TESIS DE LA UNIVERSIDAD DE ZARAGOZA

2013

16

Myriam Cilla Hernández

Mechanical effects on the atheroma plaque appearance, growth and vulnerability

Departamento
Ingeniería Mecánica

Director/es
Martínez Barca, Miguel Angel
Peña Baquedano, EStefanía

ISSN 2254-7606

Prensas de la Universidad
Universidad Zaragoza

Universidad Zaragoza
1542

Tesis Doctoral

MECHANICAL EFFECTS ON THE ATHEROMA PLAQUE APPEARANCE, GROWTH AND VULNERABILITY

Autor

Myriam Cilla Hernández

Director/es

Martínez Barca, Miguel Angel
Peña Baquedano, EStefanía

UNIVERSIDAD DE ZARAGOZA

Ingeniería Mecánica

2013

DISSERTATION

Mechanical effects on the atheroma plaque appearance, growth and vulnerability

by

Myriam Cilla Hernández

Faculty Advisors

Miguel Ángel Martínez Barca and Estefanía Peña Baquedano

Escuela de Ingeniería y Arquitectura (EINA). Departamento de Ingeniería Mecánica.
Área de Mecánica de Medios Continuos y Teoría de Estructuras
Instituto de Investigación en Ingeniería de Aragón (I3A)
Universidad de Zaragoza
Zaragoza, December 2012

Abstract

In western countries, cardiovascular disease is the most common cause of death, often related to atherosclerosis which can cause narrowing, rupture or erosion of the arterial wall, and eventually reduction or complete blockage of the blood flow. Nowadays, imaging modalities such as MRI or IVUS allow to improve the atherosclerosis diagnosis. However, in the recent years, computational techniques, which allow to approach this disease from a mechanical standpoint, have been emerged as an alternative and/or complementary diagnosis techniques, improving the understanding of the cardiovascular pathologies.

This Thesis deals with the study of the role of some mechanical factors on atherosclerotic blood vessels within the continuum mechanics framework. To achieve this goal, the atherosclerosis disease has been tackled from two different perspectives; from computational and experimental points of view. The Finite Element Method is intensively used throughout this work in order to improve the understanding of the problems at hand. Furthermore, the feasibility of the proposed methodologies as predictive tools for clinicians, which should be one of the most important aims of Computational Biomechanics, is also shown.

Regarding computational aspects, this thesis presents a computational methodology, able to accurately analyze the mechanical environment of atherosclerotic lesions and consequently identify high-risk plaques. This is accomplished by means of several finite element idealized parametric studies which predict the influence of the main mechanical and structural aspects of the atheroma plaque vulnerability; geometric risk factors such as the fibrous cap thickness, the stenosis ratio, the lipid core length and width, the remodeling index and the plaque configuration, longitudinal and circumferential residual stress and presence of microcalcifications. The idealized geometry used in these parametric studies has been validated with a patient-specific reconstruction model of human atherosclerotic lesion. Furthermore, considering the important role that the arterial wall compliance and pulsatile blood flow play in atheroma growth and,

in order to reject the effect of fluid shear stress compared to the effect of tensile wall stresses on plaque fracture dynamics, a fluid-structure interaction (FSI) model based in this parametric study is presented.

One of the main drawbacks of specific patient finite element analysis to predict the vulnerability risk are the huge memory required and the long computation times. Therefore, faster and more efficient methods to detect vulnerable atherosclerotic plaque would greatly enhance the ability of clinicians to diagnose and treat patients at risk. This thesis present two potential applications of Machine Learning Techniques, such as Artificial Neural Networks (ANNs) and Support Vector Machines (SVMs), applied to the detection of vulnerable plaques.

The experimental study of the anatomical and histological characteristics and the mechanical properties of both healthy and atherosclerotic murine aortas is also tackled. For this purpose, *in situ* inflation test, histological and immunohistochemistry analysis and a non-invasive evaluation of atherosclerosis lesions were carried out on Apolipoprotein E-Deficient and C57BL/6J mice feeding on a hyper-lipidic and a normal diet, respectively. Very different pressure-stretch curves were obtained and analyzed, pointing out the different behaviour of both groups.

Finally, focusing on atheroma plaque growth aspects, a numerical model for atheroma plaque growth including the main biological agents and processes is presented. This model based on reaction-convection-diffusion equations provide us a better understanding of the biological and mechanical interaction processes. Summarizing, these phenomena are as follows; the inflammatory process starts with the penetration of Low Density Lipoproteins (LDL) cholesterol from the circulatory system into the arterial wall, promoted by the effects of local Wall Shear Stress (WSS) on the endothelial cell layer and its effects on volume and solute flux. Part of this LDL is oxidized and becomes pathological. In order to remove it, circulating immune cells (monocytes) are recruited. Once in the intima, the monocytes differentiate to macrophages that ingest by phagocytosis the oxidized LDL. The ingestion of large amounts of oxidized LDL transforms the fatty macrophages into foam cells. Foam cells are responsible for the growth of a subendothelial plaque which eventually emerges in the artery wall. Moreover, an increase of macrophage concentration in the intima leads to the production of pro-inflammatory cytokines, which contribute to recruit more macrophages and induce the migration and proliferation of smooth muscle cells from the media to the intima layer. Finally, the smooth muscle cells may secrete a complex extracellular matrix containing collagen.

Keywords: Biomechanics, cardiovascular mechanics, atherosclerosis, constitutive model, hyperelastic material, Finite Element Model, Fluid-Structure Interaction, residual stress, vulnerability, parametric analysis, positive and negative growth, microcalcification, Machine Learning Techniques, Artificial Neural Network, Support Vector Machine, Apolipoprotein E-Deficient mice ($ApoE^{-/-}$), inflation tests, aorta stiffness, atheroma plaque growing process.

Sinopsis

Según la organización Mundial de la Salud (OMS) dieciséis millones de personas murieron en todo el mundo durante el año 2010 a causa de distintas enfermedades o patologías cardiovasculares, cerebrovasculares u otras dolencias cardíacas, por lo que constituyen la primera causa de muerte en las sociedades industrializadas. Dentro de las patologías cardiovasculares, la aterosclerosis, que consiste en un proceso progresivo de engrosamiento y endurecimiento de la pared arterial como resultado de la acumulación de depósitos de grasa en la pared interna del vaso, es una de las enfermedades más graves. Hoy en día, las técnicas de imagen que se han desarrollado (MRI, IVUS o similar) nos permiten identificar y caracterizar morefológicamente diferentes tipos de placas de ateroma. Sin embargo, en los últimos años han surgido differentes técnicas computacionales que permiten plantear la enfermedad de la aterosclerosis desde un punto mecánico, y que adicionalmente nos ayudan a entender mejor las patologías cardiovasculares.

Esta Tesis trata el estudio del papel que juegan algunos factores geométricos o mecánicos en vasos sanguíneos afectados por aterosclerosis desde el punto de vista de la mecánica de los medios continuos. Para ello, el problema de la aterosclerosis se ha enfocado desde dos perspectivas diferentes, es decir, desde un punto de vista computacional y experimental. El Método de los Elementos Finitos (MEF), que permite la aplicación de los modelos y metodologías presentados en este trabajo a problemas de interés clínico, se utiliza de manera sistemática a lo largo de todo este trabajo. Ello nos permite mostrar que los métodos computacionales aquí empleados son capaces de proporcionar resultados que pueden ayudar a tomar ciertas decisiones quirúrgicas, como uno de los principales objetivos de la Biomecánica Computacional.

Con el objetivo de analizar el comportamiento mecánico de los vasos ateroscleróticos y poder identificar el riesgo de rotura de la placa de ateroma, en esta tesis se presentan varios estudios paramétricos con geometrías idealizadas analizadas mediante el MEF. Estos modelos nos permiten determinar el papel que juegan los principales

factores mecánicos y geométricos de la placa de ateroma en la vulnerabilidad de la misma, que son; factores geométricos tales como el espesor de la capa fibrótica, ratio de estenosis, longitud y ancho del núcleo lipídico, índice de remodelado, presencia de microcalcificaciones, configuración de la placa y factores mecánicos, tensiones residuales longitudinales y circunferenciales y las propiedades del material. Se ha validado la geometría idealizada de la arteria coronaria utilizada en estos estudios con una geometría real reconstruida a partir de datos de imágenes de un paciente específico. Además, se ha realizado un estudio de interacción fluido-estructura basado en el mismo modelo geométrico usado para los estudios paramétricos. Los efectos producidos por el fluido tienen un papel fundamental en el crecimiento de la placa de ateroma, sin embargo, se ha comprobado en este trabajo que su efecto sobre las tensiones producidas en la pared arterial es prácticamente despreciable.

El alto coste computacional, tanto en tiempo como en memoria requerida, es el mayor inconveniente de utilizar el MEF para predecir el riesgo de vulnerabilidad de la placa de ateroma. Los clínicos requieren métodos más rápidos y eficientes para decidir si una placa es vulnerable o no, y por tanto la intervención. Por eso mismo, en esta tesis se presenta una herramienta para detectar placas vulnerables basada en dos diferentes técnicas "Machine Learning"; que son las Redes Neuronales Artificiales y "Support Vector Machine".

El estudio experimental de las propiedades mecánicas y de las características anatómicas e histológicas de tejido vascular sano y aterosclerótico es otro de los objetivos de esta Tesis. Concretamente, se presenta el estudio de la respuesta mecánica obtenida a partir de ensayos de inflado y el análisis histológico de aortas de ratones ApoE$^{-/-}$ (Apolipoprotein E-Deficient) y C57BL/6J alimentados con dietas hiperlipídicas y normales, respectivamente. Los resultados obtenidos muestran un comportamiento diferente de ambos grupos, y nos permite analizar el efecto que tiene la aterosclerosis en el vaso.

Finalmente, se presenta un modelo matemático basado en ecuaciones diferenciales de reacción-difusión-convección de aparición y crecimiento de placa de ateroma. Para el desarrollo de este modelo numérico se han tenido en cuenta los principales agentes biológicos y procesos que intervienen en el crecimiento de la placa. Básicamente, estos procesos son los siguientes; el paso de lipoproteínas de baja densidad (LDL) a través del endotelio al interior de la pared arterial y que es el evento desencadenante del proceso inflamatorio. Ese proceso es debido a eventos mecánicos tales como bajas tensiones tangenciales o deformaciones cíclicas del tejido que provocan que el endotelio se vuelva permeable. Parte del LDL que atraviesa la pared arterial se oxida, lo que activa al endotelio vascular reclutando monocitos. Una vez que los monocitos han atravesado la capa íntima se diferencian en macrófagos que fagocitan el LDL oxidado. La ingesión de grandes cantidades de LDL oxidado produce una acumulación lipídica en los macrófagos que da lugar a la formación de células espumosas. Por otro lado, la alta concentración de macrófagos origina la producción de células proinflamatorias

(citoquinas) que contribuyen al reclutamiento de más macrófagos e inducen la migración y proliferación de las células musculares lisas desde la capa media hacia la íntima.

Palabras clave: Biomecánica, tejidos blandos, enfermedad cardiovascular, aterosclerosis, modelo constitutivo, material hiperelástico, método de elementos finitos, análisis fluido-estructura, tensiones residuales, placa de ateroma, vulnerabilidad, análisis paramétrico, crecimiento positivo y negativo, microcalcificación, Red Neuronal Artificial, "Support Vector Machine", "Machine Learning Techniques", ratón ApoE$^{-/-}$, ensayo de inflado, rigidez de la aorta, migración, proliferación.

Contents

List of Figures

List of Tables

List of Tables

Efectos mecánicos en la aparición, crecimiento y vulnerabilidad de la placa de ateroma.

Chapter 0

Resumen

En cumplimiento de la normativa relativa a la obtención del grado de Doctorado Europeo/Internacional, se incluye en este capítulo un resumen en castellano del contenido de la Tesis. En él se especifica claramente la motivación de la misma, así como los principales objetivos globales y parciales, la estructura de la Tesis y el contenido de cada uno de los capítulos. Además, se hace balance de las conclusiones obtenidas, tanto en los ámbitos matemáticos, mecánicos y numéricos, como en los aspectos clínicos. Finalmente, se ofrece un listado de las principales contribuciones aportadas durante el desarrollo de la Tesis y se proponen algunas líneas futuras de investigación.

Contents

0.1 Motivación

0.1.1 Enfermedades Cardiovasculares

Las enfermedades cardiovasculares constituyen la primera causa de mortalidad en los países desarrollados, así como en la práctica totalidad de los países en desarrollo (Mathers and Murray, 2006; Gaziano and Gaziano, 2009; Roger *et al.*, 2011; World Health Organization. Regional Office for Europe, 2011). Dichas enfermedades presentan multitud de manifestaciones sintomáticas diferentes entre las que se cuentan, por ejemplo, los infartos de miocardio, los procesos isquémicos, aneurismas, hipertensión arterial y trombosis venosa profunda, entre otras. Como consecuencia, el 42% de las muertes acaecidas en la Unión Europea (por sexos el 37% de las mujeres y el 48% de los hombres) (Allender *et al.*, 2008), y el 51% de las muertes en Estados Unidos (Roger *et al.*, 2011) están relacionadas de forma directa o indirecta con alguna patología cardiovascular. Por consiguiente, este grupo de enfermedades tienen un elevadísimo impacto socioeconómico, lo que ha convertido a algunas de las especialidades clínicas relacionadas con ellas en destino de fuertes inversiones destinadas a profundizar en el conocimiento de las mismas a través de la investigación básica.

Desde el punto de vista mecánico, el estudio del sistema cardiovascular constituye uno de los principales pilares en el desarrollo de la Biomecánica, disciplina englobada dentro de la más amplia denominada Ingeniería Biomédica, que promueve la aplicación de las técnicas propias de la Ingeniería a los sistemas biológicos. Ambas disciplinas han experimentado un gran desarrollo en los últimos años expandiendo su alcance al estudio de fenómenos y escalas tan variadas como, por ejemplo, el estudio a escala macroscópica de órganos y tejidos (huesos, arterias, tendones, etc.) (Fung, 1990; Humphrey, 2002b), o el estudio a escala microscópica de los principales constituyentes que forman los mismos (colágeno, elastina, etc.) o de las propias células (Finlay *et al.*, 1998; Balcells *et al.*, 2005). Por consiguiente, tan variadas aproximaciones plantean desafíos de distinta naturaleza en amplias áreas de la Mecánica.

El sistema cardiovascular está formado, básicamente, por el corazón y los vasos sanguíneos (arterias, capilares y venas) que como conductos elásticos o musculares distribuyen y recogen la sangre de todos los rincones del cuerpo. La estructura de los vasos sanguíneos es repetitiva y consiste en la disposición concéntrica de tres capas, constituidas por diferentes variedades de los cuatro tejidos básicos, que son las siguientes (Rhodin, 1980; Thubrikar, 2007):

- Túnica íntima: es la capa interna y la más fina de las tres capas, formada por el endotelio, una lámina basal y tejido conectivo subendotelial laxo. Está encargada del contacto con el medio interno o lumen del vaso.

- Túnica media: es una capa formada por capas concéntricas de células musculares lisas entre las cuales se interponen cantidades variables de elastina, fibras reticulares y proteoglicanos. Por lo general, es la capa más gruesa de la pared del vaso

sanguíneo.

- Túnica adventicia: es la capa más externa, con fibras de colágeno y fibras elásticas.

Dentro de las patologías cardiovasculares, una de las enfermedades que más decesos causan hoy en día es la aterosclerosis. Dicha enfermedad, consiste en la degeneración progresiva y crónica del tejido, así como un engrosamiento y endurecimiento de la pared arterial como resultado de la acumulación de depósitos de grasa, colesterol y otras sustancias en la pared interna del vaso. Estas sustancias forman estructuras llamadas placas de ateroma y en ellas se puede diferenciar diferentes componentes; calcificaciones, lípidos y tejido fibroso. Con el tiempo, si estas placas son vulnerables pueden romperse y provocar la formación de coágulos que bloquean el flujo sanguíneo desencadenando diferentes eventos tales como infartos, trombos o gangrena entre otros (Kyriacou *et al.*, 1996; Thubrikar, 2007). A lo largo de esta Tesis se habla de "vulnerabilidad" de la placa de ateroma para hacer referencia a su propensión a la rotura.

En el proceso de formación de la placa de ateroma se pueden distinguir varias fases (Nilsson, 1986; Ross, 1986; Davies *et al.*, 1988; VanEpps and Vorp, 2007; William Jr., 2009):

- El proceso de crecimiento de la placa de ateroma comienza como una lesión del endotelio asociada a diversos factores de riesgo (tabaquismo, edad, sexo o hipertensión arterial entre otros). Normalmente las placas de ateroma crecen en áreas localizadas donde se producen alteraciones de flujo (ramificaciones, bifurcaciones o curvatura de arterias), en estas zonas aparecen bajos esfuerzos cortantes en la pared arterial y altas tasas de sedimentación de partículas. Esta lesión del endotelio permite el paso hasta la íntima de lipoproteínas de baja densidad (LDL), ricas en colesterol.

- Los leucocitos mononucleares (monocitos y linfocitos), son reclutados por moléculas de adhesión en la superficie endotelial, para posteriormente atravesar el endotelio y transformarse en macrófagos. Por otro lado, el LDL se oxida debido a la acción de radicales libres. Este LDL oxidado es captado por los macrófagos. De este modo se acumula un exceso de lípidos y macrófagos en la íntima, formando una sobreelevación denominada estría grasa.

- Cuando los macrófagos han captando gran cantidad de LDL oxidado, éstos pueden morir (apoptosis), convirtiéndose en células espumosas, o incluso romperse para liberar nuevamente lípidos en la íntima. Las citoquinas segregadas por los macrófagos estimulan la migración de células de la íntima con características de miofibroblastos (células musculares). Estas células segregan colágeno y es entonces cuando la placa comienza a fibrosarse. En esta fase las lesiones son sobreelevadas y amarillas (placas lipídicas). Al desarrollarse la lesión, la presión atrofia la capa media y se rompe la lámina elástica.

- La mayor secreción de colágeno forma un denso recubrimiento fibroso sobre la placa, que aparece ahora dura y blanquecina (placa fibrolipídica). La placa madura muestra lípidos tanto libres como en el interior de los macrófagos. La colagenización afecta también a la media, lo que debilita la pared arterial, el endotelio es frágil y a menudo se ulcera, permitiendo la agregación plaquetaria y la trombosis.

A pesar de que se dispone de numerosas técnicas de imagen invasivas y no invasivas, ninguna es capaz de identificar las principales características de una placa vulnerable. No existe documentación sobre el proceso de ruptura de una placa; una placa vulnerable sólo puede verse si se rompe y se observa el resultado final de la ruptura de la placa, normalmente en autopsias (Lee *et al.*, 1993; Fayad and Fuster, 2001; Virmani *et al.*, 2006; Kips *et al.*, 2008).

Las características y propiedades de la placa de ateroma se definen en numerosos estudios patológicos (Salunke *et al.*, 2001; Naghavi *et al.*, 2003; Fuster *et al.*, 2005; Virmani *et al.*, 2006; VanEpps and Vorp, 2007). Aunque aún sigue debatiéndose la definición exacta del término placa vulnerable, muchos investigadores básicos, científicos clínicos y médicos probablemente estarían de acuerdo en que las principales características de una placa que tiende a romperse y que, por tanto, es vulnerable, vienen dadas por su morfología, las tensiones mecánicas sobre la misma, la actividad proinflamatoria y procoagulante y las condiciones de la sangre (niveles de colesterol, azúcar, etc..) (Van der Wal and Becker, 1999; Tracqui *et al.*, 2011). Naghavi *et al.* (2003) trató de llegar a un consenso y estandarización sobre la definición de placa vulnerable en su estudio. Desde el punto de vista de las tensiones mecánicas, se considera que el factor biomecánico más importante que desencadena la rotura de la placa es la tensión principal máxima de la capa fibrótica, y por tanto, a menudo se utiliza el valor de ésta para predecir tanto placas vulnerables como la localización de la rotura (Ohayon *et al.*, 2005; Versluis *et al.*, 2006). Es muy importante detectar prematuramente aquellas placas de ateroma que son vulnerables ya que se puede producir la ruptura de la misma, su ulceración o erosión, generando de este modo la aparición de un trombo que puede bloquear un vaso situado por delante de la zona de la placa, lo que podría producir una carencia de aporte sanguíneo en la zona irrigada por la arteria correspondiente (isquemia), que puede ser mortal si el bloqueo tiene lugar en una arteria coronaria o en una arteria cerebral (Virmani *et al.*, 2006).

Sin embargo, en la práctica médica, únicamente se utiliza el valor del espesor de la capa fibrótica para definir si una placa es vulnerable o no (Lendon *et al.*, 1991; Cheng *et al.*, 1993; Ohayon *et al.*, 2005). En cambio, numerosos estudios demuestran que solamente la medida de este parámetro no es una buena aproximación para determinar un evento tan complejo como la rotura de la placa (Moreno *et al.*, 2002; Finet *et al.*, 2004; Krishna Kumar and Balakrishnan, 2005; Vengrenyuk *et al.*, 2006; Virmani *et al.*, 2006). Se deben considerar otros parámetros, tales como las dimensiones y consistencia del lípido (Finet *et al.*, 2004; Gao and Long, 2008), los niveles de inflamación (Arroyo

and Lee, 1999; Lee, 2000) o el remodelado de la arteria (Smedby, 1998; Varnava *et al.*, 2002; Ohayon *et al.*, 2008).

Esta Tesis se centra en el estudio de los efectos mecánicos en tejidos vasculares afectados por la aparición de placas de ateroma. Dentro de este amplio objetivo global, el alcance de la misma puede dividirse adicionalmente en dos partes diferenciadas como son el estudio experimental de las propiedades mecánicas de los vasos sanguíneos afectados por la aterosclerosis y el modelado del comportamiento de los mismos, bien su comportamiento mecánico e implicaciones clínicas mediante técnicas de simulación computacional, bien mediante técnicas de "Machine Learning" o bien mediante la simulación numérica a través de ecuaciones diferenciales de reacción-difusión-convección de los procesos biológicos que suceden en los instantes de aparición y crecimiento de la placa. Se describe a continuación de forma breve cada una de estas grandes líneas de investigación.

0.1.2 Modelado de vasos sanguíneos

Los modelos numéricos son una herramienta muy útil en medicina cardiovascular para el estudio del comportamiento de los tejidos biológicos, la predicción de aparición de ciertas patologías y los problemas derivados de las terapias, así como para el desarrollo y optimización de tratamientos. Para obtener resultados fiables, estos modelos necesitan incorporar ecuaciones constitutivas que representen de forma adecuada el comportamiento mecánico del vaso sanguíneo. Para la obtención de estas ecuaciones es indispensable contar con una extensa base de datos experimentales.

Los ensayos mecánicos revelan que el tejido vascular está sometido a deformaciones finitas incluso a niveles de carga fisiológicos. Además, el tejido vascular tiene un comportamiento incompresible debido al carácter acuoso de la sustancia base que lo forma (Carew *et al.*, 1968; Chuong and Fung, 1986; Holzapfel and Ogden, 2003). Por otra parte, la existencia de direcciones preferenciales de orientación para algunos de los constituyentes de la pared del vaso (Rhodin, 1980) resultan en un comportamiento mecánico altamente anisótropo, que es necesario incorporar a los modelos constitutivos (Holzapfel *et al.*, 2000; Gasser *et al.*, 2006). Dichos modelos han sido utilizados para, mediante aproximaciones analíticas (Rachev, 1997) y numéricas (Gasser, 2001; Alastrué *et al.*, 2007a,b), reproducir el comportamiento mecánico de los tejidos bajo condiciones patológicas y no patológicas.

Un rasgo característico de los tejidos biológicos es que se encuentran dotados de tensiones residuales, resultado del proceso de crecimiento desde el estado embrionario hasta la edad adulta (Fung, 1990). Dichas tensiones residuales se revelan al realizar un corte sobre un tejido libre de carga externa. Tras dicho corte, se produce una modificación de la configuración de equilibrio a causa de la liberación de dichas tensiones residuales. La función que éstas desempeñan es crucial para el funcionamiento mecánico de los vasos sanguíneos, puesto que optimizan el rendimiento mecánico de la pared del vaso, homogeneizando la distribución de tensión circunferencial a través del espesor de la pared arterial (Chuong and Fung, 1986; Fung and Liu, 1991; Ohayon *et al.*, 2007;

Holzapfel and Ogden, 2010; Cilla *et al.*, 2012a).

El modelado de vasos sanguíneos se puede enfocar de formas diferentes según los objetivos perseguidos. Entre otros, los modelos numéricos nos permiten simular los diferentes procesos biológicos a nivel celular (Olgac *et al.*, 2008; Ougrinovskaia *et al.*, 2010; Di Tomaso *et al.*, 2011; Gessaghi *et al.*, 2011; Siogkas *et al.*, 2011; Bulelzai and Dubbeldam, 2012), reproducir las tensiones mecánicas que soportan los vasos sanguíneos (Cheng *et al.*, 1993; Jaroslav *et al.*, 1999; Lee, 2000; Peterson and Okamoto, 2000; Jaroslav *et al.*, 2002; Finet *et al.*, 2004; Raghavan *et al.*, 2004; Krishna Kumar and Balakrishnan, 2005; Ohayon *et al.*, 2005, 2007, 2008) u obtener el comportamiento tanto del vaso sanguíneo como de la sangre que discurre en el interior del mismo, a través de análisis de interacción fluido-estructura (Bluestein *et al.*, 2008).

0.1.3 Técnicas "Machine Learning"

El término "Inteligencia Artificial" hace referencia a la ciencia que promueve el desarrollo de software y hardware para simular el comportamiento cognitivo humano, e incluso ampliar sus posibilidades. Una de las áreas de mayor crecimiento es el Aprendizaje de Máquinas o Aprendizaje Autónomo (Machine Learning), y se puede definir como la rama de la Inteligencia Artificial que estudia la operación y el diseño de sistemas que permitan extraer similitudes y coincidencias de un conjunto de objetos, y ayuda a establecer propiedades de o entre conjuntos de datos (Vapnik, 1982; Bishop, 1995; Scholkpof and Smola, 2002).

El Aprendizaje Autónomo se considera un proceso de generación de conocimiento. Trata de implementar sistemas que, utilizando la experiencia, sean capaces de mejorar automáticamente su rendimiento. Su objetivo es el desarrollo de métodos computacionales para la implementación de diversas formas de aprendizaje, y el desarrollo de algoritmos capaces de generalizar comportamientos a partir de una información no estructurada suministrada en forma de ejemplos (Whitehall and Lu, 1991).

En los últimos años, estas técnicas han adquirido una gran popularidad debido a su probada eficacia en la resolución de problemas de muy diversos ámbitos de la vida real, tales como biomedicina (Brown *et al.*, 2000), análisis de imágenes y visión artificial (Cosman *et al.*, 1993; Frigui and Krishnapuram, 1998), reconocimiento de caracteres escritos (Le Cun *et al.*, 1989), reconocimiento del lenguaje hablado (Rabiner, 1989) o geología y geotecnia (Taboada *et al.*, 2007; López *et al.*, 2010a,b).

0.1.4 Estudio experimental del tejido vascular

Desde un punto de vista mecánico, el estudio experimental del tejido vascular persigue la identificación de las propiedades mecánicas de los tejidos biológicos a través de la realización de ensayos. Dichas propiedades vienen determinadas por la composición microestructural del tejido (Rhodin, 1980), y son distintas para cada una de las capas que componen los vasos (en condiciones normales, íntima, media y adventicia). Además, multitud de factores como la edad, el sexo, el tipo de vaso o la posición a lo largo de la

longitud del mismo tiene influencia en el comportamiento mecánico del tejido vascular, lo que ha convertido la determinación del mismo en una tarea de gran dificultad. Por ello, se ha dedicado una gran cantidad de trabajo a la determinación de las propiedades del tejido vascular tanto en condiciones sanas (Billiar and Sacks, 2000; Sacks, 2000; Pandit *et al.*, 2005; Cox *et al.*, 2006; Wang *et al.*, 2006), como patológicas (Holzapfel and Weizsäcker, 1998; Schulze-Bauer *et al.*, 2003; Holzapfel *et al.*, 2005b).

Los ensayos mecánicos sobre vasos sanguíneos suelen clasificarse como *in vivo* o *in vitro*. Los primeros, realizados en el interior del organismo, tienen la ventaja de estudiar el tejido en su estado natural dentro del rango fisiológico, lo que les proporciona una conexión directa con el análisis médico (Cabrera Fischer *et al.*, 2006). Sin embargo, en este tipo de ensayos, existen muchas incertidumbres sobre las condiciones de contorno a las que están sometidas las muestras. Por su parte, los ensayos *in vitro*, realizados en laboratorio, permiten un mayor control sobre las variables estudiadas (Schulze-Bauer *et al.*, 2003). De los diferentes ensayos para la caracterización del comportamiento mecánico de vasos sanguíneos, los más extendidos son el de inflado (presión-diámetro) y los de tracción uniaxial y biaxial.

El animal más usado en los estudios experimentales de la enfermedad aterosclerótica es el ratón, concretamente los ratones modificados genéticamente que son deficientes en la proteína ApoE, implicada en el transporte inverso de colesterol, y cuya deficiencia promueve el desarrollo de aterosclerosis. Las principales ventajas del uso de ratones son su tamaño pequeño, fácil mantenimiento y esperanza de vida relativamente corta, además de la posibilidad de que puedan desarrollar placa de ateroma gracias a la modificación genética (Plump *et al.*, 1992; Van Ree *et al.*, 1994; Hofker *et al.*, 1998; Maeda *et al.*, 2007a). Por eso mismo, los ratones han sido objeto de numerosos estudios experimentales para la determinación de propiedades mecánicas de los vasos sanguíneos (Guo and Kassab, 2003, 2004; Vengrenyuk *et al.*, 2006).

0.2 Objetivos y metodología

El objetivo principal de esta Tesis es el estudio y modelado de vasos sanguíneos afectados por la aterosclerosis. Dentro de este amplio objetivo, se puede claramente diferenciar 4 objetivos específicos que están interrelacionados entre sí: Simulaciones mediante elementos finitos e interacción fluido estructura para estudiar el comportamiento mecánico tanto de vasos sanguíneos afectados por la aterosclerosis, como del fluido que se encuentra en el interior del mismo; implementación de una herramienta paramétrica a través de diferentes técnicas de "Machine Learning" tales como redes neuronales y "Support Vector Machines" para avanzar hacia la mejora en el diagnóstico de placa de ateroma vulnerable utilizando información mecánica; estudio y simulación numérica del proceso de crecimiento de la placa de ateroma a nivel biológico y, por último, caracterización mediante técnicas experimentales de las propiedades mecánicas y patológicas de vasos sanguíneos con placa de ateroma.

Como objetivos particulares fundamentales para obtener los anteriores pueden enumerarse a continuación los siguientes:

- Analizar la influencia de parámetros geométricos en la vulnerabilidad de la placa de ateroma. Para ello, se van a llevar a cabo estudios paramétricos mediante elementos finitos de un vaso sanguíneo aterosclerótico ideal. La morfología y dimensiones consideradas corresponderán a una arteria coronaria estándar con las siguientes partes: la pared arterial compuesta por las capas media y la adventicia, la placa fibrótica y el lípido o ateroma. Dichos estudios son los siguientes:
  - Estudio paramétrico en un modelo de tensión plana de la influencia de las microcalcificaciones en la vulnerabilidad de la placa de ateroma. Las microcalcificaciones son depósitos de calcio cuya aparición dentro de la placa de ateroma supone un riesgo añadido a su integridad. Sin embargo, hoy por hoy el papel que juegan las microcalcificaciones en el proceso de rotura de placa no está del todo claro. Los parámetros estudiados para determinar dicha influencia son; el ángulo de posición de la microcalcificación, la excentricidad de la microcalcificación respecto de la capa fibrótica, el tamaño de la microcalcificación y por último, el espesor de la capa fibrótica.
  - Estudio paramétrico mediante el cual se compara el riesgo de vulnerabilidad de la placa de ateroma en modelos de tensión plana de arterias coronarias con remodelado positivo y negativo. La placa de ateroma puede crecer de dos maneras diferentes, hacia el interior del vaso sanguíneo, lo cual provoca una reducción de la luz del vaso (remodelado negativo), o hacia el exterior, en este caso, el diámetro del vaso se ve modificado (remodelado positivo) (Glagov *et al.*, 1987; Varnava and Davies, 2001; Varnava *et al.*, 2002). Actualmente, los métodos de identificación de pacientes vulnerables que utilizan los clínicos, tienen en cuenta el remodelado negativo, sin embargo, a menudo, pacientes con placas aparentemente estables sufren roturas. Se cree, que el remodelado positivo, es el causante de este tipo de roturas de placa.
  - Estudio paramétrico en tres dimensiones (3D) de los factores geométricos en la vulnerabilidad de la placa de ateroma y de la influencia de las tensiones residuales sobre la misma. Los modelos en 3D nos permiten incluir los efectos producidos por las tensiones residuales y la orientación de las fibras de colágeno de la pared arterial que en modelos bidimensionales no es posible. Dichos modelos se van a simular para tres situaciones diferentes; sin tensiones residuales, considerando tensiones residuales en dirección longitudinal y por último, considerando tensiones residuales tanto en dirección longitudinal como circunferencial; este último caso se acercaría más a la realidad. De este modo, se podrá identificar el papel que juegan las tensiones residuales en la vulnerabilidad de la placa de ateroma y definir límites de vulnerabilidad para cada uno de los parámetros considerados.

- Validar y comparar los resultados obtenidos en los estudios paramétricos basados en una geometría 3D idealizada con geometrías personalizadas obtenidas de imágenes médicas. Se va a reconstruir una coronaria aterosclerótica de paciente específico a partir de imágenes de IVUS que posteriormente se simulará mediante el método de los elementos finitos y se compararán los resultados con la equivalente idealizada.

- Estudiar la influencia de la incorporación del fluido (sangre) en las tensiones mecánicas producidas en un vaso sanguíneo con placa de ateroma, así como calcular las tensiones tangenciales o la caída de presión debidas a la presencia de la placa. Para llevar a cabo este objetivo, se va a realizar un estudio paramétrico con interacción fluido-estructura de un modelo 3D de arteria coronaria con placa de ateroma, teniendo en cuenta tanto la geometría y posición del núcleo lipídico, como la morfología de la placa. Las dimensiones consideradas son idénticas a las usadas para la realización de los estudios paramétricos simulados en el modelo que incluye sólo el sólido.

- Implementar una herramienta paramétrica usando técnicas de "Machine Learning" que permita predecir la rotura de la placa de ateroma. Lás técnicas "Machine Learning" propuestas son redes neuronales, "Support Vector Machine" y regresión lineal. Para entrenar a la herramienta paramétrica se usarán los resultados obtenidos en los modelos paramétricos en 3D con tensiones residuales longitudinales. De este modo, gracias a esta herramienta paramétrica, los clínicos, tras medir en imágenes de un paciente diferentes parámetros, en este caso, espesor de la capa fibrótica, longitud de la placa de ateroma, ancho del lípido y ratio de estenosis, podrían obtener de una forma inmediata la tensión máxima principal correspondiente a dicha geometría con dichos parámetros de entrada. Así pues, se podría obtener una decisión inmediata sobre el riesgo de rotura de ese paciente específico y actuar en consecuencia al mismo. Se implementarán diferentes métodos de "Machine Learning" con el fin de comparar el rendimiento de todos ellos.

- Avanzar en el desarrollo de modelos matemáticos basados en ecuaciones de reacción-difusión-convección del crecimiento de la placa de ateroma desde un punto de vista biológico. Para el desarrollo de este modelo se tendrán en cuenta tanto los agentes biológicos que intervienen en el crecimiento de la placa (LDL, monocitos, macrófagos, células espumosas, citoquinas y células musculares lisas), como los procesos acontecidos en el mismo.

- Desarrollar ensayos experimentales para determinar los cambios en las propiedades mecánicas de aortas de ratones ateroscleróticos. Para ello se van a utilizar dos tipos de cepas de ratones; C57BL y ApoE$^{-/-}$. Los ratones C57BL servirán como referencia (control) para comparar los cambios ocurridos en los ratones ApoE$^{-/-}$. El estudio seriado de ambas cepas de ratones se realizará a 10, 20, 30 y 40 semanas

de edad, realizando tanto ensayos mecánicos de inflado que nos permiten comparar la rigidez de la arteria aorta de los diferentes grupos de ratones, como histologías y diferentes mediciones biológicas que nos permitan obtener más información sobre la composición de las placas de ateroma formadas.

Para la realización de todos estos objetivos, se utilizarán diferentes software: MIMICS para la obtención de la geometría real a partir de imágenes médicas (IVUS), ABAQUS 6.11 para las simulaciones mediante elementos finitos, Matlab para la implementación de la red neuronal, aunque también será necesario el uso de este software para realizar muchas otras tareas puntuales a lo largo de la Tesis, ADINA 6.8 para las simulaciones fluido-estructura y, por último, COMSOL para el modelado de los procesos biológicos en el crecimiento de la placa de ateroma. Además, se requerirá el uso de otros software como NASTRAM, ICEM, FEMAP e IDEAS para mallar y refinar las geometrías utilizadas, e Image J para postprocesar los datos obtenidos en los ensayos experimentales.

0.3 Estructura de la Tesis

La Tesis está estructurada en siete capítulos y dos apéndices, que se organizan del modo siguiente:

En el Capítulo 1 se recoge una breve descripción del sistema vascular. Se muestra detalladamente la composición microestructural de la sangre y los vasos sanguíneos en estado sano, y se presenta una clasificación de los vasos en función del tamaño, composición y función fisiológica de los mismos.

Dichas propiedades, o al menos las más relevantes en lo que a la respuesta mecánica se refiere, son descritas convenientemente. De entre ellas, la composición multicapa de los vasos sanguíneos es una de las más importantes, por lo que la consideración de las capas mecánicamente relevantes, tanto en estado sano como patológico, es de gran interés. Se hace especial hincapié en la diferenciación entre el comportamiento activo y pasivo del tejido vascular y su influencia en la respuesta mecánica del tejido. La presencia de tensiones residuales en los vasos sanguíneos es otro punto de gran interés, así como la existencia de direcciones preferenciales de orientación para algunos de los componentes de la pared arterial, que es la razón del comportamiento anisótropo del tejido vascular. Finalmente, se introduce el comportamiento incompresible y no lineal que experimenta el tejido vascular bajo grandes deformaciones.

A continuación, en la Sección 1.3, se analiza una de las principales enfermedades que afectan a los vasos sanguíneos, la aterosclerosis, que incluye una descripción de dicha patología remarcando las zonas de aparición, los factores de riesgo que acentúan su aparición, procesos de detección y tratamiento de la misma y por último, se describe el proceso de formación de la placa de ateroma.

Teniendo en cuenta el comportamiento mecánico del tejido biológico, se presenta a continuación una breve revisión de las leyes constitutivas más frecuentemente utilizadas

para el modelado de vasos sanguíneos en el rango elástico, Sección 1.4. Dichos modelos han sido clasificados en isótropos y anisótropos. El primer grupo incluye modelos originalmente utilizados para el modelado de caucho y otros materiales elastómeros, así como leyes específicamente diseñadas para el modelado de materiales biológicos. Además, cada uno de estos dos grupos se divide en dos categorías: la primera incluye aquellos modelos obtenidos desde un punto de vista fenomenológico, mientras que el segundo grupo contiene modelos que incluyen cierta información referente a la composición microestructural del tejido.

Además, se detallan las principales consideraciones que hay que tener en cuenta en los ensayos experimentales para obtener las propiedades mecánicas de tejidos biológicos, así como los principales tipos de ensayos experimentales que se realizan en este tipo de muestras.

Finalmente, se resumen las motivaciones y objetivos principales que se persiguen con la realización de esta Tesis. Como apartado final de este capítulo, se incluye un esquema de la estructura de Tesis y las partes de las que se compone.

En el Capítulo 2 se presenta un estudio paramétrico sobre la vulnerabilidad de la placa de ateroma en un modelo idealizado de una arteria coronaria aterosclerótica en tres dimensiones. Para ello se ha desarrollado un modelo de elementos finitos teniendo en cuenta tanto la composición del vaso sano (media y adventicia) como de la placa de ateroma, con el fin de establecer parámetros cualitativos del riesgo de rotura de la placa. Además, se estudia la influencia de las tensiones residuales, tanto en dirección circunferencial como longitudinal, sobre los mapas de tensiones principales máximas obtenidos.

Con el objeto de validar la geometría utilizada para el desarrollo de este estudio paramétrico en 3D, se ha reconstruido una arteria coronaria de un paciente real y se ha simulado bajo las mismas condiciones de contorno, propiedades del material y tamaño de malla. Esta geometría se ha comparado con el caso perteneciente al estudio paramétrico cuyas dimensiones son similares a la geometría real reconstruida.

Por último, con el fin de demostrar la importancia de utilizar modelos en tres dimensiones para predecir el riesgo de rotura de la placa de ateroma, se han comparado los resultados obtenidos en modelos en dos y tres dimensiones.

El Capítulo 3 incluye algunas consideraciones adicionales que sería conveniente tener en cuenta para mejorar el estudio paramétrico presentado en el Capítulo 2. Básicamente, este capítulo se divide en tres partes. En la primera se describe un estudio paramétrico que determina la influencia de las microcalcificaciones en un modelo de arteria coronaria aterosclerótica en dos dimensiones. La segunda parte, recoge un estudio paramétrico de un modelo ideal de una arteria coronaria con placa de ateroma en dos dimensiones en el cual se ha tenido en cuenta el remodelado positivo y negativo de la arteria. Mediante este estudio se pretende demostrar que las placas de ateroma con remodelado positivo son más vulnerables que aquellas con remodelado negativo. Por último, se presenta un estudio paramétrico de interacción fluido-estructura en el modelo en tres dimensiones

utilizado en el Capítulo 2. Este estudio paramétrico nos permite analizar el papel que juega el fluido en los mapas de tensiones obtenidos, así como obtener otras variables que sólo se pueden obtener en modelos de interacción fluido-estructura como son, por ejemplo, la tensión de cortadura o la caída de presión.

En el Capítulo 4 se introducen los algoritmos matemáticos "Machine Learning Techniques", denominados en castellano algoritmos de aprendizaje automático o aprendizaje de máquinas, como una herramienta para el diagnóstico y la predicción de enfermedades en el ámbito clínico, y concretamente en este caso, para predecir la vulnerabilidad de la placa de ateroma. Se presenta un breve resumen de la teoría de este tipo de algoritmos, y se profundiza en aquellos utilizados en esta Tesis, las redes neuronales artificiales, las máquinas de soporte vectorial o máquinas de vectores de soporte ("Support Vector Machine") y la regresión lineal clásica. Además, se presenta una herramienta computacional basada en algoritmos de "Machine Learning Techniques" que nos permite predecir la vulnerabilidad de la placa de ateroma en arterias coronarias. Además, se ha comparado el rendimiento de dos de estas técnicas, las redes neuronales y las "Support Vector Machine" con la regresión lineal clásica con el propósito de demonstrar la no linealidad del problema, lo que justifica la utilización de dichos algoritmos. Esta herramienta computacional se ha entrenado con los resultados obtenidos del estudio paramétrico desarrollado en el Capítulo 2.

El Capítulo 5 recoge los estudios experimentales desarrollados con objeto de determinar las propiedades mecánicas y resaltar las diferencias entre la arteria aorta de ratones ApoE$^{-/-}$ y C57BL/6. Los ratones C57BL/6 son los más susceptibles de desarrollar aterosclerosis y es, por tanto, la variedad de elección para ser genéticamente manipulada con el fin de desarrollar modelos de aterosclerosis. Los ratones ApoE$^{-/-}$ son ratones C57BL/6 a los que se ha eliminado el gen que codifica la apolipoproteína E, constituyente fundamental de diversos tipos de lipoproteínas, con el fin de desarrollar hiperlipidemia y aterosclerosis tanto con dieta normal como con dieta rica en grasa. Los ratones C57BL/6 sin alterar genéticamente se han alimentado con dieta normal y se han utilizado como control. Sin embargo, los ratones ApoE$^{-/-}$ se han alimentado con una dieta rica en grasa. Con objeto de obtener las propiedades mecánicas, se han realizado ensayos de inflado en la arteria aorta en 5 individuos de cada una de las cepas (ApoE$^{-/-}$ y C57BL/6) y a distintos tiempos (10, 20, 30 y 40 semanas) de dieta. Además, se han realizado análisis anatómicos que muestran la distribución de las placas de ateroma a lo largo de la aorta, análisis histológicos, así como la evolución del peso de los animales.

El modelado del crecimiento de la placa de ateroma teniendo en cuenta los principales agentes biológicos que intervienen en el mismo se trata en el Capítulo 6. Se presenta un modelo basado en ecuaciones reacción-difusión-convección. Los agentes biológicos que se han tenido en cuenta son; LDL, monocitos, macrófagos, células espumosas, citoquinas, células musculares lisas y colágeno. Además, se han considerado los principales procesos biológicos en los que intervienen estas especies como son diferenciación, proliferación y migración.

En el capítulo 7 se describen las conclusiones más relevantes obtenidas, las contribuciones originales en forma de publicaciones y presentaciones en congresos que se han obtenido durante el desarrollo de esta Tesis y el trabajo fututo que se podría realizar a partir del trabajo presentado.

Finalmente, se presenta en el Apéndice A un breve resumen de los principales conceptos de la mecánica de medios continuos utilizados a lo largo de la Tesis, mientras que en el Apéndice B se recoge un resumen sobre el uso del lenguaje de programación Python en el software comercial ABAQUS para poder automatizar las tareas que ABAQUS realiza. Además, en este apéndice, se incluye el código programado en este lenguaje para construir las geometrías presentadas en los Capítulos 2 y 3 y para tareas de post-procesado.

Adicionalmente a estos siete capítulos y dos apéndices, en cumplimiento de la normativa relativa a la obtención del grado de Doctorado Europeo, se ha incluido al comienzo de la Tesis, un Capítulo 0 adicional donde se resume en castellano el contenido de la misma. En este capítulo se especifica la motivación de la Tesis, los objetivos y la metodología seguida a lo largo de ésta, un esquema de la estructura, un listado de las principales contribuciones aportadas durante el desarrollo de la Tesis y se proponen algunas líneas futuras de investigación.

0.4 Conclusiones

Se muestran a continuación las principales conclusiones obtenidas en la Tesis. Teniendo en cuenta los diversos enfoques del problema clínico llevados a cabo, tales conclusiones se pueden dividir en tres grupos principales: conclusiones en el ámbito experimental, conclusiones desde el punto de vista mecánico y, por último, observaciones clínicas.

0.4.1 Aspectos experimentales

- Se ha diseñado un dispositivo para realizar ensayos *in situ* de inflado de arterias de muy pequeño calibre. Y se ha desarrollado una metodología y protocolo que permite caracterizar y estudiar el comportamiento mecánico de aortas de ratón mediante ensayos *in situ* de inflado mediante dicho dispositivo.

- Respecto al comportamiento mecánico de las aortas de ratones ApoE$^{-/-}$ y control, no existen diferencias significativas con la edad en la rigidez de la pared arterial de ratones sanos (C57BL/6). Por el contrario, sí que se han encontrado diferencias significativas en la rigidez de la pared del vaso con la edad para el caso de los ratones ApoE$^{-/-}$. Comparando ambas cepas, el comportamiento de la pared arterial obtenido en los ratones ApoE$^{-/-}$ mediante ensayos de inflado es estadísticamente diferente al del sano (C57BL/6) desde el inicio de la lesión en el ratón ApoE$^{-/-}$.

- En relación con las observaciones morfológicas realizadas, se ha observado que en las primeras semanas de dieta de los ratones ApoE$^{-/-}$ no existen diferencias significativas en el comportamiento de la aorta y no se aprecia ni de forma visual ni histológica regiones con aterosclerosis importante, únicamente en fase incipiente, sin embargo, en estadios avanzados de la enfermedad, la aterosclerosis es generalizada en todo el árbol aórtico. Para el caso de ratones control, no se han encontrado placas de ateroma ni en los ensayos histológicos ni en la evaluación visual de las lesiones. Por tanto, los resultados de los análisis histológicos y de cuantificación de placa están en concordancia con el comportamiento de presión y deformación obtenido mediante los ensayos de inflado.

- Se han encontrado correlaciones significativas entre el peso y el nivel de colesterol y triglicéridos de cada uno de los animales que seguían una dieta hiperlipídica. Sin embargo, no existe correlación en el grupo de ratones control.

- Existen diferencias significativas en todo el árbol aórtico (aorta torácica superior e inferior y abdominal) en el módulo secante y elástico al comparar ratones ApoE$^{-/-}$ con ratones control. Además, se ha encontrado una relación prácticamente lineal de estos módulos con la edad para el caso de los ratones ApoE$^{-/-}$ y, un comportamiento constante para los ratones control. Por el contrario, en el módulo tangente no se han encontrado diferencias estadísticas significativas entre ambas cepas, ni entre los diferentes grupos de ratones ApoE$^{-/-}$ al inicio y al final del desarrollo de la enfermedad. Este hecho podría deberse a la ruptura de la elastina de la capa media que se produce en los ratones ApoE$^{-/-}$ con lesiones ateroscleróticas severas. La rigidización de la pared está relacionada con la fragilización de la elastina que hace que el colágeno empiece a experimentar tracción antes, produciéndose un efecto de rigidización, y no tanto relacionado con el comportamiento propio del colágeno. Sin embargo, esta hipótesis debería ser corroborada mediante la realización de más ensayos experimentales y estudios histológicos de los vasos ensayados.

- Con respecto a las tensiones residuales longitudinales, se ha encontrado que éstas disminuyen casi linealmente con la edad en los ratones ApoE$^{-/-}$ y permanecen prácticamente constantes para los ratones control, existiendo diferencias significativas entre ambas cepas de animales con dieta durante 30 y 40 semanas. Además, se han encontrado diferencias significativas entre ratones ApoE$^{-/-}$ que han empezado a desarrollar lesiones ateroscleróticas (10 y 20 semanas) y aquellos en estadios avanzados de la enfermedad (30 y 40 semanas).

0.4.2 Aspectos matemáticos, mecánicos y numéricos

- Las simulaciones computacionales realizadas en el estudio paramétrico tridimensional de una arteria coronaria con geometría idealizada nos han permitido caracterizar fisiológica y morfológicamente la placa de ateroma, así como confirmar que

es necesario el uso de geometrías tridimensionales para predecir el riesgo de vulnerabilidad de placa. Se ha demostrado que los modelos en 2D simulados bajo la hipótesis de deformación plana tienden a sobrestimar las tensiones sobre la placa, y por tanto, no nos proporcionan una información real de la vulnerabilidad de la misma. El desarrollo de modelos computacionales de vasos sanguíneos en 3D nos permite incorporar fenómenos tales como las tensiones residuales en dirección longitudinal y circunferencial o la anisotropía que caracteriza al tejido vascular. Se ha demostrado que las tensiones residuales son muy influyentes en la predicción de las tensiones en la placa de ateroma, siendo necesario incluirlas en modelos de predicción de rotura de la misma.

- Se ha validado la hipótesis de geometría idealizada en el estudio paramétrico en 3D de una arteria coronaria mediante la reconstrucción de una geometría real paciente específico obtenida mediante ultrasonido intravascular (IVUS). La distribución de tensiones, así como la tensión máxima principal, obtenidas en el modelo real reconstruido y en un modelo paramétrico con dimensiones similares a las de la geometría personalizada obtenida a partir de imágenes médicas, se correlacionan adecuadamente.

- Se ha diseñado un modelo 3D de arteria coronaria con placa aterosclerótica excéntrica para predecir la vulnerabilidad de ésta teniendo en cuenta la interacción entre la sangre y la pared arterial (modelo de interacción fluido-estructura). Los resultados, en cuanto a la pared arterial se refiere, obtenidos con este modelo han sido comparados con los obtenidos en el modelo en el que sólo se tiene en cuenta la pared del vaso, obteniéndose los mismos resultados para todos ellos. Sin embargo, una de las variables que se deben tener presente en la progresión de la enfermedad de la aterosclerosis es la tensión tangente que el flujo genera en la pared arterial, por ello son necesarios modelos computacionales de interacción fluido-estructura.

- Las técnicas de aprendizaje autónomo son una herramienta complementaria al uso de simulaciones mediante elementos finitos en el diagnóstico de placas vulnerables debido a que estas técnicas permiten la reduccion del tiempo de respuesta. Se han obtenido errores despreciables en la predicción de placa, tanto para el caso de las redes neuronales como para las "Support Vector Machine", obteniéndose resultados ligeramente mejores para el caso de ésta última técnica. Los resultados obtenidos mediante regresión lineal de los datos muestran la alta no linealidad del problema y por tanto, se justifica la utilización de dichos algoritmos.

- Los resultados obtenidos en el estudio de la influencia de las microcalcificaciones en las tensiones producidas en la placa de ateroma, sugieren que una incorrecta elección de las propiedades del material de la microcalcificación dan lugar a conclusiones contradictorias. El papel que juegan las microcalcificaciones en la ruptura de placa no está científicamente establecido. En la literatura se pueden encontrar

numerosos estudios que indican efectos beneficiosos de las microcalcificaciones en la estabilización de las tensiones en la placa, mientras que otros tantos informan sobre las catastróficas consecuencias de la aparición de una microcalcificación en la placa de ateroma. Se ha demostrado que la controversia de los resultados encontrados en la literatura sobre la influencia de las microcalcificaciones en la vulnerabilidad de la placa podría deberse a que las propiedades del material de la microcalcificación son demasiado rígidas en algunos estudios.

- El modelo de crecimiento de placa de ateroma desarrollado basado en ecuaciones diferenciales reacción-difusión-convección permite simular de forma cualitativa el avance de la enfermedad de la aterosclerosis. Este modelo, que nos permite saber cómo interactúan los diferentes agentes que intervienen en el proceso de formación de placa, puede considerarse como un primer paso para entender esta patología.

0.4.3 Aspectos clínicos

- Se ha comprobado que desde el punto de vista mecánico el parámetro más influyente en la ruptura de placa es el espesor de la capa fibrótica. Una pequeña disminución en el tamaño de éste origina un elevado incremento en la tensión principal máxima en esa zona de la placa y por tanto magnifica el riesgo de rotura de la placa. Tradicionalmente, éste ha sido el valor que los clínicos consideran para determinar si una placa es vulnerable o no, sin embargo, los resultados obtenidos muestran que la longitud y el ancho del lípido son también factores muy influyentes a la hora de determinar si una placa es vulnerable.

- Se ha diseñado una herramienta de ayuda a la toma de decisiones para la práctica clínica basada en técnicas de aprendizaje automático (redes neuronales y máquinas de soporte de vectores), la cual nos permite ir un paso más allá en el diagnóstico preventivo.

- La influencia de la presencia de una microcalcificación en la capa fibrótica no ha sido muy significativa.

- Se ha mostrado que el remodelado positivo es siempre más vulnerable que el negativo en cualquier estadio de la enfermedad.

- Se ha mostrado que la hipertensión y la rigidización de la pared afectan negativamente a la vulnerabilidad de la placa mediante ensayos de sensibilidad de estos parámetros en modelos de elementos finitos en 2D imponiendo hipótesis de deformación plana.

0.5 Contribuciones científicas originales

Las siguientes contribuciones originales pueden extraerse de los análisis y metodologías presentadas a lo largo de esta Tesis:

- Se ha desarrollado el primer modelo paramétrico de elementos finitos en 3D que incorpora pretensión tanto en dirección circunferencial como longitudinal, para el estudio de vulnerabilidad de placa de ateroma. Dicho estudio ha sido validado mediante la reconstrucción y posterior simulación de una geometría personalizada de un paciente específico obtenida a partir de imágenes médicas de una coronaria humana. Se ha desarrollado el primer estudio sistemático de la influencia de las tensiones residuales en el riesgo de vulnerabilidad de placa de ateroma.

- Se ha presentado un estudio paramétrico que incorpora el tamaño, posición y propiedades del material de una microcalcificación para estudiar el efecto de las microcalcificaciones en la vulnerabilidad de la placa aterosclerótica.

- Se ha considerado la vulnerabilidad de placa de ateroma al incluir estenosis con remodelado negativo y positivo a través de un estudio paramétrico de placas de ateroma con estos dos tipos de remodelado. Para ello, se han comparado sistemáticamente los diferentes estados de crecimiento de dos modelos de arteria coronaria con placa de ateroma, uno con placa con remodelado positivo y otro con negativo. De este modo, se ha demostrado por primera vez por qué el remodelado positivo es clínicamente más peligroso en términos de vulnerabilidad que el negativo.

- Se ha aplicado por primera vez técnicas de aprendizaje automático como redes neuronales y máquinas de soporte vectorial para desarrollar una herramienta de ayuda a la toma de decisiones en la práctica clínica sobre vulnerabilidad de la placa de ateroma.

- Se ha diseñado un dispositivo y una metodología para realizar ensayos de inflado *in situ* que nos permite caracterizar el comportamineto mecánico de vasos sanguíneos de animales de pequeño tamaño.

- Se ha estudiado por primera vez la variación de las propiedades mecánicas a lo largo de la arteria aorta murina para dos cepas diferentes; ratones $\mathrm{ApoE}^{-/-}$ que presentan predisposición en la aparición de placa de ateroma, y ratones comunes de laboratorio (C57BL/6) para estudiar la influencia de la aparición de la placa de ateroma en función de la edad y la dieta.

- Se ha presentado un modelo matemático de crecimiento de placa de ateroma basado en ecuaciones diferenciales reacción-difusión-convección que es capaz de ilustrar las diferentes fases de desarrollo de la placa de ateroma, aportando información sobre los procesos biológicos que ocurren durante el transcurso de este proceso. Además, se ha aplicado al modelado del crecimiento de placa de ateroma en una geometría cilíndrica con una lesión inicial.

0.5.1 Publicaciones

A continuación, se enumeran las publicaciones en revistas internacionales que se han realizado durante el desarrollo de esta Tesis.

0.5.1.1 Publicaciones relacionadas con la Tesis

1. Cilla, M., Peña, E., and Martínez M.A. 3D computational parametric analysis of eccentric atheroma plaque influence of axial and circumferential residual stresses. *Biomechanical and Modeling Mechanobiology*, 11(7):1001-13 (2012).

2. Cilla, M., Martínez, J., Peña, E., and Martínez M.A. Machine Learning Techniques as a Helpful Tool Toward Determination of Plaque Vulnerability. *IEEE Transactions on Biomedical Enginering*, 9(4):1155-61 (2012).

3. Cilla, M., Monterde, D., Peña, E., and Martínez M.A. Does microcalcification increase the risk of rupture? *Proceedings of the Institution of Mechanical Engineers, Part H, Journal of Engineering in Medicine*, Under review.

4. Cilla, M., Peña, E., Martínez M.A. and D.J., Kelly Comparison of the vulnerability risk for positive versus negative atheroma plaque growth. *Journal of Biomechanics*, Under review.

5. Cilla, M., Pérez, M.M, Peña, E., and Martínez M.A. Arterial Stiffening due to Atherosclerosis in Apolipoprotein E-Deficient Mice. Effect of diet and age. *Atherosclerosis*, Submitted for publication.

6. Cilla, M., Borrás I., Peña, E., Martínez M.A. and Malvè M. Parametric analysis of atherosclerotic plaques by fluid structure interaction. Influence on the mechanics of the vulnerability. *Annals of Biomedical Engineering.*, In preparation.

7. Cilla, M., Peña, E., and Martínez M.A. On the time dependent mathematical model of atheroma plaque formation. *Journal of Theoretical Biology.*, In preparation.

0.5.1.2 Publicaciones dentro del ámbito biomecánico no incluídas en la presente Tesis

1. Araña, M., Peña, E., Abizanda, G., Cilla, M., Ochoa, I., Gavira, J.J., Doblaré, M., Pelacho, B., and Prósper F. Preparation and characterization of ADSC-cellularized patches for cardiovascular application. *Acta Biomaterialia*, Accepted.

2. Araña, M., Peña, E., Abizanda, G., Cilla, M., Pérez, M.M., Gavira, J.J., Doblaré, M., Pelacho, B., and Prósper F. Cardiac remodeling after implantation of a collagen scaffold with adipose derived stem cells. *Biomaterials*, In preparation.

0.5.2 Contribuciones a congresos

Durante el periodo de desarrollo de la Tesis, se realizaron varias contribuciones y comunicaciones a congresos de ámbito nacional e internacional. Las más relevantes se recogen seguidamente:

1. Cilla, M., Peña, E., Martínez M.A., and Doblaré, M., Estudio paramétrico tridimensional de factores geométricos en la vulnerabilidad de la placa de atheroma. *XXVII Congreso Anual de la Sociedad Española de Ingeniería Biomédica (CASEIB)*, Cádiz (Spain), 2009.

2. Cilla, M., Peña, E., Martínez M.A., and Doblaré, M., Computational modelling of atherome plaque: biomechanical factors in the risk of plaque rupture. *IV European Congress on Computational Mechanics (ECCM IV): Solids, Structures and Coupled Problems in Engineering*, Paris (France), 2010.

3. Cilla, M., Peña, E., Martínez M.A., and Doblaré, M., 3D parametric study of the biomechanical factors in evaluating the risk of plaque rupture. *17th Congress of the European Society of Biomechanics (ESB)*, Edinburgh, Scotland (United Kingdom), 2010.

4. Cilla, M., Peña, E., and Martínez M.A., Red Neuronal Artificial para la toma de decisiones en la vulnerabilidad de laca de ateroma. *Congress on Numerical Methods in Engineering (CNME)*, Coimbra, (Portugal), 2011.

5. Cilla, M., Martínez, J., Peña, E., and Martínez M.A., Red Neuronal Artificial para la toma de decisiones en la vulnerabilidad de laca de ateroma. *I Reunión del Capítulo Nacional de la Sociedad Europea de Biomecánica (ESB)*, Zaragoza, (Spain), 2011.

6. Cilla, M., Monterde, D., Peña, E., and Martínez M.A., The microcalcification influence on the ateroma plaque vulnerability. *I Jornada de Jóvenes Investigadores I3A*, Zaragoza, (Spain), 2012.

7. Cilla, M., Pérez, M.M., Peña, E., and Martínez M.A., Mechanical properties of atheroma plaque along the length of the aorta in ApoE$^{-/-}$ mice model. *18th Congress of the European Society of Biomechanics (ESB)*, Lisbon (Portugal), 2012.

8. Cilla, M., Peña, E., and Martínez M.A., A 3D parametric study of eccentric atheroma plaque: influence of geometrical factors and residual stress. *18th Congress of the European Society of Biomechanics (ESB)*, Lisbon (Portugal), 2012.

9. Cilla, M., Martínez, J., Peña, E., and Martínez M.A., Atheroma plaque vulnerability prediction using Machine Learning Techniques. *XXIII International Congress of Theoretical and Applied Mechanics (ICTAM)*, Pekin, (China), 2012.

10. Cilla, M., Pérez M.M., Peña, E., and Martínez M.A., Propiedades mecánicas de la aorta durante el proceso de formación de placa aterosclerótica en ratones ApoE$^{-/-}$. *II Reunión del Capítulo Nacional de la Sociedad Europea de Biomecánica (ESB)*, Sevilla, (Spain), 2012.

0.6 Desarrollo futuro

El trabajo de investigación que se ha llevado a cabo durante el desarrollo de la presente Tesis no es más que una pequeña aportación al estudio de la enfermedad de la aterosclerosis. A continuación se presentan algunas posibles líneas de investigación para desarrollar en el futuro y que permitirán mejorar los resultados y ampliar los conocimientos que aquí se han iniciado:

- Medidas experimentales de las tensiones residuales circunferenciales, es decir, medida del ángulo de apertura en ratones ApoE$^{-/-}$. Toma de más datos que aporten información al estudio, como medidas de colesterol, triglicéridos y otros marcadores que están directamente relacionados con el desarrollo de lesiones ateroscleróticas. Además, se propone un estudio histológico e inmunohistoquímico para la cuantificación de la microestructura (cantidades de macrófagos, citoquinas, etc...) de la placa para poderlo correlacionar con un modelo de crecimiento de placa.

- Desarrollo de un estudio equivalente al presentado para ratones pero empleando como animal de experimentación el conejo. Los conejos desarrollan unas características morfológicas de la placa de ateroma más parecidas a las humanas. Además, el tamaño de la muestra de conejos permite el desarrollo de ensayos de inflado con medida de la rigidez longitudinal que en el caso de los ratones no es posible, o en su caso la caracterización uniaxial en dirección longitudinal y/o biaxial.

- Reconstrucción 3D de la geometría del árbol aórtico de los ratones ApoE$^{-/-}$ para someterlos a un estudio CFD que nos permita correlacionar las zonas de aparición de placa de ateroma que se han identificado con zonas con bajas tensiones tangenciales.

- Desarrollo de un nuevo modelo constitutivo hiperelástico para el modelado de las propiedades mecánicas de la aorta de ratón. Este modelo permitiría reproducir de manera aproximada las curvas presión-deformación obtenidas para los ensayos experimentales de inflado realizados.

- El estudio y modelado constitutivo de las propiedades viscoelásticas y demás fenómenos inelásticos que tienen lugar arterias afectadas por la enfermedad de la aterosclerosis.

- Adquisición de una gran cantidad de geometrías de coronarias reales de pacientes específicos a partir de IVUS o RMN. Reconstrucción y simulación mediante el método de los elementos finitos de las mismas para comparar los resultados obtenidos en los estudios paramétricos realizados con geometrías idealizadas con los obtenidos para geometrías reales. Además, se propone un posterior entrenamiento de cada una de las técnicas de aprendizaje automático propuestas con los resultados correspondientes a las geometrías reales para obtener una herramienta de ayuda a la decisión sobre vulnerabilidad de placa para la práctica clínica basada en casos reales.

- Realización de un estudio paramétrico en 3D sobre una arteria coronaria idealizada que incluya remodelado positivo y negativo para poder detectar qué parámetros geométricos que definen el remodelado son más influyentes en la vulnerabilidad de la placa de ateroma. Se han realizado estudios paramétricos para determinar los factores más influyentes en la ruptura de placa en geometrías con remodelado negativo, sin embargo, no se ha llevado a cabo ningún estudio de este tipo para placas con remodelado equivalente positivo.

- Ampliación del número de modelos de interacción fluido-estructura estudiados e incorporación de tensiones residuales a estos modelos. Para el caso del estudio paramétrico que contempla la influencia del flujo sanguíneo, se ha llevado a cabo el estudio de 17 modelos. Con el fin de poder evaluar las tendencias cruzadas de todas estas variables, una posible ampliación a este estudio paramétrico es la combinación de todas las variaciones de parámetros, tal y como se ha hecho en el estudio paramétrico en 3D, de modo que sería necesario el estudio de 625 casos. Además, sería interesante obtener otras variables influyentes en la aparición de placa de ateroma, tales como la tensión tangente oscilatoria.

- Realización de un modelo de crecimiento más completo. Incorporación de más agentes biológicos que intervienen en la formación de la placa de ateroma, así como de los procesos acontecidos, tales como encimas, factores de crecimiento o radicales libres en el endotelio que regulan la oxidación del LDL.

- Realización de un completo estudio de sensibilidad de los parámetros empleados en el modelo de crecimiento para ver la influencia que tiene sobre los resultados finales obtenidos. Hay que tener en cuenta la dificultad para la obtención de dichos parámetros y constantes del modelo.

- Aplicación del modelo de crecimiento desarrollado a modelos geométricos más complejos tales como bifurcaciones en arterias coronarias o carótidas, o incluso geometrías reales.

Mechanical effects on the atheroma plaque appearance, growth and vulnerability

Chapter 1

Introduction

A brief summary of the main features and functions of the vascular system is presented in this Chapter. Specifically, the physiological role of the cardiovascular system is addressed. Blood vessels are classified as a function of their composition and physiological role, and their main mechanically relevant characteristics are presented. Furthermore, one of the most common diseases of the circulatory system, the atherosclerosis, is presented. In particular, the main features related to this cardiovascular disease are detailed; localization of atherosclerotic plaque, atherosclerosis risk factors, causes of atheroma plaque rupture, atherosclerosis plaque detection and treatment and process of the plaque formation. Next, a short state of the art in constitutive modelling of soft biological tissue and a review of the main experimental techniques commonly used to characterize the mechanical properties of soft biological tissues are stated. Finally, the motivation of this thesis, which is founded on the high social and economical impact of cardiovascular diseases, the main objectives and a brief description of the contents are included in this Chapter.

Contents

1.1 The cardiovascular system

The cardiovascular system, also called the circulatory system, is an organ system made up of the vessels that carry blood cells, hormones, nutrients, gases and lymph through the body. It also has immune function, works to stabilize body temperature, pH and homeostasis. This system may be seen strictly as a blood distribution network, but the circulatory system should be considered as composed of the cardiovascular system, which distributes blood, and the lymphatic system, which distributes lymph. The arteries and veins carry blood throughout the body, delivering oxygen and nutrients to the body tissues and taking away tissue waste matter. The lymph vessels carry lymphatic fluid (a clear, colourless fluid containing water and blood cells). The lymphatic system helps to protect and maintain the fluid environment of the body by filtering and draining lymph away from each region of the body.

This thesis is focused on the study of the atherosclerosis development on vessels belonging to the cardiovascular system, which can be roughly classified into:

- Arteries, which are the blood vessels that carry oxygenated blood away from the heart to the body. When arteries get to an organ in your body, they branch into smaller tubes called arterioles, and then arterioles branch many times into tiny tubes called capillaries.

- Veins, which carry blood from the body back into the heart. They have thinner walls than arteries because the blood is at a lower pressure. Veins have valves to keep blood going in the right direction. Capillaries join up to form larger tubes called venules, and venules join up to form veins.

- Capillaries, which are tiny blood vessels between arteries and veins. They have thin walls, to allow chemical sustances like oxygen and food pass from the blood to the body cells, while carbon dioxide and waste chemicals pass from the body cells to the blood.

Note, however, that these broad categories are composed of a number of vessel subtypes, as a function of the vessel size, composition, or physiological role (see, e.g., Rhodin, 1980; Humphrey, 2002b). A diagrammatic representation of the main veins and arteries is represented in Figure 1.1.

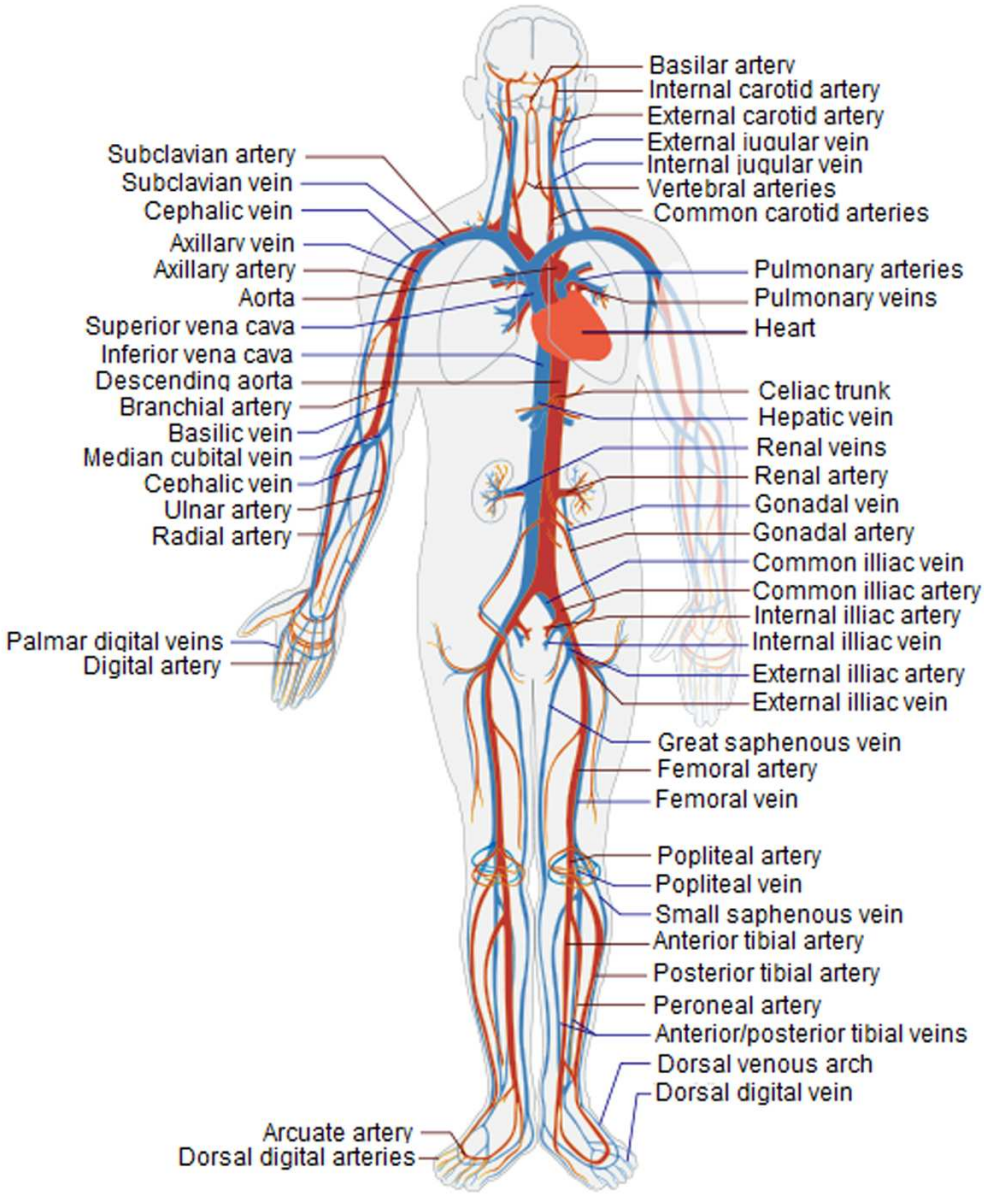

Figure 1.1: Diagrammatic representation of the cardiovascular system anatomy. Adapted from Netter (2010).

Blood moves through the circulatory system as a result of being pumped out by the heart. Blood leaving the heart through the arteries is saturated with oxygen. The arteries break down into smaller and smaller branches in order to bring oxygen and

other nutrients to the cells of the body tissues and organs (systemic circulation). As blood moves through the capillaries, the oxygen and other nutrients move out into the cells, and waste matter from the cells moves into the capillaries. As the blood leaves the capillaries, it moves through the veins, which become larger and larger to carry the blood back to the heart.

In addition to circulating blood trough the body, the cardiovascular system interacts with other body systems, i.e.:

- Respiratory system: As blood flows through the capillaries in the lungs, carbon dioxide is given up and oxygen is picked up. The carbon dioxide is expelled from the body through the lungs and trachea, and the oxygen is driven to the body tissues by the blood.
- Digestive system: As food is digested, blood flows through the intestinal capillaries and picks up nutrients, such as glucose (sugar), vitamins, and minerals. These nutrients are delivered to the body tissues by the blood.
- Kidneys and urinary system: Waste materials from the body tissues are filtered out from the blood as it flows through the kidneys. The waste material then leaves the body in the form of urine.
- Temperature control: Regulation of the body temperature is assisted by the flow of blood among the different parts of the body. Heat is produced by the body tissues as they go through the processes of breaking down nutrients for energy, making new tissue, and giving up waste matter.

Furthermore, it is worth distinguishing between systemic, pulmonary and coronary circulation systems, which play a different role in the oxygen and nutrient delivering process.

- Systemic circulation is the portion of the cardiovascular system which carries oxygenated blood away from the heart to the body, and returns deoxygenated blood back to the heart. Arteries always take blood away from the heart, regardless of their oxygenation, and veins always bring blood back. In general, arteries transport oxygenated blood to the tissues; veins bring deoxygenated blood back to the heart. Nevertheless, for the pulmonary vessels the oxygenation is reversed, that is, the pulmonary arteries take deoxygenated blood from the heart to the lungs, and oxygenated blood is pumped back through the pulmonary vein, the only vein in the body that carries oxygen rich blood in the body, to the heart. As blood circulates through the body, oxygen and nutrients diffuse from the blood into cells surrounding the capillaries, and carbon dioxide diffuses into the blood from the capillary cells (Humphrey, 2002b), see Figure 1.2.a.
- Pulmonary circulation is the portion of the cardiovascular system which carries oxygen depleted blood away from the heart, to the lungs, and returns oxygenated

blood back to the heart. Deoxygenated blood enters the right atrium of the heart and flows into the right ventricle where it is pumped through the pulmonary arteries, the only arteries in the body that carry oxygen poor blood, to the lungs. Pulmonary veins return the now oxygen rich blood to the heart, where it enters the left atrium before flowing into the left ventricle, see Figure 1.2.a.

- Coronary circulation provides a blood supply to the heart. Note, however, that contrary to the systemic and pulmonary circulations in which blood flows pumped by the systolic contraction of the heart, coronary circulation occurs at heart diastole, when heart de-contraction allows the blood to flow, see Figure 1.2.b.

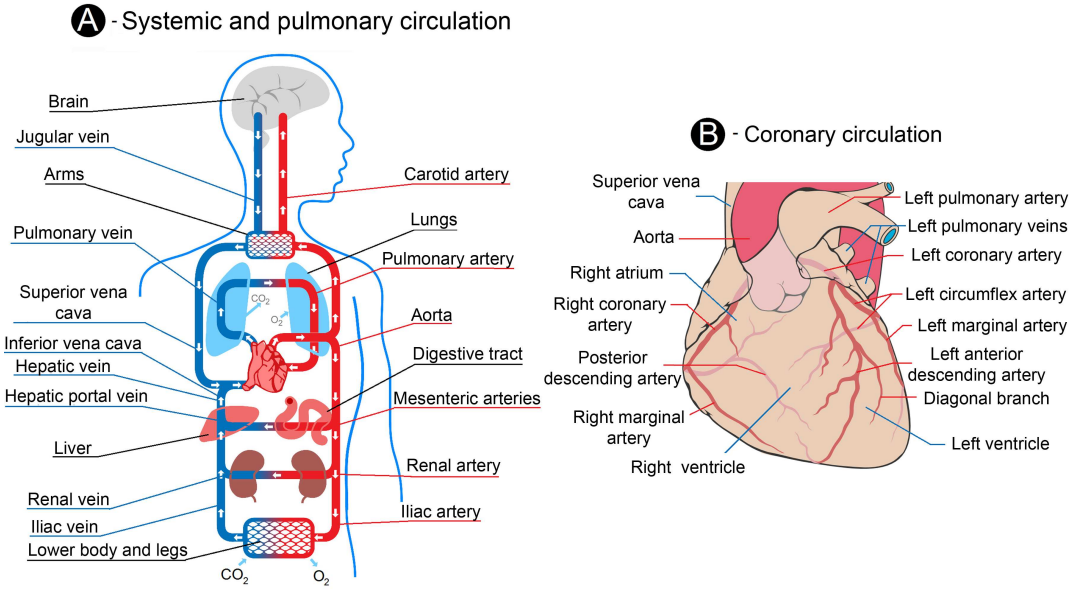

Figure 1.2: Diagrammatic representation of the three main circulations which human circulatory system is composed. A - Systemic and pulmonary circulation. B - Coronary circulation. Adapted from Netter (2010).

1.2 Vessel structure and composition

With the goal of introducing the structure and components of the blood vessels, a brief description of the histological wall composition of different vessels and their classification is presented in the following sections. Only the most relevant features of the vessel, needed for the understanding of the mechanical behaviour exhibited by the vascular tissue, are here reflected. Thus, many interesting details related to the molecular biology, angiogenesis, physiological role, or ultrastructural composition have been omitted. The interested reader is referred, for example, to the texts by Rhodin (1980), Fung (1990), or Humphrey (2002b), where these and other relevant issues are

treated in depth. As final conclusion, the main mechanical features resulting from the vessel wall composition are presented.

1.2.1 The healthy vessel wall: composition and classification

As mentioned above, the vascular system is divided into the arterial and the venous systems, which exhibit a different histological composition and play a different mechanical and physiological role in the vascular system. Arteries, for instance, usually have thicker walls and smaller cross-sectional diameters than matching veins, which can be explained by the fact that arteries carry blood to the extremities and the organs, and are, therefore, under pressure from the heart; veins, on the other hand, carry the blood back to the heart, and their physiological internal pressure is much lower, Figure 1.3. Nevertheless, there is little distinction in their histological details.

Both kinds of vessels are made of a layered structure which, when healthy, is usually composed of three different *tunicas* or layers[1]. From the inner to the outer radius, they are the intima, the media, and the adventitia, whose main features are the following (see Figure 1.4);

- Intima: The intimal layer is the innermost layer of all blood vessels, being composed of the following structures: 1) a single layer of endothelial cells lining the vascular wall; 2) a thin, about 80 [nm] thick, elastic lamina; and 3) a subendothelial layer, composed of collagenous bundles, elastic fibrils, smooth muscle cells, and perhaps some fibroblasts. The subendothelial layer, however, is only presented in large elastic arteries such as the human aorta, whereas this sublayer is missing in other smaller arteries.

- Media: The tunica media, as the name indicates, is the middle layer of the vascular wall. It is made of smooth muscle cells, a variable number of elastic laminae, bundles of collagenous fibrils and a network of elastic fibrils. This layer is thicker in arteries than in veins, in which muscle cells may be absent in large veins like vena cava. In the aorta, the media layer may reach thicknesses of 500 [μm], whereas is about 20-50 [μm] in medium sized veins (see, e.g., Wolinsky and Glagov, 1964; Clark and Glagov, 1985, for further information). The media is the main load bearing layer in vessels under physiological situations.

- Adventitia: The tunica adventitia is the outermost layer of the vascular wall. Its thickness varies considerably depending on the type and location of the blood vessel. In all arteries, and most veins, the adventitia consists of dense fibroelastic tissue without smooth muscle cells, except in large veins, such as vena cava, where bundles of longitudinally arranged smooth muscle cells may be found. Also the nutrient vessels of the vascular wall that take nutrients to the muscle cells in the media, namely the *vasa vasorum*, are part of the adventitia, as well as nerves.

[1] Note that brain arteries almost entirely lack of the tunica adventitia (Rhodin, 1980).

The adventitia renders the vascular wall a fair amount of stability, and serves to connect blood vessels to the surrounding tissue.

Depending on the wall composition, arteries are usually classified into elastic and muscular. The first group is formed by those arteries with large diameters, such as the aorta, the main pulmonary artery, the common iliac, and the carotid arteries, where the media contains both smooth muscle cells and many elastic laminae. Their most characteristic structure is a sandwich substructure of smooth muscle cells and thin elastic laminae, see Figure 1.3.a. From 40 to 70 of these substructures are found in thick vessels like the human aorta, whose thickness is nearly independent of the radial position (Wolinsky and Glagov, 1967).

On the other hand, arteries that decrease in diameter as they approach to the periphery, and in which the media is less elastic and the muscular cells prevail are called muscular arteries. In these arteries, the media appears as a single thick ring of smooth muscle cells, surrounded by the internal elastic lamina and by a less marked external elastic lamina, see Figure 1.3.b. The smooth muscle cells are embedded in a loose connective tissue matrix and arranged as a sequence of concentric layers of cells, which can reach numbers of 25-40 in larger vessels like the coronary or femoral arteries.

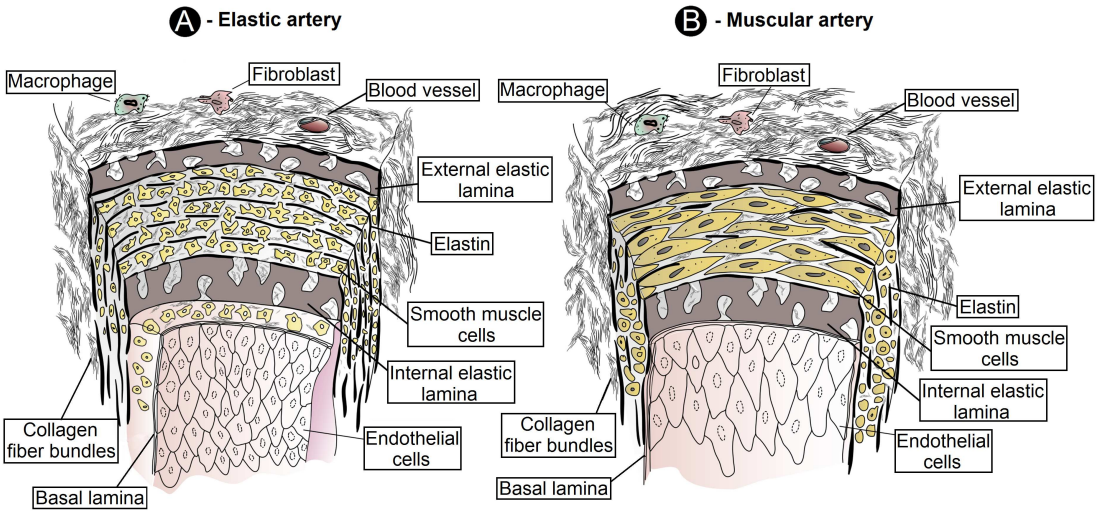

Figure 1.3: Semi-diagrammatic representation of the arterial wall. Adapted from Rhodin (1980).

It is sometimes difficult to identify clearly certain arteries as elastic or muscular, due to the fact that abrupt changes occur seldom in continuous structures like the vasculature. Instead, these transitions occur smoothly, and the corresponding artery segments loose their characteristic lamellar structure progressively, as happens in the internal and external carotid arteries.

It is not possible to distinguish between elastic and muscular veins, which are usually classified attending to their size. There is a huge confusion in the literature about large

and medium-sized veins structure and composition. The reason for this confusion is based on the fact that, as early pointed by Franklin (1928), "the intimate structure of veins varies considerably to calibre, age and species; individual veins differ from one to another according to their situation in the body, and the same vein will vary markedly in its structure in the course of its length, and even on opposite sides of the cross section. In addition, changes occur in the distribution of longitudinal and circumferential muscle at the level of valves". Furthermore, the boundaries between the intima, media and adventitia layers are not very distinct, see Figure 1.4.

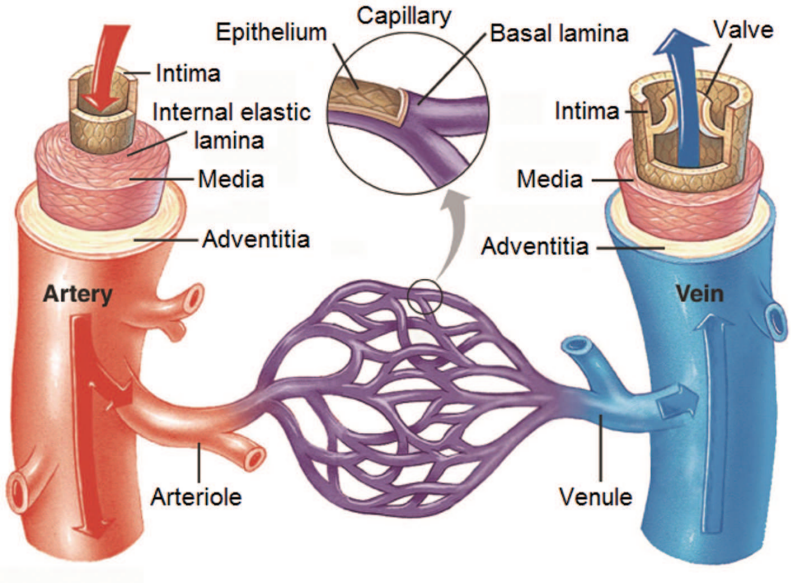

Figure 1.4: Representation of the arterial and vein wall and its layers; intima, media and adventitia.

1.2.2 Blood flow and its constituents

Blood is essentially a two-phase fluid consisting of cellular components (red blood cells, white blood cells, and platelets) and a liquid medium (plasma) whose main functions are

- Transports: Blood transports dissolved gases such as oxygen or carbon dioxide, waste products of metabolism like water or urea, hormones, enzymes, nutrients as glucose, vitamins or fatty acids, plasma proteins associated with defence such as blood-clotting and anti-bodies and body cells which includes white blood cells "leucocytes" and red blood cells "erythrocytes".

- Maintains body temperature: Blood flow to the body tissue and limbs helps to regulate body temperature in that an exchange of heat between the body and the environment takes place when the blood flows to the tissues.

- Controls pH: The pH of blood must remain in the range 6.8 to 7.4, otherwise it begins to damage cells.
- Removes toxins from the body: The kidneys filter all the blood in the body 36 times every 24 hours. Toxins removed from the blood by the kidneys leave the body in the urine or in the form of sweat.
- Regulation of body fluid electrolytes: Excess salt is removed from the body in urine.

The plasma of the blood occupies about 55% of the blood volume and carries a variety of substances including plasma proteins, non-protein nitrogen, electrolytes, hormones, enzymes and blood gases (Green, 1982). The cellular components of the blood account for approximately 40% of the blood by volume. The most numerous cellular component is the red blood cell (erythrocyte) which is soft and flexible, and can travel through the smallest capillaries. An important constituent, hemoglobin, in erythrocyte binds and transports oxygen. Another major type is the white cell (leukocyte) which primarily defends the body against invasion by infectious agents, repairs damaged tissues, and participates in immune reactions. Monocytes comprise about 3 to 8% of the total leukocyte population and their surfaces are characterized by thin folds to engulf material by endocytosis (Green, 1982). These cells are suspended in the blood, slide through the endothelium, and accumulate in regions experiencing inflammation, which play an important role in the progression of atherosclerotic disease and plaque rupture (see Figure 1.5).

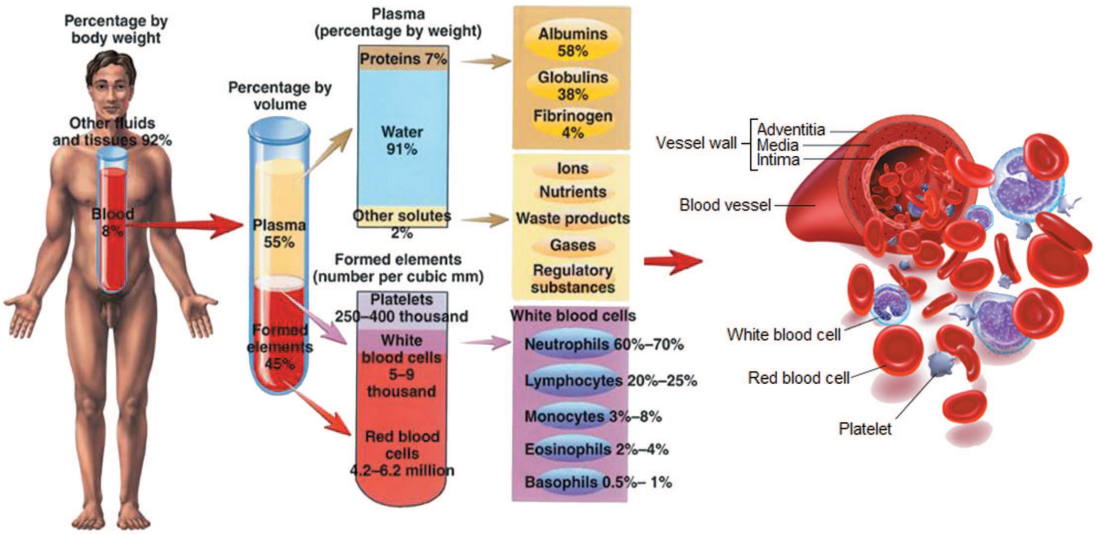

Figure 1.5: Composition of the blood and its main constituents

Under normal healthy conditions, the blood flow in carotid artery bifurcation is laminar. However, in the presence of a high stenosis degree, the flow can transit from

laminar flow to turbulence flow. Therefore, a fluid flowing in a blood vessel exhibits motion which is classified into two types: laminar or turbulent. In laminar flow the fluid particles move along smooth paths in layers with every layer sliding smoothly over its neighbor. It is also called streamline flow. As the velocity of flow increases, the different layers start interfering in each others motion due to different inertia and friction at some point and eventually the laminar flow becomes unstable, vortices start to form, and ultimately the fluid flow becomes turbulent. Hence turbulent flow is one in which different layers collide with one another and cause non uniformity. When the flow is turbulent the velocity vectors of the fluid particles at every point change rapidly with time, both in magnitude and direction. Both the laminar and turbulent flows have different developed sketches, as illustrated in Figure 1.6.

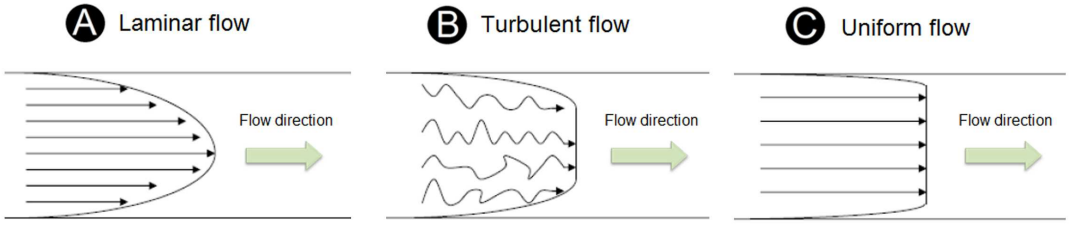

Figure 1.6: Velocity profiles for laminar (A), turbulent (B) and uniform (C) flow

For every fluid, to reach turbulent flow, there is a threshold value dependent on the average fluid velocity, density, viscosity and the diameter of the vessel (for internal flows). This characteristic value, which depends on all these quantities, is called the Reynolds number Re,

$$Re = \frac{\rho \cdot v \cdot D}{\mu} \quad , \tag{1.1}$$

where v is the average fluid velocity, D is the vessel diameter, ρ is the fluid density, μ is the fluid (dynamic) viscosity. It has been found through experiments that the fluid (blood) tends to become turbulent at a Reynolds number of approximately 2000 for internal flows (Nichols and O'Rourke., 1990).

Viscosity is a physical property of every fluid. In less viscous fluids such as water, viscosity is independent on the rate at which the adjacent fluid layers slide over one another, i.e. the relative velocities in laminar flow of parallel adjacent layers of a fluid body under shear force called (shear rate $\dot{\gamma}$), and such fluids are usually referred to as Newtonian fluids. In contrast to simple fluids as water, blood is a suspension of particles, therefore the viscous properties of blood are complex and therefore blood is a non Newtonian fluid. Newtonian behaviour to blood is only valid when it has shear rates in excess of $100s^{-1}$, which tends to occur in larger arteries (Pedley, 1980; Berger and Jou, 2000). In most cases, though, non-Newtonian blood models would provide a more accurate representation of blood flow behaviour within the arteries of interest, particularly for stenosed conditions. In some diseased conditions, blood flow is non

Newtonian regardless. Furthermore, it has been shown that if the arterial diameter is greater than 1mm, the effect of red blood cells in the flow is minimized as the size of these cells is too small compared to the arterial diameter and therefore it is pertinent to neglect, leading to a constant viscosity of blood in this case (Nichols and O'Rourke., 1990; Huo *et al.*, 2009a), and consider the asymptotic value of blood viscosity, that is the value to which the apparent viscosity tends at high shear rate of adjacent sliding layers. Its value at normal physiological conditions for an average human being is in the range of $\mu = 3 - 4 \cdot 10^{-3}$ $\frac{N \cdot s}{m^2}$ with a density of $\rho = 1050$ $\frac{Kg}{m^3}$.

Some studies have documented several non Newtonian blood properties, such as the study of Johnston *et al.* (2004) that applied different non Newtonian models onto a steady flow, and later a transient flow (Johnston *et al.*, 2006) within an artery model obtained via angiography. Specifically, these models, which are depicted in Figure 1.7.a, were the Power Law model, Walburn-Schneck model, Casson model, Carreau model and Generalised Power Law model (Johnston *et al.*, 2004). In this Thesis, non Newtonian model, and specifically the non Newtonian Carreau model (see Figure 1.7.b), has been chosen to characterize the blood rheological behaviour.

The Carreau blood model predicts decreasing viscosity at high strain rate, where μ_0 and μ_∞ are low and high shear rate asymptotic values, the parameters A and m control the transition region size. Thus, this model assumes that the viscosity of blood, μ, varies according to the law:

$$\mu = \mu_\infty + (\mu_0 - \mu_\infty) \cdot (1 + A\dot{\gamma}_{ij}^2)^m \tag{1.2}$$

where, according to the experimental values of Valencia and Baeza (2009), $\mu_0 = 0.056$ $\frac{N \cdot s}{m^2}$, $\mu_\infty = 0.00345$ $\frac{N \cdot s}{m^2}$ A=10.975 and m=-0.3216. And, the density of blood was assumed to be constant $\rho = 1050$ $\frac{Kg}{m^3}$.

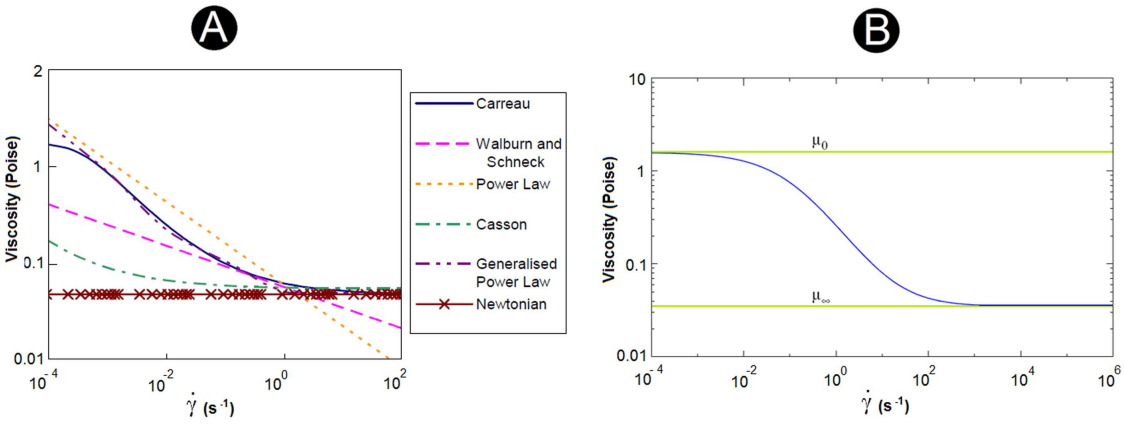

Figure 1.7: Plots of the viscosity and strain rate relationships for the different non-Newtonian models in the study by Johnston *et al.* (2004) (A) and for the model used in this Thesis, the Carreau model (B).

1.2.3 Main features of vascular tissue

The microstructural composition of the vessels wall, which has pointed out in the previous section, has several implications which must be accounted for in the creation of sophisticated constitutive laws trying to capture the mechanical behaviour of those vessels.

1.2.3.1 Mechanically relevant layers

The appropriate modelling of the arterial layers is of crucial importance in order to obtain the most accurate results from the computational simulations. In this regard, a first simplification sometimes used to model blood vessels is to consider them as thin walled tubes (Takamizawa and Hayashi, 1988; Demiray and Vito, 1991; Ballyk *et al.*, 1997). Nevertheless, the thickness-diameter ratio observed in most of the important vessels does not advice this assumption, but to consider the vessel wall as a thick walled tube.

With this consideration at hand, the next step is to determine the relevance of the load bearing capacity of the layers forming the blood vessel wall. In this regard, the tiny thickness of the intima layer in comparison with the thicknesses of the other two layers in the healthy state usually leads to neglect the mechanical contribution of this layer. Therefore, only the media and adventitia layers are included in the models. A lot of examples considering this assumption are found in the literature. To give some examples, see, e.g., Holzapfel *et al.* (2000), Holzapfel and Ogden (2003), Rachev and Greenwald (2003), Holzapfel *et al.* (2004), Driessen *et al.* (2005), Gasser *et al.* (2006) or Rodríguez *et al.* (2007).

A further simplification is to disregard the multilayer architecture of the vessels wall by assuming an homogeneous mechanical behaviour across the vessel wall (see, e.g., Demiray *et al.*, 1988). This assumption was partly motivated by the highly complicated procedure needed to separately measure the mechanical properties of these layers. Nevertheless, recent experiments have demonstrated that the mechanical response of each layer is notably different (Schulze-Bauer *et al.*, 2002, 2003; Holzapfel *et al.*, 2005b; Sommer *et al.*, 2008), which advices its consideration for the accurate modelling of the arterial wall.

Thus, it is nowadays widely accepted that at least media and adventitia layers must be included in the blood vessel models in order to obtain reliable results from the simulations of the healthy vessel wall. Note, however, that additional considerations must be accounted for in order to model, for example, the diseased arterial wall, since its composition and mechanical properties are considerably different (see, e.g., Williamson *et al.*, 2003; Holzapfel *et al.*, 2004; Ohayon *et al.*, 2007; Kiousis *et al.*, 2007).

Accordingly with these assertions, all the models presented in this Thesis consider the arteries as thick walled tubes. Furthermore, different mechanical properties have been assigned to media and adventitia layers in order to account for the wall heterogeneity. Additionally, the media has been considered as fibrotic in areas close to

atherosclerotic lesions.

1.2.3.2 Active and passive behaviour

Passive mechanical behaviour is that exhibited by most of the engineering materials, which is a result of their microstructural composition, and the way the microconstituents interact in case of composites. As mentioned above, the main role of the vascular system is to transport blood, for which they need of some load bearing capacity, associated with the passive mechanical response. Nevertheless, as other living tissues, the vascular tissue shows an active behaviour which is related to its capability, not only to change its properties in response to environmental changes, i.e. to grow or to remodel (see, e.g., Gleason *et al.*, 2007), but to react to external stimuli and exert forces. Therefore, the distinction is made between the passive behaviour and the active behaviour, typical and characteristic of muscle and vascular tissue.

As an example, a main function of this active behaviour in the arterial system is carried out by the smooth muscle cells in the medial layer, which can relax or contract in order to modify the vessel diameter, regulating this way the amount of blood which is sent to each organ (Humphrey, 2002b). Another typical example of active behaviour is the heart contraction which pumps blood into the vascular system by means of the contraction of the myocardial tissue.

Several models including the active behaviour of vascular tissues are found in the literature. For example, Bourdarias *et al.* (2003) presented a methodology for the modelling of the active behaviour of the vascular tissue within a Finite Element three-dimensional context or Fridez *et al.* (2003) investigated the dynamics of the carotid artery adaptation, considering the active behaviour of this vessel, from a biomechanical and histomorphometrical point of view. Regarding the heart, Taber and Perucchio (2000) and Ohayon *et al.* (2002) developed models to predict the development of the heart which included the active behaviour.

In the following, only the passive behaviour of the vascular tissue will be considered. Thus, all the constitutive laws and arterial models presented from now on disregard of active behaviour.

1.2.3.3 Residual stresses

The presence of residual stresses in the blood vessels wall is one of the most important features of vascular tissues. Residual stresses are defined as those stresses present in the vessels when no loads are applied, and are revealed when a cut is performed on a vessel in an unloaded configuration. Then, considering a cut in the radial direction, the vessel shortens (or lengthens) releasing part of the residual stresses in the longitudinal direction. Also when a cut is performed in the longitudinal direction, usually on a short vessel ring, it springs open releasing the residual stress associated to the circumferential direction.

The pioneering works by Chuong and Fung (1986) and Takamizawa and Hayashi (1987) are some of the first insights in the mechanical effect and implications of the residual stresses in soft tissues. Specifically, it is widely accepted in blood vessels modelling that residual stresses play an homogenizing role with regard to the circumferential stress distribution. Since a vessel ring springs open when a cut in the axial direction is performed on them, it turns out that the inner radius of the vessel is compressed and the outer tensiled in the closed unloaded configuration. Thus, the application of the internal pressure due to the blood flow will result in an almost homogeneous circumferential stress distribution across the wall thickness (Fung, 1990). In which the origin of residual stresses is concerned, Skalak (1981) suggested that residual stresses are the result of incompatible growth, and the associated elastic deformation needed to keep the material continuity (Skalak *et al.*, 1982).

Concerning the distribution of residual stresses among the vessel wall microconstituents, Saini *et al.* (1995) demonstrated, by selectively removing the components of the arterial wall, that elastin is largely responsible for the residual stress (see also Humphrey, 2002b). This effect is externally manifested in the internal elastic lamina, which is wavier in histological samples of the load-free state than in those of the stress free configuration or under *in vivo* conditions (Fung and Liu, 1992).

The presence of residual stresses in a load-free configuration leads to the consideration of the existence of a stress-free configuration, which would be taken as the starting configuration for subsequent analyses. Although, Chuong and Fung (1986) suggested that all the residual stress is released by a single cut in the radial axial direction, which is known as the opening angle experiment, other authors have shown that additional cuts still cause geometrical modifications in the open configuration, which points out to the existence of remaining residual stresses (see, e.g., Han and Fung, 1991). Anyway, the geometrical changes caused by the second and later cuts are very small compared to the first one, which points out that most of the residual stress is released with a single cut. The simplicity of this methodology has driven to the consideration of the opening angle experiment as a widely accepted measure of the residual strain field occurring in the vessels wall.

In contrast with this assumption, Greenwald *et al.* (1997), Stergiopulos *et al.* (2001), and Holzapfel *et al.* (2007) have shown that the opening angle differs for media and adventitia layers, and Matsumoto *et al.* (2004) have shown that even in the macroscopic stress-free configuration, the lamellar unit in the aorta is subjected to residual stresses at microscopic levels. All these results are mutually compatible if the stress-free configuration is considered as a boundary value problem: If the boundary conditions change (for example the vessel layers are separated), the equilibrium configuration will change accordingly.

With these considerations at hand, the inclusion of residual stresses in blood vessels models is of crucial importance for their accurate mechanical modelling and, thus residual stresses in longitudinal and circumferential direction have been included in the

majority of the simulations along this Thesis.

1.2.3.4 Anisotropy

The existence of preferred orientations for some of the microstructural components forming the vessels wall leads to the appearance of a marked anisotropic macroscopic behaviour. Specifically, anisotropy in vessels is associated to the preferred orientation of the collagen fibres, smooth muscle cells (SMC), or the elastin network in the media and adventitia layers. In the media, the preferred orientation of the collagen fibres and SMCs in each of the lamellae is different, see Figure 1.3. However, experimental studies demonstrate that the preferred orientation is almost circumferential, but with a different mismatch angle for each lamella. Furthermore, it is worth noting that the fibres average orientation exhibits certain radial component (Rhodin, 1980). In addition, histological studies show that smooth muscle cells are arranged along the preferred orientations of fibres (Holzapfel *et al.*, 2000; Holzapfel, 2006). Concerning the adventitia, its microstructure is more disorganized, which makes it difficult to determine a preferred orientation (Gasser *et al.*, 2006).

In order to try to reproduce the particular microstructure of arteries, a feasible possibility, which is widely accepted in arterial modelling, is to consider two directions of anisotropy helically oriented at $\pm\beta$ with respect to the circumferential direction (Holzapfel *et al.*, 2000). This assumption considers that the varying orientation of fibres in each lamella is mimicked by assuming a homogeneous orientation, which is frequently assumed constant across the thickness of the media and adventitia layers, that is, layers are considered homogeneous (Clark and Glagov, 1985).

In which the orientation angle is concerned, experimental measurements show that the average orientation angle of the human blood vessels is narrower for the media, in which $0° \leq \beta \leq 20°$ are typically found values, whereas wider angles are found in the adventitia, where values $40° \leq \beta \leq 60°$ are found (see, e.g., Holzapfel *et al.*, 2000; Holzapfel and Ogden, 2003; Landuyt, 2006). Concerning the fibre orientation component along the radial direction, which is not considered by this approach, the inclusion of certain dispersion with respect to the main anisotropy direction can partly compensate this lacking (Holzapfel *et al.*, 2005b; Gasser *et al.*, 2006; Alastrué *et al.*, 2009a,b).

In this thesis, the helical orientation of fibres has been assumed for the modelling of the arterial layers.

1.2.3.5 Incompressibility

Soft tissues in general and, in particular, blood vessels, are composed of elastin, collagen and smooth muscle cells, and a fluid part that is mainly an extracellular aqueous solution. The high water content of the vascular wall (70-80%) suggests that they should be considered as incompressible. Although some authors have tried to model blood vessels as a poroelastic medium (Simon *et al.*, 1998), experimental evidence collected

by Chuong and Fung (1984) revealed that despite the large amount of water, it is not free to move, which does not advice the use of the poroelastic approach.

On the other hand, the high water content of soft tissues justifies the usual assumption that they are almost incompressible. Although this is not strictly true, as there may be certain movements of fluids (Chuong and Fung, 1984) within the tissue induced by stress gradients, vascular samples undergo isochoric deformations under a wide variety of loads and, specifically, under physiological loads. This approach, which is the mainstream in blood vessels modelling and has been assumed in this Thesis, is supported by other experimental studies (Lawton, 1954; Carew *et al.*, 1968; Dobrin and Rovick, 1969).

1.2.3.6 Mechanical behaviour

Like most soft tissues, blood vessels display a highly non-linear behaviour, which progressively stiffens with increasing applied loads. In addition, blood vessels show increased circumferential stiffening with increasing axial stretch, although the axial force-length behaviour is less sensitive.

The first study that tried to quantify the non-linear mechanics of the arterial wall by considering its layered structure was carried out by Von Maltzahn *et al.* (1981). In a later experiment (Von Maltzahn *et al.*, 1984), they performed multiaxial tests in bovine carotids, both intact and free from the adventitia. They concluded that both layers are anisotropic, with a stiffer media that supported higher stresses than previously thought. Both layers were stiffer in the axial direction. Demiray and Vito (1991) published mechanical data on the mechanical response of the individual layers obtained from uniaxial experiments in the axial and circumferential directions of the canine aorta. Their results seemed to indicate that the adventitia was stiffer than the media, though both were practically isotropic. Later, however, the same authors suggested that the media was cylindrically orthotropic.

Thus, experimental tests confirm that media and adventitia behave differently, although the stress-strain relation characteristic of both layers, however, are of the same type for both of them (see, e.g., Holzapfel *et al.*, 2005b). Specifically, both layers exhibit an anisotropic non-linear behaviour which stiffens for increasing loads. Furthermore, these tissues undergo finite stretches under physiological loads, which must be accounted for in order to choose the appropriate modelling framework (Fung, 1990; Humphrey, 2002b; Holzapfel and Ogden, 2003).

1.3 Atherosclerosis and atheroma plaque formation

Cardiovascular disease refers to any disease that affects the cardiovascular system. The causes of cardiovascular disease are diverse but atherosclerosis, which is a complex disease that is believed to be initiated and promoted by linked biochemical and biomechanical pathways, is the most common. This thesis focuses on studying in depth the

mechanical environment of atherosclerotic lesions and consequently identifying high risk atheroma plaques.

1.3.1 Atherosclerosis disease

Atherosclerosis is a pathological process in which plaques, consisting of deposits of cholesterol and other lipids, calcium and large inflammatory cells called macrophages, connective tissue and other substances, are built up in the inner lining of the arterial walls of the arteries (Lusis, 2000). This fatty tissue, known as atheroma, cause narrowing or stenosis of the lumen, rupture or erosion of the arterial wall, hardening of the arteries and loss of their elasticity, which leads to an eventually or complete reduction in the blood flow through the vessels. Nevertheless, the most serious damage occurs when the plaque becomes fragile and ruptures (vulnerable plaque). Plaque rupture causes the formation of blood clots that can block blood flow or break off and travel to another part of the circulatory system thus producing heart attacks, strokes, difficulty in walking and eventually gangrene (Kyriacou *et al.*, 1996; Hanke *et al.*, 2001; Libby *et al.*, 2002; Thubrikar, 2007).

Population based studies show that atherosclerosis, the major precursor of cardiovascular disease, begins in childhood and advances throughout adulthood. Vanhecke *et al.* (2006) demonstrated that intimal lesions appear in all the aortas and more than half of the right coronary arteries of youths aged 7-9 years. Figure 1.8 shows the atherosclerosis evolution, it tends to begin as a fatty streak on the endothelial surface but usually develops into a focally thickened intima. After that, the atheroma plaque begins to grow deeply until its rupture. Moreover, the longitudinal and transversal atherosclerosis vessel sections of this figure illustrates how the atheroma plaque growth produces the blockage of the blood flow (Fuster and Kelly, 2010).

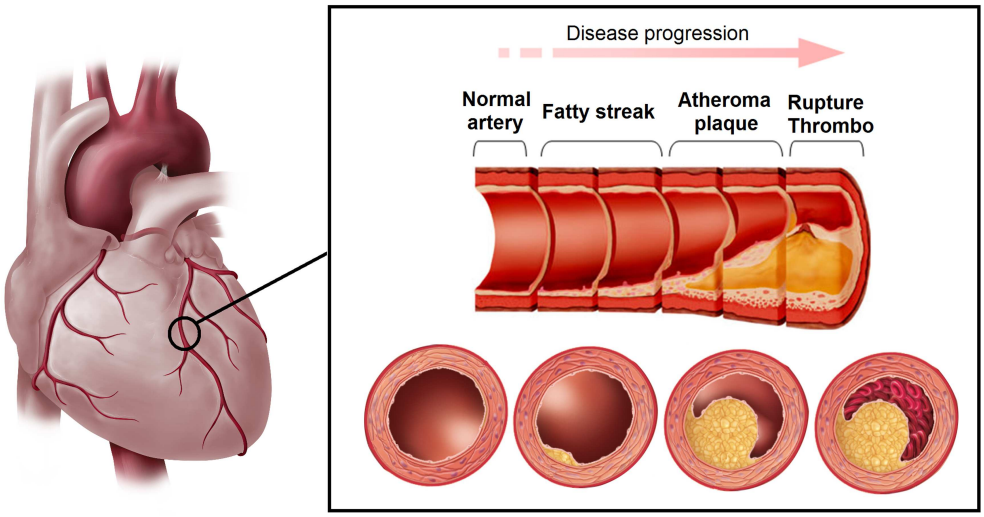

Figure 1.8: Progression of the atherosclerosis disease.

Considering that the atherosclerosis disease is associated with deficiency of blood supply due to obstruction (ischemia/angina), strokes and damage to blood vessels, muscles, or body organs, this disease leads to several important human vascular disorders, such as;

- Cerebrovascular disease: Ischemia and cerebral infarction (Figure 1.9.a).
- Coronary artery disease: Coronary thrombosis, angina, heart attack or heart failure and myocardial infarction (Figure 1.9.b).
- Diseases of the kidney: Renal ischemia (Figure 1.9.c).
- Aorta and peripheral vascular disease; gangrene and difficulty walking, embolism, leg blood clot, claudication and thrombus formation (Figure 1.9.d).

Figure 1.9 summarizes and illustrates some of the main atherosclerosis events described above. These disorders, that occur when plaques rupture, are responsible for more deaths than any other diseases in humans (Lusis, 2000; Yuan *et al.*, 2000; Libby *et al.*, 2002).

It should be highlighted that this Thesis is mainly focused on the atherosclerotic plaques developed in the coronary artery (see Chapters 2, 3, 4 and 6) and along the aortic tree (see Chapter 5).

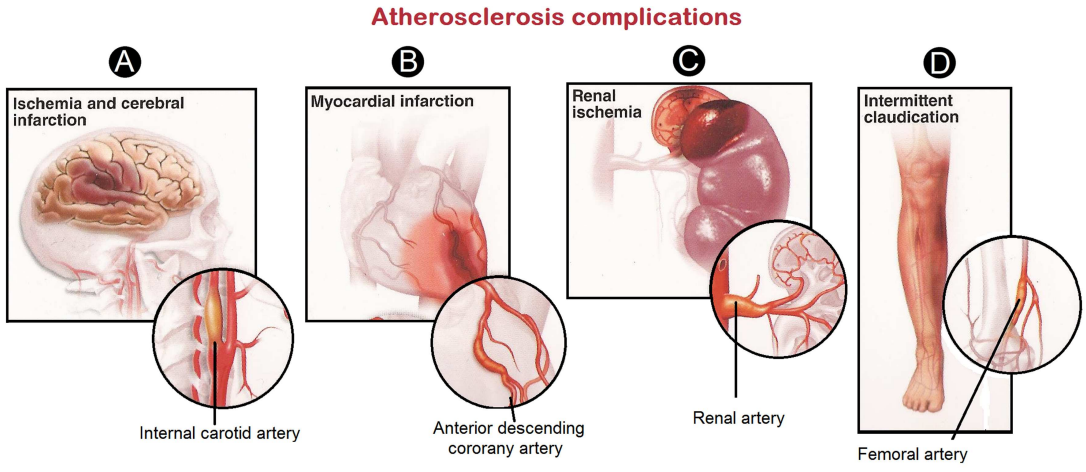

Figure 1.9: Main complications produced by atherosclerosis disease

1.3.2 Localization of atherosclerotic plaque

Atherosclerosis occurs mainly in larger and medium size arteries, which involves an abnormal accumulation of high molecular weight lipoprotein in the arterial wall (Tarbell and Qiu, 2000). In humans, atherosclerotic deposits are most frequently observed in abdominal aorta, coronary arteries, arteries of legs (femoral, iliac, etc.), arch and

descending thoracic aorta, internal carotids, and Circle of Willis (arteries of the brain). The lesions are often related with the most susceptible areas where blood flow has flow separation and recirculation, resulting in a weak net hemodynamic shear stress (Yuan *et al.*, 2000). Thus, the disease tends to be localized in regions of the outer walls of bifurcations and the inner walls of curvatures where fluid shear stress is altered from its normal patterns (Tarbell and Qiu, 2000; Ethier, 2002). These locations correspond to arterial bends, bifurcations, and in general sites presenting low velocity and wall shear stress (Tarbell and Qiu, 2000; Yuan *et al.*, 2000; Ethier, 2002).

1.3.3 Atherosclerosis risk factors

Although cardiovascular disease usually affects older adults, notably atherosclerosis begin in early life, making primary prevention efforts necessary from childhood. There is therefore increased emphasis on preventing atherosclerosis by modifying risk factors. Atherosclerosis risk factors are conditions or behaviors that increase your chances of getting a certain disease, and they can be classified as either modifiable or non-modifiable (Metha *et al.*, 1998; Grundy, 2002; Corti *et al.*, 2002; Bonetti *et al.*, 2003).

Some risk factors can be modified, treated or controlled through lifestyle changes or by taking medicine. Examples of risk factors for atherosclerosis you have control over include,

- Unhealthy blood cholesterol levels or hypercholesteremia or hyperlipidemia: This includes high LDL (low-density lipoprotein) cholesterol (sometimes called bad cholesterol) and low HDL (high-density lipoprotein) cholesterol (sometimes called good cholesterol).
- High blood pressure: Blood pressure is considered high if it stays at or above 90/140 mmHg over a period of time.
- Smoking: This can damage and tighten blood vessels, raise cholesterol levels, and raise blood pressure. Furthermore, smoking also does not allow enough oxygen to reach the body tissues.
- Overweight or obesity: Overweight is having extra body weight from muscle, bone, fat, and/or water. Obesity is having a high amount of extra body fat.
- Lack of physical activity or sedentary lifestyle: Lack of activity can worsen other risk factors for atherosclerosis.
- Insulin resistance: Insulin is a hormone that helps move blood sugar into cells where it is used and insulin resistance occurs when the body cannot use its own insulin properly.
- Diabetes mellitus: This is a disease in which the body blood sugar level is high because the body does not make enough insulin or does not use its insulin properly.

- Alcohol consumption: Heavy drinking can damage the heart muscle and worsen other risk factors for atherosclerosis.
- Stress: Research shows that the most commonly reported trigger for a heart attack is an emotionally upsetting event particularly one involving anger.

However, there are other risk factors that can not be controlled such as,

- Age: As the body ages, the risk for atherosclerosis increases and genetic or lifestyle factors cause plaque to gradually build in the arteries. By middle age or older, enough plaque has built up to cause signs or symptoms, in men, the risk increases after age 45, while in women, the risk increases after age 55.
- Family history of early heart disease or heredity.
- Gender: Generally, men have a greater risk of heart disease than women, and they have heart attacks earlier in life. Moreover, even after menopause, when the death rate from heart disease increases for women, is still lower than the death rate for men.

Scientists continue to study other possible risk factors for atherosclerosis and have found that high levels of a protein called C-Reactive Protein (CRP) in the blood may raise the risk for atherosclerosis and heart attack. High levels of CRP are a proof of inflammation in the body which is the body response to injury or infection. Damage to the inner walls of the arteries appears to trigger inflammation and help plaque grow. People with low CRP levels may get atherosclerosis at a slower rate than people with high CRP levels and research is currently under way to establish whether reducing inflammation and lowering CRP levels also can reduce the risk of atherosclerosis (Altman, 2003; Glowinska *et al.*, 2003; Fruchart *et al.*, 2004). Furthermore, high levels of fats called triglycerides in the blood also may raise the risk of atherosclerosis, specially in women. In particular, triglyceride-rich lipoprotein remnants appear to have a major impact on risk (Bhatt and Topol, 2002; Bonetti *et al.*, 2003; Glowinska *et al.*, 2003). The combination of traditional risk factors and emerging risk factors is expected to facilitate the assessment of patient global risk, thereby allowing optimal use of diagnostic and therapeutic efforts in high-risk subjects.

1.3.4 Atheroma Plaque Rupture

Atheroma plaque lesions prone to rupture which show high activity and instability are referred as vulnerable plaque (Corti *et al.*, 2002; Naghavi *et al.*, 2003; Naghavi and Falk, 2010; Finn *et al.*, 2010). The characteristics of vulnerable plaque have been well defined in several pathological studies (Salunke *et al.*, 2001; Naghavi *et al.*, 2003; Fuster *et al.*, 2005; Virmani *et al.*, 2006; VanEpps and Vorp, 2007) amongst others. The specific mechanisms by which a vulnerable plaque ruptures remain unknown and

it may occur without obvious clinical symptoms. Plaque rupture is believed to be related to plaque morphology, mechanical forces, vessel remodelling, blood conditions (levels of cholesterol, sugar, etc.), chemical environment and lumen surface conditions (inflammation) (Van der Wal and Becker, 1999). After numerous histopathological studies of disrupted plaques, there is widespread unanimity in the belief that a large lipid core occupying at least 50% of the overall plaque volume, and a thin plaque cap, in which the collagen structure is disorganized, are the major structural components of rupture prone plaques (Falk, 1989, 1992; Davies, 2000).

Several rupture mechanisms have been proposed, usually in two categories. One is the biological abnormalities in the plaque components; the other is the biomechanical factors. The biological factors can cause weakening of plaques at the regions of extreme stress situations which in turn extreme stress can affect the biological disorders at those regions (Arroyo and Lee, 1999).

Biological abnormalities in the plaques have been well considered to be related to plaque vulnerability, such as enhanced inflammatory activities, accumulation of macrophages, extracellular matrix degradation (Lendon *et al.*, 1991; Shah *et al.*, 1995; Ashwini *et al.*, 2003). The study of Moreno *et al.* (1994) on macrophage content in coronary plaque tissue from patients with stable and unstable coronary syndromes showed that macrophage rich areas are more frequently found in patients with unstable angina, suggesting that macrophage is a marker of unstable atherosclerotic plaques and may play a significant role in plaque rupture. Libby *et al.* (1996) demonstrated that ruptured plaques usually have thin fibrous cap overlying a large thrombogenic lipid core rich in lipid laden macrophages, those monocyte derived macrophages assume critical roles in plaque stability. Plaque macrophages are capable of expressing a variety of matrix degrading enzymes that can contribute to the weakening of the fibrous cap, and finally influence the lesion stability. Stefano *et al.* (2009) discussed the potential role of intraplaque angiogenesis as a risk factor for plaque vulnerability, because those immature blood vessels are aviable source of intraplaque haemorrhage providing erythrocyte derived phospholipids and free cholesterol. A recent study of Dunmore and McCarthy (2007) has found that symptomatic carotid plaques contain abnormal, immature microvessels, contributing to plaque stability by acting as sites of vascular leakage for inflammatory cell recruitment. Thin cap atheroma has also been believed to be the precursor of plaque rupture, which may account for a majority of coronary thrombi (Virmani *et al.*, 2003). Still there is a lot of research continuing to find the biological factors which could be linked to plaque vulnerability.

Biomechanical factors also have been considered to be important triggers in plaque rupture. Many studies have been carried out to associate extreme biomechanical stress situations with plaque rupture.

- Local maximum stress: Regarding the mechanical environment, several studies (see, e.g., Ohayon *et al.*, 2005; Versluis *et al.*, 2006) consider the peak circumferential stress (PCS) as the determining biomechanical factor in the mechanisms

leading to rupture of the atherosclerotic plaque and is often used as a predictor of atherosclerotic plaque rupture location. Otherwise, previous works have shown that reduced fibrous cap thickness increases the maximal value of the PCS exponentially, and leads the cap stress to exceed the rupture threshold of 300 kPa (Lendon *et al.*, 1991; Cheng *et al.*, 1993; Ohayon *et al.*, 2005) for thin fibrous caps. For the coronary artery, a fibrous cap has been defined as thin when it is less than 65μm in its minimum thickness (Moreno *et al.*, 2002; Finet *et al.*, 2004; Vengrenyuk *et al.*, 2006; Virmani *et al.*, 2006).

- Fatigue failure: Bank *et al.* (2000) hypothesized that mechanical fatigue on fibrous cap caused by pulstile blood flow may be an important factor causing plaque rupture. The growth of plaque fatigue crack based on this hypothesis has been simulated by evolving stress distribution in plaques (Versluis *et al.*, 2006).

- High wall shear stress: It has been linked to plaque rupture (Groen *et al.*, 2007, 2008) based on the findings that plaque ulceration occurs at the high wall shear stress location.

- Effect of microcalcifications: The role of microcalcifications in plaque rupture is a controversial topic. On the one hand, the hypothesis for vulnerable plaque rupture due to stress induced around cellular microcalcification in thin fibrous caps based on the fact that cellular level microcalcifications in a thin cap can cause local stress concentrations has been proposed by many authors (Vengrenyuk *et al.*, 2006; Li *et al.*, 2007b; Bluestein *et al.*, 2008; Wenk, 2011; Maldonado *et al.*, 2012, see, e.g.,). These studies suggest that the microcalcifications increase the plaque vulnerability and shift the maximal principal stress (MPS) to the region of the microcalcification. However, on the other hand, some studies indicate beneficial effects in stabilizing the plaque (Cheng *et al.*, 1993; Huang *et al.*, 2001; Wong *et al.*, 2012).

- Other hypotheses: It includes injury due to turbulent flow in the stenosis (Loree *et al.*, 1991), rupture of vasa vasorum (Barger *et al.*, 1984) or great arterial deformations in areas where atheroma plaque is found (Aoki and Ku, 1993; McCord and Ku, 1993; Mizushige *et al.*, 1993).

Comparing with the others, the local maximum stress hypothesis is the most wildly accepted one which is also the one that is followed in this Thesis. Several studies have been carried out to correlate high stress regions with rupture sites to provide evidence for plaque rupture caused by extreme stresses. Cheng *et al.* (1993) studied the stress concentration locations compared with the rupture sites based on 2D histological plaque samples, they found that the circumferential stress concentrations had a good correlation with rupture sites in their study. Ohayon *et al.* (2001) found that the peak circumferential stress areas correlated well with plaque rupture sites by comparing the plaque rupture locations on post-angioplasty intravascular ultrasound images with 3D

structure stress analysis. However the biomechanical factors related rupture hypothesis has not been fully verified *in vivo*, due to the difficulties such as there is no technique that can directly measure wall stress in the plaque *in vivo* and the geometry of a specific plaque at pre and post rupture status is practically unachievable. Nonetheless, to work on any stress related hypothesis, obtaining accurate stress distribution on the specific plaque is essential.

1.3.5 Atherosclerosis plaque detection and treatment

Atherosclerotic plaques develop over a long period of time before symptoms appear and in 50% of the population it is asymptomatic. Early detection and follow up of such vulnerable plaques are a major challenge to prevent acute coronary syndromes and cardiac events. In recent years, cardiovascular research has sought potential clinical strategies to overcome the limited ability to detect high-risk plaques and eventually guide targeted therapy (MacNeill *et al.*, 2003). Imaging techniques that enable visualization of structural and morphologic characteristics of the atherosclerotic plaque may be helpful to identify the characteristics of the vulnerable plaque *in vivo* and subsequently predict clinical outcome. Several methods have been used to evaluate the extent and location of atherosclerotic lesions which detect indicators of atherosclerosis such as classical risk factors (Lee *et al.*, 1993; Fayad and Fuster, 2001; Virmani *et al.*, 2006; Kips *et al.*, 2008). Conventional vascular imaging technologies, which either assess morphological characteristics of plaques or functional properties, rely on observation of luminal narrowing (stenosis) for the detection of atherosclerotic plaques. These technologies are either invasive, as with coronary X-ray angiography and intravascular ultrasound (IVUS), or noninvasive as with magnetic resonance imaging (MRI), duplex ultrasound and carotid intimal-medial thickness (CIMT) measurements. Preferably, imaging of atherosclerosis is performed non-invasively to minimize potential damage to the patient due to the imaging procedure itself (MacNeill *et al.*, 2003; Briley-Saebo *et al.*, 2007; Kips *et al.*, 2008). Each of these techniques has strengths and weaknesses for imaging atherosclerosis, and none have yet been determined to be the definitive diagnostic tool for atherosclerotic plaque detection.

Traditionally, only the fibrous cap thickness and the stenosis ratio have typically been identified as the key predictor of vulnerability and likelihood of rupture, and, generally, clinical procedures for detection of these vulnerable plaques are only performed by measuring these parameters on image analysis. Based on several studies (Burke *et al.*, 1997; Moreno *et al.*, 2002; Virmani *et al.*, 2006, see, e.g.,), a cap thickness of 65 μm has been suggested as a criterion of instability for coronary plaques. However, some clinical and biomechanical studies (Virmani *et al.*, 2000; Krishna Kumar and Balakrishnan, 2005; Ohayon *et al.*, 2007, 2008) shown that the fibrous cap thickness alone is not a sufficiently accurate predictor for plaque stability, since plaque stability also depends on other intrinsic properties of the plaque, such as the size and the consistency of the soft atheroma core (Finet *et al.*, 2004; Gao and Long, 2008), the presence of microcalci-

fications (Lee *et al.*, 1996; Kaazempur-Mofrad *et al.*, 2004; Vengrenyuk *et al.*, 2006), the cap and the core inflammation levels (Arroyo and Lee, 1999; Lee, 2000) and the arterial remodelling index, which is defined as the external elastic membrane area at plaque divided by the external elastic membrane area at a nearest segment judged to be free of plaque. (Smedby, 1998; Varnava *et al.*, 2002; Ohayon *et al.*, 2008). Additionally, the study by Kumar and Balakrishnan (2005) demonstrated that the extreme stress situation in plaque had a direct relation with the thickness of the lipid pool and an inverse relation with cap thickness and lumen stenosis, and stress in a positively remodeled vessel is significantly greater than more negative remodeling plaques. Positive remodeling (compensatory enlargement) is defined as the enlargement of an artery to keep the lumen area to be the same as the normal condition with plaque accumulation in the arterial wall. The negative remodeling is referred to the plaques with narrowed lumen area. The term of positive remodeling was first introduced by Glagov *et al.* (1987). Consequently, the lipid core length and width are also very important and influential parameters on maximal principal stress (MPS). Thus, these parameters should also be measured by the clinical staff. Moreover, features such as the positive and negative remodeling should be taken into account.

Procedures to detect plaque prone to rupture and to predict rupture location are very valuable for clinical diagnosis. Nowadays clinical procedures for detection of these vulnerable plaques are only performed by image analysis but not by FE analysis. However, these analyses are sometimes used in pre-operatory surgical planning when clinical staff have enough time to perform the computational model and analyze the results. However, the use of FE computations presents the disadvantage of very high computational cost, usually hours or even days, whereas an immediate response is required. Hence, there are a need to find an alternative method to available images methods and direct FE simulations to detect "vulnerable patients", specially when an instantaneous response is needed. The term "vulnerable patient" is proposed for the identification of individuals with a high likelihood of developing cardiac events in the near future (Naghavi and Falk, 2010).

Therefore, an alternative tool based on different Machine Learning Techniques (MLT), such as Artificial Neural Networks (ANN) and Support Vector Machines (SVM), applied to the study of the role of stress in plaque vulnerability in order to reduce the very long computation times and memory consumption required for 3D FE analysis is proposed in Chapter 4. The SVM (Vapnik, 1982) gives rise to a new class of theoretically elegant learning machines that use a central concept of SVM - kernels - for a number of learning tasks. Kernel machines provide a modular framework that can be adapted to different tasks and domains by the choice of the kernel function and the base algorithm (Scholkpof and Smola, 2002). MultiLayer Perceptron (MLP), as a representation of the ANN, is a feed-forward network characterized by its layered structure, each layer consisting of a set of perceptron neurons and its training algorithm (Bishop, 1995) (for more detail about the MLT, ANN and SVM theories see Section 4.3 of Chapter 4). The

alternative MLT tool developed uses an intelligent algorithm to predict the atheroma plaque rupture in terms of four of the most influential geometrical factors in the plaque rupture: (i) fibrous cap thickness; (ii) stenosis ratio; (iii) lipid core width and (iv) lipid core length. The output predicted is the maximum MPS occurred in an atherosclerotic coronary vessel with the input dimensions. Summing up, the procedure proposed would be carried as follows: for a specific patient, clinical staff should measure just four parameters in standard IVUS images and then, by using the ANN or SVM techniques, they would have an immediate response on the atheroma plaque vulnerability. Parametric FEM analysis would have been performed before in order to feed the ANN or SVM algorithms and the data base.

In summary, despite major advances on the treatment of atherosclerosis, unfortunately, the available screening and diagnostic methods are unable to reliably predict the high risk plaque associated with a particular lesion. Identifying vulnerable patients before plaque rupture occurs would help clinicians to provide early treatment as well as to take preventive measures.

Atherosclerotic lesions can be treated in several ways. The most important treatment methods can be categorized to:

- Non-surgical or pharmacological treatments such as risk-factor minimization or reduction of fat and cholesterol in blood.
- Minimally invasive treatments such as balloon angioplasty or stenting.
- Extensive surgical treatments like bypass grafting, endarterectomy, bypass grafting or amputation.

1.3.6 Stages of atherosclerosis and process of plaque formation

Stenotic atheroma plaques partly result from fatty deposits caused by hemodynamic and inflammatory factors as described previously. Besides these fatty accumulations, there are other molecules that play important roles in atheroma plaque build-up and rupture. These molecular components are listed and described below (Van der Wal and Becker, 1999).

- Calcium and microcalcifications: They contribute to the stiffening of the arterial wall. Arterial wall calcification has always been associated with severe stenosis. The role of calcium and microcalcifications in the vulnerable plaque rupture mechanics is still debated. Some studies indicate beneficial effects in stabilizing the plaque (Cheng *et al.*, 1993; Huang *et al.*, 2001), whereas others suggest that they increase the plaque vulnerability and shift the MPS to the calcified region (Bluestein *et al.*, 2008; Wenk, 2011).
- Collagen: It is a group of naturally occurring proteins found in animals, especially in the flesh and connective tissues of vertebrates. It is the main component of

connective tissue, and is the most abundant protein in mammals, making up about 25% to 35% of the whole-body protein content. It is non-uniformly distributed in the plaque and contributes to local hardening of the plaque (Di Lullo *et al.*, 2002).

- Endothelial cells: Thin flattened cells lining the inside surfaces of blood vessels that provide an anticoagulant barrier between the vessel wall and blood. In addition to its role as a selective permeability barrier, the endothelial cell is a unique multifunctional cell with critical basal and inducible metabolic and synthetic functions. The endothelial cell reacts with physical and chemical stimuli within the circulation and regulates hemostasis, vasomotor tone, and immune and inflammatory responses. Their lesions or dysfunctions are the principal cause of plaque development since endothelial cell injury, activation or dysfunction is a hallmark of many pathologic states including atherosclerosis, loss of semi-permeable membrane function, and thrombosis.

- Low-Density Lipoproteins (LDL): Proteins that act as carriers for cholesterol and fats in the bloodstream. They are involved in the initiation of the atherosclerotic plaque. LDL level over 130-160 mg/dl is considered as positive risk factor for the development of atherosclerosis.

- Macrophages: Small, active white blood cells produced by the differentiation of monocytes in tissues. Macrophages function is both non-specific defense (innate immunity) as well as help initiate specific defense mechanisms (adaptive immunity) of vertebrate animals. Their role is to phagocytose, or engulf and then digest, cellular debris and pathogens, either as stationary or as mobile cells. They also stimulate lymphocytes and other immune cells to respond to pathogens. They are specialized phagocytic cells that attack foreign substances, infectious microbes and cancer cells through destruction and ingestion. In the atheroma plaque development, they are specializing in engulfing, killing and digesting LDL proteins. Furthermore, they can assault collagen and then weaken the plaque locally.

- Metalloproteinase: Enzymes that utilize metal in the catalytic mechanism (accelerating chemical reaction without being consumed or changed). It is always associated with plaque rupture.

- Monocytes: Monocytes are a type of white blood cell and are part of the innate immune system of vertebrates including all mammals (humans included), birds, reptiles, and fish. Monocytes play multiple roles in immune function. Such roles include replenish resident macrophages and dendritic cells under normal states, and in response to inflammation signals, monocytes can move quickly (approximately 8-12 hours) to sites of infection in the tissues and divide/differentiate into macrophages and dendritic cells to elicit an immune response.

- Platelets or thrombocytes: Small, irregularly shaped clear cell fragments (i.e. cells that do not have a nucleus containing DNA) found in large number in blood. They are important for blood coagulation and reparations of breaches in the walls of blood vessels.

- T-Cells: Also called T-Lymphocytes, coordinate the immune system by secreting growth factors called lymphokine hormones. Their activations by macrophages or vascular smooth muscle cells through oxidized LDL result in secretion of cytokines which stimulate inflammatory response. Thereby they favor disruption of the lesion.

- Vascular smooth muscle cells: They are found in blood vessel walls and contribute largely to mechanical properties of the artery.

The normal muscular artery and the cell changes that occur during disease progression to thrombosis are shown in Figure 1.10. Figure 1.10.a shows the normal artery which contains the three layers described in Section 1.2.1 of this Chapter. Figure 1.10.b depicts the initial steps of atherosclerosis, which corresponds to endothelial dysfunction, which is characterized by increased endothelial permeability to lipoproteins and other plasma constituents. Formation of atherosclerotic lesions is proceeded by intimal thickness and lipid accumulation (Yuan *et al.*, 2000; Libby *et al.*, 2011). The adhesion of blood leukocytes to the activated endothelial monolayer, directed migration of the bound leukocytes into the intima is produced. After that, it takes place the maturation of monocytes (the most numerous of the leukocytes recruited) into macrophages, and their uptake of lipid, yielding foam cells. Fatty streak is the first macroscopically visible stage of atherosclerosis, which initially consists of lipid-laden molecules: monocytes, macrophages (foam cells) and T-lymphocytes (Ross, 1986; Yuan *et al.*, 2000; Libby *et al.*, 2011). As Figure 1.10.c shows, lesion progression involves the migration of SMCs from the media to the intima, the proliferation of resident intimal SMCs and media-derived SMCs, and the heightened synthesis of extracellular matrix macromolecules such as collagen, elastin and proteoglycans. Plaque macrophages and SMCs can die in advancing lesions, some by apoptosis. Extracellular lipid derived from dead and dying cells can accumulate in the central region of a plaque. Advancing plaques also contain cholesterol crystals and microvessels. Thus, intermediate and advanced lesions tend to form a fibrous cap that walls off the lesion from the lumen. Fibrous cap covers a mixture of leukocytes, lipid and debris, which give rise to a necrotic core. These lesions expand at their shoulders by means of continued leukocyte adhesion and infiltration. Finally, the ultimate complication of atherosclerosis is shown in Figure 1.10.d, disruption of plaque leads to the formation of an occlusive thrombus, leading to unstable plaque surface or fibrous cap; this produces clinical complications like angina, myocardial infarction, or sudden death (Ross, 1986; Nemirovsky, 2003; Libby *et al.*, 2011).

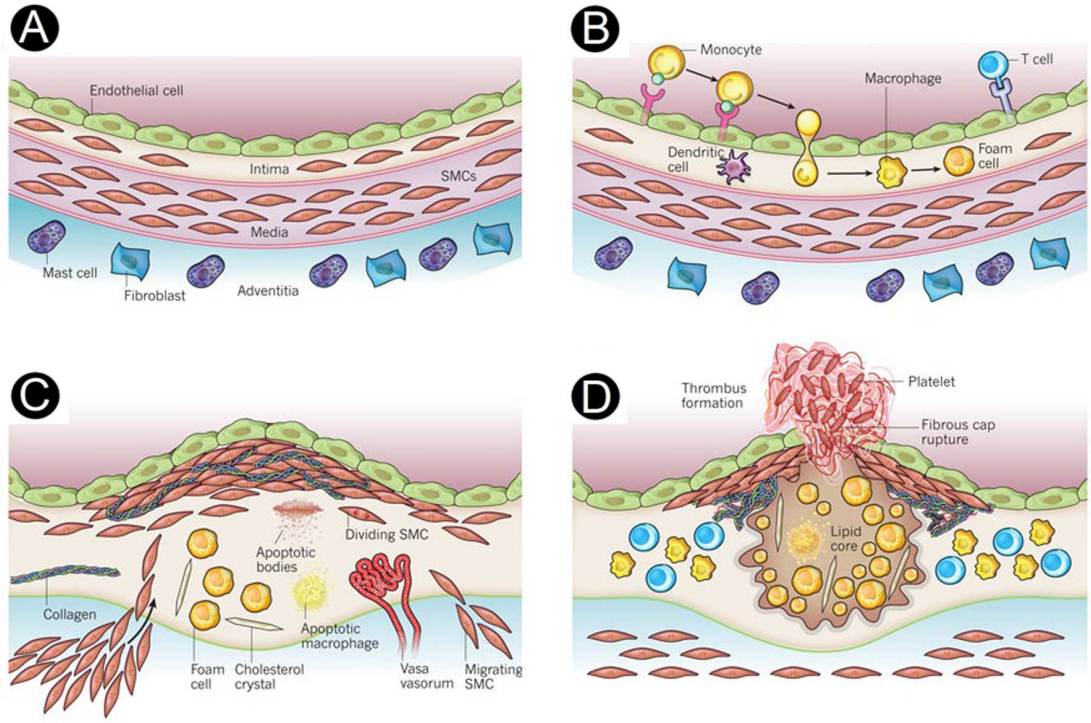

Figure 1.10: Stages in the development of atherosclerotic lesions. Illustration based on Libby *et al.* (2011)

Inflammation during macrophage foam cell formation plays an important role during the progression of atherosclerosis, because it is involved with lesion initiation, lesion progression, and with thrombotic complications. Hence, inflammation of the artery is the main factor leading to early atheromas. From this stage on, the stenosis can either progress into a stable plaque or a vulnerable plaque (see Figure 1.11). Figure 1.11 presents each of the histopathological features that precede the formation of an advanced atherosclerotic lesions. The main characteristics of these atherosclerotic lesions are as following:

- Stable: The fibrous plaque is localized under the intima resulting into thickening and expansion of the wall, and often into spotty localized narrowing of the lumen, with some atrophy of the muscular layer. The fibrous plaque contains mostly collagen fibres, precipitates of calcium, and rarely lipid-laden cells.
- Vulnerable: The plaque is characterized by an accumulation of lipid-laden cells underneath the intima, typically without narrowing the lumen due to compensatory expansion of the bounding muscular layer of the artery wall. Beneath the endothelium there is a fibrous cap covering the atheromatous core of the plaque. The core, or lipid pool consists of macrophages and smooth muscle cells, fibrin, collagen, and cellular debris. In advanced plaques, the central core of the plaque

usually contains extracellular cholesterol deposits. The periphery of the plaque is composed by younger foamy cells and capillaries.

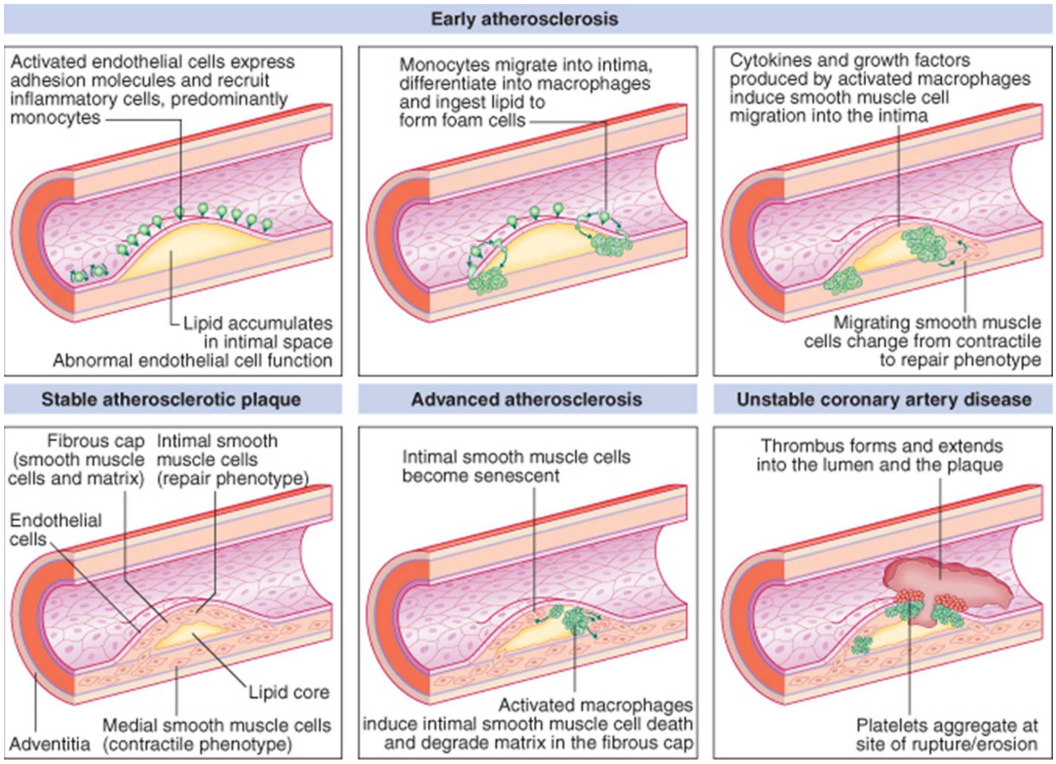

Figure 1.11: Atheroma plaque progress into a stable plaque or a vulnerable plaque.

In Chapter 6 a simplified model which takes into account these mechanobiological processes is presented.

1.4 Cardiovascular modelling - Constitutive modelling of anisotropic material

In the context of mathematical modelling and FE simulation, the experimental data are used to estimate the material model parameters through a strain energy function (SEF) within the framework of the continuum theory of large deformation hyperelasticity. A brief review of the most widely used constitutive laws in the modelling of passive elastic behaviour of blood vessels is here presented.

In order to define the mathematical model of the tissue behaviour (blood vessel wall, atheroma plaque and lipid core) several considerations should be taken account. Firstly, the tissue samples experienced finite strains for small loads. Secondly, a strongly marked nonlinearity was found. Thirdly, there is a remarkable anisotropy behaviour in the tissue belong to the blood vessel wall. Thus, a preferential direction of anisotropy

is considered, through the angle β referred to the circumferential direction. Atheroma plaque and lipid core tissue are considered as isotopic materials.

1.4.1 Constitutive modelling of the passive elastic behaviour

Within the framework of hyperelasticity, a brief review of the constitutive laws frequently used for modelling the passive behaviour of soft biological tissues, in particular of the vascular tissue, is presented in this section. Accounting for the nature of the models, they have been grouped into isotropic and anisotropic (see, e.g., the reviews by Vito and Dixon, 2003; Kalita and Schaefer, 2008, and references therein).

The considered strain energy functions are suitable for modelling fully three dimensional load states, and have been presented as a function of the invariants of the right Cauchy-Green tensor (and the invariants for the anisotropic functions) (Spencer, 1971), or the principal stretches of the deformation gradient tensor (see Appendix A).

A common way to formulate an elastic constitutive law under isothermal conditions for soft tissues is to postulate the existence of a SEF. For nearly incompressible materials, the strain energy function is additively split into volumetric and isochoric contributions (Flory, 1961) as

$$\Psi = \Psi_{\text{vol}} + \Psi_{\text{ich}}, \tag{1.3}$$

where the volumetric contribution $\Psi_{\text{vol}}(J)$ accounts for the energy variations due to volume variations as a function of the local volume ratio $J = \det(\boldsymbol{F})$ (see Appendix A). On the other hand, Ψ_{ich} represents the volume changes due to purely shear deformations, which are defined by the isochoric deformation gradient.

$$\bar{\boldsymbol{F}} := J^{-1/3}\boldsymbol{I} \cdot \boldsymbol{F}. \tag{1.4}$$

Thus, note that it is possible to apply the decomposition in (1.3) to the aforepresented constitutive relations by considering them as the isochoric contributions to the total strain energy. Accordingly, the dependence on the principal stretches should be replaced by their isochoric version $\bar{\lambda}_{1,2,3} = J^{-1/3}\lambda_{1,2,3}$, and the right Cauchy-Green tensor by its isochoric counterpart $\bar{\boldsymbol{C}} = J^{-2/3}\boldsymbol{C}$ (see the expressions for the isochoric invariants in Section A.3.2.1).

The constitutive equation for quasi-compressible hyperelastic materials can be defined from the Clausius-Planck inequality as:

$$\boldsymbol{S} = 2\frac{\partial \Psi(\boldsymbol{C})}{\partial \boldsymbol{C}} = \boldsymbol{S}_{\text{vol}} + \boldsymbol{S}_{\text{ich}} = J\,\text{p}\,\boldsymbol{C}^{-1} + 2\frac{\partial \Psi_{\text{ich}}(\bar{\boldsymbol{C}})}{\partial \bar{\boldsymbol{C}}} \tag{1.5}$$

where the second Piola-Kirchhoff stress $\boldsymbol{S}$ consists of a purely volumetric contribution $\boldsymbol{S}_{\text{vol}}$ and a purely isochoric one $\boldsymbol{S}_{\text{ich}}$; being $\text{p} = \dfrac{\partial \Psi_{\text{vol}}(J)}{\partial J}$ the hydrostatic pressure. The Cauchy stress tensor $\boldsymbol{\sigma}$ is $1/J$ times the push-forward of $\boldsymbol{S}$ ($\boldsymbol{\sigma} = J^{-1}\boldsymbol{\varphi}(\boldsymbol{S})$) (Holzapfel *et al.*, 2000).

Knowing the second Piola-Kirchhoff stress $\boldsymbol{S}$, the elastic tensor $\mathbf{C}$ is defined in the material configuration as follows:

$$\mathbf{C} = 2\frac{\partial \boldsymbol{S}(\boldsymbol{C})}{\partial \boldsymbol{C}} \tag{1.6}$$

The elastic tensor $\mathbf{C}$ consists of a purely volumetric contribution and a purely isochoric response (Holzapfel *et al.*, 2000):

$$\mathbf{C} = \mathbf{C}_{\text{vol}} + \mathbf{C}_{\text{ich}} = 2\frac{\partial \boldsymbol{S}_{\text{vol}}}{\partial \boldsymbol{C}} + 2\frac{\partial \boldsymbol{S}_{\text{ich}}}{\partial \boldsymbol{C}} \tag{1.7}$$

The elastic tensor in the spatial configuration, denoted by $\mathbf{c}$, is $1/J$ times the push-forward of $\mathbf{C}$ ($\mathbf{c} = J^{-1}\boldsymbol{\varphi}(\mathbf{C})$) (Holzapfel *et al.*, 2000).

1.4.1.1 Isotropic models

As discussed above, the microstructural composition of blood vessels is responsible of their anisotropic properties. Nevertheless, the first steps in the modelling of vascular tissue were to assume isotropic behaviour by analogy with the constitutive laws earlier developed for modelling rubber, with which soft biological tissues share some common features, such as the very low volumetric changes undergone under finite strains. Thus, it was straightforward to apply some of the constitutive laws elaborated for rubber-like materials to soft biological tissues and, specifically, to the vascular tissue behaviour.

Furthermore, although the histological composition of blood vessels renders an anisotropic behaviour, the use of isotropic constitutive laws to model the vessel behaviour in low load ranges, where the mechanical effect of collagen fibres is irrelevant, is an adequate approach. At those ranges, even though the tissue remains anisotropic (Holzapfel *et al.*, 2005b), the isotropic assumption provides an accurate approximation of the vascular tissue mechanical behaviour (see, e.g., Ohayon *et al.*, 2007).

The isotropic models can be classified into two groups. The first comprises the macroscopic models, in which a strain energy function is obtained disregarding the nature of the microstructural components of the tissue (see, e.g., Mooney, 1940; Demiray, 1972; Demiray *et al.*, 1988; Arruda and Boyce, 1993; Yeoh, 1993). Second, a group of microstructurally based models are presented, in which the macroscopic mechanical properties are obtained by assuming a constitutive relation for the microscopic components along each direction, whereas the macroscopic behaviour is obtained by integration of the contributions in all directions of space (see, e.g., Bažant and Oh, 1986; Carol *et al.*, 2004; Driessen *et al.*, 2005; Alastrué *et al.*, 2009a; Sáez *et al.*, 2012).

Since the macroscopic perspective has been selected to model the material mechanical properties on this Thesis, a more detailed description of macroscopic models is presented. Most isotropic macroscopic constitutive laws are particular cases of the polynomial model (1.8), which is obtained as the Taylor series expansion of a function $f(I_1 - 3, I_2 - 3)$, where I_1 and I_2 are the first and second invariants of the right

Cauchy-Green tensor $\boldsymbol{C}$, namely $I_1 = \mathrm{tr}\,(\boldsymbol{C})$ and $I_2 = \frac{1}{2}\left[[\mathrm{tr}\,(\boldsymbol{C})]^2 + \mathrm{tr}\left(\boldsymbol{C}^2\right)\right]$ (see Appendix A), getting

$$\Psi = \sum_{i+j=1}^{N} c_{ij}\,[I_1 - 3]^i\,[I_2 - 3]^j\,. \tag{1.8}$$

In this expression, the constants c_{ij} are stress-valued model parameters. Among all particular cases used to model the vascular tissue mechanical behaviour, the neo-Hookean constitutive law

$$\Psi = \mu\,[I_1 - 3] \tag{1.9}$$

is the simplest one, which determines the mechanical response of the material as a function only of the first invariant I_1 and the single constant $\mu \equiv c_{10}$ (Treloar, 1943b,a).

Also the well-known Mooney-Rivlin constitutive model (Mooney, 1940) in (1.10) has been used to model vascular tissue. This model is able to reproduce a wider range of mechanical non-linear behaviours, since additionally incorporates a term depending on the second invariant of $\boldsymbol{C}$, namely I_2, and the stress-valued constant c_{01}.

$$\Psi = c_{10}\,[I_1 - 3] + c_{01}\,[I_2 - 3] \tag{1.10}$$

The Yeoh constitutive law (Yeoh, 1993) is obtained accounting for the three first terms in (1.8) and setting the coefficients c_{ij} with $j \neq 0$ to zero, which omits the dependence with respect to I_2. It reads

$$\Psi = \sum_{i=1}^{3} c_{i0}\,[I_1 - 3]^i\,. \tag{1.11}$$

The model by Valanis and Landel (1967) is expressed as a function of the principal stretches $\lambda_{1,2,3}$. Furthermore, the total strain energy function is additively decomposed on functions solely depending on one of the principal stretches, which is known as the Valanis-Landel hypothesis, getting

$$\Psi = \sum_{i=1}^{3} f\,(\lambda_i)\,. \tag{1.12}$$

Another model which is naturally expressed as a function of the principal stretches was proposed by Ogden (1972). Ogden provided a very general expression for the strain energy density function for rubber-like materials, that is written as

$$\Psi = \sum_{i=1}^{N} \frac{2\,\mu_i}{\alpha_i}\,[\lambda_1^{\alpha_i} + \lambda_2^{\alpha_i} + \lambda_3^{\alpha_i} - 3]\,, \tag{1.13}$$

where the constraint

$$\mu = \sum_{i=1}^{N} \mu_i\,\alpha_i, \tag{1.14}$$

must be satisfied. Hence, the first part of the Ogden's strain energy function depends only on $I_1 = \lambda_1^2 + \lambda_2^2 + \lambda_3^2$ and $I_2 = \lambda_1\lambda_2 + \lambda_1\lambda_3 + \lambda_2\lambda_3$, see Equation (A.36). However, it is not possible to explicitly express this function as a function of the invariants. Note that the Mooney-Rivlin function is obtained for $N = 2$, $\alpha_1 = 2$, and $\alpha_2 = -2$, whereas it degenerates to the neo-Hookean model for $N = 1$ and $\alpha_1 = 2$.

The hyperelastic potential proposed by Arruda and Boyce (1993), widely known as the eight-chain model since it was developed starting out from a representative volume element where eight springs emanate from the centre of a cube to its corners[2], has the form

$$\Psi = \mu \sum_{i=1}^{5} \frac{A_i}{\lambda_{\mathrm{m}}^{2i-1}} \left[I_1^i - 3^i \right] \tag{1.15}$$

where the coefficients

$$A_1 = \frac{1}{2}, \qquad A_2 = \frac{1}{20}, \qquad A_3 = \frac{11}{1050}, \qquad A_4 = \frac{19}{7000}, \quad \text{and} \quad A_5 = \frac{519}{673750} \tag{1.16}$$

arise from a series expansion of the inverse Langevin function, which arises in the statistical treatment of non-Gaussian chains. The series expansion is truncated after the fifth term. The λ_{m} coefficient is referred to as the locking stretch, at which the slope of the stress-strain curve will rise significantly[3].

All these models, which were developed in order to reproduce the rubber mechanical behaviour, can reproduce the kind of non-linear behaviour exhibited by vascular tissues. Nevertheless, there exist other constitutive laws specifically designed to capture the stress-stretch curves obtained from tests on blood vessels tissue. Among them, it is worth mentioning the strain energy density function proposed by Ballyk *et al.* (1997)

$$\Psi = a \, [I_1 - 3]^2 + b \left[[I_2 - 3] - 2 \, [I_1 - 3] \right], \tag{1.17}$$

where a and b are stress-like constants.

Another isotropic constitutive law for vascular tissues was developed by Demiray (1972), Equation 1.18. Its most noticeable characteristic is the exponential dependence on the first invariant I_1 which helps to mimic the characteristic stiffening of the vascular tissue.

$$\Psi = \frac{a}{2\,b} \left[\exp\left(b \, [I_1 - 3] \right) - 1 \right]. \tag{1.18}$$

This strain energy density function was modified in a later contribution (Demiray *et al.*, 1988) by including a neo-Hookean term and the quadratic dependence of the term $[I_1 - 3]$ in (1.18). With these modifications, it results

$$\Psi = \mu \, [I_1 - 3] + \frac{a}{2\,b} \left[\exp\left(b \, [I_1 - 3]^2 \right) - 1 \right], \tag{1.19}$$

where the constants a and μ have stress units, whereas b is dimensionless.

[2]Notice that this assumption is based on the consideration of information at micro-structural level.

[3]Note that the Arruda-Boyce potential in (1.15) depends on the first invariant only; the physical interpretation is that the eight chains are stretched equally under the action of a general deformation state. The first invariant I_1 directly represents this elongation.

1.4.1.2 Anisotropic models

In spite of the wide variety of stress-stretch curves that can be obtained with the constitutive relations presented above, they miss the anisotropic behaviour inherent to the vascular tissue. Therefore, the use of models including anisotropy is required in order to get accurate results, specially under large-stretch ranges, in which the role of collagen fibres is of crucial importance.

Anisotropic constitutive laws can be classified into non-structural and structural. The former group comprises those strain energy density functions that use certain components of some measure of strain in the definition of the constitutive law expression. That way, anisotropy is straightforwardly introduced in the model.

Non-structural models: Considering the tube-like shape exhibited by the blood vessels, most of these non-structural anisotropic functions are usually expressed in cylindrical coordinates, so the radial, circumferential and longitudinal characteristic directions are explicitly included in the strain energy density function.

One of the most widely used constitutive laws of this group is due to Fung *et al.* (1979), who assumed the exponential form

$$\Psi \,=\, c\,\left[\exp\left(Q\right)-1\right], \tag{1.20}$$

where c is a model constant and Q is a function of the components of the Green-Lagrange strain tensor $\boldsymbol{E}$. Depending on the shape of Q, different Fung-type relations can be obtained, Fung (see, e.g., 1990, and references therein). Among this type of strain energy density functions, the proposed in Fung (1990) assumed

$$\begin{aligned} Q \,=& b_1\,E_{\Theta\Theta}^2 \,+\, b_2\,E_{ZZ}^2 \,+\, b_3\,E_{RR}^2 \\ &+ 2\,b_4\,E_{\Theta\Theta}E_{ZZ} \,+\, 2\,b_5\,E_{ZZ}E_{RR} \,+\, 2\,b_6\,E_{RR}E_{\Theta\Theta}, \end{aligned} \tag{1.21}$$

where b_i, $i = 1, \cdots, 6$ are dimensionless parameters weighting the contribution to the strain energy of the deformations in the principal cylindrical directions which are obtained from the experimental tests (Chuong and Fung, 1984). Thus, seven parameters determine the mechanical behaviour in this model, which can be reduced to four by neglecting the contribution to the strain energy density function of strains in the longitudinal direction.

Humphrey and Na (2002a), maintaining the assumption of cylindrical orthotropy, proposed a different expression for Q in order to model the passive behaviour of the arterial mechanical response. Contrary to the expression proposed by Chuong and Fung (1984), Humphrey and Na (2002a) included the shear terms in Q, although this result naturally from their assumed material symmetry (Humphrey, 2002b). Considering these

terms, Q yields

$$\begin{aligned} Q =& c_1\, E_{\Theta\Theta}^2 + c_2\, E_{ZZ}^2 + c_3\, E_{RR}^2 \\ &+ 2\, c_4\, E_{\Theta\Theta} E_{ZZ} + 2\, c_5\, E_{ZZ} E_{RR} + 2\, c_6\, E_{RR} E_{\Theta\Theta} \\ &+ c_7\, \left[E_{R\Theta}^2 + E_{\Theta R}^2\right] + c_8\, \left[E_{\Theta Z}^2 + E_{Z\Theta}^2\right] + c_9\, \left[E_{ZR}^2 + E_{RZ}^2\right], \end{aligned} \tag{1.22}$$

where $c_i, i = 1, \cdots, 9$ are dimensional parameters. These models are intuitive and easily implementable within, e.g., a Finite Element code, since stress and elasticity tensors are directly obtained from (1.20). Nevertheless, they include a big number of constants that, usually, cannot be identified from experimental tests. Furthermore, not all combinations of these constants ensure the convexity of the strain energy function (see, e.g., the work by Holzapfel *et al.*, 2000; Holzapfel, 2006, and references therein), therefore, additional constraints should be accounted for the definition of those constants.

An alternative to the exponential form of the strain energy function in (1.20), is to assume a logarithmic form for the strain energy density function, as proposed by Takamizawa and Hayashi (1987), i.e.

$$\Psi = -c \ln (1 - Q), \tag{1.23}$$

with

$$Q = \frac{1}{2}\, a_{\Theta\Theta}\, E_{\Theta\Theta}^2 + \frac{1}{2}\, a_{ZZ}\, E_{ZZ}^2 + a_{\Theta Z}\, E_{\Theta}\, E_Z, \tag{1.24}$$

where the stress-valued coefficient c, and the dimensionless coefficients $a_{\Theta\Theta}$, a_{ZZ}, and $a_{\Theta Z}$ characterize the mechanical properties of the material. As it happened with the Fung-type models, these coefficients cannot take arbitrary values, but some constraints must be satisfied in order to ensure the convexity of the function, which is the main drawback of this model. Nevertheless, the capabilities of both types of models to capture experimental data is similar (see Takamizawa and Hayashi, 1987).

Furthermore, the application of Fung-type models is limited to cylindrical geometries, since the definition of radial, circumferential and longitudinal directions in patient-specific geometries is unclear.

An innovative approach for the modelling of vascular tissue, specifically to the arterial wall, was proposed by Holzapfel and Weizsäcker (1998), where the strain energy function was additively split into isotropic and anisotropic contributions as

$$\Psi = \Psi_{\text{iso}} + \Psi_{\text{ani}} = c_1\, [I_1 - 3] + c_2\, [\exp (Q) - 1], \tag{1.25}$$

where c_1 and c_2 are stress-like parameters. A neo-Hookean term was assumed to model the isotropic contribution to the total strain energy density function, whereas the anisotropic contribution was represented by the model by Fung (1990) Q, shown in Equations (1.20) and (1.21).

Structural models: The microstructural architecture of the blood vessels is the basis for the macroscopic anisotropic behaviour exhibited by the vascular tissue. Specifically, the existence of preferred orientation directions for the collagen fibre network forming the vessel layers is widely accepted (see, e.g. Holzapfel *et al.*, 2000). Furthermore, the particular shape of other wall constituents, such as the spindle-shaped smooth muscle cells, determine the appearance of anisotropy. Thus, the development of models in which these directions are explicitly included is justified, for which the inclusion of additional information in the strain energy density function is required.

At this point, by analogy with the classification presented for the isotropic models, two alternatives to include anisotropy in the macroscopic behaviour can be taken. First, it is the consideration of a macroscopic direction along which the mechanical behaviour is explicitly specific (see, e.g., Humphrey and Yin, 1987; Holzapfel *et al.*, 2000, 2005b; Gasser *et al.*, 2006). The second, it is based on the development of a constitutive relation for the microconstituents causing the anisotropy, whose contribution in all the directions of space is usually weighted by means of the inclusion of an orientation density function. Finally, the macroscopic mechanical behaviour is obtained by integration of all the contributions of the microconstituents (see, e.g., Lanir, 1979; Arruda and Boyce, 1993; Caner and Carol, 2006; Alastrué *et al.*, 2009a; Sáez *et al.*, 2012).

Again, a more detailed description of macroscopic models is presented here due to the material mechanical behaviour on this Thesis has been modeled from a macroscopic point of view. A frequently used strategy to incorporate anisotropy in macroscopic continuum models is based on the explicit consideration of vectors, defined in the reference configuration, characterizing each direction of anisotropy at each material point. In this regard, it is worth mentioning the pioneering work by Spencer (1971), who postulated that transverse isotropy can be described with a unit vector $\boldsymbol{a}_1$ describing the anisotropy direction, and introduced the concept of pseudo-invariants, describing the invariants associated to this vector and the deformation tensor, that can be used to capture this information. Therefore, the following pseudo-invariants

$$\begin{aligned} I_4 &:= \boldsymbol{a}_1 \cdot \boldsymbol{C} \cdot \boldsymbol{a}_1 = \boldsymbol{C} : \boldsymbol{A}_1 \\ I_5 &:= \boldsymbol{a}_1 \cdot \boldsymbol{C}^2 \cdot \boldsymbol{a}_1 = \boldsymbol{C}^2 : \boldsymbol{A}_1 \end{aligned} \tag{1.26}$$

are additionally introduced to the formerly presented $I_{1,2,3}$, where $\boldsymbol{A}_1 = \boldsymbol{a}_1 \otimes \boldsymbol{a}_1$ is a structural tensor. Thus, the strain energy density function will be dependent on the set of invariants $I_{1,\cdots,5}$. Furthermore, the expression

$$\Psi\left(\boldsymbol{C},\, \boldsymbol{A}_1\right) = \Psi\left(\boldsymbol{Q} \cdot \boldsymbol{C} \cdot \boldsymbol{Q}^{\mathrm{t}},\, \boldsymbol{Q} \cdot \boldsymbol{A}_1 \cdot \boldsymbol{Q}^{\mathrm{t}}\right), \qquad \forall\, \boldsymbol{Q} \in \mathbb{Q}^3_+ \tag{1.27}$$

such that $\boldsymbol{Q} \cdot \boldsymbol{a}_1 = \boldsymbol{a}_1$ must be satisfied for a transversely isotropic constitutive law (see, e.g., Holzapfel *et al.*, 2000).

For materials with two directions of anisotropy, it is necessary to introduce an additional referential vector $\boldsymbol{a}_2$ and its associated structural tensor $\boldsymbol{A}_2 = \boldsymbol{a}_2 \otimes \boldsymbol{a}_2$, for

which the invariants I_6 and I_7 are defined analogously to (1.26). Furthermore, two additional anisotropic invariants representing the interaction between the two directions of anisotropy are defined as

$$\begin{aligned} I_8 &:= [\boldsymbol{a}_1 \cdot \boldsymbol{a}_2]\, \boldsymbol{a}_1 \cdot \boldsymbol{C} \cdot \boldsymbol{a}_2 \\ &= [\boldsymbol{a}_1 \cdot \boldsymbol{a}_2]\, \boldsymbol{C} : [\boldsymbol{a}_1 \otimes \boldsymbol{a}_2]\,, \\ I_9 &:= [\boldsymbol{a}_1 \cdot \boldsymbol{a}_2]^2\,. \end{aligned} \tag{1.28}$$

Note that I_9 is not a function of the deformation state and, therefore, will not be included in the definition of strain energy functions. Nevertheless, it has been here introduced for completeness. With all these definitions at hand, the anisotropic constitutive laws including two directions of anisotropy can be formulated as a function of the invariants $I_{1,\cdots,8}$.

However, the complexity associated to the experimental characterisation of the mechanical behaviour dependence on each of the invariants, and the high number of material parameters resulting from considering the eight invariants, has leaded to the assumption of several simplifications. Specifically, the most widely used models in the literature neglect the contribution of the pseudo-invariants I_5 and I_7, since their effect can be mostly reproduced just by considering I_4 and I_6, respectively. Furthermore, the mechanical coupling between both anisotropy directions is usually neglected, and therefore no terms depending on I_8 are considered. Thus, the strain energy function can be written

$$\Psi \,=\, \Psi\,(I_1,\, I_2,\, I_3,\, I_4,\, I_6)\,. \tag{1.29}$$

With these consideration at hand, several functionals are found in the literature. Among them, it is worth mentioning the transversely isotropic model by Weiss (1994), specifically designed for tendons and ligaments, i.e.,

$$\Psi\,(\boldsymbol{C},\, \boldsymbol{A}_1) \,=\, c_1\,[I_1 - 3] \,+\, c_2\,[I_2 - 3] \,+\, c_3\,[\exp\,(I_4 - 1) - I_4]\,, \tag{1.30}$$

which assumes the isotropic-anisotropic additive decomposition of the strain energy density function introduced in (1.25) (Holzapfel and Weizsäcker, 1998). The isotropic ground substance is modelled by means of a Mooney-Rivlin term (1.10), whereas the contribution of fibres in introduced by means of a term depending on I_4. This model satisfies that $\Psi\,(\boldsymbol{I},\, \boldsymbol{A}) = 0$, and can be efficiently implemented in a FE code (Weiss *et al.*, 1996), and has been extended to handle transversely isotropic viscoelastic materials (Puso and Weiss, 1998).

Several strain energy density functions for soft tissues were proposed in Humphrey and Yin (1987). Among them, it is worth remarking the exponential considered for the modelling of the passive behaviour of the cardiac tissue. By means of the additive decomposition of isotropic and anisotropic contributions, the function

$$\Psi\,(\boldsymbol{C},\, \boldsymbol{A}_1) \,=\, c\,[\exp\,(b\,[I_1 - 3]) - 1] \,+\, A\,\left[\exp\left(a\,[\lambda - 1]^2\right) - 1\right], \tag{1.31}$$

was proposed, where c and A are stress-like and b and a dimensionless parameters, and $\lambda = \sqrt{\boldsymbol{C} : \boldsymbol{A}_1}$. In that expression, the non-muscular contributions are represented by the isotropic term depending on I_1 (compare (1.18)), whereas the anisotropic contribution, represented by the anisotropic term, is assumed to correspond to the smooth muscle cells bundles. This function has been also applied to skeletal muscles (Martins *et al.*, 1998).

Another transversely isotropic function for modelling the cardiac tissue, specifically the left ventricular myocardium, was proposed by (Lin and Yin, 1998), i.e.

$$\Psi\left(\boldsymbol{C},\, \boldsymbol{A}_1\right) \,=\, C_1 \left[\exp\left(Q\right) \,-\, 1\right], \tag{1.32}$$

with

$$Q \,=\, C_2 \left[I_1 \,-\, 3\right]^2 \,+\, C_3 \left[I_1 \,-\, 3\right]\left[I_4 \,-\, 1\right] \,+\, C_4 \left[I_4 \,-\, 1\right]^2, \tag{1.33}$$

where the material constants $C_2 \,>\, 0$, $C_4 \,>\, 0$, and C_3 are dimensionless, whereas $C_1 \,>\, 0$ is a stress-like parameter. As the most noticeable feature of this function, note the explicit coupling between the isotropic and anisotropic contributions. Furthermore, note that the convexity of this function is not guaranteed for all the combinations of the constants in (1.33).

Humphrey and Na (2002a) proposed an exponential transversely isotropic constitutive law for the modelling of the atherosclerotic plaque mechanical behaviour with the form

$$\Psi\left(\boldsymbol{C},\, \boldsymbol{A}_1\right) \,=\, c \,\left[\exp\left(c_1 \left[I_1 - 3\right] \,+\, c_2 \left[I_4 - 1\right]^2\right) \,-\, 1\right], \tag{1.34}$$

where the model parameter c has stress units, and c_1, c_2 are dimensionless parameters. In that work, the direction of anisotropy was assumed to correspond to the circumferential direction.

A model including two directions of anisotropy, specifically designed for the arterial tissue was developed by Holzapfel *et al.* (2000). An exponential behaviour to represent the collagen fibres contribution, which was only considered under tension, was chosen, i.e.

$$\begin{aligned} \Psi\left(\boldsymbol{C},\, \boldsymbol{A}_1,\, \boldsymbol{A}_2\right) \;&=\; \mu \,\left[I_1 - 3\right] \,+\, \frac{k_1}{2\,k_2}\left[\exp\left(k_2 \left[I_4 - 1\right]^2\right) - 1\right] \\ &+\; \frac{k_3}{2\,k_4}\left[\exp\left(k_4 \left[I_6 - 1\right]^2\right) - 1\right], \end{aligned} \tag{1.35}$$

where the neo-Hookean term is associated to the ground substance with constant μ, and the parameters k_1 and k_3 are stress-like, whereas k_2 and k_4 are dimensionless. As its main contribution, it is worth remarking that the directions of anisotropy were helically distributed, with an orientation angle of $\pm\beta$ degrees with respect to the circumferential direction. This assumption is an attempt to mimic the real fibre distribution. In addition, this model has been extended to inelastic phenomena, such as viscoelasticity (Holzapfel and Gasser, 2001; Peña *et al.*, 2007) or plasticity (Gasser and Holzapfel, 2002), and has been proved to be strongly elliptic, which is crucial for its numerical implementation and stability.

In order to include certain amount of fibre dispersion around the anisotropy directions characterized by the invariants I_4 and I_6, Holzapfel's model was modified in Holzapfel *et al.* (2005b), where the functional

$$\begin{aligned} \Psi\left(\boldsymbol{C},\, \boldsymbol{A}_1,\, \boldsymbol{A}_2\right) &= \mu\,[I_1-3] \\ &+ \frac{k_1}{k_2}\left[\exp\left(k_2\left[[1-\rho]\,[I_1-3]^2 \,+\, \rho\,[I_4-1]^2\right]\right)-1\right] \\ &+ \frac{k_3}{k_4}\left[\exp\left(k_4\left[[1-\rho]\,[I_1-3]^2 \,+\, \rho\,[I_6-1]^2\right]\right)-1\right], \end{aligned} \tag{1.36}$$

was proposed. This expression includes the exponential dependence on the factor $[I_1-3]$ as well as the dimensionless weighting parameter $\rho \in [0,\, 1]$, compare with (1.34), in order to improve the ability of the original model to reproduce the experimental curves (Gasser *et al.*, 2006). By means of this parameter, which has a purely phenomenological basis, it is possible to regulate the degree of anisotropy in such way that (1.35) is recovered when $\rho = 1$, whereas the isotropic exponential model in (1.18) is obtained when $\rho = 0$.

With the same spirit, Gasser *et al.* (2006) proposed the strain energy density function

$$\begin{aligned} \Psi\left(\boldsymbol{C},\, \boldsymbol{A}_1,\, \boldsymbol{A}_2\right) &= \mu\,[I_1-3] \\ &+ \frac{k_1}{2\,k_2}\left[\exp\left(k_2\big[\kappa\, I_1 \,+\, [1-3\kappa]\; I_4-1\big]^2\right)-1\right] \\ &+ \frac{k_3}{2\,k_4}\left[\exp\left(k_4\big[\kappa\, I_1 \,+\, [1-3\kappa]\; I_6-1\big]^2\right)-1\right], \end{aligned} \tag{1.37}$$

where $\kappa \in [0,\, 1/3]$ is a measure of the dispersion around the preferred orientations determined by I_4 and I_6. However, contrary to the expression in (1.36) where ρ basically couples the invariants I_1 and I_4 (or I_1 and I_6), a structurally consistent derivation where the structural components of the vessel wall are reflected by associated entities in the formulation leads to the derivation of κ. Specifically, this parameter is a result of considering the fibres oriented following the von Mises orientation density function. Thus, isotropy is reached for $\kappa = 1/3$, whereas $\kappa = 0$ renders no fibre dispersion.

Summarizing, during the last years, the constitutive modelling of soft biological tissues has constituted a very active field of research (see e.g., Ogden, 2003). Commonly, these materials have been modelled as hyperelastic continua embedded into continuum mechanical formulations. Accordingly, one of the main tasks consisted in the determination of appropriate strain energy density functions, from which local mechanical quantities are derived (Truesdell and Noll, 2004). First constitutive laws for soft tissue modelling were purely phenomenological and also assumed to be isotropic (Demiray, 1972). Fung's exponential model (Fung *et al.*, 1979), accounting for anisotropy induced by fibres, became one of the most popular models used in soft tissue modelling. However, the inclusion of structural tensors into constitutive laws nowadays is the most widely used technique to introduce anisotropy in material models (Menzel and Steinmann, 2001, 2003). In view of the problem at hand, we here place emphasis on the approach developed by Weiss *et al.* (1996) for transversely isotropic materials and the models by Humphrey and Yin (1987) and Holzapfel *et al.* (2000) that account for two

preferred directions. The latter was lately modified in order to incorporate fibre dispersion with respect to the deterministic preferred orientation direction (Holzapfel *et al.*, 2005b). The more recent work by Gasser *et al.* (2006) included microstructural information in the model by means of the assumption of a fibre orientation distribution function; the reader is also referred to the remodelling framework proposed in Menzel (2007). Furthermore, the large variability concerning the mechanical behaviour and the particular composition exhibited by soft biological tissues (Sacks, 2000), has led other points of views, which incorporates the representative structural information into associated constitutive models in order to appropriately recapture the response of these materials. Consequently, micro-structurally based models which account for at least some micro-mechanical information of the underlying tissue constituents - for example elastin and collagen fibres - and include their individual response into the overall constitutive equations has been also developed. Notwithstanding, the presented review of the more frequently constitutive laws used for modelling the hyperelastic passive behaviour of soft biological tissues has been mainly focussed from a macroscopic perspective, and the microstructurally based models have not taken into account, therefore, for more details about this micro-structurally models, the interested reader is referred, for example, to the texts by Carol *et al.* (2004), Alastrué *et al.* (2009a), or Sáez *et al.* (2012) and references therein.

Along this Thesis, the strain energy density functions proposed by Holzapfel *et al.* (2005b) and Gasser *et al.* (2006) have been used to characterize the mechanical properties of the different biological tissues.

1.5 Experimental characterization of soft tissues

1.5.1 Main experimental test considerations

The experimental study of the mechanical properties of the soft biological tissues and, in particular, of the vascular tissue, is of vital importance. The thorough research of the mechanical response of tissues and organs is the basis for the creation of models which can accurately reproduce their mechanical behaviour. In order to obtain the material properties of these tissues, the classical engineering testing techniques have been applied to biological materials (see e.g., Fung *et al.*, 1979; Fung, 1990; Humphrey, 2001, and references therein).

Nevertheless, the particular characteristics of these tissues noticeably complicate the obtaining of valid results. Because of this reason, the experimental study of soft biological tissues is one of the field of biomechanics in which more research effort is required. Some of the more relevant features of the soft biological tissues are itemized bellow:

- Test conditions: The interest of the mechanical tests is to obtain the mechanical properties of the materials at their work conditions. Thus, the environment in

which the mechanical tests are carried out should mimic *in vivo* conditions as accurately as possible. Aimed by this goal, most of the experimental tests reported in the literature propose highly complicated experimental set-ups, including thermostatic baths in which variables as the pH or the temperature are fixed to some assumed physiological values, at which the experimental test is developed (see, e.g., Hayashi *et al.*, 1981; Fung, 1990; Hayashi and Imai, 1997; Sacks, 2000, and references therein). Nevertheless, no matter how complicated the experimental set-up is, the test conditions will be always far from the working *in vivo* conditions since some factors as, e.g., the interaction with the surrounding tissues or the chemical signalling appearing under loading, will never be captured in the testing environment. Very few studies comparing the effect of the tests conditions on the measured mechanical properties have been reported (Miller, 2001; Hrapko *et al.*, 2008).

- Tissue degeneration: Soft biological tissues are living tissues and, therefore, their mechanical response is affected by a multitude of factors whose effects are negligible when dealing with classical engineering materials. Tissue degeneration, i.e., the loose of mechanical properties due to modifications of the material structure after the tissue harvesting, is one of them. The most effective technique in order to minimize its influence is to carry out the tests immediately after the tissue harvesting. However, it usually happens that it is necessary to store the tissue samples until the tests are carried out.

  In those cases in which the testing is developed in the next hours following the harvesting, tissues are usually immersed in a preserving physiological solution, e.g., Krebs-Ringer solution, and kept at low temperature, usually at 4 [°C], until the sample preparation is performed (see, e.g., Hayashi *et al.*, 1980, 1981). Nevertheless, tissue samples are frozen in those studies in which long periods occur between tests, where it is usually claimed that the freezing process does not affect the mechanical properties of the tissue (Silver *et al.*, 2003). Nevertheless, this assertion is lacking from a solid experimental basis.

- Anisotropic behaviour: As already mentioned in the previous sections, most of the soft biological, and blood vessel in particular, exhibit a marked anisotropic behaviour. This feature notably complicates the mechanical characterization of the tissue. Thus, the developing of multiaxial tests or tension tests in different directions is needed to capture the mechanical behaviour (Holzapfel *et al.*, 2004, 2005b).

- Sample size: The small size of the testing specimens is an added complication to the biological experimental tests, since it sometimes prevents the use of the optimal testing techniques. However, for biological tissue samples in which the measurement of mechanical properties is difficult to perform due to its size, alternative techniques such as indentation techniques which offer quite a simple method for

measurement of these biological mechanical properties (see e.g., Carmines *et al.*, 1991; Oyen, 2011).

- Variability: The huge variability in the mechanical properties of the vascular tissues is one of the most important difficulties in the determination of their mechanical properties. Due to the different physiological role of each vessel and the different mechanical loading it is subjected to, their mechanical properties are highly variable between different vessels (Fung *et al.*, 1979; Fung, 1990). Furthermore, the mechanical properties of a vessel also vary depending on the position along its length, which is due to the variation of the microstructural composition (see Section 1.1) (Humphrey, 2002b; Vande Geest *et al.*, 2004). Different mechanical behaviour is found between different individuals, where a multitude of factors such as sex, age, or species influence on the mechanical properties of the vascular tissue.

In which the testing procedures used for the characterization of the vascular tissue is concerned, three different techniques are mainly used for the measurement of their mechanical response; simple tension, planar biaxial and inflation test, where a schematic representation of each of these three experimental tests is shown in Figures 1.12.a, 1.12.b and 1.12.c, respectively.

- Simple tension tests: This type of test, widely used for the determination of the mechanical properties of all kinds of materials, has been also applied to soft biological tissues (see, e.g., Hayashi *et al.*, 1981; Hayashi and Imai, 1997; Schulze-Bauer *et al.*, 2003; Holzapfel *et al.*, 2005a). Among its main advantages, it is worth noting its simplicity and versatility, which allows its application to very small-sized samples. Nevertheless, it allows obtaining the mechanical properties only in the testing directions. This is irrelevant when dealing with isotropic materials, but it is an important shortcoming in testing anisotropic materials. A feasible possibility to complete the information provided by simple tension tests, is to apply them to different tension directions (Holzapfel *et al.*, 2005b), which partly compensates this limitation.

  Figure 1.12.a shows a device to carry out simple tension tests; this kind of test involves gripping a sample specimen at both ends and pulling it at a specified rate until the sample breaks. During the test, the force is recorded as a function of elongation, and then the mechanical behavior of the tissue is extracted. By considering the dimensions of the sample, it is possible to determine the properties of the biological material.

- Biaxial tests: These tests have been extensively used in the last years in order to obtain the mechanical properties of planar biological tissues (see, e.g., Lanir and Fung, 1974a,b; Pandit *et al.*, 2005; Cox *et al.*, 2006, 2008). Their application allows obtaining more complete information about the mechanical response of

the biological tissue than the simple tension test since they cause a multiaxial loading state, which is closer to the *in vivo* state. Nevertheless, their set up and preparation is much more complicated, and the interpretation of the obtained results is also difficult. Also the small size of some biological tissues can prevent the application of this technique which, joined to the poor standardization and the influence of boundary effects, difficult the generalized use of biaxial tests (Sacks, 2000).

Nevertheless, to determine the parameters for the anisotropic hyperelastic models from biaxial test, techniques such as the inverse finite element method have been proposed (Krishnamurthy *et al.*, 2008; Nguyen and Boyce, 2011). The inverse finite element method is a numerical approach in which an optimization algorithm is coupled with a finite element method in order to find optimal values for a set of target parameters which enter the finite element simulation. A user defined objective function serves to measure the optimality of the parameters. The finite element method is used to simulate the physical process which depends on the target parameters. The target parameters can be various physical quantities like the material parameters in inverse material parameter estimation related to experimental testing (Krishnamurthy *et al.*, 2008; Nguyen and Boyce, 2011).

In planar biaxial testing, the biological sample is gripped at four locations and loaded along two orthogonal axes as illustrated in Figure 1.12.b. As in the uniaxial test, the force as a function of elongation is stored in order to characterize the mechanical properties of the tissue.

- Inflation tests: As biaxial tests, this kind of test provides measurements of the mechanical properties of a vessel under a multiaxial loading state. Furthermore, the manipulation of the testing specimens is minimal, which notably reduces the influence of the sample preparation process in the measurements. Because of that, this testing technique has been widely used for the determination of the mechanical properties of blood vessels (see, e.g., Hayashi *et al.*, 1980; Carmines *et al.*, 1991; Schulze-Bauer *et al.*, 2002; Hayashi *et al.*, 2003; Carboni *et al.*, 2007). Concerning the main drawbacks of this methodology, the highly difficult tuning of the testing machine (which can cause the buckling of the vessel), the sealing of the vessel in order to prevent fluid leakage, and the interpretation of the results, are some of the most important shortcomings of this testing procedure.

  Inflation testing is made possible by the machine shown in Figure 1.12.c. This test consists of filling a blood vessel by PBS dissolution or similar, controlling the applied pressure. Then, the variation of the blood vessel diameter and the applied pressure are recorded during the experimental test in order to determine the mechanical properties of the blood vessel.

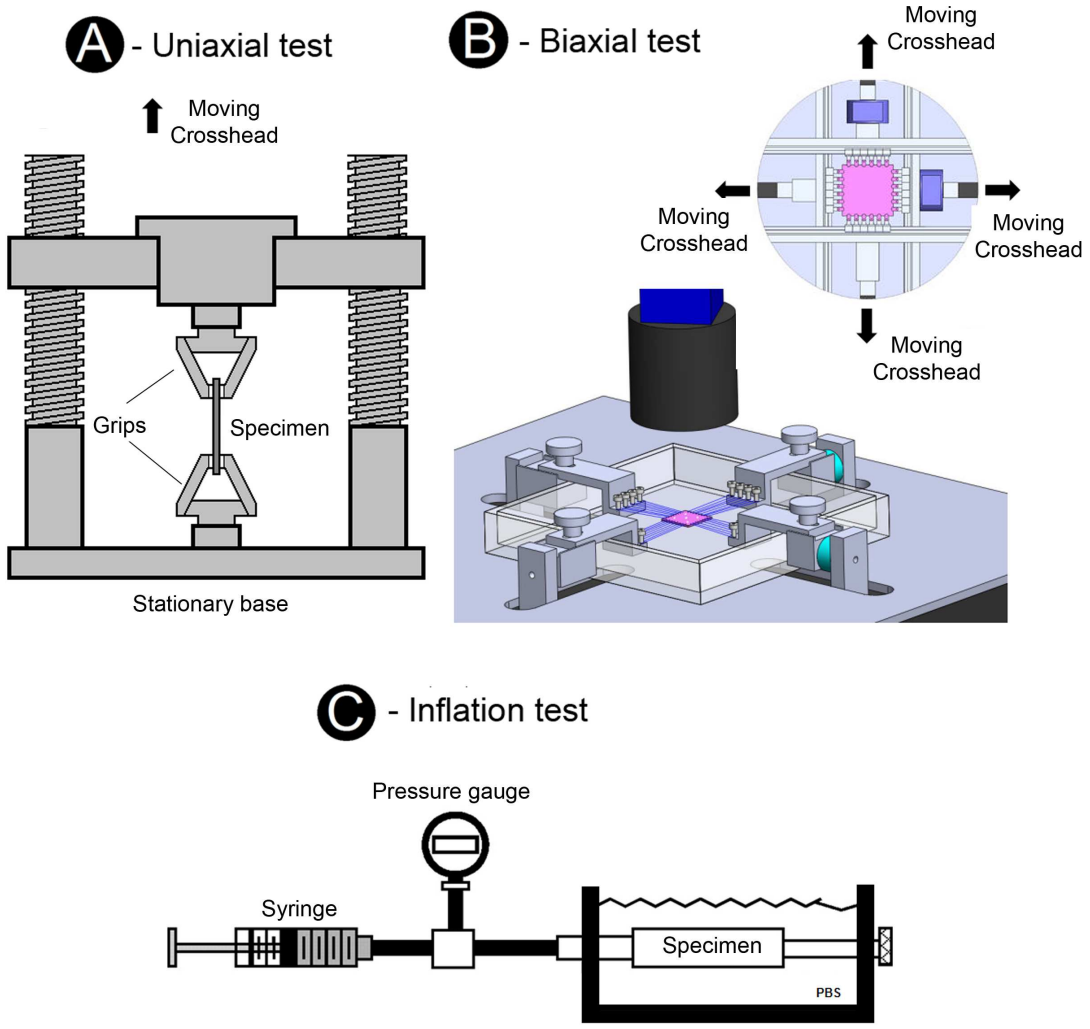

Figure 1.12: Techniques for the mechanical response of biological tissues. A - Uniaxial test. B - Biaxial test. C - Inflation test.

1.5.2 Experimental test focused on atherosclerosis pathology

Due to the limitations on studying human lesions of atherosclerosis, numerous animal species have been used to study the pathogenesis and potential treatment of the lesions of atherosclerosis (see, e.g., Wagner, 1978; Reitman *et al.*, 1982; Buja *et al.*, 1983; Faggiotto *et al.*, 1984; Schwartz *et al.*, 1985). The first evidence of experimental atherosclerosis came into view as early as in 1908 when Ignatowski (1908) reported thickening of the intima with formation of large clear cells in the aorta of rabbits fed with a diet rich in animal proteins (meat, milk, eggs). The most useful animal models have thus far been restricted to relatively large animals, such as nonhuman primates, swine, and rabbits.

Hamsters and pigeons have been used occasionally but present problems peculiar to their species (Singh *et al.*, 2009). Rats and dogs are not good models for atherosclerosis because they do not develop spontaneous lesions and require heavy modifications of diet to produce vascular lesion. Despite the fact that rabbits do not develop spontaneous atherosclerosis, they are useful because they are highly responsive to cholesterol manipulation and develop lesions in a fairly short time (Rosenfeld *et al.*, 1987; Drobnik *et al.*, 2000; Singh *et al.*, 2009). The lesions are much more fatty and macrophage-rich (inflammatory) than the human lesions and plasma cholesterol levels are extraordinarily high (very dissimilar to humans). Pigs and monkeys are better suited to model human atherosclerotic lesions. However, nowadays monkeys are not widely used due to specific concerns (risk of extinction) and cost (Faggiotto *et al.*, 1984). The pig is a very good model since when fed with cholesterol, they reach plasma levels and atherosclerotic lesions that are quite similar to those seen in humans (Gerrity, 1981; Breslow, 1993). Problems with the pig model are costs, the difficulties involved in maintaining the colonies and in their handling. However, murine models of atherosclerosis could help to overcome the many problems and deficiencies of larger animals and, in particular, would permit studies of possible therapies that require relatively large numbers of animals (Breslow, 1993; Singh *et al.*, 2009). In recent years, there has been an explosion in the number of *in vivo* and *ex vivo* studies that is largely attributable to the use of mouse models to study atherogenic mechanisms (Guo and Kassab, 2003; Gleason *et al.*, 2007; Santelices *et al.*, 2007; Agianniotis *et al.*, 2012a). The mouse is a uniquely suited model system for studies of complex diseases. Its overall biology is closely comparable to that of humans and the characteristics of many pathologic conditions are very similar between the two species. However, the structure of mouse atherosclerotic lesions may differ from that of humans (Wessel and Sedmera, 2003; Hoyt Jr. *et al.*, 2007; Iwaki *et al.*, 2001) and, in addition, mouse strain does not generate spontaneous arterial lesions (Jawien *et al.*, 2004).

A revolution in murine atherosclerosis research began by applying transgenic techniques to create mouse models of human lipoprotein metabolism. With the emerging technique of gene inactivation through homologous recombination, came the ability to recreate important aspects of human lipid metabolism in mice. Thus, since its introduction in the early 1990s, the apolipoprotein E-deficient transgenic mice ($ApoE^{-/-}$) created by homologous recombination in embryonic stem cells, has been the most widely studied animal model for atherosclerosis (Zhang *et al.*, 1992; Nakashima *et al.*, 1994; Daugherty, 2002; Coleman *et al.*, 2006) since they are hypercholesterolemic and develop spontaneous arterial lesions. Additionally, the outstanding success of this animal model is due to its ready availability, relatively easy breeding and colony maintenance, spontaneous elevated cholesterol levels and rapid development of atherosclerotic lesions with histopathological progression, similar to that found in humans (Plump *et al.*, 1992). Numerous potential applications to basic research and drug development have been achieved thanks to $ApoE^{-/-}$ mice (Plump *et al.*, 1992). However, despite the common

use of this experimental model for the study of biological mechanisms underlying plaque development, very few data are available regarding the mechanical behaviour of healthy and atherosclerotic blood vessels in ApoE$^{-/-}$ mice. Summarizing, some of the developed studies in order to characterize the mechanical behaviour of ApoE$^{-/-}$ mice are oriented to quantify the mechanical properties of atheroma plaques in ApoE$^{-/-}$ mouse models (Dye *et al.*, 2007; Humphrey *et al.*, 2009; Broisat *et al.*, 2011; Eberth *et al.*, 2011; Hayenga *et al.*, 2011; Agianniotis and Stergiopulos, 2012b) and other asses the aortic aneurysms behaviour in these mice (Daughtery and Cassis, 2004; Sheth *et al.*, 2010; Collins *et al.*, 2011; Goergen *et al.*, 2011), even though computational models have been carried out to predict stresses in these lesions (Vengrenyuk *et al.*, 2010; Ohayon *et al.*, 2012).

Consequently, ApoE$^{-/-}$ mice model has been chosen to perform experimental tests oriented to the better understanding of atherosclerosis lesions (Chapter 5). Furthermore, the experimental inflation test has been selected to characterize the atherosclerotic tissue since the small size of the aorta mice makes impossible to realize other kind of experimental tests.

1.6 Motivation

The main motivation of this Thesis is mainly founded on the high social and economical impact of cardiovascular diseases. Cardiovascular diseases (CVD) related to atherosclerosis are nowadays primary causes of mortality in the developed world and it has been calculated that they will become the first cause of death worldwide in 2020 (Mathers and Murray, 2006; Lloyd-Jones *et al.*, 2009). Estimations of the cause of death are given by the Roger *et al.* (2011) and World Health Organization. Regional Office for Europe (2011), accounting for 42% of all deaths in Europe (by sex, 37% of all women and 48% of men) and 51% in the US (World Health Organization. Regional Office for Europe, 2011; Petersen *et al.*, 2005; Gaziano and Gaziano, 2009).

For example, an illustration of the main death causes for adults in Europe in 2008 is shown in Figure 1.13. This Figure depicts clearly what is the number one cause of death throughout the world. Cardiovascular diseases kill more people every year than any others. In 2008, 7.3 million people died from ischaemic heart disease and 6.2 million from stroke or another form of cerebrovascular disease. Figure 1.13 also shows differences between rich and poor countries with respect to causes of death. People from middle and high income countries predominantly die due to cardiovascular disease. In low income countries, despite of the fact that cardiovascular diseases are not found on the top three causes of death, they affect to a significative number of population and an important increment of deaths per year is expected in further analysis (World Health Organization. Regional Office for Europe, 2011).

The 10 leading causes of death by broad income group

	Low-income countries	Deaths in millions	% of deaths
1-	Lower respiratory infections	1.05	11.3
2-	Diarrhoeal diseases	0.76	8.2
3-	HIV/AIDS	0.72	7.8
4-	Ischaemic heart disease	0.57	6.1
5-	Malaria	0.48	5.2
6-	Stroke and other cerebrovascular disease	0.45	4.9
7-	Tuberculosis	0.40	4.3
8-	Prematurity and low birth weight	0.30	3.2
9-	Birth asphyxia and birth trauma	0.27	2.9
10-	Neonatal infections	0.24	2.6

	Middle-income countries	Deaths in millions	% of deaths
1-	Ischaemic heart disease	5.27	13.7
2-	Stroke and other cerebrovascular disease	4.91	12.8
3-	Chronic obstructive pulmonary disease	2.79	7.2
4-	Lower respiratory infections	2.07	5.4
5-	Diarrhoeal diseases	1.68	4.4
6-	HIV/AIDS	1.03	2.7
7-	Road traffic accidents	0.94	2.4
8-	Tuberculosis	0.93	2.4
9-	Diabetes mellitus	0.87	2.3
10-	Hypertensive heart disease	0.83	2.2

	High-income countries	Deaths in millions	% of deaths
1-	Ischaemic heart disease	1.42	15.6
2-	Stroke and other cerebrovascular disease	0.79	8.7
3-	Trachea, bronchus, lung cancers	0.54	5.9
4-	Alzheimer and other dementias	0.37	4.1
5-	Lower respiratory infections	0.35	3.8
6-	Chronic obstructive pulmonary disease	0.32	3.5
7-	Colon and rectum cancers	0.30	3.3
8-	Diabetes mellitus	0.24	2.6
9-	Hypertensive heart disease	0.21	2.3
10-	Breast cancer	0.17	1.9

	World	Deaths in millions	% of deaths
1-	Ischaemic heart disease	7.25	12.8
2-	Stroke and other cerebrovascular disease	6.15	10.8
3-	Lower respiratory infections	3.46	6.1
4-	Chronic obstructive pulmonary disease	3.28	5.8
5-	Diarrhoeal diseases	2.46	4.3
6-	HIV/AIDS	1.78	3.1
7-	Trachea, bronchus, lung cancers	1.39	2.4
8-	Tuberculosis	1.34	2.4
9-	Diabetes mellitus	1.26	2.2
10-	Road traffic accidents	1.21	2.1

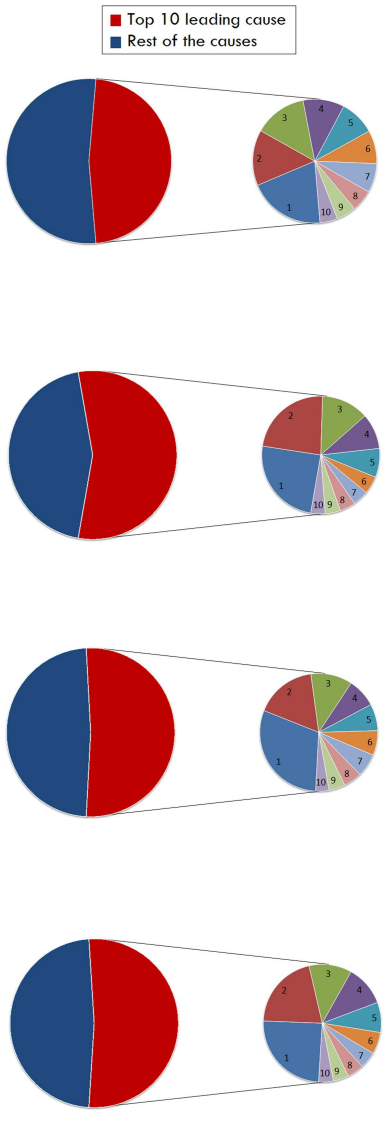

Figure 1.13: The 10 leading causes of death by broad income group (2008) (World Health Organization. Regional Office for Europe, 2011). Note that the low, middle and high income categories are defined by the World Bank. Countries are grouped based on their 2009 gross national income per capita.

As an overview of the people death across the globe, imagine a diverse international group of 1000 individuals representative of the women, men and children from all over the world who died in 2008. Of those 1000 people, 159 would have come from high income countries, 677 from middle income countries and 163 from low income countries. What would be the top 10 causes of their deaths? Figure 1.14 is the answer.

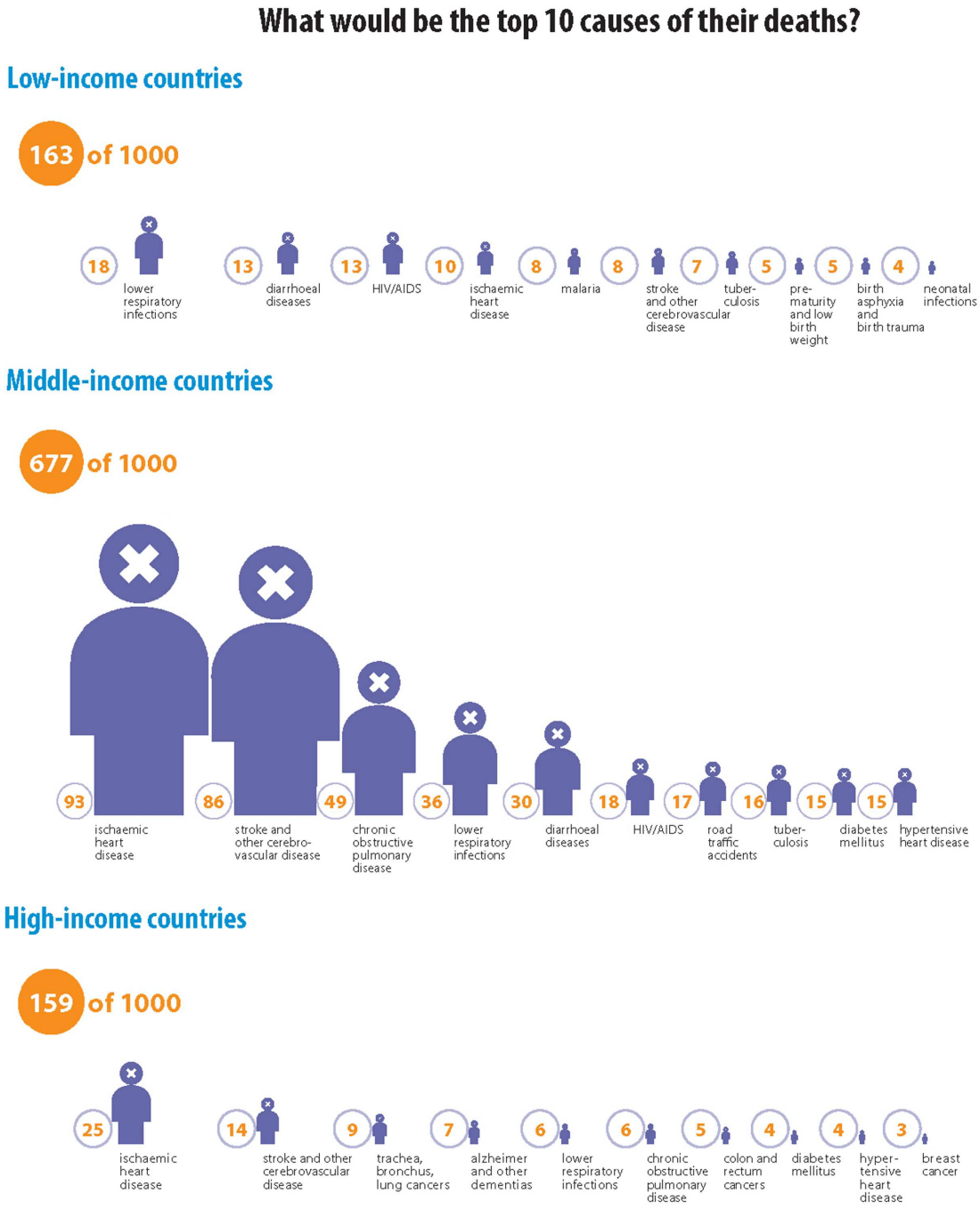

Figure 1.14: Overview of the main people death around the world.

Combined with these figures, it is also interesting to note that the life expectancy in these countries has increased significantly in the past thirty years, which means that better health policies and practices have decreased the prevalence of other illnesses, and simultaneously enabled progressive ageing of the population. These findings support the

notion that cardiovascular disease is strongly related to age, with a large proportion of fatal events occurring at 65 or later (over 80% of all CVD deaths in the US (Gaziano and Gaziano, 2009; World Health Organization. Regional Office for Europe, 2010), in spite of the fact that nearly two thirds of all CVD affected Americans are under this age). Despite this fact, the future trends in global mortality are not encouraged, as Figure 1.15. The resulting estimates suggest a massive shift in the distribution of deaths over the coming 25 years. Globally, deaths from cardiovascular diseases will rise from 17.1 million to 23.4 million in 2030. By 2030, deaths due to cardiovascular diseases, cancer and traffic accidents will collectively account for 56% of the projected 67 million deaths due to all causes (Gaziano and Gaziano, 2009; World Health Organization. Regional Office for Europe, 2010).

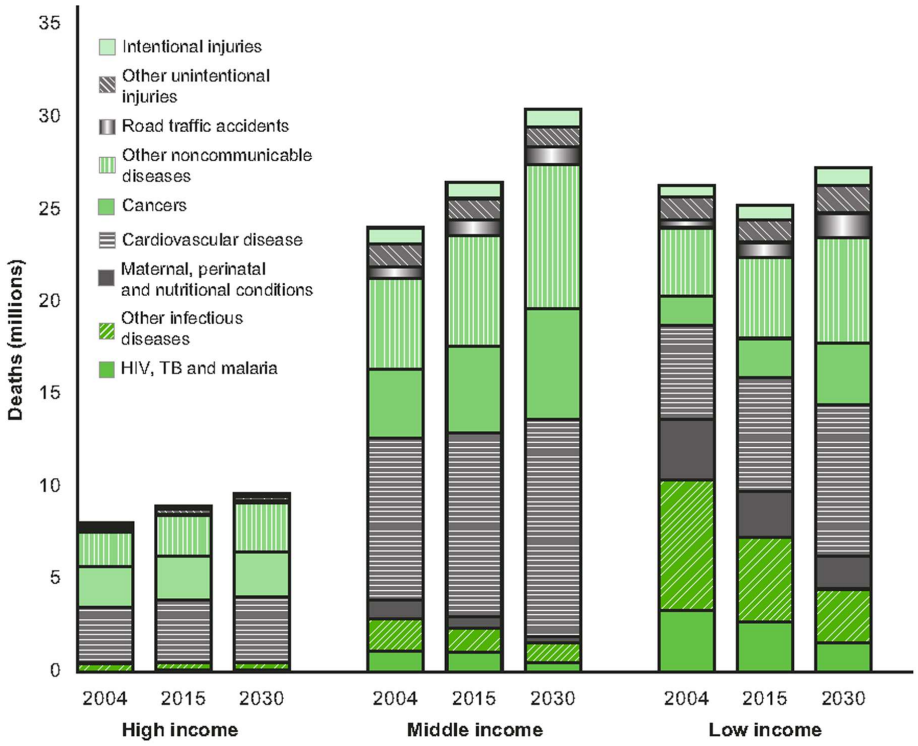

Figure 1.15: Projected deaths by cause for high, middle and low income countries.

The Spanish population follows these trends too, although the numbers are in all cases under those given above. Traditionally, this lower incidence of CVD in Spain and other Mediterranean countries has been associated to dietary habits. However, as noted in the latest European Cardiovascular Disease Statistics report (Petersen *et al.*, 2005; Gaziano and Gaziano, 2009), this pattern is now converging with that of northern European countries due to changes in the diet. Figure 1.16 schematizes the Spanish situation concerning the leading causes of mortality and the number of death that these diseases produced during the 2009 and 2010 years according to Spanish National

Statistics Institute (INE) (2010). Again, the cardiovascular diseases are the leading cause of death, accounting for approximately 120000 deaths per year. Furthermore, the evolution between the 2009 and 2010 years can be compared, observing a slightly reduction on the number of cardiovascular disease deaths.

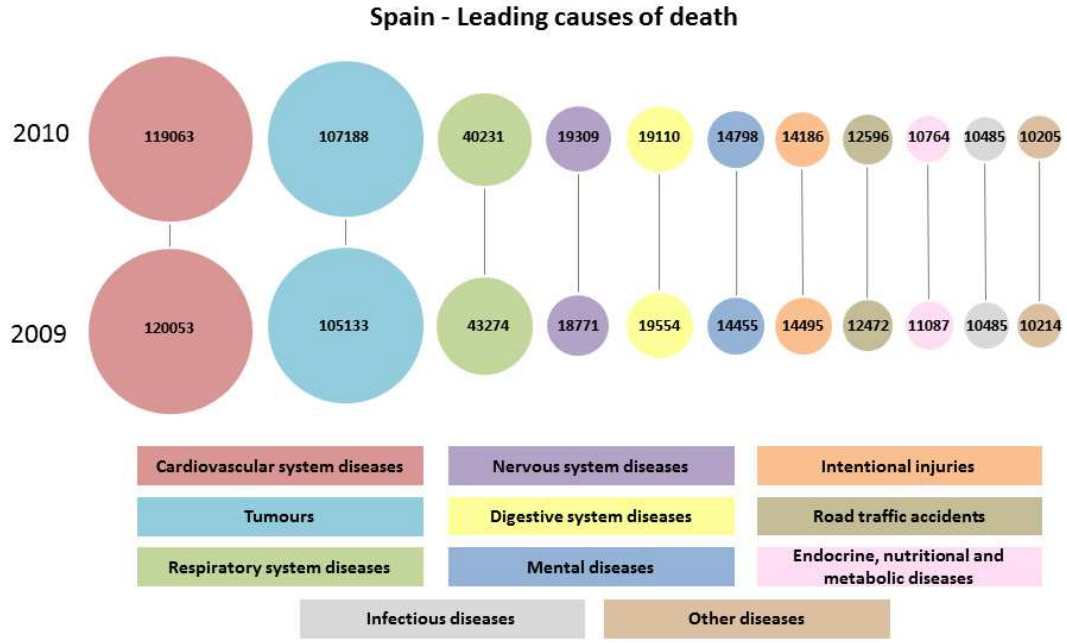

Figure 1.16: Spanish causes of death during the 2009 and 2010 years according to Spanish National Statistics Institute (INE) (2010).

Cardiovascular disease is divided into several categories of subclasses. The most important one, in terms of annual deaths, is Coronary Heart Disease (CHD), also referred to as Coronary Artery Disease (CAD), which refers to the disease of the blood vessels supplying the heart muscle. Stroke is another important affection caused by the disruption of blood supply to the brain, which may result from either blockage, with the resulting oxygen shortage (ischaemic stroke), or from rupture of a vessel, the haemorrhagic stroke. These two categories account for over two thirds of all CVD deaths in developed countries. In addition to these two, important CVD categories include aneurysm, especially in the larger vessels and at critical spots in the body, such as the brain; peripheral artery disease, which is similar to CHD but happens in the vessels supplying blood to the arms and legs; deep venous thrombosis, where blood coagulates in the peripheral veins (mainly in the legs), and dislodged clots move to the heart and lungs, causing embolism; finally, other less frequent illnesses like congenital heart disease, congenital abnormalities in the main vessels and rheumatic heart disease also find a place in official reports. All these disease processes are caused for the syndrome of the atherosclerosis, which is the main focus of this Thesis. Therefore, the atherosclerosis could be considered as the main responsible of the mentioned death related to cardio-

vascular diseases. Moreover, hypertension, a chronic increase in the blood pressure, is often encountered in combination with most of the above mentioned CVDs, and its presence is a major risk factor.

Due to the huge social and economical impact of CVDs, the study of the blood vessel and their associated pathologies have been one of the main research topics in medicine in the last decades. More recently, the mechanical factors influencing the vascular pathologies have been considered in Biomechanics (see, e.g., Fung, 1990). Specifically, arteries have been focused most of the efforts due to their higher tendency to develop disease pathologies, whereas veins have not been so deeply studied. The studies developed until the date demonstrate that mechanics play a determinant role in the development and evolution of a variety of pathologies (Humphrey, 2002b), which itself justifies the thorough investigation of their mechanical response both in healthy and diseased states.

1.7 Objectives

Based on the arguments above, the objective of this Thesis is to go deeper in the understanding and modelling of atherosclerotic blood vessel behaviour, being able to analyze the 3D mechanical environment of complex atherosclerotic lesions, and to identify high risk plaques. In particular, firstly, the analysis of plaque mechanics, by application of the nonlinear static finite element method and fluid-structure interaction, has been performed in order to identify the biomechanical stresses inside the arterial tissues, and to assess the rupture risk for atheroma plaque mechanical models. Secondly, a parametric tool to predict the vulnerability on atheroma plaques based on different Machine Learning Techniques (MLT) such as Artificial Neural Network (ANN) or Support Vector Machine (SVM). Thirdly, experimental characterization of the mechanical and pathological murine tissue properties affected by the atherosclerosis has been carried out. And, finally, a mathematical modelling of the atheroma plaque growth taking account the biological complex processes occurred during the atheroma plaque formation, has been developed. With this purpose, the main work and their partial objectives presented in this Thesis are itemized below:

- To improve the understanding of the role of mechanical factors in the vulnerability risk of atheroma plaque in coronary arteries. For this purpose several finite element idealized parametric studies will be carried out. The morphology and dimensions of the idealized geometry used will correspond to a standard coronary artery composed by media and adventitia layers. These parametric studies are as follows:
  - Mechanical effects of the atheroma plaque vulnerability by a 3D parametric model including the main biomechanical risk factor. Furthermore, the role of the residual stress will be assessed. 3D models allow to include residual stress effects and other features as fibre orientation, which can not be considered in 2D models. The influence of residual stresses on the risk of atheroma

plaque will be shown by comparing three sets of idealized 3D geometries incorporating residual stresses (one set taking into account just the longitudinal residual stress and other with the longitudinal and the circumferential residual stress included) and without them.

  - Parametric study by means of a plane strain model in order to evaluate the microcalcifications influence on the atheroma plaque vulnerability risk. Atherosclerotic plaques with microcalcifications located at the fibrous cap are more susceptible to rupture. However, the role of microcalcifications in the vulnerable plaque rupture mechanics is still debated. The parameters studied will be: the microcalcification angle, eccentricity and radius and the fibrous cap thickness.
  - Comparison of the atheroma plaque rupture risk between models with positive and negative remodelling. For this purpose, a parametric study under the plane strain hypothesis will be accomplished. As the plaque grows, two types of remodeling occur; positive and negative remodeling. Positive remodeling is an outward compensatory remodeling in which the arterial wall bulges outward and the lumen remains constant, the negative one is defined as the local shrinkage of vessel size (Glagov *et al.*, 1987; Varnava and Davies, 2001; Varnava *et al.*, 2002). The positive remodeling could explain why many heart attacks seem to come from out of the blue. Available screening and diagnostic methods are insufficient to identify the victims before the event occurs since they do not take into account the positive remodeling.

- To compare and validate the results obtained in the 3D idealized parametric analysis by means of the reconstruction of a patient-specific geometry obtained from IVUS medical images. This reconstructed geometry will be simulated by the finite element method.

- To study the role of the fluid (blood) on the mechanics of the atheroma plaque. For this goal, a 3D parametric fluid-structure interaction (FSI) analysis of a coronary model which atheroma plaque will be modeled, thereby the fluid effects of the blood will be included. Through this study, important variables as the wall shear stress (WSS) or the pressure drop along the artery will be obtained. Moreover, the stress field will be computed and compared with the results obtained in the 3D parametric study which include just the solid part.

- To advance towards the use of biomechanical models in artery clinical practice by means of the implementation of a parametric tool using Machine Learning Techniques (MLT) to take faster decisions about atheroma plaque vulnerability. The used techniques will be Artificial Neural Network (ANN) and Support Vector Machine (SVM). Furthermore, the results obtained will be compared with the classical linear regression in order to detect the presence of high nonlinearities in the problem and justify the use of such alternative techniques to solve the regression

problem. The procedure proposed to use this parametric tool would be carried as follows: for a specific patient, clinical staff should measure just four parameters in standard IVUS images and then, by using the ANN or SVM techniques, they would have an immediate response on the atheroma plaque vulnerability.

- To experimentally study the mechanical and pathological behaviour of atherosclerotic blood vessels by means of C57BL and ApoE$^{-/-}$ mice. The progressive development of atherosclerotic lesions along the aorta of both ApoE$^{-/-}$ and C57BL/6 mice (used as control) feeded on hyper lipidic and normal chow diets, respectively, is studied. Mechanical (inflated test and axial residual stress measurement) and histological properties between both strains at the same time and, the same strain at different time have been compared.

- To establish a methodology for the modelling of atheroma plaque growth in order to the better understanding of the biological processes. A mathematical model based on reaction-diffusion-convection equations which take account the main biological agents (LDL, monocytes, macrophages, foam cell, cytokines and smooth muscle cells) and processes have been developed.

Several commercial software such ABAQUS to the finite element simulations, MIMICS to reconstruct the patient-specific geometry obtained from IVUS, Matlab to implement the parametric tool based on MLT and other punctual tasks such as fit the material properties curves, ADINA to the fluid-structure interaction analysis and COMSOL to the modelling of the atheroma plaque growth have been handled during the develop of this Thesis. Furthermore, other commercial software like ICEM, FEMAP or IDEAS have been used for the meshing and smoothing of the geometries, and ImageJ to post-process the images obtained in the experimental inflation test.

Summarizing, the Thesis goal is to aid to bridge the gap between the medical and engineering community by providing clinicians with an index of vulnerability, linked to the mechanical strength and stress of the clinically important fibrous cap. The experimental tests performed and the models developed have the potential to serve as a tool for the understanding, diagnosis, prevention and better treatment of atherosclerotic plaques.

1.8 Organisation of the Thesis

The remaining of this Thesis is composed of seven Chapters and two Appendices. A schematic summary of the organization of the Thesis can be found in Figure 1.17. This work is organized as follows:

The main features of the vascular system are presented in Chapter 1. Special emphasis is put in the description of the wall composition of large and medium sized vessels, as well as in their classification as a function of their physiological role and composition. The most mechanically relevant features of blood vessels, which will be accounted for

in the elaboration of constitutive laws are presented, including the vessel layers, the definition of active and passive behaviour, the presence of residual stresses, and the anisotropic incompressible non-linear behaviour under finite strains. Furthermore, one of the most fatal cardiovascular diseases which affect to large and medium-sized arteries, the atherosclerosis, is presented. A review of the state of the art in cardiovascular modelling is provided in Section 1.4. Specifically, the constitutive laws most frequently used in the modelling of the vessel wall are presented, and a brief note about the volumetric-isochoric decomposition of the strain energy function, widely used in computational soft tissue biomechanics is given. After that, some of the experimental techniques frequently used to determine the mechanical properties of soft biological tissues are introduced. Finally, the main reasons and objectives that have motivated the development of this Thesis and a schematic description of the contents included in it are exposed.

Chapter 2 includes a 3D parametric study of the atheroma plaque vulnerability based on an idealized atherosclerosis coronary artery geometry. The steps to develop the computational model are detailed; geometry creation, studied parameters, model mesh and, finally the assignation of the material properties, boundary conditions and loads. Furthermore, the influence of both circumferential and longitudinal residual stress on the stress field is evaluated. In order to validate the idealized geometry hypothesis used in the 3D parametric study, a patient specific coronary artery has been reconstructed from IVUS images and simulated under the same boundary conditions, loads, material properties and size mesh than those of the 3D parametric study. The real reconstructed geometry has been compared with the corresponding idealized model. Finally, in order to show up the importance of using 3D blood vessel models to predict accurately the atheroma plaque rupture, the results obtained in idealized 3D and 2D models have been compared.

Chapter 3 which is closely related to Chapter 2, presents some new features for considering in order to improve the performance of the 3D idealized parametric study. The Chapter is divided in three parts. In the first part, a 2D parametric study performed on an idealized coronary artery to asses the microcalcification influence on the atheroma risk rupture is described. The second part consists of the comparison of the vulnerability risk of atheroma plaques with negative and positive remodeling by means of a 2D parametric study based on a idealized coronary artery. Finally, the last part resumes a 3D FSI parametric study performed in the same geometry model than the parametric study presented in Chapter 2. This study reproduces the pulsatile nature of physiological blood pressure and allows us to calculate some important biomechanical variables such as the wall shear stress distribution, which is considered essential in plaque formation and growth, or the pressure drop.

Chapter 4 comprises an alternative parametric tool based on MLT, such as AAN and SVM, to detect vulnerable atheroma plaques in coronary arteries. Furthermore, a comparison of the performance of these techniques (SVM and ANN) with the classical linear regression, in order to prove the non-linearity of the problem which justify the

use of MLT, is provided. This computational tool has been trained with the results obtained in the 3D parametric study presented in Chapter 2.

An experimental study carried out in order to determine the changes in vascular mechanical properties due to development of atherosclerosis, and specifically, the mechanical properties of the aortic tree of ApoE$^{-/-}$ and C57BL/6 mice is presented in Chapter 5. Among available animal models, the ApoE$^{-/-}$ mice are particularly popular because of its propensity to spontaneously develop atherosclerotic lesions on a standard chow diet. At the time they were aged 7 weeks, ApoE-/- mice have been fed on a Harlan-Teklad 88137 Western Diet (hyper-lipidic diet) in order to ease the development of atheroma plaque and C57BL/6 mice have been maintained on a normal chow diet so as to prove that ApoE-/- mice develop atherosclerosis. Forty individuals (five animals of each strain aged 10, 20, 30 and 40 weeks) were used for the study, in which both the longitudinal residual strain field and the mechanical properties by means of inflated tests, were investigated. The methodologies followed for harvesting, conservation, preparation, and mechanical testing of the specimens are exhaustively presented. Furthermore, anatomical analyses by gross examination of each animal have been performed by microscopy in order to show the predilection zones of atheroma plaque development and the evolution of the atheroma plaque growth as the time increases. Finally, analytical analyses, such as body weight, plasma levels of total cholesterol and triglycerides measurements of each animal, and histological and immunochemistry analysis were performed.

Modeling of the atheroma plaque growth is faced in Chapter 6. An atherosclerotic lesion growth model relying on the biomolecular processes that take place in the intima with blood flow dynamics and mass transfer is presented. The Navier-Stokes equations that govern the blood motion in the lumen, the Darcy law used to model blood filtration, as well as the reaction-diffusion-convection equations which model the evolution of the species, are the main equations involved in the atheroma plaque growth process both in the lumen and in the intima. The species considered are LDL, monocytes, macrophages, foam cell, cytokines, SMC and collagen are displayed.

The main conclusions of this Thesis, together with a brief summary of the original contributions here presented and the future work lines are collected in Chapter 7.

Finally, a summary of basic continuum mechanics has been included in Appendix A for completeness. Likewise, Appendix B comprises a brief summary of Python programming language and the main advantages of using this object oriented programming language combining with ABAQUS software. Furthermore, the Python code programmes for accomplishing several specific tasks such as the building of the parametric models of Chapters 2, 3 and 4 as well as the post-processing of these models, are included.

Additionally, at the beginning of the document, a spanish summary of the Thesis, which reports the motivation, structure, objectives and methodology as well as the main conclusions, original contributions and future work of this work, is presented

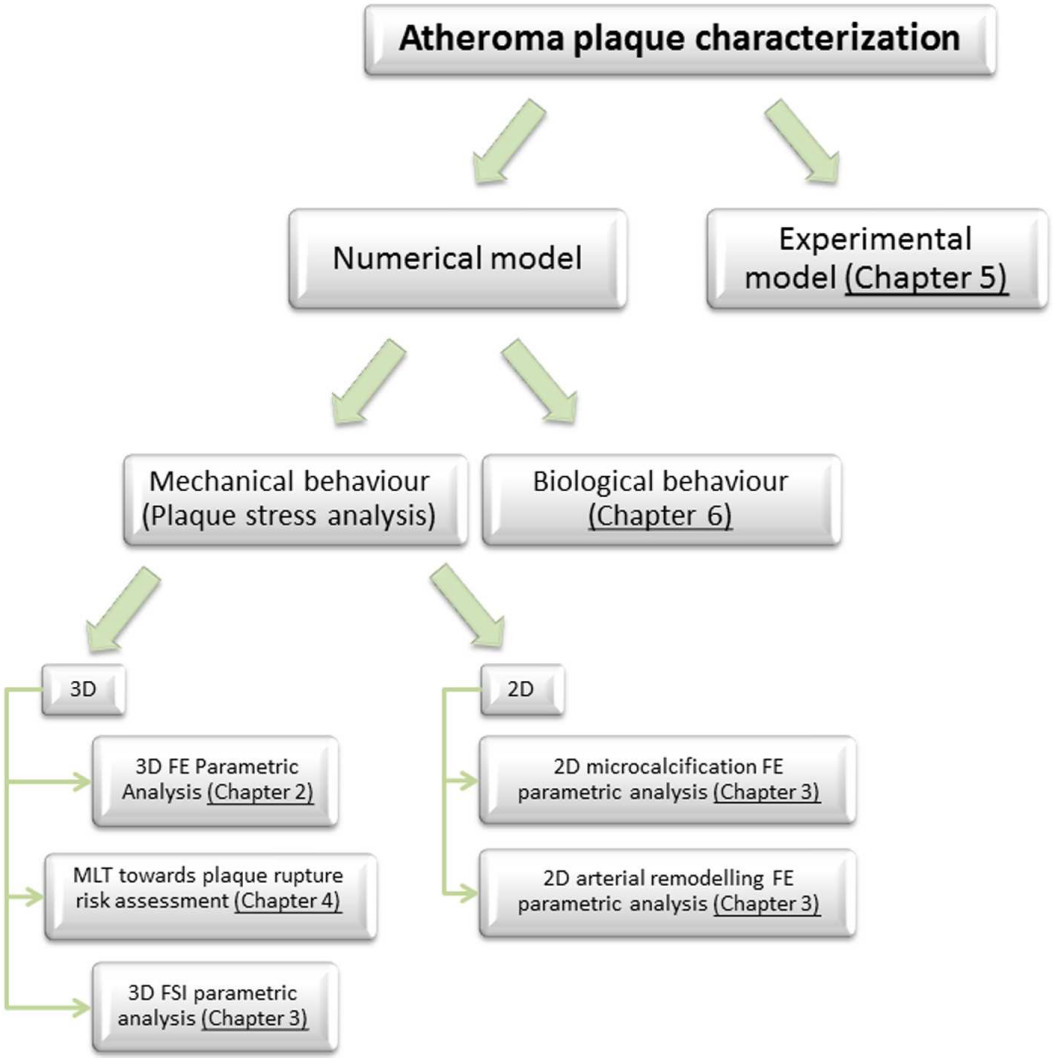

Figure 1.17: Scheme which summarizes the organization of the Thesis.

Chapter 2

Atheroma plaque vulnerability based on a three dimensional idealized parametric geometry

In this Chapter, a 3D idealized parametric finite element model is presented in order to evaluate the influence of morphology on the risk of plaque rupture, including the main geometrical factors, and to assess the role of circumferential and axial residual stresses. Since it is believed that mechanical stresses play an important role in atherosclerotic plaque rupture process and may be used for better plaque vulnerability assessment and rupture risk predictions, the maximal principal stress (MPS) has been considered as the key mechanical factor for the purposes of comparison in this parametric study.

Viewing the results, residual stresses should be considered in the modeling of this kind of problems since they cause a significant alteration of the vulnerable plaque region limits. The obtained results show that the fibrous cap thickness and the lipid core length, in combination with the lipid core width, appear to be the key morphological parameters that play a determinant role in the maximal principal stress (MPS). However, the stenosis ratio is found not to play a significant role in vulnerability related with the MPS. Plaque rupture should therefore be observed as a consequence, not only of the cap thickness, but also as a combination of the stenosis ratio, the fibrous cap thickness and the lipid core dimensions.

Contents

2.1 Introduction

Cardiovascular diseases related to atherosclerosis are nowadays primary causes of mortality in the developed world and it has been calculated that they will become the first cause of death worldwide in 2020 (Lloyd-Jones *et al.*, 2009) (see Chapter 1, Section 1.6). Until now, several methods have been used to evaluate the extent and location of atherosclerotic lesions; invasive methods such as IVUS (intravascular ultrasound) or X-ray angiography and non-invasive methods, which detect indicators of atherosclerosis such as classical risk factors (Lee *et al.*, 1993; Fayad and Fuster, 2001; Kips *et al.*, 2008) (see Chapter 1, Subsection 1.3.5). Despite advances in treating atherosclerosis disease, a large number of patients die suddenly without prior symptoms due to the atherosclerosis, showing that available screening and diagnostic methods are insufficient for the accurate diagnosis of atheroma plaque rupture. As a result, there is a huge interest in the detection of preclinical or subclinical atherosclerosis in order to provide early treatment as well as to take preventive measures.

A limited number of biomechanical and imaging studies started to emerge in the early 1990s addressing the role of mechanical stress in the destabilization of vulnerable plaques (see, e.g., Zarins *et al.*, 1983; Getz and Roberts, 1990; Loree *et al.*, 1992; Slager *et al.*, 2005b; Gijsen *et al.*, 2008). Plaque rupture is highly complex, multifactorial, and morphological criteria alone cannot reliably identify high risk plaques. Early studies based on structural mechanics (Richardson *et al.*, 1989; Loree *et al.*, 1992; Cheng *et al.*, 1993), identified a strong connection between plaque fracture and mechanical loading through blood pressure. It was especially shown that large, eccentric lipid cores impose a mechanical disadvantage to the plaque by redistributing circumferential stress to the shoulders regions of the plaques; hence to the location where fibrous caps in most cases tend to rupture (Burke *et al.*, 1997). These investigations provided strong evidences that acute plaque fracture is linked to plaque composition and to high mechanical stresses which exceed the ultimate tensile strength of the fibrous cap. Thus, it is now accepted that computational mechanics is necessary for the assessment of the vulnerability lesions. Regarding the mechanical forces, some authors (Ohayon *et al.*, 2005; Versluis *et al.*, 2006) consider the peak circumferential stress (PCS) as the most important biomechanical factor in the mechanisms leading to rupture of the atherosclerotic plaque, and have often used it as a predictor of atherosclerotic plaque rupture location. Previous works have shown that reduced fibrous cap thickness increases the maximal value of the PCS exponentially, and leads the cap stress to exceed the rupture threshold of 300 kPa (Lendon *et al.*, 1991; Cheng *et al.*, 1993; Ohayon *et al.*, 2005) when the cap thickness becomes lower than 65 μm (Moreno *et al.*, 2002; Finet *et al.*, 2004;

Vengrenyuk *et al.*, 2006; Virmani *et al.*, 2006).

Therefore, in recent years more attempts come from the biomechanics community by applying numerical tools in conjunction with imaging modalities such as MRI (Magnetic Resonance Imaging) and IVUS(Intravascular ultrasound) to provide deeper insights on plaque fracture. Several studies support the interrelation between the tissue structure and material properties and the overall mechanical environment of the plaque, and especially the fibrous cap responsible for acute cardiovascular events. However, the majority of published efforts have utilized simplified modeling approaches based on two dimensional model plaques or assumed plane-strain states (Richardson *et al.*, 1989; Loree *et al.*, 1992; Cheng *et al.*, 1993; Lee *et al.*, 1996; Bank *et al.*, 2000; Lee, 2000; Huang *et al.*, 2001; Finet *et al.*, 2004; Ohayon *et al.*, 2005; Krishna Kumar and Balakrishnan, 2005; Zheng *et al.*, 2005; Li *et al.*, 2006b; Versluis *et al.*, 2006; Ohayon *et al.*, 2008). Loree *et al.* (1992) studied the effects of plaque structure features including stenosis severity and fibrous cap thickness on stress distributions based on idealized plaque models. They found that decreasing the fibrous cap thickness considerably increased the peak circumferential stress, while increasing the stenosis severity decreased peak stress, suggesting that ruptured plaques may not associate with high stenosis degree. Cheng *et al.* (1993) studied the relation between the locations of peak stress in ruptured plaques and rupture sites for the same plaque. The results showed that most plaque rupture sites occurred very close to regions of high stress. They also found the maximum circumferential stress in plaques that ruptured was significantly higher than maximum stress in stable specimens. Finet *et al.* (2004) studied the effect of fibrous cap thickness to plaque stress with 2D idealized models. They found that irrespective of plaque geometry and composition, an atheroma plaque with a fibrous cap thickness of less than 60μm is considered as vulnerable. By using heterogeneous material model for stress analysis in human atherosclerotic aortas, Beattie *et al.* (1998) found that the distribution of stress and strain energy was strongly influenced by plaque structure and compositions, indicating that a proper material model with multi-components in plaque stress analysis is of very importance. Williamson *et al.* (2003) studied the sensitivity of wall stresses in diseased human coronary arteries to varied material properties. They showed that stresses in the artery have low sensitivities to variations in elastic modulus and comparable among isotropic nonlinear, isotropic nonlinear with residual strains, and transversely isotropic linear models. Huang *et al.* (2001) and Veress *et al.* (2000) investigated the effect of calcification towards plaque stability in human atherosclerotic coronary arteries. Furthermore, stress analysis has been combined with the findings from histological analysis to study the possible interaction between inflammatory activities and extreme stress environments in fibrous cap (Lee *et al.*, 1996; Howarth *et al.*, 2007; Hallow *et al.*, 2009). Ohayon *et al.* (2001) used IVUS images of human atherosclerotic coronary arteries before angioplasty to predict plaque rupture locations. Chau *et al.* (2004) performed a stress and strain study by using optical coherence tomography images and compared those results with models from histological images. Though the stress distributions were

comparable between those two models, the maximum stress was higher in the histological models. Tang *et al.* (2004) used *ex-vivo* MRI images for stress analysis and compared the results with histological models of human carotid plaques. From high resolution of *in vivo* multispectral magnetic resonance imaging of 5 human carotid atherosclerotic plaques, Li *et al.* (2006b) built up multicomponents of 2D plaque models. Incompressible hyperelastic material properties were used for the stress analysis. Results showed that the mean maximum stresses in ruptured plaques were much higher than those in non-ruptured plaques. In their following study (Li *et al.*, 2007b), they compared the stress concentrations between symptomatic and asymptomatic patients by 2D structure analysis based on *in vivo* magnetic resonance imaging, found that maximal predicted plaque stresses in symptomatic patients were significantly higher, indicating the possibility that plaques with higher stresses may be more prone to be symptomatic and rupture in the near future. Similar results can be found in the study by Trivedi *et al.* (2004). Nevertheless, other studies show that 2D structural analyses tend to overestimate the maximal value of the PCS (Ohayon *et al.*, 2005). In addition, longitudinal residual stress effects and other features such as the anisotropy or the longitudinal length of the plaque can not be considered in 2D models. Other promising approaches (Wu *et al.*, 2003; Tang *et al.*, 2005a,b; Li *et al.*, 2006) have presented 3D analyses of plaques based on fluid-structure interaction (FSI) to identify flow and stress conditions and to computationally assess the fracture risk factor of structurally different atherosclerotic lesions. In all mentioned studies, though, the arterial tissues were assumed to be isotropic, an assumption that does not reflect the experimentally observed anisotropic behavior of non-diseased (Weizsacker and Pinto, 1988; Abè *et al.*, 1996; Zhou and Fung, 1997; Schulze-Bauer *et al.*, 2002, 2003; Holzapfel *et al.*, 2005b; Holzapfel, 2006) and diseased (Holzapfel *et al.*, 2004) vascular tissues. The aforementioned studies undoubtedly offer notable insights on the mechanics of plaque vulnerability. However, isotropic material models do not yield reliable quantitative results (Holzapfel *et al.*, 2002), and restrict the biomechanical interpretation of the findings significantly. Furthermore, the performed 3D structural studies related to the atheroma plaque are usually carried out on geometries obtained from IVUS or MRI (Imoto *et al.*, 2005; Ohayon *et al.*, 2005; Auer *et al.*, 2006; Briley-Saebo *et al.*, 2007). Consequently, there is a need for modeling the complex 3D arterial tissue geometry and the related mechanics in a more realistic way.

Concerning the vulnerability risk factors, the fibrous cap thickness has typically been identified as the key predictor of vulnerability and likelihood of rupture, but some clinical and biomechanical studies have shown that this single parameter is not a reliable predictor of plaque stability (Virmani *et al.*, 2000; Krishna Kumar and Balakrishnan, 2005), since plaque stability also depends on other intrinsic properties of the plaque, such as the size and the consistency of the soft atheroma core (Finet *et al.*, 2004; Gao and Long, 2008), the cap and the core inflammation levels (Arroyo and Lee, 1999; Lee, 2000) and the arterial remodelling index, which is defined as the external elastic mem-

brane area at plaque divided by the external elastic membrane area at a nearest segment judged to be free of plaque. (Smedby, 1998; Varnava *et al.*, 2002; Ohayon *et al.*, 2008). Moreover, several studies have shown the importance of including residual stresses (RS) on arterial models to get an accurate calculation of the stress distribution across the arterial wall (Jaroslav *et al.*, 1999; Peterson and Okamoto, 2000; Jaroslav *et al.*, 2002; Raghavan *et al.*, 2004; Ohayon *et al.*, 2007; Alastrué *et al.*, 2007b). Holzapfel *et al.* (2005b) performed statistical analysis to test for significant correlations between age and axial *in situ* stretch and there were significant negative correlations between both. This suggests that axial *in situ* stretches of the human LAD coronary artery decrease with age. Varnava *et al.* (2002) simulated the effects of tissue aging on residual strain in the main right and left human coronary arteries based on experimental data. They found that experimental opening angle scatters considerably with age. The factors affecting the opening angle are age, sex and the degree of atherosclerosis. Besides, their study showed the effect of including the circumferential RS in the final stress distribution. The vessel artery wall is under tension in the inner layers and under compressive stress in the outer layers, for positive opening angles. The difference between both layers increases as the opening angle increases. This fact tends to make the circumferential stress more uniform in the arterial wall under the constant internal pressure. However, the influence of RS on the wall stress distribution in pathological coronaries remains unclear since the relationship between RS and atheroma plaque configuration is very complex. Longitudinal and circumferential RS present in a vulnerable coronary plaque dramatically influences the spatial stress distribution and could cause new sites of stress concentration. RS could play a major role in the biomechanical stability of vulnerable coronary plaque and in the growth process of the lipid core. This study shows that plaque rupture is to be viewed as a consequence not only of external pressure but rather of a subtle combination of external loading, geometrical configuration and intraplaque RS. Surprisingly, residual stresses are neglected in the great majority of the models mentioned above. Although simplified approaches have contributed to the current level of understanding of plaque rupture mechanics, there is a need to model the 3D morphology including RS.

Even though the performance and importance of 3D models has been demonstrated to identify vulnerable plaques (Ohayon *et al.*, 2005; Chun *et al.*, 2010), no idealized and parametric 3D studies have attempted to analyze the influence of residual stresses on the biomechanical stability of vulnerable coronary plaques. For this reason, a 3D parametric study of the geometric risk factors in an idealized coronary vessel to quantify and investigate the biomechanical interaction between the most influential values of the geometry of the vessel in the plaque rupture: (i) the fibrous cap thickness; (ii) the stenosis ratio; (iii) the lipid core width and (iv) the lipid core length, is presented in this chapter. Although similar studies in the literature include other parameters such as the lipid core angle or the remodelling index which is related to the lumen radius (see, e.g., Versluis *et al.*, 2006; Ohayon *et al.*, 2008), previous tests were performed in

order to choose the most influential parameters. Furthermore, the influence of residual stresses on the risk of atheroma plaque has been shown by comparing three sets of idealized 3D geometries incorporating residual stresses (one set taking into account just the longitudinal RS and other with the longitudinal and the circumferential RS included) and without them.

2.2 3D Computational modeling of atheroma plaque

2.2.1 Modeling of the atherosclerotic coronary artery

2.2.1.1 Idealized geometry

A 3D parametric study of the influence of the geometric factors was performed to check the vulnerability of the atherosclerotic plaque. For this purpose, a 3D finite element model was developed in the commercial finite element code ABAQUS 6.9, taking into account both the composition and the dimensions of the different layers of the tissue (media and adventitia), the fibrous plaque and the lipid core.

An idealized geometry corresponding to a coronary vessel with an eccentric atheroma plaque was modelled. The plaque was characterized by a large lipid pool with a thin fibrous cap (Davies, 1996; Ohayon *et al.*, 2001; Finet *et al.*, 2004). Atherosclerotic vessel morphology and average dimensions were obtained from Versluis *et al.* (2006) and Bluestein *et al.* (2008). A vessel length of 20 mm, an external radius of 2 mm and a vessel wall thickness of 0.5 mm were considered to create the basic geometry.

The arterial wall was assumed as a hollow cylinder and the lumen was consider circular. The atherosclerotic plaque, which is located inside the vessel, was assumed to be symmetric with respect to the central cross section. Finally, the lipid core was approximated as a blunt volume. In areas with atheroma plaque, the whole media layer was considered as fibrotic, whereas only the adventitia was considered to be a healthy tissue. Figure 2.1.a shows the longitudinal section of the atherosclerotic coronary vessel described and the main parts of the model considered; wall vessel composed by the adventitia and the media layers, lipid core and atheroma plaque.

2.2.1.2 Parameters studied

The parametric model consists of a series of idealized plaque morphology models, mimicking different stages and variations of the atherosclerotic lesion growth. Previous analyses were first performed on the model in order to identify the most influential geometric parameters on the atheroma vulnerability risk and their critical range values. Geometric parameters such as the lipid core angle (α, Figure 2.1), which is constant for all the geometries in the parametric study performed, were rule out as one of the most influential parameters. These previous tests consisted on a 3D parametric analysis performed on the same model shown in Figure 2.1 and with similar material properties and boundary conditions, which are described on Subsection 2.2.2.6.

Following the results of these previous tests and several works of the literature (Cheng *et al.*, 1993; Finet *et al.*, 2004; Ohayon *et al.*, 2008; Williamson *et al.*, 2003), the most influential geometric parameters considered were the fibrous cap thickness *(fc)*, the stenosis ratio *(sr)* - which is obtained by dividing the lumen radius by the lumen radius of a normal artery ($R = 1.5$ mm), $sr(\%) = \frac{r(mm)}{R(mm)}100$ - the lipid core length *(l)* and the lipid core width *(w)*. The lipid core width *(w)* was defined as the ratio between the percentage of the atheroma plaque width *(w_1)* and the distance from the inner point of the lipid core to the outer point of the fibrotic plaque *(w_2)*, $w(\%) = \frac{w_2(mm)}{w_1(mm)}100$. The central cross section of the 3D model with the parameters studied marked is shown in Figure 2.1.b, where the lipid core length was measured along the longitudinal direction (Figure 2.1.a).

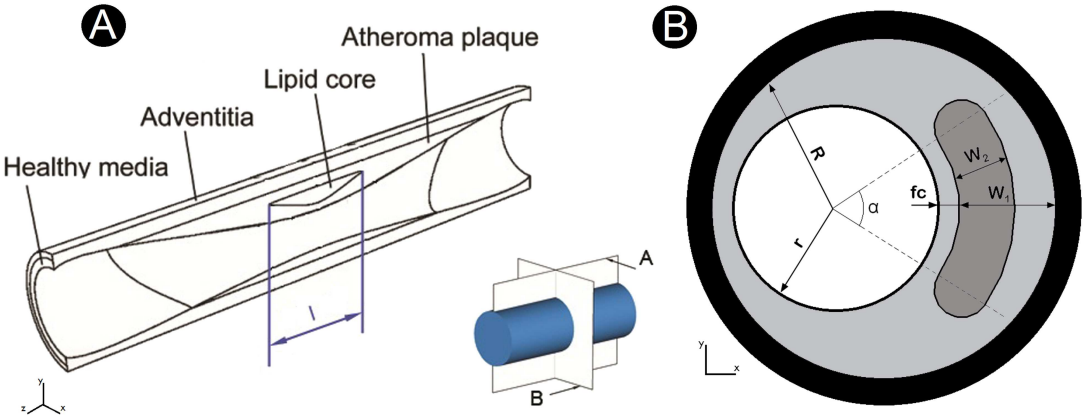

Figure 2.1: (A) Idealized geometry of an atherosclerotic arterial model and its main parts. Longitudinal section. (B) Geometrical parameters shown on the central cross section of the atherosclerotic vessel.

Five values for each parameter were considered and combined, which makes a total of $625 = 5^4$ idealized eccentric vessel models with atherosclerotic lesions. Realistic morphological data was investigated by varying the lipid core length ($1 \leq l \leq 8$, in mm), the stenosis ratio ($46.7 \leq sr \leq 66.7$, in %), the fibrous cap thickness ($0.025 \leq fc \leq 0.25$, in mm) and the lipid core width ($30 \leq w \leq 90$, in %) (Fujii *et al.*, 2005). The values of the geometrical parameters used to define the idealized coronary plaque models are shown in Table 2.1.

Level	***l*[mm]**	***sr*[%]**	***fc*[mm]**	***w*[%]**
1	1	46.7	0.025	30
2	2	53.3	0.05	45
3	4	56.7	0.1	60
4	6	60	0.15	75
5	8	66.7	0.25	90

Table 2.1: Geometrical parameters used to generate the parametric 3D models.

Residual stresses (RS) in longitudinal and circumferential directions were incorporated into the model to analyze the influence of the important mechanical factors in the vulnerability of the plaque. In order to assess the role of circumferential and axial residual stresses on the atheroma plaque ruptures, the set of 625 simulations described in this subsection were performed under three different hypothesis;

- (i) without RS,
- (ii) just considering longitudinal RS
- (iii) and taking account both circumferential and axial RS.

In total, 1875 (625 x 3) analyses have been performed. Each of these 1875 geometrical models, were created, meshed and defined by the means of a python programming code which allows the automation of the process (see Appendix B).

2.2.1.3 Mesh

A fine mesh was created in the various regions of the model and the fibrous cap region was meshed with an adaptive mesh. Previous sensitivity analyses were performed on the mesh to choose the definitive one. In order to show the influence of the mesh, two meshes with different number of elements and nodes are shown in Figure 2.2. The maximum MPS value and its localization is approximately the same for both cases.

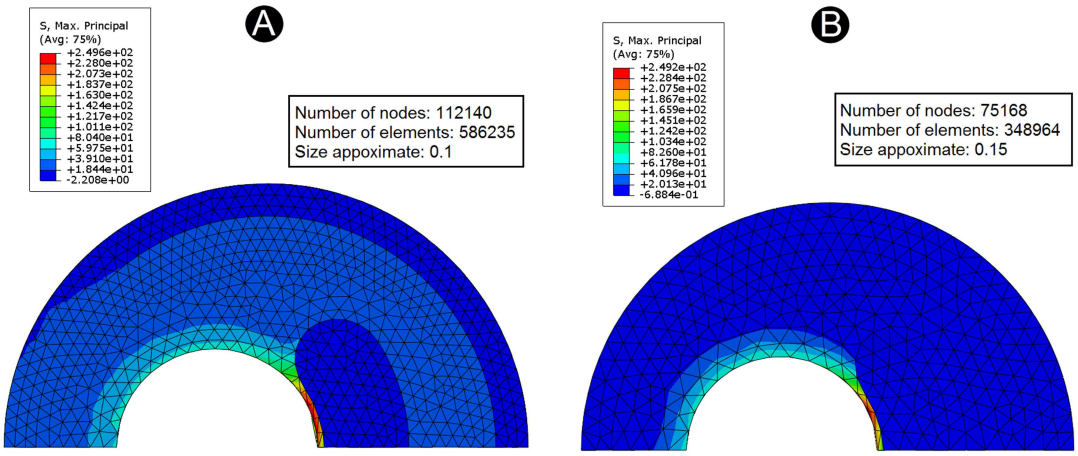

Figure 2.2: Comparison between the results obtained with two different mesh sizes. A- Fine mesh. B- Coarse mesh.

Due to the symmetry of the problem only a quarter of the model with approximately 150.000 hybrid linear tetrahedral elements and 30.000 nodes were considered. In general, the hybrid elements are used for incompressible materials to avoid volumetric locking. The mesh used and the number of nodes and elements vary from one simulation to another due to the geometry undergoes small alterations as the parameters are changed.

Figure 2.3 shows a longitudinal section of the mesh corresponding to one of the 625 models simulated.

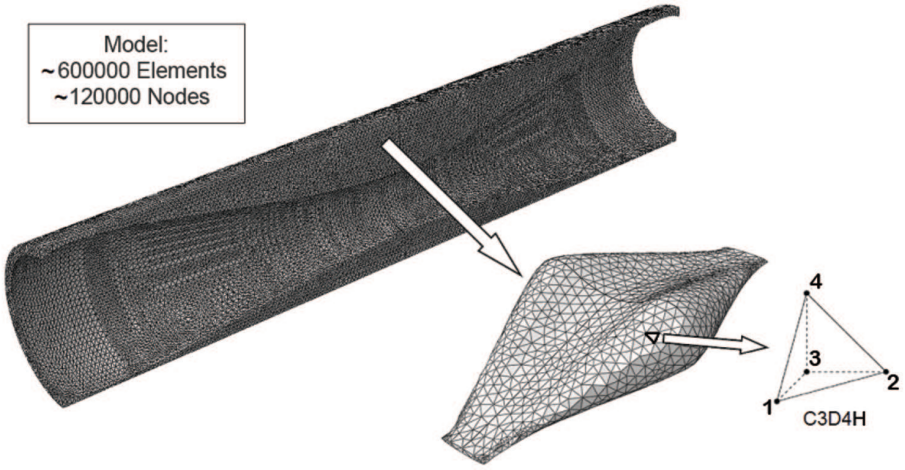

Figure 2.3: Representative longitudinal section of the mesh used for one of the 625 models simulated. Detail of the lipid core mesh. C3D4H is the type of elements used, which corresponds to linear and hybrid tetrahedral elements in ABAQUS commercial software.

2.2.1.4 Material properties

All tissues were modelled as nonlinear, hyperelastic and incompressible materials (Carew *et al.*, 1968; Holzapfel *et al.*, 2005b). The lipid core and the atherosclerotic plaque were modelled as isotropic materials, while healthy wall was considered as an anisotropic material with two families of fibres, oriented at $\pm$ 61.8° and $\pm$ 28.35° with respect to the circumferential direction in the adventitia and the media layers, respectively. Both families of fibres were assumed to have the same mechanical properties (Holzapfel *et al.*, 2005b) (see Figure 2.4).

The behaviour of the tissue was modelled by using the Gasser, Ogden and Holzapfel (GOH) strain energy function (SEF) (Gasser *et al.*, 2006)

$$\Psi = \mu[I_1 - 3] + \frac{k_1}{2k_2} \sum_{i=4,6} \exp\big(k_2\big[\kappa[I_1 - 3] + [1 - 3\kappa][I_i - 1]\big]^2\big) - 1, \qquad (2.1)$$

where $\mu > 0$ and $k_1 > 0$ are stress-like parameters and $k_2 > 0$ and $0 \leq \kappa \leq \frac{1}{3}$ are dimensionless parameters (when κ=0 the fibres are perfectly aligned (no dispersion) and when κ=$\frac{1}{3}$ the fibres are randomly distributed and the material becomes isotropic), $I_1 = \mathrm{tr}(\boldsymbol{C})$ is the first invariant of $\boldsymbol{C}$, with $\boldsymbol{C} = \boldsymbol{F}^T\boldsymbol{F}$ the right Cauchy-Green tensor and $\boldsymbol{F}$ the deformation gradient tensor, $I_4(\boldsymbol{C}, \boldsymbol{a}_1) = \boldsymbol{a}_1 \cdot \boldsymbol{C} \cdot \boldsymbol{a}_1$ and $I_6(\boldsymbol{C}, \boldsymbol{a}_2) = \boldsymbol{a}_2 \cdot \boldsymbol{C} \cdot \boldsymbol{a}_2$ are invariants which depend on the direction of the family of fibres at a material point

$\boldsymbol{X}$ that is defined by the unit vectors field $\boldsymbol{a}_1$ and $\boldsymbol{a}_2$ (Spencer, 1971) (for more details, see Appendix A).

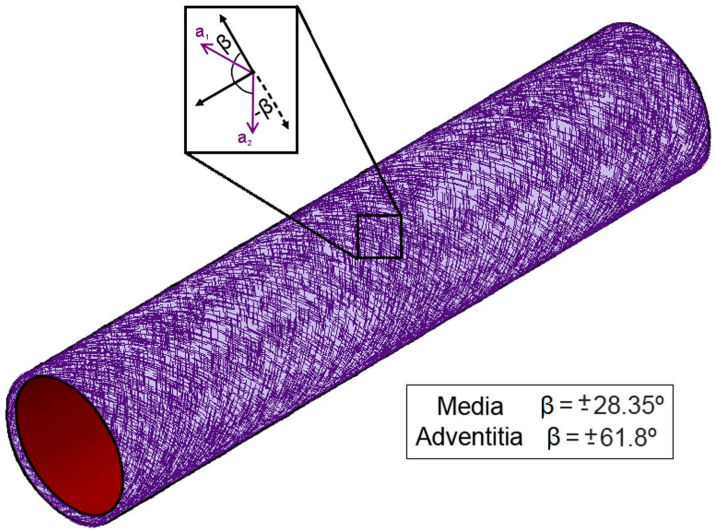

Figure 2.4: Fibres distribution in the adventitia and media layers. $\pm\,\beta$ is the orientation angle of the fibres with respect to the circumferential direction. $\boldsymbol{a}_1$ and $\boldsymbol{a}_2$ are the vectors which define the fibre orientations of each family of fibres.

A least-square minimization procedure was used to identify the set of constants that better reproduce the experimental curves coming from simple tension tests. For this purpose, an objective function relating the measured stress-stretch data to the stress values provided by each specific constitutive model is used. Due to the anisotropic nature of the blood vessels, tissue experimental data in different tests directions were included simultaneously in the objective functions, so that the resulting constants account for this tissue feature.

The general form of this function for stress data measured at n stretch values is represented in Equation (2.2).

$$\chi^2 = \sum_{i=1}^{n} \left[\left[\sigma_{\Theta\Theta} - \sigma_{\Theta\Theta}^{\Psi} \right]_i^2 + \left[\sigma_{ZZ} - \sigma_{ZZ}^{\Psi} \right]_i^2 \right]. \tag{2.2}$$

There, $\sigma_{\Theta\Theta}$ and σ_{ZZ} are the Cauchy stress data obtained from the tests in circumferential and longitudinal directions, respectively. In the same way, $\sigma_{\Theta\Theta}^{\Psi}$ and σ_{ZZ}^{Ψ} represent the Cauchy stresses in circumferential and longitudinal directions provided by each constitutive law for the ith stretch level.

The expressions that allows a straightforward computation of the Cauchy stress value as a function of the stretch level in each direction are obtained by standard derivation of the strain energy density function (see, e.g., Holzapfel *et al.*, 2000), and are expressed as

$$\left[\sigma^{\Psi}_{\Theta\Theta}\right]_i = \left[\lambda_\Theta \frac{\partial \Psi}{\partial \lambda_\Theta}\right]_i, \qquad \left[\sigma^{\Psi}_{ZZ}\right]_i = \left[\lambda_Z \frac{\partial \Psi}{\partial \lambda_Z}\right]_i. \tag{2.3}$$

After that, the material constants set that better recaptures the experimental curves was obtained by minimizing Equation 2.2 by means of an, e.g., Levenberg-Marquardt (Marquardt, 1963) or quasi-Newton optimization algorithm (see, e.g., Gill *et al.*, 1981, and references therein).

For this least squares based iteration scheme, experimental data reported in previous works (the adventitia and the media properties from Holzapfel *et al.* (2005b) and the plaque and the lipid core properties from Versluis *et al.* (2006)) were fitted using the Levenberg-Marquardt minimization algorithm (Marquardt, 1963). Notice that all tissues have been considered as incompressible (J = 1) for this material parameter identification. Figure 2.5 shows the experimental stress-stretch model responses for each part of the model considered (Holzapfel *et al.*, 2005b; Versluis *et al.*, 2006) and the fit obtained after the least squares based iteration scheme. Adventitia and media layers have different behaviour in the longitudinal and circumferential direction due to its anisotropy.

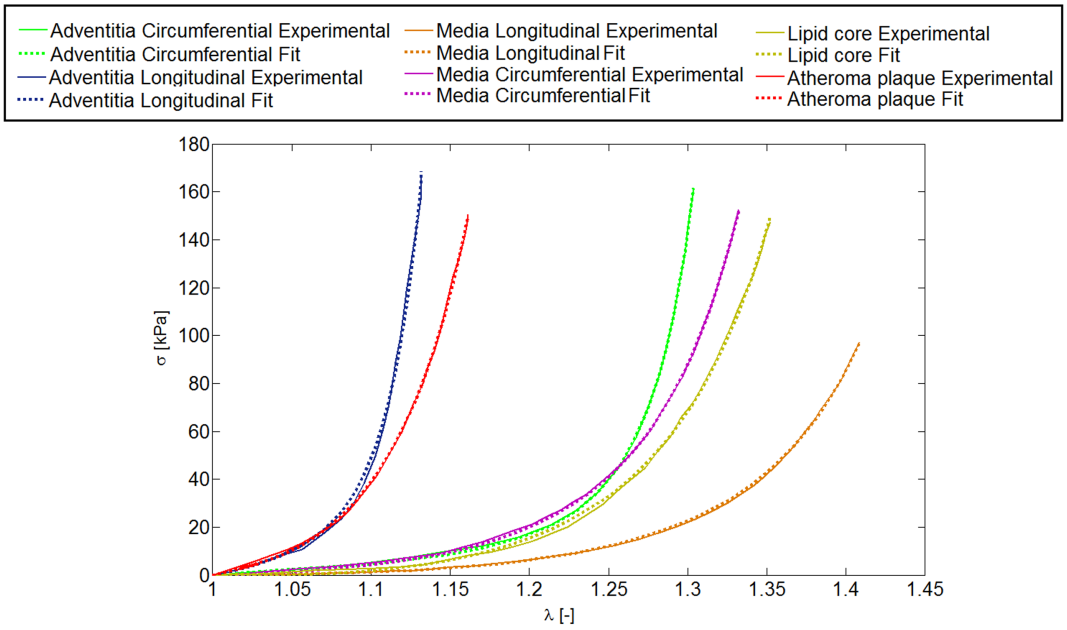

Figure 2.5: Stress-stretch model responses of experimental data taken from the literature (dot line) (Holzapfel *et al.*, 2005b; Versluis *et al.*, 2006) and fit performed by a least-square minimization procedure (normal line) for each tissue of the model considered; adventitia and healthy media layers in both directions (circumferential and longitudinal), lipid core and atheroma plaque.

Table 2.2 shows the results of the parameter identification for each tissue fitted according the Gasser, Ogden and Holzapfel strain energy function (Gasser *et al.*, 2006).

Furthermore, the normalized mean square root error (ε) which is defined as

$$\varepsilon = \frac{\sqrt{\frac{\chi^2}{n-q}}}{\sigma_{mean}}, \tag{2.4}$$

was used to check the goodness of the fit. Where q is the number of parameters of the strain energy function, n is the number of data points, $n-q$ is the number of degrees of freedom, and σ_{mean} is the mean stress.

	$\mu[kPa]$	$k_1[kPa]$	$k_2[-]$	$\kappa[-]$	$\beta[°]$	$\varepsilon[-]$
Adventitia	8.44	547.67	568.01	0.26	±61.8	0.041
Healthy media	1.4	206.16	58.55	0.29	±28.35	0.014
Atheroma plaque	9.58	17654.91	0.51	0.33	-	0.056
Lipid core	0.052	965.76	70	0.33	-	0.03

Table 2.2: Material parameters of the GOH strain energy function (SEF) (Gasser *et al.*, 2006) used in the finite element analysis for the adventitia, the healthy media, the atheroma plaque and the lipid core.

2.2.1.5 Boundary conditions and loads

Regarding the boundary conditions, the longitudinal displacements were constrained at the end of the blood vessel, whereas the free radial displacement allows the model to expand. Symmetry conditions were imposed in the corresponding symmetry planes to avoid the solid rigid behaviour of the model and only a quarter of the model was simulated.

Firstly, in order to introduce the circumferential residual stress, a cut with an opening angle of 23.5° was performed in the opposite side of atheroma plaque location according to the experimental data of severe atherosclerosis obtained by Jaroslav *et al.* (1999). The opened model was closed such that finally the configuration shown in Figure 2.6.a is obtained. Secondly, to introduce the longitudinal residual stress, the model was stretched 4.4% of the vessel length in the longitudinal direction, representing *in vivo* conditions reported by Holzapfel *et al.* (2005b), as Figure 2.6.b shows. Thirdly, a constant internal pressure load of 140 mmHg (18.7 kPa) was imposed in the inner surface of the lumen, simulating the blood flow pressure (Ohayon *et al.*, 2008) (Figure 2.6.c).

Summarizing, in the simulation set without RS included, just the internal pressure load is applied (Figure 2.6.c), in the simulation set with the longitudinal RS included the longitudinal RS boundary condition and the internal pressure load are assigned (Figure 2.6.b + Figure 2.6.c), and finally, in the simulation set where longitudinal and circumferential RS are incorporated, the longitudinal and circumferential RS boundary conditions and the internal pressure load are implemented (Figure 2.6.a + Figure 2.6.b + Figure 2.6.c).

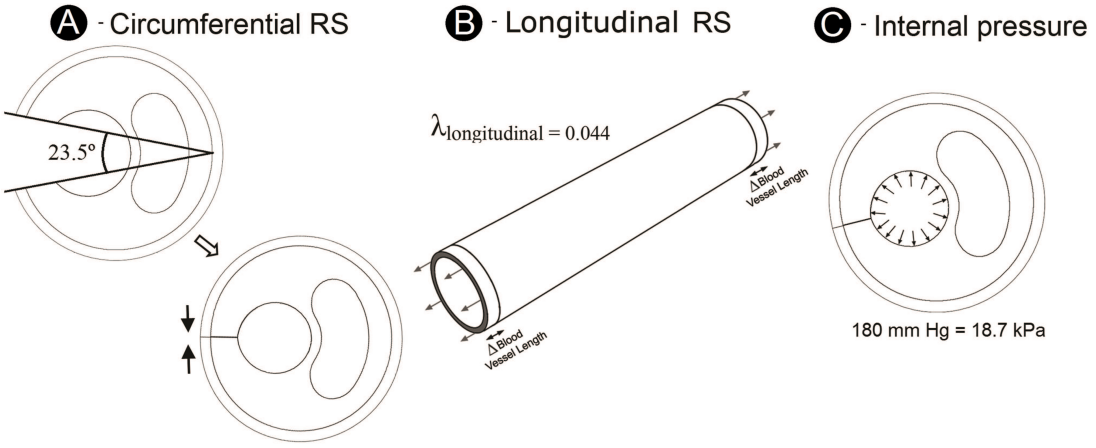

Figure 2.6: Boundary conditions and loads applied for the different simulation set. A - Circumferential RS boundary condition. B - Longitudinal RS boundary condition and C - Internal Pressure load.

Maximal Principal Stresses (MPS) were considered as the key mechanical factor for the purposes of comparison in this study. It is important to remark that the maximum MPS was measured at the critical zones (fibrous cap and plaque shoulders) and always appears in the circumferential direction. Some authors have shown that the maximum MPS sometimes appears at healthy areas, where rupture is unlikely (Arroyo and Lee, 1999; Tang *et al.*, 2005a, 2008, 2009). Healthy areas where rupture is not probable, even if a local stress maximum occurred there, have been excluded from the analysis of the results.

2.2.2 Influence of the morphology and the axial and circumferential residual stresses on the risk of atheroma plaque rupture

2.2.2.1 Contour maps of maximal principal stress

Figure 2.7 illustrates the difference between the results obtained in an idealized 3D coronary artery model with the longitudinal RS included (Figure 2.7.a), a 3D model with the circumferential and the longitudinal RS (Figure 2.7.b) and the equivalent 3D model without residual stresses (Figure 2.7.c). The dimensions of the presented case are; 4 mm long lipid core, 53.3% of stenosis ratio, 0.025 mm thick of fibrous cap and 60% of lipid core width. The maximum MPS is located at the fibrous cap in every case, however this value varies from 451.7 kPa in the model with the longitudinal RS included, to 254.4 kPa in the model with circumferential and the longitudinal RS included and to 385.7 kPa in the model without residual stress effects. The maximum MPS decreases with the incorporation of circumferential and longitudinal RS, but increases when just the longitudinal RS are considered, see Figure 2.7. However, although this trend is observed in a great number of the studied cases, it could not be completely generalized.

The maximum MPS also highly depends on the geometrical factors, as it is shown in Figure 2.12.

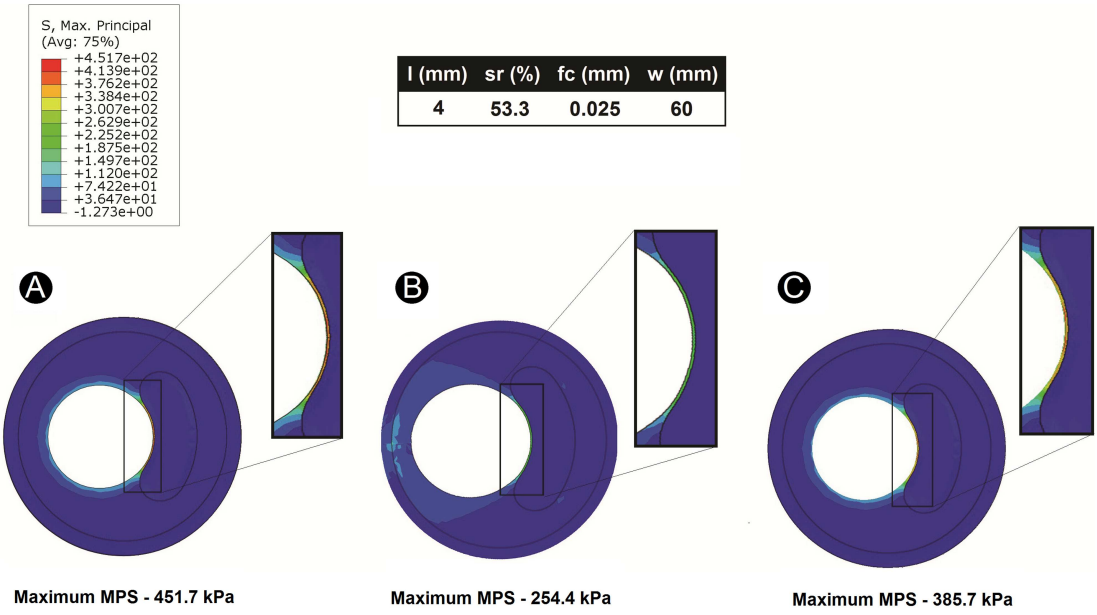

Figure 2.7: Contour maps of MPS. Comparison between a model with the longitudinal RS included (A), a model with the longitudinal and the circumferential RS included (B) and without them (C). The dimensions of the presented model are as follows: 4 mm long lipid core, 53.3% of stenosis ratio, 0.025 mm thick of fibrous cap and 60% of lipid core width.

There is an explanation for the fact that maximum MPS decreases with the incorporation of circumferential and longitudinal RS, but increases when just the longitudinal RS are considered. Longitudinal RS produces an increment of the MPS. This fact is due to the MPS in the fibrous cap occurs in the circumferential direction if just internal pressure load is considered (without any residual stress), Figure 2.8.a. Moreover, when just the longitudinal RS are included (without internal pressure load), Figure 2.8.b, the circumferential stresses are positive as well due to the incompressibility of the lipid core. Thus, if longitudinal RS and internal pressure load are imposed, Figure 2.8.c, the circumferential stresses are higher than without considering longitudinal RS. Thus, if the circumferential RS are not considered (0° opening angle), the whole blood vessel wall is under tensile stresses, being this stress bigger on the inner layer of the blood vessel wall.

In addition, the circumferential residual stress in arteries is a compressive stress at the inner boundary and a tensile stress at the outer boundary, for positive opening angles (opening angle greater than 0°). The difference between both layers increases as the opening angle increases. This fact tends to redistribute the total stress and also

gives a more uniform stress distribution in the arterial wall under the constant internal pressure.

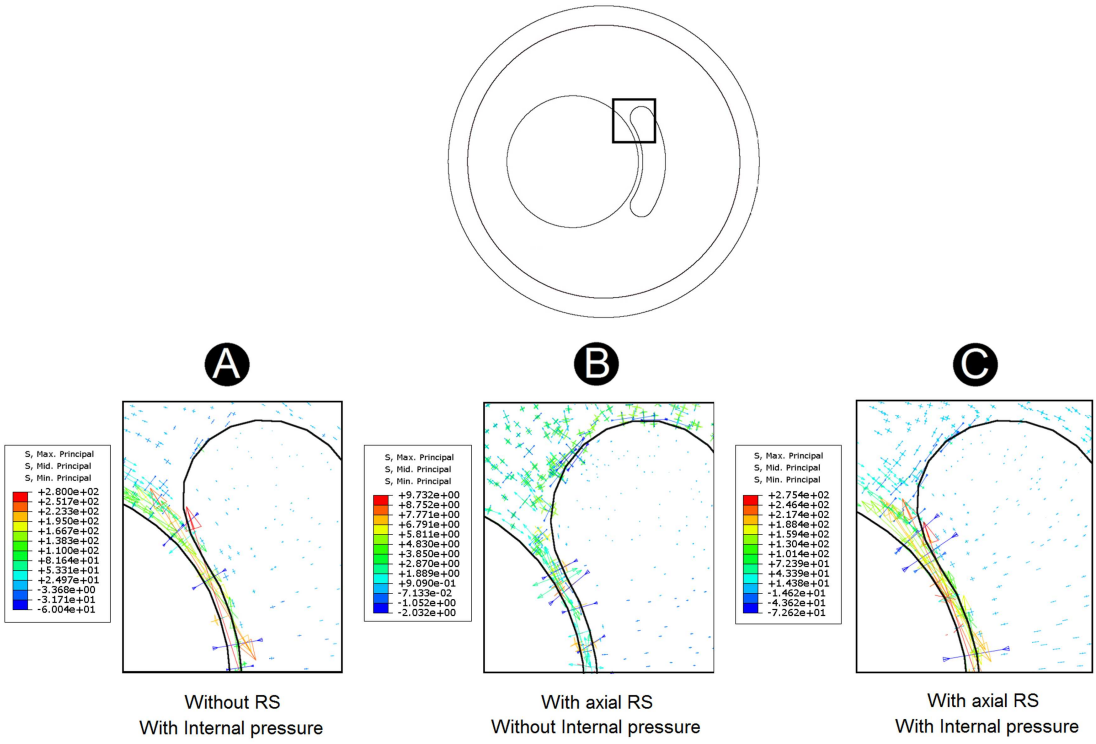

Figure 2.8: Detail of the principal stresses (maximum, minimum and media) in the fibrous cap thickness area. A - Without RS and with internal pressure load. B - With longitudinal RS and without internal pressure load. C - With longitudinal RS and internal pressure load.

2.2.2.2 Statistical Analysis

In order to assess the influence of the geometrical parameters on the MPS, a statistical analysis was performed. The Lilliefors test (to check the normality of the distribution) (Lilliefors, 1967), the Student's t-tests and the analysis of variance (ANOVA) were used (Fisher, 1925). The ANOVA test and the Student's t-test were performed at 1% and 5% significance level, respectively. For further details of the statistical analysis performed see e.g. (Wasserman, 2005; Rice, 2006).

Figure 2.9 shows the statistical analysis performed on the maximum MPS value in the critical region with respect to the distinct geometrical parameters (lipid core length, stenosis ratio, fibrous cap thickness and lipid core width) for the three different simulation sets studied (with just the longitudinal RS included, with the longitudinal and the circumferential RS included and without RS). Each subfigure represents the

results grouped for the different levels of each geometrical parameter, and the variation of this parameter becomes influential if the MPS is modified significantly as this parameter varies. In this Figure, the means of group n and the groups marked with $*^{(n)}$ are significantly different with the probability (p) indicated in the legend which is located in the top of each figure. Subfigures without any mark mean that, performing two sample comparisons, the means are always significantly different. On each box, the central mark is the median, the edges of the box are the 25th and 75th percentiles, the whiskers extend to the most extreme data points not considered outliers, and outliers are plotted individually.

In the first row of Figure 2.9, the median for each variation of the lipid core length increases slightly with the lipid core length for all the cases, especially for the longitudinal and circumferential RS simulation sets. For the models with longitudinal RS and without RS, considering all the two-sample comparisons (paired t-test), some significant differences are found, between the second group ($l = 2$ mm) and the groups marked with $*^{(2)}$ and between the fifth group ($l = 8$ mm) and the groups marked with $*^{(5)}$ ($p < 0.01$, see Figure 2.9). However, when the circumferential and the longitudinal RS are considered, the lipid core length becomes more influential since the means are always significantly different for all the two sample lipid core length comparisons considered ($p < 10^{-5}$).

The stenosis ratio statistical analysis is shown in the second row of the Figure 2.9. In this case, the medians and the dispersion are similar and very few significant differences between the means of the groups for the three simulation sets considered are found, showing that the stenosis ratio does not play a significant role in vulnerability related to the MPS.

The statistical analysis of the fibrous cap thickness is shown in the third row of Figure 2.9 and demonstrate the big influence of this parameter on the MPS for the three analyzed simulation sets. A noteworthy remark is that the median and the dispersion of each variation of the fibrous cap thickness decrease dramatically as the fibrous cap thickness increases. In addition, considering all the two sample fibrous cap thickness combinations, the means are always significantly different ($p < 10^{-5}$), reflecting the huge influence of this parameter on the MPS values, even if the residual stress are not considered.

Finally, the lipid core width statistical analyses exhibited in the fourth row of Figure 2.9, shows that both medians and dispersions increase with the lipid core width. In a similar way than in the case of the fibrous cap thickness, for all the two sample lipid core width considered comparisons, the means are always significantly different ($p < 10^{-5}$) for the three simulations sets considered, showing again a high dependence of this parameter.

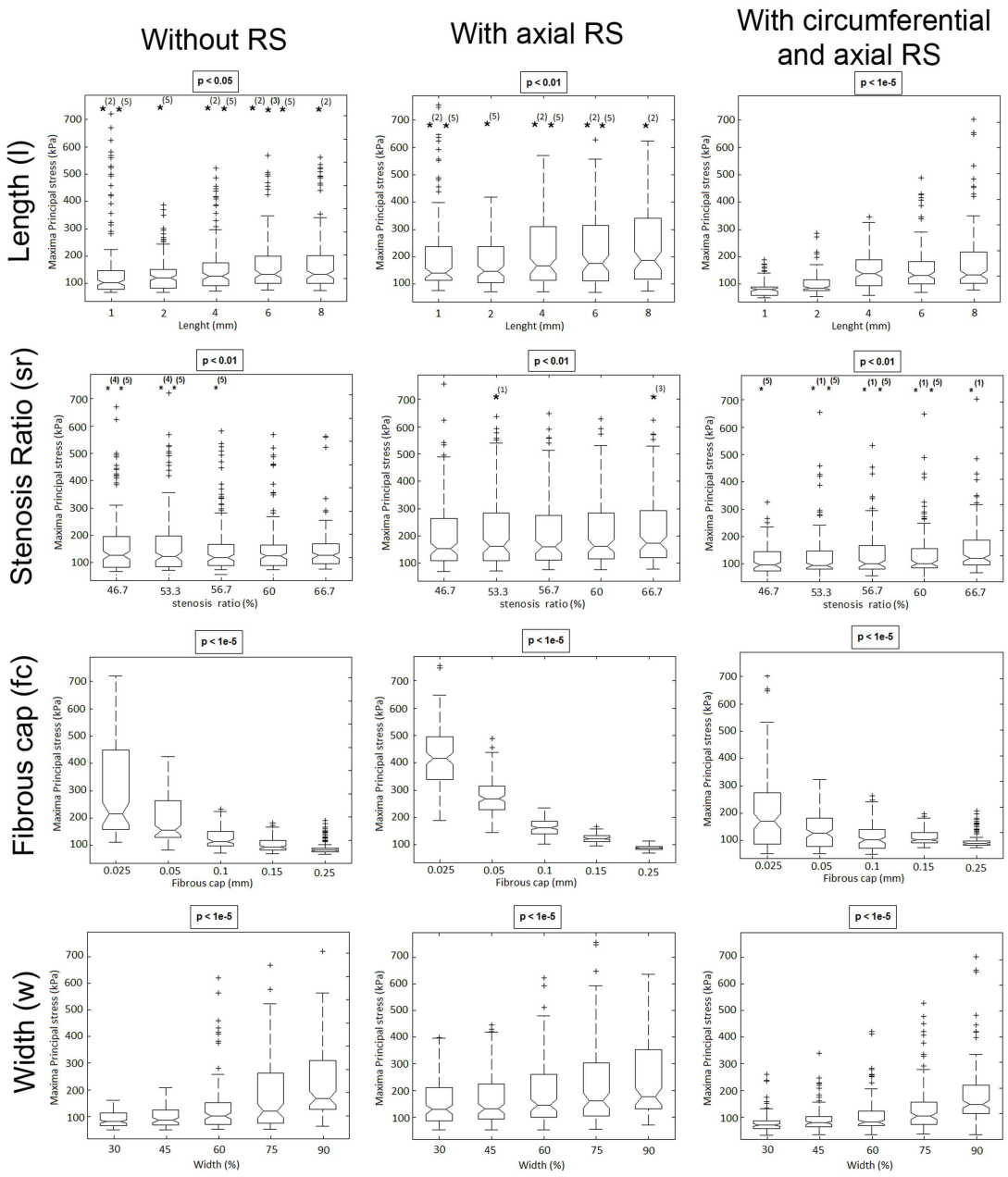

Figure 2.9: Statistical analysis: Maximum MPS vs. the variation of each parameter for the three different simulation sets; without RS, with the axial RS included and with the circumferential and the axial RS included. The means of group n and the groups marked with $*^{(n)}$ are significantly different with the probability p. Figures without any mark mean that, performing two sample comparisons, the means are always significantly different.

2.2.2.3 Trend analysis

In order to compare the variation of circumferential stress versus the geometrical parameters considered in 3D parametric study, a normalized variation of each parameter has been defined. This parameter (ν_{param}) is obtained as $\nu_{param} = \frac{a_{param}-a_{max}}{a_{max}-a_{min}}$, where the variable "$a_{param}$" represents each of the four parameters (lipid core length (ν_l), lumen radius (ν_r), fibrous cap thickness (ν_{fc}) and lipid core width (ν_w)) in whatever position, and a_{min} and a_{max} are the lowest and highest values, respectively, of each parameter. Figure 2.10 represents the maximum MPS vs. normalized variation ν_{param} of each parameter. There are 5 variations for each parameter, therefore 125 cases have been represented in each normalized variation of each parameter.

A trend analysis has been performed in order to show the influence of the variation of each parameter in the maximum MPS. Therefore, a linear trendline ($MPS(kPa) = p_1\nu_{param} + p_2$) has been added to the experimental data in each graph. The general trend observed is that the maximum MPS increases respect to the models without RS if axial RS are considered, whereas the MPS decreases and the dispersion is reduced if circumferential and axial RS are included, as Figure 2.10 shows.

In Figure 2.10.a, the results for the lipid core length are shown. The linear trendline has a positive gradient for the three simulation sets studied ($p_1 = 37.48$ kPa, $p_1 = 45.3$ kPa and $p_1 = 98.2$ kPa for the cases without RS, with circumferential RS included and axial and circumferential RS included, respectively) and p_1 increases more than twice from the cases without RS to those with axial and circumferential RS included, reflecting an increased influence of this parameter on the MPS when the axial and circumferential RS are considered.

Stenosis ratio evolution (Figure 2.10.b) has negative gradient for the models without RS included ($p_1 = -32.6$ kPa), so maximum MPS decreases as the lumen radius increases from 167.3 kPa to 134.7 kPa for $sr = 46.7\%$ and $sr = 66.7$ %, respectively. However, p_1 is positive for the cases with RS considered, so the trend changes and maximum MPS increases as the lumen radius increases when RS are taken account. Furthermore, the gradient concerned to the stenosis ratio are the lowest, reflecting a low influence of this parameter on the MPS.

The gradients related to the fibrous cap thickness (Figure 2.10.c) are the steepest and they are negative ($p_1 = -204.7$ kPa, $p_1 = -293.6$ kPa and $p_1 = -58.8$ kPa for the simulations set without RS, with circumferential RS included and axial and circumferential RS included, respectively). In this case the inclusion of RS tends to relax the acute dependence on this parameter.

Finally, the lipid core width analysis, (Figure 2.10.d), shows a pronounced slope with a positive value for the three set of cases studied (with axial RS, with circumferential and axial RS and without them). Eventually, p_1 decreases from the case without RS ($p_1 = 164.2$ kPa) to the cases with RS considered ($p_1 = 84.5$ kPa and $p_1 = 88$ kPa for the simulations set with circumferential RS included and axial and circumferential RS included, respectively).

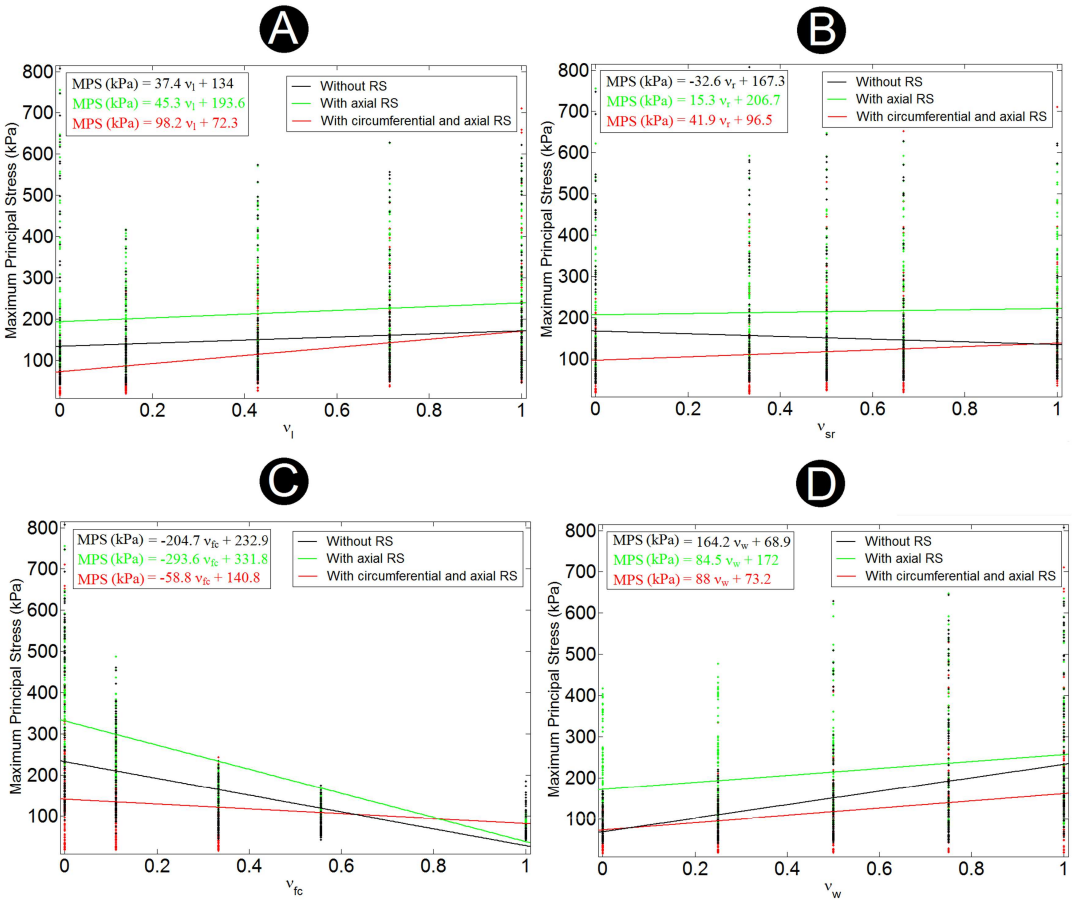

Figure 2.10: Maximum MPS vs. the variation of each normalized parameter. Linear polynomial approximation is included ($MPS(kPa) = p_1\nu_{param} + p_2$).

2.2.2.4 Vulnerability study

Regarding the vulnerability of the plaque, different threshold stress values have been proposed by different authors (Lendon *et al.*, 1991; Cheng *et al.*, 1993; Loree *et al.*, 1994). In this study, a threshold value of 247 kPa has been used according to the set of experimental data obtained by Loree *et al.* (1994), assuming a normal distribution of the data. This threshold value indicates that the probability of having plaque rupture is 0.05 for the cases whose combination of parameters have a maximum MPS equal or higher than 247 kPa, according to the data by Loree *et al.* (1994).

The maximum MPS for each combination of parameters is shown in Figures 2.11 and 2.12. In Figure 2.11, the two most influential parameter, the fibrous cap thickness and the lipid core width (fc and w), were chosen as the variable represented by the surfaces. In each subfigure, five surfaces are presented, one for each stenosis ratio (sr) variation. The safety threshold plane at 247 kPa is presented. The results obtained for the three simulations sets (with axial RS, with circumferential and axial RS and

without them) have been compared both in Figures 2.11 and 2.12.

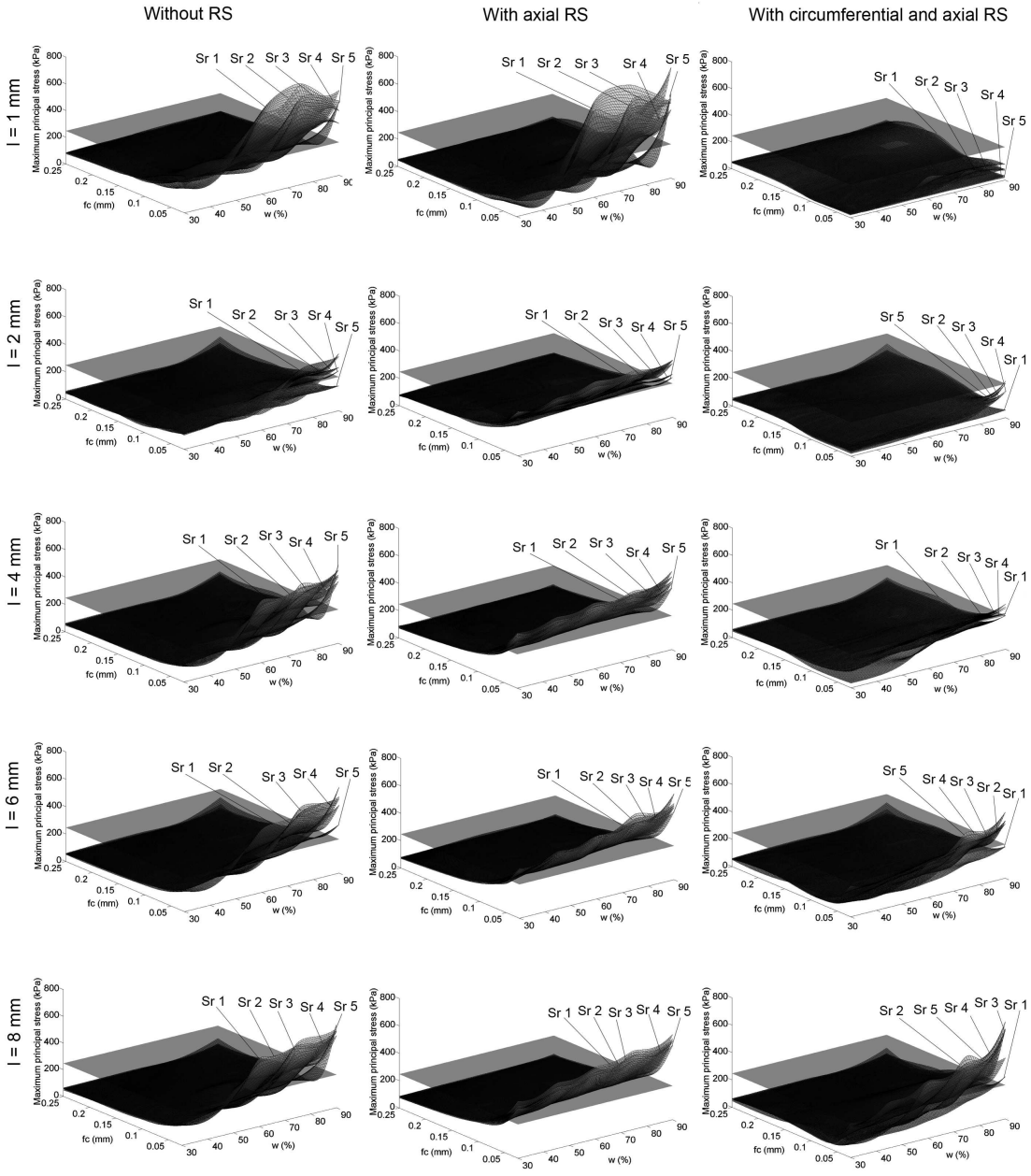

Figure 2.11: Maximum MPS surfaces (in kPa) for a given lipid core length (l) and for the three simulations sets considered; (i) without RS, (ii) with the axial RS included and (iii) with the circumferential and the axial RS included. In each subfigure, five surfaces are presented, one for each stenosis ratio (sr) variation.

For the sake of clarity, the contour maps of the maximum MPS that are higher than the safety threshold plane defined (the intersections between each surface of Figure 2.11

and the safety threshold of 247 kPa plane for a lipid core length given) are shown in Figure 2.12.

Interestingly, the obtained contour maps change for the different studied cases. For the models without RS, similar contour maps are obtained for l=4 mm, l=6 mm and l=8 mm, showing that the lipid core width has a strong dependency on the MPS (vulnerability limit of $w > 60\%$). Despite the fact that the lines corresponding to each variation of the stenosis ratio intersect in some cases, the vulnerability area increases as the stenosis ratio decreases. In every case, the vulnerable threshold of the fibrous cap thickness is between 0.025 and 0.01 mm.

However, the obtained contour maps can be classified into two groups according to the value of the lipid core length if axial RS are included, showing the high dependency of that parameter on the MPS. The first group includes the small atheroma plaques ($l \leq 2$ mm) and, the lipid core width and the stenosis ratio have an important influence on the MPS (atheroma plaque becomes vulnerable for $w > 50\%$). The second group includes the long ones ($l \geq 4$ mm), the influence of the lipid core width is less important, being more vulnerable for high values of this parameter. A linear trendline is observed, being the vulnerable fibrous cap thickness threshold around 0.05 mm for low lipid core width values and 0.075 mm for high lipid core width values. Again, despite the fact that the lines corresponding to each variation of the stenosis ratio intersect in some cases, the vulnerability area increases as the stenosis ratio decreases.

Finally, if circumferential and axial RS are included, the obtained contour maps can be also classified into two groups as a function of the lipid core length, showing a strong dependency of that parameter on the MPS. First group for the small atheroma plaques ($l \leq 2$ mm), where there is not vulnerable geometries, and second group for the long ones ($l \geq 4$ mm), where the influence of the lipid core width is important (atheroma plaque become vulnerable for $w > 55\%$). In every case, the vulnerable fibrous cap thickness threshold is around 0.05 mm.

By observing the contours of the intersection between the safety threshold plane (247 kPa) and the maximum MPS surfaces, depicted in Figure 2.12, it can be appreciated how the axial residual stresses reduce the dependency between the MPS and the lipid core width except for the smallest lipid core length (l= 1 mm). Interestingly, the axial residual stresses dramatically increase the vulnerable area showing MPS values higher than 247 kPa for small values of the lipid core width. However, the circumferential and the axial residual stresses together produce again a strong dependency between the MPS and the lipid core width, and the vulnerable area highly decreases due to the effects of compression stress in the inner layer of the vessel fibrous cap zone, produced by the circumferential RS. Consequently, this fact shows the relevance of considering the residual stresses (circumferential and longitudinal) in the vulnerability computational analysis of the atheroma plaque.

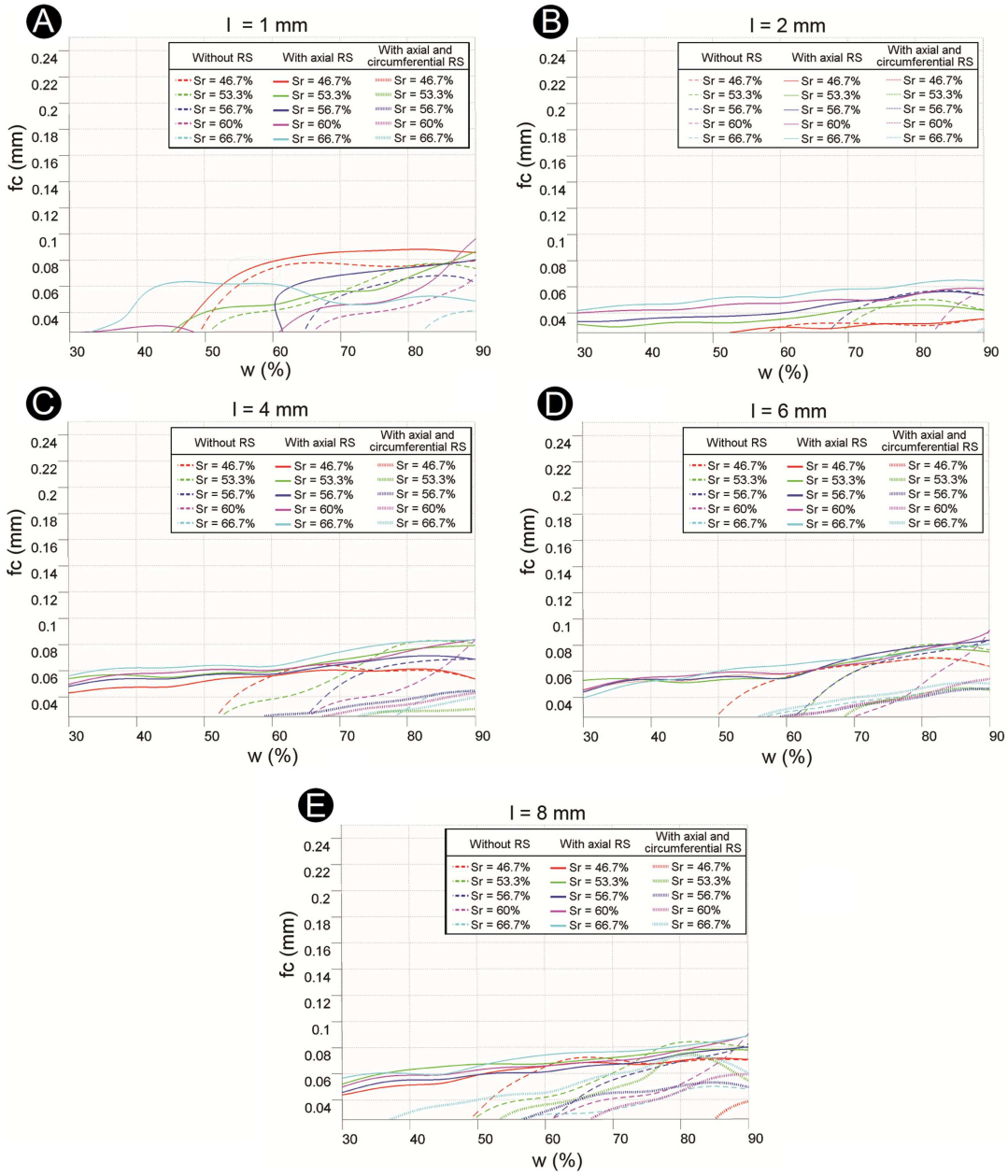

Figure 2.12: Contours of the intersection between the safety threshold plane (247 kPa) and the maximum MPS surfaces for all lipid core lengths studied and for the results without RS, with the axial RS included and with the circumferential and the axial RS included.

2.2.2.5 Vulnerability factor

In order to quantify the vulnerability risk of atheroma plaque rupture, a vulnerability factor *(VF)* was defined. This factor is computed as

$$VF = \frac{Maximum\ MPS\ (kPa)}{Critical\ MPS\ (kPa)}, \tag{2.5}$$

where the critical MPS value is assumed to be 247 kPa (Loree *et al.*, 1994).

The value of the VF for the main combinations of parameters which produce a maximum MPS higher than 247 kPa (vulnerable areas of Figure 2.12) are shown in the following tables. In Tables 2.3, 2.4 and 2.5, the VF values for the cases without residual stress are shown. Tables 2.6, 2.7, 2.8, 2.9 and 2.10 resume the VF values for the cases with the longitudinal RS included and finally, the VF values for the cases with longitudinal and circumferential RS included are shown in Tables 2.11, 2.12 and 2.13. In each table, the lipid core width is considered constant, the fibrous cap thicknesses are 0.025 mm (left sides of the tables) and 0.05 mm (right sides of the tables) and the lipid core length and the stenosis ratio vary.

Without residual stress: Generally, the VF values in Table 2.4 and 2.5 are higher than in Table 2.3 for the same values of lipid core length (l) and stenosis ratio (sr), showing the dependency of the lipid core width on MPS. Moreover, the VF values increase with the lipid core width. A negative relation was observed between the decrease of the fibrous cap thickness and the VF since the values of the VF are significantly higher in the left sides of the tables ($fc = 0.025$ mm) than in the right sides ($fc = 0.05$ mm). The highest vulnerability factor is 3.27 ($l = 1$ mm, $sr = 56.3\%$, $fc = 0.025$ mm and $w = 90\%$), exceeding the safety threshold value (247 kPa) by a factor of three, Table 2.5. The dependence of the lipid core length on MPS is unclear since the highest values of the VF are produced for the smallest value of the lipid core length (l= 1 mm).

	fc = 0.025 mm					fc = 0.05 mm				
sr(%)/l(mm)	1	2	4	6	8	1	2	4	6	8
46.6	2.81	1.06	1.67	1.86	1.94	1.71	0.74	1.09	1.13	1.23
56.3	2.55	0.64	1.83	0.87	1.66	0.42	0.54	0.47	0.64	0.64
56.6	0.43	0.59	0.71	0.95	0.96	0.41	0.49	0.5	0.63	0.63
60	0.55	0.62	0.73	1.00	0.98	0.5	0.54	0.51	0.66	0.68
66.6	0.6	0.48	0.79	1.05	1.05	0.55	0.61	0.58	0.76	0.76

Table 2.3: Vulnerability factors for the cases without residual stress included. Parameter values of $fc = 0.025, 0.05$ mm and $w = 60\%$.

	fc = 0.025 mm					fc = 0.05 mm				
sr(%)/l(mm)	1	2	4	6	8	1	2	4	6	8
46.6	3.03	1.09	1.79	1.95	2.15	1.87	0.79	1.15	1.25	1.27
56.3	2.35	1.25	1.92	2.23	2.18	1.38	0.94	1.31	1.35	1.38
56.6	2.61	1.5	1.68	2.08	2.26	1.34	1.01	1.22	1.44	1.32
60	2.08	0.62	2.01	1.18	2.03	0.42	0.55	0.57	0.75	0.74
66.6	0.65	0.72	0.93	1.22	1.2	0.43	0.54	0.66	0.86	0.84

Table 2.4: Vulnerability factors for the cases without residual stress included. Parameter values of $fc = 0.025, 0.05$ mm and $w = 75\%$.

	fc = 0.025 mm					fc = 0.05 mm				
sr(%)/l(mm)	1	2	4	6	8	1	2	4	6	8
46.6	2.22	1.18	1.83	2.01	2.19	1.84	0.79	1.06	1.21	1.32
56.3	3.27	1.28	2.01	2.25	2.34	1.54	0.9	1.42	1.36	1.44
56.6	2.34	1.6	1.97	2.19	2.39	1.18	1.05	1.25	1.43	1.47
60	2.02	1.69	2.16	2.54	2.31	1.22	1.12	1.54	1.5	1.53
66.6	2.5	0.73	2.32	1.44	2.52	0.41	0.57	0.71	0.95	0.9

Table 2.5: Vulnerability factors for the cases without residual stress included. Parameter values of $fc = 0.025, 0.05$ mm and $w = 90\%$.

With longitudinal residual stress: The dependence of the fibrous cap thickness (fc) on MPS is shown since the VF values are greater in the left side of Tables 2.6, 2.7, 2.8, 2.9 and 2.10 ($fc = 0.025$ mm) than in the right side of these tables ($fc = 0.05$ mm), for the same values of lipid core length (l) and stenosis ratio (sr). The influence of the lipid core width on MPS decreases when longitudinal residual stress are considered since there is VF higher than 1 for all considered values of the lipid core width. However, it can be observed that the VF values increase as the lipid core width increases. The highest vulnerability factor is 3.06 and the dimensions of the case with this VF are; 1 mm long lipid core, 46.6% of stenosis ratio, 0.025 mm thick of fibrous cap and 75% of lipid core width, exceeding again the safety threshold value of 247 kPa more than three times over, Table 2.9. Furthermore, most of the VF values are lower than 1 for the small values of the lipid core length ($l \leq 2$ mm) and higher than 1 for the long ones ($l \geq 4$ mm) in all of these tables, which show the dependence of the lipid core length on MPS.

	fc = 0.025 mm					fc = 0.05 mm				
sr(%)/l(mm)	1	2	4	6	8	1	2	4	6	8
46.6	0.77	0.91	1.37	1.43	1.49	0.59	0.70	0.89	0.93	0.88
56.3	0.92	1.10	1.60	1.45	1.46	0.78	0.76	1.06	1.04	1.03
56.6	0.81	1.11	1.53	1.39	1.48	0.97	0.81	0.97	0.91	0.93
60	1.00	1.31	1.62	1.48	1.54	0.74	0.84	0.99	0.93	1.00
66.6	0.96	1.31	1.63	1.26	1.69	0.77	0.88	1.09	0.86	1.10

Table 2.6: Vulnerability factors for the cases with longitudinal residual stress included. Parameter values of $fc = 0.025, 0.05$ mm and $w = 30\%$.

	fc = 0.025 mm					fc = 0.05 mm				
sr(%)/l(mm)	1	2	4	6	8	1	2	4	6	8
46.6	0.93	0.97	1.50	1.65	1.62	0.63	0.80	0.96	1.04	1.04
56.3	1.00	1.12	1.70	1.64	1.74	0.80	0.78	1.08	1.02	1.22
56.6	0.88	1.21	1.61	1.69	1.68	0.82	0.81	1.06	1.05	1.08
60	1.08	1.36	1.63	1.63	1.80	0.70	0.88	1.12	1.09	1.14
66.6	1.00	1.42	1.80	1.59	1.93	1.12	0.96	1.18	1.06	1.15

Table 2.7: Vulnerability factors for the cases with longitudinal residual stress included. Parameter values of $fc = 0.025, 0.05$ mm and $w = 45\%$.

	fc = 0.025 mm					fc = 0.05 mm				
sr(%)/l(mm)	1	2	4	6	8	1	2	4	6	8
46.6	2.52	1.06	1.67	1.87	1.95	1.77	0.74	1.09	1.13	1.24
56.3	2.4	1.14	1.83	1.77	2.07	0.79	0.82	1.15	1.08	1.31
56.6	0.87	1.27	1.82	1.86	1.87	0.99	0.85	1.12	1.08	1.18
60	0.96	1.46	1.89	1.87	1.89	0.74	0.95	1.17	1.13	1.23
66.6	1.08	1.63	1.95	1.84	2.12	1.1	1.03	1.2	1.21	1.38

Table 2.8: Vulnerability factors for the cases with longitudinal residual stress included. Parameter values of $fc = 0.025, 0.05$ mm and $w = 60\%$.

	fc = 0.025 mm					fc = 0.05 mm				
sr(%)/l(mm)	1	2	4	6	8	1	2	4	6	8
46.6	3.06	1.09	1.79	1.96	2.16	1.98	0.79	1.15	1.25	1.27
56.3	3.02	1.25	1.92	2.23	2.18	1.22	0.94	1.31	1.35	1.39
56.6	2.62	1.5	1.68	2.07	2.27	1.61	1	1.22	1.44	1.33
60	2.4	1.52	2.01	1.96	2.04	0.85	0.99	1.28	1.27	1.32
66.6	1.25	1.65	1.93	1.96	2.32	0.96	1.12	1.39	1.29	1.47

Table 2.9: Vulnerability factors for the cases with longitudinal residual stress included. Parameter values of $fc = 0.025, 0.05$ mm and $w = 75\%$.

	fc = 0.025 mm					fc = 0.05 mm				
sr(%)/l(mm)	1	2	4	6	8	1	2	4	6	8
46.6	1.95	1.18	1.83	2.01	2.19	1.84	0.79	1.06	1.21	1.32
56.3	2.58	1.28	2.01	2.25	2.34	1.56	0.89	1.41	1.36	1.44
56.6	2.26	1.59	1.97	2.19	2.39	1.5	1.04	1.25	1.43	1.47
60	1.57	1.68	2.15	2.54	2.31	1.52	1.11	1.53	1.49	1.53
66.6	2.24	1.69	2.31	2.14	2.52	0.93	1.17	1.49	1.4	1.61

Table 2.10: Vulnerability factors for the cases with longitudinal residual stress included. Parameter values of $fc = 0.025, 0.05$ mm and $w = 90\%$.

Longitudinal and circumferential residual stress: As it is observed for the cases without residual stress considered (Tables 2.3, 2.4 and 2.5), for the cases with longitudinal and circumferential residual stress included, the VF values shown in Table 2.12 and 2.13 are higher than in Table 2.11 for the same values of lipid core length (l) and stenosis ratio (sr), showing the dependency of the lipid core width on MPS. Furthermore, the VF values increase as the lipid core width increases. Most of the VF values are lower than 1 for the small values of the lipid core length ($l \leq 2$ mm) and higher than 1 for the long ones ($l \geq 4$ mm), which show the dependence of the lipid core length on MPS. Regarding the influence of the fibrous cap thickness, the values of the VF are significantly higher in the left sides of the tables ($fc = 0.025$ mm) than in the right sides ($fc = 0.05$ mm) of these tables. The highest vulnerability factor value is 2.98 and the dimensions of the case with this VF are; 8 mm long lipid core, 66.6% of stenosis ratio, 0.025 mm thick of fibrous cap and 90% of lipid core width, exceeding the safety threshold value of 247 kPa by almost a factor of three, Table 2.13.

	fc = 0.025 mm					fc = 0.05 mm				
sr(%)/l(mm)	1	2	4	6	8	1	2	4	6	8
46.6	0.08	0.16	0.73	0.44	0.51	0.09	0.10	0.52	0.41	0.47
56.3	0.66	0.20	0.75	0.52	1.66	0.09	0.20	0.25	0.39	0.41
56.6	0.11	0.27	1.02	1.02	1.12	0.11	0.19	0.72	0.59	0.68
60	0.14	0.19	0.98	1.00	0.79	0.10	0.20	0.68	0.41	0.44
66.6	0.28	0.51	0.80	1.10	1.70	0.23	0.38	0.63	0.75	0.89

Table 2.11: Vulnerability factors for the cases with longitudinal and circumferential residual stress included. Parameter values of $fc = 0.025, 0.05$ mm and $w = 60\%$.

	fc = 0.025 mm					fc = 0.05 mm				
sr(%)/l(mm)	1	2	4	6	8	1	2	4	6	8
46.6	0.08	0.18	0.86	0.71	0.79	0.08	0.11	0.61	0.52	0.63
56.3	0.59	0.44	1.04	1.52	1.82	0.35	0.39	0.67	0.65	1.09
56.6	0.11	0.32	1.16	1.31	2.14	0.10	0.25	0.81	0.72	0.85
60	0.55	0.22	1.10	1.64	1.70	0.11	0.23	0.77	0.52	0.59
66.6	0.32	0.59	1.05	1.34	1.94	0.25	0.47	0.71	0.88	1.16

Table 2.12: Vulnerability factors for the cases with longitudinal and circumferential residual stress included. Parameter values of $fc = 0.025, 0.05$ mm and $w = 75\%$.

	fc = 0.025 mm					fc = 0.05 mm				
sr(%)/l(mm)	1	2	4	6	8	1	2	4	6	8
46.6	0.08	0.23	1.00	0.93	1.25	0.08	0.14	0.67	0.71	0.85
56.3	0.48	0.79	1.05	1.69	2.67	0.45	0.36	0.82	0.89	1.12
56.6	0.13	0.76	1.33	1.70	1.80	0.10	0.30	0.93	0.91	0.98
60	0.30	1.02	1.25	1.95	2.64	0.36	0.45	0.92	1.07	1.19
66.6	0.33	1.08	1.21	1.61	2.98	0.27	0.47	0.86	1.00	1.25

Table 2.13: Vulnerability factors for the cases with longitudinal and circumferential residual stress included. Parameter values of $fc = 0.025, 0.05$ mm and $w = 90\%$.

The general trend observed in this study is that the maximum MPS increases with the lipid core length, the lumen radius and the lipid core width, and also when the fibrous cap thickness decreases. Furthermore, regarding the influence of each parameter on the MPS, it is observed that the fibrous cap thickness is the most influential parameter on the MPS. However, the the lipid core length and width has a moderate influence over the MPS and, finally, it has not been found a clear influence of the stenosis ratio on the MPS.

Figure 2.11 and 2.12 and Tables 2.3, 2.4, 2.5, 2.6, 2.7, 2.8, 2.9, 2.10, 2.11, 2.12 and 2.13 show that most of the parameter combinations have MPS values lower than 247 kPa (VF<1), however, an important vulnerable plaque region, where the maximum MPS value is higher than the safety threshold ($VF\geq$ 1) was found. This region is generally formed by low fibrous cap thickness values. Moreover, this unsafe region changes from the analysis in which longitudinal RS are considered to the analysis in which RS effects are neglected (see Figure 2.12). Since when just longitudinal RS are included (without take into account internal pressure load), the circumferential stresses are positive. Thus, if longitudinal RS and internal pressure load are imposed, the circumferential stresses

are higher than without considering longitudinal RS. However, due to the effects of compression stress in the inner layer of the vessel fibrous cap zone produced by the circumferential RS, when circumferential RS are considered, the circumferential stresses decrease.

To summarize, the vulnerable plaque region corresponds to a combination of the following parameters: $w \geq 50\%$, $fc \leq 0.088$ mm for any lumen radius and lipid core length. For each of the three set of cases studied (with just longitudinal RS included, with longitudinal and circumferential RS included and without RS included), Table 2.14 shows the fibrous cap thickness (fc) and lipid core width (w) vulnerable limits for each lipid core length (l) and for all values of the lumen.

	With axial RS		With circumferential and axial RS		Without RS	
	fc (mm)	w (%)	fc (mm)	w (%)	fc (mm)	w (%)
l=1	$fc \leq 0.088$	$w \geq 50\%$	No vulnerable zone		$fc \leq 0.077$	$w \geq 50\%$
l=2	$fc \leq 0.085$	No limit	$fc \leq 0.025$	$w \geq 95\%$	$fc \leq 0.050$	$w \geq 58\%$
l=4	$fc \leq 0.080$	No limit	$fc \leq 0.052$	$w \geq 62\%$	$fc \leq 0.079$	$w \geq 52\%$
l=6	$fc \leq 0.081$	No limit	$fc \leq 0.055$	$w \geq 64\%$	$fc \leq 0.079$	$w \geq 50\%$
l=8	$fc \leq 0.082$	No limit	$fc \leq 0.080$	$w \geq 38\%$	$fc \leq 0.080$	$w \geq 50\%$

Table 2.14: Summary of vulnerable limits of the fibrous cap thickness (fc) and lipid core width (w) for each different lipid core length (l) independently of the stenosis ratio (sr) parameter. The results are grouped according to the three set of cases studied (with just longitudinal RS included, with longitudinal and circumferential RS included and without RS included)

2.2.2.6 Parameters excluded as an influential parameter

As it has been mentioned on Section 2.2.1.2 of this Chapter, previous tests on 3D geometries were performed in order to choose the most influential parameters on the risk of atheroma plaque vulnerability. These previous test were performed with the same boundary conditions, material parameters and dimensions than the 3D parameter model described in previous sections. In order to simplify the structural analyses the effects of RS were neglected.

Figure 2.13 shows the influence of the lipid core angle. Three subfigures (A, B and C) are presented, where in each subfigure, the lipid core angle (α) is always chosen as one of the variable represented by the surfaces and the other chosen parameter as the variable represented by the surfaces changes in each of the three subfigures. The other two parameters are constant at the intermediate value studied ($l = 4$ mm, $sr = 56.6\%$, $fc = 0.1$ mm). The lipid core width has been excluded for these previous analyses in order to reduce the number of models studied. As Figure 2.13 shows, for all the parameter combinations, the maximum MPS remains practically constant as the lipid core angle varies. Furthermore, each subfigure has been turned in order to show other point of view and see better that the MPS value is constant for the different lipid core angle values.

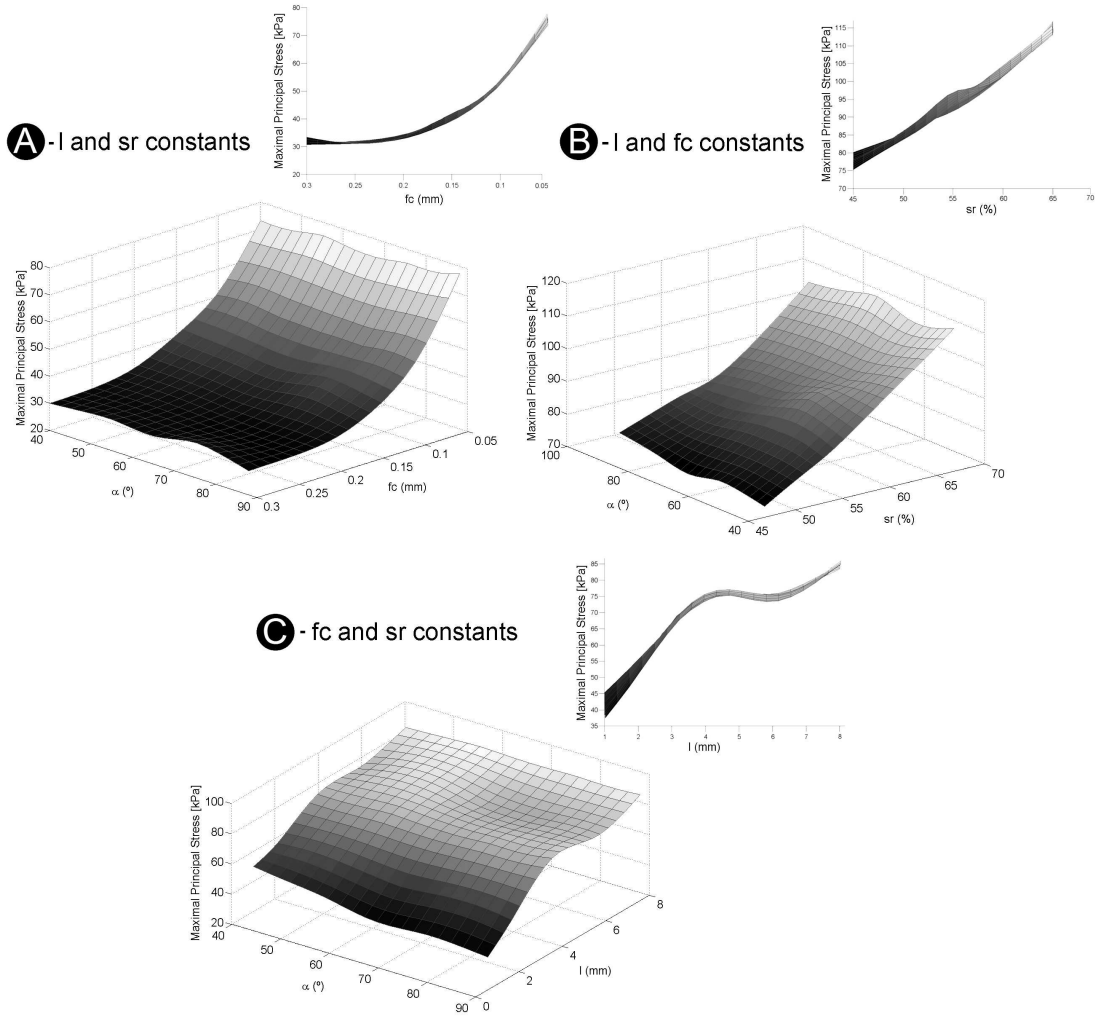

Figure 2.13: Maximum MPS surfaces for the lipid core angle and the fibrous cap thickness (A), the stenosis ratio (B) and the lipid core length (C).

2.3 Comparison between two and three-dimensional models

2D structure stress analysis has been extensively applied to plaque models for predicting stress distributions from idealized or from patient specific models. One of the main advantages of using idealized models is the reduction the long computation times and memory consumption required for 3D FE analysis. Furthermore, 2D models are simpler than 3D models, thus they allow easy changing of geometrical parameters to investigate effects of individual plaque features. Most of parametric studies have been performed only in two dimensions (2D) assuming a plane strain hypothesis (Cheng *et al.*, 1993; Lee, 2000; Finet *et al.*, 2004; Ohayon *et al.*, 2005, 2008) in order to define the site of MPS concentrations. A brief review of the main 2D structural analysis found

in the literature can be found in the Section 2.1 of this Chapter. Although two dimensional mechanical models of atherosclerotic plaques are abundant and the findings could shed some lights on the plaque rupture mechanism, the results from such models may be inaccurate because of the assumptions of plane strain/stress and the geometry simplification. Furthermore, some studies show that a 2D analysis tends to overestimate the amplitude of the peak circumferential stress (Ohayon *et al.*, 2005). Ohayon *et al.* (2005) calculated the stress in a single diseased human coronary artery from IVUS images to decide the possible relation between high stress concentrations and plaque rupture sites. The diseased arterial wall was modeled by components of adventitia, media, dense fibrosis, and cellular fibrosis with isotropic materials. They found the peak stress locations from 3D model well coincided with plaque rupture location, but not in the corresponding 2D models, which may overestimate the stress levels. Thus, 3D finite element models of atherosclerotic coronaries may be very valuable and more accurate than the 2D finite element analysis in helping cardiologists to evaluate the risk of spontaneous plaque rupture in a patient since they incorporate more information, such as anisotropic material model considering fiber directions, the residual stress and no plain stress or strain assumptions as in 2D finite element models.

Therefore, in this section, the results obtained by the 3D model used in the parametric study described in Section 2.2 have been compared with a plane strain 2D model usually employed in the literature to study the vulnerability of plaque (Cheng *et al.*, 1993; Lee *et al.*, 1996; Veress *et al.*, 2000; Ohayon *et al.*, 2001; Baldewsing *et al.*, 2004; Ohayon *et al.*, 2005; Versluis *et al.*, 2006; Howarth *et al.*, 2007; Ohayon *et al.*, 2007, 2008; Hallow *et al.*, 2009). Since both models should be simulated with the same dimensions, material properties, boundary conditions and applied loads, a 3D model without any residual stress included has been chosen to compare with the equivalent plane strain model. Longitudinal RS are not possible to include in the 2D plane strain model, and a 3D model with just circumferential RS implemented has not been considered. The plane strain model has been obtained from the central cross section of the equivalent 3D model. This section was extruded at a small length in order to introduce some purely 3D parameters such as the fiber orientation and to compare both models with the same exactly material parameters.

The MPS distribution of the central cross section of both models is shown in Figure 2.14. The dimension of the presented case are; 2 mm long lipid core, 46.6 % of stenosis ratio, 0.025 mm thick of fibrous cap and 90% of lipid core width. The maximum MPS is located in the fibrous cap in both cases, however, its value is about 205 kPa in the 3D model vessel (Figure 2.14.a) and 510 kPa (Figure 2.14.b) in the plane strain vessel. According to the threshold value of 247 kPa (Lendon *et al.*, 1991; Cheng *et al.*, 1993; Loree *et al.*, 1994; Ohayon *et al.*, 2005), the 3D plaque model could be considered stable (maximum MPS is lower than 247 Kpa), but the plane strain plaque model could be considered vulnerable (maximum MPS is much greater than the threshold value). These results could be related to the incompressibility of the material.

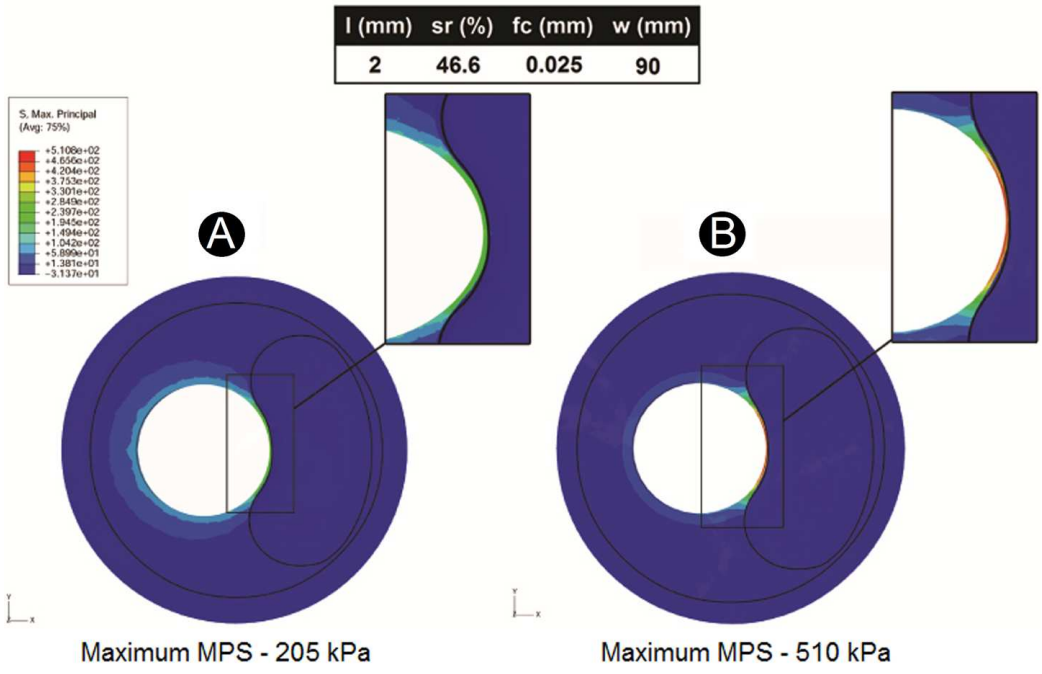

Figure 2.14: MPS distribution (kPa) in the comparison between 3D and plane strain plaque model. A - 3D model vessel. B - Plane strain model.

2.4 Patient-specific geometry reconstruction. Real geometry versus idealized geometry

In order to validate the assumption of an idealized geometry of the atherosclerotic artery, a patient-specific geometry of a coronary vessel has been segmented and modelled using the same material parameters, boundary conditions and dimensions. The performance of the 3D model used to carry out the 3D parametric analysis have been compared with an *in vivo* reconstruction.

A real geometry of a left coronary artery with atherosclerosis disease was obtained by *in vivo* intravascular ultrasound (IVUS) images. The artery, which belongs to an adult male patient of 50 years old, was imaged using an automatic pullback with a speed of 0.5mm/s, from the distality of the lesion to the tip of the guiding catheter, see Figure 2.15.a. The commercial code MIMICS 10.0 was used to reconstruct the 20 cross-sections of the human coronary vulnerable plaque. The 3D plaque geometry of the patient is reconstructed by piling up and following the trajectory of the center of the catheter, see Figure 2.15.a. Plaque components were characterized by their appearance on IVUS images, the contours delimiting lumen border, media, adventitia and plaque components (lipid core and atheroma plaque) were manually traced on each IVUS cross sectional image.

Figure 2.15.b and 2.15.c show transversal and longitudinal sections, respectively, of

the 3D *in-vivo* atherosclerotic vessel obtained by IVUS. A noteworthy remark is that the cross section obtained by IVUS shown in Figure 2.15.a is the same cross section as that shown in 2.15.b.

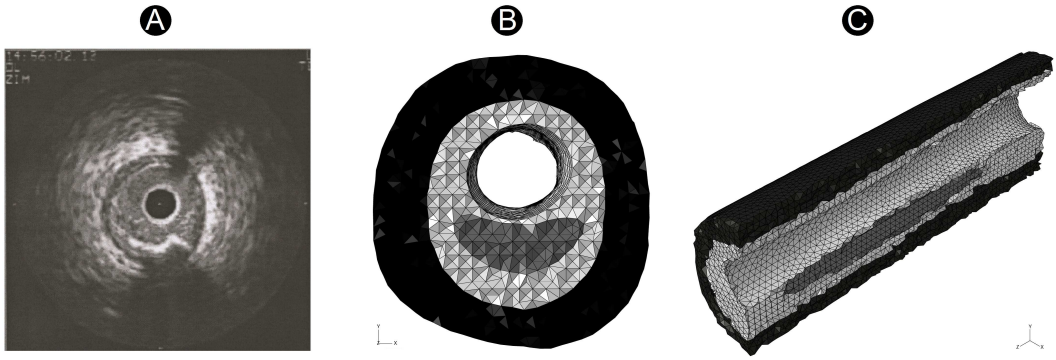

Figure 2.15: 3D reconstruction of a vessel with an atherosclerotic lesion obtained by IVUS. A - One of the 20 cross-sections of the human coronary obtained by IVUS. B - Cross section reconstructed from a real geometry. C - Transversal section reconstructed from a 3D real geometry.

Dimensions of lipid core and fibrous cap thickness were measured in the geometrical reconstruction from the IVUS for purposes of comparison with a case with similar dimensions and properties of the 3D parametric study. The model was meshed with 252.216 linear tetrahedral elements of type C3D4H of similar size to those of the 3D parametric mesh, Figures 2.15.b and 2.15.c. Furthermore, in order to simplify the finite element analysis, both models (idealized and patient-specific model) have been simulated without RS.

Amongst all the 3D parametric models, the geometry with more similar parameters to the real geometry segmented from IVUS has been chosen, see Table 2.15. The lipid core length is 2 mm shorter in the idealized geometry than in the specific-patient model because 8 mm is the largest value studied for the lipid core length in the parametric study. However, Figure 2.12.a shows that the influence of lipid core length variation on the maximum MPS is not relevant for long lipid core lengths, so this can be considered as a good approximation. The dimensions measured on both the real geometry obtained by IVUS images and the idealized geometry are shown in Table 2.15.

	l(mm)	sr(%)	fc(mm)	w(%)
Real geometry	10	46.6	0.04	55
Idealized geometry	8	46.6	0.05	60

Table 2.15: Parameters measured in the 3D reconstruction of a vessel with atherosclerotic lesion obtained by IVUS and parameters selected to compare the idealized 3D with the real geometry.

Both in the real reconstructed vessel and in the idealized model, the spatial distri-

bution of the MPS is quite similar and the maxima are both located in the fibrous cap. The maximum MPS of the real and idealized geometries are 322 kPa (Figure 2.16.a) and 305 kPa (Figure 2.16.b), respectively, showing an error of 5%, and the MPS maps are similar in both cases, showing the validity of the idealized geometry, see Figure 2.16. In both models the maximum MPS is greater than 247 kPa, so according to the defined threshold of 247 kPa defined in previous chapters, both cases could be considered as vulnerable plaque.

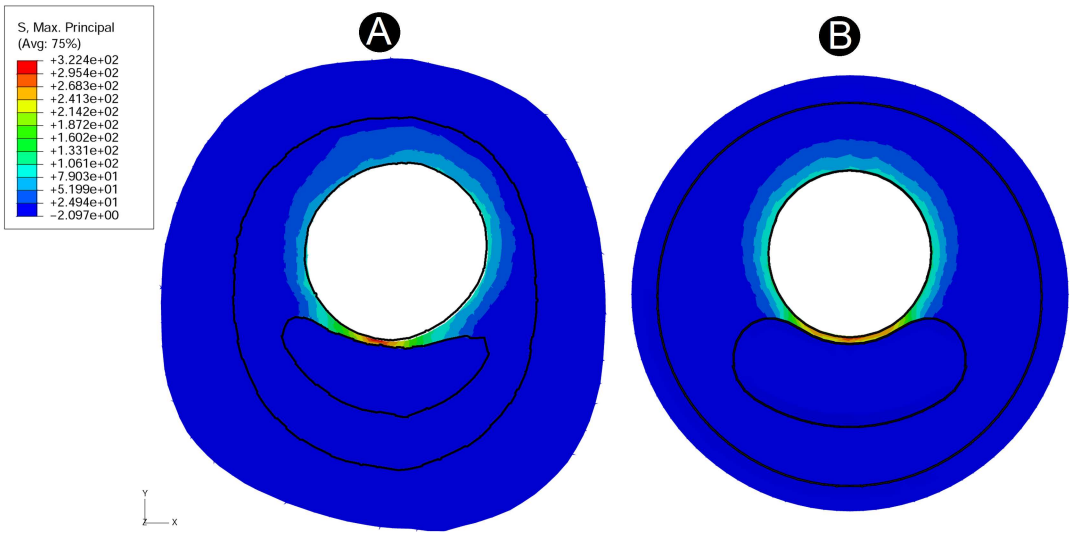

Figure 2.16: MPS distribution (kPa). Comparison between the real geometry reconstructed from the IVUS and the idealized geometry of the 3D parametric study. A - Real geometry reconstructed from the IVUS. B - Idealized geometry.

2.5 Discussion

Quantifying the mechanical stress in the wall of an atherosclerotic vessel and, more specifically, in the fibrous cap, is a vital step in predicting the risk of plaque rupture based on biomechanical features, especially in 3D geometries (Creane *et al.*, 2010). For this reason, the mechanical behaviour of a 3D parametric atheroma plaque in a coronary vessel with atherosclerosis disease has been studied by varying the four most influential geometrical parameters; lipid core length (l), stenosis ratio (sr), fibrous cap thickness (fc) and lipid core width (w) Furthermore, the influence of residual stress effect has been studied. Static finite element analyses were performed in order to study a group of idealized plaque morphologies and to try to predict the vulnerable plaque rupture.

Additionally, the performance of 2D plane strain plaque models versus 3D models have been analyzed, concluding that plane strain plaque models are not accurate enough to calculate MPS distribution. Plane strain hypothesis overestimates the maximum MPS; 510 kPa for plane strain versus 205 kPa for 3D analysis in the case presented in

Figure 2.14. Leading to similar results as those presented by Ohayon *et al.* (2005, 2007). In the case presented in Section 2.3 the plane strain analysis exceeds the threshold of 247 kPa, but the 3D analysis does not, showing the limitation of the plane strain approach for such complex plaques due to the material incompressibility. In addition, Figure 2.16 summarizes a first validation of the 3D idealized model, showing that the 3D model behaves in a very realistic way.

Historically, fibrous cap thickness has been considered the most important and almost the exclusive factor determining plaque vulnerability (Arroyo and Lee, 1999; Briley-Saebo *et al.*, 2007), but it is not the only one. To date, very few 3D computational studies have been performed specifically to investigate the effect of the lipid core size on plaque stress distribution, and the distribution of residual stress and its effects on the stress field in 3D parametric atherosclerotic coronary plaques have never been studied in detail. Owing to the difficulty of estimation of stresses and strains in real geometries, the influence of residual stresses is usually ignored in structural analyses intended to predict plaque rupture location, even though authors such as Ohayon *et al.* (2007) have assessed RS and its impact on the *in vivo* stress distribution in human vulnerable coronary plaques.

The findings in the present study show a high dependency on some purely 3D parameters and factors on the MPS distribution, such as the lipid core length and the axial RS, affecting the vulnerability risk of the plaques. Figures 2.12 and 2.7 clearly show the influence of residual stresses since the vulnerable unsafe areas changes when residual stresses are considered. The predominant trend is that the incorporation of axial RS increases the maximum MPS. However, the incorporation of axial and circumferential RS reduces the maximum MPS. Therefore, 3D plaque models could produce more accurate predictions, since plane strain plaque models could not be enough to calculate a sufficiently accurate MPS distribution. Plane strain models not only overestimate the maximum MPS, as it is shown in the literature by Krishna Kumar and Balakrishnan (2005); Ohayon *et al.* (2005, 2007), but they also miss RS effects and other features as fibre orientation, which can not be consider in 2D models (Holzapfel *et al.*, 2005b).

The fibrous cap thickness, the lipid core width and length have been shown in this study to be critical geometric parameters to the overall plaque stability, whereas it has been shown that the lumen radius influence is lower, but non-negligible. Furthermore, the influence of the lipid core angle has not been found significative. The influence of these parameters on plaque rupture is shown in Figure 2.9.

Similar results were previously obtained by other authors. Ohayon *et al.* (2008) obtained slight higher limits of these parameters, probably because they performed a 2D study. However, the global trends were similar. The remodelling index (a parameter equivalent to the stenosis ratio) and the lipid core width had a positive correlation with the maximum MPS, while the fibrous cap thickness had a negative correlation with the maximum MPS. Similar trends were found by Virmani *et al.* (2000) where they suggested that atherosclerotic lesions with a fibrous cap thickness of less than 65 μ are

most likely to rupture. Several studies in the literature shown that plaques containing a highly thrombogenic lipid rich core are more at risk for rupture if the size of the lipid core is large and is less consistent. Several investigators have reported on the relation of the amount of extracellular gruel and plaque fissuring (Gertz and Roberts, 1990; Davies *et al.*, 1993; Pasterkamp *et al.*, 2000; Douglas *et al.*, 2011). Davies *et al.* (1993) estimated that when at least 40% of the plaque consists of lipid, an atheroma is at risk for rupture.

Some limitations of this study should be mentioned. First, an idealized straight geometry has been used to perform the parametric analysis, however this geometry has been validated in Section 2.4. Second, the material properties and residual stresses have been taken from experimental data in the literature (Jaroslav *et al.*, 1999; Holzapfel *et al.*, 2005b; Versluis *et al.*, 2006). Furthermore, there is no data of axial RS for isolated plaques in the literature, so the axial RS used corresponds to a non-stenotic but intima thickening artery. The opening angle was assumed to be constant for all of the geometries though it is known that it depends on the plaque geometry. Third, viscoelastic effects were not considered (Armentano *et al.*, 1995, 2006; Peña *et al.*, 2010). Fourth, the analysis does not reproduce the pulsatile nature of physiological blood pressure. Also, the fluid-structure interaction effects resulting from such cyclic loading were not considered (Kock *et al.*, 2008). It was assumed that there were no shear stresses, torques, time varying forces or flow related forces. Only static blood pressure was considered to be acting on the lesion in the models. Nevertheless, it has been documented that the effect of fluid shear stress is insignificant when compared to the effect of tensile wall stresses as a direct component in plaque fracture dynamics (Huang *et al.*, 2001; Himburg *et al.*, 2004), although it is considered essential in plaque formation and growth. The estimation of stresses induced by the static pressure load has been proved to be valid to identify stress concentrations in atherosclerotic lesions (Cheng *et al.*, 1993) since the location of stress concentration does not significantly differ between models including static pressure and models with complex dynamic pressure profiles. Fifth, calcifications were not considered in order to simplify the study (Vengrenyuk *et al.*, 2006; Bluestein *et al.*, 2008; Wenk, 2011). Different properties of the atheroma plaque were not taken into account in this parametric study. Properties of calcified, cellular and hypocellular plaques have been identified by other authors (Loree *et al.*, 1994). Finally, the 3D parametric study only could be validated qualitatively. It is not possible to measure the stress concentration in real atheroma plaques and to correlate with the main geometrical risk factors under *in vivo* conditions and later verify the plaque rupture. Actually, in the literature, the only way to extract stress information is by performing computational simulations reproducing geometry and *in vivo* conditions, and validate the model qualitatively, measuring the geometrical risk factors, but not measuring directly the stresses.

The 3D parametric study presented on this chapter can be considered as an additional step towards the development of a tool to assist clinicians in the identification of

vulnerable atheroma plaques. The large-scale computational analysis aids the clinical staff to identify the critical morphological parameters that indicate plaque vulnerability and the likelihood of rupture.

Chapter 3

Some new features to improve the performance of the idealized parametric study

The 3D parametric study presented in Chapter 2 could be carried further by the inclusion of other features such as (i) the influence of microcalcifications, (ii) the consideration of other atheroma plaque anatomies such as positive and negative remodeling, and (iii) the incorporation of the fluid-structure interaction effects.

Therefore, this chapter includes three parametric studies; the first one investigates the effect of microcalcifications on the stress field of an atheroma plaque vessel section. This is achieved by performing a parametric finite element study, assuming a plane strain hypothesis of a coronary artery section with eccentric atheroma plaque and one microcalcification incorporated. The geometrical parameters used to define and design the idealized coronary plaque anatomy and the microcalcification were: the fibrous cap thickness and the microcalcification ratio, angle and eccentricity. Viewing the results, it could be concluded that microcalcifications should be considered in the modeling of this kind of problems since they cause a significant alteration of the vulnerable risk by increasing the maximum maximal principal stress up to 40%, although this increase of stress is not uniform (12% on average). The obtained results show that the fibrous cap thickness, the microcalcification ratio and the microcalcification eccentricity, in combination with the microcalcification angle, appear to be the key morphological parameters that play a determinant role in the maximal principal stress, and accordingly in the rupture risk of the plaque.

The second one assesses the role of positive growth in the vulnerable plaque rupture mechanics, which could explain why many sudden heart attacks occur without prior symptoms. Plane strain finite element models of a coronary artery with positive and negative growth have been compared by systematically varying the most influential values of the geometry of the vessel on plaque stresses: (i) the fibrous cap thickness,

(ii) the stenosis ratio, (iii) the lipid core dimensions and (iv) the atheroma plaque distribution (eccentric or concentric). All models have been developed with the same average dimensions and material properties. Vessel wall stress concentrations were always predicted to be higher in the fibrous cap of atheroma plaques with positive growth compared to those with negative growth. Furthermore, these conclusions are independent of the fibrous cap and the degree of stenosis considered. These results may explain why plaque rupture is often apparent at sites with only modest luminal stenoses but marked positive growth. The results of this study support the hypothesis that coronary arteries with positive growth are more vulnerable to rupture than those arteries with negative growth for comparable geometrical conditions.

Finally, the third one consists of a Fluid-Structure Interaction (FSI) analysis which allows to compare the results of considering or not the blood effects. It has been documented that the effect of fluid shear stress is insignificant when compared to the effect of tensile wall stresses as a direct component in plaque fracture dynamics (Huang *et al.*, 2001; Himburg *et al.*, 2004), although it is considered essential in plaque formation and growth.

Contents

3.1 Introduction

Plaque disruption tends to occur at points where the plaque surface is the weakest and most vulnerable which coincide with points where stresses, which are affected mainly

by tissue properties and plaque geometry, are concentrated (Falk *et al.*, 1995; Van der Wal and Becker, 1999). The risk of plaque rupture depends on plaque type and size (Schroeder and Falk, 1995). Chapter 2 provided some guidelines to asses the atheroma plaque vulnerability according to four of the most influential geometrical parameters on the risk of plaque rupture. Traditionally, coronary atheroma plaques with a thin fibrous cap thickness and high stenosis ratio have been considered as prone to rupture. However, several pathological and biomechanical studies and the results obtained in the 3D parametric study presented in the previous Chapter, have provided morphological descriptions of the vulnerable risk, and it can be concluded that the fibrous cap thickness alone is not a sufficiently accurate predictor for plaque stability. The lipid core length and width are also very important parameters on vulnerability (Virmani *et al.*, 2000; Krishna Kumar and Balakrishnan, 2005). Nevertheless, apart from plaque morphology, there are other factors which could play a key role in the initiation of failure such as the presence of microcalcifications, the anatomy of the atheroma plaque related to the positive and negative remodeling since the positive growth increases plaque vulnerability from a structural perspective, or hemodynamic features such as blood flow separation and circulation.

Concerning to the composition of the plaque, more careful examination of stress distributions in atherosclerotic plaques reports that it could be due to local stress behaviors at critical sites caused by cap thinning, inflammation, macroscopic heterogeneity, and recently, the presence of microcalcifications. However, the role of microcalcifications is not yet fully understood and most finite element models of blood vessels with atheroma plaque ignore the heterogeneity of the plaque constituents at the microscale. Therefore, the presence of calcium, which is a common phenomenon, also appears to have an important role in the evolution of atherosclerosis. Initially, the calcium deposits develop in the form of both intracellular and extracellular granules. After that, these granules can either join into large deposits or remain as dispersed collections of microcalcifications along the arterial wall (Roijers *et al.*, 2008). Plaque calcifications are both in intravascular ultrasound (IVUS) and multislice computed tomography (MSCT) easily recognized. However, small microcalcifications might be missed on MSCT due to its lower resolution (Van der Giessen *et al.*, 2011). Therefore, there are no reliable means of viewing these microstructures (Friedrich *et al.*, 1994). Only some proposed novel imaging methods could detect the presence of microcalcifications in and around the fibrous cap of plaque lesions, such as that developed by Vengrenyuk *et al.* (2006). They examined autopsy specimens of coronary atheromatous lesions using *in vitro* imaging techniques whose resolution far exceeds conventional magnetic resonance imaging, intravascular ultrasound, and optical coherence tomography approaches. These high resolution imaging modalities, which include confocal microscopy with calcium specific staining and micro-computed tomography imaging, provide images of cellular level calcifications within the cap proper.

The role of microcalcifications in the mechanics of vulnerable plaque rupture is still

debated. Some studies indicate beneficial effects in stabilizing the plaque (Cheng *et al.*, 1993; Huang *et al.*, 2001; Wong *et al.*, 2012), whereas others suggest that the microcalcifications increase the plaque vulnerability and shift the maximal principal stress (MPS) to the region of the microcalcification (Bluestein *et al.*, 2008; Wenk *et al.*, 2010; Wenk, 2011; Maldonado *et al.*, 2012). Several parametric studies have investigated the effects of varying key parameters that influence stress in diseased arteries (Ohayon *et al.*, 2005; Cheng *et al.*, 1993; Finet *et al.*, 2004; Lee, 2000; Krishna Kumar and Balakrishnan, 2005; Ohayon *et al.*, 2008). However, microcalcifications are not usually considered in their studies. Huang *et al.* (2001) tested the hypothesis that calcification impacts biomechanical stresses in human atherosclerotic lesions by Fluid Structure Interaction (FSI) models. Their conclusion was that calcification does not increase fibrous cap stress in typical ruptured or stable human coronary atherosclerotic lesion. However, their study is related with relatively large calcification areas. Williamson *et al.* (2003) performed a finite element (FE) study to test the sensitivity of predicted levels of stress and strain to the variations of material properties of the atheroma plaque components (normal wall, fibrous plaque, calcified regions, lipid pools). Li et al. (Li *et al.*, 2007b) implemented a sensitivity study on an idealized two dimensions (2D) longitudinal cross-section model using FSI simulations. They studied the effect of the fibrous cap thickness and the stenosis degree on the stress in an isolated plaque cap while assuming that the artery walls were rigid. Tang *et al.* (2005b) carried out three dimensional FSI simulations using modified magnetic resonance imaging data of atherosclerotic plaques with varying luminal stenosis, cap thickness, material properties. Their sensitivity results indicate that vessel and plaque material properties, plaque structure, component volume and pressure conditions have large impact on stress/strain behaviors. Vengrenyuk *et al.* (2006) performed a finite element analysis on a model of patient-specific geometry with three microcalcifications embedded in the cap. The stress around the inclusions was found to increase significantly when the cap thickness was decreased, while the position of the three inclusions was fixed. Similar FSI simulations were performed by Bluestein *et al.* (2008). Wenk (2011) investigated the effects of localized regions of microcalcifications on the stress field of atherosclerotic plaque caps in a section of carotid artery using a global sensitivity analysis method known as Sobol indices (Sobol, 2001). They conclude that the MPS always shifted to the region of microcalcification and the amplification of the stress depend of the zone where the microcalcification appears. Maldonado *et al.* (2012) found a great microcalcification influence on the atheroma plaque vulnerability, however, their results could be related to the stiff material properties used for the microcalcification tissue.

Regarding the anatomy of the atheroma plaque related to the positive and negative remodeling, Glagov *et al.* (1987) demonstrated that in the early stages of atherosclerosis, coronary arteries enlarge in relation to plaque area to preserve lumen diameter until plaque area occupies approximately 40% of vessel area. This phenomenon, commonly referred to as arterial remodeling, describes the process by which the arterial wall adapts

to physiological or pathological insults by a change in vessel size, or area, within the external elastic lamina. According to the analyses of Glagov *et al.* (1987), coronary arteries may respond to plaque growth by either outward expansion of the vessel wall (positive) or vessel shrinkage (negative). The compensatory remodeling process can maintain luminal dimensions during early atherosclerosis. These plaques grow further and the plaque does not generally begin to encroach on the lumen until it occupies 40% of the cross-sectional area. There is evidence to suggest that positive remodeling may be advantageous, providing benefit in terms of avoiding luminal stenosis, but also harmful in that such marked compensatory remodeling may make the plaque more vulnerable to rupture. In contrast, lesions with negative remodeling may be associated with higher stenoses grade but may appear more stable (Varnava *et al.*, 2002).

Despite major advances in the treatment of coronary heart disease, a large number of victims of the disease who are apparently healthy die suddenly without prior symptoms. Available screening and diagnostic methods could be insufficient to identify the victims before the event occurs (Sipahi *et al.*, 2006) since the plaques that rupture do not necessarily protrude very far into the blood channel and so, may not cause angina or appear on angiograms. Positive growth could potentially explain why many heart attacks occur suddenly by potentially increasing the vulnerability of the plaque rupture.

A structural parametric study considering the possibility of positive or negative remodeling was carried out by Ohayon *et al.* (2008), who included in their element finite study a remodeling index, which takes into account positive and negative vascular remodeling, as a parameter effecting plaque stability. The aim of their study was to investigate the biomechanical interaction between vessel and plaque geometry and the risk of plaque rupture. Their study demonstrated that in the early stages of positive remodeling, lesions were more prone to rupture, motivating the need for further research into the influence of positive and negative remodeling on plaque stability.

Finally, as regards the effects of the blood flow in plaque rupture, the complex blood flow dynamics in the arterial system has been considered to be a key role in the initiation and development of plaques (Steinman, 2004; Chien, 2008). When lumen narrowing occurs, the upstream part of the plaque is exposed to a high WSS while the downstream part is still exposed to low WSS and inverse flow. Thus, the change in lumen diameter due to plaque growth will influence the blood flow pattern and therefore the WSS (Slager *et al.*, 2005a). Even in an inflammatory environment, endothelial cells are capable of responding to signals induced by the WSS (Dimmeler *et al.*, 1999; Tricot *et al.*, 2000). Therefore, the low shear stress region of the plaque will remain athero-prone while the high shear stress region is thought to activate alternative signaling pathways leading to matrix degradation and eventually resulting in destabilization of the cap covering the plaque (Slager *et al.*, 2005b). Weakening of the cap will eventually result in plaque rupture. Great effort has been made to calculate those hemodynamic factors and tried to link the disturbed flow features to the atherosclerosis disease. However, owing to the practical difficulties of measuring local hemodynamic factors, computational fluid

dynamics (CFD) has been applied to quantify the flow patterns in diseased and non-diseased arteries. These analyses provide a way to identify the role of geometric and hemodynamic factors for atherosclerosis and therapeutic options. Until now, a variety of factors related to hemodynamics in plaque region have been proposed to quantify flow disturbances as potential predictors for arterial wall dysfunction, including the time averaged of the wall shear stress (TΔWSS) (Caro *et al.*, 1971), the oscillatory shear index (OSI) (Kaazempur-Mofrad *et al.*, 2004), the relative residence time (RRT) (Himburg and Friedman, 2006), the WSS spatial gradient (WSSG) or the WSS angle gradient (WSSAG) (Hyun *et al.*, 2000). In addition, various conducted physiological experiments have shown that the hemodynamic forces play an important role of initiation, formation and growth of atherosclerotic lesions (Malek *et al.*, 1999).

In general, fluid computational results range from steady (Fei *et al.*, 1994; Lee and Chen, 2000) to unsteady flows (Perktold *et al.*, 1997; Long *et al.*, 2001), simplified or realistic geometries with either deformable (Perktold and Rappitsch, 1995) or rigid walls and Newtonian or non-Newtonian blood rheology (Johnston *et al.*, 2004, 2006). The rheological properties of blood have also been studied by employing different constitutive equation models (Johnston *et al.*, 2004) as well as the formation of vortices at post-stenotic regions (Bertolotti and Deplano, 2000; Liepsch, 2002). The influence of elasticity on the arterial walls has also been investigated concerning the blood flow patterns in carotid bifurcation models (Maurits *et al.*, 2007), in both symmetric and non-symmetric stenotic fields (Valencia and Villanueva, 2006), in abdominal aortic aneurysms (Scotti and Finol, 2007), showing that WSS varies from 3 to 25% from the shear stress obtained with rigid models and in patient-specific geometries (Torii *et al.*, 2007; Malvè *et al.*, 2012). It is concluded from these studies that the influence of wall elasticity on the haemodynamic parameters depends on the arterial geometries.

Nevertheless, the understanding of the impact the flow has on structures, both within the flow and encompassing the flow, which is provided by FSI numerical analysis, is also an important point to bear in mind. While originally FSI was used to simulate cases of aeroelasticity for aerodynamic research interests (Milne-Thomson, 1958), this method has been actively incorporated in various biomechanical researches, including those involving blood flows through stenosed arteries (Steinman, 2004; Chien, 2008), but also many of the accomplished structural analysis in atherosclerotic blood vessel were limited by the unrealistic uniform pressure often assumed (e.g., Cheng *et al.*, 1993; Lee, 2000; Finet *et al.*, 2004; Ohayon *et al.*, 2005, 2008). In general, FSI approach has been applied to cardiovascular problems such as abdominal/thoracic aortas (see e.g., Figueroa *et al.*, 2006) including aortic aneurysm (see e.g., Scotti and Finol, 2007), carotid artery bifurcation (see e.g., Gao and Long, 2008), cerebral aneurysm (see e.g., Torii *et al.*, 2006; Tezduyar *et al.*, 2008; Torii *et al.*, 2010), and coronary artery (see e.g., Tang *et al.*, 2004). Incorporating FSI into the models is considered to be a big step in research on stenosed arteries as it allows to determine the locations where arterial lesions are most likely to occur and how they happen; providing a method of understanding

that helps to prevent potentially fatal results. Moreover, Torii *et al.* (2009) and Malvè *et al.* (2012) compared the computational results of a computerized tomography scan reconstructed geometries of a stenotic right and left coronary artery, respectively, by CFD and FSI techniques. And the FSI and rigid-wall models showed that the WWS distributions were substantially affected by the arterial wall compliance. In particular, the minimum and maximum WSS values significantly vary. These results confirm that for WSS evaluation, arterial wall compliance can be neglected only in first approximation since, for an accurate WSS computation, wall displacements can play an important role. Besides, Huo *et al.* (2009a) and Huo and Kassab (2009b) studied the effect of the compliance on the WSS computation for a porcine right coronary artery comparing rigid wall and FSI simulations.

Within the atherosclerosis on coronary arteries, studies on these diseased arteries are normally focused on hemodynamic aspects, neglecting the interaction between blood flow and arterial walls, evaluating the WSS at the rigid walls and connecting it with atheromatous pathologies (Asakura and Karino, 1990; Caro *et al.*, 1971). Many works put their attention only in particular regions of the coronary tree (Giannoglou *et al.*, 1986, 2002) neglecting not only the vessel compliance but also the bifurcations, considering only the main branch. Some other studies are focused on coronary stenting technique (Balossino *et al.*, 2008; Gori and Boghi, 2011; Morlacchi *et al.*, 2011; Chiastra *et al.*, 2012). Gijsen *et al.* (2006) analyzed a left arterial bifurcation showing the hemodynamics of a left main arterial bifurcation of just one patient. Soulis *et al.* (2006) studied a left arterial bifurcation of the ascending and the circumflex arterial branches but used a mean geometry. Finally, Goubergrits *et al.* (2007) performed a CFD simulation of a rigid wall based left arterial bifurcation comparing the results with an *in silico* experimental model. Additionally, an important feature of the coronary arteries, which is addressed in limited CFD studies, is their predisposition to undergo large displacements during the cardiac cycle (Bovendeerd *et al.*, 2006). Coronary arterial motion can be described by overall vessel translation, stretching, bending and twisting and to a lesser degree by radial expansion and axial torsion (Ramaswamy *et al.*, 2004). Although still debated in literature, arterial motion may alter the fluid mechanics in the coronaries (Delfino *et al.*, 1994; Weydahl and Jr. Meister, 2001).

Regarding 2D and 3D models, several FSI simulations has been performed in 2D models; Yamagushi *et al.* (1996) analyzed the plaque and wall motion by means of arterial stenosis and abdominal aneurysm models. Yamagushi *et al.* (1998) suggested that the dragging force from fluid flow impacts on the wall compression. Li *et al.* (2006b), who used a 2D flow-plaque interaction model and tried to answer how critical is fibrous cap thickness to carotid plaque stability. They concluded that the presence of a moderate carotid stenosis (30% to 70%) but with a thin fibrous cap can also present a high risk for plaque rupture. Kock *et al.* (2008) developed a 2D FSI model based on *in vivo* MR images of two symptomatic atherosclerosis patients, and the longitudinal stress levels for each patient were computed. They suggested that the longitudinal fibrous cap

stresses may be useful in assessing plaque vulnerability. Notwithstanding, some studies on patient specific flow analysis based on *in vivo* MR images from patients (Long *et al.*, 1997, 2000) show the importance of the use of 3D models to obtain accurate results since the flow pattern in the carotid bifurcation was greatly influenced by 3D bifurcation geometry, and this flow pattern results were significantly different from those found in simplified planar carotid bifurcation models. Moreover, comparison between the predicted flow patterns and MR measurement showed good quantitative agreement. Therefore, 3D models have also been utilized to perform FSI analysis. Zhao *et al.* (2002) firstly introduced MRI-based FSI models to predict wall shear stress and wall stress patterns in healthy subjects, and tried to define regions of low wall shear stress and high wall stress. Their results demonstrated that there are certain regions with low wall shear stress and high mechanical stress, corresponding to the areas where atherosclerotic plaque develops. Younis *et al.* (2004) used finite element simulations of FSI to investigate inter individual variations in flow dynamics and wall mechanics at carotid artery bifurcations from three healthy subjects. Subject specific calculations were based on MR images of carotid artery geometries and ultrasound measured flow boundaries. Various biomechanical parameters such as wall shear stress, oscillatory shear index, and cyclic strain have been compared among subjects. Kaazempur-Mofrad *et al.* (2004) proposed cyclic strain in describing the arterial wall dynamics under pulsatile blood pressure loading. They found that the regions of highest variations in cyclic strain are identified at frequent sites of atherosclerosis. Tang *et al.* (2002, 2003, 2004) used FSI as a basis to perform experimental and numerical investigation of plaque rupture, and to provide new insights on the effects of FSI on strain and stress distributions. A non-linear thick wall model was used to simulate blood flow in diseased carotid arteries in order to assess the physical conditions leading to wall compression and ultimately occlusion (Tang *et al.*, 2004). The results of this study show that severe stenosis causes considerable compressible stress in the arterial wall and, affects stress localizations and flow characteristics. Maximum compressive stress and maximum tensile stress are localized within the stenosis. Li *et al.* (2007a) constructed an idealized 3D atheroma plaque model with varying stenosis degree of 30%, 50% and 70%, to study the wall motion in plaque throat. The results suggested that severe stenosis may inhibit wall motion. Ohayon *et al.* (2011) quantify WSS and stiffness in coronary bifurcations and investigate correlations with atheroma plaque sites.

With all these considerations at hand, firstly, a parametric study to assess the influence of microcalcifications on the stresses in the fibrous cap using an idealized coronary vessel with one microcalcification included has been carried out. In addition, we investigate the biomechanical interaction between the most influential parameter of the vessel geometry, the fibrous cap thickness, and the size and the position of the microcalcification in the mechanical risk factor of vulnerable plaque. The geometrical parameters used to define and design the idealized cross-sectional coronary plaque anatomy and the microcalcification were as follows: (i) the fibrous cap thickness; (ii) the microcalcifica-

tion ratio; (iii) the microcalcification angle and (iv) the microcalcification eccentricity. Secondly, a parametric finite element study has been accomplished in order to test the hypothesis that coronary artery atheroma plaques with positive growth are more vulnerable than those with negative growth. Therefore, the effect of positive and negative growth on plaque stability by considering the arterial growth process that occurs in response to plaque growth has been investigated. Various idealized cross-sectional plaque morphologies, mimicking different stages and variations in atherosclerotic lesion growth, were modelled. The possible relevant anatomical diversity was simulated by continuously varying the most influential values of the diseased vessel geometry: (i) the fibrous cap thickness, (ii) the stenosis ratio, (iii) the lipid core dimensions and (iv) the atheroma plaque distribution (eccentric or concentric). Finally, a 3D FSI parametric study of the geometric risk factors in an idealized coronary vessel to quantify and investigate the biomechanical interaction between the most influential values of the geometry of the vessel in the plaque rupture: (i) the fibrous cap thickness; (ii) the stenosis ratio; (iii) the lipid core width and (iv) the lipid core length, has been also conducted. Both distributions on the solid part model such as the MPS or the blood vessel deformations, and on the fluid part model like the WSS, the vorticity or the drop pressure, have been obtained. Furthermore, the influence of including the fluid effects has been shown by comparing the results of the 3D parametric study presented in Chapter 2, which was performed considering a constant internal pressure, with the obtained results on this FSI analysis.

3.2 Microcalcification influence on the risk of atheroma plaque rupture

Since the role of microcalcifications in the vulnerable atheroma plaque rupture mechanics is still debated; some studies suggest that the microcalcifications increase the atheroma plaque vulnerability, while other studies indicate beneficial effects in stabilizing the atheroma plaque, there is a urgent need to clarify this fact. To the sake of simplicity, a coronary artery plain strain model was chosen as the baseline anatomy although the performance and importance of 3D models has been previously demonstrated to identify vulnerable atheroma plaques (Ohayon *et al.*, 2005; Wong *et al.*, 2012). Nevertheless, the goal of this study is to show the relative contribution of the microcalcification. The accurately calculation of the plaque stress field is not so relevant to show the microcalcification influence.

3.2.1 Modeling of the atherosclerotic coronary artery

3.2.1.1 Idealized geometry, parameters studied and mesh

Two dimensional idealized geometry corresponding to a cross-section coronary vessel with atheroma plaque was modelled. The model was extruded at a small length in

order to introduce some purely 3D parameters, such as the fiber orientation due to the anisotropy of the tissue, and plane strain boundary conditions were applied. The basic geometry was built considering a coronary vessel with an external radius of 2 mm and a vessel wall thickness of 0.5 mm. These dimensions as well as the atherosclerotic vessel morphology were the same than those dimensions of the central cross-section of the 3D parametric model presented in Chapter 2 (Versluis *et al.*, 2006). A microcalcification, which was considered as spherical and located in the fibrous cap, was also introduced in the model. Similar to the 3D parametric model, the basic geometry was created taking into account both the composition and the dimensions of the tissue (adventitia), the fibrous plaque, the lipid core and the microcalcification. The whole media layer has been considered as fibrotic non-healthy tissue, whereas the adventitia has been considered as the only healthy layer of the vessel (see Figure 3.1).

The microcalcification influence was evaluated by carrying out a parametric study of the geometric factors. ABAQUS 6.10 software was used to perform static FE analyses on 108 idealized plaque morphologies. The geometric parameters analyzed, which are represented in Figure 3.1, were the following: the fibrous cap thickness *(fc)*, the microcalcification ratio *(r)*- which is obtained by dividing the microcalcification diameter by the fibrous cap thickness, $r(\%) = \frac{D(mm)}{fc(mm)}100$- , the microcalcification position angle (α_m) and the microcalcification eccentricity *(x)*- which is defined as the ratio between the distance from the lumen to the microcalcification center point *(d)* and the fibrous cap thickness *(fc)*, $x(\%) = \frac{d(mm)}{fc(mm)}100$-. These parameters were selected for the analysis because of their great influence on the atheroma vulnerability and the microcalcification position and dimensions (Finet *et al.*, 2004; Bluestein *et al.*, 2008; Ohayon *et al.*, 2008; Wenk *et al.*, 2010).

A fine adaptive mesh was created in some regions of the model such as the fibrous cap area and the microcalcification. This mesh was chosen after previous sensitivity analysis, and it consisted on 40,000 linear hybrid tetrahedral elements and 10,000 nodes. The geometrical model, the parameters studied and the mesh used are shown in Figure 3.1.

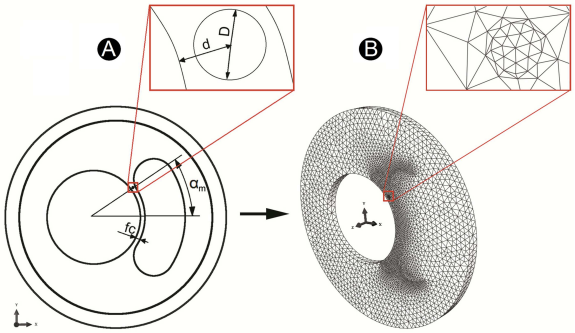

Figure 3.1: (A) Geometrical parameters shown on the cross-section coronary model. (B) Finite element mesh used.

Figure 3.2 presents one case of the sensitivity analysis carried out to assess the performance of the mesh. In this Figure two mesh sizes are compared, the element size of the first mesh, Figure 3.2.a, is 0.1 mm, excepting in the fibrous cap area and around on the microcalcification where the mesh has been refined with elements size of 0.06 mm. However, the second mesh, Figure 3.2.b, has been building with elements of the half size than the first one, i.e, elements of 0.05 mm in the model and 0.03 in the fibrous cap and microcalcification areas. It can be observed that the results do not depend of the size mesh since the maximum MPS value and its localization is approximately the same for both cases.

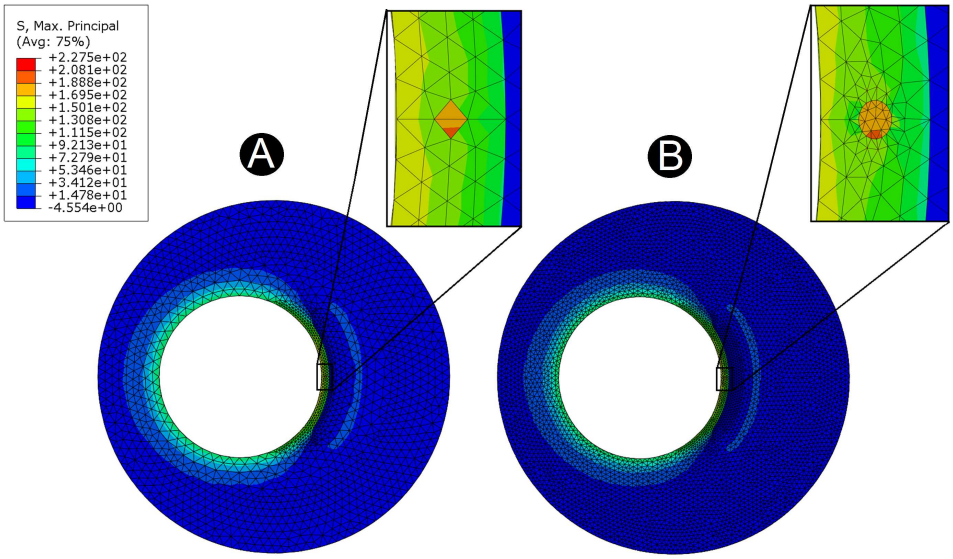

Figure 3.2: Comparison between the results obtained with two different mesh sizes. A- Coarse mesh. B- Fine mesh.

The values considered for each parameter are shown in Figure 3.3. Realistic morphological data were investigated by varying the microcalcification angle ($0° \leq \alpha \leq 32.5°$), the fibrous cap thickness (0.05 mm $\leq fc \leq 0.1$ mm), the microcalcification eccentricity ($25\% \leq x \leq 75\%$) and the microcalcification ratio ($10\% \leq r \leq 20\%$). The minimum and maximum values of the microcalcification angle correspond to the central point of the fibrous cap and the shoulders, respectively (Finet *et al.*, 2004; Fujii *et al.*, 2005; Bluestein *et al.*, 2008).

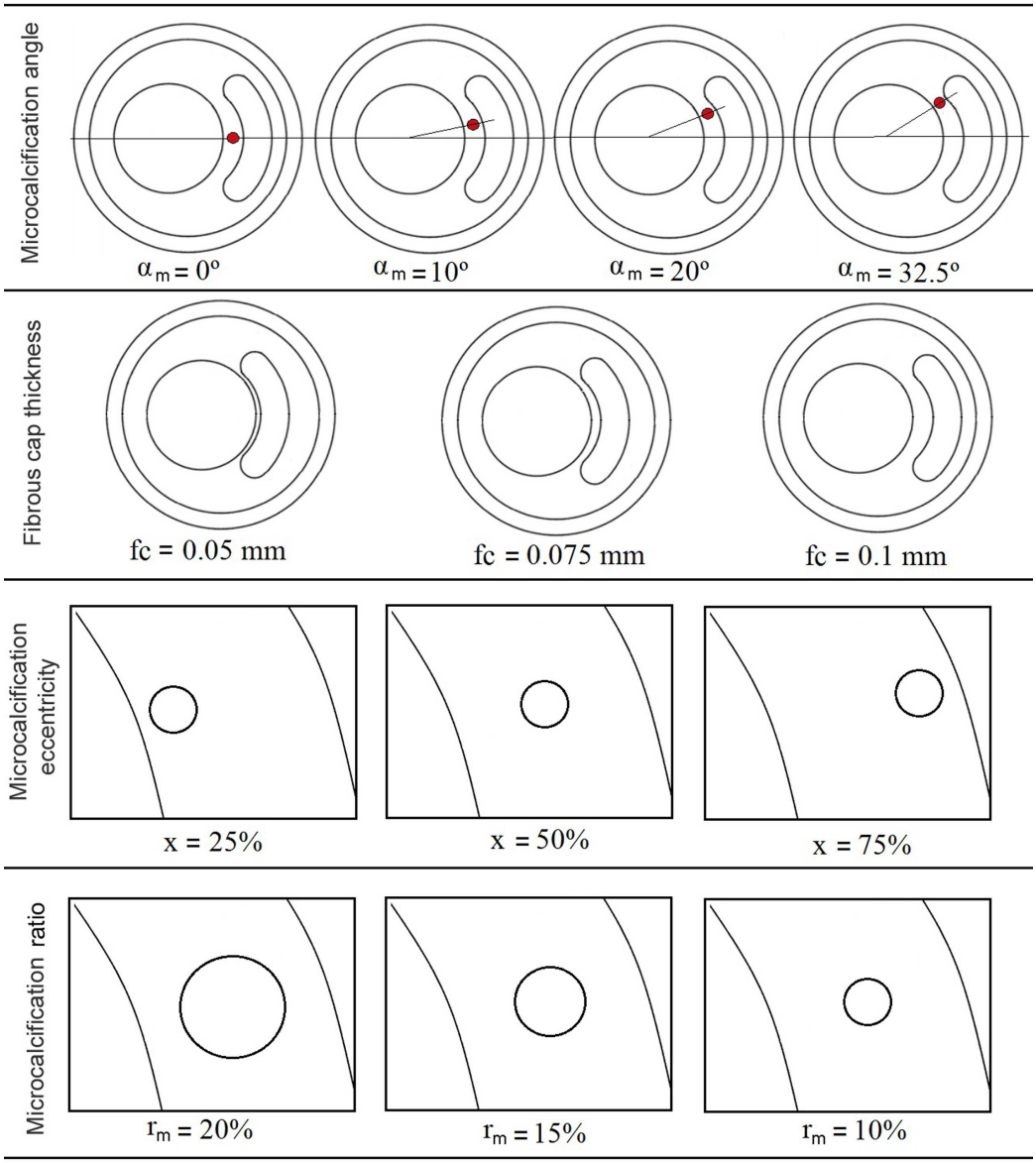

Figure 3.3: Variations of the geometrical parameters in the parametric models.

3.2.1.2 Material model and boundary conditions

As for the 3D parametric model, all tissues were modelled as nonlinear (Roy, 1881; Patel *et al.*, 1969; Cox, 1978), hyperelastic (Holzapfel *et al.*, 2005b) and incompressible materials (Carew *et al.*, 1968; Chuong and Fung, 1984). The behaviour of the lipid core, the atheroma plaque and the vessel wall were modelled by using the strain energy function (SEF) proposed by Gasser et al. (Gasser *et al.*, 2006) and were the same than those described in the Subsection 2.2.1.4 of Chapter 2. Nevertheless, the behaviour of the microcalcification was modelled by using the isotropic Neo-Hookean model with a SEF, $\Psi = C_1[I_1 - 3]$.

The material parameters for the constitutive law of the tissue were obtained using the least-square minimization procedure based on the Levenberg-Marquardt minimization algorithm (Marquardt, 1963) which has been presented in the Subsection 2.2.1.4 of Chapter 2. The experimental data used for the simulations, which were obtained from previous works, were the following: the adventitia properties from Holzapfel *et al.* (2005b), the plaque and the lipid core properties from Versluis *et al.* (2006) and finally, the microcalcification properties from Loree *et al.* (1994). The literature gives rise to a wide range of mechanical properties for the microcalcification tissue, therefore a sensitivity analysis of MPS to small changes of microcalcification mechanical properties, which is presented in Subsection 3.2.2.3, has been carried out in order to investigate the influence of material properties on the conclusions. Figure 3.4 shows the experimental stress-stretch model responses for each part of the model considered (Loree *et al.*, 1994; Holzapfel *et al.*, 2005b; Versluis *et al.*, 2006) and the fit obtained after the least-squares-based iteration scheme.

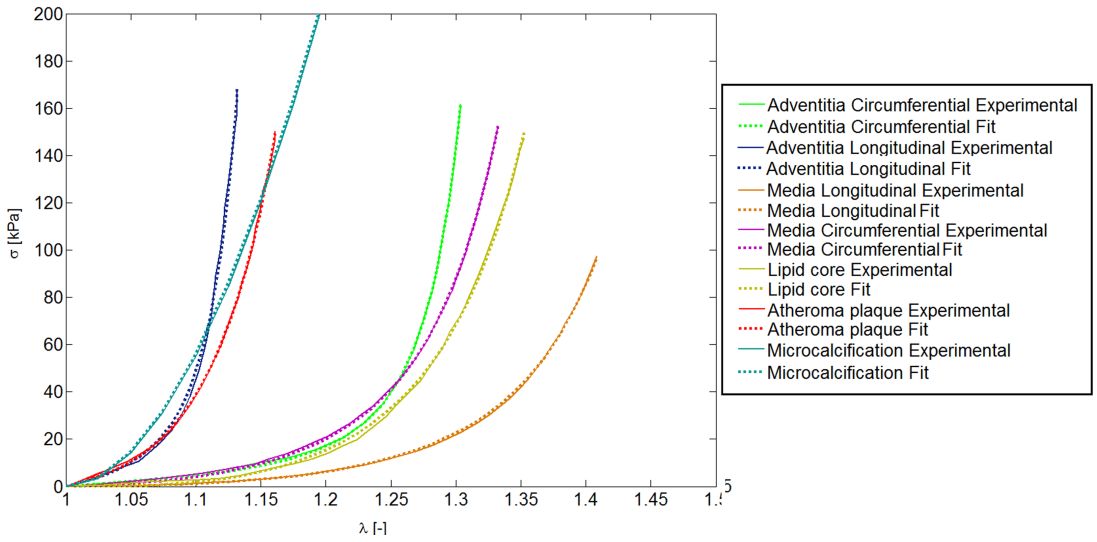

Figure 3.4: Stress-stretch model responses of experimental data taken from the literature (dot line) (Loree *et al.*, 1994; Holzapfel *et al.*, 2005b; Versluis *et al.*, 2006) and fit performed by a least-square minimization procedure (normal line) for each tissue of the model considered; adventitia and healthy media layers in both directions (circumferential and longitudinal), lipid core and atheroma plaque.

Table 3.1 shows the results of the material parameter identification for each tissue considered. Again, the goodness of the fit was checked by the normalized mean square root error (ε).

	C_1 [kPa]	k_1 [kPa]	k_2 [-]	κ [-]	ε [-]
Adventitia	8.44	547.67	568.01	0.26	0.041
Atheroma plaque	9.58	17654.91	0.51	0.33	0.056
Lipid core	0.052	965.76	70	0.33	0.03
Microcalcification	977.3	-	-	-	0.024

Table 3.1: Material parameters used in the finite element analysis, fitted according to the GOH strain energy function (SEF) (Gasser *et al.*, 2006) for the adventitia, the atheroma plaque and the lipid core, and to the Neo-Hookean SEF for the microcalcification.

Regarding the boundary conditions, symmetry conditions were imposed in the corresponding symmetry planes. Therefore, only the half of the microcalcification (half of a small sphere) was considered due to the symmetry conditions. The models were solved imposing conditions to reproduce the assumption of plane strain. A constant internal pressure of 140 mmHg (18.7 kPa) was imposed on the inner surface of the lumen, simulating the blood flow pressure (Ohayon *et al.*, 2008).

MPS was considered again as the mechanical factor for the purpose of comparison in this study. And, regarding vulnerability of the plaque, the threshold stress value of 247 kPa according to the set of experimental data obtained by Loree et al. (Loree *et al.*, 1994), and defined in the 3D parametric study of Chapter 2, has been used.

3.2.2 Results

3.2.2.1 Parametric study

The obtained contour maps can be classified into two main groups according to the influence of including the microcalcification on the results. The first group includes the models in which the geometry without microcalcification has already maximum MPS in the zone where the microcalcification is located. Generally, geometries with small microcalcification angles ($\alpha \leq 10°$), the smallest fibrous cap thickness ($fc \leq 0.05$ mm) and the small microcalcification eccentricity (x=25%) belong to this group. In that case, the microcalcification hardly increases the MPS. The second group includes the rest of the models which microcalcifications are located far away from the maximum MPS. In that case, the microcalcification considerably increase the MPS. Figure 3.5 illustrates the difference between both groups. Figure 3.5.a shows a case that belongs to the first group where the dimensions are: 0.05 mm thick of fibrous cap, 32.5° of microcalcification angle, 25% of microcalcification eccentricity and 20% of microcalcification ratio. The maximum MPS, which is located at the fibrous cap thickness, does not increase when the microcalcification is considered. Figure 3.5.b shows a case belonging to the second group whose dimensions are 0.1 mm thick of fibrous cap, 32.5° of microcalcification angle, 75% of microcalcification eccentricity and 20% of microcalcification ratio. The maximum MPS is located in the central part of the fibrous cap in the non-calcified model, but the MPS shifts to the region around of the microcalcification in the calcified one. The MPS increases around 40% from the case with microcalcification to the case

without.

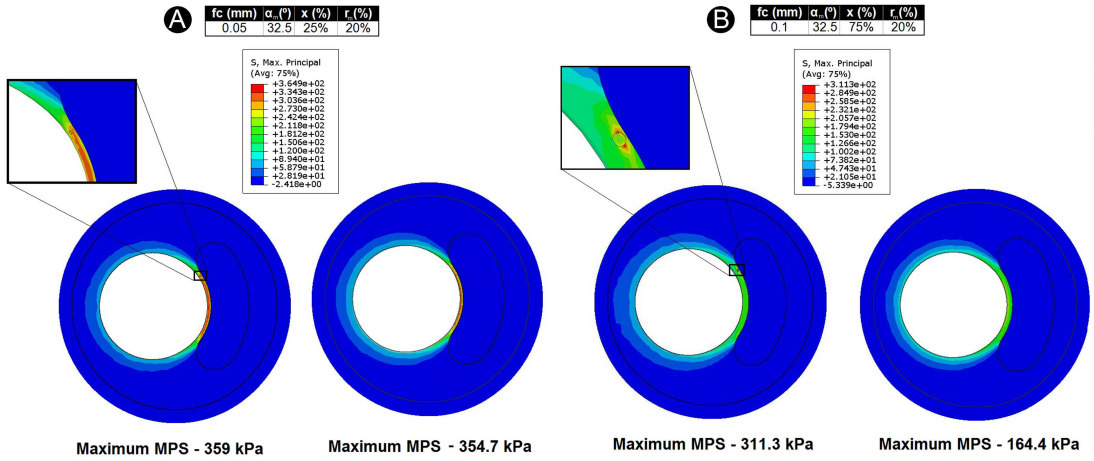

Figure 3.5: Contour maps of MPS. Comparison between models with and without microcalcification. (A) belongs to the first group where the maximum MPS is located at the fibrous cap thickness in both models. (B) belongs to the second group, the maximum MPS is located in the central part of the fibrous cap in the non-calcified model, but the MPS shifts to the region around of the microcalcification in the calcified one.

Maximum MPS for each combination of parameters is shown in Figure 3.6. For each subfigure, that corresponds to each microcalcification angle, there are four surfaces, one for each microcalcification ratio and one for the case without microcalcification. The fibrous cap thickness fc and microcalcification eccentricity x were the variables represented in each surface. All subfigures include the safety threshold plane at a maximum MPS of 247 kPa.

In all studied cases, the maximum MPS increases slightly as the microcalcification ratio increases, showing a dependency of this parameter on the MPS. As expected, the reduction of the fibrous cap thickness dramatically increase the MPS, showing the relevance of the fibrous cap thickness on MPS (Finet *et al.*, 2004; Ohayon *et al.*, 2005). The influence of the microcalcification eccentricity depends on the microcalcification angle; for the small microcalcification angles ($\alpha \leq 20°$) the microcalcification eccentricity has not influence on the MPS, however, for long ones ($\alpha > 20°$) the microcalcification located at $x = 75\%$ increases the MPS, while for $x = 25\%$, the microcalcification has a protective effect.

It can be noticed that the majority of parameter combinations are above the threshold plane of 247 kPa due to the values of the fibrous cap thickness chosen are the most critical, and thus, vulnerable even without microcalcification included (see Section 2.2.2 of Chapter 2).

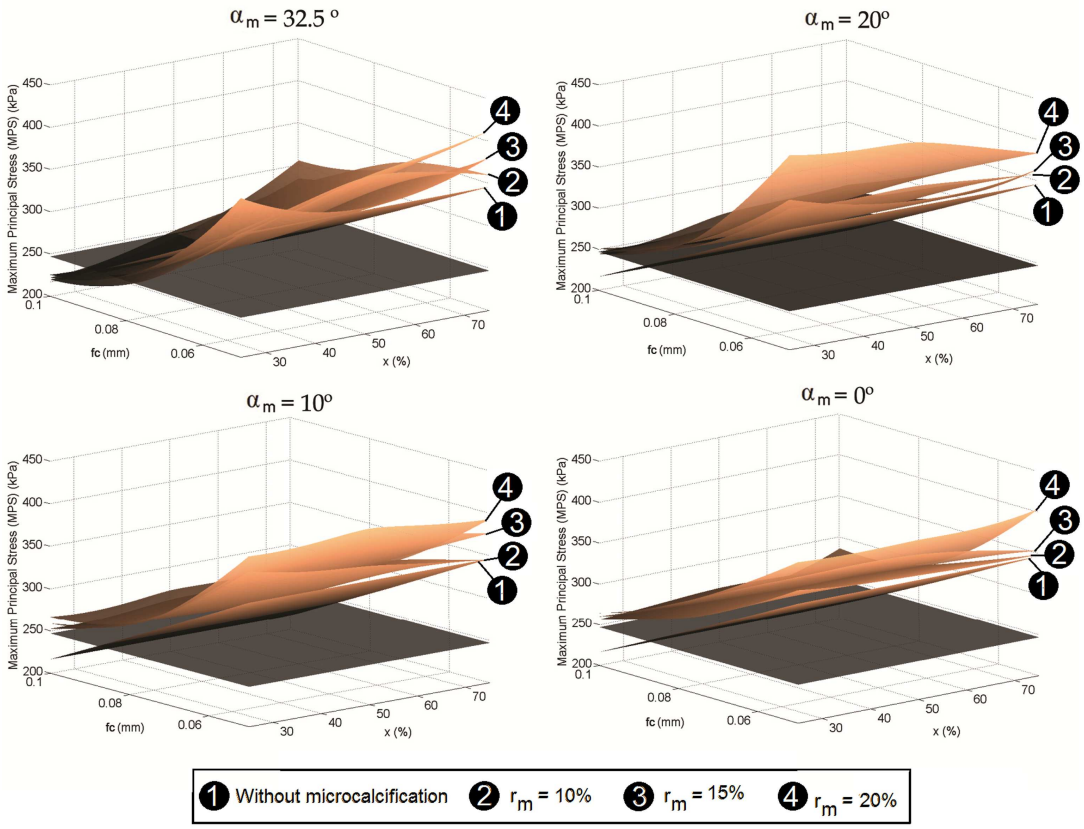

Figure 3.6: Maximum MPS surfaces for a given microcalcification angle.

3.2.2.2 Statistical Analysis

To assess the influence of the geometrical parameters on the MPS, a statistical analysis was performed. The Lilliefors test (checking the normality of the distribution), the Student's *t*-tests and the analysis of variance (ANOVA) were used. The Student's t-test was performed at 5% of significance level.

Figure 3.7 shows the statistical analysis performed on the relative increment of the maximum MPS ratio (ΔMPS) between the model with and without microcalcification, in the critical region.

$$\Delta MPS(\%) = \frac{MPS\ with\ (kPa) - MPS\ without\ (kPa)}{MPS\ without\ (kPa)} 100. \tag{3.1}$$

The results of the ANOVA analysis grouped for the different levels of each geometrical parameter studied are presented in Figure 3.7. The studied parameter becomes influential on the results if the relative increment of MPS is modified significantly when this parameter varies. The ANOVA statistical analysis related to the fibrous cap thickness is shown in Figure 3.7.a and proofs the influence of this parameter on MPS. The median of each variation of fibrous cap thickness decreases from 19.8% to 8.3% for $fc =$

0.05 mm and $fc = 0.075$ mm respectively, and slightly increases again for $fc = 0.1$ mm A noteworthy remark is that the presence of microcalcification is more influential for low values of fibrous cap. Regarding to microcalcification ratio, the median and dispersion for each variation of microcalcification ratio increase slightly as the microcalcification ratio increases, Figure 3.7.b. The median of the relative variation of MPS is between 8.8% and 12.3% when the microcalcification ratio varies between 10% and 20%. Microcalcification angle statistical analysis is presented in Figure 3.7.c, showing that the medians are very similar, taking a value around 10% for all angle values. Finally, for the microcalcification eccentricity, the results show that the medians and dispersion increase as this parameter increases from 9.9% to 16.3% for x=25% and x=75% respectively, Figure 3.7.d.

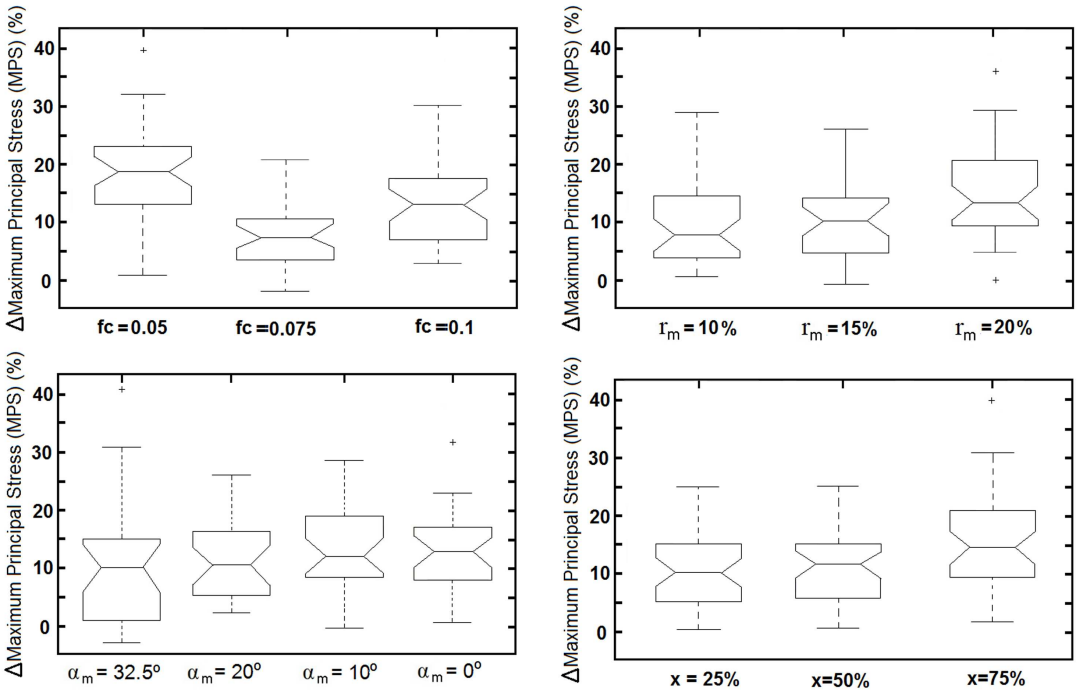

Figure 3.7: ANOVA Statistics analysis: Relative increment of maximum MPS measured in % (ΔMPS) vs. the variation of each studied parameter; fibrous cap thickness and microcalcification radius, angle and eccentricity. On each box, the central mark is the median, the edges of the box are the 25th and 75th percentiles, the whiskers extend to the most extreme data points not considered outliers, and outliers are plotted individually.

The results of the paired Student's t-test performed on the maximum MPS value from the cases with and without microcalcification grouped as exposed in Figure 3.7 are promising. The results of this test are returned in h and p-value. $h = 1$ indicates that there are significant differences between both groups at the 5% significance level, and $h = 0$ indicates the rejection of the hypothesis. The p value is the probability of

not observing the fact reflected in h (there are no differences between the results with and without microcalcification). All paired Student's t-test performed presents $h = 1$ and $p < 10^{-5}$, thus, there is always significant differences between the cases with and without microcalcification, which indicates the impact of microcalcifications.

3.2.2.3 Sensitivity of MPS to the microcalcification material properties

A sensitivity analysis of MPS to changes on microcalcification mechanical properties have been carried out. In the literature there is a wide range of calcified material properties and some conclusions presented by other authors could be related to material property values. Notice that for the case of a Neo-hookean material a relation can be established between C_1 and E; $C_1 = \frac{E}{1+\nu}$, where E is the Young's modulus valid for lineal elastic materials and ν the Poisson's ratio, whose value has been considered 0.5 (incompressible material).

In the studies performed by Cheng *et al.* (1993), Lee *et al.* (1994) and Vengrenyuk *et al.* (2006), the Young´s modulus of calcified was estimated as 10-fold that of plaque E_θ, is that, approximately $C_1 = 6666.6$ kPa (E = 10000 kPa) for the calcified areas. The experimental analysis performed by Loree *et al.* (1994), in which our study and many others works in the literature are based (Huang *et al.*, 2001; Williamson *et al.*, 2003; Tang *et al.*, 2005b; Bluestein *et al.*, 2008), reported $C_1 = 977.3 \pm 856$ kPa (E = 1466±1284 kPa) for the calcified tissue. Similar results magnitude was found by Beattie *et al.* (1998) ($C_1 = 2660$ kPa or E = 3990 kPa for the calcification tissue). Holzapfel et al. Holzapfel *et al.* (2002) modeled in their study the calcification as a rigid body, however, in a later paper of the same authors (Holzapfel *et al.*, 2004), they performed their own experiments and the microcalcification properties obtained were $C_1 = 8400 \pm 3133.3$ kPa (E = 12600±4700 kPa), after that, Wong et al. Wong *et al.* (2012) amongst others authors used these results to carry out their studies. Kiousis *et al.* (2009) used to characterize the calcified mechanical behaviour $C_1 = 90000$ kPa (E = 135000 kPa). Finally, (Maldonado *et al.*, 2012) accomplished their study with the stiffest calcified material properties ($C_1 = 6.6$ GPa or E = 10 GPa).

Viewing this wide range of calcified material parameters, the sensitive analysis has been performed by varying the initial values of C_1. The constant C_1 has been varied 100 and 10000 times higher than the proposed by Loree *et al.* (1994) and used in our study ($C_1 = 977.3$ kPa, which corresponds to E = 1465.95 kPa). Thus, the values of C_1 used to perform the sensitive analysis are; 977.3 kPa, $9.773 \cdot 10^4$ kPa and $9.773 \cdot 10^6$ kPa. These analyses have been performed on a representative geometry with the following dimensions: 0.05 mm of fibrous cap thickness, 20% of microcalcification ratio, 0° of microcalcification angle and 50% of microcalcification eccentricity. Figure 3.8 shows the results obtained for the sensitivity analysis to the microcalcification material properties. The results show that MPS amplitude increases dramatically and the way in which the soft tissue works also changes as the stiffness increases . For $C_1 = 977.3$, the microcalcification is mainly under tensile stresses (344.1 kPa) and the compressive

stress can be neglected (4.87 kPa), this fact allows the deformation of the microcalcification. However, for C_1 values of $9.773 \cdot 10^4$ kPa and $9.773 \cdot 10^6$ kPa, the tissue around of microcalcification is under compressive and tensile stress which restricts the microcalcification deformation. The tensile stress increases until 1256 and 1300 kPa for C_1 values of $9.773 \cdot 10^4$ kPa and $9.773 \cdot 10^6$ kPa, respectively, which means a MPS increase of 3.65 and 3.77 times respect to the reference case, respectively. And the compressive stress reaches 676.4 and 725.4 kPa, respectively. Such results indicate that deviation in the microcalcification material constant value would modify the conclusions regarding the influence of the microcalcifications on plaque vulnerability.

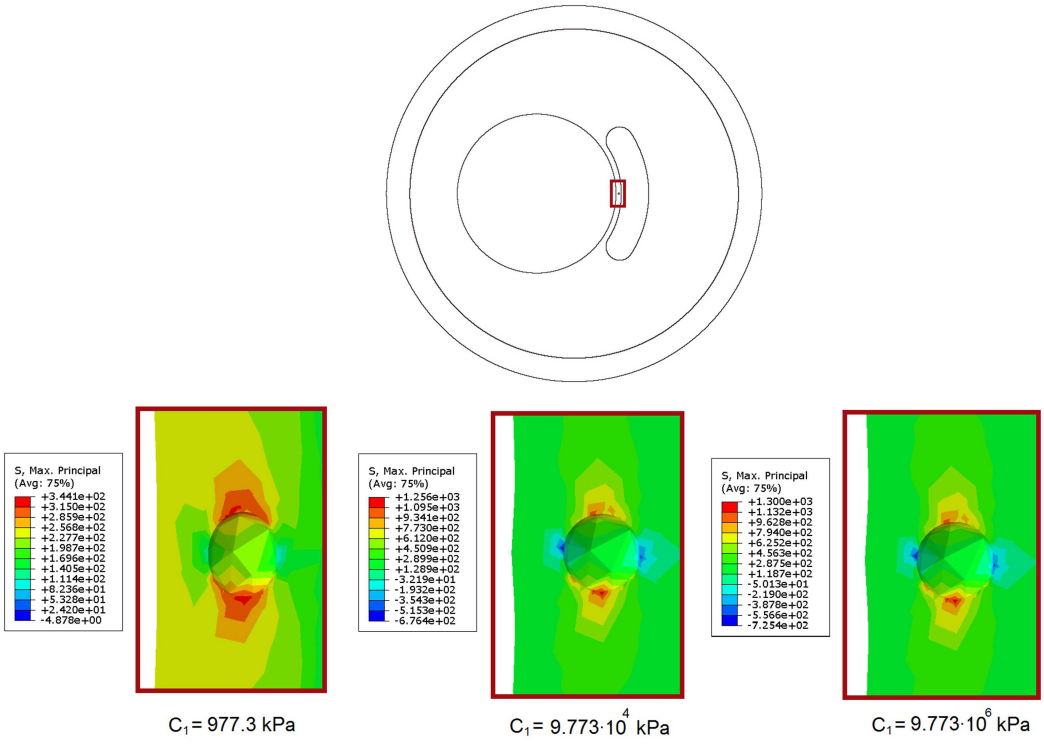

Figure 3.8: Sensitivity analyses of MPS to the microcalcification material properties. The constant C_1 has been varied 100 and 10000 times higher than that used in our study ($C_1 = 977.3$), is that, 977.3 kPa, $9.773 \cdot 10^4$ kPa and $9.773 \cdot 10^6$ kPa for the microcalcification tissue.

3.3 Comparison of the vulnerability risk for positive versus negative atheroma plaque growth

As plaque develops in arteries two types of remodeling can occur according to the process defined by Glagov *et al.* (1987); positive and negative remodeling. Positive remodeling is an outward compensatory remodeling phenomenon in which the arterial

wall grows outward in an attempt to maintain a constant lumen diameter, while negative remodeling is defined as a local shrinkage of vessel lumen size. The majority of the structural models do not include this anatomy variety and, even more, the available screening and diagnostic methods do not allow to visualize positive remodeling. Therefore, it is essential to strengthen the importance of positive remodeling, showing that it is more dangerous in terms on plaque vulnerability than negative remodeling. Since the goal of the study is to compare two geometries between them, it is not necessary to perform the analysis with 3D geometries. An arterial 2D cross-section with an atheroma plaque was used to perform the test.

3.3.1 Modeling of the atherosclerotic coronary artery

3.3.1.1 Idealized geometry, parameters studied and mesh

Three idealized geometries corresponding to a coronary vessel with atheroma plaque have been chosen: (i) a vessel with positive arterial growth, (ii) a vessel with negative arterial growth and an eccentric atheroma plaque and (iii) a vessel with negative arterial growth and a concentric atheroma plaque. The models were extruded at a small length in order to introduce some purely 3D parameters such as the fiber orientation. Atherosclerotic vessel morphology and average dimensions were similar to those presented in the 3D parametric model of Chapter 2 for the negative remodeling model. However, the positive remodeling geometry has been modelled following the works of Varnava and Davies (2001) and Versluis *et al.* (2006). Again, the whole media layer has been considered as fibrotic, whereas the adventitia was modelled as the only healthy layer of the vessel

Various idealized cross-sectional plaque morphologies, mimicking different stages and variations in atherosclerotic lesion growth, were modelled to evaluate the influence of plaque remodeling (positive and negative growth) on the maximum MPS occurred in the plaque fibrous cap. The possible relevant anatomical diversity was generated by continuously varying the size of the lipid core, the stenosis ratio, the fibrous cap thickness and the atheroma plaque distribution (eccentric or concentric), following previous works (Cheng *et al.*, 1993; Williamson *et al.*, 2003; Finet *et al.*, 2004; Ohayon *et al.*, 2008). Thus, the most influential geometric parameters considered were the fibrous cap thickness (fc), the stenosis ratio (sr) and the lipid core size (lc) determined by the width (w) and the angle (α). The lipid core size (lc) was defined as the ratio between the area of the fibrotic plaque (a_p) and the area of lipid core (a_{lc}), $lc(\%) = \frac{a_{lc}(mm^2)}{a_p(mm^2)}100$, (see Figure 3.9).

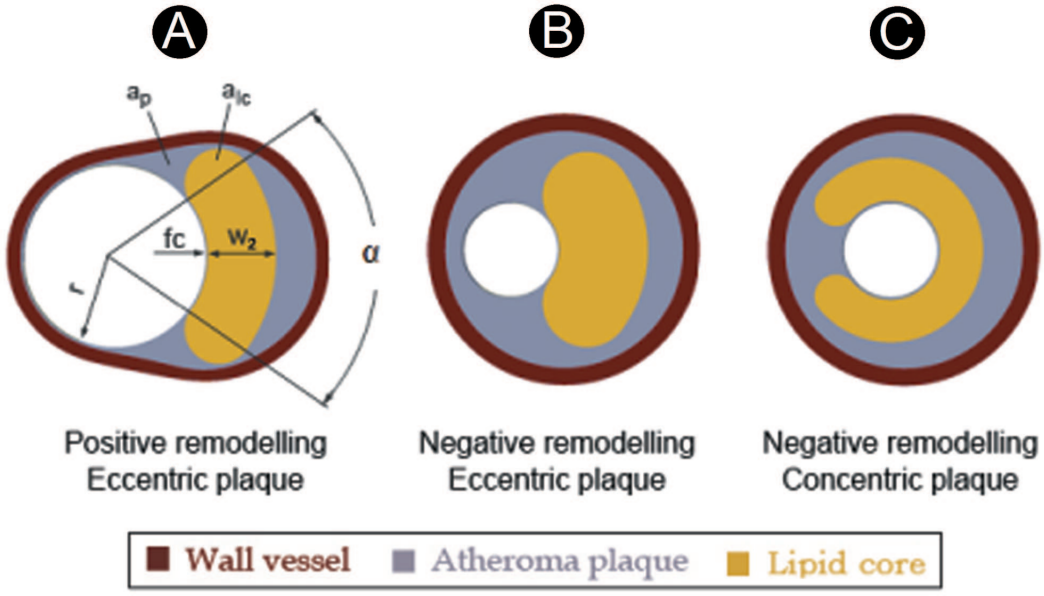

Figure 3.9: Idealized cross-sectional models and geometrical parameters studied. (a) Positive arterial growth. (b) Negative arterial growth with an eccentric atheroma plaque. (c) Negative arterial growth with a concentric atheroma plaque.

A fine mesh was created with an adaptive mesh implemented for the fibrous cap region. The mesh size was chosen based on the sensitive analyses executed for the microcalcification study previously presented and for the 3D parametric study of Chapter 2. Thus, finally approximately 20.000 linear hexahedral elements and 25.000 nodes were used to mesh the geometry.

3.3.1.2 Material model and boundary conditions

As in the parametric analysis shown in the Section 3.2 of this Chapter, the material properties used for the lipid core, the atherosclerotic plaque and the adventitia layer were assumed the same than in the 3D parametric model of Chapter 2 (see Table 2.2 of Chapter 2 or Table 3.1 of this Chapter).

Concerning the boundary conditions, symmetry conditions were imposed in the corresponding symmetry planes. The atheromatous plaque is considered as a 3D structure, however, plane strain conditions were assumed as the plaque length is large with regard to the radial dimension and neighbouring cross-sectional morphologies remain similar. A systolic pressure of 140 mmHg (18.7 kPa) was imposed in the inner surface of the lumen, simulating the blood flow pressure (Ohayon *et al.*, 2008).

Once more, MPS were considered as the key mechanical factor for the purposes of comparison in this study.

3.3.2 Results

To compare positive versus the negative growth, several tests were performed. Six successive stages (n = 6) of vulnerable plaque evolution, simulating atheroma plaque growth, were carried out in this analysis. Three different growth processes were modeled by increasing the size of the lipid core and the fibrous cap thickness and decreasing the stenosis ratio.

It should be noted that the MPS was predicted at the critical zones (fibrous cap and plaque shoulders areas) and always appeared in the circumferential direction. Furthermore, it is assumed that an atherosclerotic vessel is more vulnerable to rupture as the maximum mechanical stress in the plaque increases. In order to quantify the change in atheroma plaque vulnerability, a relative vulnerability factor (VF_{rel}) is defined. If this factor is greater than 1, it indicates that the model predicts that a plaque with positive growth is more prone to rupture than a plaque with negative growth under the same boundary conditions, material properties, geometry and dimensions. This factor is defined as,

$$VF_{rel} = \frac{Maximum\ MPS\ Positive\ Remodeling}{Maximum\ MPS\ Negative\ Remodeling}. \tag{3.2}$$

The predicted MPS with positive arterial growth (eccentric plaque, Figure 3.10.a) and the equivalent with negative growth were compared (eccentric plaque, Figure 3.10.b and concentric plaque, Figure 3.10.c). The maximum MPS is located in the fibrous cap in all three cases, however it is about 1009 kPa for the positive growth model compared to 283.1 kPa and 417.5 kPa for negative growth with eccentric and concentric plaques, respectively.

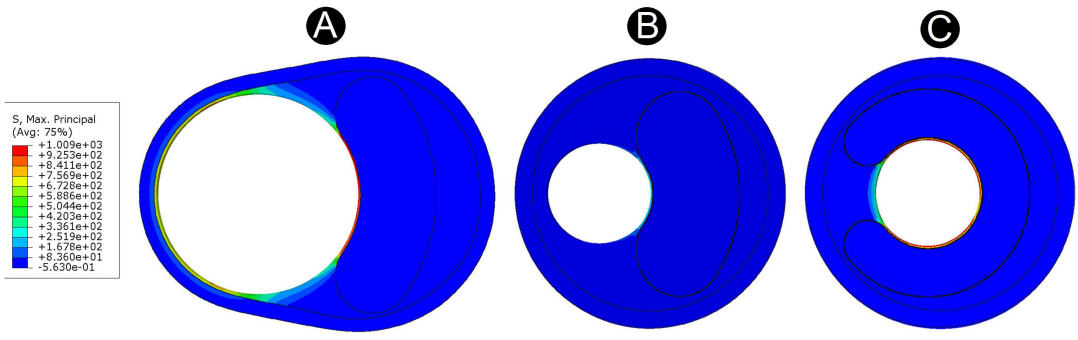

Figure 3.10: Contour maps of MPS. Comparison between a positive growth model and the negative growth models with concentric and eccentric plaques. The three cases presented have the same general dimensions: 75% lipid core, 46.6 % stenosis ratio and 0.03 mm of fibrous cap thickness. The models correspond to the third simulation set - stage 6.

All of the simulations predict that the MPS in the models with positive growth is much higher than in the models of negative growth for the same geometry, properties and boundary conditions. This is even the case when the atheroma plaque is concentric which is more unfavorable to plaque stability than the eccentric case according to the MPS obtained results.

3.3.2.1 Case 1 - Modeling plaque growth by increasing the size of the lipid core and decreasing the stenosis ratio

The first simulation set consists in six successive stages (n = 6) of eccentric vulnerable plaque evolution. Despite of the fact that the absolute area of lipid core increases, the % of the total plaque consisting of lipid remains constant (40 %) because the area of fibrotic plaque also increases. The growth process and the geometry used in each stage are illustrated in Figure 3.11.

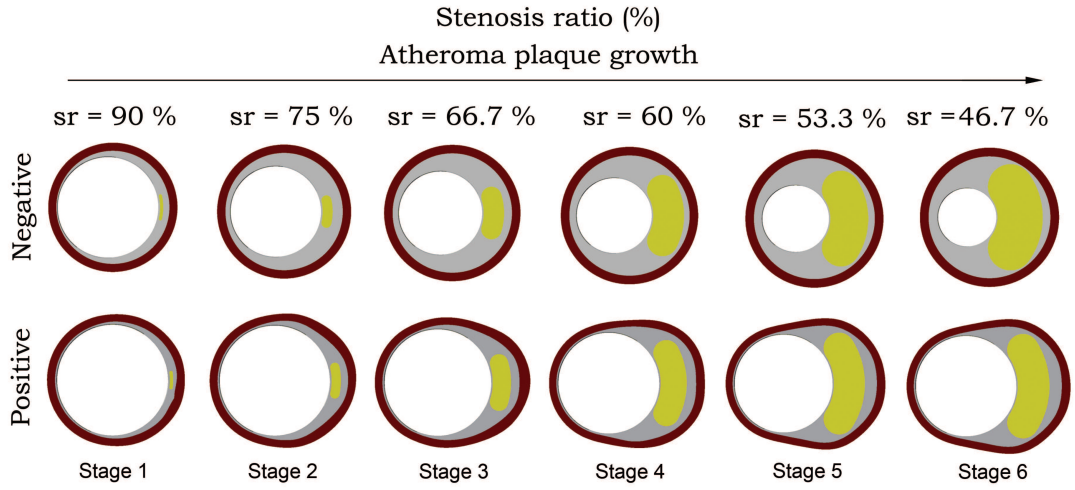

Figure 3.11: Growth process and geometry used in each stage for the first simulation set. In each of the six models both the absolute size of the lipid core (varying w_2 and α at the same time) and the stenosis ratio (sr) increases.

Table 3.2 shows the results obtained for this first simulation. VF_{rel} is always higher than 1, demonstrating that the MPS in the model with positive vascular growth is always higher than in the corresponding model with negative vascular growth. The vulnerability factor is the highest (3.45; fc = 0.03 mm) at stage 6 of plaque growth, with the relative difference in vulnerability between plaque undergoing positive and negative growth increasing at the plaque develops (see Table 3.2). The MPS in the fibrous cap for the positive growth models increases as sr decreases. However, the MPS in the fibrous cap is predicted to be constant as the plaque grows for the negative growth models.

		Fibrous cap thickness (fc)		
Stage	sr [%]	fc = 0.03 mm	fc = 0.04 mm	fc = 0.05 mm
1	90	460.3/276.7=1.66	403.8/249.9=1.62	387.8/216.6=1.79
2	75	535.8/302.7=1.77	411.2/254.6=1.61	398.4/218.9=1.82
3	66.7	831.3/307.6=2.70	654.4/248.8=2.63	598.8/217.7=2.75
4	60	877.5/332.4=2.64	693.1/245.8=2.82	645.4/220.3=2.93
5	53.3	923.9/331.9=2.78	794.8/273.1=2.91	691.5/244.3=2.83
6	46.7	998.5/289.4=3.45	782.3/249.9=3.13	779.8/243.7=3.20

Table 3.2: VF_{rel} for the first simulation set, $fc = 0.03, 0.04, 0.05$ mm. VF_{rel} is obtained by dividing the maximum MPS of the case with positive remodeling by the maximum MPS of the homologous case with negative remodeling. Absolute maximum MPS values are given in units of kPa.

3.3.2.2 Case 2 - Modeling plaque growth by increasing the size of the lipid core while maintaining a constant lumen diameter

The second simulation set (Figure 3.12) models six successive stages (n = 6) of eccentric vulnerable plaque evolution by increasing the size of the lipid core (varying w and α at the same time). The size of the lipid core, measured as a % of the total plaque size, increases while the stenosis ratio (sr) is maintained constant (sr = 53.3 %). The area of fibrotic plaque is also constant.

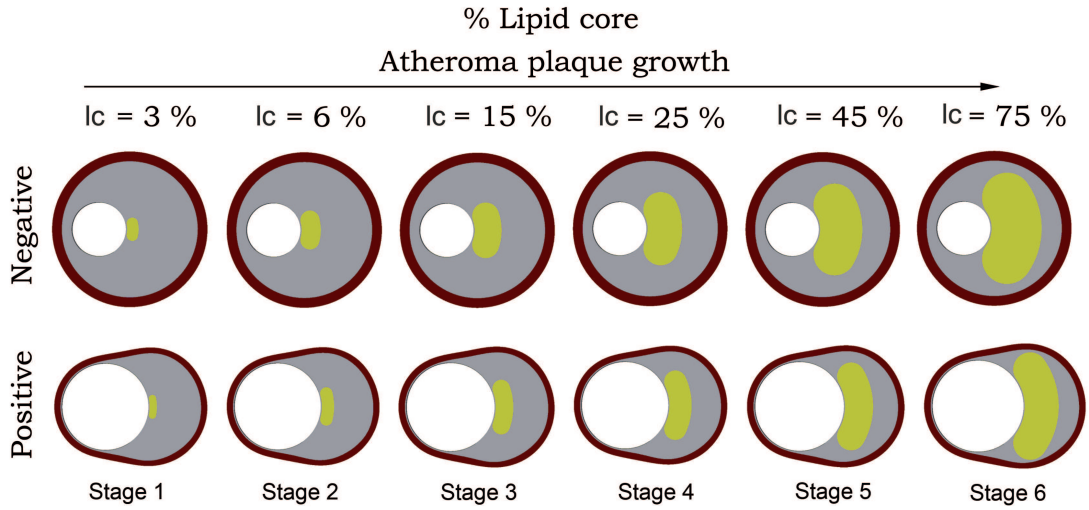

Figure 3.12: Growth process and geometry used in each stage for the second simulation set.

Again, VF_{rel} is always predicted to be higher than 1 and the relative vulnerability factor is higher at stage 6 of plaque development (3.42; fc = 0.04 mm), but does not increase dramatically as the size of the lipid core increases (see Table 3.3). The MPS in the fibrous cap increases as the lipid core grows for both models.

		Fibrous cap thickness (fc)		
Stage	lc [%]	fc = 0.03 mm	fc = 0.04 mm	fc = 0.05 mm
1	3	398.5/161.3=2.47	390.7/145.8=2.68	355.5/120.1=2.69
2	6	601.3/192.4=3.13	535.4/170.5=3.14	441.5/145.7=3.03
3	15	779.6/239.1=3.26	662.6/201.4=3.29	506.2/160.7=3.15
4	25	846.8/281.5=3.01	766.6/254.7=3.01	590.7/198.9=2.97
5	45	904.3/281.9=3.21	860.9/259.3=3.32	672.7/201.4=3.34
6	75	958.6/282.6=3.39	892.6/261=3.42	685.1/201.5=3.40

Table 3.3: VF_{rel} for the second simulation set, $fc = 0.03, 0.04, 0.05$ mm. VF_{rel} is obtained by dividing the maximum MPS of the case with positive remodeling by the maximum MPS of the homologous case with negative remodeling. Absolute maximum MPS values are given in units of kPa.

3.3.2.3 Case 3 - Modeling plaque growth by increasing the size of the lipid core and the fibrous cap thickness

The third simulation test is similar to the second one, but the fibrous cap thickness (fc) varies in each stage (see Figure 3.13). The central point of the lipid core is always located at the same position in order to best simulate the growth process.

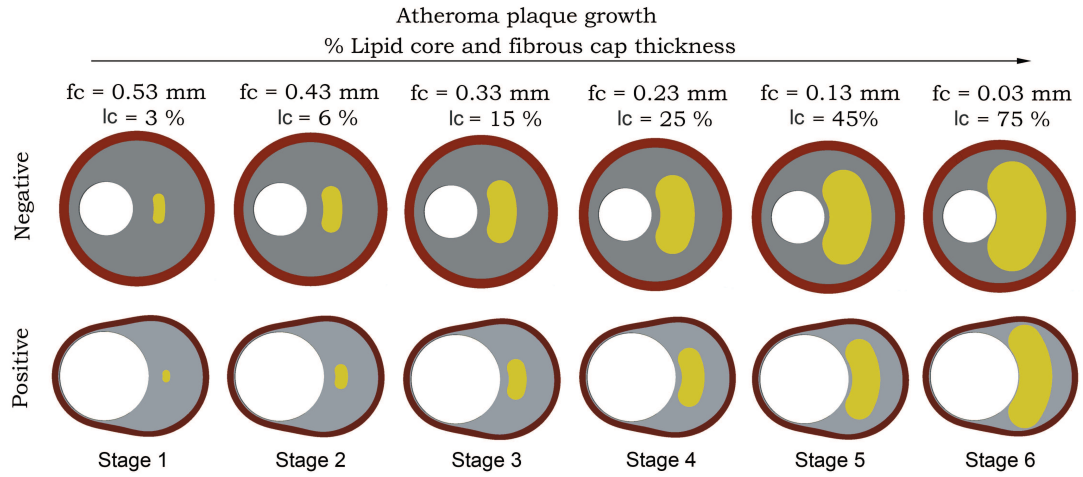

Figure 3.13: Growth process and geometry used in each stage for the third simulation test.

Again, VF_{rel} is always predicted to be higher than 1 (Table 3.4). The vulnerability factor peaks at a value of 14.33 for stage 1 of plaque development and a sr of 46.6%, suggesting that the relative risk of rupture for positive remodeling (compared to negative remodeling) decreases dramatically as the plaque cap thickness reduces. The MPS on the fibrous cap increases as the size of the lipid core increases for both models, however the relative increase is higher for negative remodeling.

			Stenosis ratio (sr)		
Stage	fc [mm]	lc [%]	sr = 75 %	sr = 60 %	sr = 46.6 %
1	0.53	3	639.3/45.7=13.99	669.2/47.8=14.00	761.4/53.1=14.33
2	0.43	6	633.4/47.2=13.42	640.6/48.2=13.29	760.8/56.8=13.38
3	0.33	15	633.2/52.9=11.97	670.1/55.7=12.03	760/61.1=12.43
4	0.23	25	628.5/85.4=7.36	671.9/71.4=9.41	759.8/73.7=10.30
5	0.13	45	604.96/86.3=7.01	721.8/87.6=8.24	762.3/88.4=8.63
6	0.03	75	829.6/278.4=2.98	879.5/281=3.13	1009/283.1=3.56

Table 3.4: VF_{rel} for the third simulation set, $sr = 75, 60, 46.6$ %. VF_{rel} is obtained by dividing the maximum MPS of the case with positive remodeling by the maximum MPS of the homologous case with negative remodeling. Absolute maximum MPS values are given in units of kPa.

3.3.2.4 Case 4 - Concentric versus eccentric atheroma plaque models

The last set of simulations compare concentric and eccentric plaque growth with negative growth to that with positive growth. The lipid core size, the fibrous cap thickness and the stenosis ratio remained constant. VF_{rel} was calculated with the same eccentric positive growth atheroma plaque for both models, as concentric positive atheroma plaque growth is unrealistic. The predicted value of VF_{rel} was 2.42 and 3.56 for the concentric and eccentric plaque, respectively (see Table 3.5).

Atheroma plaque distribution	VF
Concentric	1009/417.5=2.42
Eccentric	1009/283.1=3.56

Table 3.5: VF_{rel} for the fourth simulation set. Absolute maximum MPS values are given in units of kPa.

3.3.2.5 Sensitivity of MPS to the material properties

The sensitivity of MPS to small changes of lipid core and atheroma plaque mechanical behavior were analyzed in order to investigate the influence of the lipid core and atheroma plaque stiffness on the MPS. Since the parameter k_2 from the GOH strain energy function is the main parameter driving the increase of lipid core stiffness with strain, the sensitivity analysis has been restricted based on this material constant only (Ohayon *et al.*, 2011). Computations were performed by varying the initial values of k_2 ($k_2 = 70 \pm 10\%$ and $k_2 = 0.51 \pm 10\%$ for the lipid core and plaque, respectively). This analysis was conducted on the first and second tests with 0.03 mm of fibrous cap thickness and the third test with 46.6% of stenosis ratio.

Table 3.6 shows the results obtained for the sensitivity analyses to the lipid core properties for the four test performed. The material properties marked in bold letter, which are the ones used in the parametric study, have been used as control. It has been found that the MPS amplitude increases almost linearly within the considered range of material constants and that VF_{rel} remains nearly constant, being independent to

material variations. This indicates that deviations to this material constant would not modify our primary conclusions regarding the higher vulnerability risk associated with positive growth.

Test	$k_2 = 76.99$	$\mathbf{k_2 = 69.99}$	$k_2 = 62.99$
First	459.7/272.2=1.69	**460.3/302.7 = 1.77**	462.1/279.3=1.65
	523.4/300.3=1.78	**535.8/302.7 = 1.77**	538.8/303.9=1.77
	831.2/304.7=2.73	**831.3/307.6 = 2.7**	832.4/309.7=2.69
	876.4/331.9=2.64	**877.5/332.4 = 2.64**	878/333.6=2.63
	922.7/331.7=2.78	**923.9/331.9 = 2.78**	924.1/332.1=2.78
	996/286.7=3.47	**998.5/289.4 = 3.45**	999.2/291.9=3.42
Second	398.7/160.9=2.48	**398.5/161.3 = 2.47**	399/162=2.46
	600.1/191.3=3.14	**601.3/192.4 = 3.13**	601.6/192.9=3.12
	778.78/238.7=3.26	**779.6/239.1 = 3.26**	780/239.9=3.25
	846.2/279.4=3.03	**846.8/281.5 = 3.01**	847.9/282.4=3
	904.1/208.7=4.33	**904.3/281.9 = 3.21**	905.5/283=3.2
	957.8/280.9=3.41	**958.6/282.6 = 3.39**	960.9/283.9=3.38
Third	760.5/52.01=14.62	**761.4/53.1 = 14.33**	762.4/54.75=13.93
	758.4/56.98=13.31	**760.8/56.8 = 13.38**	761.8/57.01=13.36
	759.4/60.45=12.56	**760/61.1 = 12.43**	760/62.45=12.17
	758.1/72.05=10.52	**759.8/73.7 = 10.30**	761.9/75.01=10.16
	761.2/85.84=8.87	**762.3/88.4 = 8.63**	763/88.94=8.58
	1009/282.4=3.57	**1009/283.1 = 3.56**	1009/284.2=3.55
Fourth	1009/416.4=2.42	**1009/417.5 = 2.42**	1009/418.7=2.41
	1009/282.4=3.57	**1009/283.1 = 3.56**	1009/284.2=3.55

Table 3.6: VF_{rel} for sensitive analyses of MPS to the lipid core material properties

Figure 3.14 illustrates the tendency of the MPS as the lipid core material properties varies. The case presented corresponds to the stage 4 of test 1 for the negative remodeling geometry.

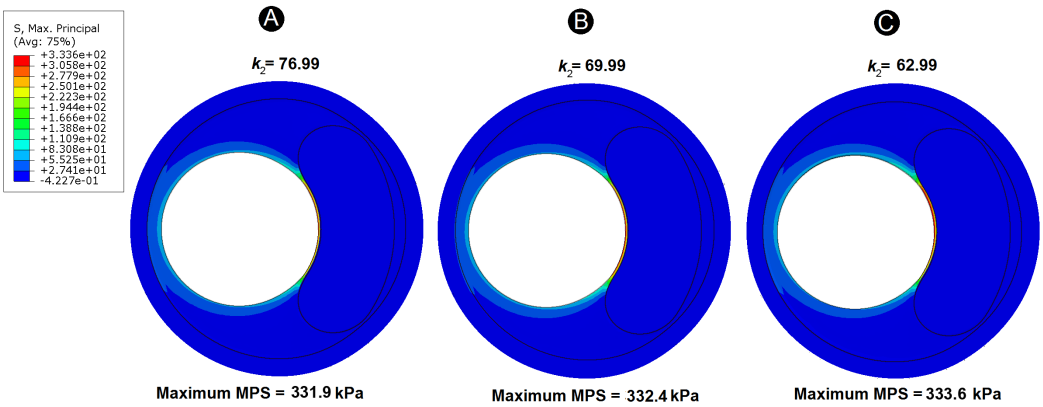

Figure 3.14: MPS variation with the parameter k_2 of the lipid core material properties. This negative remodelling model corresponds to the first simulation set - stage 4.

Meanwhile, Table 3.7 shows the obtained VF_{rel} by varying the atheroma plaque properties in the four test carried out, similar conclusions than for the case of varying the lipid core material properties could be drawn. Again, the results in bold letters correspond to those obtained in the parametric study.

Test	$k_2 = 0.56$	$\boldsymbol{k_2 = 0.51}$	$k_2 = 0.46$
First	451.7/271.7=1.66	**460.3/276.7 = 1.66**	468.6/283.5=1.65
	532.4/297.54=1.79	**535.8/302.7 = 1.77**	547.9/314.1=1.74
	829.94/301.5=2.75	**831.3/307.6 = 2.7**	834.5/319.5=2.61
	875.4/328.9=2.66	**877.5/332.4 = 2.64**	881.4/335.4=2.63
	918.6/327.4=2.81	**923.9/331.9 = 2.78**	926.4/333.4=2.78
	953.7/276.9=3.44	**998.5/289.4 = 3.45**	962.2/294.6=3.27
Second	394.6/158.7=2.49	**398.5/161.3 = 2.47**	401.9/163.9=2.45
	577.9/185.9=3.11	**601.3/192.4 = 3.13**	602.6/195.4=3.08
	765.4/235.7=3.25	**779.6/239.1 = 3.26**	785.4/243.4=3.23
	824.7/276.9=2.98	**846.8/281.5 = 3.01**	851.6/284.6=2.99
	901.6/277.5=3.25	**904.3/281.9 = 3.21**	905.7/385.4=2.35
	955.4/273.9=3.49	**958.6/282.6 = 3.39**	962.4/286.9=3.35
Third	758.4/49.78=15.24	**761.4/53.1 = 14.33**	762.4/55.94=13.63
	758.3/52.94=14.32	**760.8/56.8 = 13.38**	764.9/57.98=13.19
	757.5/57.64=13.14	**760/61.1 = 12.43**	763/62.94=12.12
	751.6/71.94=10.45	**759.8/73.7 = 10.30**	761.9/79.61=9.57
	760/82.94=9.16	**762.3/88.4 = 8.63**	768.9/91.46=8.41
	1006/286.7=3.51	**1009/283.1 = 3.56**	1014/285.6=3.55
Fourth	1006/416.7=2.41	**1009/417.5 = 2.42**	1014/423.7=2.39
	1006/286.7=3.51	**1009/283.1 = 3.56**	1014/285.6=3.55

Table 3.7: VF_{rel} for sensitive analyses of MPS to the atheroma plaque material properties

Analogous to the lipid core material properties, Figure 3.15 illustrates the tendency of the MPS as the atheroma plaque material properties changes. The case presented is the same than for the lipid core material properties variation (First simulation test - Stage 4).

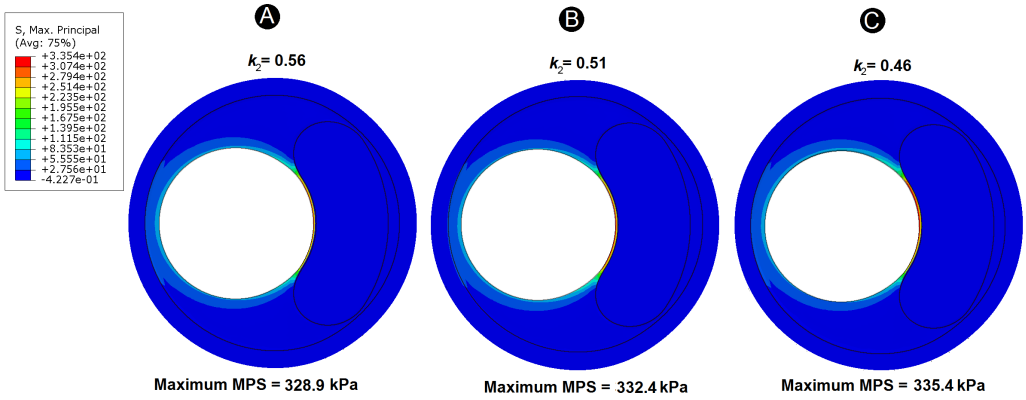

Figure 3.15: MPS variation with the parameter k_2 of the atheroma plaque material properties. This negative remodelling model corresponds to the stage 4 of the first simulation set.

3.3.2.6 Sensitivity of maximum MPS to the internal pressure

The sensitivity of MPS to changes in the applied internal pressure *(p)* was also investigated. The pressure was varied between $140 \pm 10\%$ mmHg. As expected, our

simulations show that the maximum MPS value increases linearly as the internal pressure increases, and again, that VF_{rel} is similar for all applied pressures. Thus, considering different internal pressures would not significantly modify the main findings of this study. This analysis was performed on the same models than the sensitivity analysis of MPS to the material properties, and, the results are shown in Table 3.8.

Test	$p = 154mmHg$	$\mathbf{p = 140mmHg}$	$p = 126mmHg$
First	520.5/315.1=1.65	**460.3/276.7 = 1.66**	421/229.8=1.83
	576.6/330.3=1.75	**535.8/302.7 = 1.77**	500.6/270.1=1.85
	896.2/349.8=2.56	**831.3/307.6 = 2.7**	779.3/273.1=2.85
	939.5/368.9=2.55	**877.5/332.4 = 2.64**	798.6/307.9=2.59
	1021/396.9=2.57	**923.9/331.9 = 2.78**	826.9/297.8=2.78
	1060/319.4=3.32	**998.5/289.4 = 3.45**	887.1/267.8=3.31
Second	432/201.6=2.14	**398.5/161.3 = 2.47**	329.6/121.6=2.71
	635.8/213.4=2.98	**601.3/192.4 = 3.13**	583.7/159.9=3.65
	843.6/263.8=3.20	**779.6/239.1 = 3.26**	716/201.2=3.56
	935.3/312.6=2.99	**846.8/281.5 = 3.01**	758.5/253.6=2.99
	969.7/338.3=2.87	**904.3/281.9 = 3.21**	829.3/241.9=3.43
	1030/318.4=3.23	**958.6/282.6 = 3.39**	907.3/254.5=3.57
Third	805.6/71.7=11.24	**761.4/53.1 = 14.33**	739.8/49.01=15.09
	799.4/61.45=13.01	**760.8/56.8 = 13.38**	733.9/48.03=15.28
	789.4/63.46=12.44	**760/61.1 = 12.43**	732.5/57.21=12.80
	781.5/81.95=9.54	**759.8/73.7 = 10.30**	729.4/60.03=12.15
	781.9/92.96=8.41	**762.3/88.4 = 8.63**	740.6/79.46=9.32
	1103/318.4=3.46	**1009/283.1 = 3.56**	993.6/226.4=4.39
Fourth	1103/424.1=2.60	**1009/417.5 = 2.42**	993.6/403=2.47
	1103/318.4=3.46	**1009/283.1 = 3.56**	993.6/226.4=4.39

Table 3.8: VF_{rel} for sensitive analyses of MPS to the internal pressure

Figure 3.16 illustrates how the MPS increases as the internal pressure applied increases (see Table 3.8). Again, the negative remodeling case shown belongs to the stage 4 of the first simulation test.

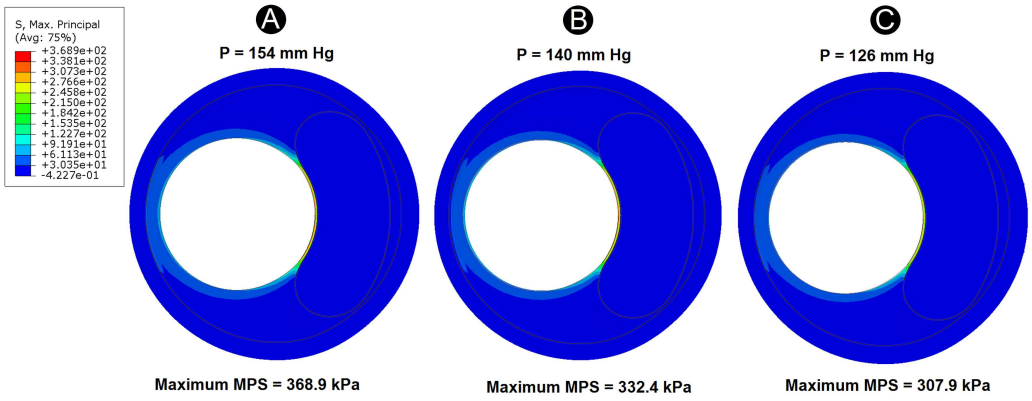

Figure 3.16: MPS variation with the internal pressure applied. The case presented belongs to the Stage 4 of test 1.

3.4 Fluid-Structure (FSI) Analysis

Due to the important role of high pulsating blood pressure and wall shear stress effects in atheroma growth, FSI phenomenon has been incorporated into the 3D geometric model described in Chapter 2. Thus, the influence of including the blood flow in the model can be assessed by comparing the results of the FSI study with those obtained in Chapter 2. Furthermore, the relationship between the shape of the stenotic artery and blood flow, using an idealized geometry, as well as other influential hemodynamic variables in the atheroma plaque development such as WSS, can be studied by FSI.

3.4.1 Modeling of the atherosclerotic coronary artery

3.4.1.1 Idealized geometry, parameters studied and mesh

The idealized model of coronary artery with an eccentric stenosis described in Chapter 2 was used as the solid model to perform the 3D FSI parametric study. The fluid part corresponds to the volume inside of the solid model part (see Figure 3.17). The parameters studied were also the same than in the 3D parametric model of Chapter 2, i.e. the fibrous cap thickness, fc; the stenosis ratio in the central cross-section, sr; the lipid core length, l and the lipid core width, w. For more details of the geometric model and the parameters studied, see Subsection 2.2.1 of Chapter 2.

Five realistic morphological data were considered for each parameter. However, since for the FSI simulations higher computational cost than for FEM simulations are required, less variations of the parameters than for the FEM parametric study of Chapter 2 have been considered. Combining these five values for each parameter from the following way makes a total of 17 idealized models of coronary artery with atherosclerotic plaque. Therefore, considering the intermediate value of each parameter, the reference model or base case **(Cb)** is defined. The remaining 16 models were obtained changing only one parameter each time, from the range described above, and unchanging the another three parameters (see Table 3.9).

Parameters	1	2	**Cb**	4	5
fc [mm]	0.025	0.035	**0.05**	0.1	0.15
sr [mm]	46.7	53.3	**56.7**	60	66.7
l [mm]	1	2	**4**	6	8
w [%]	30	45	**60**	75	90

Table 3.9: Geometrical parameters used to generate the parametric 3D models.

Regarding the mesh of the model, the election of the mesh size has to take into consideration limitations on the software capability as well as its degree of accuracy. A compromise between the number of elements and nodes of the fluid and the solid part was elected in order to obtain a suitable mesh. Therefore, a 3D fine mesh was created in each region of the solid model, building a more precise mesh in the fibrous cap

region. And, in order to evaluate the fluid-structure interaction, the fluid volume must be defined for each studied idealized vessel models with eccentric atherosclerotic, then the inner surface or lumen for each model was meshed using the commercial softwares NX NASTRAN 8.0, ICEM, FEMAP 9.3.

The mesh used and the number of nodes and elements vary from each of the 17 studied models because the geometry undergoes small alterations as the parameters are changed, but approximately 125.000 and 800.000 tetrahedral elements, and 25.000 and 140.000 nodes, for the solid and fluid part, respectively, were used. The mesh sensitivity is tested on the velocity and WSS, by varying the number of grid cells. The computational domain is considered to be sufficient for this study, when further mesh refinement can only result in less than 2% change in velocity and 1% change in WSS at some examined sections.

Figure 3.17 shows both the solid and the fluid mesh and geometry, Figures 3.17.a and 3.17.b, respectively, corresponding to one of the 17 models simulated.

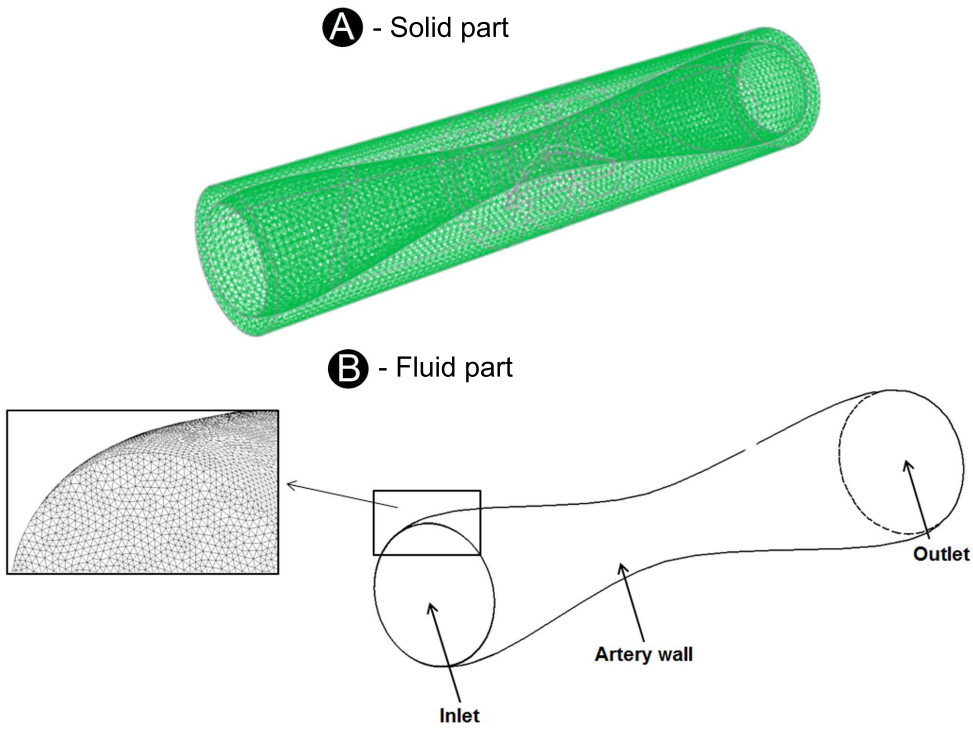

Figure 3.17: A - Solid geometry and mesh. B - Fluid geometry and mesh. The three surfaces which define the fluid volume are indicated; inlet, outlet and artery wall.

3.4.1.2 Material properties

The material properties of the solid part were based on the same experimental data than the 3D parametric model presented in Chapter 2 (Holzapfel *et al.* (2005b),

for the media and adventitia layers; and Versluis *et al.* (2006), for the lipid core and the atherosclerotic plaque). Due to ADINA software has implemented other SEF than ABAQUS software, the material constants were fitted using the process described in the Subsection 2.2.1.4 of Chapter 2 by the SEF proposed by Holzapfel *et al.* (2005b) (see Table 3.10). Therefore, non-linear, hyperelastic and incompressible material properties were assumed for the different tissues. Healthy wall was modelled as an anisotropic material with two families of fibres, oriented at $\pm 36°$ and $\pm 30.28°$, with respect to the circumferential direction, for the adventitia and media layer, respectively. The hyperelastic SEF developed by Holzapfel *et al.* (2005b) has the form

$$\Psi = C_1[I_1 - 3] + \frac{k_1}{2k_2} \sum_{i=4,6} \exp\big(k_2\big[[1-\rho][I_1-3]^2 + \rho[I_i - 1]^2\big]\big) - 1, \tag{3.3}$$

where $C_1 > 0$ and $k_1 > 0$ are stress-like parameters and $k_2 > 0$ and $0 \leq \rho \leq 1$ are dimensionless parameters (when ρ=1 the fibres are perfectly aligned and when ρ=0 the fibres are randomly distributed and the material is considered as isotropic), I_1 is the first invariant, and I_4 and I_6 are invariants which depend on the direction of the family of fibres at a material point (Spencer, 1971).

	$C_1[kPa]$	$k_1[kPa]$	$k_2[-]$	$\rho[-]$	β [°]	$\varepsilon[-]$
Adventitia	1.99	89.97	97.30	0.77	± 36	0.036
Media	1.02	25.11	8.58	0.32	± 30.28	0.019
Atheroma plaque	10.99	950.88	5.00	0	-	0.054
Lipid core	0.01	66.24	4.99	0	-	0.031

Table 3.10: Material parameters used in the finite element analysis for the adventitia, the media, the atheroma plaque and the lipid core.

As described in Section 1.2.2, the fluid (blood) was modeled as incompressible (density, ρ_f=1050 $\frac{Kg}{m^3}$) and non-Newtonian with a Carreau constitutive law with shear rate ($\dot{\gamma}$; s^{-1}) dependent viscosity:

$$\mu = \mu_\infty + (\mu_0 - \mu_\infty) \cdot (1 + A\dot{\gamma}_{ij}^2)^m, \tag{3.4}$$

where μ_0 = 0.056 $\frac{N \cdot s}{m^2}$, μ_∞ = 0.00345 $\frac{N \cdot s}{m^2}$ A=10.975 and m=-0.3216 (Valencia and Baeza, 2009).

3.4.1.3 Boundary conditions

As usual for FSI analyses, mixed velocity-pressure boundary conditions are required in order to correctly compute flow features and structural stresses, strains and displacements. Therefore, a typical physiological coronary flow waveform, $\mathbf{u(t)}$, was imposed at the inlet and a time varying pressure, $p(t)$, was applied at the outlet. This physiological velocity-pressure waves are obtained from the experimental data of Davies *et al.* (2006),

who measured simultaneous pressure and Doppler velocity with intracoronary wires in the left main stem, left anterior descending, and circumflex arteries of 20 subjects after a normal coronary arteriogram (see Figure 3.18). In addition, it should be noted that the maximum pressure and velocity of the physiological cycle occurs at 0.36 s and 0.56 s, respectively.

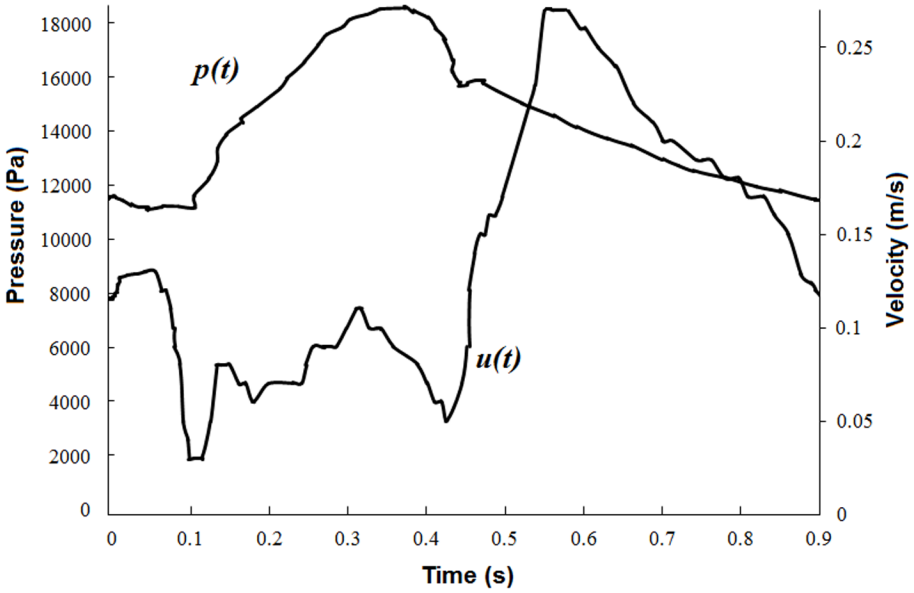

Figure 3.18: Time varying physiological pressure and flow profiles applied at the inlet and outlet (Davies *et al.*, 2006).

The FSI condition in the fluid-structure interface is obtained with the following boundary conditions:

$$d^s = d^f, \text{ at the inner wall, and} \tag{3.5}$$

$$\sigma_{ij}{}^s n_j = \sigma_{ij}{}^f n_j, \text{ at the lumen wall interface,} \tag{3.6}$$

where d^s and d^f are the displacements for the solid and fluid domain, respectively, and, $\sigma_{ij}{}^s$ and $\sigma_{ij}{}^f$ are the stress tensor for the solid wall and fluid flow, respectively.

The blood flow and pressure fields were calculated by solving the continuity (Equation 3.7) and momentum (Equation 3.8) equations for incompressible, viscous and laminar blood flow along the stenosis section; within the arterial wall stress equilibrium equation (Equation 3.9):

$$\nabla \cdot u = 0 \tag{3.7}$$

$$\rho \left(\frac{\partial u}{\partial t} + [(u - u_m) \cdot \nabla] u \right) = -\nabla p + \nabla \cdot (\mu \nabla u) \tag{3.8}$$

$$\sigma^s_{ij,i} = 0, \tag{3.9}$$

where u is the flow velocity field, u_m the mesh velocity, p the pressure field, μ and ρ the dynamic viscosity and density of the blood, respectively, and σ_{ij}^s the stress tensor for the arterial wall.

Therefore, using the boundary conditions described above within the arbitrary Lagrangian-Eulerian (ALE) formulation, the Equations (3.7)-(3.9) are solved. A finite-element scheme was used to solve the coupled fluid-structure interaction equations using the commercial software ADINA 8.5 which employs the iterative Newton-Raphson scheme. Furthermore, in order to avoid the movement of the model as solid rigid all the displacements were constrained at the ends of the coronary artery despite this boundary condition is unrealistic. However, the blood vessel is subjected to extreme movements when the pressure and velocity conditions are applied, and then this boundary conditions is needed for the FSI analysis convergence.

3.4.2 Results

The obtained results in the 17 FSI models of an idealized coronary artery with atheroma plaque are shown beneath. Firstly, the variables related to the solid part are presented; the MPS and the maximal principal strain occurring in the model due to the fluid effects. Furthermore, the MPS results of this FSI study are compared with those obtained in the 3D parametric study applying internal constant pressure in order to evaluate the fluid influence on the atheroma plaque vulnerability risk. Secondly, the variables linked to the fluid volume are analyzed; the flow pattern, the WSS, the drop pressure and the vorticity.

3.4.2.1 MPS distribution in the solid part

The MPS distribution occurring on each of the 17 models studied has been obtained. Figure 3.19 shows the obtained 17 MPS contour maps in the cross-central section of each model for the instant of time in which the pressure is maximum (t= 0.36 s). These contour maps show that the maximum MPS is produced in the fibrous cap region in all models. Furthermore, it should be noted that any of the 17 studied models exceeds the threshold stress of 247 kPa. This fact is due to the most unfavourable case studied that correspond to the model with 0.025 mm of cap thickness, 56.7% of stenosis ratio, 4 mm of lipid core length and 60% of lipid core width, is considering stable according to the obtained results of Chapter 2. Therefore, no further conclusions about vulnerability limits can be obtained by means of this FSI study.

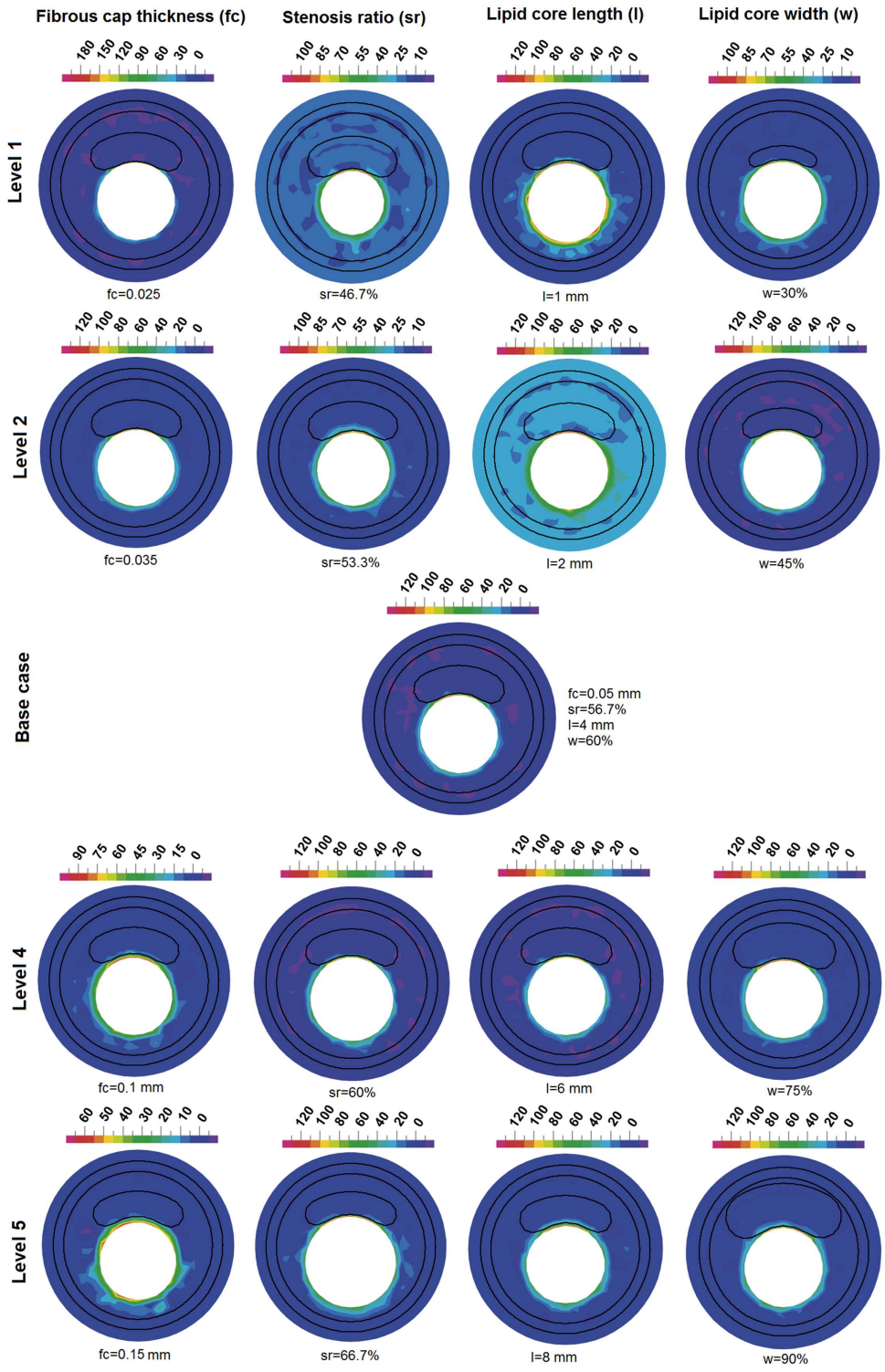

Figure 3.19: Contour maps of the MPS for the central cross section of each of the 17 models studied.

For the sake of clarity, Figure 3.20 shows the maximum MPS at the maximum pressure applied (t = 0.36 s) in order to compare the variation of circumferential stress versus each of the geometrical parameters considered in this 3D FSI parametric study. Thereby, the tendency of the maximum MPS versus each geometrical parameter can be observed. Figure 3.20.a shows the MPS evolution with fibrous cap variation, showing a dramatically increase of MPS as this parameter decreases. Comparing the models with 0.15, 0.1 and 0.05 mm of cap thickness, the maximum MPS values obtained are 64.3, 73.98 and 139.11 kPa, respectively. For the stenosis ratio and lipid core parameters, Figures 3.20.b and 3.20.d, respectively, the maximum MPS increase slightly as these parameters increase. Finally, for the lipid core length, Figure 3.20.c, the maximum MPS increases as the lipid core length increases until 4 mm, and after that, the maximum MPS remains practically constant. These results are in agreement with those obtained in the 3D parametric study presented in Chapter 2.

Furthermore, as alluded before, any conclusion about vulnerability limits could be obtained from these results since any model exceed the vulnerability threshold stress value of 247 kPa.

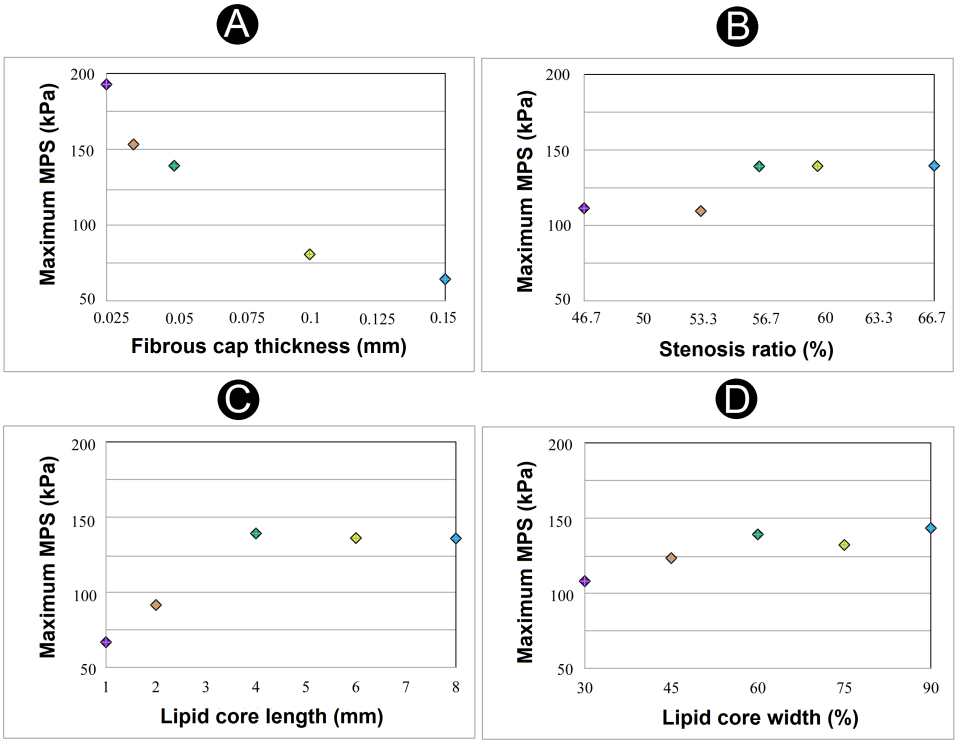

Figure 3.20: Maximum MPS for each of the 17 models at the maximum pressure applied (t = 0.36 s).

Figures 3.19 and 3.20 show the MPS contour maps and the maximum MPS, respectively, of each studied model at t = 0.36 s, which corresponds to the maximum pressure

instant. However, since the applied pressure varies with the time, the maximum MPS also varies along the imposed physiological cardiac cycle. Therefore, Figure 3.21 illustrates the tendency of the maximum MPS along this cycle ($\Delta t = 0.9$ s). The trend observed in the maximum MPS variation along the time is similar to the applied time varying pressure cycle, being the maximum MPS reached at 0.36 s which corresponds to the moment of maximum pressure applied. This fact is expected since the pressure is the main responsible of the occurred maximum circumferential stress, which is the MPS in this case.

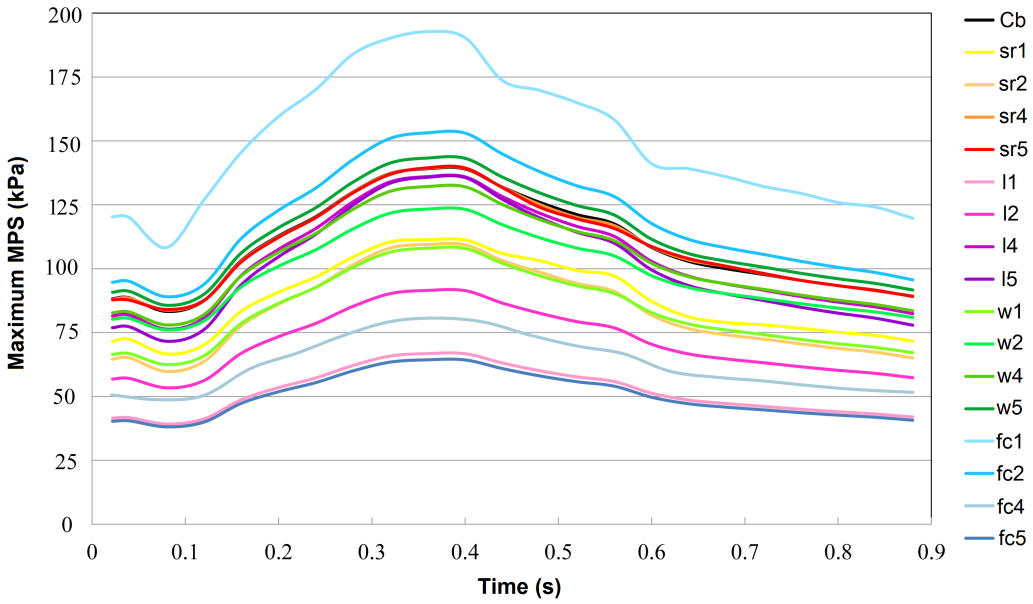

Figure 3.21: MPS variation along a physiological coronary flow waveform in the central section of each of the 17 models.

3.4.2.2 Comparison of the obtained MPS results in the FSI and FEM models

The obtained results in this FSI study and in the 3D FEM parametric study of Chapter 2 have been compared in order to rule out the influence of considering the blood effects on the MPS distribution, and thus, to asses atheroma plaque vulnerability risk. Since the geometric model and the material properties used in both cases are the same, and the maximum pressure reached in the application of the physiological coronary cycle (see Figure 3.18) for the FSI study is equivalent to that used as internal constant pressure (140 mm Hg or 18.3 kPa) for the FEM study, the models can be compared at this moment of maximum pressure (t = 0.36 s).

Figure 3.22 shows the results of this comparison by means of MPS contour maps in the cross central section of the reference case model. Both contour map distributions are similar and the maximum MPS reached is also analogous and located in the fibrous

cap for both models, showing that the fluid-structure interaction effects resulting from the physiological pulsatile nature of blood pressure are insignificant for the assessing of the MPS distribution.

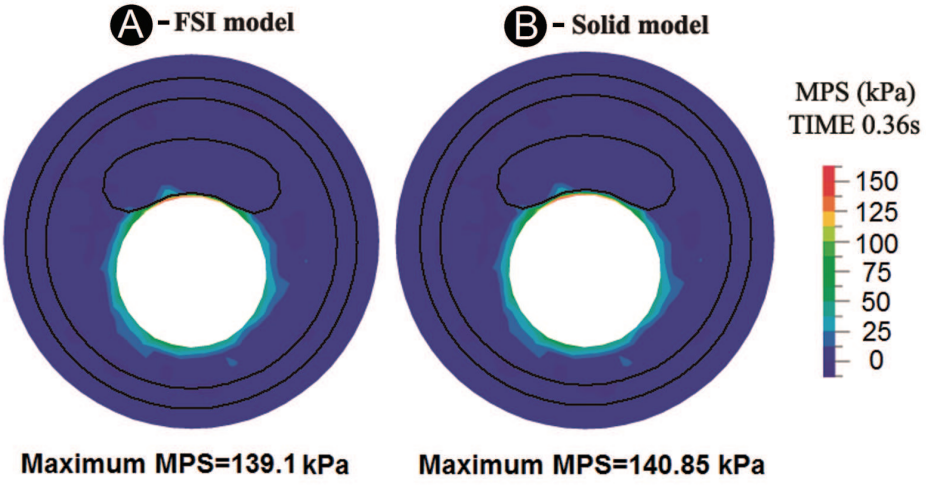

Figure 3.22: Contour maps of the MPS on the base case model for the FSI model (A) and FEM model (B).

3.4.2.3 Arterial deformation

Plaque rupture occurs when the plaque structure cannot resist the hemodynamic blood pressure and shear stress. Hemodynamic blood flow acts as an extrinsic factor exerting pressure and shear stress on the plaque. The deformation of the plaque in turn will affect blood flow. Collapse of severe but compliant stenoses due to negative transmural pressures may produce highly concentrated compressive stresses from buckling of the wall with bending deformation, preferentially involving plaque edges, and theoretically, this could contribute to plaque disruption (Aoki and Ku, 1993). Furthermore, the propagating pulse wave causes cyclic changes in lumen size and shape with deformation and bending of plaques, particularly the soft ones (Mizushige *et al.*, 1993), and therefore, the repetitive deformations caused by the cardiac cycle may play an important role in lesion stability (McCord and Ku, 1993).

Therefore, the arterial deformation has been deeper studied. Figure 3.23 shows the undeformed and maximum deformed model geometries for one of the 17 studied models (Reference case) in order to observe the differences between both states. Furthermore, the contour maps of the maximal principal strain, which corresponds to the radial direction, in logarithmic scale for the instant of maximum pressure applied (t = 0.36 s) are also shown. Observing these contour maps, the maximum maximal principal strain occurs in the artery wall close to the ends of the artery. Mainly, this fact is related to the great stiffness of the central zone of the coronary model due to the presence of

atheroma plaque, allowing more radial displacement in zones without atherosclerotic lesions. However, in order to predict atheroma plaque rupture, the maximal principal strain should be observed in the critical zones of the model, i.e, in the internal surface of the atheroma plaque.

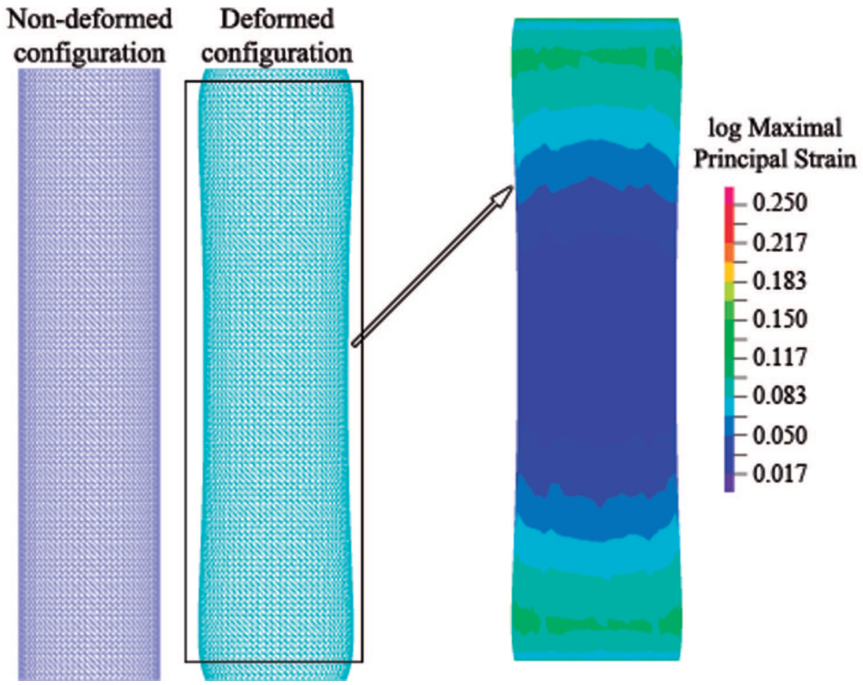

Figure 3.23: Deformed and non-deformed configuration belonging to the reference case, and its corresponding contour maps of the maximal principal strain in logarithmic scale.

Therefore, Figure 3.24 depicts the maximum deformation measuring in percentage of each of the 17 studied model occurring at the central part of the atheroma plaque internal surface. A trend is observed between the parameters and the maximum principal deformation since it increases as the lipid core width and length and the stenosis ratio increase, but on the contrary, it decreases as the fibrous cap thickness increases. Additionally, since the deformations are directly related with the stresses, this observed trend is analogous than that found for the case of the maximum MPS. Furthermore, the maximum deformation of the atheroma plaque is quite similar for all the considered models, varying around a 6%, being these deformations allowable as an artery deformation. Notwithstanding, the maximum maximal principal strain varies from one to another parameter, reaching deformation variations of 4.5% and 5%, for the fibrous cap thickness and for the lipid core length, respectively, which are slightly higher than for the other two studied parameters (3%).

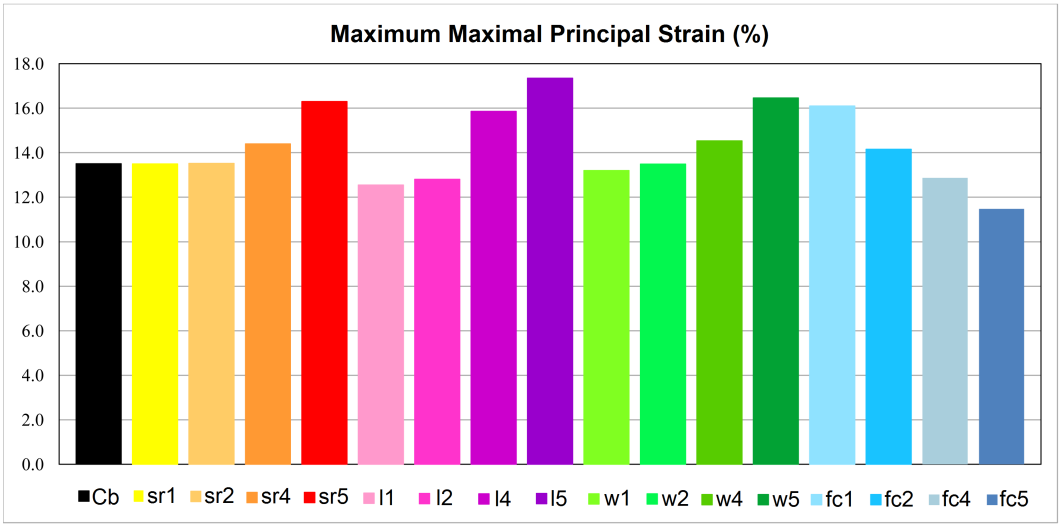

Figure 3.24: Maximum Maximal Principal Strain (in percentage) of each studied model.

3.4.2.4 Drop pressure

The total flow rate, which is the volume of fluid that flows through the artery per unit time, is given by the equation

$$Q = \frac{\Delta P}{Zr}, \tag{3.10}$$

where ΔP is the pressure variation along the artery and Zr is the flow resistance along the blood vessel. Therefore, the calculation of the drop pressure along the artery is essential in order to determine the volume flow through the blood vessel.

Otherwise, in fluid dynamics, the Hagen-Poiseuille equation is a physical law that gives the pressure drop in a fluid flowing through a long cylindrical pipe. The assumptions of the equation are that the fluid is viscous and incompressible; the flow is laminar through a pipe of constant circular cross-section that is substantially longer than its diameter; and there is no acceleration of fluid in the pipe. According to this law, the drop pressure can be expressed as

$$\Delta P = \frac{8\mu \cdot L \cdot Q}{\pi \cdot R^4}, \tag{3.11}$$

where ΔP in the drop pressure, L is the length of the blood vessel, μ is the blood dynamic viscosity, Q is the volumetric flow rate and R is the radius of the artery. In addition, from the Hagen-Poiseuille equation, the parabolic velocity profile occurring in a fully developed flow can be obtained (see Figure 3.25):

$$\boldsymbol{u}_z(r) = -\frac{1}{4\mu}\frac{\partial P}{\partial z}(R^2 - r^2), \tag{3.12}$$

where $\mathbf{u_z}$ is the velocity in the longitudinal direction of the artery and r is the radius of the blood vessel. Furthermore, the maximum velocity occurs at the artery centerline (r = 0):

$$u_{zmax} = -\frac{R^2}{4\mu}\frac{\partial P}{\partial z}. \tag{3.13}$$

Figure 3.25 shows this parabolic profile, showing the maximum velocity at the central point of the artery.

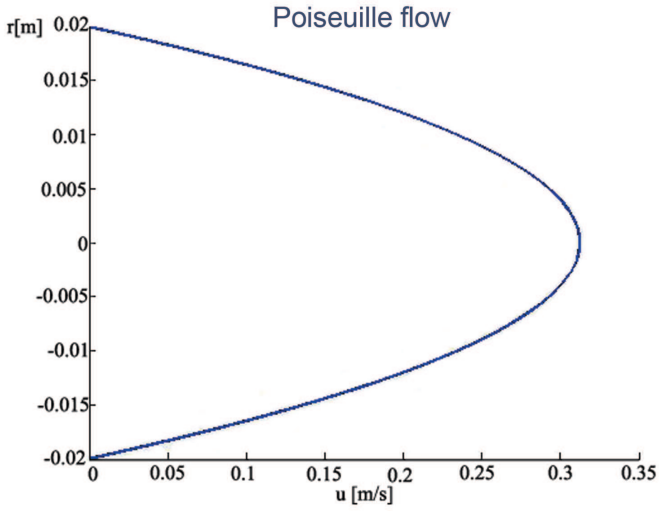

Figure 3.25: Parabolic profile of Poiseuille which describes the velocity profile for laminar flows.

Concerning the obtained drop pressure results, comparing the results of this variable along the blood vessel for all studied models, it hardly varies from one to another model. Therefore, just the results for the reference case are shown in Figure 3.26.a, where the contour map of the pressure along the coronary artery model of the reference case at the instant of time in which the velocity is maximum (t = 0.56 s) is shown. In Figure 3.26.b can be observed that the drop pressure experimented by the volume flow through the blood vessel is determined by the stenosis ratio.

Furthermore, Figure 3.26.b shows the pressure of this reference model at specific time instants of the FSI simulation, showing how the drop pressure varies along a physiological cardiac cycle. Mainly, the drop pressure along the cardiac cycle varies because of the difference phase between the applied pressure and velocity boundary conditions. It is observed that for the maximum velocity applied (t = 0.56 s), the pressure drop is linear in the pre stenotic and post stenotic areas because of the laminar character of the fluid. Moreover, in the stenosis zone, where the pressure is maximum, the drop pressure is also linear, but with a higher slope due to the velocity variation occurs in this zone. For the rest of the instant of time, the pressure gradient describes

a curve in the stenotic zone due to the friction load losses, specially at the outlet of the artery due to the turbulence of this zone.

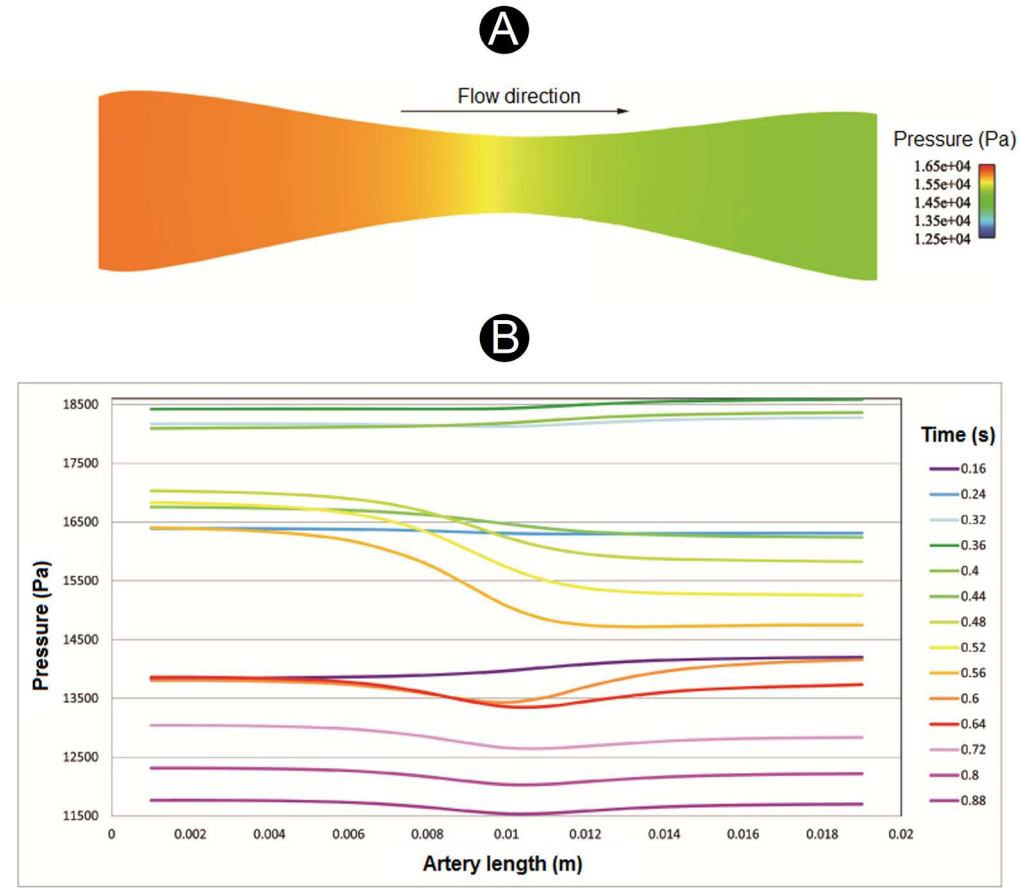

Figure 3.26: A - Contour map of the pressure along the reference case blood vessel. B - Pressures along the reference case geometry at different instants of time.

3.4.2.5 Flow pattern

Streamline descriptions of flow pattern show the paths of each particle within the flow and they are specially convenient for highlighting flow disturbances such as regions of recirculations. Besides, these flow disturbances commonly arise in arterial bends and bifurcations.

Flow pattern with the fluid velocity magnitude for the reference case model is showed in Figure 3.27. Due to the stenosis effect in the plaque region, a jet flow can be found at plaque throat, and the reverse flow zone can be found right after plaque throat. As expected, the parabolic profile of Poiseuille of the fluid is followed, confirming that the flow is complete developed. Thus, the velocity profile at the central section of the model is shown in Figure 3.27.

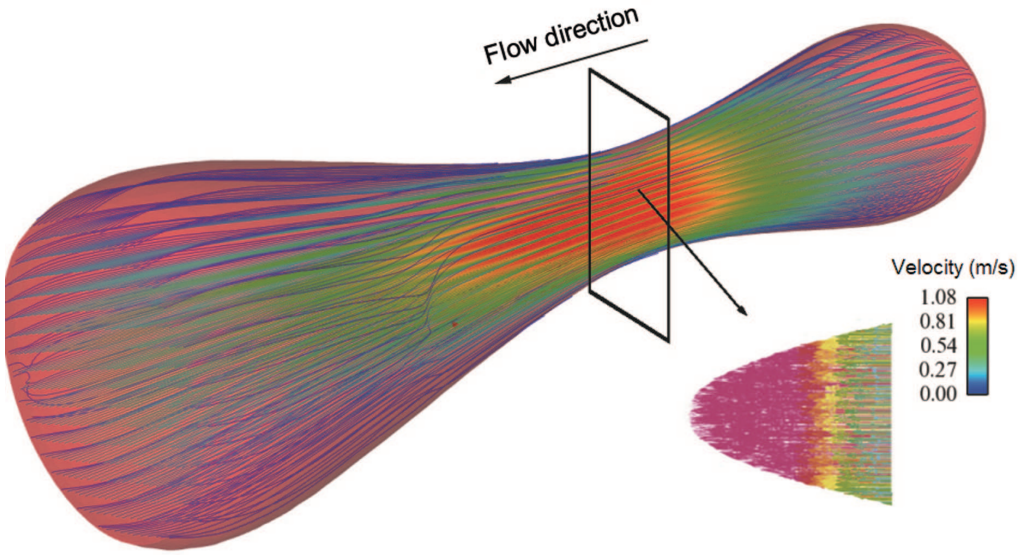

Figure 3.27: Flow pattern and flow velocity for the reference model.

In order to present detailed velocity contours in the plaque region, the flow pattern and the fluid velocity at the longitudinal central section of the reference case model is depicted in Figure 3.28, being the velocity maximum at the center of the stenosis area, and minimum at the ends of the artery (inlet and outlet), specially in the zones closed to the arterial wall. Strong secondary flow can be found after plaque throat due to the lumen section variation. Furthermore, for plaques with high stenosis degree, the fluid flow shows more complex patterns in post plaque region compared to the flow pattern in less stenosis plaques.

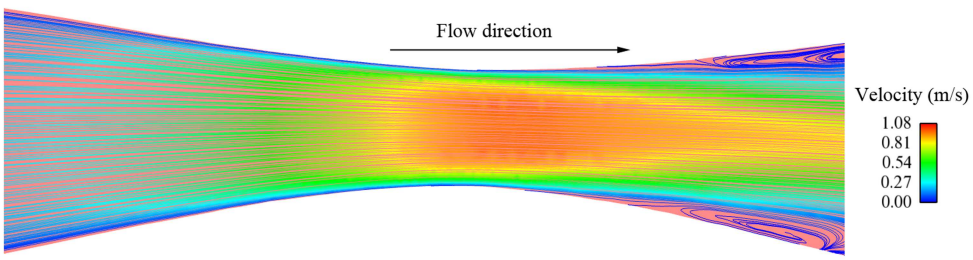

Figure 3.28: Flow pattern in the longitudinal section for the reference model. Recirculation is presented.

3.4.2.6 Wall Shear Stress

As it has been commented in the introduction section, the WSS is believed to play an important role in the plaque initiation and development. Low WSS or highly oscillatory WSS on vessel segments appear to be at the highest risk for development of atherosclerosis, since these phenomena modulate endothelial gene expression through. This fact is complex mechanoreception and mechanotransduction processes, inducing an atherogenic endothelial phenotype and formation of an early atherosclerotic plaque (Chatzizisis *et al.*, 2007), and favouring the LDL particle decantation and adherence to the artery wall (Fuster, 2002). Furthermore, some authors such as Groen *et al.* (2007, 2008) proposed that the high WSS in the fibrous cap could produce the rupture of vulnerable plaques.

Additionally, because WSS is affected by luminal dimensions, some authors have argued that the local WSS can be estimated from purely anatomic measures such as angiography or intravascular ultrasound (Zarins *et al.*, 1987; Steinman, 2004). However, in addition to luminal geometry, local hemodynamics and ultimately WSS depends on flow rate, blood velocity, vessel angulation, curvatures in multiple planes, and bifurcations, providing a link between WSS and pathological atherosclerotic lesions (Weydahl and Jr. Meister, 2001; Fuster, 2002).

Therefore, due to the importance of WSS in the atherosclerosis development, the study of the distribution of this hemodynamic variable has been carried out. Figure 3.29 shows the WSS contour maps for the different stenosis ratio considered at the maximum velocity (t = 0.56 s), which it is expected to be the physiological cardiac cycle instant with greater WSS. Moreover, since the WSS distribution in the studied coronary artery model mostly depends of the stenosis severity, similar WSS contour maps have been obtained for models with the same value of stenosis ratio, although the other three parameters, which modify the geometry of the atheroma plaque but not the internal geometry of the blood vessel, varies from one to another model. Therefore, only 5 WSS patters have been found in this study, corresponding to the reference case and the four variations of the stenosis ratio respect to the base case.

Concerning the WSS results shown in Figure 3.29, it can be observed that the WSS is maximum in the stenosis zone (atheroma plaque area), founding greater WSS values as the stenosis ratio decreases. This WSS difference rises from 45.8 Pa to 28.9 Pa, for the most and less stenosis ratio considered (sr = 46.7% and sr = 66.7%), respectively. Although the direct link between the plaque rupture and high shear stress has not been established, it is proposed that this high WSS could induce thinning of the fibrous cap and destabilising the plaque (Groen *et al.*, 2008). However, the minimum WSS occurs in the pre and post stenotic areas, corresponding to the zones where blood recirculation areas are found. The minimum WSS remains practically constant despite of the stenosis ratio variation, since the minimum WSS varies from 0.78 Pa to 0.1 Pa, for the most and less severe atherosclerotic lesion considered, respectively. This small variations are related to the inverse flow where the recirculation is lesser as the stenosis ratio increases,

and thus the WSS will be lesser too. Finally, it should be highlighted the acute variation of WSS from the pre and post stenotic zones to the central point of the stenosis for all the models simulated but specially for greater stenosis degree. The WSS increases from the minimum value of 0.78 Pa to the maximum one, 45.8 Pa, in a short length of the artery.

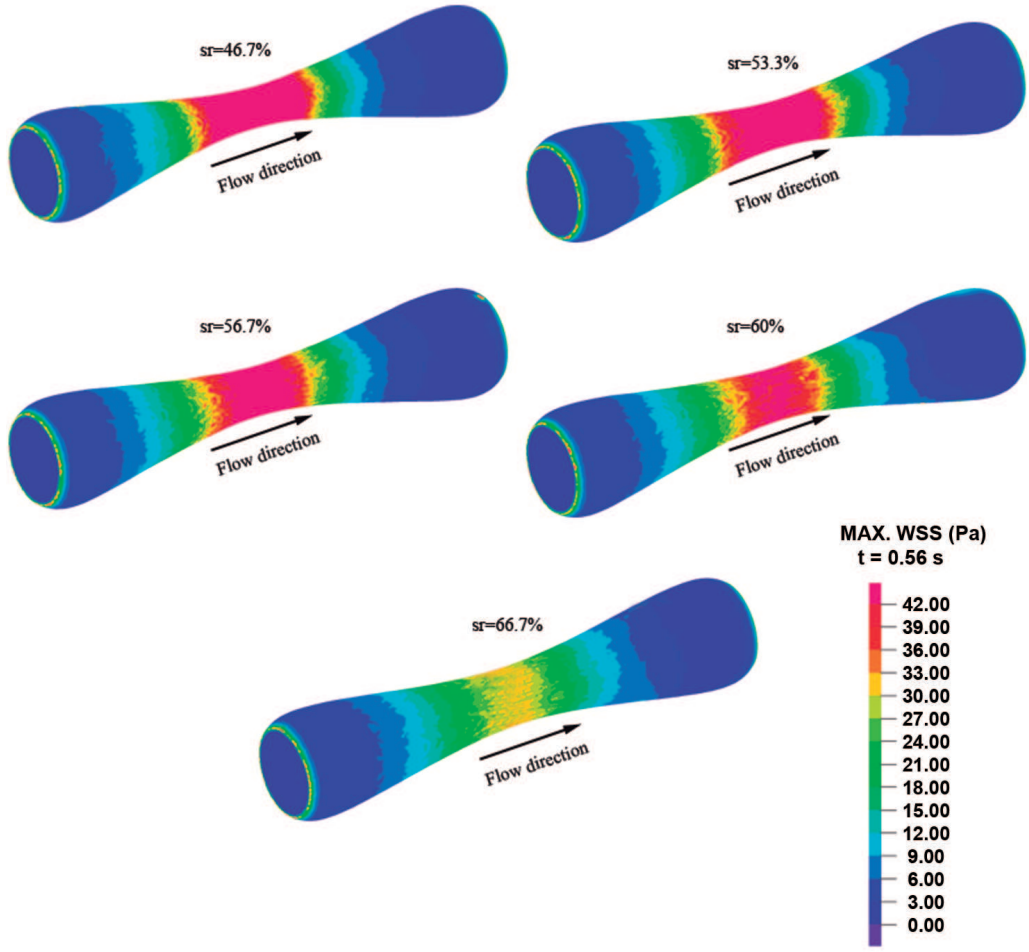

Figure 3.29: Contour maps of the WSS for the five stenosis ratio variations considered.

For the sake of clarity, Figure 3.30 is shown in order to demonstrate the linking between the WSS distribution along the coronary artery wall vessel and the laminar velocity of the blood flow. In this Figure, both the WSS and the velocity contour map indicated by streamlines for the reference case model is depicted. Consequently, the maximum velocity and WSS are located in the fibrous cap surface at the luminal side, close to atheroma plaque throat. However the minimum WSS areas are clearly related to those with flow recirculation.

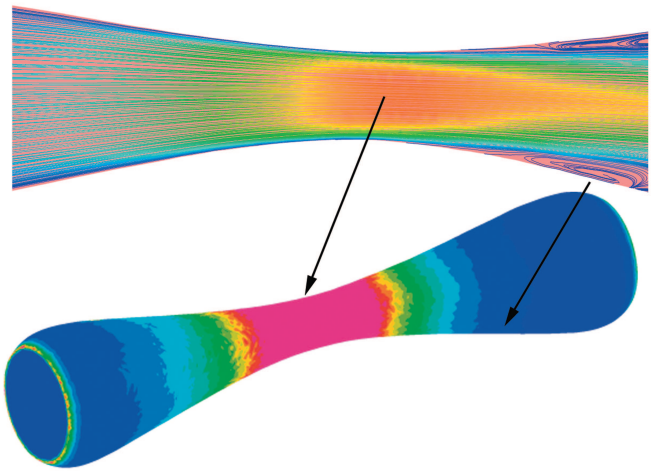

Figure 3.30: Relation between WSS and velocity distributions for the reference case model.

Finally, Figures 3.31 and 3.32 illustrated the evolution of the maximum and minimum WSS, respectively, during a cardiac cycle ($\Delta t = 0.9$ s) for each of the 17 simulated parametric models. The trend of both variables follows the typical physiological coronary flow waveform applied. Furthermore, it can be again observed that the WSS distribution increases just as the stenosis ratio decreases but not as the variation of the other three parameters.

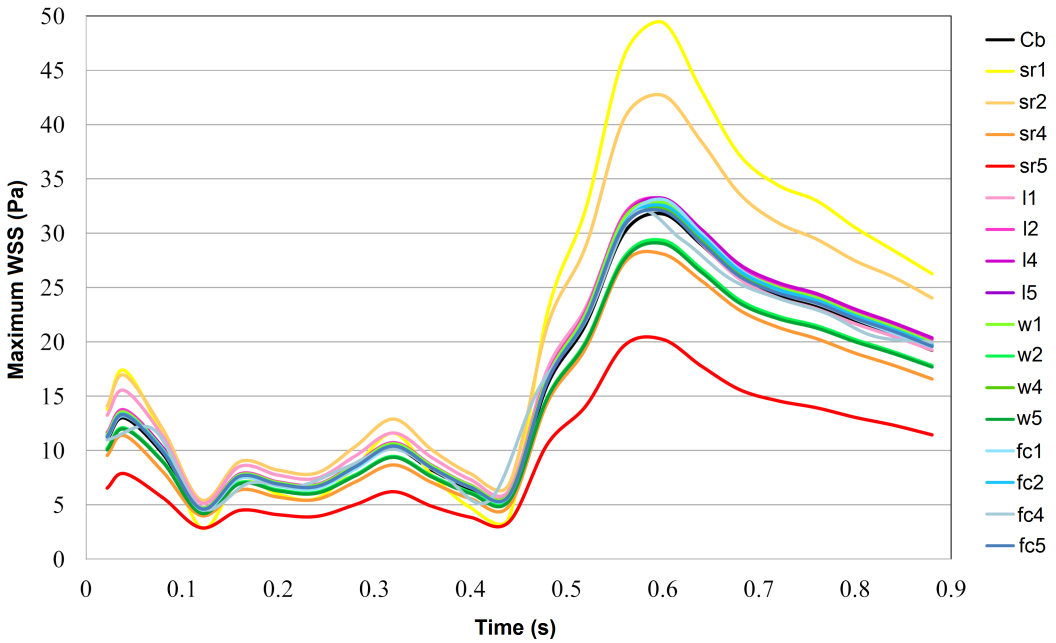

Figure 3.31: Maximum WSS along a cardiac cycle for the 17 simulated models.

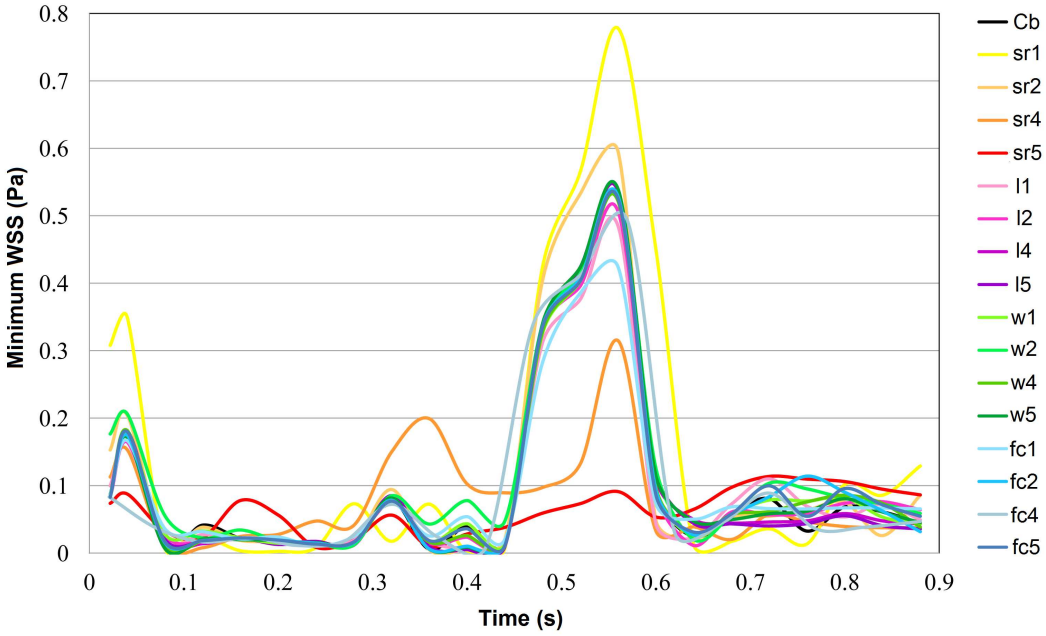

Figure 3.32: Minimum WSS along a cardiac cycle for the 17 simulated models.

3.4.2.7 Vorticity

In fluid dynamics, the vorticity is a vector that describes the local spinning motion of a fluid near some point, as would be seen by an observer located at that point and traveling along with the fluid. Conceptually, the vorticity could be determined by marking the particles of the fluid in a small neighborhood of the point in question, and watching their relative displacements as they move along the flow (Fuster, 2002). The vorticity field can be related to the presence of WSS as well as the traveling of fluid particles along curved trajectories such as Figure 3.33 shows. Furthermore, the vorticity vector is twice the mean angular velocity vector of those particles relative to their center of mass, oriented according to the right-hand rule. Nevertheless, this quantity must not be confused with the angular velocity of the particles relative to some other point (Fuster, 2002; Stouffer, 2007). As discussed before, the occurrence of vortices or an oscillatory nature of the flow could explain the formation of an atherosclerotic lesion at this position.

Mathematically, the vorticity of a three-dimensional flow is a vector field, $\boldsymbol{\omega}$, defined as the curl or rotational of the velocity field $\boldsymbol{u}$. Thus, the vorticity can be defined as:

$$\boldsymbol{\omega}(x,t) = \nabla \times u(x,t) = \left(\left(\frac{\partial u_3}{\partial x_2} - \frac{\partial u_2}{\partial x_3} \right) i, \left(\frac{\partial u_1}{\partial x_3} - \frac{\partial u_3}{\partial x_1} \right) j, \left(\frac{\partial u_2}{\partial x_1} - \frac{\partial u_1}{\partial x_2} \right) k \right), \quad (3.14)$$

where ∇ is the nabla operator.

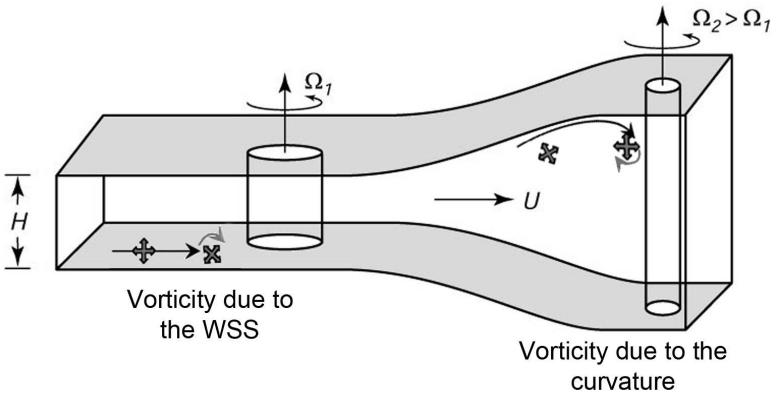

Figure 3.33: Factors affecting the fluid vorticity.

In Figure 3.34 is shown the vorticity contour map for the reference case model in a longitudinal plane to the flow circulation. The maximum vorticity occurs in the zones in which the WSS is maximum, i.e. in the stenotic area. Furthermore, it would be expected a correlation between the maximum vorticity and the minimum WSS areas since the recirculation, which is related to the vorticity, occurs in zones with low WSS, however due to the fact that this recirculation is produced at low velocities, their magnitude is not comparable to the magnitude of the WSS.

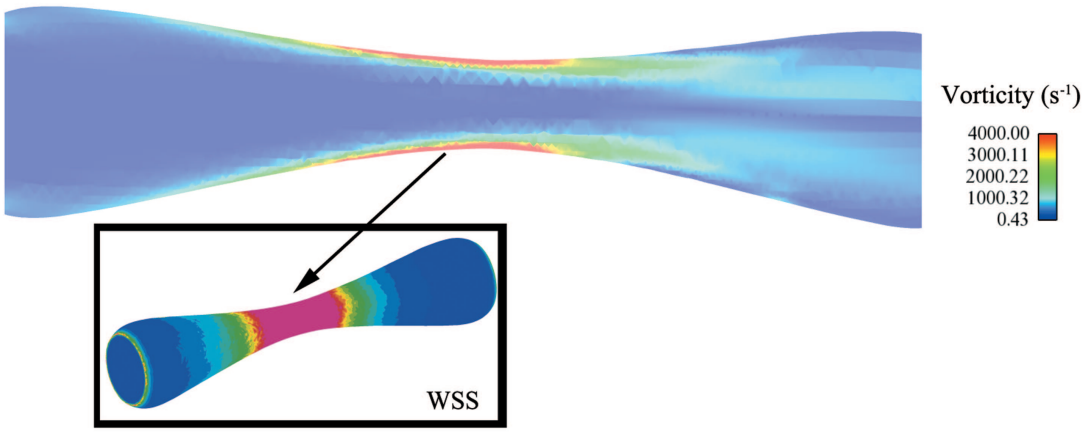

Figure 3.34: Vorticity contour map for the reference case model in a longitudinal plane to the flow circulation.

3.5 Discussion

3.5.1 Microcalcification influence on the risk of atheroma plaque rupture

In this Chapter, the vulnerability risk of plaque rupture due to the presence of microcalcifications in the fibrous cap of an atheroma plaque vessel was investigated using a plane strain FE model. From the obtained results, it can be concluded that the dimensions and location of the microcalcification had a significant influence on the magnitude of stress in the fibrous cap. In some cases, the presence of microcalcifications increases the MPS up to 40% respect to the case without it. However, this increase of MPS is not uniform for all cases (12% on average). The influence of the microcalcification on the magnitude of the MPS is correlated with the location of the MPS in the non-calcified case. It was found that when the microcalcification is located in a region where the MPS of the model without microcalcification appears, the influence of the microcalcification is not relevant. Nevertheless, if the microcalcification is located in a region far away from the maximum MPS in the equivalent non-calcified plaque, the MPS shifts around to the microcalcification and the global value of MPS increase considerably (see Figure 3.5).

Historically, fibrous cap thickness has been considered the most important and almost the exclusive factor determining plaque vulnerability (Arroyo and Lee, 1999; Briley-Saebo *et al.*, 2007). To date, very few computational studies have been performed to investigate the effect of others geometric parameters in a model with microcalcifications included. It has been shown in the literature that microcalcifications can have a significant effect on the stress in fibrous caps (Vengrenyuk *et al.*, 2006; Li *et al.*, 2007b; Bluestein *et al.*, 2008; Wenk *et al.*, 2010; Maldonado *et al.*, 2012). However, the main difference between the current work and previous in the literature is an additional focus on the effects of both the dimensions and location of a microcalcification by using a parametric model. The results of the present work predict a significant increase in MPS due to variations of the fibrous cap thickness. However, the influence of others parameters such as the microcalcification ratio, angle and eccentricity has been found also as significant although with a lower influence. Figures 3.6 and 3.7 show the fibrous cap thickness is the most influential parameter on MPS and the MPS increases as this parameter decreases reaching ΔMPS=19.8% for fc=0.05 mm. The MPS increases slightly as the microcalcification ratio, angle and eccentricity increase. The influence of the microcalcification eccentricity is different according to the microcalcification angle; for the small microcalcification angles ($\alpha \leq 20°$) the microcalcification eccentricity has not influence on the MPS, however, for the long ones ($\alpha > 20°$) the microcalcification located at $x = 75\%$ increases the MPS.

However, the results about the microcalcification influence on the MPS of this study and others previously presented in the literature could be affected by the calcified material properties defined (Cheng *et al.*, 1993; Lee *et al.*, 1994; Huang *et al.*, 2001;

Holzapfel *et al.*, 2002; Williamson *et al.*, 2003; Tang *et al.*, 2005b; Vengrenyuk *et al.*, 2006; Bluestein *et al.*, 2008; Kiousis *et al.*, 2009; Maldonado *et al.*, 2012). This fact is shown by the results of the sensitivity analysis performed on the microcalcification material properties. According to our results, the stress state around the microcalcification highly depends on the relative stiffness of both materials (microcalcification and fibrous cap). While for a low C_1 microcalcification parameter, only tensile stresses appear in circumferential direction when C_1 increases a high compression occurs in radial direction and an abrupt increment is produced in the tensile circumferential stress.

Some limitations of this parametric study should be mentioned. First, the use of an idealized plane strain geometry does not fully capture the complexity of the plaque lesion. Several studies have demonstrated the performance and importance of 3D models to identify vulnerable plaques accurately (Ohayon *et al.*, 2005; Wong *et al.*, 2012). However, detecting the vulnerable areas and limits in an atherosclerosis model with a microcalcification included is out of the scope of this work. The authors performed previous tests in an idealized 3D model with a microcalcification and similar results where found about the influence of the microcalcifications. Furthermore, an idealized straight geometry with just one spherical microcalcification has been used to perform the parametric analysis in order to simplify the study and to clearly detect the isolated influence of each parameter. Second, viscoelastic effects were not considered (Armentano *et al.*, 1995; Peña *et al.*, 2010), and the influence of residual stress has been ignored in this study (Alastrué *et al.*, 2007b) due to the difficulty of estimation in real geometries (Ohayon *et al.*, 2007). Finally, the analysis does not reproduce the pulsatile nature of physiological blood pressure. Also, the fluid-structure interaction effects resulting from such cyclic loading were not considered (Kock *et al.*, 2008). Nevertheless, it has been documented that the effect of fluid shear stress is insignificant when compared to the effect of tensile wall stresses as a direct component in plaque fracture dynamics, although it is considered essential in plaque formation and growth (Huang *et al.*, 2001; Himburg *et al.*, 2004). The estimation of stresses induced by the static pressure load has been proved to be valid to identify stress concentrations in atherosclerotic lesions since the location of stress concentration does not significantly differ between models including static pressure and models with complex dynamic pressure profiles (Cheng *et al.*, 1993).

Calcification is commonly found in atherosclerosis, and the presence and extent of calcifications is usually associated with worse prognosis (Raggi *et al.*, 2000). However, the impact of calcification within a specific atherosclerotic lesion is still unclear. Despite these limitations, this study shows that microcalcifications could cause an important increase in peak stress, but it might depends on other geometrical factors that also affect the location of points of maximum stress. These results have potential implications for the estimation of interventions for coronary artery disease and they can be considered as an additional step towards the understanding of the role of microcalcifications on the MPS in an atheroma plaque vessel.

3.5.2 Comparison of the vulnerable risk for positive versus negative atheroma plaque growth

The results presented in this Chapter provide strong support for the hypothesis that positive growth (or remodeling) increases the risk of plaque rupture and hence the likelihood of cardiac arrest and sudden death compared to plaques that remodel inward. The relative increase in plaque vulnerability for positive growth compared to negative growth, as given by the metric VF_{rel}, was greater than 1 for all simulations. Significantly, this metric reached a value as high as 14.33 for the third simulation set in the initial stages of plaque development (i.e. the maximum MPS for positive growth exceeds the maximum MPS for negative growth by a factor of fourteen). A number of sensitivity analyses were performed in order to rule out the influence of material properties and applied pressure on the model predictions. The predicted maximum MPS increases almost linearly as the internal pressure and the material constant k_2 of the lipid core and the atheroma plaque increase.

For the first two sets of simulations, the metric VF_{rel} was predicted to increase with plaque growth. For the first simulation the MPS in the fibrous cap for negative and positive growth models increases as the atheroma plaque develops, but they increase at different rates, producing that VF_{rel} increases as well with each stage of plaque development. For the third simulation set, this tendency is not predicted since the most influential parameter on atheroma plaque vulnerability, namely the fibrous cap thickness, decreases as the plaque grows, increasing its vulnerability (Virmani *et al.*, 2000; Krishna Kumar and Balakrishnan, 2005).

All simulations have been performed with the same size of lipid core for both cases (positive and negative growth), however according to the literature (Varnava *et al.*, 2002) lesions with positive growth, compared with lesions with vessel shrinkage, have a higher lipid content and macrophage count, which are both markers of plaque vulnerability. This will further increase the vulnerability of such plaques. It should also be noted that for the first simulation set, the lumen radius remains constant for the positive growth, while it decreases as the atheroma plaque develops for the negative growth model. The predicted differences between positive and negative remodeling could be affected by this fact. To rule out the influence of the lumen radius on models predictions, the second, third and fourth simulations were performed with a constant lumen radius for all models.

Although this study presents potentially promising concepts for the identification of atherosclerosis sites, several limitations exist. Firstly, the use of an idealized plane strain geometry does not fully capture the complexity of the plaque lesion. Several studies have demonstrated the performance and importance of 3D models to identify vulnerable plaques accurately (Ohayon *et al.*, 2005; Wong *et al.*, 2012). The authors performed previous tests in idealized 3D models with both positive and negative remodeling and similar results were found concerning plaque vulnerability. Furthermore, an idealized model has been chosen due to the difficulty associated with obtaining clinical images

with positive remodeling with the same dimensions and quantity of lipid core as those with negative remodeling. Viscoelasticity and the influence of residual stresses were not considered as previous studies have not characterized residual stresses in atheroma plaques with positive remodeling (Armentano *et al.*, 1995, 2006; Peña *et al.*, 2010; Alastrué *et al.*, 2007b). The analysis does not reproduce the pulsatile nature of physiological blood pressure. Also, the fluid-structure interaction effects resulting from such cyclic loading were not considered (Kock *et al.*, 2008). Calcifications were not considered in order to simplify the study. In addition, the material properties have been taken from experimental data in the literature (Holzapfel *et al.*, 2005b; Versluis *et al.*, 2006). Furthermore, the orientation angle of the collagen fibers has been estimated through fitting mechanical test data while in reality collagen organization is much more complicated and should ideally be measured from histological or microscopy images. However, these assumptions have been widely accepted as allowable for the assessment of the biomechanical properties of atherosclerotic lesions. More advanced constitutive models such as non-cohesive models, damage models or fracture mechanic models should be implemented in order to reproduce the real physiology of the problem. Finally, different properties of the atheroma plaque were not taken into account; i.e. whether the plaques were calcified, cellular or hypocellular (Lee *et al.*, 1991; Maher *et al.*, 2009, 2011).

Summarizing, despite these limitations, the performed parametric study strongly suggests that coronary arteries that undergo positive growth are more vulnerable to rupture than those diseased arteries that remodel inwards. Arterial enlargement during plaque growth prevents luminal narrowing but, nevertheless, such non-stenotic lesions could paradoxically be considered more dangerous than stenotic lesions as they are vulnerable and prone to rupture, increasing the risk of a thrombus mediated acute myocardial infarction.

3.5.3 Fluid structure analysis

Plaque stress has been studied for several decades from 2D structure, only fully coupled 3D plaque stress in both structure dynamics and hemodynamics are recently explored, demonstrating better performance than 2D models (Ohayon *et al.*, 2005; Chun *et al.*, 2010). Regarding atheroma plaque vulnerability, the extremely high stress locations in the fibrous cap and shoulders regions have been mostly considered to be main factors responsible for plaque rupture. However, other features such as great arterial deformations, high wall shear stress values at the arterial wall or the blood flow vorticity could also contribute to the atheroma plaque instability (Aoki and Ku, 1993; McCord and Ku, 1993; Mizushige *et al.*, 1993). Moreover, some variables, which can be obtained by FSI analysis, such as the low WSS or the occurrence of oscillatory vortices has been linked to the initiation of atherosclerotic lesions (Steinman, 2004; Chien, 2008). Consequently, the importance of cardiovascular FSI modeling is shown since this kind of analysis allow to accurately predict not only potential sites of vulnerable plaque rupture but also the initiation and progression of the lesions.

Additionally, the effect of complex loading experienced under pulsatile flow conditions has been shown as neglected for the accurately prediction of the MPS, as Figure 3.22.a and Figure 3.22.b reflect, which shown similar obtained MPS contour maps by the FSI and structural analysis, respectively. Therefore, as regards the MPS distribution along the coronary artery model, similar conclusion than those obtained for the models without residual stress of Chapter 2 can be highlighted. The fibrous cap thickness is the most influential parameter in terms of plaque vulnerability, increasing the MPS as this parameter decreases. The lipid core length and width are less influential parameters on plaque stability, however, they should be taken into account to asses atheroma plaque vulnerability risk. MPS increases as these parameters increase. Finally, the stenosis degree may not be a good predictor for plaque rupture risk, occurring a slight increase of MPS as this parameter increases. Furthermore, any of the 17 simulated models by FSI analysis has been predicted as vulnerable (MPS higher than the vulnerability threshold of 247 kPa) since the considered geometric models are built from combination of parameter values out of the vulnerability limits defined in Chapter 2. Moreover, as expected, the MPS distribution follows a tendency similar to the applied cardiac cycle.

Maximal arterial deformation can be found in the non-stenotic zones of the model. However, the maximal principal strains should be observed at the critical zones (stenotic areas) in order to extract conclusions about atheroma plaque vulnerability. Then, the maximum deformation at these sites remains around 6% for all studied model. Furthermore, as for the maximum MPS, the maximum deformation increases as the stenosis ration and lipid core width and length increase, and it decreases with the fibrous cap thickness.

As regards the WSS distribution along the artery wall, high WSS values have been found in the central part of the stenosis, which could exacerbate the atheroma plaque unstability. On the contrary, low WSS values are identified in the post stenotic zone, zones of flow recirculation, providing an indication of atheroma plaque initiation. As expected, the distribution of this variable varies just with the stenosis degree. Therefore, the stenosis ratio which was defined as not influential in term of plaque stability, plays an important role in the appearance of atheroma plaque.

Finally, the vorticity which is directly related to the WSS and it could also help to atheroma plaque rupture have been calculated.

Although FSI simulation can provide a more realistic stress prediction than structure stress analysis, some major limitations needed to be acknowledged in the FSI modeling carried out. Firstly, the idealized straight arterial wall model used is crude, however this geometry has been validated in Section 2.4 of Chapter 2. Secondly, the material properties have been taken from experimental data in the literature (Holzapfel *et al.*, 2005b; Versluis *et al.*, 2006). Thirdly, the real arterial wall is viscoelastic. Furthermore, the effect of including residual stress was not considered. Fourthly, laminar flow assumption may not be valid in the post-stenosis flow due to the flow instability. Fifthly, the constrained displacements applied at the ends of the blood vessel are unrealistic,

however, they are necessary to the FSI model convergence. Furthermore, a constant velocity has been applied at the cross artery section, nevertheless a parabolic profile velocity should be applied instead. Sixthly, plaques have been classified histologically as either cellular, hypocellular or calcified, however this variety of atheroma plaque has not taken into account (Loree *et al.*, 1994; Vengrenyuk *et al.*, 2006; Bluestein *et al.*, 2008; Wenk, 2011). Seventhly, only 17 models has been studied, which correspond to the variation of just one of the four parameters studied from a reference case model. However, it should be interesting the simulation of the same 625 models than in the 3D parametric study presented in Chapter 2, which result from all the possible combinations of the four parameters considered. Finally, as the 3D parametric study presented in Chapter 2, this FSI study only could be validated qualitatively. It is not possible to measure all the studied variables in real atheroma plaques and to correlate with the main geometrical risk factors *in vivo* conditions, and later verify the plaque rupture.

Summarizing, the progress in numerical modeling has made possible FSI analysis, providing useful information and correlations for the clinical practice. Therefore, the presented FSI parametric study could be considered as a forward step towards the better understanding of cardiovascular pathologies.

Chapter 4

Machine Learning Techniques: Application to predict the atheroma plaque risk of vulnerability

Initially, a brief introduction about the theory of Machine Learning Techniques (MLT) and, in particular, about the Artificial Neural Network (ANN) and the Support Vector Machine (SVM) algorithms as well as the classical linear regression, are exposed. MLT have been previously used by researchers to solve different classification and regression engineering problems. Hence, these techniques are presented in this Chapter as an alternative tool to complex FE simulations for detection of vulnerable plaques, when an instantaneous response is needed.

Therefore, a parametric tool, using machine learning techniques, to assist the clinicians on decisions of the vulnerability of the atheroma plaque is exposed in this Chapter. In practice, the main drawbacks of 3D finite element analysis to predict the vulnerability risk are the huge main memories required and the long computation times. Thus, the use of these methods which are faster and more efficient is essential. The tool is based on two potential methodologies of computational technologies, Artificial Neural Networks and Support Vector Machines, used to estimate the maximum principal stress in a coronary artery with atheroma plaque as a function of the main geometrical features. Furthermore, in order to prove the non-linearity of the problem, the results have been fitted by a linear regression.

Contents

4.1 Introduction

Computer science has been widely adopted by modern medicine and advances in technologies and computers have enabled to become a vital tool in conventional clinical practice. Nowadays, the medical information in hospitals become larger and larger, which causes great difficulties in extracting useful information for decision support, specially when traditional manual data analysis has become inefficient and methods for computer based analysis are indispensable (Itchhaporia *et al.*, 1996). Therefore, there is a need to introduce more efficient and effective computational methods in medical analysis for decision support to help clinicians. The idea is to build decision support tools based on numerical methods that store and use knowledge from sources such as experienced clinicians, statistical analysis or computer simulations, and after that, these tools gather knowledge automatically, and use optimization methods to return appropriate answers to queries or accurate predictions on future data (Mitchell, 1997; Lavrac *et al.*, 2000). There are many different methods to achieve this goal, however, Machine Learning Techniques (MLT) have shown to be quite useful for this automation process (Langley and Simon, 1995). These techniques are based on the ability to learn from examples which is an important facet of intelligence that has been an especially fertile area of study in the last decade.

Notwithstanding, since there is no intelligence without learning, MLT are one of major branches of artificial intelligence, which is the part of computer science that tries to make computers more intelligent, and, indeed, they have been applied successfully to a high variety of problems and data for prediction tasks and real problems of practical interest (Widrow *et al.*, 1994; Mitchell, 1997). Drawing from computer science, statistics, mathematics, and engineering, the multidisciplinary nature of machine learning is underscored by its applicability to many different areas, such as industry (see e.g., Evans and Fisher, 1992), electronic (see e.g., Jabbour, 1987), space science (see e.g., Fayyad *et al.*, 1993), geology (see e.g., Taboada *et al.*, 2007; López *et al.*, 2010b) or language (see e.g., Liu *et al.*, 2005) amongst many others. Within the medical context,

these techniques have been also successfully applied to different clinical applications, for instance; diagnosis of breast cancer or melanomas, interpreting electrocardiograms, diagnosing dementia or predicting prognosis and survival rates (see e.g., Handels *et al.*, 1999; Gniadecka *et al.*, 2004; Huang and Kecman, 2005). And, they have been used for treating cardiovascular diseases (see e.g., Poli *et al.*, 1991; Itchhaporia *et al.*, 1995, 1996). Furthermore, it has been proven some benefits of introducing MLT into medical analysis such as an increase of diagnostic accuracy, reduction of costs and human resource (Cheung, 2001; Kononenko, 2001).

Within the atherosclerosis disease framework, as mentioned in Chapter 1, cardiovascular diseases related to atherosclerosis are the first cause of death in the western world; more people die annually from cardiovascular diseases than from any other cause (Hanke *et al.*, 2001). And, the best way to prevent a cardiovascular accident related to the atherosclerosis disease is to discover it in the early stages. In the later ones, when the atheromatous lesion expands causing severe stenosis of the arterial lumen, the problem could be irreversible, causing fatal events such as heart attacks or strokes. Furthermore, the current clinical procedures for detection of these vulnerable plaques can be classified into two areas: image diagnosis and data analysis. Image diagnosis is the use of screening medical tests to capture an image of the lesion in order to analyze the injury status (see Subsection 1.3.5, Chapter 1). On the other hand, data analysis focuses on the analysis of a patient's condition from observed symptoms or measured test results. Nevertheless, despite recent advances in the diagnosis and treatment of symptomatic atherosclerosis, available traditional methods for early detection and treatment of asymptomatic coronary artery disease are grossly insufficient and fail to identify the majority of victims prior to the onset of a life threatening event.

All these relevant facts have motivated the development of numerical models for arterial behaviour in order to better understanding of cardiovascular pathologies. Mostly of these numerical models are based on FE methods. However, the use of FE methods for the analysis and design of bioengineering processes often requires a large memory consumption and long computational time cost, usually hours or even days, which is an important drawback for fast diagnosis in real time. Nonetheless, the simulation time can be significantly reduced combining FE method with MLT. Therefore, a quantitative method using MLT for cumulative risk assessment of vulnerable patients based on atheroma plaque morphology, which could replace the time consuming biomechanical simulations used in cardiovascular mechanics, has been developed in this Thesis. For this purpose, different MLT, such as ANN and SVM, have been used to study the role of stress in plaque vulnerability as a function of the main geometrical features. It has been proved that these techniques are very powerful tools for classification or regression (Taboada *et al.*, 2007; López *et al.*, 2010a,b).

ANN are mathematical models inspired by biological neural networks which consists of an interconnected group of artificial neurons, where it processes information using a connectionist approach to computation (McCulloch and Pitts, 1943; Gurney, 1997).

Additionally, the MultiLayer Perceptron (MLP), as a representation of the ANN, is a feed-forward network characterized by its layered structure where each layer consists of a set of perceptron neurons and its training algorithm (Bishop, 1995). The SVM (Vapnik, 1982) constructs a hyperplane or set of hyperplanes in a high or infinite dimensional space. A good separation is achieved by the hyperplane that has the largest distance to the nearest training data point of any class (so called functional margin), since in general the larger the margin the lower the generalization error of the classifier or regressor (Cortes and Vapnik, 1995; Meyer *et al.*, 2003). Whereas the original problem may be stated in a finite dimensional space, it often happens that the sets to discriminate are not linearly separable in that space. For this reason, it was proposed that the original finite dimensional space be mapped into a much higher dimensional space, presumably making the separation easier in that space. To keep the computational load reasonable, the mappings used by SVM schemes are designed to ensure that dot products may be computed easily in terms of the variables in the original space, by defining them in terms of a kernel function selected to suit the problem (Burges, 1998; Scholkpof and Smola, 2002).

In order to train the machine learning developed for the vulnerability prediction, a parametric coronary vessel model have been performed using FEM. This parametric model consists of a series of idealized plaque morphology models, mimicking different stages and variations in atherosclerotic lesion growth. Consequently, the 3D parametric coronary vessel study described in Chapter 2 has been used for this purpose. According to previous works (Cheng *et al.*, 1993; Williamson *et al.*, 2003; Finet *et al.*, 2004; Ohayon *et al.*, 2008), the developed tool uses the MLT algorithms to predict the atheroma plaque rupture in terms of four of the most influential geometrical factors in the plaque rupture which are the input of the MLT: (i) fibrous cap thickness; (ii) stenosis ratio; (iii) lipid core width and (iv) lipid core length. The output predicted by the MLT is the maximum MPS occurred in an atherosclerotic coronary vessel with the input dimensions.

4.2 The learning paradigm

The problem of learning has been investigated by philosophers throughout history, under the name of inductive inference. Although this might seem surprising today, it was not until the 20th century that pure induction was recognized as impossible unless one assumes some prior knowledge. This conceptual achievement is essentially due to the fundamental work of Karl Popper (Popper, 1934, 1959) (based on Hume's ideas (Hume, 1748)).

Valiant (1984) developed the first formal approach of machine learning, emphasizing in the computational problems. However, other works emerged parallel such as the theory of the empirical process (Vapnik and Chervonenkis, 1971, 1981; Vapnik, 1982; Pollard, 1990) or the theory of decisions (Berger, 1985), as well as contributions which generalize the initial formulations of the problem incorporating the mentioned theory

of decisions and the data noise concept (Haussler, 1992). Later, the computational field (Vidyasagar, 1997; Anthony and Barlett, 1999), the statistics (Valiant, 1984) and other disciplines (Bousquet and Elissee, 2001, 2002) refined and developed the existing theory.

The main idea of the machine learning is that it is possible to gain knowledge starting from experience or data (i.e. a collection of objects) without understanding the internal mechanism that has generated such data. Knowledge gained through learning partly consists of descriptions of what we have already observed, and is partly obtained by making inferences from (past) data in order to predict (future) outcomes. Obviously if data have no regularities, in the sense that it does not possess any law as a part of themselves, we can not be able to find any new knowledge. From all the contributions mentioned above, the basic components of a learning problem could be extracted (Martínez, 2011):

- A input vectors: Because machine learning methods derive from so many different traditions, its terminology is rife with synonyms. For example, the input vector ($\boldsymbol{x} \subset \mathbb{R}^n$) is called by a variety of names. Some of these are: input vector, pattern vector, feature vector, sample, example, and instance. The components, $\boldsymbol{x}_i$, of the input vector are variously called features, attributes, input variables, and components. The values of the components can be numerical (real-valued numbers or discrete-valued numbers), categorical values (e.g. "A", "B", "AB" or "O", for blood type), ordinal (e.g. "large", "medium" or "small") and integer-valued (e.g. the number of occurrences of a part word in an email). An important specialization uses Boolean values, which can be regarded as a special case of either discrete numbers (1,0) or of categorical variables (True, False). Of course, mixtures of all these types of values are possible.

- A supervisor: It produces for each $\boldsymbol{x}$ an output response $y \subset \mathbb{Y}$, and it can be determinist or random.

- A machine learning: It implements a set of measurable functions ($\mathcal{F}$) in order to correlate the input and output variables. Furthermore, the main problem of learning processes is related to the selection of a function in the hypothesis space ($\mathcal{F}$) according to some criterion of interest.

The output may be a real number, in which case the process embodying the function is called a function estimator or regressor, and the output is called an output value or estimate. Alternatively, the output may be a categorical value, in which case the process embodying is variously called a classifier, a recognizer, or a categorizer, and the output itself is called a label, a class, a category, or a decision. Therefore, regarding the type of task solved, the learning machine can be resolved into two categories as it is shown in Figure 4.1; classification or pattern recognition, when the labels are members of a finite and discrete set and, regression or function estimation, when the labels belongs to a continuous set (Alpaydin, 2001; Kotsiantis, 2007).

- Classification or pattern recognition problem: It is the problem of identifying to which of a set of categories a new set of observations belong, on the basis of a training set of data containing observations whose category membership is known. The individual observations are analyzed into a set of quantifiable properties, known as various explanatory variables, features, etc. An algorithm that implements classification, especially in a concrete implementation, is known as a classifier. The term "classifier" sometimes also refers to the mathematical function, implemented by a classification algorithm, that maps input data to a category. The task of the classifier is to learn the mapping function. A classification task with only two class is named binary classification or dichotomic classification. In this case the mapping function belongs to the class of indicator functions. If the classes are more than two we are dealing with a multiclass classification task problem (see e.g., Platt *et al.*, 2000; Kotsiantis, 2007).

- Regression or function estimation problem: In the regression task problem the output is a continuous value. A typical regression problem is the well-known fitting problem. In this case the learning machine has to choose a fitting function and then it has to estimate the parameters that minimize the risk functional associated with the loss (see e.g., Werbos, 1974; Drucker *et al.*, 1997).

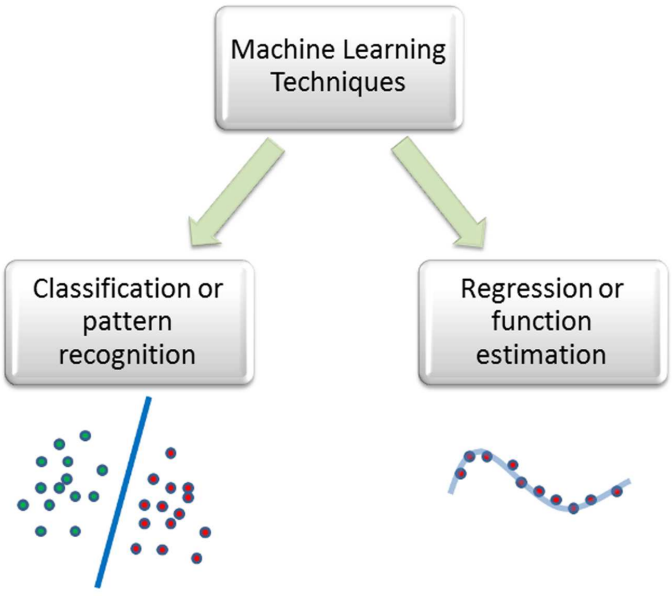

Figure 4.1: Machine learning categories grouped according the task problem solved; classification or regression.

It should be highlighted that the machine learning developed in this Thesis are focus on regression tasks, since the output will be a real number.

4.3 Mathematical background of Machine Learning Techniques

MLT theory aims to understand the fundamental principles of learning as a computational process. The area of MLT deals with the design of programs that can learn rules from data, adapt to changes, and improve performance with experience. Furthermore, these methods provide an increasing of automation levels in the knowledge engineering process, replacing much time consuming human activity with automatic techniques that improve accuracy or efficiency by discovering and exploiting regularities in training data (Michie *et al.*, 1994; Alpaydin, 2001).

Many machine learning algorithms have been found to have direct counterparts with other disciplines. Here is a brief listing of some of the separate disciplines that have contributed to the development of MLT (Carbonell, 1983; Michie *et al.*, 1994).

- Statistics: A standing problem in statistics is how best to use samples drawn from unknown probability distributions to help to decide from which distribution some new sample is drawn. A related problem is how to estimate the value of an unknown function at a new point given the values of this function at a set of sample points. Statistical methods for dealing with these problems can be considered instances of machine learning because the decision and estimation rules depend on a corpus of samples drawn from the problem environment. More details about the statistical theory underlying these methods can be found in statistical textbooks (see, e.g., Anderson, 1958).

- Brain models: Non-linear elements with weighted inputs have been suggested as simple models of biological neurons. Networks of these elements have been studied by many researchers (Hebb, 1949; McCulloch and Pitts, 1943; Sejnowski *et al.*, 1988; Gluck and Rumelhart, 1989). Brain modelers are interested in how closely these networks approximate the learning phenomena of living brains.

- Adaptive control theory: Control theorists study the problem of controlling a process having unknown parameters which must be estimated during operation. Often, the parameters change during operation, and the control process must track these changes. Some aspects of controlling a robot based on sensory inputs represent instances of this sort of problem (Sastry and Bodson, 1989; Kasabov *et al.*, 1999).

- Psychological models: Psychologists have studied the performance of humans in various learning tasks. Reinforcement learning is an important theme in machine learning research (Sastry and Bodson, 1989).

- Artificial intelligence: From the beginning, this discipline research has been concerned with MLT. Artificial Intelligence explores the role of analogies in learning

(Carbonell, 1983) and how future actions and decisions can be based on previous exemplary cases (Kolodner, 1993).

- Evolutionary models: In nature, not only individual animals learn to perform better, but species evolve to be better fit in their individual niches. Since the distinction between evolving and learning can be blurred in computer systems, techniques that model certain aspects of biological evolution have been proposed as learning methods to improve the performance of computer programs (Koza, 1992).

As the following taxonomy shows, machine learning algorithms may be categorised in at least four ways according the type of reasoning, the type of task solved, the kind of learning process and the manner in which the training data are presented to the learner. At a general level, there are three main types of reasoning: deductive, inductive, and transductive, see Figure 4.2 (Vapnik, 1998b; Kasabov *et al.*, 1999).

- Inductive: It uses observed cases and generate hypotheses based on the similarities between them. It attempts to extract general rules and patterns based on the limited training experience.

- Deductive: It learns, following a procedure, new rules which are actually conclusions of existing rules. Deductive learning does not generate new knowledge at all, it simply memorizes the logical consequences of what is known already and applies this learning to new data.

- Transductive: It attempts to learn specific examples, and not general rules as in the case of inductive learning, from specific train training examples. Transductive learning is more straightforward and less demanding than inductive learning in cases when the test examples are known beforehand, as it involves less steps and assumptions: it is not necessary to induce general rules and then to deduce the needed knowledge for the specific test data but, rather, to find directly the most probable predictions, based on the training data.

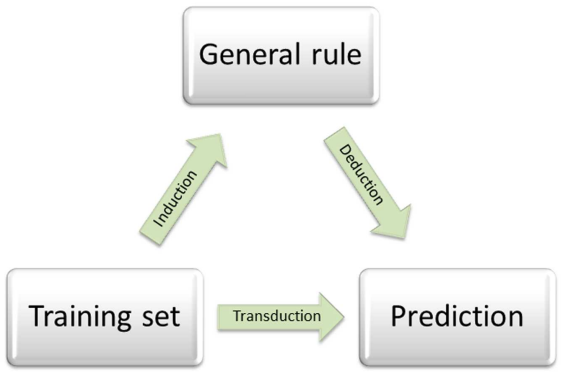

Figure 4.2: Types of machine learning approaches.

Finally, the learning process can be broadly characterized as supervised, unsupervised, semi-supervised and reinforcement. Figure 4.3 shown a schematic representation of the main tasks performed for applying each type of learning to a real world problem (Vapnik, 1998b; Kasabov *et al.*, 1999; Batista and Monard, 2003; Alpaydin, 2001; Martínez, 2011).

- Supervised: We have a set of data points or observations for which we know the desired target or label. Then, the outcome may take one of many values called classes or labels. The target variable is providing some level of supervision in that it is used by the learning algorithm to adjust parameters or make decisions that will allow it to predict labels for new data (Batista and Monard, 2003; Kotsiantis, 2007) (see Figure 4.3.a).

- Unsupervised: Instead of trying to predict a set of known classes like in the supervised algorithms, it tries to identify the patterns inherent in the data that separate like observations in one way or another. In some cases we do not necessarily know what makes them similar, but the algorithms are capable of finding these relationships between data points and group them in significant ways. While supervised algorithms aim to minimize the classification or regression error, unsupervised algorithms aim to create groups or subsets of the data where data points belonging to a cluster are as similar to each other as possible, while making the difference between the clusters as high as possible (Alpaydin, 2001; Antkowiak, 2006) (see Figure 4.3.b).

- Semi-supervised: It combines both labeled and unlabeled examples to generate an appropriate function. This learning process has either to learn the most suitable mapping between possible examples and the available labels, or reveal an underlying structure, using the label information as constraint. Many machine-learning researchers have found that unlabeled data, when used in conjunction with a small amount of labeled data, can produce considerable improvement in learning accuracy (see Figure 4.3.c).

- Reinforcement: It attempts to learn from interaction, receiving feedback for its actions. Every action has some impact in the environment, and the environment provides feedback in the form of rewards or punishments that guides the learning algorithm (see Figure 4.3.d).

Accordingly with the learning processes classification presented above, all the machine learning models presented in this Thesis (see Chapter 4) are based on supervised learning algorithms. Because of this reason, the theory of supervised learning algorithms are presented here in detail.

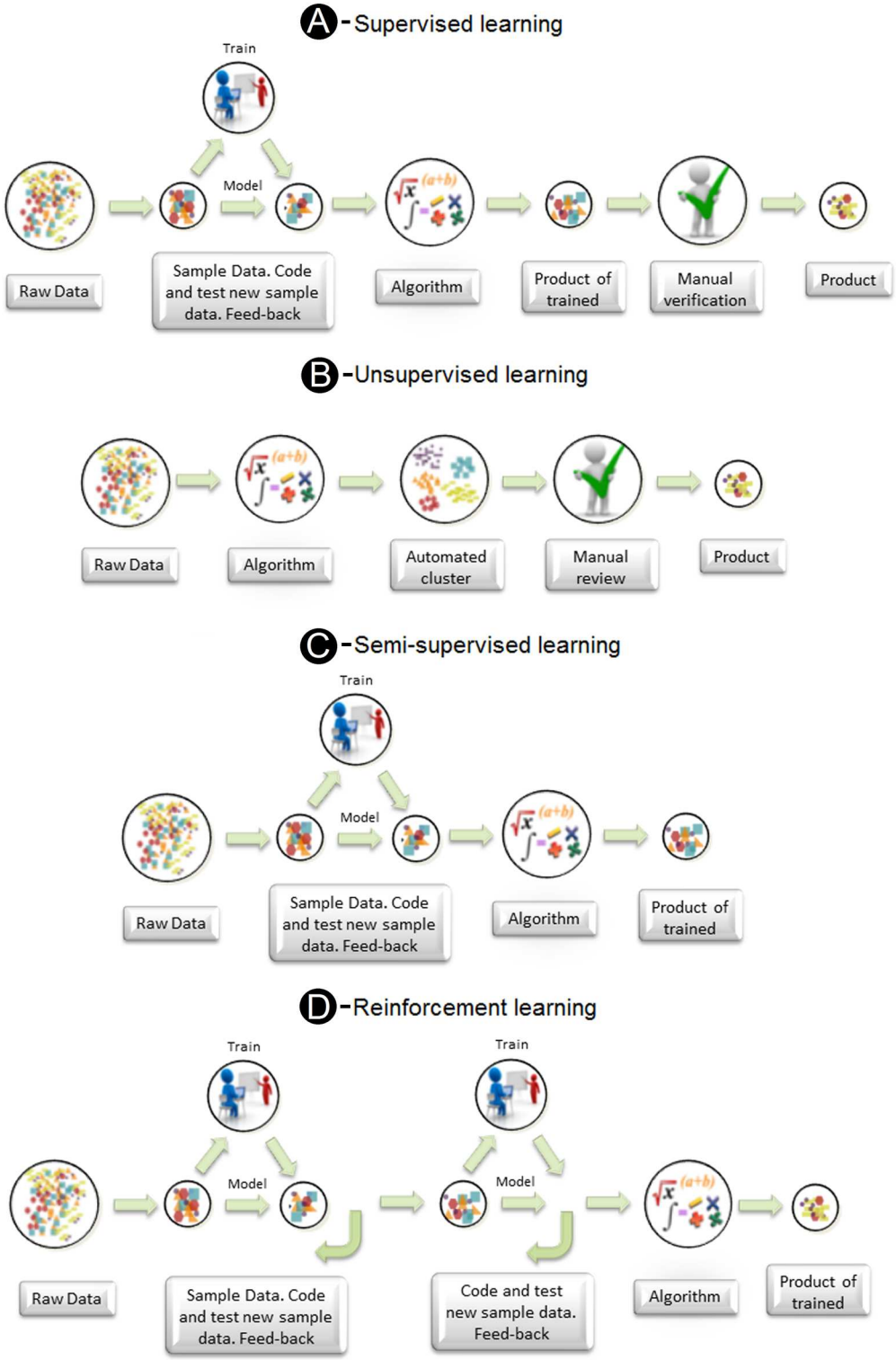

Figure 4.3: Types of learning process.

Supervised Machine Learning Techniques: As Figure 4.3.a shows, the MLT supervised process consists of several steps. Once the problem has been identified, defined and analyzed, the data set should be collected. If a requisite expert is available, then the most informative fields can be suggested by this expert. If not, then the simplest method is that of "brute-force", which means measuring everything available in the hope that the relevant features can be isolated. However, a data set collected by the "brute-force" method is not directly suitable for induction. It contains in most cases noise and missing feature values, and therefore requires significant pre-processing (Zhang *et al.*, 2002). The second step corresponds to the data preparation and pre-processing. The training data are scaled and prepared as input vectors properly for feeding into our supervised learning algorithm. Depending on the circumstances, there are a great number of methods to choose from to handle missing data (Batista and Monard, 2003; Hodge and Austin, 2004). For example, instance selection is an optimization problem that attempts to maintain the quality while minimizing the sample size in the data set (Liu and Motoda, 2001; Reinartz, 2002), or feature subset selection, which is the process of identifying and removing as many irrelevant and redundant features as possible in order to reduce the dimensionality of the data to operate faster and more effectively (Yu and Liu, 2004). Furthermore, training and validation sets are created by randomly splitting the universe of data. The training set is the data that the classifier uses to learn how to classify or regress the data, whereas the validation set is used to feed the already trained model in order to get an error rate (or other measures and techniques) that can help us to identify the performance and accuracy of the classifier or regressor. Typically, more training data than validation data are used. About the 80% of the entire universe is usually used for training data and, from the 20% of the available data used for validation processes, the half is used for test processes (fourth step) and the other half for validation processes (fifth step). Note that these parameters may be adjusted by optimizing performance on a subset of the training set through different methods such as cross-validation algorithms, among others (see Subsection 4.3.3). Third, the algorithm is fed by the training data and, the end result is a model that has learned (hopefully) how to predict our outcome given new unknown data. After the model has been created, the fourth step corresponds to test the model accuracy. It is critical to measure the efficiency on data that the model has not yet seen, otherwise you are cheating. For this reason, we separated out a subset of the data that was not used for training. In addition, it is very easy to learn every single combination of input vectors and their mappings to the output as observed on the training data with very low errors. However, the question is how the very same rules or mappings perform on new data that may have different input to output mappings. If the error of the validation set is very big compared to the error of the training set, then go back and adjust model parameters. The model will have essentially memorized the answers seen in the training data, losing its generalization capabilities. This is called overfitting, and there are various techniques for overcoming it as it is exposed below in Subsection 4.3.3. Finally,

in the fifth step, the performance of the model is validated. The accuracy of the model can be improved by changing its structure or the underlying training data. However, if the performance of the model is not satisfactory, change model parameters, inputs and or scaling, go to the first step and try again (Bousquet and Elissee, 2001; Kotsiantis, 2007).

There is no universally "best" learning algorithm (Wolpert, 1995). That is, there is no learning method that provides superior predictive accuracy for all problems. Therefore, often one of the tasks involved in tackling a learning problem is to try to select the algorithm with the most suitable inductive bias for the problem. In the area of supervised learning, there are a wide variety of algoritms, and among them it should be highlighted: Linear classifiers such as the Naive Bayes classifier, Learning Vector Quantization (LVQ), Classification and Regression Trees (CART), Logistic regression, Artificial neural network (ANN) and Multi Layer Perceptron (MLP) which is a particular case of ANN or Support Vector Machine (SVM) (Bishop, 1995; Alpaydin, 2001; Kotsiantis, 2007). In this Thesis, the supervised MLT algorithms which have been employed are ANN and SVM algorithms.

4.3.1 Artificial Neural Network (ANN) and Multi Layer Perceptron (MLP)

The term "Artificial Neural Network" (ANN), when is used without qualification, usually is referred to a Multilayer Perceptron Network (MLP), which is a particular case of ANN with a layered structure where each neuron is a perceptron. A perceptron is the first, and therefore the simplest, ANN developed by Rosenblatt (1958). However, there are many other types of neural networks including Probabilistic Neural Networks, General Regression Neural Networks, Radial Basis Function Networks, Cascade Correlation, Functional Link Networks, Kohonen networks, Gram-Charlier networks, Hebb networks, Adaline networks, Heteroassociative networks, Recurrent Networks and Hybrid Networks (Whitehall and Lu, 1991; Langley and Simon, 1995; Mitchell, 1997; Alpaydin, 2001).

ANN are mathematical models that are inspired by the structure and functional aspects of biological neural networks (McCulloch and Pitts, 1943). The human brain consists of around 10^{11} nerve cells called neurons (see Figure 4.4). The nucleus, where the main processes take place, can be treated as the computational center of a neuron. The output duct of a neuron is called axon whereas dendrite is its input. One neuron can have many dendrites but only one axon; biological neurons have thousands of dendrites. Connections between neurons are called synapses; their quantity in a human brain is greater than 10^{14}. A neuron receives electrical impulses through its dendrites and sends them to the next neurons using axon. An axon is split into many branches ending with synapses. Synapses change power of received signal before the next neuron will receive it. Changing the strengths of synapse effects is assumed to be a crucial part of learning process and that property is exploited in models of a human brain in its artificial

equivalent (Minsky and Papert, 1969; Bishop, 1994). However, the structure of an artificial neuron, which is also shown in Figure 4.4, consists of two modules: summation module $\sum$ and activation module F. Roughly the summation module corresponds to biological nucleus. The algebra summation of weighted input signals is realized and the output signal is generated. Furthermore, output signal can be calculated using the following formula:

$$\varphi = \sum_{i=1}^{n} w_i x_i = \boldsymbol{w}^t \boldsymbol{x}, \tag{4.1}$$

where $\boldsymbol{w}$ is the vector of weights (synapses equivalent), $\boldsymbol{x}$ the vector of input signals (dendrites equivalent), n the number of inputs. Signal φ is processed by the activation module F, which can be specified by different functions according to needs (Rumelhart *et al.*, 1994).

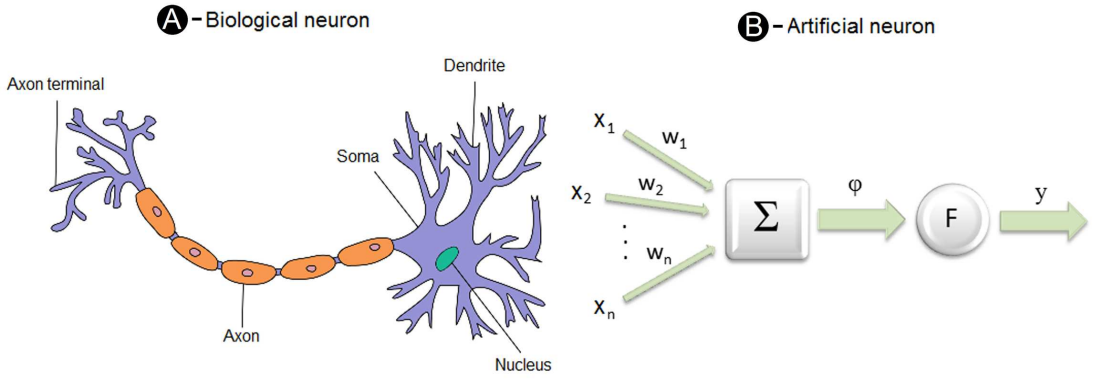

Figure 4.4: A - Model of a biological neuron. The green area inside a cell body is called nucleus. A signal is sent along the axon and through the synapse is transferred to dendrites of the other neuron. B - Model of an artificial neuron. In this neuron, the weighted sum of the inputs is transformed by the activation function to give the final output.

Additionally, information capacity and processing ability of a single neuron is relatively small. However, it can be raised by the appropriate connection of many neurons. In 1958 the first ANN prototype, called perceptron, was developed by Rosenblatt (1958). It was used for alphanumerical character recognition. Although the perceptron initially seemed promising, the results were not satisfactory due to problems when characters were more complex or the scale was changed, however it can be considered successfully as the first system built, which simulated a neural network (Rosenblatt, 1958). An artificial network consists of a pool of simple processing units which communicate by sending signals to each other over a large number of weighted connections (Anthony and Barlett, 1999).

Summarizing, an ANN model basically consists of two basic elements:

- A structure consisting in a set of basic units, called neurons, organized in different layers.

- A training algorithm for calibrating the network weights and other parameters as a function of deviations of the outputs provided by the network and the actual values.

Concerning this layered structure, is should be remarked that neurons in the multilayer ANN are grouped into three different types of layers: input, output, and hidden layer (see Figure 4.5). There can be one or more hidden layers in the network but only one output and one input layer. The number of neurons in the input layer is specified by the number of data attributes. The number of output neurons corresponds to the type of answer of the network. The amount of hidden layers and their neurons is more difficult to determine (Minsky and Papert, 1969; Bishop, 1994; Lisboa, 2002). A network with one hidden layer suffices to solve most tasks. Each unit consists of the following neuronal components,

- A set of input connections, along with a set of weights that regulate the input signals intensity.

- The activation threshold, which is subtracted from the aggregation of the input signals transmitted.

- An activation function which focuses on the input signals.

- The output of the neuron as a function of the input signals, called transfer function.

This mentioned structure is often called the network architecture, being able to make a classification of the networks as a function of the number of networks layers, the interconnection degree of the structure or according to the character of the connections.

With regards to the architecture, two types of a multilayer artificial neural networks can be distinguished: feed-forward and feed-back networks. In the feed-forward networks signal can move in one direction only and can not move between neurons in the same layer (see Figure 4.5.a). Such networks can be used in the pattern recognition. Feed-back networks are more complicated, because a signal can be sent back to the input of the same layer with a changed value. Signals can move in these loops until the proper state is achieved. These networks are also called interactive or recurrent networks (see Figure 4.5.b).

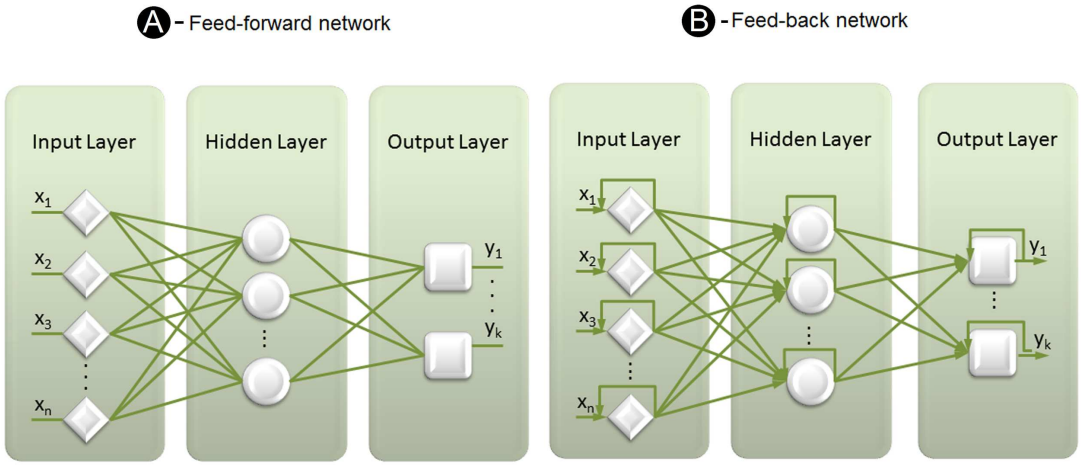

Figure 4.5: Multi-layer neural networks architecture. A - Feed-forward network. From the neurons in the input layer signals are propagated to the hidden layer and then finally to the output layer. B - Feed-back network. A signal can be returned to the same layer to adjust the proper state.

However, as regards the training algorithm, it should be noted that one of the best-known learning algorithms is the back-propagation algorithm (Bishop, 1995). This basic supervised learning algorithm for multilayered feed-forward networks gives a recipe for changing the weights of the elements in neighbouring layers. It was developed by Werbos (1974) and rediscovered independently by Parker (1985) and Rumelhart *et al.* (1985), and it consists in the minimization of the combination of squared errors and weights starting from randomly distributed weights, and then it determines the correct combination. The error data at the output layer is "back propagated" to earlier ones, allowing incoming weights to these layers to be updated. What makes this algorithm different than the others is the process by which the weights are calculated during the learning network. In general, the difficulty with multilayer perceptrons is calculating the weights of the hidden layers in an efficient way that result in the least output error. To update the weights, one must calculate an error. At the output layer this error is easily measured; this is the difference between the actual and desired (target) outputs. At the hidden layers, however, there is no direct observation of the error; hence, some other technique must be used. To calculate an error at the hidden layers that will cause minimization of the output error, as this is the ultimate goal. The back propagation algorithm is an involved mathematical tool; however, execution of the training equations is based on iterative processes, and thus is easily implementable on a computer. Despite of the fact that back-propagation algorithm is an ill-conditioned optimization problem (Eriksson *et al.*, 1998), thanks to specific way of the errors propagation, this algorithm has become one of the most effective learning algorithms (Minsky and Papert, 1969; Bishop, 1994; Lisboa, 2002).

Moreover, the activation and transfer functions can have many forms. Figure 4.6

lists some of these functions. In the original work on perceptrons (McCulloch and Pitts, 1943; Rosenblatt, 1958) which generally had no hidden layers, the activation functions were a simple linear function and a threshold function. For the linear function, Figure 4.6.a, the output signal y has the form

$$y = \tau\varphi, \tag{4.2}$$

where τ is a coefficient. Networks using this function are called Madaline and their neurons are called Adaline (Adaptive Linear Element). They are the simplest networks, which have found practical application. And, for the threshold function, Figure 4.6.b, the form of y is

$$y = \begin{cases} 1, & \varphi > \varphi_h \\ 0, & \varphi \leq \varphi_h \end{cases}. \tag{4.3}$$

But Minsky and Papert (1969) showed that perceptrons could only solve linearly separable problems. Two sets of points are linearly separable if and only if there exist a hyperplane such that all points of the first set are on one side of it and all points of the other set are on the other side of it. Besides, these functions have the disadvantage of not being differentiable everywhere, and, hence, does not work with gradient descent optimization algorithms. The linear and threshold functions were therefore replaced by the sigmoid function (Figure 4.6.c),

$$y = \frac{1}{1 + e^{-\tau\varphi}}, \tag{4.4}$$

where τ is a given parameter, or by the hyperbolic tangent function (see Figure 4.6.d),

$$y = \frac{e^{-\tau\varphi} - 1}{e^{-\tau\varphi} + 1}, \tag{4.5}$$

where τ is a given parameter. Many other functions were also studied, such as the ramp (continuous piece-wise linear), Figure 4.6.e,

$$y = \begin{cases} 0, & \varphi < 0 \\ \tau\varphi, & 0 \geq \varphi < \varphi_h \\ 1, & \varphi \geq \varphi_h \end{cases}, \tag{4.6}$$

or radial basis functions such as the Gaussian function, Figure 4.6.f,

$$y = e^{-(\tau\varphi)^2} \tag{4.7}$$

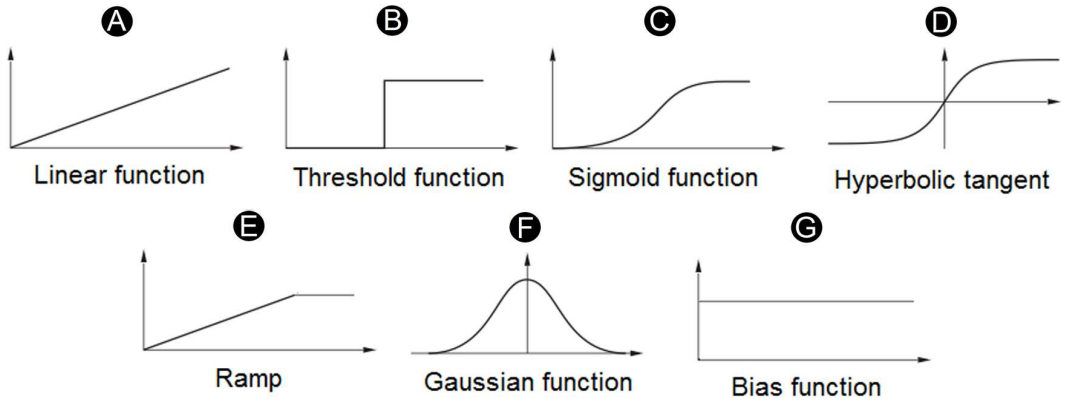

Figure 4.6: Activation and transfer type functions.

where τ is a given parameter.

Since this Thesis is focused on feed-forward network structures (see Figure 4.5) with specific activation functions and weights, the ANN mathematical model defined below is based on that the feed-forward network structure. Moreover, the back-propagation algorithm has been chosen to implement the models.

Within the feed-forward network structure, the network implements a function $f : \mathcal{X} \subset \mathbb{R}^n \to \mathcal{Y} \subset \mathbb{R}^k$ where n is the input space dimension and k is the output space dimension. The functions implemented by a network feed-forward can be formulated by the following general model,

$$\begin{aligned} f(\boldsymbol{x}) &= \varphi(\psi(\boldsymbol{x})) = (\varphi \circ \psi)(\boldsymbol{x}) \\ \psi&\colon \mathcal{X} \subset \mathbb{R}^n \to \mathcal{U} \subset \mathbb{R}^m \\ \varphi&\colon \mathcal{U} \subset \mathbb{R}^m \to \mathcal{Y} \subset \mathbb{R}^k \end{aligned} \tag{4.8}$$

where $\mathcal{U}$ is the hidden variables space with dimension m (number of neurons of this layer), and it is called feature space. And, based on the architecture defined above for the case of MLP (Bishop, 1995),

1. $\psi_j(\boldsymbol{x}) = \psi(\boldsymbol{w}_j^t \boldsymbol{x} + w_{j0})$ being ψ the hidden layer activation function, $w_j \in \mathbb{R}^n$ the parameter vector of the hidden layer and $w_{j0} \in \mathbb{R}$ its threshold value. The function ψ can be a sigmoid, a logistic or a hyperbolic tangent.

2. $\varphi_j(\boldsymbol{u}) = \varphi(\boldsymbol{c}_j^t \boldsymbol{u} + c_{j0})$ being φ the output layer activation function, $c_j \in \mathbb{R}^m$ the weights and $c_{j0} \in \mathbb{R}$ its threshold value. The activation function φ can be the identity function, threshold function or any dichotomous function.

The process of training the ANN consists in changing the weights assigned to connections of neurons until the achieved result is satisfactory. ANN is considered to have learned when computed errors are minimized. For completeness, the steps which should

be carried out in order to teach an ANN using feed-forward structure for each pattern in the learning set are described below (Antkowiak, 2006). The complex mathematical background of these techniques has been already described for many authors, however it has been here introduced for completeness. For more rigorous description, the interested reader is referred to see e.g., Mitchell (1997), Vidyasagar (1997), Anthony and Barlett (1999) and references therein.

1. Insert the learning vector $\boldsymbol{u}^{\mu_P}$ as an input to the network, being μ_P the index of actual learning patterns, $\mu_P = 1, ..., P$, and P the number of learning patterns.

2. Evaluate the output values $\boldsymbol{u}_j^{m\mu_P}$ of each element for all layers using the formula

$$u_j^{m\mu_P} = f(\varphi_j^{m\mu_P}) = f(\sum_{i=0}^{n_{m-1}} w_{ji}^m u_i^{(m-1)\mu_P}, \tag{4.9}$$

   where m is the index of actual layer, $m = 1, ..., M$ and M the number of layers without including the input layer. j is the index of actual element, $j = 1, ..., n_m$ and n_m the number of elements or neurons in layer m. $\varphi_j^{\mu_P}$ is the weighted sum of input values for element j in layer μ_P, f the activation function, w_{ji}^m the weight between element j in layer m and element i in layer $m-1$ and $u_i^{(m-1)\mu_P}$ is the output of element i in layer $m-1$ for pattern μ_P.

3. Evaluate error values $\pi_j^{M\mu_P}$ for the output layer using the formula

$$\pi_j^{M\mu_P} = f'(\varphi_j^{M\mu_P})\pi_j^{\mu_P} = f'(\varphi_j^{M\mu_P})(\widehat{y}_j^{\mu_P} - y_j^{\mu_P}), \tag{4.10}$$

   where $\pi_j^{M\mu_P}$ is learning error for element j for pattern μ_P, $\widehat{y}_j^{\mu_P}$ the expected network output value for element j for pattern μ_P and $y_j^{\mu_P}$ the actual network output value for element j for pattern μ_P,

4. Evaluate sum of squares errors ε_{μ_P} from

$$\varepsilon_{\mu_P} = \frac{1}{2}\sum_{j=1}^{n}(\pi_j^{\mu_P})^2. \tag{4.11}$$

5. Carry out the back propagation of output layer error $\pi_j^{M\mu_P}$ to all elements of hidden layers (see Figure 4.7) calculating their errors $\pi_j^{m\mu_P}$ from

$$\pi_j^{m\mu_P} = f'(\varphi_j^{m\mu_P}) \sum_{l=1}^{n_{m+1}} \pi_l^{(m+1)\mu_P} w_{lj}^{(m+1)}. \tag{4.12}$$

6. Update the weights of all elements between output and hidden layers and then between all hidden layers moving towards the input layer. Changes of the weights can be obtained from

$$\Delta_{\mu_P} w_{ji}^{m} = \eta \pi_{l}^{m\mu} u_{i}^{(m-1)\mu_P}, \tag{4.13}$$

where $\Delta_{\mu_P} w_{ji}^{m}$ is the change of given weight for pattern μ_P and η the proportion coefficient.

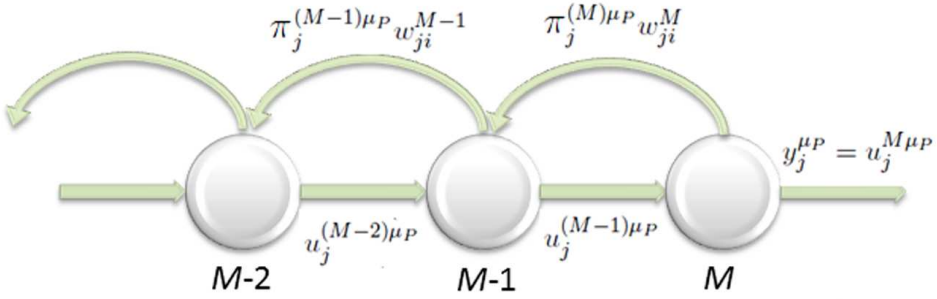

Figure 4.7: Back-propagation of errors values.

Above steps have to be repeated until satisfactory minimum of complete error function is achieved:

$$\varepsilon = \sum_{\mu_P=1}^{P} \varepsilon_{\mu_P} = \frac{1}{2} \sum_{\mu_P=1}^{P} \sum_{j=1}^{n} (\widehat{y}_j^{\mu_P} - \varphi_j^{\mu_P})^2. \tag{4.14}$$

Every iteration of these instructions is called epoch. After the learning process is finished another set of patterns can be used to verify the knowledge of the ANN. For complicated networks and large sets of patterns the learning procedure can take a lot of time. Usually it is necessary to repeat the learning process many times with different coefficients selected by trial and error. Furthermore, there is a variety of optimization methods which can be used to accelerate the learning process such as the momentum technique (Moreira and Fiesler., 1995).

The advantages of neural networks are quite apparent, in particular a list of advantages might be made for feed-forward ANN (Tu, 1996).

- Feed forward neural networks have a fixed computation time.
- Computation speed is very high, as a result of the parallel structure.
- Fault tolerant, because of distributed nature of network knowledge.
- Learns general solutions of presented training data.

- Ability to generalize to situations not taught to network previously.
- It does not use pre-programmed knowledge base.
- It suits to analyze complex pattern.
- It has no restrictive assumptions.
- It allows for qualitative data.
- It can handle noisy data and incomplete data, the solution will just be less precise. Besides, neural networks can model parts of a process that cannot be modeled or are unidentified.
- It can overcome autocorrelation.
- It is user-friendly, clear output, robust and flexible.

However, like any technique, artificial neural networks have certain drawbacks as:

- It requires high quality data.
- The variables must be carefully selected a priori.
- There is a risk of overfitting.
- It requires a definition of architecture.
- It takes long training processing time.
- There is a possibility of illogical network behavior.
- Large training sample is required.

4.3.2 Support Vector Machine (SVM)

Vapnik (1982) is considered the pioneer in introducing the concept of optimum separating hyperplane of a sample of data in a classification or regression problem, which is the core of the Support Vector Machines method (SVM). The SVM original algorithm was invented by Vapnik (1982), however the current standard approach (soft margin) was proposed by Vapnik (1995). The essence of SVM method is the construction of optimal hyperplane, which can separate data from opposite classes using the maximum margin. Margin is a distance between optimal hyperplane and a vector which lies closest to it (Boser *et al.*, 1992; Vapnik, 1995, 1998b,a).

Different historical facts could be highlighted in the development of support vector machine techniques,

1. The feature space generation from input space by the transformation $f : \mathcal{X} \subset \mathbb{R}^n \rightarrow \mathcal{Z} \subset \mathbb{R}^g$ with $g \geq n$ (can be ∞). By the reverse transformation, the linear boundaries of the separating hyperplanes in the feature space result in non-linear boundaries in the input space. This transformation is called the Kernel Trick (Boser *et al.*, 1992).

2. The appearance of soft-margin algorithm for problems where perfect separability is not reachable (problems with noise in the sample data).

3. The SVM generalization to regression problems by way of Vapnik's ε-insensitive loss function (Drucker *et al.*, 1997).

An example of such hyperplane is illustrated in Figure 4.8, where for a linearly separable set of 2D points which belong to one of two classes, a separating straight line is needed. In the Figure 4.8.a, it is observed that there exists multiple lines that offer a solution for the problem. However, a line is bad if it passes too close to the points because it will be noise sensitive and it will not generalize correctly. Therefore, the goal should be to find the line passing as far as possible from all points. Then, the operation of the SVM algorithm is based on finding the hyperplane that gives the largest minimum distance to the training examples. This distance receives the name of margin within theory of SVM. Therefore, the optimal separating hyperplane maximizes the margin of the training data, Figure 4.8.b.

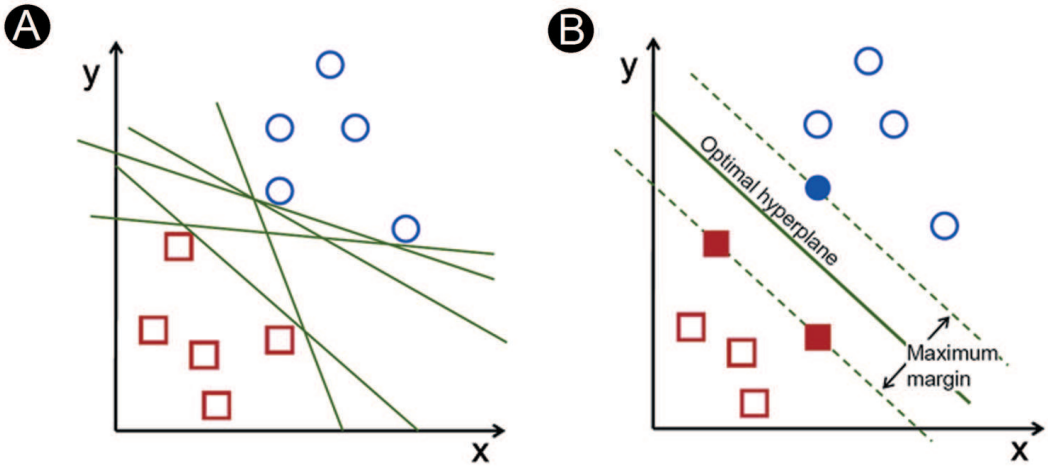

Figure 4.8: A - set of 2D points which belong to one of two classes separated by straight lines. B - Optimal hyperplane separating two classes.

Further, optimal hyperplane should satisfy

$$\frac{y_n f(x_n)}{\|\boldsymbol{w}\|} \leq \tau_m, \tag{4.15}$$

where $\boldsymbol{w}$ is the normal vector to the hyperplane, τ_m is a margin and $f(\boldsymbol{x})$ is defined as:

$$f(\boldsymbol{x}) = \boldsymbol{w}^t \boldsymbol{x} + \beta_0, \tag{4.16}$$

where the parameter $\frac{b}{\|\boldsymbol{w}\|}$ determines the offset of the hyperplane from the origin along the normal vector $\boldsymbol{w}$. And this function is not suitable for solving more complicated linearly non-separable problems.

Possibility of occurrence of the linearly non-separability in the input space is the main cause why the idea of SVM is not optimal for hyperplane construction in the input space but rather in high dimensional so called feature space ($\mathcal{Z}$). The feature space is usually defined as a non-linear product of base functions $\phi(\boldsymbol{x})$, defined in the input space. The solution can be expressed as a linear combination of the training vectors β_i. And, given a new point $\boldsymbol{x}_i$ to classify or regress, the solution is obtained by means of the inner product with the sample points $\boldsymbol{x}$. Thus, the function of the optimal hyperplane is now:

$$f(\boldsymbol{x}) = \sum_{i=1}^{n} \beta_i K(\boldsymbol{x}_i, \boldsymbol{x}) + \beta_0 \tag{4.17}$$

where $K(\boldsymbol{x}_i, \boldsymbol{x})$ is the inner product kernel of the base functions $\phi(\boldsymbol{x})$. Inner product may be defined as:

$$K(\boldsymbol{x}, \boldsymbol{x}') = \langle \phi(\boldsymbol{x}), \phi(\boldsymbol{x}') \rangle \tag{4.18}$$

We are now looking for solution in other space, but the problem is linearly separable, so it is more effective, even if the problem was linearly non-separable in the input space (see Figure 4.9). It is known as Kernel trick (Boser *et al.*, 1992).

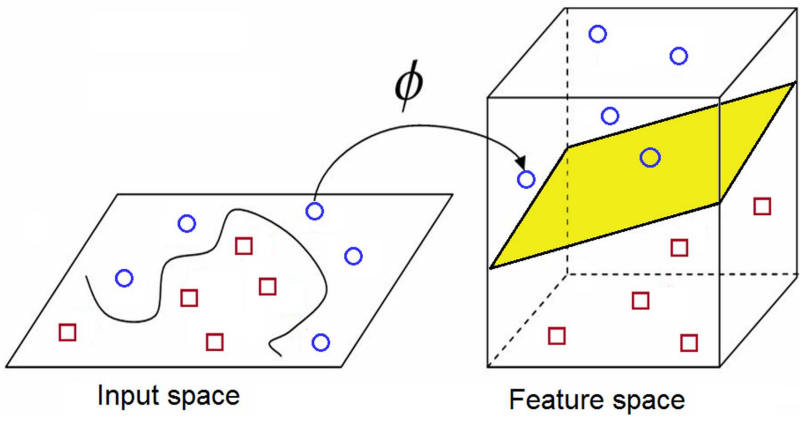

Figure 4.9: Transformation of input space into feature space.

The kernel function can have many different forms. Some of the commonly used functions are: linear, polynomial, gaussian or sigmoidal (see Figure 4.6). Choosing the most appropriate kernel highly depends on the problem at hand, and fine tuning its parameters can easily become a tedious and cumbersome task. Automatic kernel selection is possible and is discussed in the works by Howley and Madden (2005). The choice of a Kernel depends on the specific problem which is going to be solved because it depends on what we are trying to model. The motivation behind the choice of a particular kernel can be very intuitive and straightforward depending on what kind of information we are expecting to extract about the data. Consequently, different elections of this kernel function will provide better or worse performance of the SVM. But generally, the linear and the polynomial kernel functions are used in problems without high nonlinearity, the radial basis functions allows to pick out circles (or hyperspheres), and finally the sigmoid and the gaussian kernel functions are indicated for problems with high nonlinearity.

Therefore, the optimum hyperplane problem is obtained by means of the following constrained problem:

$$\begin{aligned} &\max_{\boldsymbol{w},b} \left\{ \min_{i\in\{1:n\}} |\langle \boldsymbol{w}, \boldsymbol{x}\rangle + \beta_0| \right\} \\ &\text{Subject to: } \|\boldsymbol{w}\| = 1 \end{aligned} \tag{4.19}$$

Or equivalently it can be also expressed as:

$$\begin{aligned} &\min_{\boldsymbol{w},b} \frac{1}{2}\|\boldsymbol{w}\|^2 \\ &\text{Subject to: } y_i(\langle \boldsymbol{w}, \boldsymbol{x}\rangle + \beta_0) \geq 1,\ i = 1, 2...n \end{aligned} \tag{4.20}$$

Then,this problem can now be solved by standard quadratic programming techniques and programs, and the Karush-Kuhn-Tucker condition are necessaries and sufficient (Vapnik, 1998a).

And the solution, which can be obtained from the dual problem, is a linear combination of a subset of sample points denominated support vectors (SV) and it can be written as follows:

$$\begin{aligned} \mathbf{w} &= \sum_{i\in \mathrm{SV}} \beta_i \phi(\mathbf{x_i}) \Rightarrow \\ f_{\mathbf{w},\beta_0}(\mathbf{x}) &= \sum_{i\in \mathrm{SV}} \beta_i \left\langle \phi(\mathbf{x_i}), \phi(\mathbf{x})\right\rangle + \beta_0 = \sum_{i\in \mathrm{SV}} \beta_i K\left(\mathbf{x}_i, \mathbf{x}\right) + \beta_0 \end{aligned} \tag{4.21}$$

Although SVM method is naturally adapted for separating or regretting data from two classes, it can be easily transformed into very useful tool for the classification of more than two classes.

Consequently, given a sample of data $\{(\mathbf{x}_i, y_i)\}_{i=1}^n$, the SVM regression problem (Drucker *et al.*, 1997) can be formulated as follows:

$$\min_{\mathbf{w},b,\boldsymbol{\xi}} \frac{1}{2}\left\{\left\|\mathbf{w}^2\right\| + C\sum_{i=1}^{n}(\xi_i + \xi_i')\right\}$$
$$\left\{\begin{array}{c|l} \langle \mathbf{w}, \phi(\mathbf{x}_i)\rangle + \beta_0 - y_i \geq \epsilon + \xi_i & \\ y_i - (\langle \mathbf{w}, \phi(\mathbf{x}_i)\rangle + \beta_0) \geq \epsilon + \xi_i' & i = 1, ..., n \\ \xi_i, \xi_i' \geq 0 & \end{array}\right. \tag{4.22}$$

where ξ_i, ξ_i', are slack variables that ensure that the solution does not contain, within the band of radius ϵ, all the points $(\mathbf{x}_i, y_i)$ of the sample (thus avoiding possible outliers and overfitting), where C is the cost parameter and expresses the importance of the slack variables in each point, and where $\phi : \mathcal{X} \to \mathcal{Z}$ is a transformation of the input space into a new space $\mathcal{Z}$ usually of larger dimension, where we define an inner product by means of a positive definite function K (kernel).

Furthermore, it is possible to introduce the parameter ν in the SVM regression model (Nu-SVR) in order to control the number of support vectors determined (Scholkopf *et al.*, 2000). Then, the SVM problem can be formulated as follows:

$$\min_{\mathbf{w},b,\boldsymbol{\xi}} \frac{1}{2}\left\{\left\|\mathbf{w}^2\right\| + C\left(\nu\epsilon + \frac{1}{n}\sum_{i=1}^{n}(\xi_i + \xi_i')\right)\right\}$$
$$\left\{\begin{array}{c|l} \langle \mathbf{w}, \phi(\mathbf{x}_i)\rangle + \beta_0 - y_i \geq \epsilon + \xi_i & \\ y_i - (\langle \mathbf{w}, \phi(\mathbf{x}_i)\rangle + \beta_0) \geq \epsilon + \xi_i' & i = 1, ..., n \\ \xi_i, \xi_i' \geq 0 & \end{array}\right. \tag{4.23}$$

where ν $(0 \leq \nu \leq 1)$ represents the upper bound on the function of margin errors in the training set and establishes the lower bound on the fraction of support vectors.

Obviously, all learning techniques have advantages and disadvantages, which are more or less important according to the data which are being analysed, and thus have a relative relevance. The advantages of the SVM technique could be summarized as follows:

- By introducing the kernel, SVM gain flexibility in the choice of the form of the threshold separating plane, which needs not be linear and even needs not have the same functional form for all data, since its function is non-parametric and operates locally.

- Since the kernel implicitly contains a non-linear transformation, no assumptions about the functional form of the transformation, which makes data linearly separable, is necessary. The transformation occurs implicitly on a robust theoretical basis and human expertise judgement beforehand is not needed.

- SVM provide a good out of sample generalization.

- SVM deliver a unique solution, since the optimality problem is convex. This is an advantage compared to ANN, which have multiple solutions associated with local minimum, and for this reason may not be robust over different samples.

- SVM classifier or regressor depends only on the support vectors, and the classifier or regressor function is not influenced by the whole data set, as it is the case for many ANN systems.
- With the choice of an appropriate kernel and parameters, SVM are faster than ANN in training. SVM uses a subset of training points in the decision function called support vectors, so it is also memory efficient.
- Effective in high dimensional spaces.
- High computational efficiency.

In contrast, the main disadvantages of this technique are:

- A common disadvantage of non-parametric techniques such as SVM is the lack of transparency of results. The parameters can not inform us of the importance of each independent variable since its dimension may be very high. In addition, high dimensionality of data can represent another limitation for SVM techniques.
- We need to select and appropriate kernel and its parameters. This is the same situation as that of ANN where we need to set the number of hidden units, initial values of weights, and so on.
- If the number of features is much greater than the number of samples, the method is likely to give poor performance.

4.3.3 Assuring the quality of the machine

In a perfect world we would always have all the data we need to represent a given classification or regression problem. However, the world is far from perfect in this respect. Consequently, some previous consideration should be taken to improve the performance of these techniques on the medical field. Many patterns will be banal and uninteresting. Others will be spurious, contingent on accidental coincidences in the particular data set used. In addition real data, specially in the medical field, are imperfect; some parts will be garbled, and some will be missing. Anything discovered will be inexact; there will be exceptions to every rule and cases not covered by any rule. Thus, algorithms need to be robust enough to cope with imperfect data and to extract regularities that are inexact but useful. A MLT useful to solve medical diagnostic tasks should include the following desirable features (Itchhaporia *et al.*, 1995; Cheung, 2001; Kononenko, 2001):

- Good performance: The algorithm has to be able to extract significant information from the available data. The diagnostic accuracy on new cases has to be as high as possible. Furthermore, if there is a possibility to measure an accuracy prediction of clinicians in the given problem, their performance can be used as

the lower bound on the required accuracy of the MLT. In the majority of learning problems, various approaches typically achieve similar performance in terms of the classification or regression accuracy, although in some cases some algorithms may perform significantly better than others (Michie *et al.*, 1994). Therefore, a priori, almost none of the algorithms can be excluded with respect to the performance criterion. Rather, several learning approaches should be tested on the available data and the one or few with best estimated performance should be considered for the development of the application.

- Dealing with missing data: In medical diagnosis very often the description of patients in records lacks certain data. The algorithms have to be able to appropriately deal with such incomplete descriptions of patients.

- Dealing with noisy data: Medical data typically suffer from uncertainty and errors. Therefore MLT appropriate for medical applications have to have effective means for handling noisy data.

- Transparency of diagnostic knowledge: The generated knowledge and the explanation of decisions should be transparent to the clinicians. They should be able to analyse and understand the generated knowledge.

- Explanation ability: The system must be able to explain decisions when diagnosing new patients. When faced with an unexpected solution to a new problem, the clinicians shall require further explanation, otherwise they will not seriously consider the suggestions of the system.

- Reduction of the number of tests: In medical practice, the collection of patient data is often expensive, time consuming, and harmful for the patients. Therefore, it is desirable to have a classifier/regressor that is able to reliably diagnose with a small amount of data about the patients.

Moreover, we have to be very careful not to overfit our models. Overfitting essentially occurs when a model begins to adapt too well to the specific training set. This will lead to an increase of the error when measured on an independent data set not previously seen by the model. As mentioned above, the data set is split such that 80% of the instances are randomly selected for training and the remainder are used for testing (10% for validation tasks and 10% for test tasks), and in principle they are used for different stages during the construction of a prediction model. An example of overfitting is presented in Figure 4.10 where the error of the model, during training and testing, is plotted against its complexity.

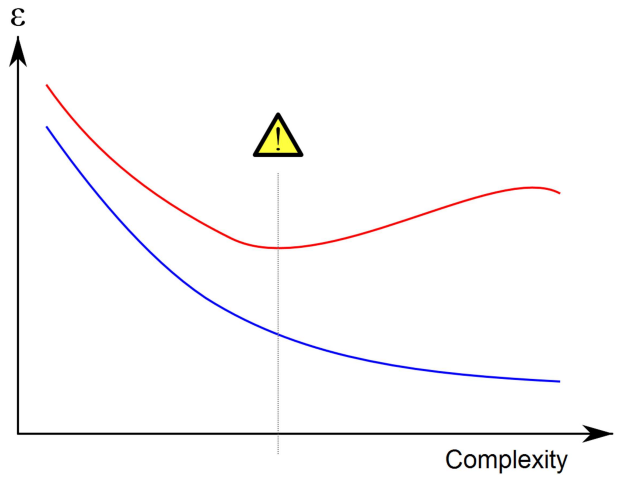

Figure 4.10: Plot of the training and validation error against the complexity of the model. The blue and red line represents the error from the training and validation data, respectively. The dashed line marks the point indicates where overfitting starts to occur.

This means that when developing models and later adapting them to data, we need to have an independent data set to validate the performance on. Otherwise we would never know if our model just memorized the data or if it actually has learned something. You will most likely get different results depending on the way you divide the data. Thus, you would have to do this splitting several times and use the average of all the validation results as the performance measurement. Several methods have been proposed to generate these repeated training and validation sets such as the hold out method which cuts the data in half, using the first half for training and the other one for testing or the bootstrap approach which samples from the original data with replacement meaning that some data points will be present more than once in the new re-sampled data set, but there will also be some data points left out which are used as the validation set (Efron and Tibshirani, 1997; Wehrens *et al.*, 2000). Nevertheless, probably the currently most used method of re-sampling in order to quantify generalization performance of a classifier or regressor is K-fold cross validation, which is the method used to develop the machine learning tools developed in this Thesis (Stone, 1974; Kohavi, 1995; Efron and Tibshirani, 1997).

K-fold cross validation: This method basically randomly splits the data set into K equally sized parts. Of the K subsamples, two single subsamples are retained as the validation and test data, respectively, and the remaining K-2 subsamples are used as training data. The cross-validation process is then repeated K times (the folds), with each of the K subsamples used exactly once as the validation and test data. The K results from the folds then can be averaged to produce a single estimation. The

advantage of this method over repeated random sub-sampling is that all observations are used for both training, validation and test, and each observation is used for validation and test exactly once. 10-fold cross-validation is commonly used, but in general K remains an unfixed parameter (Seymour, 1993).

An example of this sample division strategy can be found in Figure 4.11 where K = 10 has been chosen. The original set of training data is split into three groups: the first group consists of a training data set with the 80% of the data patterns; the remaining groups are the validation data set with the 10% of the patterns and, the remaining 10% of the data patterns are used to evaluate the performance of the MLP. The weight configuration for the best performance reached is stored and only replaced if a better performance has occurred. In this way, the best weight configuration can be determined. This process is repeated 10 times (10-fold cross validation) (Stone, 1974; Efron and Tibshirani, 1997; Kohavi, 1995).

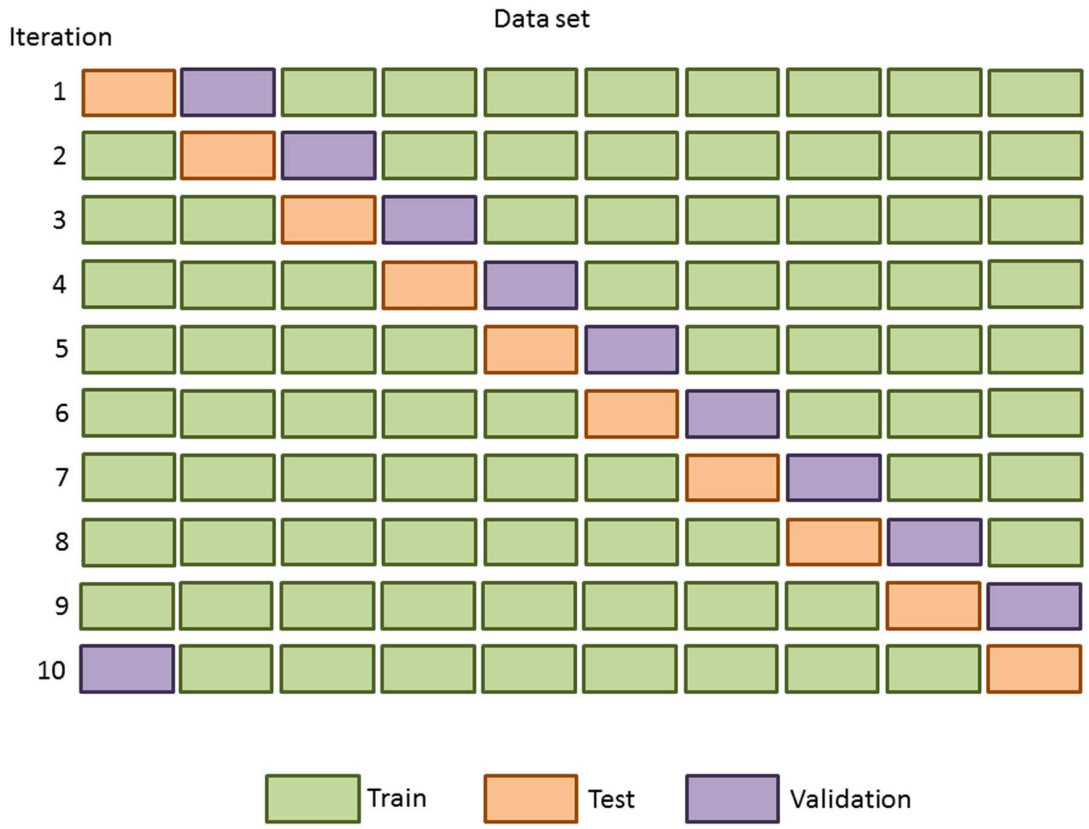

Figure 4.11: Illustration of a K-fold cross validation with K = 10. The green boxes correspond to the training data, the orange ones to the data that will be used for testing and the purple ones to the validation set.

4.4 Machine Learning Techniques as a helpful tool towards determination of plaque vulnerability

Detection of vulnerability in the process of atheroma plaque development would be of considerable value for clinical diagnosis. Nowadays, image analysis techniques are the only procedure used by clinicians for detection of vulnerable atheroma plaques and also, FEM models have sometimes been used as preoperative planning tools, when clinical staff have enough time to segment and reconstruct the patient-specific geometry for computational simulation, and after that analyze the obtained results. Nevertheless, the use of FEM computations presents the disadvantage of very high computational cost (long computational times and huge memory requirements), usually hours or even days, when an immediate response is required. Therefore, below an alternative tool based on different MLT, such as ANN and SVM, applied to the study of the role of stress in plaque vulnerability in order to reduce the very long computation times and memory consumption required for 3D FE analysis, is presented.

4.4.1 Data acquisition and pre-processing

The 3D parametric study with longitudinal residual stress performed in Chapter 2 to asses the atherosclerotic plaque vulnerability as a function of the main geometrical factors: (i) the fibrous cap thickness; (ii) the stenosis ratio; (iii) the lipid core width and (iv) the lipid core length, has been used to generate the source or input data to train the different machine learning techniques implemented. MPS, which is the output data, was also considered as the mechanical factor for the purpose of comparison between different models in order to define vulnerability risk. Furthermore, the threshold value of 247 kPa calculated from the set of experimental data obtained by Loree *et al.* (1994) has also used to determine if an atheroma plaque is considered as vulnerable or not. Therefore, the source data to train the machine learning tool developed correspond to those shown in Figure 2.11 of Chapter 2.

Pre-processing of raw data is necessary as a first step to remove weak or flagged measurements, handle background estimates, and do further transformations. Normalization is commonly used to remove systematic bias from the data and to make comparable empirical distributions. Thus, a normalized variation of each of the four parameter studied has been defined for all of the techniques. This parameter (ν_{param}) is obtained as $\nu_{param} = \frac{a_{param} - a_{max}}{a_{max} - a_{min}}$, where the variable "$a_{param}$" represents each of the four parameters (lipid core length (ν_l), lumen radius (ν_r), fibrous cap thickness (ν_{fc}) and lipid core width (ν_w)) in whatever position, and a_{min} and a_{max} are the lowest and highest values, respectively, of each parameter.

4.4.2 Mathematical Methods for Regression

The methods used in this comparative study are briefly presented below. The mathematical description of MLT, which are concerned with the design and development

of algorithms that allow computers to evolve behaviours based on empirical data, has been presented in Section 4.3, thus just the specific considerations related to the tool built are exposed below.

4.4.2.1 Artificial Neural Network (ANN)

MLP with three layers (one input layer, one hidden layer and one output layer) which is a particular case of ANN with a layered structure where each neuron is a perceptron has been defined as the structure baseline. Furthermore, the feed-forward architecture in which each layer is connected with the following forward direction only, so that can be represented by an acyclic graph, has been chosen to perform the parametric tool. A typical feature of MLP is the training algorithm of back-propagation (Bishop, 1995). In this case, the training algorithm used has been the Bayesian regularization back-propagation which is a network training function that updates the weight and bias values according to Levenberg-Marquardt optimization. It minimizes a combination of squared errors and weights starting from randomly distributed weights, and then determines the correct combination so as to produce a network that generalizes well (Rumelhart *et al.*, 1994). Once a MLP is trained, it has input data fed into it, and from that, generates an appropriate output. The structure of the MLP, combined with the non-linearity and its weights, adjusted by the training algorithm, creates general function approximations that allow for the generation of practically any non-linear function. Additionally, among all the possible transfer functions (Bishop, 1995), the sigmoid-type and the linear functions have been selected for the hidden layer and the output layer, respectively. And the maximum number of epochs to train and the minimum performance gradient have been chosen as 5000 and 10^{-20}, respectively.

A cross-validation process was implemented in order to minimize the selection of the test set. The original set of training data is split into three groups: the first group consists of a training data set with the 80% of the data patterns; the remaining groups are the validation data set with the 10% of the patterns and, the remaining 10% of the data patterns are used to evaluate the performance of the MLP. The weight configuration for the best performance reached is stored and only replaced if a better performance has occurred. In this way, the best weight configuration can be determined. This process is repeated 10 times (fold cross validation) (Stone, 1974).

Figure 4.12 shows the structure and architecture used to implement the MLP algorithm to estimate a decision about atheroma plaque vulnerability. The three layers are clearly depicted. The input layer represented in red color has four neurons that correspond to the four parameters studied; fibrous cap thickness, stenosis ratio and lipid core width and length. The hidden layer, blue color, has an undetermined number of neurons which will be calculated by trial and error during the training process. And finally, the output layer depicted in orange color has only one neuron and shows the response predicted by the ANN, in this case, the maximum MPS value which correspond to the 3D coronary artery model with the parameters selected as input of the network.

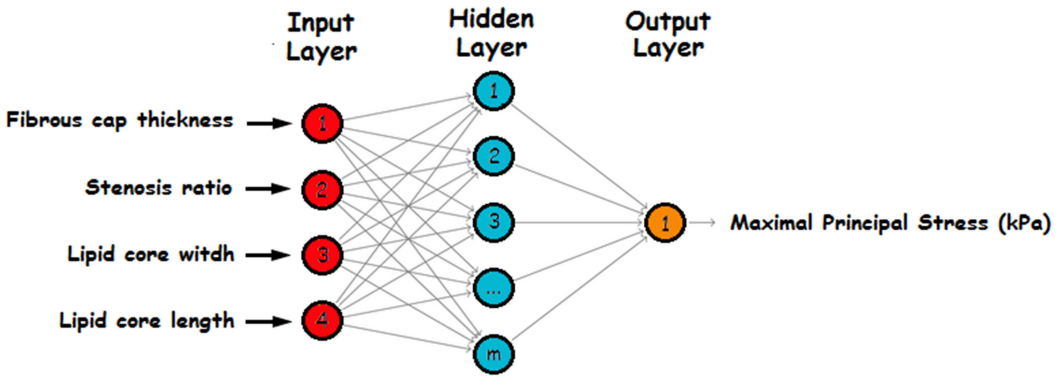

Figure 4.12: Artificial Neural Network structure

4.4.2.2 Support Vector Machine (SVM)

To implement the SVM, the radial basis kernel function has been selected due to its better performance against the sigmoid kernel function. The linear and the polynomial kernel functions are used in problems without high nonlinearity, however, the sigmoid and the radial basis kernel functions are indicated for problems with high nonlinearity, as is the case of the current problem.

Furthermore, as it is indicated above in Section 4.3, it is possible to introduce a parameter in the SVM regression model (Nu-SVR) in order to control the number of support vectors determined (Scholkopf *et al.*, 2000). Therefore, the SVM algorithm has been implemented with and without including this parameter and the performance of both algorithms has been compared.

Finally, a 10-fold cross validation has been again implemented in order to determine the optimal SVM parameters according to the best fit criterion.

4.4.2.3 Classical Linear regression

Comparing MLT models with classical linear regression is an important step in the development procedure. If the results show that the gain of using a non-linear model, such as the ANN or SVM, is limited, one should usually go for the less complicated model. Therefore, the results have been fitted by a linear regression in order to prove the non-linearity of the problem which justify the use of MLT.

A regression equation of the form

$$y_i = \beta_0 + \sum_{i=j}^{n} (\beta_j x_{ij}) + \epsilon_i \tag{4.24}$$

explains the value of a dependent variable y_i in terms of a set of n observable variables in x_i and an unobservable random variable ϵ_i. The vector $\boldsymbol{\beta}$ contains the parameters

of a linear combination of the variables in x_i. A set of n successive realizations of the regression relationship can be compiled into a system

$$\boldsymbol{y} = \beta_0 + \boldsymbol{\beta x} + \boldsymbol{\epsilon}, \tag{4.25}$$

wherein $\boldsymbol{y}$ and $\boldsymbol{\epsilon}$ are vectors of order i and $\boldsymbol{x}$ is a matrix of order ixn. We shall assume that $\boldsymbol{x}$ is a non-stochastic matrix with $\text{Rank}(\boldsymbol{x}) = n$ which requires that $i \geq n$. $\boldsymbol{\epsilon}$ is the error to explain the variable $\boldsymbol{y}$ by the hyperplane $\beta_0 + \boldsymbol{\beta x}$. β_0 and $\boldsymbol{\beta}$ are the constants of the regression model estimated from the sample data by the principle of ordinary least squares regression.

Furthermore, the coefficient of determination R^2 is a measure of the global fit of the model. Specifically, the coefficient R^2 can assume values between 0 and 1, and represents the proportion of variability in $\boldsymbol{y}$ that may be attributed to some linear combination of the regressors (explanatory variables) in $\boldsymbol{x}$. Thus, $R^2 = 1$ indicates that the fitted model explains all variability in $\boldsymbol{y}$, while $R^2 = 0$ indicates no linear relationship for straight line regression. An interior value such as $R^2 = 0.7$ may be interpreted as follows: "Approximately seventy percent of the variation in the response variable can be explained by the explanatory variable. The remaining thirty percent can be explained by unknown, lurking variables or inherent variability". Regression models were implemented between the explanatory variable and each predictor variables in order to establish the order of importance of each variable of the problem by analyzing the coefficient of determination which is defined as follows,

$$R^2 = 1 - \frac{\frac{1}{n}\sum_{i=1}^{n}(y_i - \widehat{y}_i)^2}{S_Y^2} \tag{4.26}$$

where y_i, $\widehat{y}_i$ are the real and estimated values respectively and S_Y^2 is the variance of $\boldsymbol{y}$.

4.4.3 Performance and accuracy of the regressor

Regressor performance evaluation is an indispensable step in diagnostic system design. The same regressor performs differently from application to application. Given that no single regressor is always superior over others for all applications, common practice for designing regressors for a given problem, therefore, involves experimenting with many different regressors, comparing their performance, and selecting the one with the best performance. The performance between ANN with different number of neurons in the hidden layer, SVM with and without Nu-regression and with different radial basis function types as kernel function; Gaussian and normal and, classical linear regression are compared.

In order to evaluate regressor performance, which generally refers to both computational and regression efficacy, a regressor performance measure, which is a single index that measures the goodness of the regressors considered, has to be defined. Depending

on the design or application requirements, different problems may call for different performance measures to ensure that the regressors considered can be properly compared and selected.

In this particular case, in order to predict the accuracy of the technique, the absolute of relative error (ER) and the correlation coefficient (RSQ) have been chosen as the error functions that will be measured in the test set and will provide us with information of how well the network fits the data.

$$ER = abs(\frac{\widehat{\text{MPS}} - \text{MPS}}{\text{MPS}}) \tag{4.27}$$

$$RSQ = \frac{cov_{MPS\ \widehat{MPS}}}{S_{MPS} S_{\widehat{MPS}}} \tag{4.28}$$

where $\widehat{\text{MPS}}$ is the predicted maximum MPS, MPS is the real maximum MPS, $cov_{MPS\ \widehat{MPS}}$ is the covariance and S_{MPS} and $S_{\widehat{MPS}}$ are the standard deviations of the predicted an real maximum MPS, respectively.

4.4.4 How the Decision Support System works

The decision support system is the knowledge source, and the optimization method is the mechanism for problem solving, which returns a customized recommendation based on the query's individual information. The optimization method should provide a feasible recommendation which would be used by the expert clinicians to asses the stability of the atheroma plaque. Therefore, once the ANN and SVM has been trained, the three easy steps should be taken to use this parametric tool to assist the clinical professionals on decisions of the vulnerability of the atheroma plaque;

1. For a specific patient, clinical staff should measure in standard coronary artery IVUS images or simular just the four dimensions defined as the most influential parameters in the risk of plaque vulnerability. This parameters which has been used in the algorithms as input are: (i) fibrous cap thickness, (ii) stenosis ratio, (iii) lipid core length and (iv) lipid core width.

2. The value of these four geometrical measurements will be introduced in the MLT tool developed (using either the ANN or the SVM algorithms as input).

3. Then, the clinical staff would have an immediate response on the atheroma plaque vulnerability. They will get as the output of the decision support system the maximum MPS value occurred in an idealized coronary artery model with the same dimensions than those measured in the specific patient. The obtained response will be used by the experienced clinician to decide the therapies and treatments necessaries.

Figure 4.13 provides an overview of the process of applying MLT to atheroma plaque vulnerability prediction. Each step is described in detail above.

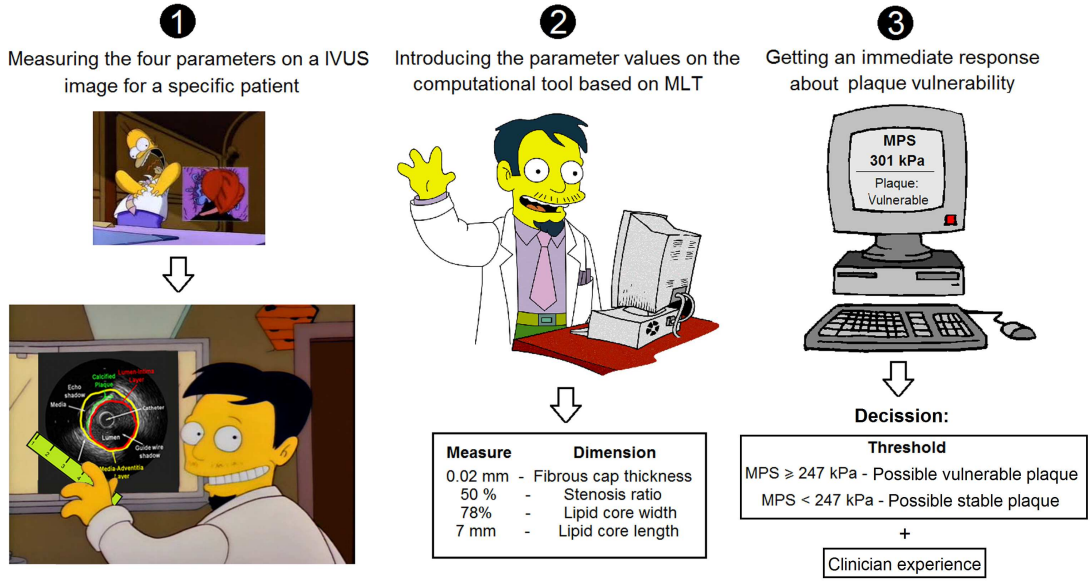

Figure 4.13: The three steps that should be taken to use this parametric tool to assist the clinical professionals on decisions of the atheroma plaque vulnerability.

4.4.5 Results of the vulnerability prediction

Below, the results obtained by the three mathematical methods used in this study; linear regression, Artificial Neural Networks through the particular case of a Multilayer Perceptron Network and Support Vector Machines, are presented. Firstly, the results of each method are presented separately and, later a comparison between the obtained results of the three techniques is carried out. The absolute of relative error (ER) and the correlation coefficient (RSQ) have been used to predict the accuracy of each of the techniques used. Furthermore, in order to show the computational efficiency of each method related to the computational costs, the time requirements of each of the techniques presented have been compared with the computational time of one finite element structural analysis.

Artificial Neural Network (ANN): The optimum number of neurons in the hidden layer has been chosen by trial and error approach searching through an enormous range of values so that the error in prediction is minimized. Furthermore, different test size has been tried in order to obtain the better performance. Table 4.1 summarizes the absolute of relative errors and the correlation coefficients for two different size test; 5 and 10 elements, and for 50, 75, 100 and 150 neurons in the hidden layer. In that case, the most accurate prediction has been for 100 neurons in the hidden layer neuron (Test

ER = 6.76% and RSQ = 0.9953). It can be observed that an increase of the number of neurons in the hidden layer, increases the computation time, but the ER remains constant. However, decreasing the number of neurons in the hidden layer increases the ER.

		Test size 5				Test size 10			
	Neurons	50	75	100	150	50	75	100	150
Train	RSQ	0.965	0.978	0.9996	0.9995	0.975	0.987	0.9997	1
	ER	0.053	0.047	0.0013	0.0125	0.048	0.054	0.0112	0.0013
Test	RSQ	0.92	0.924	0.9953	0.9952	0.917	0.909	0.9513	0.9465
	ER	0.125	0.101	0.0676	0.0692	0.128	0.098	0.1097	0.1153

Table 4.1: ER and RSQ obtained by the MPL technique for the train and test processes, and for a number of 50, 75, 100 and 150 neurons in the hidden layer and a test size of 5 and 10 elements.

In addition, Figure 4.14 depicts the maximum MPS values obtained for the best combination of neurons in the hidden layer, i.e. 100 neurons, which has been shown in Table 4.1, in a set of 50 observations. Viewing the results, it can be corroborated that the MLP models present very accurate fits between the real and the estimated points with a high correlation between them. Furthermore, the maximum absolute error occurred in the MPS prediction has been 2.77 kPa over a MPS value of 746.95 kPa (26^{th} observation), this error allow us to know that in the worst case the MLP technique will be produce an relative error of 0.37% on the MPS estimation.

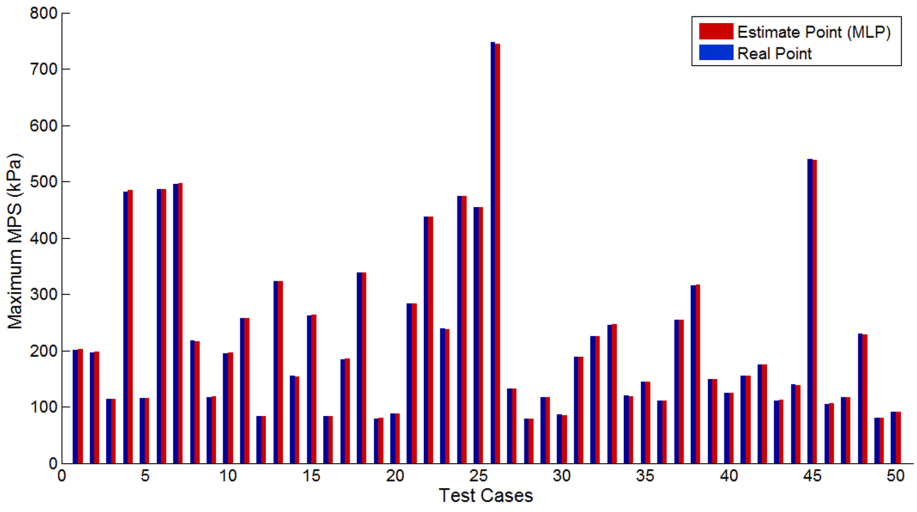

Figure 4.14: Maximum MPS real and predicted by the MLP technique for a set of 50 observations.

Support Vector Machine (SVM): The absolute of relative errors and the correlation coefficients for SVM technique is shown in Table 4.2. The performance of gaussian and normal radial basis kernel functions have been compared, as well as the accuracy for

models implemented with and without Nu-regression. The optimum values of the cost parameter (C) the band of radius (ϵ) and the parameter of the gaussian kernel function (τ) have been found by trial and error approach between a wide range of values. As Table 4.2 shows, the gaussian distribution with Nu-regression is the best combination (Test ER = 4.14% and RSQ = 0.9997). In Addition, SVM has greater updating capacity than the MLP, because once the model is generated and presented a new observation to itself, if the model is unable to estimate correctly the value, it simply adds this observation to the support vectors set without the need of a new training loop. However, MLP would need a new training to build a new model which includes information on the new observation presented.

		With Nu regression		Without Nu regression	
		Gaussian	*Normal*	*Gaussian*	*Normal*
Train	RSQ	1	1	1	1
	ER	5.13E-06	5.13E-06	0.000281	0.000281
Test	RSQ	0.9997	0.9996	0.9995	0.9995
	ER	0.041442	0.044532	0.073469	0.073469

Table 4.2: ER and RSQ for the SVM Technique.

As in the MLP case, the results obtained for the best combination (C equals to 80, ϵ equals to 0.00001 and the parameter of the gaussian kernel function equals to 0.001) in a set of 50 observations are shown in Figure 4.15. Again, the models present very accurate fits between the real and the estimated points with a high correlation between them, however, the results obtained by SVM are in fact even better than the MLP ones. Moreover, the maximum ER occurred in the MPS prediction, which allow us to know the worst prediction made by the SVM technique, has been 0.998 kPa over a MPS value of 481.78 kPa (4^{th} observation), which corresponds to a 0.207% MPS prediction error.

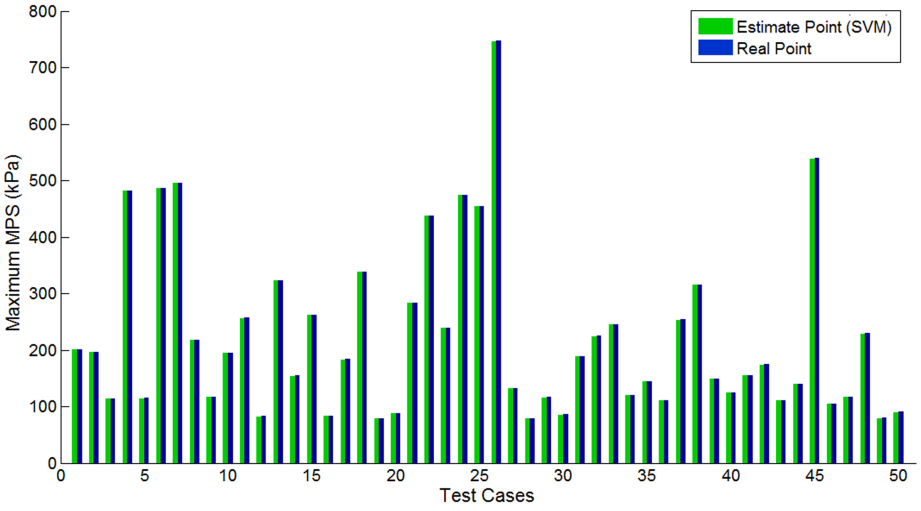

Figure 4.15: Maximum MPS real and predicted by the SVM technique for a set of 50 observations.

Linear regression: Regarding simple linear regression, Table 4.3 shows the results of the coefficient of determination R^2 for each simple regression model implemented between the explanatory variable and each predictor variable. Taking this data into account, it can conclude that the variable v_{fc} is the most influential of the explanatory variables since its coefficient is clearly the closest to 1 ($R^2 = 0.7181$). The other three parameters are less influential on the MPS prediction, being the lipid core width slightly more influential of these last three parameters. These results which show the influence of each parameter studied on the maximum MPS value are consistent with those obtained in Chapter 2, in which the fibrous cap was also assessed as the most influential parameter on the atheroma vulnerability risk.

Variable	R^2
v_l	0.01506
v_{sr}	0.01533
v_{fc}	0.7181
v_w	0.04774

Table 4.3: Coefficients R^2 for the different predictor variables; fibrous cap thickness, stenosis ratio and lipid core width and length.

Henceforth, the results are calculated based on the test and train sets. The train set is used to generate the model, so, a high fit accurate (R^2 value closes to 1) in this set indicates that the model has been well trained, while the test set is used to validate it, therefore a high fit accurate between the estimated and the actual values indicate that the model is appropriate to simulate the problem.

In order to strengthen the use of ANN and SVM techniques, the classical linear regression model has been included, and the results obtained are shown in the Table 4.4. Two test set sizes of 5 and 10 observations were used to contrast the different presented models, with the aim of deciding if the test size has influence in the error for each technique. The low value of RSQ and the high relative error of this model using classical linear regression indicate the high nonlinearity of the problem and justify the use of these techniques.

		Test size 5	Test size 10
Test	RSQ	0.4792	0.4585
	ER	0.5458	0.5580

Table 4.4: ER and RSQ for the Linear Regression Model.

Furthermore, the very poor fit between the real and estimated points provided by the linear regression for a set of 50 observations is shown in Figure 4.16, being the maximum absolute error occurred of 533.94 kPa over a MPS value of 746.95 kPa, detected in the 26^{th} observation of the set of 50 observations. Besides, this maximum absolute error corresponds to a relative error of 71.48%, much more higher than the mean relative error obtained for this technique (54.58 %).

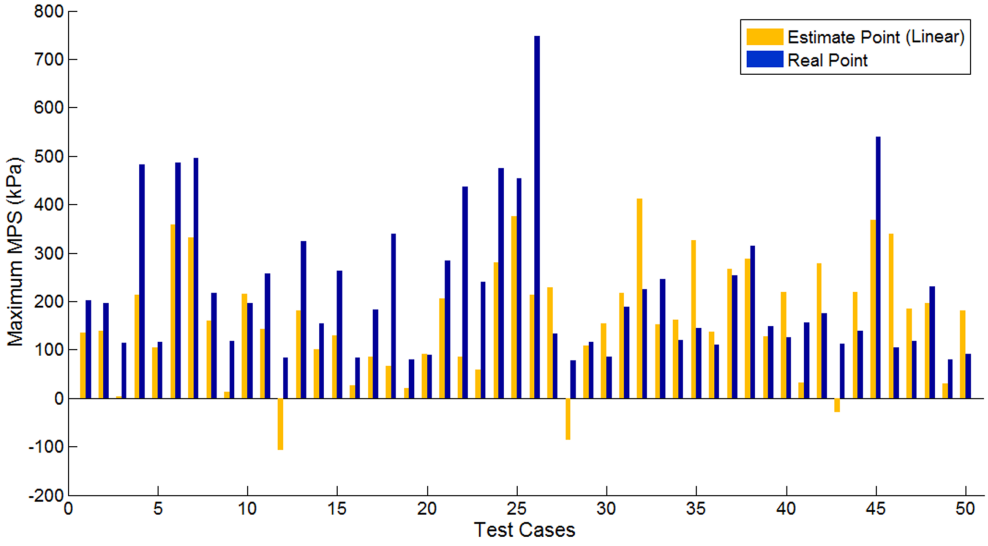

Figure 4.16: Maximum MPS real and predicted by the linear regression technique for a set of 50 observations.

Comparison of the obtained results by the three mathematical models for regression implemented: In order to compare the results obtained by the three prediction methods (MLP, SVM and classical linear regression), Figure 4.17 shows the comparison of real MPS points and estimated MPS points by using linear regression, SVM and MLP methods in a set of 25 observations. Subsequently, it can be clearly observed that the SVM and MLP models present very accurate fits between the real and the estimated MPS points with a high correlation between them. Furthermore, the results obtained by SVM technique are in fact even better than the MLP ones. However, the classical linear regression model provides a very poor fit between the real and estimated points.

Further, in order to play up the importance of computational efficiency, the computational costs of the different methods studied have been compared. For the ANN and SVM, the computation train time is 7 ± 3 and 5 ± 2 minutes, respectively (once the optimal parameters have been chosen by 10 fold cross validation and depending on the stopping criterion used), and the validation process time is negligible due to ANN and SVM techniques, which only evaluate a function, provide an immediate estimated response. However, once the FEM model has been constructed, the computational cost of each structural analysis is 10 ± 3 hours if the model is running in a super computer cluster of 1526 CPUs in total, using 8 compute nodes with the following characteristics; 2992 MHz of frequency, 32.96 and 32.77 Gb of total memory and swap space total, respectively.

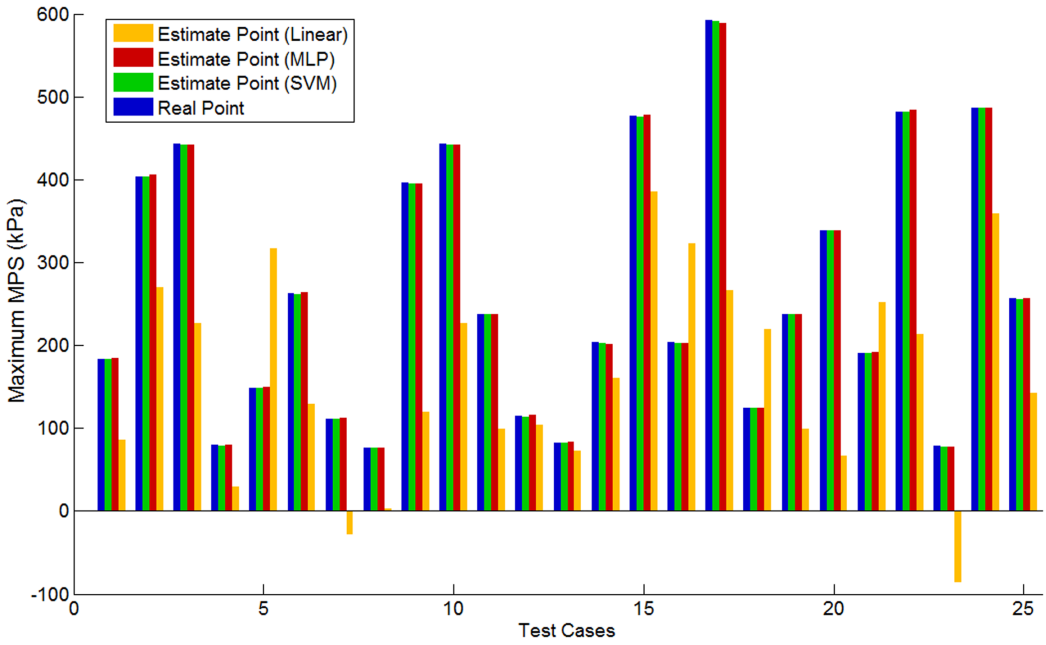

Figure 4.17: Comparative of real points (blue color) and estimated points by linear regression (yellow color), SVM (green color) and MLP (red color) models in a set of 25 observations.

4.5 Discussion

Quantifying the mechanical stress in the wall of an atherosclerotic vessel and, more specifically, in the fibrous cap, is a vital step in predicting the risk of plaque rupture based on biomechanical features. FEM is playing an increasing role in medical practice, being used in pre-operatory surgical planning when clinical staff have enough time to perform the computational model and analyze the results. However, FEM presents the disadvantage of very high computational cost. From the results of this study, we can conclude that both ANN and SVM techniques represent a powerful tool to replace FEM simulations used in cardiovascular mechanics to quantify the vulnerable risk since they provide an immediate response and the relative errors obtained are less than 10% for both methods.

The presence of high nonlinearities in the problem, as reflected by the results of classical linear regression model, reinforces the use of such alternative techniques to solve the regression problem. It was demonstrated that the SVM technique used in this study has the capacity to produce higher overall prediction accuracy than a particular specific MLP architecture since the relative error obtained is 4.14% and 6.76% in the SVM and ANN techniques, respectively. Based on this observation, we could conclude that SVM represents a useful method for vulnerable atheroma plaque detection. On the contrary, linear regression is not an appropriate technique to solve this problem due to the extremely high relative error obtained (55%).

A particular advantage of SVM is that this regressor depends only on the support vectors, and the regressor function is not influenced by the whole data set, as it is the case for many neural network systems. Additionally, SVMs are faster in training, but requires an appropriate choice of kernel function and parameters.

Some limitations of this study should also be mentioned. First, an idealized straight geometry has been used to perform the parametric analysis, thus the local curvature and other features such as the blood pressure have not been consider. Second, the material constitutive properties has not been considered. However, these assumptions have been widely accepted as allowable for the assessment of the biomechanical properties of atherosclerotic lesions (Cheng *et al.*, 1993). Third, global RS has been considered since there is any technique to measure the RS pointwise. Fourth, a huge set of real clinical data should be used in conjunction with the data obtained from the idealized geometry to train the ANN or SVM in order to quantitatively validate the results.

Despite these limitations, and according to the results obtained, the following conclusion could be drawn; the ANN and SVM techniques are able to replace FEM simulations to predict the maximum MPS on an idealized coronary model with a good error tolerance and avoiding the time consuming 3D FE analysis. However, the use of both techniques, FEM and MLT, in clinical practice remains unclear because it is necessary to clarify the real role of stress in plaque vulnerability and to perform a quantitative validation with clinical data.

Chapter 5

Experimental study of the arterial Stiffening due to Atherosclerosis in Apolipoprotein E-Deficient Mice

Apolipoprotein E-deficient mice, since their introduction in the early 1990s, have proved to be a very popular model for studying spontaneous hypercholesterolemia and the subsequent development of atherosclerotic lesions. The pathogenesis of atherosclerotic lesions in these mice mimics the lesions found in humans on a very short time-scale. Thereupon, the experimental progressive development of atherosclerotic lesions along the aorta of both apolipoprotein E-deficient ($ApoE^{-/-}$) and C57BL/6 mice (control) feeding on a Harlan-Teklad 88137 Western Diet and normal chow diet, respectively, is presented in this Chapter.

Experimental mechanical tests were performed in order to compare the different behaviours of the aorta between both strains at the same time on a diet and, between the same strain at different time on a diet. For this purpose, tissue samples were subjected to *in situ* mechanical inflation tests in order to determine the mechanical properties of the aortic $ApoE^{-/-}$ and control mice tissue. Furthermore, the longitudinal residual strain field in the aortic tree of both strains was measured.

In addition, anatomical analysis were carried out in order to evaluate the localization of the atheroma plaques along the aorta. For this goal, gross examination of each animal studied ($ApoE^{-/-}$ and control) have been performed by microscopy in order to show the predilection zones of atheroma plaque development and the evolution of the atheroma plaque growth. Concerning anatomical analysis, body weight measurements of each animal studied were performed once weekly since an increase of weight is directly related to high cholesterol levels and, therefore atherosclerosis lesions. Moreover, before animals were sacrificed, blood samples were taken directly from the heart for further analysis of total cholesterol and triglycerides by commercially available kits. Finally, the samples were processed in order to accomplish histological analysis. These analyses

are necessary since it allows direct identification the underlying tissue type, revealing his morphological composition.

Contents

5.1 Introduction

Experimental research constitutes the fundamental basis of the study of the role and behaviour of soft biological tissues. In particular, experimental studies provide basic information about multiple mechanically-relevant features of vascular tissue such as their layered nature, composite-like anisotropic micro-structure, physiological state configuration, and mechanical properties, among many others (see e.g., Fung, 1990; Humphrey, 2001, and references therein). From an engineering approach, the determination of mechanical and mechanobiological vascular tissue properties is the first stage in the understanding of mechanisms that regulate the vessel behaviour.

As it was indicated in Section 1.5 of Chapter 1, a wide variety of mechanical tests have been developed in order to obtain the macroscopic mechanical properties of soft biological tissues, which can be classified into simple tension tests, planar biaxial tests, and inflation tests. Each of these methods present advantages and drawbacks which

determine their applicability on the different tissues. Nevertheless, all of them have been applied to the measurement of the mechanical response of blood vessels (Fung *et al.*, 1979; Vande Geest *et al.*, 2004).

Simple tension tests are the most versatile and widely used procedure to get mechanical properties of soft biological materials due to its simplicity both in preparation of the sample, developing of the tests process, measuring of data, and interpretation of the obtained results (Hayashi *et al.*, 1981; Hayashi and Imai, 1997). Nevertheless, this method presents several drawbacks for the non isotropic materials group, where most of the biological soft tissues are included. The main disadvantage of the application of simple tension tests to the determination of the mechanical properties of anisotropic soft biological tissues is that they decouple the mechanical response of the tissue in the test direction, which makes it impossible to determine the mechanical properties of a three-dimensional material depending on the load direction (Fung *et al.*, 1979; Hayashi *et al.*, 1981). This shortcoming may be partially overcome by carrying out tests in different directions, so additional information about the mechanical properties of the tissue is obtained (Carmines *et al.*, 1991).

Regarding planar biaxial tests, they were firstly used in biomechanics for the determination of the mechanical properties of skin (Lanir and Fung, 1974a,b). Later,they were applied to other planar biological tissues and, specifically, to the determination of the mechanical properties of blood vessels (see e.g, Vande Geest *et al.*, 2004; Pandit *et al.*, 2005). Biaxial tests provide more accurate information than simple tension tests about the material since they account for a loading state very similar to the physiological one, and measurements are simultaneously obtained in two directions. Nevertheless, they are difficult to perform, especially when dealing with small samples since the preparation of tissue samples for biaxial tests requires a more complicated procedure. The complex mechanical behaviour of soft tissues (Sacks, 2000) together with the strong influence of the boundary conditions, which limit the validity of the analyses to a small central portion of the test sample in the measurements (Sun *et al.*, 2005; Cox *et al.*, 2006), and the little standardization of this method make difficult the spreading of biaxial tests.

In which the application of inflation tests to the determination of the mechanical properties of biological tissues is concerned, their most noticeable advantage is that they allow getting measurements of the response of the tissue of interest in a configuration that is very close to the real one. This feature is certainly satisfied in the testing of those organs which are subjected to a load due to a fluid in the *in vivo* configuration, such as the blood vessels. Furthermore, the preparation of the test samples is simplified, since the whole organ is tested at once and, therefore, there is no need to cut the vessel in rectangular or squared pieces, what could cause alterations in the tissue. Regarding the deformation state caused by the inflation tests, they provoke the loading of vessels in multiple directions simultaneously, as well as planar biaxial tests, what supplies more exact information about tissue functioning. Because of these reasons, inflation test

has been employed to determine the mechanical properties of different vessels (Hayashi *et al.*, 1980; Takamizawa and Hayashi, 1987; Hayashi *et al.*, 2003; Schulze-Bauer *et al.*, 2003; Van Andel *et al.*, 2003). Moreover, the particular geometry and small size of the tissue samples lead sometimes to the application of this method, since it allows testing small size samples.

Additionally to the mechanical properties, it is also necessary to determine the configuration in which vascular tissue is found *in vivo* conditions. In this regard, it is of great relevance to consider the existence of residual stresses (Fung, 1990). Their presence in blood vessels is revealed when an unloaded vessel is cut, which makes part of the residual stress to be released, and a new equilibrium configuration to be reached. Then, the strain caused by that stress releasing can be measured by comparing both equilibrium configurations (see e.g., Vaishnav and Vossoughi, 1987; Matsumoto and Hayashi, 1994, 1996).

With these considerations at hand, the use of experimental techniques is of crucial importance for understanding pathologies, and in particular, the effect of these pathologies on the mechanics of soft tissues. Due to the high impact of diseases related to the arterial system such as the atherosclerosis, most of the experimental researches are devoted to the study of arteries, specifically, those arteries related to the most extended pathologies as coronary artery. A huge amount of work has been done in order to obtain the mechanical properties of this group of arteries, both in animals (Vaishnav *et al.*, 1973; Carmines *et al.*, 1991; Pandit *et al.*, 2005; Wang *et al.*, 2006) and in humans (Gow and Hadfield, 1979; Ozolanta *et al.*, 1998; Holzapfel *et al.*, 2005b; Tracqui *et al.*, 2011). Another arteries such as the aorta (Wolinsky and Glagov, 1964; Carew *et al.*, 1968; Saini *et al.*, 1995; Patel *et al.*, 1969; Guo and Kassab, 2004), or carotid arteries (Zhao *et al.*, 2002; Fridez *et al.*, 2003; Roy *et al.*, 2005; García *et al.*, 2011) have been also studied in depth. Those experiments reveal that artery tissue passive behaviour is highly non-linear and anisotropic under elastic finite strains, which is usually modelled within the framework of hyperelasticity.

Within the atherosclerosis framework, several experimental studies showed that this disease modifies the mechanical properties of the arterial tissue where inflammatory, biological and mechanical processes act in concert to remodel the arterial wall structure and composition (Tracqui *et al.*, 2011). Therefore, the study of the change of the morphology and mechanical properties during the atheroma plaque development is particularly important to understand the mechanisms of vascular adaptation in response to changes in physical stress. Although histopathological analyses of postmortem specimens have provided important data on histological features of ruptured human plaques, there is an urgent need for good representative animal models of plaque rupture. Such experimental models would allow investigators to examine the events leading to plaque rupture and the rupture itself prospectively (Jawien *et al.*, 2004). Moreover, it has been proved that the benefits of the use of animals in cardiovascular research are invaluable to increase the understanding of those diseases or processes occurred in humans (Zaragoza

et al., 2011).

Due to the existence of this evident need of modelling atherosclerosis disease through animal models, numerous animal species have been used to study the pathogenesis and potential treatment of the lesions of this disease (see e.g., Wagner, 1978; Reitman *et al.*, 1982; Buja *et al.*, 1983; Faggiotto *et al.*, 1984; Schwartz *et al.*, 1985) as it was exposed in Subsection 1.5.2 of Chapter 1. Nevertheless, over the past two decades the laboratory mouse has emerged as the preferred model system for biomedical cardiovascular research. Atherosclerosis is a disease that develops very slowly and leads to clinical events late in life. Mice have a short life span and develop atherosclerosis in a matter of weeks or months, compared to several decades in humans. The outstanding success of this animal model is due to its ready availability, relatively easy breeding and colony maintenance, spontaneous elevated cholesterol levels and rapid development of atherosclerotic lesions with histopathological progression, similar to that found in humans (Plump *et al.*, 1992). Moreover, they are small in size and thus are easy to house and can be maintained at low costs. However, with the small body size it follows limitations in amount of tissue and blood samples that can be collected.

However, atherosclerosis does not develop spontaneously in any animal species and mice are no exception, this fact is mainly related to the lipid profile of these animals, with high HDL levels and low LDL levels, which significantly differ from humans (Smith and Breslow, 1997). However, targeted deletion of specific genes (knockout) can provide strains that develop atherosclerosis. Gene targeting in mice via homologous recombination in embryonic stem cells was developed during the latter half of the 1980s (Doetschman *et al.*, 1987; Thomas and Capecchi, 1987; Zhang *et al.*, 1992) and revolutionized the use of mice as genetic tools for biomedical research. This technique allows precise and predetermined changes in a chosen mouse gene and allows their consequences to be studied in living animals. One such mouse strain is ApoE$^{-/-}$ mice, where the gene for apolipoprotein E is knocked out in order to stimulate atherosclerosis lesions. Thus, these mice display severe hypercholesterolemia and spontaneously develop atherosclerosis (Breslow, 1993), and they have emerged as the preferred model animal for atherosclerosis research (see e.g., Zhang *et al.*, 1992; Nakashima *et al.*, 1994; Daugherty, 2002; Coleman *et al.*, 2006). Therefore, in the case of the present Thesis, ApoE$^{-/-}$ and C57BL/6J wild type mice as control group have been chosen as animal models to obtain the mechanical response of atherosclerotic blood vessels.

Several studies have investigated the morphological, structural, and biochemical changes of the aorta during development as well as the relation between these changes and the mechanics of the aorta (Davis, 1995; Wong and Langille, 1996; Machii and Becker, 1997; Wells *et al.*, 1999; Katsuda *et al.*, 2002; Huang *et al.*, 2006). These studies confirmed the aorta to increase its stenosis ratio, wall thickness, and mechanical stiffness during development and, atherosclerotic plaque appears throughout the arterial tree, with the heaviest plaque seen in the aortic arch (Nakashima *et al.*, 1994). Further, there has been little attention directed towards quantifying the mechanical properties

of plaques in the ApoE$^{-/-}$ mice, even though computational models can now predict stresses in these lesions such as the study of Vengrenyuk *et al.* (2010) that used histology based finite element analysis to evaluate peak circumferential stresses in aortic and brachiocephalic arteries lesions from six 42-56 week-old fat-fed ApoE$^{-/-}$, or the work performed by Ohayon *et al.* (2012) that proposed an original finite element strategy that reconstructs the *in vivo* stress/strain distributions in ApoE$^{-/-}$ atherosclerotic vessels based on cross substitution of ApoE$^{-/-}$ mouse and human plaque components stiffnesses and including residual stress, by means of the opening angle measurement of the aorta blood vessel, or the research work of Broisat *et al.* (2011) that combined immunohistology, atomic force microscopy measurements, and finite element computational analysis for the accurate quantification of stress amplitude and distribution in ApoE$^{-/-}$ mice aortic atherosclerotic lesions. Most of the studies that reveals the underlying mechanics of ApoE$^{-/-}$ mice have focused mainly on the proximal aorta, and none have systematically characterized the geometric and mechanical properties along the entire length of the aorta for young and old ApoE$^{-/-}$ mice. Guo and Kassab (2003) studied the mechanical properties along entire length of the aorta, and analogous, Santelices *et al.* (2007) developed and rigorously validated an *ex vivo* system for measuring stiffness of the mouse aorta, however both studies were focused on the C57BL/6J strain, and it has been widely reported ApoE$^{-/-}$ is the only model genetically engineered that develops extensive atherosclerotic lesions on a chow diet (Jawien *et al.*, 2004). In the same direction, (Agianniotis *et al.*, 2012a) studied the mechanical properties of the thoracic aorta of C57BL/6J mice and described experimentally the active stress under isometric conditions and proposed an analytical expression for the active stress component in the axial direction. Nevertheless, in a more recent work performed by the same authors (Agianniotis and Stergiopulos, 2012b), they quantified the dysfunction of thoracic aortas of ApoE$^{-/-}$ mice, determined structural and elastic properties by means of a biaxial experimental device for the inflation and extension of mechanical tests at three different axial stretches, and provided histological data of these thoracic aortas of ApoE$^{-/-}$ mice, but their study just a population of six young 10-12 weeks old ApoE$^{-/-}$ and C57BL/6J wild type mice of both sexes. Hayenga *et al.* (2011) assessed the regional atherosclerotic plaque properties in ApoE$^{-/-}$ mice by means of atomic force, immunofluroescence, and light microscopy and, Tracqui *et al.* (2011) quantified the highly heterogeneous mechanical characteristics of atherosclerotic plaques by force mapping experiments using atomic force microscopy conducted in ApoE$^{-/-}$ mice aged 30 weeks. In order to understand the aortic aneurysms behaviour in mice, several studies have been accomplished (Daughtery and Cassis, 2004; Sheth *et al.*, 2010; Goergen *et al.*, 2011), among which could be highlighted the study of (Collins *et al.*, 2011) that compared the biaxial mechanical behaviors of suprarenal and infrarenal abdominal aorta of six male mice aged from 8 to 12 week and quantify the data using a nonlinear constitutive relation. Moreover, other mice blood vessels affected by the atherosclerosis such as carotid arteries have been characterized (Dye *et al.*, 2007; Humphrey *et al.*,

2009; Eberth *et al.*, 2011).

The presented work is focussed on ApoE$^{-/-}$ and C57BL/6J wild type mice because ApoE$^{-/-}$ mice is the most widely strain used for the study of atherosclerosis lesions since they are predisposed to hypercholestermia (Zhang *et al.*, 1992). C57BL/6J wild type mice, which were used as control, are best known of all inbred strains. In order to characterize mechanically the aortic tissue of these mice strains, inflation test performed on the aorta blood vessel was chosen due to the size of the sample studied. These experimental tests were developed to obtain a systematic set of data on the mechanical response along the entire aortic root in ApoE$^{-/-}$ and C57BL/6J mice for a set of 5 animals for different time on a specific diet; 10, 20, 30 and 40 weeks, which makes a total of 40 animals studied (n=5 mice in each group). For this purpose, a special designed inflation setup system was designed. The ascending aorta of each mouse was cannulated near the aortic valve, and the aorta was preconditioned with several cyclic changes in pressure. The perfusion pressure was then increased in 25-mmHg increments from 0 to 250 mmHg. Apart from experimental inflation test, the progressive change of the morphology and its correlation with mechanical properties of the whole aorta tree of these strains was obtained by histological analysis, morphological lesion evaluations, residual stress assessments and other anatomical measurements such as gain in body weight. Furthermore, the results of the mechanical and anatomical analysis were submitted to statistical analyses. Such statistical analyses were conduced in order to study the possible significant variations in the behavior between the aortic tissue of ApoE$^{-/-}$ and control mice by means of a paired one-tailed t-test which is based solely on the order in which the observations from the two samples fall, Lilliefors test which is used to test the null hypothesis that data come from a normally distributed population, and Wilcoxon rank sum test which is a nonparametric alternative to the two sample Student's t-test. A $p < 0.05$ was established to indicate statistical significance for all the statistical analysis performed.

5.2 Murine and human cardiovascular system

The cardiovascular systems in humans and mice, with the exception of cardiac size, rapid heart rate, and small variations in the anatomy, are very similar. The mouse heart is about the same size as a pencil eraser, weighs approximately from 100 to 200 mg and beats around 500 to 800 times per minute. The human heart weighs about 250 to 300 gr and beats an average of 60 to 70 times per minute (Cook, 1965; Wessel and Sedmera, 2003; Hoyt Jr. *et al.*, 2007). Because the murine body is parallel to the ground, the mouse heart does not rest on the diaphragm like the human heart and, therefore, has more room to move around within the pericardial cavity. As such, the murine heart has more of an ellipsoidal, like a "rugby ball" shape (Iwaki *et al.*, 2001; Wessel and Sedmera, 2003; Hoyt Jr. *et al.*, 2007). Nevertheless, despite the small size of the mouse, many researchers have turned to mouse models for studying many physiologic processes

due to recent advances in science and technology. An important milestone has been the completion of the sequencing of both the mouse (Mouse genome sequencing consortium, 2002) and human genomes (Venter *et al.*, 2001). This fact has resulted in a number of genetic and physical maps of the mouse genome being published that demonstrated a great deal of synteny between the two species. In classical genetics, synteny describes the physical co-localization of genetic loci on the same chromosome within an individual or species. Despite their clear physical differences, genes from humans and mice are approximately 99% identical (Mouse genome sequencing consortium, 2002) with approximately 30.000 - 40.000 human genes having murine counterparts (Grieder and Strandberg, 2003).

Although pathologies like those developed by humans can be often replicated in mice, the phenotype does not always model all aspects of the human diseases precisely, even when identical genetic defects to those occurring in humans are introduced into the mouse genome. In many cases, however, phenotypic differences between humans and mice are not because there is a fundamental difference in the biology of the gene products in the two species but is due to differences in the overall physiologic set point of the system in mice and in humans. Considering that the two species differ greatly in body size and heart rate, species differences are expected. One must also bear in mind that humans are genetically very diverse, whereas a study made in genetically uniform mice is comparable to studying a single individual out of all human populations (Wessel and Sedmera, 2003; Hoyt Jr. *et al.*, 2007).

However, despite the fact that "mice are not humans", over the last decade, mice have become the predominant species used to create models of atherosclerosis. The initial interest was based on the great diversity of inbred strains with defined genetic backgrounds that provides a means of linking genes to the development of atherosclerosis. More recently, the ability to genetically modify mice to over or under express specific genes has facilitated the definition of pathways in the atherogenic process. All of the current mouse models of atherosclerosis are based on perturbations of lipoprotein metabolism through dietary and genetic manipulations. Although hyperlipidemia is necessary for the development of atherosclerosis, mouse models have demonstrated that many non-lipid factors can influence the severity and characteristics of lesions (Daugherty, 2002).

Additionally, several research studies have focussed on the determination of the similarities and differences in the developmental cardiac anatomy in mice and human species in order to extrapolate the obtained results in mice experiments to the human reality (Hamlin and Altschuld, 2001; Mestas and Hughes, 2001; Wessel and Sedmera, 2003, among many others). From the data presented in these studies, it can be concluded that, apart from the obvious differences in size, the mouse and human cardiovascular systems are anatomically remarkably similar throughout development (Wessel and Sedmera, 2003). Figure 5.1 illustrates the basic cardiovascular murine anatomy, which could be compared with the human cardiovascular anatomy shows in Figure 1.1 in Chapter

1. Arteries, which carry oxygen-rich blood away from the heart, are depicted in Figure 5.1.a, while veins, which carry oxygen-poor blood back to the heart, are shown in Figure 5.1.b. For more details of the gross anatomy of the mouse, the readers are referred to Cook (1965) or Iwaki *et al.* (2001).

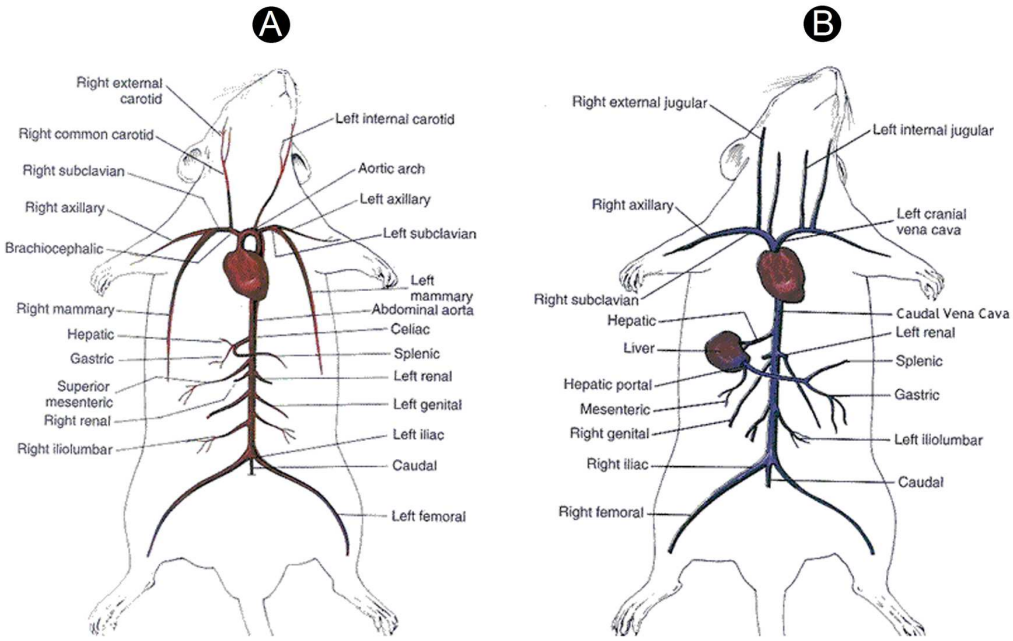

Figure 5.1: Murine cardiovascular system. A - Arteries circulation system. B - Veins circulation system.

5.3 Experimental study of the properties of the murine aortic tree

5.3.1 Specimens

A set of 5 animals were sacrificed at 10, 20, 30 and 40 weeks on a diet for ApoE$^{-/-}$ and C57BL/6 control groups, which makes a total of 40 individuals (n=5 mice in each group considered) which were used for the experiments, i.e, 5 animals of 2 different strains were sacrificed at 4 different ages on a diet. C57BL/6J wild type mice were used as control mice since the anatomical differences and atherosclerosis lesions between these strains have been assessed by Maeda *et al.* (2007b), suggesting that the differences found may contribute to the effects of genetic background on atherosclerosis. Female specimens were used in this study since the effect of gender on the development of aortic atherosclerotic lesions in ApoE$^{-/-}$ mice has been reported in several studies (King *et al.*, 2007; Smith *et al.*, 2010), having the female ApoE$^{-/-}$ mice marked increases in atherosclerotic lesions compared to males. It should be noted that the

sacrifice of mice was performed by skilled veterinarians under the approval of the Animal Experimentation Ethics Commission of the University of Zaragoza and they have also been performed in accordance with the national ethical guidelines and directives of the European Council (ETS 123) and European Union (Council Directive 86/609/EEC Norm, incorporated into Spanish legislation through the RD 1021/2005).

Basically, two different mechanical and statistical comparisons have been made in the presented experimental study of the progressive change of the morphology and mechanical properties along the aorta tree of ApoE$^{-/-}$ and C57BL/6 (control) mice:

1. At the same age: ApoE$^{-/-}$ and control mice have been compared in order to analyze the development of atheroma plaque in both strains.

2. At different ages: ApoE$^{-/-}$ mice have been compared between themselves and control mice between themselves as well in order to study the effect of diet and age in each strain.

Female ApoE$^{-/-}$ and C57BL/6 mice (control) strains housed in a temperature-controlled room with a 12-hour light/dark cycle and had free access to water and food, have been used in this experimental study. At the time they were aged 7 weeks, ApoE$^{-/-}$ mice were fed on a Harlan-Teklad 88137 Western Diet (hyper-lipidic diet) in order to ease the development of atheroma plaque and C57BL/6 mice have been maintained on a normal chow diet.

Figure 5.2 shows the formula of the Harlan-Teklad 88137 Western Diet. In % by weight, this diet mainly consists of 17.3% of proteins, 48.5 of carbohydrate and 21.2% of fat amongst others and, in % kcal from is formed by 15.2% of proteins, 42.7 of carbohydrate and 42% of fat amongst others. And chiefly, the source of fat cames from the anhydrous milk fat. These overall levels of fat and the saturated nature of the fat are representative of diets that are linked to risk of cardiovascular diseases in humans. The formula originated with researchers at Rockefeller University and is used primarily with genetically manipulated mouse models that are susceptible to atherosclerosis. The diet may also be useful in diet-induced obesity, diabetes, and metabolic syndrome models.

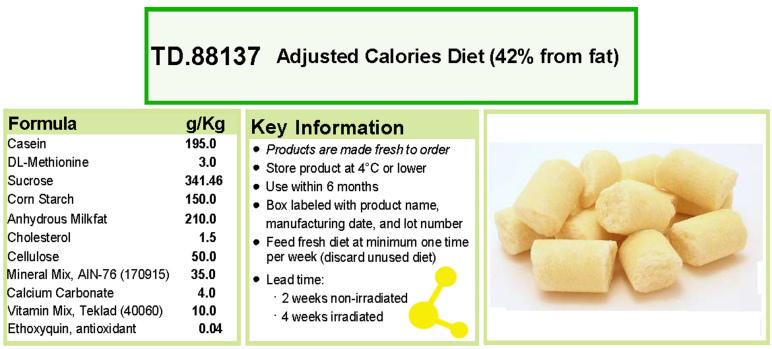

TD.88137 Adjusted Calories Diet (42% from fat)

Formula	g/Kg
Casein	195.0
DL-Methionine	3.0
Sucrose	341.46
Corn Starch	150.0
Anhydrous Milkfat	210.0
Cholesterol	1.5
Cellulose	50.0
Mineral Mix, AIN-76 (170915)	35.0
Calcium Carbonate	4.0
Vitamin Mix, Teklad (40060)	10.0
Ethoxyquin, antioxidant	0.04

Key Information

- *Products are made fresh to order*
- Store product at 4°C or lower
- Use within 6 months
- Box labeled with product name, manufacturing date, and lot number
- Feed fresh diet at minimum one time per week (discard unused diet)
- Lead time:
  - 2 weeks non-irradiated
  - 4 weeks irradiated

Figure 5.2: Harlan-Teklad 88137 Western Diet data sheet.

The animals were sacrificed by anesthetic overdose of anesthesia; *Sedator DFV*® and *Imalgène*® *(Merial)*. Specifically, the dose which contained 0.3 ml of sedator, which has 1 mg of medetomidine hydrochloride for each ml of product, and 0.23 ml of imalgène, which has 0.1 gr of Ketamine Hydrochloride for each milligram of product have been punctured to each individual on the heart of the animals, using a needle mounted on a syringe and, causing it a painless death.

Figure 5.3 shows a scheme of the specimens tested grouped according their strain and time on a diet, and the mentioned different comparisons performed between them.

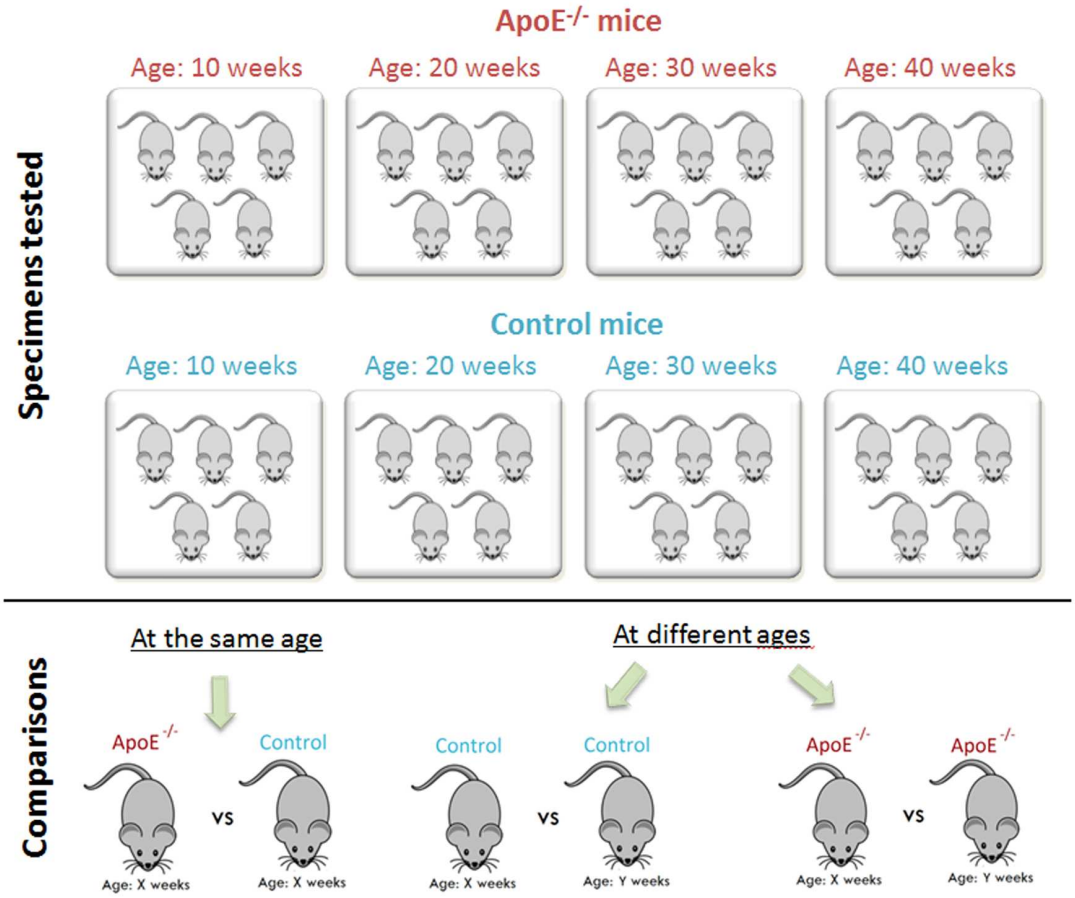

Figure 5.3: Scheme of the specimens tested and the comparisons performed between them.

5.3.2 Dissection protocol

After the animals were sacrificed, blood samples were taken directly from the right ventricle of the heart for further analysis of total cholesterol and triglycerides by commercially available kits. After that, the specimen was carefully dissected by a veterinarian scientist. Then, all the internal organs including stomach, intestines, lungs, liver,

and kidney, were removed in order to have a complete sight of the aortic tree, from the heart to the iliac bifurcation. These organs were preserved in formaldehyde to further analysis of them such as lipid levels or anomaly detection. The ramification of the aortic tree were bound and burned with a scalpel in order to remain the aorta as a closed circuit, having the smallest number of leaks. At the end of the dissection process, the aorta from the aortic valve to the common iliac bifurcation was carefully exposed on the anterior portion, dissected away the surrounding connective and adipose tissue from the outer surface of the vessel and leaving the posterior portion attached. This procedure was very carefully developed in order to avoid damaging aorta structure, what was not always achieved. However, the experiments in which the aorta dissection process described above was inadequate or failed, were rejected. Moreover, all the experimental test and measurements were performed immediately after the sacrifice of the animal in order to minimize the variation of the mechanical properties due to tissue degeneration. Moreover, the animals were often refreshed by ion-free physiologic saline solution (0.9% NaCl) at 4° C in order to minimize tissue degradation. For all the dissection process described, several labware tools and utensils were used. These laboratory instruments were:

- A electronic cautery: To suture the aorta branches in order to avoid leaks of fluid during the experimental inflation tests.
- Microsurgical instruments: This instrument set, which is shown in Figure 5.4, includes different sizes of tweezers, scissors, needles, cannulas and clamps. Microsurgical instruments are needed due to the small size of the mouse aortic tree. Furthermore, special care should be taken for not puncturing the aorta which would produce leaks during the inflation tests.
- Suture thread so as to tie the aortic blanches.
- Bio adhesive silicone elastomer for the leaks.

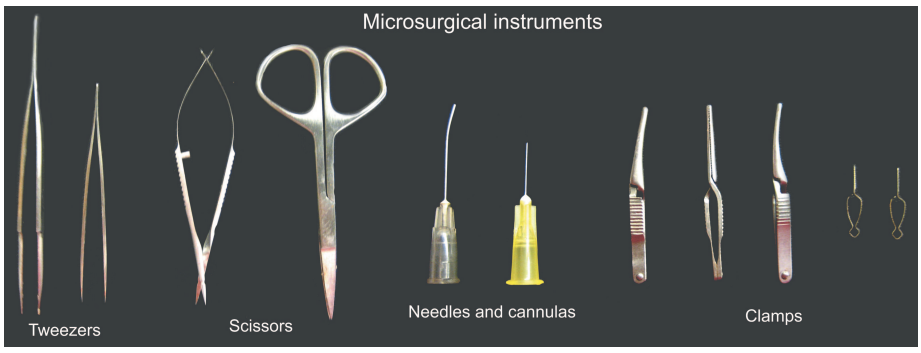

Figure 5.4: Labware tools and utensils used to the dissection process.

5.3.3 Experimental protocol

In order to characterize the aorta tissue of ApoE$^{-/-}$ and control mice, several type of analysis were carried out. Anatomical analysis which consisted on body weight measurements and non-invasive evaluations of atherosclerosis lesions, histological study by means of different stainings such as Hematoxiling and Eosin or Red Oil and mechanical analysis which involved inflation test and measurements of the initial stretches in longitudinal direction have been developed.

Once the specimen has been completely dissected, photographies from different perspectives were taken using the *Mantis Elite*® magnifying glass from *Vision Engineering*®, which is a "eyepieceless" stereo microscope, with truly superb 3D imaging and magnification options up to x20 (see the specifications of this magnifying glass in Figure 5.5), in order to perform a non-invasive evaluation of atherosclerosis lesions which allow us to define and quantify the zones with a high probability of atheroma plaque appearing at different time on a diet.

Optical Data

Objective Lenses	Working Distance	Field of View
x2	160mm	57.0mm
x4	96mm	34.0mm
x6	68mm	23.0mm
x6 SLWD*	112mm	20.0mm
x8	59mm	17.0mm
x10	54mm	13.5mm
x15	40mm	8.8mm
x20	29mm	6.5mm

* cannot be used together with x2 or x20 objective lens

Illumination

Mantis Elite	Substage (Bench Stand Only)
24 LEDs	13 LEDs
11,000 LUX	1,200 - 4,000 LUX

Power Supply

9V DC external plug transformer, available in all worldwide plug configurations.

Figure 5.5: Technical specifications of the *Mantis Elite*® magnifying glass.

Next, the animal was cannulated through the beginning of its intercostal aorta by a 18-gauge needle (1.270 mm and 0.838 mm of nominal outer and inner diameter, respectively) at the beginning of the intercostal aorta, in order to perform the experimental inflation test. This inflation test has been achieved by means of a inflation *in situ* system designed in order to measure the pressure-diameter relationship and compare the aorta stiffness of each mice group. Furthermore, equivalent arterial stiffness was computed from the pressure-stretch curves, and different moduli were computed to compare the stiffness of the aorta at different pressure levels. Three different modules were defined depending the pressure levels; secant modulus which indicates the global stiffness (from pressure 0 mmHg to 250 mmHg), elastic modulus which shows the stiffness at low pressures (from 0 mmHg to 50 mmHg) and tangent modulus which points out the stiffness at high pressures (from 200 mmHg to 250 mmHg).

After the experimental inflation test is finished and before the aorta harvesting, separated markers were placed along the aorta length in order to have a reference to determine its length in the *in situ* configuration. Photographies from different perspectives were taken and, a ruler and a specially-designed cube of 1 cm length were used as scale measure to determine the real size of taken pictures, being able to reconstruct the 3D real geometry by means of the different perspectives of the cube using a software such as the PhotoModeler, which is a software application that performs image-based modeling and close range photogrammetry - producing 3D models and measurements from photography. Then, the aortic tree was harvested. Just after the cuts, the aorta suffered a marked contraction in the axial direction associated to the existence of longitudinal residual stresses. In order to quantify the axial stretch along this blood vessel, photographies of the aorta were taken immediately after harvesting. Again, a ruler and the metal cube were placed close to the samples to have a reference of the real scale so that the *ex situ* length could be obtained from the photographies, see Figure 5.18. To get an estimation of the longitudinal residual strain field, the distance before (*in situ* length) and after harvesting (*ex situ* length) was calculated. Finally, the samples of the aortic tree were conserved frozen for their histological and immunochemistry studies in order to observe the murine aorta microstructure.

Furthermore, statistical analyses were performed on the obtained anatomical and mechanical results with the purpose of showing statistical significant differences in the comparisons studied. These results were compared by means of the t-test for paired samples, the Lilliefors test in order to check the normality of the distribution, and the Wilcoxon rank sum test, which is usually taught as nonparametric alternatives for the Student's t-test in situations where the data appear to arise from non-normal distributions. All these tests were performed at 5% significance, thus a $p < 0.05$ was established to indicate statistical significance for all the statistical analysis performed. For further details of the statistical test used to perform the statistical analysis, see e.g. Wasserman (2005); Rice (2006).

5.4 Anatomical analysis

The anatomical analysis, which consists of body weight and morphological observations of the atherosclerosis lesions, reveals differences between the behaviour of both strains and enable comparing directly the data of ApoE$^{-/-}$ and control mice.

5.4.1 Body weight measurements

Body weight measurements of each animal studied were performed once weekly at the same hour of the day using a digital balance, in order to observe the weight evolution of each of the 8 animal groups considered. The gain in body weight was calculated using the body weight values at the beginning of the diet and compared with body weight values until the sacrifice. Figure 5.6 shows this gain in body weight (average $\pm$ SD) for

ApoE$^{-/-}$ and control mice. For the ApoE$^{-/-}$ mice, a linear relationship with age is observed ($R^2 = 0.94$). However, the weight remains practically constant for the control mice groups, reflecting the different behavior between animals feeding on a Western-type and normal diet. Statistical analyses of these results were carried out in order to find significant dependencies among the different groups studied. Comparing the ApoE$^{-/-}$ and control gain in body weight results at the same time on diet, the means are always significantly different ($p < 0.0005$ for 10, 30 and 40 weeks and $p < 0.05$ for 20 weeks), showing the effect of the diet on both groups, even in the first weeks of the diet. The statistical analysis developed in order to find significant dependencies among the same strain at different times on diet, reveals that no statistical significance was found between control mice at different times on diet, however for ApoE$^{-/-}$ mice at different times on diet, a statistical significance ($p < 0.005$ between ApoE$^{-/-}$ mice aged 10 and 40 weeks, $p < 0.05$ between ApoE$^{-/-}$ mice aged 10 and 30 weeks and $p < 0.005$ between ApoE$^{-/-}$ mice aged 20 and 40 weeks) was exhibited (see Figure 5.6).

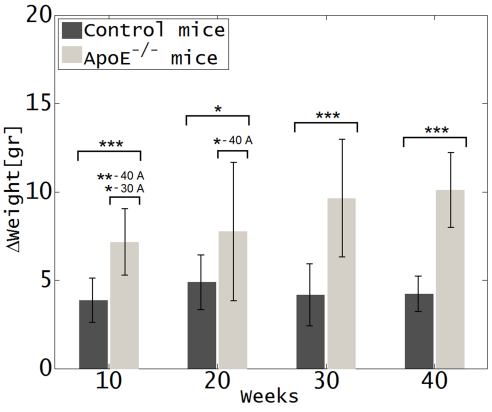

Figure 5.6: Variation in mouse body weight for each strain at different time on a diet (mean ± SD). For the comparisons between groups of the same strain, the means of group n and the groups marked with *-n are significantly different with the probability $*p < 0.05$, $**p < 0.005$ and $***p < 0.0005$, being appointed the ApoE$^{-/-}$ and control groups by the letters A and C, respectively. For the comparisons between both strains at the same time on diet, the means which are significantly different are just marked with $*p < 0.05$, $**p < 0.005$ and $***p < 0.0005$.

Additionally, Figure 5.7 shows the absolute mean values (mean ± SD) in the evolution on body weight (in grams) for the ApoE$^{-/-}$ mice at the four different ages studied. The growth rate is always positive, thus the ApoE$^{-/-}$ mice are fatter with the evolution time. Furthermore, a great gain in body weight is observed in the first weeks, and after that the increase of gain in body week is less pronounced. Body weight did not vary significantly in the control groups.

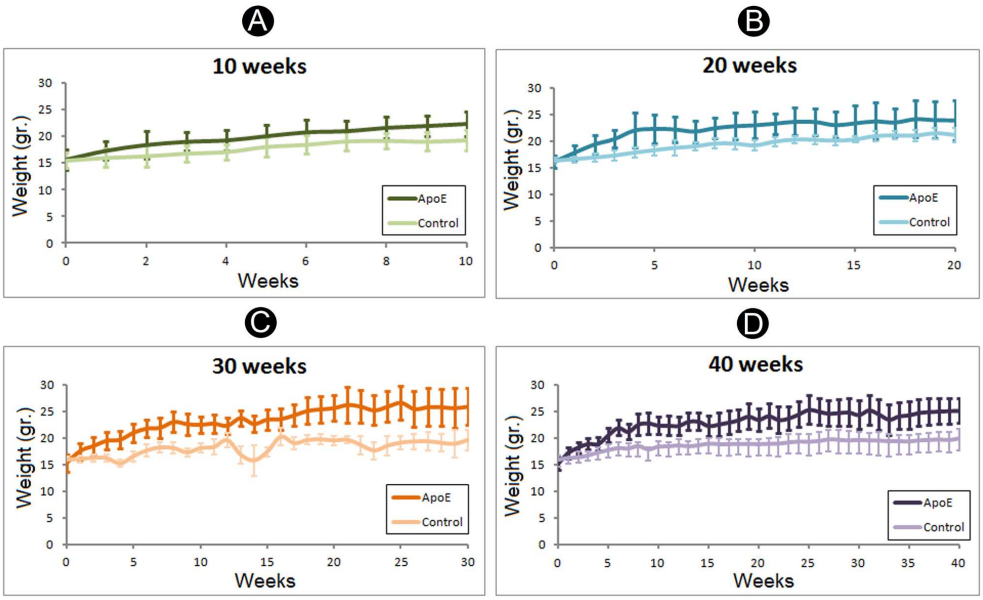

Figure 5.7: Mean values in the evolution on body weight (in grams) for the ApoE$^{-/-}$ mice at the four different ages studied.

5.4.2 Evaluation of the atherosclerosis lesions

Hemodynamic features such as blood flow separation and circulation, which result in a weak hemodynamic shear stress, appear to play a major role in the development of atherosclerotic plaque (Zarins *et al.*, 1983; VanderLaan *et al.*, 2004). In the aorta blood vessel, susceptible sites for plaque formation are found at branch points of the tree and in the lesser curvature radius of the aorta, where blood flow is characterized by low shear, oscillatory and turbulent flow. Thence, in order to obtain the distribution of atherosclerotic lesions over time in ApoE$^{-/-}$ and control mice, a non-invasive evaluation of atherosclerosis lesions using a powerful magnifying glass have been carried out. The zones with a high level of atheroma plaque are defined and quantified for both ApoE$^{-/-}$ and control mice by means of morphological observations from the different perspective photographies that were taken before the inflation experimental test.

Conducive to define a comparison measurement of this study of the atheroma plaque development at different times on diet, four levels of atheroma plaque quantity (l_i with $i = 1, 2, 3$ and 4) were establish, which correspond to 0%, 33%, 66% and 100% of atheroma plaque found. Moreover, they were normalized from 0 to 1, being assigned the 0 value for zones without atheroma plaque and 1 value for zones with atheroma plaque in everywhere. Consequently, for each mice specimen, a level of atheroma plaque was assigned to the different zones of the aorta and its main branches according the observations performed from the photographies taken using a magnifying glass. Thus, the normalized mean level of atheroma plaque found in each zone, l_{plaque}, was computed as:

$$l_{plaque} = \frac{\sum_{i=1}^{4} (l_i \cdot n_i)}{n}, \tag{5.1}$$

were n_i, i=1, 2, 3, and 4, are the number of animals with an atheroma plaque quantity of l_i, i=1, 2, 3, and 4, respectively. And n is the number of specimens in each group considered ($n = 5$).

The morphological observations of the site preferences for lesion development under the influence of strain and age, have confirmed that lesions occurs only in the ApoE$^{-/-}$ mice, since no evidence of atheroma plaque development has been found on the control mice groups. As alluded to earlier, the development of atherosclerotic lesions in the vasculature of mice also occurs at very reproducible sites that are consistent with being determined predominately by the hemodynamic forces experienced by the endothelium. This distribution for ApoE$^{-/-}$ mice is depicted in Figure 5.8.a. The control mice atherosclerotic plaque distribution has not been shown due to the lack of atheroma plaque found. The normalized mean level of atheroma plaque found at different zones of the aorta and its principal branches has been plotted by the color scale on Figure 5.8.a. Sites of predilection for lesion development were indicated in red color and healthy sites were plotted in blue color.

Clearly, Figure 5.8.a shows that the severity of the lesions increases as the age advances and, the time course of lesion distribution in the aortic tree of ApoE$^{-/-}$ mice illustrates the susceptibility of the sites with low wall shear stress or highly oscillatory wall shear stress. The earliest atherosclerosis lesions begin to appear in the intersections between the thoracic aorta and its principal branches for the groups of 10 and 20 weeks on a diet. The normalized quantity of atheroma plaque found in the thoracic aorta at these weeks on a diet is low, as the green color areas shown, and really unlikely in the abdominal aorta (blue color areas). Lesions are present chiefly in the proximal aorta near the aortic sinus and around aortic valve attachment sites and at branch points of the right and left common carotid, brachiocephalic and left subclavian arteries. However, for longer times on diet there is a gradual progression of lesions from this area to other sites in the aortic tree and associated vessels. Over time, the complexity of the lesion changes and progress through the fatty streak stage of development to atheromatous plaques. Therefore, for the ApoE$^{-/-}$ group of 30 weeks aged, lesions become more severe as the red color areas indicate and, lesions have not been only found in the aorta, but also in its main branches. Thus, an important quantity of atheroma plaque is found at the thoracic aorta and its aortic arch and in the right and left common carotid, left subclavian, celiac and mesenteric arteries. Furthermore, lesions are again found in all the aortic intersections with its main branches. At this stage, the abdominal lesions start to developing, founding an normalized atheroma plaque quantity of 0.5 in the abdominal aorta and, moreover extension of the plaques into renal and common iliac arteries may occur. Finally, in the oldest mice studied, ApoE$^{-/-}$ mice of 40 weeks on a diet, atherosclerotic plaques are found practically along all the aorta, main branches

and intersections, being the normalized quantity atheroma plaque found slightly smaller in the abdominal aortic zone than in the thoracic one. Furthermore, a representative microscopic image from the thoracic aorta, the right and left common carotid arteries, left subclavian artery and the heart of each of the group studied with the main location of lesions indicated by black arrows is shown in Figure 5.8.b to illustrate the process. It is observed that the results of both photographies are consistent between them, showing that atheroma plaques in specimens aged 10 weeks could hardly find, but on the contrary, specimens which are 40 weeks old have lesions everywhere.

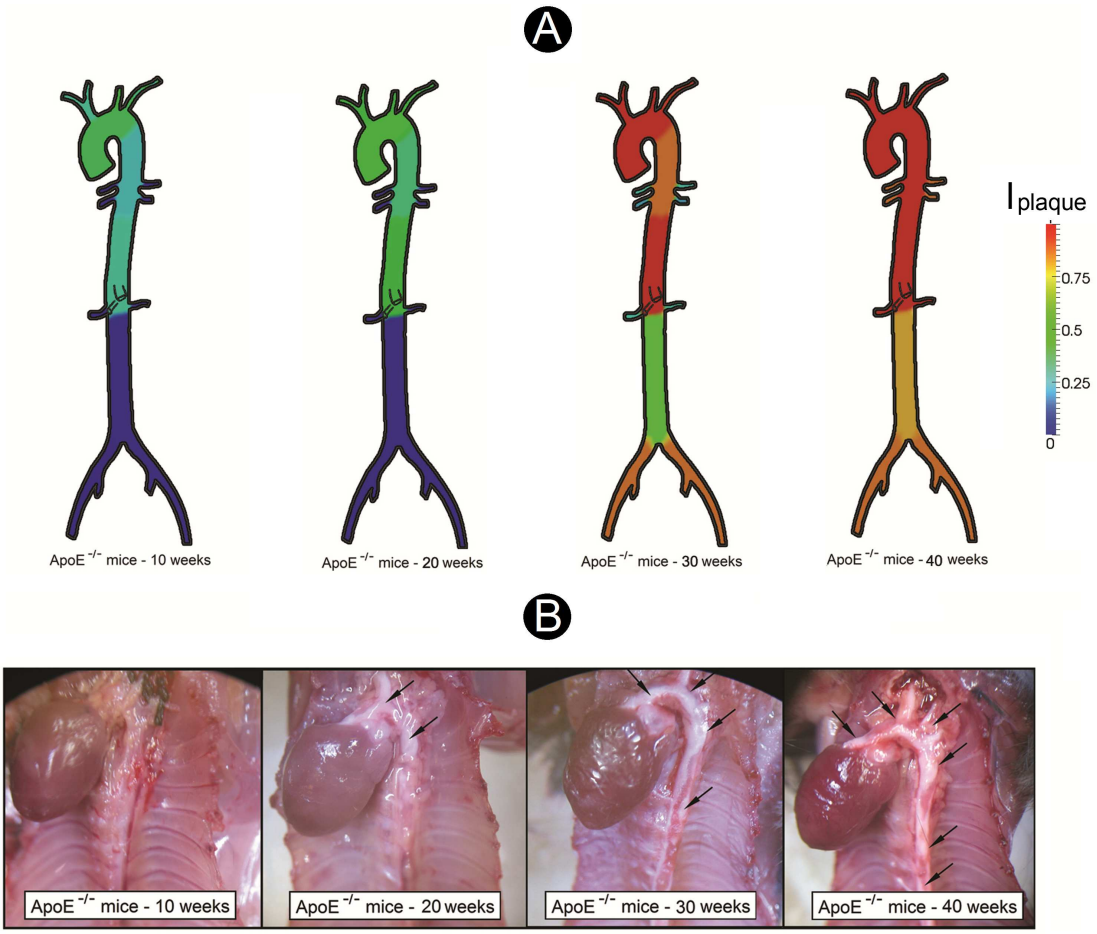

Figure 5.8: A - Graphs showing the normalized mean level of atheroma plaque found located on ApoE$^{-/-}$ mice at different sites of the aorta and its main branches for 10, 20, 30 and 40 weeks on a diet. B - Microscopic images of the thoracic aorta, the right and left common carotid arteries, left subclavian artery and the heart for ApoE$^{-/-}$ specimens of different weeks old, indicating by arrows the main atheroma plaques.

5.5 Mechanical properties analysis

The mechanical properties of the aorta mice are experimentally assessed. For this purpose, inflation tests and measures of the longitudinal residual stress were performed. Furthermore, the small size of mice has motivated the use of inflation test in order to characterize the mechanical properties of the aorta affected by the atherosclerosis disease.

5.5.1 Inflation mechanical testing

5.5.1.1 Experimental setup device

In order to obtain the different mechanical properties of ApoE$^{-/-}$ and control mice, a inflation *in situ* system has been designed. The experimental inflation test consists of measuring the outer diameter along the trunk of the aorta mice at different pressure levels to compute the aorta stiffness. Mainly, this experimental setup, which is shown in Figure 5.9, where each component part of the system has been indicated by numbers, consisted of:

1. A test cage to place the animal.
2. A syringe pump which injects phosphate buffered saline (PBS) into the mouse aorta.
3. A Hg-manometer with a data logger *OpSens*® which transduce the data from the pressure catheter.
4. A pressure catheter to measure the pressure during the development of the experimental test.
5. A plastic tube of 6 mm used to conduct the PBS solution from the syringe pump to the aorta.
6. Several plastic T-shaped connectors used to join the plastic tubes and the pressure catheter.
7. A motor which drove the syringe pump.
8. A video camera system mounted in order to measure the radial deformation. This video system consists of two cameras *Pulnix*® TM/RM-1405GE Series Gigabit Ethernet Cameras to record the whole experiment. The video recorded by this high performance digital cameras with a 1.4 megapixel sensor (4.65 μm square pixels) and image resolution of 1392 x 1040 at 30 frames per second, enable the posterior measurements of the aorta mice diameter as well as the reconstruction of the blood vessel.

9. A specially designed cube of 1 cm length which is placed close to the animal and it is used as a measurement reference.

10. A computer used as acquisition system to manage and visualize the experiment recorded by the cameras with a installed specially designed software (Termix) to control all the items namely.

11. A magnify glass used in order to observe all details of the experimental test and, check how the aorta expands.

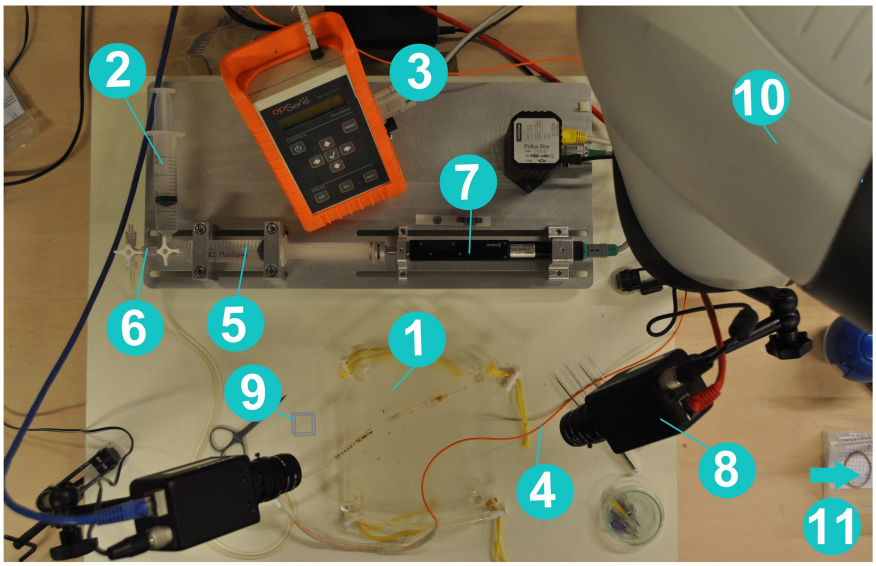

Figure 5.9: Experimental setup and mechanical testing device designed in order to evaluate the stiffness of the mouse aorta, indicating by numbers each of its component parts.

Once the animal has been killed, the aorta from the aortic valve to the common iliac bifurcation was then carefully exposed on the anterior portion, leaving the posterior portion attached. The specimen was placed horizontally in the test cage and was connected to the pump system through its ascending aorta, being the mice cannulated at the beginning of the intercostal aorta. Pressure was measured at 0 mmHg - 250 mmHg (0 kPa -33.3 kPa, respectively) by means of the Hg-manometer. The pressure transducer was connected to the pressure line between the pump and the specimen at one end and, to the computer on the other side. Information on the deformation of aortic outer diameter was provided by the two high resolution cameras, which were mounted at the lateral sides of the test cage. The cameras are placed for the purpose of taking pictures and recording from different angles, which allow afterwards a 3D reconstruction. The specially-designed cube of 1 cm length was recorded by the cameras at the same time than the experiment in order to know the real deformation measurements, being able

to reconstruct the 3D real geometry. This reconstruction will be performed by the PhotoModeler software, which creates accurate 3D models and accurate 3D measurements from photographies. The output signal of the cameras were displayed and recorded on the computer. Thereby, the computer allows us to process the whole data obtained in the experiment. Finally, the computer also controls the flow of the pump syringe system, which consists of a motor to propel PBS inside of the mice's aorta, and the pressure. Figure 5.10 shows a schematic representation of this device (Figure 5.10.a) as well as a real photography of the system (Figure 5.10.b), where each of the components described above can be easily identified.

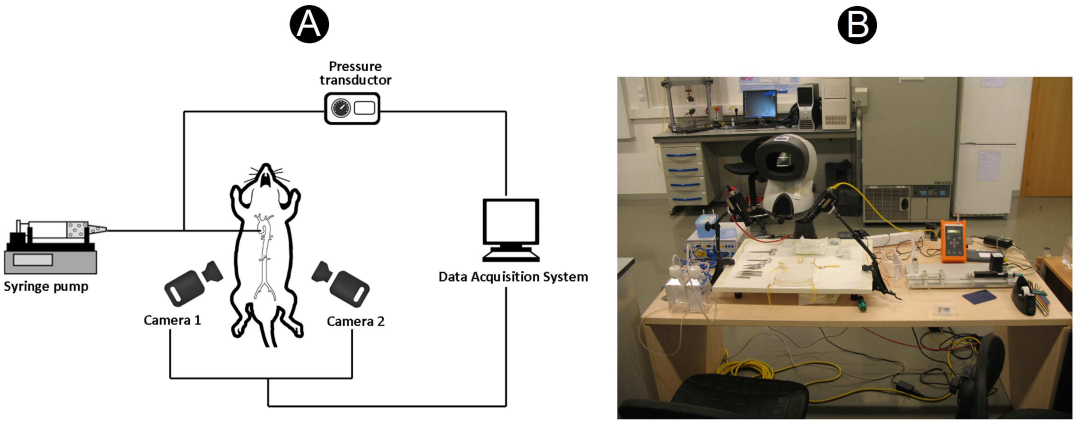

Figure 5.10: Experimental setup and mechanical testing device used to evaluate the stiffness of the mouse aorta. A - Schematic representation. B - Real device.

Furthermore, some parameters could be changed in the Termix software designed,

- Velocity of pump syringe flow. Normally, this parameter has been fixed at 0.150 mm/s.
- Approximation velocity of the pump syringe system. Usually, this value has been assumed equals to the velocity of the pump syringe system.
- Reverse velocity, as a rule taken 0.5 mm/Hg.
- Tolerance of the pressure measurements, which has been considered as 0.5 mmHg.
- Pressure range. The pressure measurements were defined as 25, 50 ,75, 100, 125, 150, 175, 200, 225 and 250 mmHg.

A screenshot of the software designed with the parameters which could be adjust in each experiment indicated is shown in Figure 5.11.

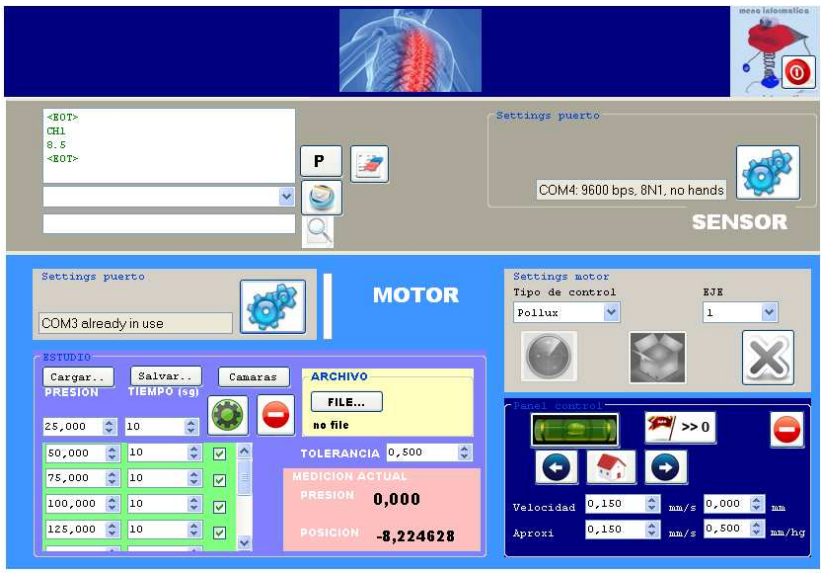

Figure 5.11: A screenshot of the software designed to the experimental inflation test.

Before to perform the experiments, several considerations should be taken. Firstly, it should be checked that there is not leaks along the aortic root and the cannula is inserted in the specimen correctly. Secondly, any air bubbles inside of the circuit should be placed since it may alter the value of the measurement. Finally, the cameras should be calibrated ir order to get a clear image. After that, the inflation test performed in order to measure the pressure-diameter-length relationship and compare the aorta stiffness of each mice group could be carried out. After all these regards, the aorta was preconditioned with three cyclic changes in pressure from 0 mmHg to 200 mmHg. Then, the perfusion pressure (Pr) was increased in 25-mmHg step increments from 0 mmHg to 250 mmHg (Guo and Kassab, 2003) and the loaded outer diameter along the trunk of the aorta at each pressure step was recorded.

5.5.1.2 Pressure-stretch behaviour

Once the experimental inflation test has been carried out, the information stored on the video recorded during the experiment and on the different taken photographies has been post-processed. Then, the blood vessel was divided into a series of short segments (about 3-4 mm per segment) and the outer diameter-pressure relation for each of the segments was measured serially in order to obtain pressure-stretch curves. As the results of the anatomical analysis carried out, the atheroma plaque development was not uniform along the whole vessel, therefore, the aortic tree was divided in three zones for the inflation test post-processing attending to the atheroma plaque quantity found. These portions of the aortic tree are; upper and lower thoracic and abdominal aorta (see Figure 5.12).

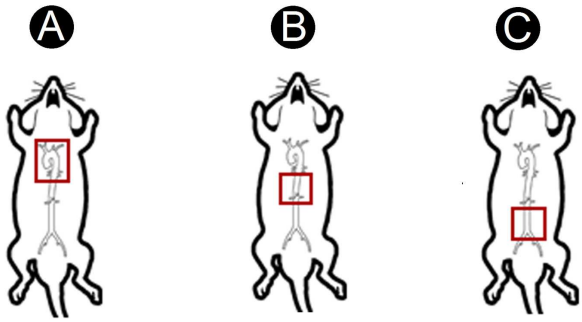

Figure 5.12: Studied portions of the aortic tree are; A - Upper thoracic aorta. B - Lower thoracic aorta. C - Abdominal aorta.

Figure 5.13 shows the inflation test results obtained by plotting the mean and the standard deviation (mean ± SD) for all specimens of each group considered at the three aortic zones studied (upper and lower thoracic and abdominal aorta), which are pointed out in the right of this Figure 5.13. Then, six subfigures are shown, one for each of the three zones of the aorta studied; upper and lower thoracic and abdominal aorta for both ApoE$^{-/-}$ and control mice. In each subfigure, four curves are presented, one for each group of time on a diet (10, 20, 30 and 40 weeks). The different behavior of ApoE$^{-/-}$ mice at different times on diet is noticeable since the circumferential stretch decreases as the age increases for all pressures tested. In contrast, the control mice results show similar pressure-stretch curves for all ages.

Additionally, as mentioned before, several statistical analyses were performed by means of Lilliefors, one-tailed Student's t-test and Wilcoxon rank sum tests. Firstly, ApoE$^{-/-}$ and control mice at the same weeks on a diet and, next, each strain at different time on a diet, were compared. For this goal, stretch values for each corresponding test were extracted at several different pressure levels, 25, 50, 75, 100, 125, 150, 175, 200, 225 and 250 mmHg. The stretch values which were divided into several subgroups, corresponding to the 10, 20, 30 and 40 weeks on a diet for each aortic zone studied (upper and lower thoracic and abdominal aorta), were compared. Comparing the results of each strain at different times on a diet and for the pressures described above, ApoE$^{-/-}$ aorta stiffness increases dramatically as the age of feeding on a Western-type diet increases for all the aortic zones studied ($p<0.05$). In contrast, control aorta stiffness remain practically constant as the age on a diet increases. However, comparing the ApoE$^{-/-}$ and control results obtained, the ApoE$^{-/-}$ pressure-stretch curve of 10 weeks on a diet for the upper thoracic aorta and, 10 and 20 weeks on a diet for the lower thoracic and abdominal aorta, are similar to the control ones for all weeks ($p>0.05$). This shows that a short period on a high fat diet does not affect the mechanical properties of the ApoE$^{-/-}$. Furthermore, the different behaviour of the three zones studied for the ApoE$^{-/-}$ mice is highlighted, being the upper thoracic aortic stiffer than the lower thoracic aortic and this, in turn, stiffer than the abdominal aorta, while the stiffness for

the three zones considered for the control mice remains constant.

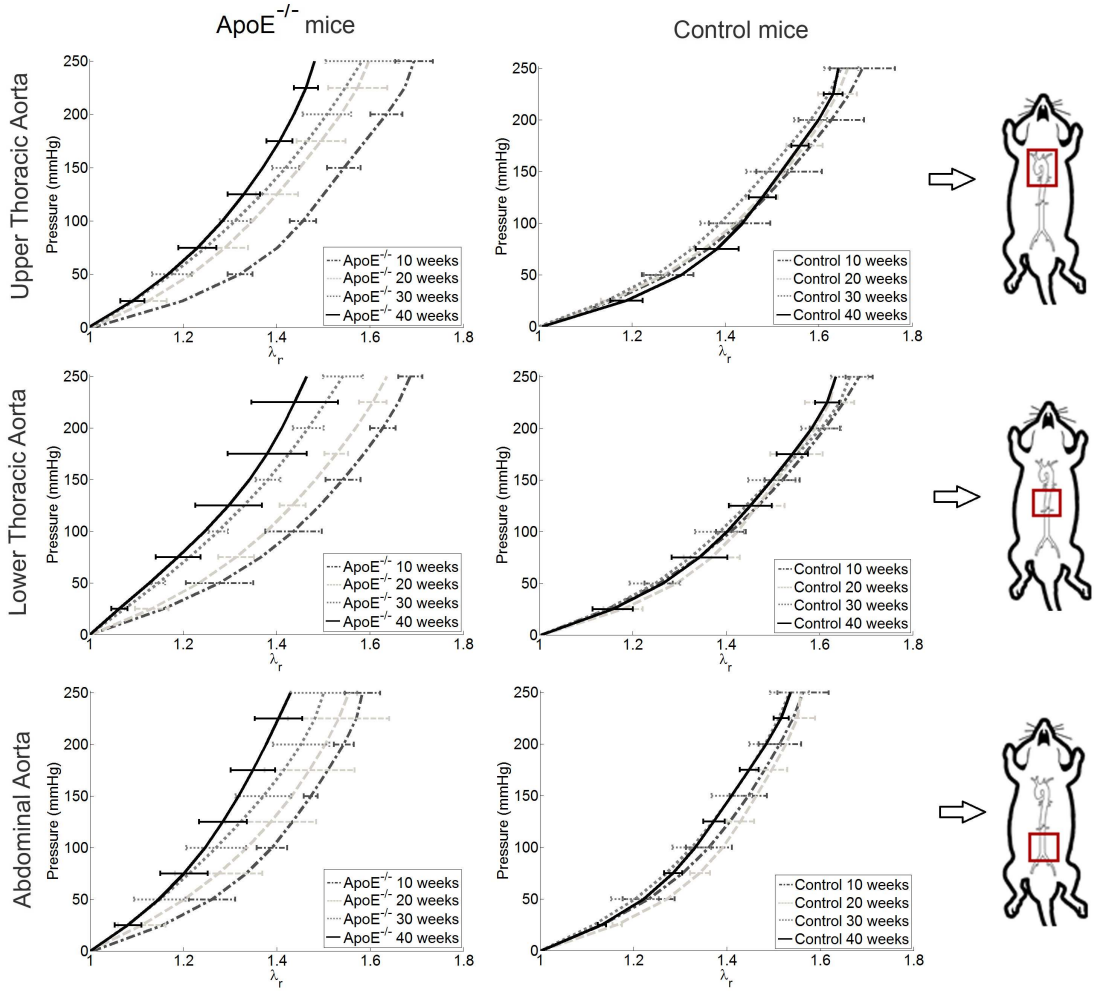

Figure 5.13: Experimental curves obtained by means of an inflation experimental test. Applied pressure versus circumferential stretch for ApoE$^{-/-}$ and control mice at different times on diet and locations on the aorta; upper and lower thoracic aorta and abdominal aorta are plotted (mean ± SD).

5.5.1.3 Equivalent stiffness - Modules

Furthermore, in order to quantitatively compare the stiffness of the aorta at different pressure levels, three stiffness modules, which are defined as the slope of the pressure-stretch curve,

$$\frac{\Delta Pr}{\Delta \lambda_r} \tag{5.2}$$

were defined, where Pr (mmHg) is the pressure applied and λ_r the stretch in radial direction, therefore a stiffer aortic tissue of a group of animals will have a higher modules. These three different modules were defined depending the pressure levels; secant modules which indicates the global stiffness (pressure from 0 mmHg to 250 mmHg), elastic modules which is the mathematical description of an sample tendency to be deformed elastically, showing the stiffness at low pressures (pressure from 0 mmHg to 50 mmHg) and tangent modules which is useful in describing the behavior of materials that have been stressed beyond the linear region, pointing out the stiffness at high pressure levels (pressure from 200 mmHg to 250 mmHg). Thereby, equivalent stiffness of the aorta mice trunk for each of the three aortic zones studied at different pressure levels was obtained.

The obtained results for the equivalent stiffness through the different modules defined are shown below in Figures 5.14, 5.15 and 5.16. For the sake of clarity, a plot indicating the part of the pressure-stretch curve which is referred each of the different modules defined has been added to the top part of this Figures. Generally, the obtained results indicate that the tangent modules are higher than the secant modules, and the latter is higher than the elastic one. Despite of the results are within an acceptable range, it is noticeable in all cases the important inter-individual variability found, specially for the tangent modules results.

Figures 5.14 shows the global mechanical behaviour of the aorta by means of the secant modules (from 0 mmHg to 250 mmHg). At a first glance, the different behaviour of both strains can be observed. First, results for the ApoE$^{-/-}$ mice, present an almost linear behaviour for the three aortic parts considered; R^2 values of 0.97, 0.95 and 0.93 have been obtained by fitting the results with a linear trendline for the upper and lower thoracic aorta and abdominal aorta, respectively, reflecting a stiffening character as stretch increases. Second, the secant modules obtained for the control mice are afresh similar for all ages.

Moreover, similar statistical analysis than in the pressure-stretch curves were performed at 5% significance level to the three different modules defined above; secant, elastic and tangent modules. Significant differences between the mechanical behaviour of ApoE$^{-/-}$ and control mice were revealed. The t-test showed that significant differences between ApoE$^{-/-}$ and control specimens aged 40 weeks for the three zones studied; $p < 0.0005$ for the upper thoracic aorta and $p < 0.05$ for the lower thoracic and abdominal aorta. For specimens aged 30 weeks the statistical significance between both strains was found on the whole thoracic aorta ($p < 0.05$), and finally, for the specimens aged 20 weeks the results were statistical different just for the upper thoracic aorta ($p < 0.05$). Regarding the comparisons between the same strain at different ages, no statistical significance was again found among the different control groups, however, for the ApoE$^{-/-}$ groups, several statistical differences were shown between young and old mice (see Figure 5.14).

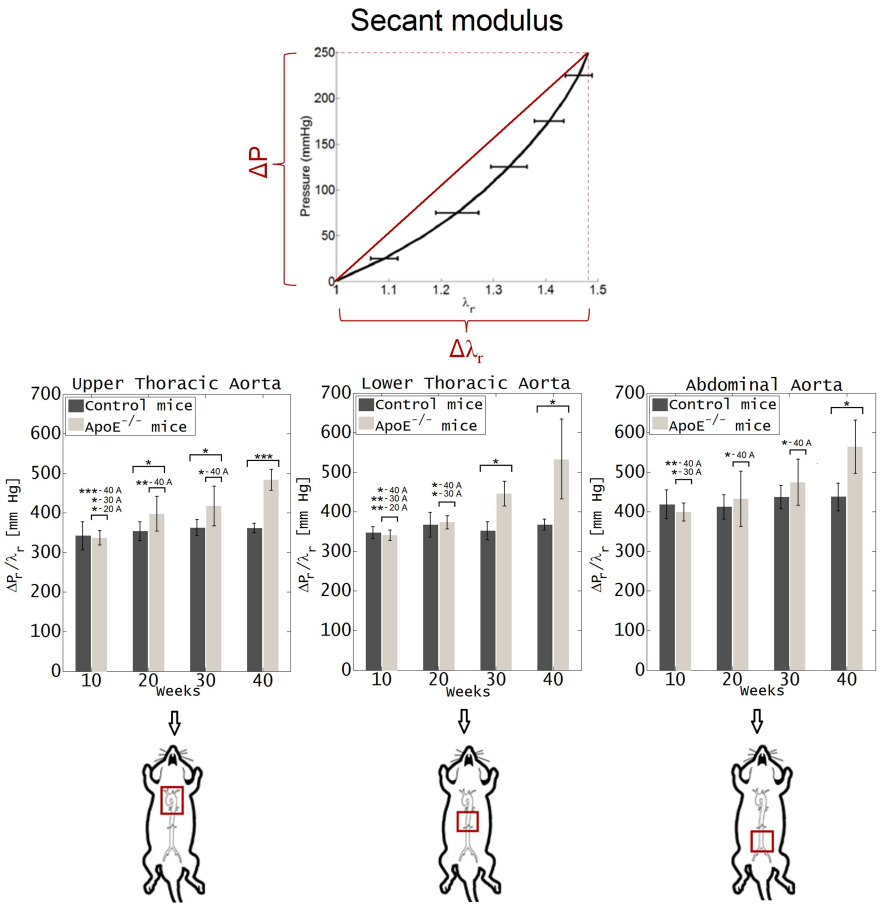

Figure 5.14: Secant modules (from 0 mmHg to 250 mmHg). Equivalent stiffness of the aorta for the whole pressure range (mean ± SD). For the comparisons between groups of the same strain, the means of group n and the groups marked with *-n are significantly different with the probability *p $<$ 0.05, **p $<$ 0.005 and ***p $<$ 0.0005, being appointed the ApoE$^{-/-}$ and control groups by the letters A and C, respectively. For the comparisons between both strains at the same time on diet, the means which are significantly different are just marked with *p $<$ 0.05, **p $<$ 0.005 and ***p $<$ 0.0005.

Figure 5.15, which shows the behaviour of the aortic tissue at low pressures (Pr from 0 mmHg to 50 mmHg), serves as an illustrative example of the marked differences existing between the mechanical behaviour of both strains studied. The elastic modules for the ApoE$^{-/-}$ mice increases almost linearly as the age increases, obtaining R^2 values of 0.92, 0.97 and 0.9 for the upper and lower thoracic and abdominal aorta, respectively. These elastic modules for the ApoE$^{-/-}$ mice are higher than the control ones, which are practically constants for all weeks on a diet considered. Regarding the statistical analysis performed, comparing ApoE$^{-/-}$ and control mice at the same ages for the upper thoracic aorta, $p = 0.049$, 0.018 and 0.002 were obtained for the ages of 20, 30 and 40

weeks, respectively. For the case of the lower thoracic aorta, the values of p obtained for 20, 30 and 40 weeks on a diet were 0.028, 0.0006 and 0.0032, respectively. Finally, for the abdominal aorta, p equals to 0.042, 0.048 and 0.038 were reached for specimens aged 20, 30 and 40 weeks. All these p values confirm that there is a marked statistical significance in the mechanical differences between both strains. However, comparing the specimens of the same strain at different ages, for the control mice groups it was found that elastic modules did not present differences at different weeks on a diet in a statistically significant manner. In contrast, the very different behaviors of ApoE$^{-/-}$ mice at different ages is clearly depicted, founding again statistical differences between specimens aged 10 and 20 weeks with those of 30 and 40 weeks.

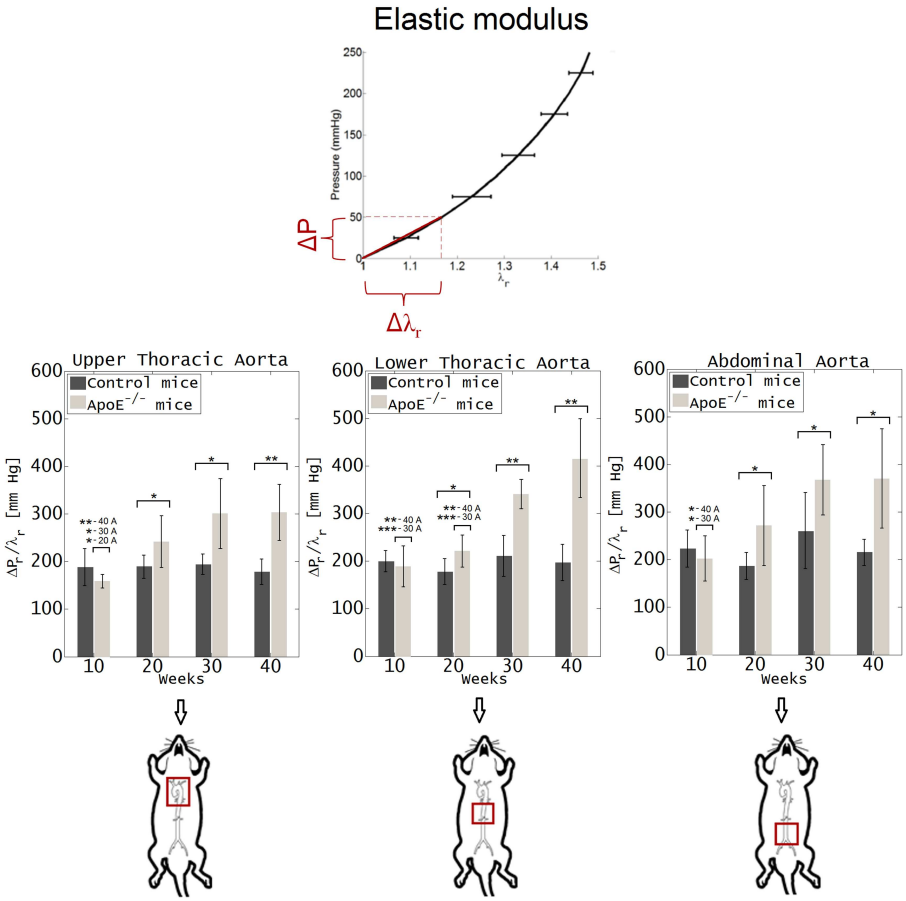

Figure 5.15: Elastic modules (from 0 mmHg to 50 mmHg). Equivalent stiffness of the aorta for low pressure range (mean ± SD). For the comparisons between groups of the same strain, the means of group n and the groups marked with *-n are significantly different with the probability *p $<$ 0.05, **p $<$ 0.005 and ***p $<$ 0.0005, being appointed the ApoE$^{-/-}$ and control groups by the letters A and C, respectively. For the comparisons between both strains at the same time on diet, the means which are significantly different are just marked with *p $<$ 0.05, **p $<$ 0.005 and ***p $<$ 0.0005.

Finally, the general trend found for secant and elastic modules changes for the tangent modules. Figure 5.16 points out the analogous behaviour of the both strain studied at high pressures (P from 200 mmHg to 250 mmHg), showing similar modules for both ApoE$^{-/-}$ and control mice for all weeks studied. The results for the tangent modules for the ApoE$^{-/-}$ and control mice was subjected to statistical analysis in order to find correlations between the different groups. Nevertheless, the t-test for paired samples was not statistically significant, excepting the ApoE$^{-/-}$ mice groups of 10 and 40 weeks on a diet for the upper thoracic aorta ($p = 0.0011$).

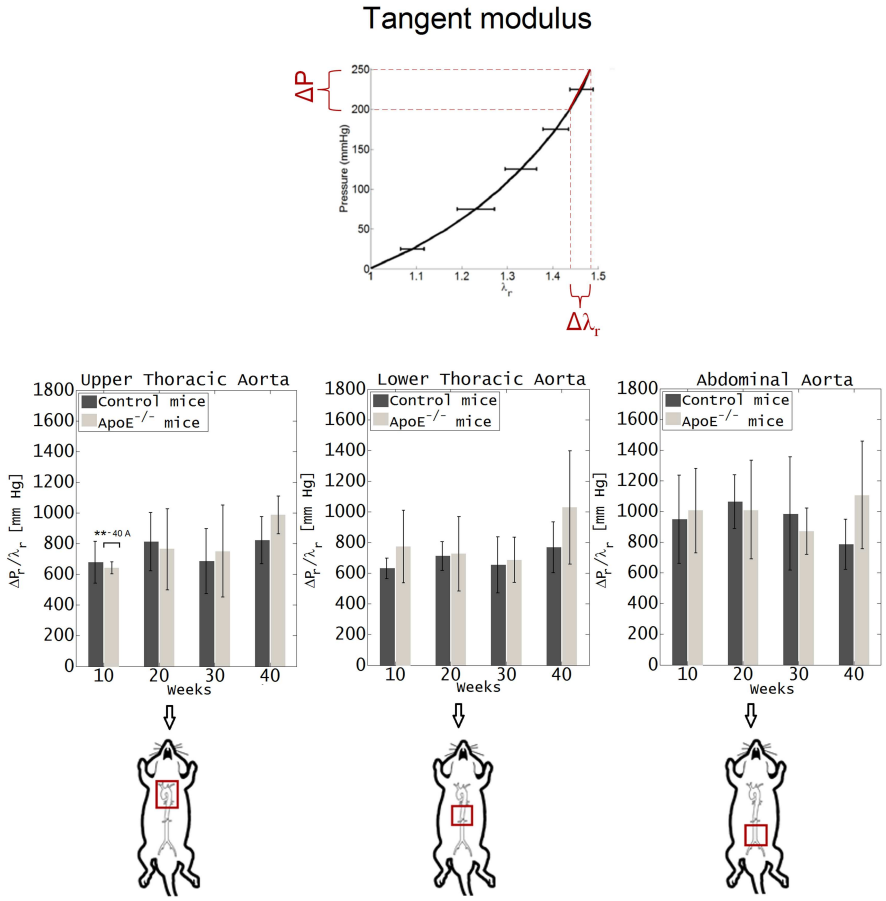

Figure 5.16: Tangent modules (from 200 mmHg to 250 mmHg). Equivalent stiffness of the aorta at high pressure range (mean ± SD). For the comparisons between groups of the same strain, the means of group n and the groups marked with *-n are significantly different with the probability *p < 0.05, **p < 0.005 and ***p < 0.0005, being appointed the ApoE$^{-/-}$ and control groups by the letters A and C, respectively. For the comparisons between both strains at the same time on diet, the means which are significantly different are just marked with *p < 0.05, **p < 0.005 and ***p < 0.0005.

The fact that the global and low pressure stiffness varies for ApoE$^{-/-}$ mice at

different ages, while the high pressure stiffness remains constant for this strain, as Figures 5.14, 5.15 and 5.16 show, could be related to the breakdown of the elastin in the aortic wall of old ApoE$^{-/-}$ specimens. These obtained results are consistent with the findings by Carmeliet *et al.* (1997) and Wang *et al.* (2000), who reported fragmentation of elastic laminae and rupture of all elastic layers across the media of the aortic wall in old ApoE$^{-/-}$ mice, but not in the wild-type mice. Furthermore, (Agianniotis and Stergiopulos, 2012b) reported that at low stretch ratios ApoE$^{-/-}$ mice present stiffer aortas and this can possibly be explained by the elastin rupture of ApoE$^{-/-}$ mouse arteries compared to control arteries. Roach and Burton (1957) demonstrated that the resistance to stretch at low pressures is mainly due to elastin, whereas at high pressures collagen dominates. It is known that the artery tissue passive behaviour is highly non-linear and anisotropic under elastic finite strains. The integrity of the media elastin in the conduit vessels is a major determinant of the arterial elasticity and the capacitive function of these arteries (Wolinsky and Glagov, 1964; Clark and Glagov, 1985). As Figure 5.17 shown, the artery is mainly composed by elastin and a tangled structure of collagen fibers. Elastin is the main load-bearing component of the arteries at low pressures since the wavy collagen fibers of these soft collagenous tissues are not active at this pressures (see part I of the pressure-stretch curve). However, as the stretch increases due to the applied pressure, the fibers extent and contribute to the mechanical response (see part II of the pressure-stretch curve), being the main mechanical component at high pressures (see part III of the pressure-stretch curve). Furthermore, the histologies of the right side of Figure 5.17, which demonstrate the microstructure of the media, show unstretched and stretched human aorta samples. In the unstretched aorta histology, the wavy pattern of the collagen fibers is observed, however, in the stretched one the elastin laminae and the collagen fibers are straighten (Sommer *et al.*, 2008).

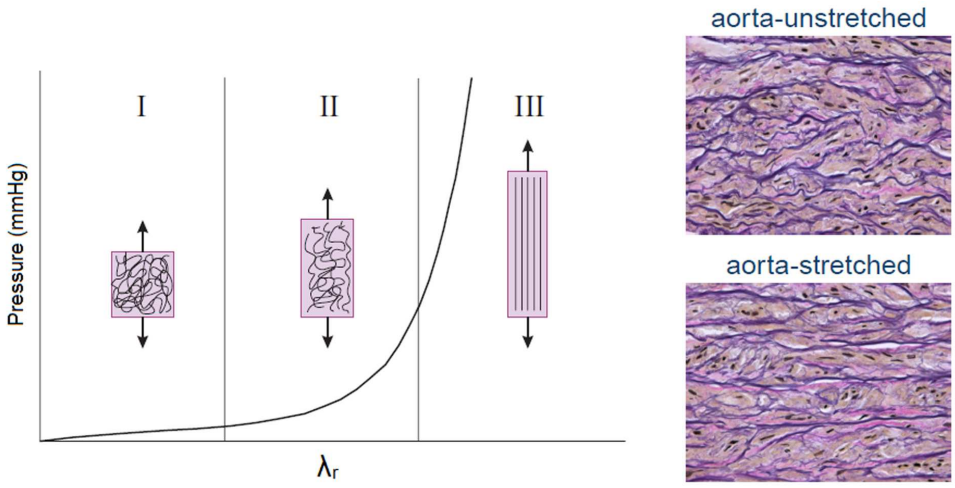

Figure 5.17: Non-linear behaviour of the pressure-stretch curve due to the collagen fibers. Adapted from Gasser (2001).

Therefore, with all this considerations at hand, since the breakdown elastin in the old ApoE$^{-/-}$ mice, but not in the control mice, the elastic and secant modules vary from ApoE$^{-/-}$ mice at different time on diet and remain constant for the control mice. Nevertheless, the tangent modulus remains practically constant for both species since the collagen is the main mechanical component of the artery wall at high pressures, being the mechanical contribution of elastin neglected. However, this is just an hypothesis and more experimental test as well as deeper histological analyses are needed in order to prove it.

5.5.2 Residual stress in longitudinal direction

As mentioned before, after the distension protocol, the aorta was then carefully dissected to measure the axial residual stretch. For this purpose, separated markers were fixed to the aorta. Longitudinal lengths before and after harvesting were determined by measuring the distance between markers, obtaining the *in situ* and *ex situ* dimensions, respectively. Then, the residual axial stretch, defined as the ratio between the *in situ* and *ex situ* measured lengths, determined as

$$\lambda_L = \frac{l_{in-situ}}{l_{ex-situ}}, \tag{5.3}$$

was computed (García *et al.*, 2011). Longitudinal residual stretch has been calculated for the whole aorta vessel. The morphological measurements were made from the images using the ImageJ software. Figure 5.18 shows an example of the *in situ* (Figure 5.18.a) and *ex situ* (Figure 5.18.a) photographies taken to the specimens in order to measure the residual stress in longitudinal direction.

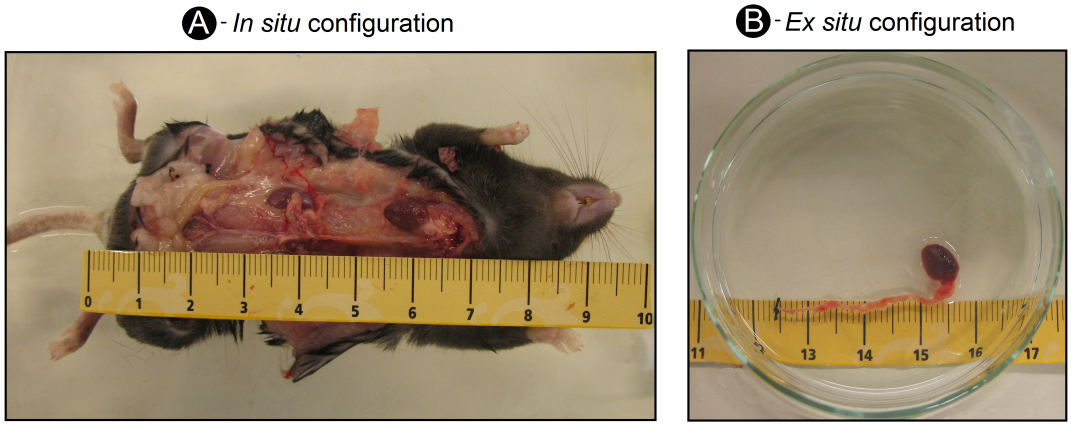

Figure 5.18: Photographies of the aortic tree of any individual used for the determination of the longitudinal residual stretch. A - *In situ* configuration. B - *Ex situ* configuration immediately after harvesting.

Figure 5.19 shows the results related to the axial residual stress of ApoE$^{-/-}$ and control mice. As the figure shows, λ_L for control mice is constant, 1.31 ± 0.1123, for all weeks on a diet considered. Nevertheless, the longitudinal residual stress decreases as the time on diet increases from 1.33 ± 0.13 to 1.15 ± 0.095 for 10 and 40 weeks on a diet, respectively. Furthermore, a linear correlation with $R^2 = 0.97$ was found between λ_L and age for ApoE$^{-/-}$ mice. These longitud residual stress data were subjected to statistical analysis in order to find correlations between the different groups studied. And, as expected, the longitudinal residual stress for ApoE$^{-/-}$ and control mice are significantly different at 30 and 40 weeks on a diet ($p = 0.00009$ and 0.041, respectively). By contrast, similar longitudinal stress were found at 10 and 20 weeks on a diet for both strains studied, showing again, that the mechanical properties of ApoE$^{-/-}$ are less affected at low weeks on a diet. Furthermore, the axial residual stretch for ApoE$^{-/-}$ specimens aged 10 differs statistically from those aged 30 and 40 weeks ($p < 0.05$), whereas for control mice any significative difference was found.

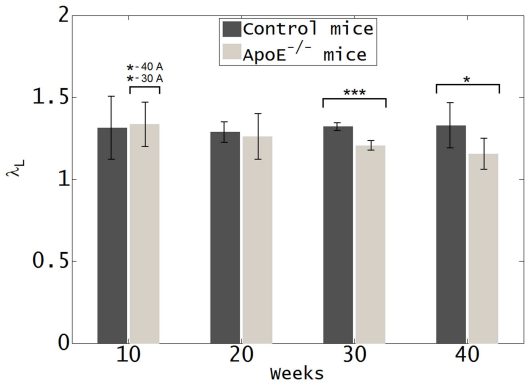

Figure 5.19: Longitudinal residual stress for all the subgroups considered (mean $\pm$ SD). For the comparisons between groups of the same strain, the means of group n and the groups marked with *-n are significantly different with the probability *p < 0.05, **p < 0.005 and ***p < 0.0005, being appointed the ApoE$^{-/-}$ and control groups by the letters A and C, respectively. For the comparisons between both strains at the same time on diet, the means which are significantly different are just marked with *p < 0.05, **p < 0.005 and ***p < 0.0005.

5.6 Histological and immunohistochemistry analysis

The mechanical response of aorta tissue is determined by its highly variable histological composition. Regarding large arteries, among which aorta artery is included, most authors recognize the existence of three layers in their wall, namely tunica intima, tunica media and tunica adventitia. As a general statement, the media layer in large arteries contains both smooth muscle cells and many elastic laminae, and the adventitia layer consists of dense fibroelastic tissue without smooth muscle cells. However,

because of the boundaries are not very distinct, whether the bulk of smooth muscle cells in the wall is located in the intima, media, or adventitia is a matter of individual judgement (Rhodin, 1980). Furthermore, the blood vessel is formed, among other mechanically non-relevant substances, of connective tissue composed of collagen and elastin in different proportions.

Regarding the plaque composition, it varies with time (Nakashima *et al.*, 1994; Reddick *et al.*, 1994). Early lesions in ApoE$^{-/-}$ mice consist mainly of foam cells, similar to the fatty streaks found in early stages of human atherosclerosis. Over time, smooth muscle cells from the tunica media proliferate and migrate to the intima where they form a fibrous cap that covers a necrotic core containing foam cell debris and cholesterol crystal deposits (Rhodin, 1980). Smooth muscle cells within plaques contain lipid droplets in their cytoplasm and show prominent increase in rough endoplasmic reticulum. Adjacent to these lesions, the elastic layers of the media are irregular and often dilated or disrupted. All of these findings are typical of those observed in mature human atherosclerotic lesions. Large plaques are often associated with adventitial thickening, chronic inflammation, and the formation of new capillaries (Wolinsky and Glagov, 1964; Clark and Glagov, 1985). Occlusion of more than 70% of the enlarged vessel lumen is not uncommon, but the lesions are consistently eccentric, that is, growing away from the lumen as seen in some human coronary arteries, and the net size of the actual luminal diameter may remain normal (Wolinsky and Glagov, 1967).

Since the highest resolution for assessment of plaque components is obtained by histological examination, two different stainings have been used for the histological and immunohistochemistry characterization of the aorta tissue for ApoE$^{-/-}$ and control mice; Hematoxylin and Eosin (H-E) and red oil staining. For this purpose, firstly the aortic tissue was frozen, and after that, it was sectioned at 4 [μm] thickness slides by means of a cryostat. Once cuts have been performed, the sections were fixed in 10% buffered formaldehyde. Then, the different stainings were applied on them in order to observe the aorta microstructure. For more precise information about what histological analysis are intended for, as well as the specific steps involved in preparing histology slides see e.g., Ross and Pawlina (2010).

5.6.1 Hematoxylin and Eosin staining

In order to observe a global view of the structural microconstituents of the atherosclerosis aorta blood vessels, Hematoxylin and Eosin, staining has been used. This type of stain gives the possibility to see all the microconstituents (collagen, elastin and smooth muscle cells) in the same histology, which allows to clarify the global disposition at micro level. With that, a first visual idea of the different density of the collagen, elastin and smooth muscle cells can be regarded (Ross and Pawlina, 2010). The cell nuclei are observed in blue and muscle and connective tissue composed of collagen and elastin in different shades of pink (Ross and Pawlina, 2010). Figure 5.20 depicts two slice examples of atherosclerotic aorta microstructure belong to a 30 weeks aged ApoE$^{-/-}$

mice. As mentioned before, atherosclerotic lesions were not developed by control mice, thus control histological analysis are not shown. Figure 5.20 shows two samples of histological preparations by means of Hematoxylin and Eosin staining. A higher degree of cellular and extracellular components of atherosclerotic lesions including cholesterol clefts is illustrated.

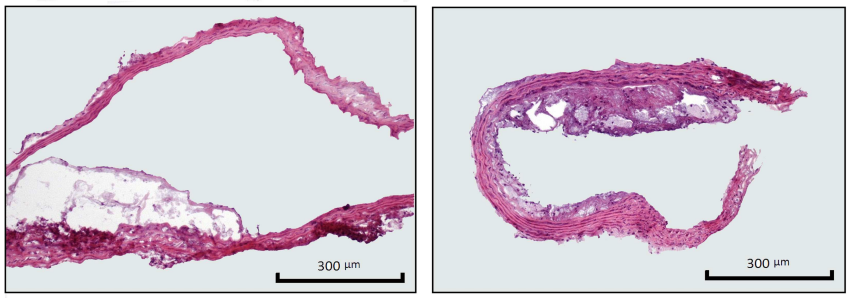

Figure 5.20: Histological samples of atherosclerosis aorta stained with Hematoxylin and Eosin. The two slices correspond to a 30 weeks aged ApoE$^{-/-}$ mice.

5.6.2 Red oil staining

Oil Red is one of the dyes used for Sudan staining. It mainly targets fat deposits on the surface of porous exhibits, and it is a non-destructive technique, which does not destroy the exhibit and does not prevent the use of other techniques. Thus, the lipid core was identified by red oil staining. Representative photomicrographs of aortic roots of an ApoE$^{-/-}$ specimen of 30 weeks on a diet are illustrated in Figure 5.21, where the red oil stained sections present the presence of lipid-rich atherosclerotic lesions, and the extent and severity of the atherosclerotic lesions are well illustrated (Ross and Pawlina, 2010).

5.7 Discussion

Recent progress in our ability to produce genetically altered animals that model human conditions has contributed greatly to the development of a better understanding of the complex pathogenesis of human (Hoyt Jr. *et al.*, 2007). The ApoE$^{-/-}$ mouse is a well-established animal model in atherosclerosis research. On standard chow, ApoE$^{-/-}$ mice develop severe hypercholesterolemia and advanced atherosclerotic lesions spontaneously throughout the arterial system (Zhang *et al.*, 1992; Nakashima *et al.*, 1994). A high-fat Western-type diet may double the plasma cholesterol level and accelerate the development of atherosclerosis. An experimental device for the *in situ* inflation of aortas of ApoE$^{-/-}$ and wild type mice has been developed. Furthermore, histological data, anatomical analysis and measurements of the longitudinal residual stress have been provided. The obtained results, which are discussed in this section, demonstrate

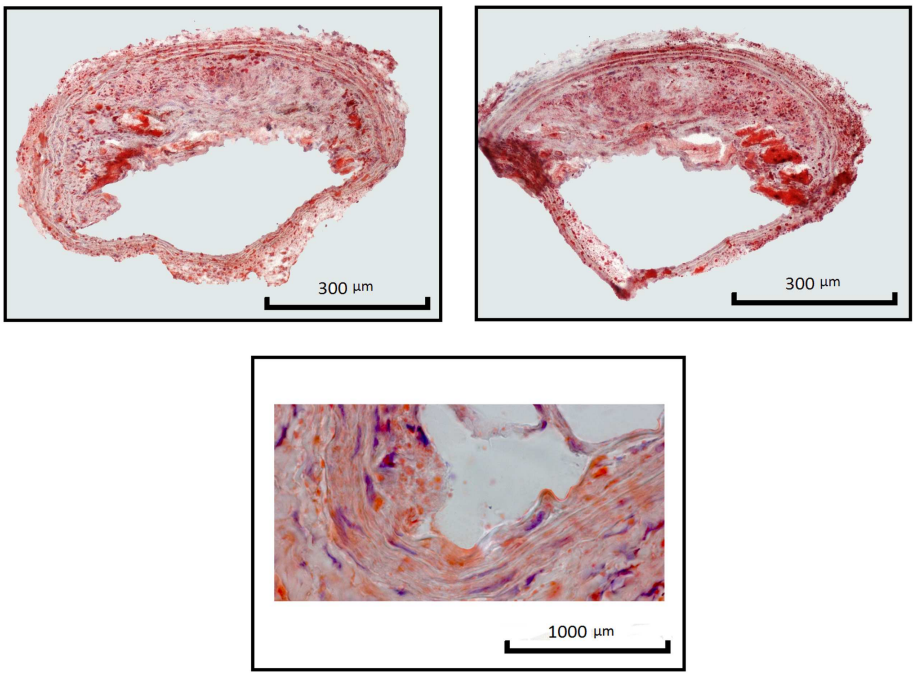

Figure 5.21: Histological samples of atherosclerosis aorta stained with red oil. The slices correspond to a 30 weeks aged ApoE$^{-/-}$ mice.

substantial changes in the mechanical behaviour and in the structural properties of the aorta blood vessel of genetically engineered ApoE$^{-/-}$ mice as compared to control group (C57BL/6). These findings are important for a better understanding of the cardiovascular system of mice and could serve as a reference state for the study of atherosclerosis disease in knock-in and knock-out models of this species.

5.7.1 Anatomical analysis

Regarding the gain in body weight measurements, a linear weight gain is observed since the first week on a diet for ApoE$^{-/-}$ mice, becoming most of the ApoE$^{-/-}$ mice studied severely obese, while the gain in body weight for control mice remains constant from 10 weeks. (Hirano *et al.*, 2001) reported that plasma insulin, glucose and cholesterol levels were elevated by 213, 23, and 51%, respectively, in obese ApoE$^{-/-}$ mice aged 15 weeks, which is directly related with the development of atherosclerosis.

Because the time scale of plaque development differs along the aortic tree, morphological evaluations of plaque development must take this into account. The observations with ApoE$^{-/-}$ and C57BL6 mice maintained on regular and hyper-lipidic chow, respectively, has shown that for ApoE$^{-/-}$ mice plaques begin to appear at same zones of the aortic root at about 10 weeks of age and increase in size rapidly with time. At about 40 weeks the growth rate of mature plaques increases, and atheroma plaque is found along the whole aortic tree, while any evidence of atheroma plaque was found for control mice.

Disturbed blood flow patterns such as flow separation, recirculation, reattachment, stasis, and reflux occur naturally at certain vascular regions (e.g. arterial branch points and curvatures and the aortic and venous valve sinuses). The flow disturbances that occurred naturally or associated with vascular diseases and interventions can lead to development or acceleration of atheroma plaque, as it has correlated by the presented morphological observations. This atheroma plaque distribution results are consistent with those found by Hoyt Jr. *et al.* (2007) or Chiu and Chien (2011) amongst others.

5.7.2 Mechanical properties analysis

The presented work characterizes the mechanical behaviour of the aortic wall of ApoE$^{-/-}$ mice affected by the atherosclerosis and C57BL/6 mice for different times on diet, using a sufficiently large population of mice. This is an original experimental work, which could be considered as a step forward for the understanding of the atherosclerosis diseases. Any study with all this characteristics can be found in the literature.

Pressure-stretch measured curves were marked by the wide variability caused by the highly variable composition of the aortic wall, that determines the aorta tissue mechanical response. In addition to this feature, observed in inflation tests, the study of the pressure-stretch behaviour showed very clearly the different behaviour of the aortic tissue belonging to ApoE$^{-/-}$ and control mice. ApoE$^{-/-}$ specimens were always stiffer than the control ones, increasing their stiffness with the age. The obtained nonlinear pressure-stretch curves present an increasing of stiffness with the stretch.

The equivalent stiffness results computed by means of the secant, elastic and tangent modules could be classified into two groups. The first group, which includes results of the secant and elastic modules, shows an almost linear behaviour between the modules and the age on a diet. Furthermore, important statistical differences have been found between ApoE$^{-/-}$ and control mice at the same age, as well as between ApoE$^{-/-}$ mice at different ages. Agianniotis and Stergiopulos (2012b) suggested that the collagen fibers are recruited at lower pressures in ApoE$^{-/-}$ mouse arteries than in their control counterparts, which limits the elastic response of these arteries and results in a stiffer vessel. The second group included the results of the tangent modules, these results are characterized by a marked variability and, few significative differences were found between the different groups defined, presenting similar mechanical behaviour between ApoE$^{-/-}$ and control mice. The fact that elastic and secant modules increase for ApoE$^{-/-}$ mice as the time on diet increases, but not the tangent modulus, which is practically constant for all the ApoE$^{-/-}$ mice groups studies, could be possibly caused by the breakdown of the elastin in the aortic wall of old ApoE$^{-/-}$ specimens. Similar behavior was found by Carmeliet *et al.* (1997) and Wang *et al.* (2000). Previous studies suggest that 10% of collagen fibers are engaged at physiological pressure (Greenwald *et al.*, 1997), whereas at higher pressures, the vessel becomes progressively less distensible as collagen fibers are recruited to support passive wall tension and restrict aortic distension. With additional increases in wall strain or stretch ratio, there is little further

change in radius as additional collagen fibers are recruited, accounting for the nonlinear nature of vascular elasticity (Roach and Burton, 1957; Wolinsky and Glagov, 1967). Therefore, the tangent modulus for ApoE$^{-/-}$ mice do not vary since the elastin do not apport mechanical properties at high pressure levels, and the collagen remains intact. However, the elastic and secant modules for ApoE$^{-/-}$ mice, which point out the stiffness at the pressure ranges where the elastin is the main component responsible for the resistance to stretch, vary due to the elastin rupture.

Measurements of longitudinal *in situ* stretch are collected in Figure 5.19. These measurements provided a lower value as the time on diet increases for the ApoE$^{-/-}$ mice, and a constant value for control mice. The structural protein elastin endows large arteries with unique biological functionality and mechanical integrity, hence its disorganization, fragmentation, or degradation can have important consequences on the progression and treatment of vascular diseases (Cardamone *et al.*, 2009). Thus, age and the development of atherosclerosis lesions cause a decrease of longitudinal residual stretch for ApoE$^{-/-}$ mice.

5.7.3 Histological and immunohistochemistry analysis

The histological analyses, which let observe the microstructure and composition of the atherosclerotic lesions, have confirmed the existence of mature atheroma plaque for ApoE$^{-/-}$ mice.

5.7.4 Limitations and open problems

Some points of the developed study should be commented in order to show its limitations and how the obtained results could be improved in future works. Firstly, the application of an alternative kind of test would provide more accurate additional information about aorta mechanical properties. *In situ* inflation test provide just pressure-stretch information, and other features such as the strongly anisotropic properties of blood vessels cannot be capture by this kind of inflation test. Furthermore, since these inflated tests are performed *in situ*, the measurement of longitudinal forces, and thereby the longitudinal stiffness can not be assessed. *Ex situ* inflation test combined with extension test could be carried out, however the control of the liquid leaks in this kind of test is difficult due to the great number of branches of the aortic root. Moreover, uniaxial or planar biaxial test should be needed in order to characterize the aortic mice tissue. On this subject, the experience acquired during the development of inflation tests does not advice the use of simple tension or planar biaxial test on the mice aorta, since its small size would make it difficult the development of these tests.

Secondly, the mechanical properties have been obtained from the whole aorta wall, however, the arteries are composed of three different layers (see Section 1.2 of Chapter 1), so it is expected that their different histological composition would result in different mechanical properties for each layer. However, the mechanical separation of these layers is extremely complicated or almost impossible due to the small size of the aorta.

The third consideration concerns the size of the mouse aorta; although mice were dissected carefully, there is many branches in the aortic root which usually leads to small leaks during the inflation test.

Fourth, circumferential residual stretch measurement were not obtain due to the difficulty of its estimation. Nevertheless, (Ohayon *et al.*, 2012) were able to measure the circumferential residual stress on ApoE$^{-/-}$ mice aged 20, 25 and 30 weeks by means of radially cutting aortic rings. After a while, the opening angle was defined as the angle formed between the two extremities of the opened ring and the point of the intima crossed by the perpendicular bisector of the segment bounded by these two extremities. For this purpose, a liquid substance was placed inside of the blood vessel, and after that, the vessel was frozen with the liquid inside, making easier the opening angle measurement technique.

Finally, only the determination of the aorta elastic properties was considered in this study. Inelastic procedures such as plastic or viscoelastic phenomena were considered out of the scope of this research. As an example of the influence of these phenomena, the assumed 15 [mm/min] strain rate supplies data to model physiological load states such as those caused by the breath cycle, the interaction with the surrounding organs or vena cava filter implantation or retrieving.

Chapter 6

Atheroma plaque growth process modeling

In this Chapter a numerical approach to model the atheroma plaque growth is presented. This model employs the Navier-Stokes equations and Darcy's law for fluid dynamics, convection-diffusion-reaction equations for modeling the mass balance in the lumen and intima, and Kedem-Katchalsky equations for interfacial coupling at membranes, i.e., endothelium, and it includes fluid dynamics and solute dynamics in the blood lumen and the arterial wall. The volume flux and the solute flux across the interface between the fluid and the porous domains are governed by a three pore model. And the main species which play a role in the early atherosclerosis lesions development have been considered in the presented model, i.e. LDL, oxidized LDL, monocytes, macrophages and foam cells. Furthermore, experimental data taken from the literature have been used in order to determine physiologically realistic model parameters. The developed model has been implemented on a representative geometric coronary artery model. Results showed that the mathematical model is able to capture the atheroma plaque development observed in the intima layer.

Contents

6.1 Introduction

Atherosclerosis is related to nanoscale fluid dynamics and macromolecular transport at the arterial endothelium (Ciofalo *et al.*, 1998). The behavior of atherosclerosis is time-dependent and the dominant phenomena may occur in the range of 0-1$\cdot$ 10^{-7} mm from the endothelium. The location of atherosclerosis is associated with flow separation and turbulence. Therefore, many studies have identified hemodynamic shear stresses, which are due to the frictional force acting on the endothelial cell surface as a result of blood flow, as an important determinant of endothelial function and phenotype on atherosclerosis disease (see e.g., Zarins *et al.*, 1983; Malek *et al.*, 1999; Slager *et al.*, 2005b,a; Groen *et al.*, 2008, and references therein). On the one hand, wall shear stress is related to the plaque rupture since this phenomenon has been more frequently observed at the proximal upstream side of the minimal lumen diameter, which is supposedly exposed to higher WSS. Groen *et al.* (2007) suggested that there is ample evidence that the endothelium responds to high WSS such that it induces antiproliferative action, which may lead to cap thinning (Malek *et al.*, 1999). For that reason, they hypothesized that high WSS at the upstream side of the plaque has a biological effect on the fibrous cap and therefore enhances plaque vulnerability (Slager *et al.*, 2005b). Moreover, a WSS dependence on the thrombosis event has been reported by Ku (1997). For the arterial system, thrombosis is initiated by the adherence of platelets at the surface with rapid accumulation of additional platelets. In vitro experiments have produced conflicting results, but in vivo studies with nonanticoagulated blood indicate that platelets stick at the throat of the stenosis. The adherence and accumulation of these platelets are shear dependent with more accumulation at higher shear rates. Then, arterial-level shear stress approximately greater than 1.5 Pa induces endothelial quiescence and an atheroprotective gene expression profile (Malek *et al.*, 1999). On the other hand, atherosclerosis disease preferentially affects to predisposed areas of the blood vessel where the hemodynamic shear stress are low such as bifurcations or zones with flow recirculation. And shear stress approximately lower than 0.4 Pa stimulates an atherogenic phenotype and eases the atherosclerotic lesion initiation (Malek *et al.*, 1999).

The onset and progression of atherosclerosis involves many processes, however, the fundamental cause of the plaque development is believed to be the abnormal enlargement of the intima by the infiltration and accumulation of macromolecules such as lipoproteins and the associated cellular and synthetic reactions. It is well accepted that the early atherogenesis tends to be hallmarked by an abnormally high accumulation of macromolecules, i.e. LDL, within the arterial wall. This fact suggests that the macro-

molecular transport in the arterial wall must have some impact on the initiation and development of atherosclerosis (Ethier, 2002; Yang and Vafai, 2006). Therefore, the general picture is that zones of elevated LDL tend to colocalize with areas of atherosclerotic lesion development and intimal thickening, and such zones also tend to have "abnormal" wall shear stress patterns, which are also believed to be atherogenic. The endothelium, which is the internal lining of the entire cardiovascular system, is uniquely positioned to be a sensor, responding and transducing these hemodynamic signals. Taken together, these results suggest, but do not prove, a role for mass transport in atherogenesis (Ethier, 2002; Taylor and Humphrey, 2009).

As a result, additionally to the study of the hemodynamic forces which impact upon the vascular endothelium, mathematical modeling of the transport of the biological agents which play a role on the atheroma plaque development in the arterial wall has received considerable attention in recent years. So far, most models either concentrate on explaining a specific clinical trial result about the growth and rupture of atherosclerotic plaques (Wang, 2001), or focus on the initiation of atherosclerosis related to the mass transport of LDL molecules. Since locally elevated concentrations of LDL in the arterial wall are considered to be the initiator of atherosclerotic plaque formation (Ross, 1993; Lusis, 2000), both experimental (see e.g., Preobrazhensky *et al.*, 1983; Lin *et al.*, 1989; Tompkins *et al.*, 1989; Mandarino *et al.*, 1992; Truskey *et al.*, 1992; Meyer *et al.*, 1996; Cancel *et al.*, 2007, amongs others) and computational (see e.g., Karner and Perktold, 2000; Karner *et al.*, 2001; Stangeby and Ethier, 2002b; Wada *et al.*, 2002; Kaazempur-Mofrad *et al.*, 2004; Prosi *et al.*, 2005; Ai and Vafai, 2006; Sun *et al.*, 2006; Olgac *et al.*, 2008; Dabagh *et al.*, 2009; Chung and Vafai, 2012; Lantz and Karlsson, 2012, amongs others) studies have been conducted to comprehend the pathways and mechanisms governing LDL transport from the artery lumen into the arterial wall and within the arterial wall.

The simplest models used so far are wall-free models, in which the arterial wall is substituted by a simplified boundary condition (Prosi *et al.*, 2005). Rappitsch and Perktold (1996) and Wada and Karino (2000) applied these models for the analysis of the macromolecular LDL transport in the arterial wall. A more realistic approach is named lumen-wall models, which couple the transport within the lumen and the wall. In these models, the arterial wall is simplified as a homogeneous monolayer. Such models, originally proposed by Moore and Ethier (1997), have been used to study the mass transport of LDL within the arterial wall by many authors (Stangeby and Ethier, 2002a,b; Ibragimov *et al.*, 2006; El Khatib *et al.*, 2007, 2009; Gessaghi *et al.*, 2011). Finally, the most realistic models are multilayer models, which break the arterial wall down into several layers, and model the transport within the wall, either at the microscopic (Yuan *et al.*, 1991; Huang *et al.*, 1994; Huang and Tarbell, 1997; Tada and Tarbell, 2004) or macroscopic (Fry, 1985, 1987; Karner *et al.*, 2001; Prosi *et al.*, 2005; Sun *et al.*, 2005; Ai and Vafai, 2006; Sun *et al.*, 2006; Yang and Vafai, 2006; Hong *et al.*, 2008; Olgac *et al.*, 2008; Dabagh *et al.*, 2009; Olgac *et al.*, 2009; Chung

and Vafai, 2012) levels. Several works pertinent to arterial LDL transport models were analyzed by Khakpour and Vafai (2008), and a critical assessment of these models was presented, with an emphasis on the role of porous media. Arterial LDL transport models were assessed and classified based on their ability to physically prescribe the arterial anatomy as well as the related transport processes. Pertinent models such as wall-free, homogeneous-wall, and multi-layer models as well as the governing equations and different types of boundary conditions utilized in each model were analyzed in their study.

In addition, the Staverman-Kedem-Katchalsky membrane equations (Kedem and Katchalsky, 1958) are usually used to model the transport processes in the endothelium and internal elastic lamina (IEL) in the majority of the previous multilayer models. However, these equations have at least couple of substantial disadvantages despite of the fact that they are widely used to model the mass transport through the endothelium: (i) it is derived based on the existence of steady state condition, which is in conflict with the real physiological conditions existing within both endothelium and IEL, and (ii) it ignores the boundary effects on the flow across the membrane, which is not valid when the boundaries of the porous membrane have to be accounted for (Yang and Vafai, 2006). Furthermore, there are three pathways of transport through the endothelium: vesicular transcytosis, which is regulated by receptors on the endothelial cells (Snelting-Havinga *et al.*, 1989), and through leaky and normal junctions, most of which are located at the sites of dying or replicating cells (Lin *et al.*, 1989, 1990).

Apart from the LDL molecules, many studies have been focused on the governing mechanics interaction of the different biological species which play a role in the atheroma plaque development, again, both from experimental (see e.g., Steinman and Cohn, 1972; Steinberg *et al.*, 1977; Lehoux and Tedgui, 2003; Zhao *et al.*, 2006; Howarth *et al.*, 2007, amongs others) and computational (see e.g., Zohdi *et al.*, 2004; Ougrinovskaia *et al.*, 2010; Di Tomaso *et al.*, 2011; Gessaghi *et al.*, 2011; Fok, 2012, amongs others) points of view. Furthermore, a wide variety of complexity exists between these computational studies according to the number of species considered and the development of the equations proposed. Zohdi *et al.* (2004) modeled the adhesion of monocytes to the endothelial surface, which is controlled by the intensity of the blood flow and the adhesion molecules stimulated by the excess LDL, the penetration of the monocytes into the intima and subsequent inflammation of the tissue, and the rupture of the plaque accompanied with some degree of thrombus formation or even subsequent occlusive thrombosis. Their modeling approach, a priori predict the time to rupture as a function of arterial geometry, diameter of the monocyte, adhesion stress, bulk modulus of the ruptured wall material, blood viscosity, flow rate and mass density of the monocytes. Cobbold *et al.* (2002) and Gessaghi *et al.* (2011) studied the oxidation process of LDL cholesterol within the context of an in vitro framework, however Cobbold *et al.* (2002) considered additionally the action of different vitamins such as vitamin E or C. Mathematical analysis of this behaviour predicts that vitamin E supplementation

is not as beneficial as high density lipoproteins (HDLs) and vitamin C. Di Tomaso *et al.* (2011) considered the interaction between just two species, LDL and monocytes, but the monocytes behaviour was modelled in a very simple and unrealistic way. Fok (2012) proposed a mathematical model of intimal thickening, posed as a free boundary problem. Intimal thickening was driven by damage to the endothelium, resulting in the release of cytokines and migration of SMCs. More complex studies were presented by Siogkas *et al.* (2011), who included in their model oxidized LDL, macrophages and cytokines, considering that all the LDL molecules and the monocytes were oxidized and differentiated, respectively, at the instant in which these agents pass through the endothelium. A similar study was presented by Calvez *et al.* (2009) and Calvez *et al.* (2010) from a mathematical point of view, but their study included also the foam cell. Ougrinovskaia *et al.* (2010) explored the uptake of cholesterol by different scavenger receptors of macrophages during early stage atherosclerosis was investigated, using an ODE model.It was found that macrophage proliferation rather than an increased influx of LDL particles drives lesion instability. Finally, Bulelzai and Dubbeldam (2012) presented a qualitative mathematical model which consists of a number of ordinary differential equations for the concentrations of the most relevant constituents of the atherosclerotic plaque; macrophages, monocytes, foam cell and oxidized LDL. However, a reliable model to simulate atheroma plaque growth has not yet carried out.

It should be noted that the main drawback of these atheroma growth computational models lies on the lack of experimental data about the interaction between the different biological species. The scarce experimental test of atherosclerotic transport species found in the literature are mainly performed *in vitro*, which does not reproduce accurately the biological complexity of the atheroma plaque development since the *in vitro* experiments may not achieve time scale accuracy of the process. However, some of the challenges met in the experimental works include the suitability of animal models for the human disease condition, the challenge of properly controlling all relevant experimental conditions in animal models in order to obtain measurements with adequate spatial and time resolution has also explored. Consequently, some studies have been carried out in animals in order to investigate the LDL transport in the arterial wall. The main method was systemic injection of LDL solution with subsequent harvesting and examination of the animal's arteries. Lin *et al.* (1989) observed thoracic aortas of rats with this method and counted the number of leakage sites of LDL, as well as the portion of leakage sites associated with mitotic cells. Their results support the hypothesis that transiently opened leaky junctions provide pathways for LDL transport. Truskey *et al.* (1992) used the same method on rabbits to quantify the apparent permeability of the endothelium to LDL. Tompkins *et al.* (1989) measured LDL concentration at various sites in the circulatory system of monkeys. Meyer *et al.* (1996) used a different method and excised aortic segments of rabbits to incubate them in vitro at various pressure levels with LDL solutions. With this method, they were able to assess the effect of intraluminal pressure on LDL transport. Cancel *et al.* (2007) used endothelial cell cultures to study LDL

transport under pressurized conditions and found that LDL transport through leaky junctions constitutes the major part of total LDL transport (90.9%), whereas only a small portion occurs via the vesicular pathway (9.1%). Because the occurrence of leaky junctions is governed by the adjacent endothelial cells, and because the behavior of the endothelial cells is in turn influenced by the shear stress acting on their surface, LDL transport in the arterial wall is in part governed by local blood flow characteristics that determine the level of wall shear stress.

With all these considerations at hand, there is a evidently need for developing models that relate hemodynamic factors to cell-mediated biochemomechanical processes that are responsible for atherosclerosis. High dependency of the genesis and development of atherosclerosis upon transport processes within the arteries has led scientists to employ advanced tools and sophisticated models to study the hemodynamics and mass transport within the arteries. Consequently, a computational modeling based on reaction-convention-diffusion equation of coupled blood-wall mass transport of the main biological species which lead to atheroma plaque development is presented in this Chapter. These biological agents are namely as; LDL, oxidized LDL, monocytes, macrophages and foam cells. However, there are two important challenges in the mass transport modeling within the arteries; proper set of governing equations, and appropriate choice of boundary conditions (Khakpour and Vafai, 2008). Therefore, the dependence of fluid and transport mass through the endothelium on local blood flow characteristics have been modeled using a three pore model since it is more accurately than the use of a single pathway approach (Karner *et al.*, 2001; Prosi *et al.*, 2005; Sun *et al.*, 2005, 2006; Olgac *et al.*, 2008), and this model is represented by the vesicular pathway, normal junctions, and leaky junctions. The transport properties of the leaky junctions, i.e., hydraulic conductivity, diffusive permeability, and reflection coefficient, are calculated locally in dependence of the fraction of leaky junctions. The fraction of leaky junctions is correlated to wall shear stress using the available experimental data as outlined above (Olgac *et al.*, 2008). Furthermore, the constants which defines the biological interaction between the different species have been obtained from experimental studies of the literature.

The Chapter is organised as follows: firstly, the simplified modeled inflammatory process is described qualitatively in Section 6.2. Then, section 6.3 deals with the mathematical equations defining the fluid and mass transport behaviour both in the lumen and wall artery. Based on this, a representative numerical simulation example has been modeled in order to test the equation which governs the model. For this purpose, the propose atheroma lesion growth process in an axisymmetric idealized geometry of a coronary artery with a perturbation which allow to reproduce low WSS patterns, has been implemented in section 6.4. Discussion on the presented findings is shown in Section 6.5.

6.2 Atherosclerotic process modeled

The model focus on the inflammatory process and then on its links with hemodynamics features. A plenty of molecular particles and cells interfere in the atherosclerotic process, interacting between them by means of a different complex processes. However, the developed model just included the most important of this substances and processes. Therefore, a simplified disease progression has been used to model the atheroma plaque growth. Furthermore, several assumptions related to the arterial wall, blood and mass transport should be made in order to mathematically define the biological process.

6.2.1 Main assumptions of the model

Going from the lumen to the most external layer, a large artery is comprised of the following parts: endothelium, intima, internal elastic lamina, media, and adventitia. As section 1.2 of Chapter 1 described, the endothelium is a single layer of endothelial cells, which are elongated in the direction of blood flow. Endothelial cells are interconnected through intercellular junctions. Internal elastic lamina is an impermeable elastic tissue with fenestral pores and lies between intima and media. In contrast to the media, which contains alternating layers of smooth muscle cells and elastic connective tissue, the intima is mainly comprised of proteoglycan and collagen fibers. The media layer is surrounded by a loose connective tissue, called the adventitia, which contains some capillaries (lymphatic and vasa vasorum) (Wolinsky and Glagov, 1967). The processes which leads to plaque evolution take place in the intima and media layer. Therefore, it should be noted that in the context of arterial mass transport and atheroma plaque formation, the arterial wall refers to the intima and the media, with the adventitia as the outer boundary layer (not included in the model).

Many of the risk factors that predispose to atherosclerosis (see Section 1.3 of Chapter 1) can also cause endothelial dysfunction, and the presence of multiple risk factors has been found to predict endothelial dysfunction (Davignon and Ganz, 2004). Nevertheless, this model focused on the pure mechanical factors which promote endothelial dysfunction such as low shear stress. Clinical observations indicate that atherosclerotic lesions develop often at branches and bifurcations where disturbed flow patterns are observed (Ku, 1997; Quarteroni *et al.*, 2000). Therefore, the endothelium permeability has been linked to the WSS distribution along the internal artery wall in this model.

In the developed model the arterial mass transport is coupled with both the bulk blood flow in the lumen and the transmural flow in the wall. Therefore, fluid dynamic models and solute dynamic models have been included. Regarding the fluid dynamic model part, from a rheological point of view, blood can be thought of as a solid-liquid suspension, with the cellular and molecular elements being the solid phase, and plasma is the liquid phase of the blood. A standard assumption made in arterial flow modelling is that blood is a homogeneous, isothermal and incompressible fluid. The incompressibility assumption breaks down if the fluid velocity approaches the speed of sound in

the fluid, but since arterial blood velocities are significantly below 1% of the sound speed, the incompressibility assumption is valid (Caro *et al.*, 1978). Despite the fact that blood is formed by a suspension of particles, it is also valid to treat it as a homogeneous fluid. This is because the diameter of the suspended particles, such as red blood cells, is much smaller than the interna1 diameter of the artery (Caro *et al.*, 1978; Nichols and O'Rourke., 1990). In the smaller vessels, such as capillaries, the homogeneity assumption cannot be applied; however, this work is focus on medium to large sized arteries such as coronary arteries, hence blood is assumed to be homogeneous. Moreover, assuming that blood acts as a Newtonian fluid is also an established approach, due to the predominantly high shear rates in medium to large arteries. Under this assumption the fluid viscosity is taken to be equal to the high shear rate limit of the viscosity of blood (Newtonian fluid, i.e. viscosity independent of shear rate) (Nichols and O'Rourke., 1990). In order to validate this assumption, Perktold *et al.* (1991) conducted a study in which pulsatile Newtonian and non-Newtonian results were compared in a three dimensional human carotid bifurcation model. It was found that the flow phenomena were essentially unchanged and that there were only minor differences in the basic flow characteristics when non-Newtonian effects were included. Under the above assumptions, the laminar flow of blood is governed by the Navier-Stokes and continuity equation.

Additionally, arterial wall, like a great majority of other human tissues, can be treated as a porous medium. As such, it is of great importance to characterize the porous media transport models used in describing biological phenomena. A porous medium is characterized by its porosity represented as the ratio of the void space to the total volume of the medium. Most human tissues can be treated as porous media as they are composed of dispersed cells separated by connective voids where blood flows (Khaled and Vafai, 2003; Huyghe *et al.*, 2004). Earlier studies in fluid flow through porous media have revealed the classical Darcy law which represents a linear relationship between the flow velocity and the pressure gradient across the porous medium. Darcy model has been utilized in several biomedical studies (Huyghe *et al.*, 1992; Bulter *et al.*, 1997; Sun *et al.*, 2006, see e.g.,). Although useful, Darcy's law has several substantial shortcomings. It neglects the effects of a boundary or the inertial forces on the fluid flow and heat transfer through porous media (Vafai and Tien, 1981). As such, a number of modified models have been proposed such as the Brinkman model which takes into account the effect of solid boundaries and permits the application of no-slip boundary condition along the solid walls that confine the porous medium (Huyghe *et al.*, 1992).

Concerning the solute dynamics part model, mass transfer across the arterial wall occurs via two mechanisms: convection associated with the gradient of pressures which promotes transmural flow and mass diffusion caused by concentration gradients. Molecular diffusion is driven by solute concentration gradients within the arterial walls. These gradients are caused by metabolic uptake and production of proteins and cells within tissue. The substances transported from blood through the endothelial, intimal and

media layers usually encounter some mass-transfer resistance. The resistance can be quite high depending on the size and charge of the protein or cell (Lin *et al.*, 1989, 1990).

6.2.2 Atherosclerosis stages modeled

The stages of atherosclerosis and process of plaque formation are described in section 1.3 of Chapter 1. Many protein, enzymes and cells play a role by means of different biological processes in the atheroma plaque growth. However, as alluded before, a simplified fluid-wall model was formulated in order to obtain an approach of atheroma plaque evolution due to the iteration between biological agents as the time increases, introducing numerical procedures to carry out time-dependent simulations. Therefore, just the main biological species and processes have been taken account. These considered species are; LDL, oxidized LDL, monocytes, macrophages and foam cell (see Figure 6.1).

Figure 6.1: Biological species which interfere in the atheroma plaque growth process

Simplifying, the atherosclerosis process starts with the accumulation of low density lipoproteins in the intima, where part of them are oxidized and become pathological. In order to remove the oxidized particles, circulating immune cells (monocytes) are recruited. Once in the intima, the monocytes differentiate and become macrophages that phagocyte the oxidized LDL. Fatty macrophages then transform by apoptosis into foam cells. Foam cells are responsible for the growth of a subendothelial plaque which eventually emerges in the artery lumen. Therefore, as Figure 6.2 shown, the processes considered by the model are as follows:

1- Transport of the LDL and monocytes by laminar flow into the artery lumen

Blood is composed of two parts: the fluid portion is called plasma, and the solid portion or formed elements (suspended in the fluid) consists of the blood cells, platelets, proteins and other substances are suspended and transported. Plasma accounts for about 55 per cent of the volume and the formed elements account for about 45 per cent (Green, 1982). Therefore, as the blood flows through an artery, macromolecules and cells such as LDL and monocytes, respectively, are carried in longitudinal direction due to the axial component of the flow as Figure 6.2 shown.

The purpose of the cardiovascular system is to transport your blood to the cells of the body, but it has to protect itself from this blood too. The inside of the blood vessels are lined with a layer of thin cells called the endothelium. This is a living system that is in constant change based on the things it comes in contact with. A good example of this is how it responds to toxic chemicals called free radicals. Your blood contains free radicals coming from many different places. These free radicals come from all the thousands of cells of your body, your environment, and the food we eat. The problem is they can cause damage to the endothelium when they interact with it. Dysfunction arises when the endothelium can not respond completely or adequately to the damage or oxidation created by the toxins. A normal response is for antioxidants produced by the endothelium to neutralize the free radicals. Moreover, blood vessels respond to changes in mechanical load from circulating blood in the form of shear stress and mechanical strain as the result of heart propulsions by changes in intracellular signaling leading to changes in vascular tone, production of vasoactive molecules, and changes in vascular permeability, gene regulation, and vascular remodeling. And many reports indicate that altered levels of shear stress or changes in cyclic stretch induce profound changes in the endothelium permeability (Davies *et al.*, 1988; Davignon and Ganz, 2004; Chiu and Chien, 2011).

In the model, the LDL and monocytes are captured by the endothelium in those areas in which it is injured, and thus permeable. And the permeability of this membrane is regulated by the wall shear stress pattern. A transmural flow of plasma is always occurred in radial direction due to the presence of transmural pressure difference, however, if the endothelium is injured, substances and cells are also transported by this flow.

2 - LDL retention

Once the endothelium cells have experienced the impact of the WSS perturbation occurring in the blood. In these arterial prone areas, the initial event that takes place and the penetration of LDL in the intima occurs. The LDL is a heterogeneous class of lipoprotein particles consisting of a hydrophobic core containing triglycerides and cholesterol esters in a hydrophilic shell of phospholipids, free cholesterol, and apolipoprotein. Thus, the intima LDL retention depends on the blood LDL concentration, thus as the cholesterol level increases in the blood, the penetrated LDL in the intima increases. The retained LDL moves into the arterial wall by diffusion and convection (see Figure 6.2).

The response to retention hypothesis of early atherosclerosis, put forward by Williams and Tabas (1995), defines the subendothelial retention of atherogenic lipoproteins as the main pathogenic process in early atherogenesis. Because aortic fatty streaks have been observed in infancy, and even in human fetal aortas, bidirectional flux of lipids could be regarded as a part of normal physiological metabolism. Although the most important aspect in initial lesion development is the retention of LDL in the subendothelial space, with a marked preference for lesion-prone sites, this process does not always happen in

parallel with increased levels of circulating lipids and an increased rate of influx into the arterial wall. Schwenke and Carew (1989) demonstrated that the early accumulation of lipoproteins occurs selectively in lesion-prone sites of the arterial wall, but the delivery rates of lipoproteins into lesion-prone and resistant sites were not different, meaning that there is a natural saturation of LDL penetration. Although the LDL suspended quantity in the blood would be abnormally high, the LDL retained amount by the artery wall should be similar for all pathological LDL concentration since the accumulation of LDL can not grow indefinitely.

3 - LDL oxidation

LDL molecules placed in the artery wall can be oxidized. Moreover, LDL cholesterol becomes even more dangerous when it is oxidized. The oxidized LDL itself then becomes more reactive with the surrounding tissues, which can produce tissue damage. A complex set of biochemical reactions, which have been neglected in this model, regulates the oxidation of LDL particles, chiefly stimulated by presence of necrotic cell debries, free radicals in the endothelium and enzimes.

4 - Monocytes recruitment

After the LDL penetration and oxidation, recruitment of leukocytes to the vessel wall, which is a multi-step process consisting of capture, rolling, arrest, adhesion, and transmigration through the endothelium, occurs. These steps require expression and interaction of adhesion molecules and their ligands on the vascular endothelium and on the monocyte surface (Eriksson *et al.*, 2001). The mechanisms of monocyte recruitment to the vessel wall have been reviewed in Bobryshev (2006) and Quehenberger (2005). The monocytes are recruitment into the arterial wall due to the presence of LDL (see Figure Figure 6.2). The oxidized LDL particles have several pro-inflammatory properties, including activation of endothelial cells, causing them to express the adhesion of vascular cell. It should be noted that only a part of the monocytes carried by the blood passes trough the endothelium, i.e. despite the fact that the endothelium is injured, it becomes semi-permeable. Thus, the monocytes recruitment will be proportional to the blood monocytes concentration. Moreover, since the role of monocytes is neutralized the oxidized LDL, the monocytes concentration should be greater in those areas plenty of oxidized LDL.

5 - Monocytes differentiation into macrophages

Furthermore, a strong interaction between monocytes and components of the extracellular matrix (ECM), e.g., collagen and proteoglycans, is a prerequisite for the formation of lipid-laden macrophages. Therefore, the monocytes are differentiated into macrophages, which are responsible for protecting tissues from foreign substances such as pathogens, cellular debris and other compounds harmful to the body, and to activate

other immune cells through secretion of signal molecules and as an antigen presenting cell. They are cells that possess a large smooth nucleus, a large area of cytoplasm, and many internal vesicles for processing foreign material.

6 - Oxidized LDL uptaken by macrophages and foam cell formation

Then, the macrophages engulf oxidized LDL by endocytosis via scavenger receptors, and the oxidized LDL accumulates in the macrophages and other phagocytes, which are then known as foam cells. As macrophages accumulate oxidized lipid, lesions form as nodular areas of lipid deposition that are also known as fatty streaks, and these represent lipid-filled macrophages (i.e., foam cells). Continued foam cell formation and macrophage necrosis can produce lesions that contain small extracellular pools of lipid. Foam cells are not dangerous as such, but can become a problem when they accumulate at particular foci thus creating a necrotic centre of atherosclerosis.

6.3 Model governing equations

6.3.1 Fluid dynamics

As alluded before, the model considers both the blood and plasma which flow inside the lumen and the artery wall, respectively. Navier-Stokes equations were employed to model bulk blood flow in the lumen, whereas Darcy's Law was used to model transmural flow in the intima.

A - Blood flow along the artery lumen:

The nature pulsatile of blood flow has not taken into account. The laminar motion of pure fluids is completely described by the Navier-Stokes equations, which express Newton's law of conservation of momentum in the fluid as it passes trough a control volume and are combined with the equation of conservation of mass or continuity equation. Then, blood flow was assumed to be steady, incompressible, laminar, Newtonian, and, hence, governed by the Navier-Stokes equation,

$$\rho_b(\boldsymbol{u}_l \cdot \nabla)\boldsymbol{u}_l = \nabla \cdot \Big[- p_l 2\boldsymbol{I} + \mu_b\big(\Delta \boldsymbol{u}_l + (\Delta \boldsymbol{u}_l)^t\big)\Big] + F_l, \tag{6.1}$$

and the continuity equation,

$$\rho_b \nabla \cdot \boldsymbol{u}_l = 0, \tag{6.2}$$

where ∇ and Δ, denote the gradient and the Laplacian operator, respectively. The subscript l is used to represent the lumen, meaning that the velocity, pressure or whatever variable with this subscript is referred to the lumen volume, then, $\boldsymbol{u}_l$ is the velocity

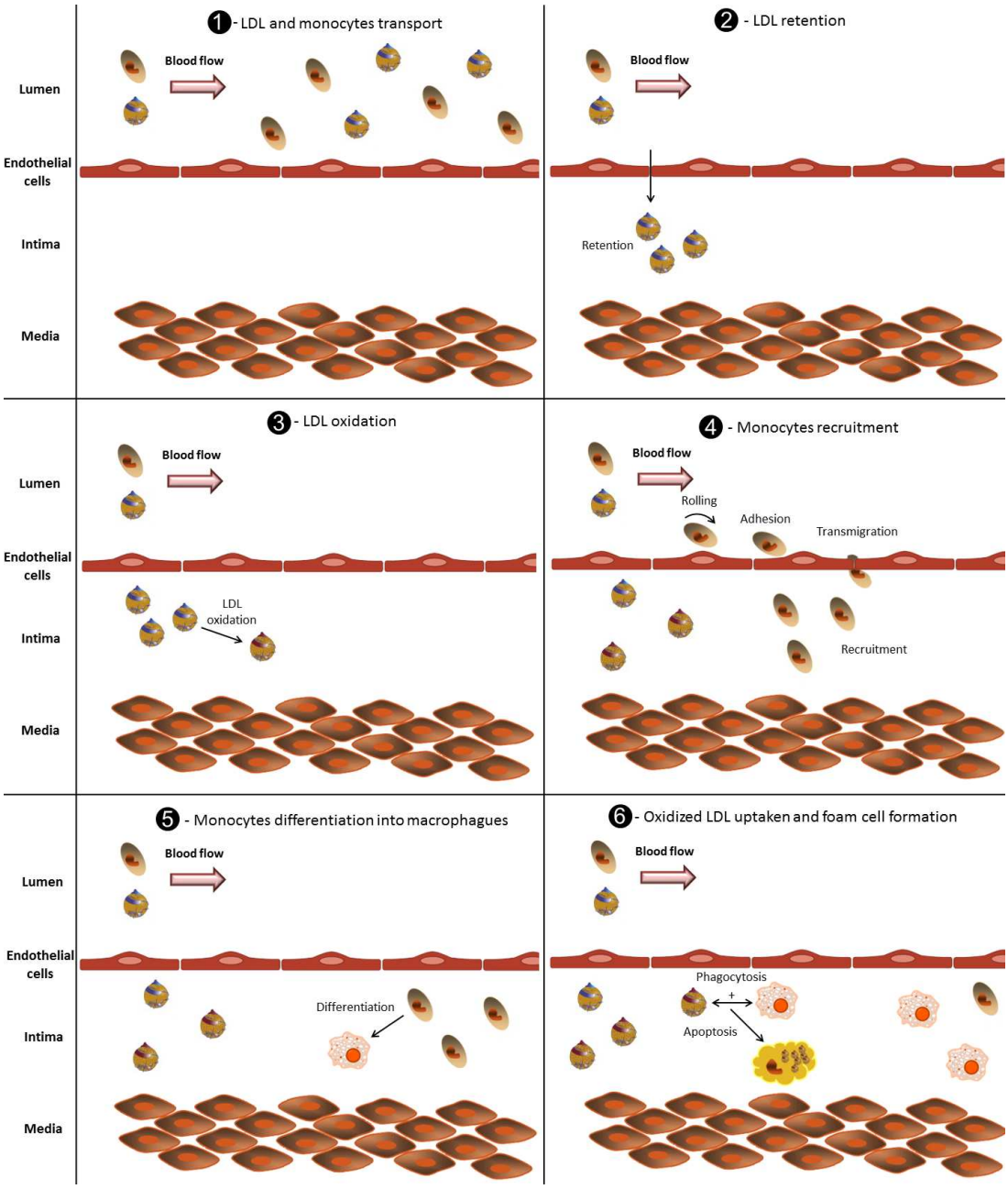

Figure 6.2: Steps to the atheroma plaque initiation considered in the developed model.

vector field in the lumen, p_l is the lumen pressure and F_l are the internal forces which are neglected in this model. μ_b and ρ_b, the blood density and viscosity, respectively, are well defined in the literature. In the present study, blood density and viscosity were assumed to be $\rho_b = 1050\ \frac{kg}{m^3}$ and $\mu_b = 0.0035$ Pa $\cdot$ s, respectively, although blood is not a Newtonian fluid and therefore the viscosity depends on local shear rate (Milnor, 1989; Stouffer, 2007).

Suitable boundary conditions need to be specified in order to obtain numerical solutions to the above equations. These include, a given parabolic velocity profile imposed at the inlet of the artery and a given pressure at the outlet. This velocity profile can be assumed as:

$$u_r = 2u_0\left(1 - \left(\frac{r}{R_a}\right)^2\right), \tag{6.3}$$

where u_0 is the mean inlet velocity taken to be $u_0 = 0.24\ \frac{m}{s}$ as the average of the mean diastolic and systolic velocities in the left anterior descending coronary artery according to the experimental data of Iliceto *et al.* (1991), R_a is the internal radius of the artery in which the model is simulated and r is the radius of the artery at the axial location. The geometry used to validated the geometry corresponds to a normal coronary artery of $1.85 \cdot 10^{-3}$ m of internal radius. Furthermore, following the experimental conditions of Meyer *et al.* (1996), a constant pressure boundary condition of 9332.089 Pa (70 mmHg) is used at the outlet of the artery. Finally, a no slip boundary condition was applied at the lumen and endothelium interface. In fluid dynamics, the no-slip condition for viscous fluids states that at a solid boundary, the fluid will have zero velocity relative to the boundary.

B - Transmural plasma flow throughout the artery wall:

The transmural velocity vector field $\boldsymbol{u}_w$ in the arterial wall is calculated with the Darcy's Law,

$$\boldsymbol{u}_w = \frac{\kappa_w}{\mu_p}\nabla p_w, \tag{6.4}$$

and the corresponding continuity equation,

$$\frac{\partial(\rho_p \epsilon_p)}{\partial t} + \rho_p \nabla \cdot \boldsymbol{u}_w = J_v, \tag{6.5}$$

where the subscript w is used to represent the artery wall, indicating that the velocity, pressure or whatever variable with this subscript is referred to the artery wall volume. κ_w, the Darcian permeability of the arterial wall, is a measure of the flow conductivity and is one of the key parameters characterizing a porous medium, and it has been taken as $1.2 \cdot 10^{-18}\ m^2$, which agrees well with the literature values of $1 - 2 \cdot 10^{-18}\ m^2$ (Vargas *et al.*, 1979; Huang *et al.*, 1994; Prosi *et al.*, 2005). ρ_p and μ_p are the density and viscosity of the blood plasma, respectively, and its value have been well assessed in the literature as $\mu_p = 0.001$ Pa $\cdot$ s and $\rho_p = 1000\ \frac{kg}{m^3}$, respectively. p_w is the pressure within the arterial wall which is determined by the blood flow simulation along the artery lumen, and $J_v\ \left[\frac{m}{s}\right]$ is the transmural volume flux specified in the normal direction to the endothelium for the artery lumen which is calculated by means of a

three pore model. Finally, the porosity of the wall, ϵ_p, has been taken as 0.96, which corresponds to the intima porosity value according to Ai and Vafai (2006).

Concerning the boundary conditions defined to compute the transmural flow through the intima, a volumetric flux (J_v) was applied perpendicular to the endothelium surface, and in order to specify a pressure drop across the arterial wall, a constant pressure of 2333.022 Pa (17.5 mmHg) was assumed at the intima-media interface (Olgac *et al.*, 2008; Gefen, 2012).

As explained before, the coupling of flow dynamics in the artery lumen with that in the arterial wall is achieved by a three pore model, and the volumetric flux through the endothelium is calculated by this theory which takes into account the vesicular pathway, normal endothelial junctions, and leaky junctions (see Figure 6.3).

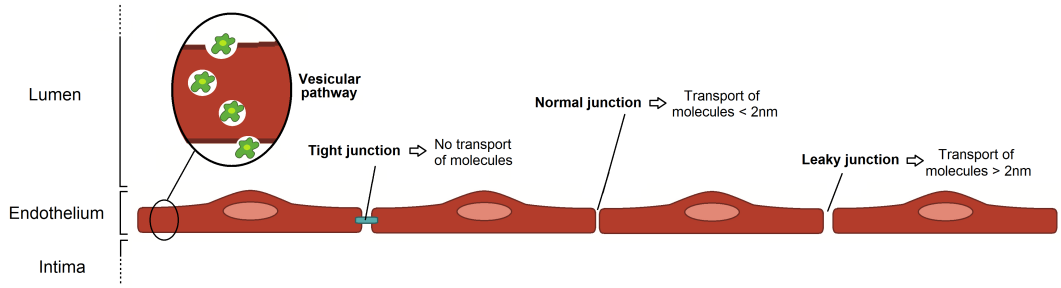

Figure 6.3: Transport pathways across the endothelium. The major transport pathways are: the tight junctions, normal junctions which block the passage of molecules with a radius larger than 2 nm, vesicles, and leaky junctions which allows the transport of molecules with a radius larger than 2 nm.

Therefore, at the fluid-tissue interface (i.e. the endothelium), volume flux was defined by the Kedem and Katchalsky (1958) equations. Then, following Curry (1984), the volume flux J_v $\left[\frac{m}{s}\right]$ through a single pathway is given by

$$J_v = Lp(\Delta p - \sigma_d \Delta \Pi), \tag{6.6}$$

where Lp and σ_d are the hydraulic conductivity and the osmotic reflection coefficient of a single pathway, respectively, and Δp and $\Delta \Pi$ are the hydraulic and osmotic pressure differences across the endothelial layer, respectively. However the osmotic pressure difference is neglected in order to decouple the fluid dynamics from the solute dynamics (Olgac *et al.*, 2008; Gefen, 2012). Therefore, the equation above can be written as

$$J_v = Lp\Delta p, \tag{6.7}$$

being Δp 18 mmHg (Tedgui and Lever, 1984).

In a three pore model, the total volume flux, J_v, can be obtained by summing the fluxes over each single pathway, i.e.,

$$J_v = \underbrace{J_{v,lj}}_{Leaky\ junctions} + \underbrace{JJ_{v,nj}}_{Normal\ junctions} + \underbrace{J_{v,v}}_{Vesicular\ pathways}, \tag{6.8}$$

where $J_{v,lj}$, $J_{v,nj}$ and $J_{v,v}$ are the volume flux through leaky and normal junctions and vesicular pathway, respectively. Volume flux occurs through normal and leaky junctions (Ogunrinade *et al.*, 2002; Tarbell, 2003), therefore,

$$J_{v,v} = 0, \tag{6.9}$$

and then, Equation 6.8 becomes

$$J_v = J_{v,lj} + J_{v,nj}. \tag{6.10}$$

Moreover, the volume flux through leaky and normal junctions can be expressed as:

$$J_{v,lj} = L_{p,lj}\Delta p \tag{6.11}$$

and

$$J_{v,nj} = L_{p,nj}\Delta p, \tag{6.12}$$

respectively. $L_{p,nj}$ is the hydraulic conductivity for the normal junction taken as 1.58 $\cdot 10^{-9}$ $\frac{m}{s \cdot mmHg}$ (Tedgui and Lever, 1984) and $L_{p,lj}$, the hydraulic conductivity for the leaky junction, can be defined as

$$L_{p,lj} = \frac{A_p}{S} L_{p,slj}, \tag{6.13}$$

where $\frac{A_p}{S}$ represents the fraction of the surface area S occupied by the leaky junctions, and $L_{p,slj}$ the hydraulic conductivity of a single leaky junction.

The endothelium is modeled as a boundary between the artery lumen and the arterial wall with endothelial clefts and leaky junctions in and between the endothelial cells, respectively. Adopting the approaches of Huang *et al.* (1994) Weinbaum *et al.* (1985) and Yuan *et al.* (1991), the normal endothelial junctions are considered to be cylindrical pores on the junction strands at the endothelial clefts, whereas the leaky junctions are modeled as ring-shaped pores surrounding the leaky cells. The leaky junctions are assumed to be randomly distributed and spaced $2\varepsilon_{lj}$ apart, as shown in Figure 6.4. Additionally, a periodic unit can be constructed by drawing a circle of radius ε_{lj} centered at each leaky junction.

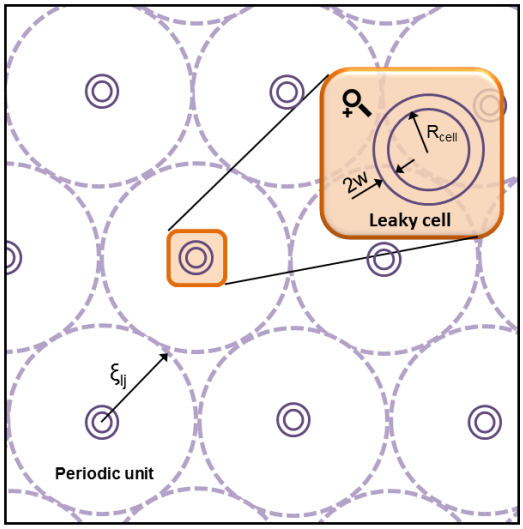

Figure 6.4: Illustration of randomly distributed leaky cells. A leaky cell is present at the center of each periodic circular unit of radius (ε_{lj}) represented by dashed lines. The gray background represents the normal cells. Cells have a radius of R_{cell}, and leaky junctions have a half-width of w.

Therefore, according to Figure 6.4, the fraction of leaky junctions, ϕ_{lj}, is defined as the ratio of the area of leaky cells to the area of all cells (Huang *et al.*, 1994), using this definition,

$$\phi_{lj} = \frac{{R_{cell}}^2}{{\varepsilon_{lj}}^2}, \tag{6.14}$$

and the fraction of the surface area S occupied by the leaky junctions as

$$\frac{A_p}{S} = \frac{A_{slj}}{\pi {\varepsilon_{lj}}^2}, \tag{6.15}$$

where A_{slj} is the area of a single leaky junction, which can be calculated by

$$A_{slj} = 2\pi R_{cell} 2w, \tag{6.16}$$

with the endothelial cell radius, R_{cell}, is 15 μm (Huang *et al.*, 1994; Weinbaum *et al.*, 1985; Yuan *et al.*, 1991), and w, the half-width of a leaky junction, 20 nm (Huang *et al.*, 1994; Weinbaum *et al.*, 1985; Yuan *et al.*, 1991). Combining equations 6.14, 6.15 and 6.16, $\frac{A_p}{S}$ can also be represented as

$$\frac{A_p}{S} = \frac{4w}{R_{cell}} \phi_{lj}. \tag{6.17}$$

Therefore, once ϕ_{lj} is known, the transport properties of the leaky junctions can be calculated accordingly. In the presented model, ϕ_{lj} is assigned locally at the endothelium as a function of WSS. The correlation between WSS and ϕ_{lj} is obtained using published experimental data used in the study of Olgac *et al.* (2008), where the several steps described in the following paragraphs are carried out.

Levesque *et al.* (1986) studied stenosed dog aortas and correlated the cell shape with levels of shear stress. Cell shape is generally expressed in terms of a shape index (SI) defined as

$$SI = \frac{4\pi\ area}{perimeter^2}, \tag{6.18}$$

where area and perimeter correspond to the dimensions of a single cell. Consequently, SI is one for a circle and approaches zero for a line.

Suciu (1997) and Chiu *et al.* (1998) used cell cultures to observe the cell alignment of endothelial cells as a response to shear stress. Based on experimental data from these studies (Levesque *et al.*, 1986; Suciu, 1997; Chiu *et al.*, 1998), an empirical correlation between wall shear stress and endothelial cell shape index, SI, has been defined (Olgac *et al.*, 2008):

$$SI = 0.380\exp(-0.79WSS) + 0.225\exp(-0.043WSS). \tag{6.19}$$

Chien (2003) observed rabbit thoracic aortas and counted the number of mitotic cells in regions of specific shape indexes. Then, the experimental data of Chien (2003) to correlate the shape index to the number of mitotic cells, MC, per unit area of 0.64 mm^2 have been used:

$$MC = 0.003797\exp(14.75SI). \tag{6.20}$$

Lin *et al.* (1989) observed thoracic aortas of 10 rats to determine the total number of mitotic cells and the total number of leakage sites. He found that 45.3% of total leakage sites are formed by mitotic cells and that 80.5% of total mitotic cells are leaky. Adopting the proportions by Lin *et al.* (1989), the number of leaky cells associated with mitotic cells is calculated by multiplying the number of mitotic cells with 0.805, and the total number of leaky junctions by dividing the number of leaky cells associated with mitotic cells by 0.453. Moreover, Olgac *et al.* (2008) determined the number of leaky junctions associated with nonmitotic cells to be 0.307. Therefore, the correlation between the number of leaky cells, LC, per unit area of 0.64 mm^2, and the number of mitotic cells results as:

$$LC = 0.307 + \frac{0.805MC}{0.453}. \tag{6.21}$$

Because the fraction of leaky junctions ϕ_{lj} is defined as the ratio of the area of leaky cells to the area of all cells (Huang *et al.*, 1994), ϕ_{lj} can also be written as

$$\phi_{lj} = \frac{LC\pi {R_{cell}}^2}{unit\ area}, \tag{6.22}$$

where as indicated before, the unit area is considered 0.64 mm^2.

Furthermore, to calculate the the hydraulic conductivity for the leaky junction by solving the Equation 6.13, the hydraulic conductivity of a single leaky junction, $L_{p,slj}$, should be defined. The transport properties of the leaky junctions, i.e., hydraulic conductivity, diffusive permeability, and reflection coefficient, are estimated using the pore theory (Curry, 1974, 1984; Olgac *et al.*, 2008). Accordingly, the hydraulic conductivity of a single leaky junction is given by

$$L_{p,slj} = \frac{w^2}{3\mu_p l_{lj}}, \tag{6.23}$$

where l_{lj} is the length of the leaky junction (Huang *et al.*, 1994; Weinbaum *et al.*, 1985; Yuan *et al.*, 1991) taken to be 2 μm.

Finally, with all this consideration, the volume flux J_v through a single pathway can be estimated.

6.3.2 Solute dynamics

In order to modeled the mass transfer across the lumen and artery wall, two different steps have been taken account; the first step corresponds to a steady-state diffusion and convection along the lumen of the LDL particles and the monocytes cells, and the second one is related to the transmural time dependent process of mass transport, where the monocytes transmigration and later differentiation into macrophages, the LDL accumulation and further oxidation, the ingest of oxidized LDL by the macrophages and its apoptosis, leading to foam cells. Furthermore, it should be noted that the concentrations of the molecules and cells are measured in $\frac{mol}{m^3}$ and $\frac{cell}{m^3}$, respectively.

STEP 1 - Steady-state diffusion and convection along the lumen

A - LDL particles:

The LDL transport in the blood fluid domain along the artery lumen is governed by the convection-diffusion equation:

$$\underbrace{\nabla \cdot (-D_{LDL,l} \nabla C_{LDL,l})}_{Diffusion} + \underbrace{\boldsymbol{u}_l \cdot \nabla C_{LDL,l}}_{Convection} = 0, \tag{6.24}$$

and a convective flux condition is used to ensure that LDL is convected out of the domain with flow:

$$\boldsymbol{N} = -D_{LDL,l}\nabla C_{LDL,l} + \boldsymbol{u}_l C_{LDL,l}, \tag{6.25}$$

where $D_{LDL,l}$ is the LDL diffusion coefficient in the lumen blood flow, which is taken as $5 \cdot 10^{-12}$ $\frac{m^2}{s}$ (Curry, 1984; Olgac *et al.*, 2008), and $C_{LDL,l}$ is the LDL concentration. For the mass transport calculations at the lumen, a constant concentration boundary condition of 1.2 $\frac{mg}{ml}$ or equivalent 3.1 $\frac{mol}{m^3}$ considering the molar mass of the LDL as 386.65 $\frac{g}{mol}$ (Guarino *et al.*, 2006), is used at the lumen inlet in accordance with the common human blood LDL concentration level which is considered 0.5-2 $\frac{mg}{ml}$ (Goldstein and Brown, 1977; Ai and Vafai, 2006). Therefore, the LDL concentration distribution at the lumen inlet was assumed to have a uniform profile. Finally, an outflow and no flux boundary conditions were applied at the lumen outlet and lumen-artery wall interface, respectively.

B - Monocytes:

Analogous, the monocyte diffusion and convection processes along the lumen are regulated by

$$\underbrace{\nabla \cdot (-D_{m,l}\nabla C_{m,l})}_{Diffusion} + \underbrace{\boldsymbol{u}_l \cdot \nabla C_{m,l}}_{Convection} = 0 \tag{6.26}$$

and

$$\boldsymbol{N} = -D_{m,l}\nabla C_{m,l} + \boldsymbol{u}_l C_{m,l} \tag{6.27}$$

equations. Where $D_{m,l}$ is the diffusion coefficient of the monocytes in the lumen which is taken as $1 \cdot 10^{-10}$ $\frac{m^2}{s}$ (Petty *et al.*, 1980), and $C_{m,l}$ the monocytes concentration in the lumen. Since the normal range for the monocyte count is 200 - 950 $\frac{cells}{mm^3}$ (Khan, 2009), a intermediate value of 550 $\frac{cells}{mm^3}$ has been chosen as initial concentration of monocytes at the inlet of the artery. Then, as for the LDL substance, the monocytes concentration distribution at the lumen inlet was assumed to have a uniform profile. Again, an outflow and no flux boundary conditions were applied at the lumen outlet and lumen-artery wall interface, respectively.

STEP 2 - Time dependent diffusion and convection along the artery wall

A - LDL particles:

The LDL diffusion and convection through the artery wall can be modelled as

$$\frac{\partial C_{LDL,w}}{\partial t} + \underbrace{\nabla \cdot (-D_{LDL,w} \nabla C_{LDL,w})}_{Diffusion} + \underbrace{\boldsymbol{u}_w \cdot \nabla C_{LDL,w}}_{Convection} = \underbrace{-d_{LDL} C_{LDL,w}}_{LDL\ oxidation}. \tag{6.28}$$

where $C_{LDL,w}$ and $D_{LDL,w}$ are the LDL concentration in the artery wall and the LDL diffusive coefficient in the plasma, respectively. Different diffusive coefficient of LDL into the wall artery can be found in the literature, to name few, Prosi *et al.* (2005) and Dabagh *et al.* (2009) reported a LDL diffusive coefficient of $8 \cdot 10^{-13}$ and $5 \cdot 10^{-10}$ $\frac{m^2}{s}$, respectively. Therefore, a intermediate value of $8 \cdot 10^{-11}$ $\frac{m^2}{s}$ has been chosen as LDL diffusive coefficient. d_{LDL} is the degradation rate of LDL. Published LDL degradation rates vary from 1.4 to $6.05 \cdot 10^{-4}$ s^{-1} (Esterbauer *et al.*, 1989; Prosi *et al.*, 2005; Sun *et al.*, 2005; Ai and Vafai, 2006; Sun *et al.*, 2006), thus an average value of $3.0 \cdot 10^{-4}$ s^{-1} has been chosen as LDL degradation rate.

Apart from the diffusive and convective terms of the Equation 6.28, the term of the right side, $d_{LDL} C_{LDL,w}$, corresponds to the LDL oxidation formation, indicating the concentration per second which is oxidized.

Besides, insulation boundary conditions were applied at both axial ends of the artery wall,

$$\boldsymbol{N} = -D_{LDL,w} \nabla C_{LDL,w} + \boldsymbol{u}_w C_{LDL,w}. \tag{6.29}$$

Moreover, at the media-adventitia interface, a constant LDL concentration value of 0.005 times of the LDL concentration retained at the lumen-intima interface have been assigned as Meyer *et al.* (1996) reported. The lumen artery wall interface coupling of solute dynamics is achieved by a three pore model that takes into account the vesicular pathway, normal endothelial junctions, and leaky junctions. Thus, the solute flux of LDL at the endothelium was defined by the Kedem and Katchalsky (1958) equations.

The total LDL solute flux, $J_{s,LDL}$ $\left[\frac{mol}{m^2 s}\right]$, through a single pathway is given by (Curry, 1984)

$$J_{s,LDL} = P_i (c_l - c_w) \frac{Pe_i}{\exp(Pe_i) - 1} + J_v (1 - \sigma_{f,i}) c_l, \tag{6.30}$$

with c_l and c_w the luminal and arterial wall side LDL concentrations at the endothelium, respectively, P_i and $\sigma_{f,i}$ the diffusive permeability and the solvent-drag reflection coefficient of the single pathway, respectively, and Pe_i is a modified Peclet number that is defined as the ratio of convective to diffusive fluxes through the pathway (Olgac *et al.*, 2008)

$$Pe_i = \frac{J_v(1-\sigma_{f,i})}{P_i}. \tag{6.31}$$

The endothelium has a high resistance to LDL transport (Ogunrinade *et al.*, 2002; Stangeby and Ethier, 2002b; Tarbell, 2003) and, as a result, is c_w much smaller compared with c_l, therefore c_w is neglecting. Furthermore, since the whole c_l is not retained at the endothelium, it has been considered that just one of each thousand of LDL particles of the blood flow is deposited at the artery wall in order to pass through the leaky and normal junctions and vesicular paths, then (LDL_{dep} was chosen as $1 \cdot 10^{-3}$). Furthermore, since the entrance of LDL into the arterial wall can not grow indefinitely, there is a natural saturation incorporated by the ${C_{LDL}}^{th}$ in the denominator. Meaning that the LDL retention increases as the cholesterol level of the blood flow increases, however, it has been considered that this natural saturation occurs when the LDL levels on the blood are pathological, i.e., high levels of total cholesterol (270 $\frac{mg}{m^3}$) (National Institutes of Health, 2002). In order to obtain coherent ${C_{LDL}}^{th}$ units $\left[\frac{mol}{m^3}\right]$, the considered high level of total cholesterol has been divided by the molar mass of the LDL, 386.65 $\frac{g}{mol}$ (Guarino *et al.*, 2006). Therefore, 6.98 $\frac{mol}{m^3}$ has been assigned as ${C_{LDL}}^{th}$. Therefore, Equation 6.30 can be reformulated as:

$$J_{s,LDL} = LDL_{dep}\frac{c_l}{1+\frac{c_l}{{C_{LDL}}^{th}}}P_{app}, \tag{6.32}$$

where LDL_{dep} is the LDL deposition coefficient which indicates the percentage of LDL particules from the blood flow deposited at the endothelium and P_{app} is the apparent permeability coefficient given as

$$P_{app} = P_i Z_i + J_v(1-\sigma_{f,i}), \tag{6.33}$$

and Z_i is a fractional reduction factor in solute concentration gradient at the pore entrance defined as

$$Z_i = \frac{Pe_i}{\exp(Pe_i)-1}. \tag{6.34}$$

In the absence of flow through the pore, i.e., when convection vanishes, $Pe_i \to 0$ and $Z_i \to 1$, which represents the pure diffusion case. As $Pe_i \to \infty$, i.e., convection dominates over diffusion, $Z_i \to 0$.

Additionally, P_{app} is the total apparent permeability of the endothelial layer given as the sum of apparent permeabilities of each single pathway:

$$P_{app} = P_{app,nj} + P_{app,lj} + P_v, \tag{6.35}$$

where $P_{app,nj} = P_{nj}Z_{nj} + J_{v,nj}(1 - \sigma_{f,nj})$ and $P_{app,lj} = P_{lj}Z_{lj} + J_{v,lj}(1 - \sigma_{f,lj})$ are the apparent permeabilities of the normal junctions and the leaky junctions, respectively, and P_v is the permeability of the vesicular pathway. Applying the proportion between the leaky junction pathway and vesicular transport reported by Cancel *et al.* (2007), P_v is calculated to be $1.92 \cdot 10^{11}$. However, as Figure 6.3 shown, LDL flux occurs by vesicular transport and through leaky junctions, but not through normal junctions since they block the passage of solutes with a radius larger than 2 nm, which is the LDL case with a radius of 11 nm (Prosi *et al.*, 2005; Ogunrinade *et al.*, 2002). Consequently, the diffusive permeability and the solvent-drag reflection coefficient become P_{nj}=0 and $\sigma_{f,nj}$=0, respectively, resulting in $P_{app,nj}$=0. Thus, Equation 6.35 results as

$$P_{app} = P_{lj}Z_{lj} + J_{v,lj}(1 - \sigma_{f,lj}) + P_v, \tag{6.36}$$

where P_{lj}, the diffusive permeability of the leaky junction pathway, is defined as

$$P_{lj} = \frac{A_p}{S}\Phi P_{slj}, \tag{6.37}$$

being $\Phi = 1 - \alpha_{lj}$ the partition coefficient, i.e., the ratio of the pore area available for solute transport to the total pore area, $\alpha_{lj} = \frac{a}{w}$ the ratio of the radius a of the transported molecule to the half-width of the leaky junction and P_{slj} the diffusive permeability of a single leaky junction, which is given by

$$P_{slj} = \frac{D_{lj}}{l_{lj}}, \tag{6.38}$$

where D_{lj} is the diffusion coefficient in a leaky junction, which is related to the free diffusion coefficient in the lumen, D_l, by the expression

$$\frac{D_{lj}}{D_l}F(\alpha_{lj}) = 1 - 1.004\alpha_{lj} + 0.418{\alpha_{lj}}^3 - 0.16{\alpha_{lj}}^5, \tag{6.39}$$

where $F(\alpha_{lj})$ is a function describing the restricted diffusivity in a pore.

Finally, the solvent drag coefficient σ_{lj} for the leaky junctions is given by

$$\sigma_{lj} = 1 - \frac{2}{3}{\alpha_{lj}}^2(1 - \alpha_{lj})F(\alpha_{lj}) - (1 - \alpha_{lj})(\frac{2}{3} + \frac{2\alpha_{lj}}{3} - \frac{7{\alpha_{lj}}^2}{12}). \tag{6.40}$$

Following all this considerations, the total LDL solute flux, $J_{s,LDL}$ $[\frac{mol}{m^2 s}]$, can be estimated.

B - Monocytes:

The diffusion and convection governed equations for the monocytes cells are:

$$\frac{\partial C_{m,w}}{\partial t} + \underbrace{\nabla \cdot (-D_{m,w} \nabla C_{m,w})}_{Diffusion} + \underbrace{\boldsymbol{u}_w \cdot \cancel{\nabla C_{m,w}}}_{Convection} \tag{6.41}$$

$$= - \underbrace{d_m C_{m,w}}_{Differentiation} - \underbrace{m_d C_{m,w}}_{Death} + \underbrace{C_{m,w} C_{LDL_{ox},w} \exp \frac{-C_{m,w}^2}{2 C_{m,w}^{th\ 2}}}_{Chemotaxis},$$

and

$$\boldsymbol{N} = -D_{m,w} \nabla C_{m,w} + \boldsymbol{u}_w C_{m,w}, \tag{6.42}$$

where $C_{m,w}$ and $D_{m,w}$ is the concentration and diffusive coefficient of monocytes, respectively, and d_m is the rate of monocytes which differentiate into macrophages. According to Bulelzai and Dubbeldam (2012), d_m has been considered as $1.15 \cdot 10^{-6}\ s^{-1}$, and $D_{m,w}$ as $8 \cdot 10^{-13}\ \frac{m^2}{s}$ since according to the literature it can be considered the cells diffusion coefficients two order of magnitude more than the molecular substances (Budu-Grajdeanu *et al.*, 2008). m_d indicated the frequency of the monocytes natural death, the life span of monocytes is about 30-90 days as Krstic (1997) reported. Therefore, m_d is chosen as $2.572\ s^{-1}$, considering the intermediate value of 45 days of life expectancy. The monocytes undergo random motion, are chemotactically attracted to the chemicals in the presence of oxidized LDL, and grow up to a maximal value $C_{m,w}^{th}$. Therefore, the last term on the right hand side of Equation 6.41 corresponds to the chemotaxis of monocytes due to the oxidized LDL presence. The natural saturation at this maximum value have been included by means of a gaussian function. This gaussian function is set to 1 while there is not monocytes in the artery wall, and it decreases slightly to 0. The gaussian function is set to 0 when the monocytes concentration is bigger than $C_{m,w}^{th}$, a threshold monocyte concentration which has been set to the same value than monocyte blood concentration.

As equation 6.41 shown, the monocytes can move by diffusion and convection, however, due to the size of the monocytes, the convection term has been neglected. Moreover, regarding the boundary conditions, insulation conditions were applied at both axial ends of the wall and media-adventitia interface, and a perpendicular monocytes inflow to the endothelium have been defined. The solute flow dependence on the WSS has been modeled based on the study of Bulelzai and Dubbeldam (2012). The monocytes solute flux per unit of surface, $J_{s,m}$ $[\frac{celulas}{m^2\ s}]$, is modelled as

$$J_{s,m} = \frac{m_r}{1 + \frac{WSS}{WSS_0}} C_{LDL_{ox},w} C_{m,l} \tag{6.43}$$

which is consistent with the fact that larger shear rates imply a smaller growth coefficient for the monocytes (Malek *et al.*, 1999; Gijsen *et al.*, 2008). The value of WSS_0 designates the wall shear stress at which the growth rate of the monocyte concentration due to the signaling response by the endothelium is reduced with a factor of two compared to the zero wall shear rate response by the endothelium and it is taken as 1 Pa (Bulelzai and Dubbeldam, 2012). Since the monocytes captation for the artery wall is due to the presence of oxidized LDL in the intima, the second term on the right hand side of Equation 6.43 contemplates $C_{LDL_{ox},w}$ in the numerator. The entrance of monocytes into the arterial wall will be regulated by the oxidized LDL concentration, being the monocytes flux unnecessary when the oxidized LDL would be complectly eliminated. Moreover, the monocytes flux depends on the lumen concentration of this specie, indicating that the flux increases as the monocytes blood concentration increases. Finally, the factor m_r is a constant which determines the rate at which monocytes enter the intima for small wall shear stress and per $\frac{mol}{m^3}$ of oxidized LDL. According to the experimental test performed by Steinberg *et al.* (1977), the 90% of monocytes which were injected into a mutant rabbit disappear from the blood flow at 72 hours. So, each day the 30% of the monocytes of the blood flow is recruitment by the artery wall. Then, considering a unit surface of the model, i.e $\frac{\pi R^2 dh}{2\pi R dh}$, the m_r constant should satisfied that $\frac{m_r}{1+\frac{WSS}{WSS_0}}$ divided per unit of surface is equal to 0.3 $\frac{m^3}{mol\ day_{-1}}$. Thus, m_r has been taken $5.5 \cdot 10^{-4}$ $\frac{m^3}{mol\ day_{-1}}$.

C - Oxidized LDL:

For the oxidized LDL process we came to the followings equation:

$$\frac{\partial C_{LDL_{ox},w}}{\partial t} + \underbrace{\nabla \cdot (-D_{LDL_{ox},w} \nabla C_{LDL_{ox},w})}_{Diffusion} + \underbrace{\boldsymbol{u}_w \cdot \nabla C_{LDL_{ox},w}}_{Convection} \tag{6.44}$$

$$= \underbrace{d_{LDL} C_{LDL,w}}_{Oxidated\ from\ LDL} - \underbrace{LDL_{oxr} C_{LDL_{ox},w} C_{M,w}}_{Uptaken\ by\ macrophages},$$

$$\boldsymbol{N} = -D_{m,w} \nabla C_{m,w} + \boldsymbol{u}_w C_{m,w}, \tag{6.45}$$

where $C_{LDL_{ox},w}$ and $D_{LDL_{ox},w}$ are the concentration and diffusive coefficient of oxidized LDL, respectively. $D_{LDL_{ox},w}$ values varies from $1 \cdot 10^{-8}$ to $2.4 \cdot 10^{-5}$ $\frac{m^2}{s}$ in the literature

(Siogkas *et al.*, 2011; Bulelzai and Dubbeldam, 2012), However, it has been considered the same diffusion coefficient for the LDL than for the oxidized one, thus a value of $8 \cdot 10^{-11}$ $\frac{m^2}{s}$ has been considered. $d_{LDL}C_{LDL,w}$ modeled the oxidized LDL process from the LDL, whose constant has been previously defined. Finally, the quantity of LDL uptaken by the macrophages per second $\left[\frac{mol}{m^3\ s}\right]$ is defined by the first term on the right hand side of Equation 6.44, where $C_{M,w}$ is the concentration of macrophages. LDL_{oxr} is the rate of LDL uptaken by a macrophage, which has been asses as $0.0012 \cdot 10^{-15}$ $\frac{m^3}{cells\ s}$ based on the experimental data of Kruth *et al.* (2002), and knowing that 10^6 macrophages are approximately $25 \cdot 10^{-9}$ kg of cell proteins (Steinman and Cohn, 1972).

Finally, insulation boundary condition were applied at all the walls, i.e. at the lumen-intima and media-adventitia interface and at the axial ends of the wall.

D - Macrophages:

The evolution for the macrophages cells is modelled by

$$\frac{\partial C_{M,w}}{\partial t} + \underbrace{\nabla \cdot (-D_{M,w}\nabla C_{M,w})}_{Diffusion} + \underbrace{\cancel{\boldsymbol{u}_w \cdot \nabla C_{M,w}}}_{Convection} \tag{6.46}$$

$$= \underbrace{d_m C_{m,w}}_{Differenciates\ from\ monocytes} - \underbrace{\frac{M_{r1}}{M_{r2}} LDL_{oxr} C_{M,w} C_{LDL_{ox},w}}_{Converted\ to\ foam\ cells},$$

and

$$\boldsymbol{N} = -D_{M,w}\nabla C_{M,w} + \boldsymbol{u}_w C_{M,w}, \tag{6.47}$$

where $D_{M,w}$ is the diffusive coefficient of macrophages in the arterial wall considered as $8 \cdot 10^{-13}$, taken equals to the monocytes diffusion coefficient. The first term on the right side of Equation 6.46 corresponds to the monocytes which have been differentiated into macrophages and whose constant has previously defined. And the second term of this equation models the foam cell formation. The foam cell formation depends on the quantity of oxidized LDL ingested by the macrophages ($LDL_{oxr}C_{M,w}C_{LDL_{ox},w}$), which has been multiply and divided by the constants M_{r1} $\left[\frac{m^3}{mol\ s}\right]$ and M_{r2} $\left[\frac{m^3}{cells\ s}\right]$, respectively, which corresponding to the oxidized LDL concentration per second that a macrophage should ingest to convert into a foam cell and the rate of foam cell formation per second depending of the macrophage concentration. Based on the experimental study of Zhao *et al.* (2006), M_{r1} and F_{M2} have been estimated as $2.0375 \cdot 10^{-6}$ $\frac{m^3}{mol\ s}$ and $9.25 \cdot 10^{-22}$ $\frac{m^3}{cells\ s}$, respectively. Insulation boundary condition were again applied at all the walls of the intima-media layers. As for the equation which models the monocytes behaviour, the convective term for the macrophages has been neglected.

E - Foam cells:

Finally, the foam cells production is governed by

$$\frac{\partial C_{F,w}}{\partial t} + \underbrace{\nabla \cdot (-D_{F,w} \nabla C_{F,w})}_{Diffusion} + \underbrace{\boldsymbol{u}_w \cdot \nabla C_{M,w}}_{Convection} = \underbrace{\frac{M_{r1}}{M_{r2}} LDL_{oxr} C_{M,w} C_{LDL_{ox},w}}_{Converted\ from\ macrophages}, \tag{6.48}$$

and

$$\boldsymbol{N} = -D_{M,w} \nabla C_{M,w} + \boldsymbol{u}_w C_{M,w}, \tag{6.49}$$

where $C_{F,w}$ and $D_{F,w}$ is the concentration and diffusive coefficient of foam cells in the arterial wall. The convection and diffusion of the foam cells is neglected since the dimensions of them are too large, then the convection transmural velocity flow can not drag these cells. The reaction term corresponds to the macrophage apoptosis, whose constant have been already defined. Once, boundary conditions of no flux have been defined at the contour of the artery wall volume.

6.3.3 Plaque formation

Finally, as the volume of the atheroma plaque is mainly due to the foam cells, the volume contribution of the rest of the species has been neglected, thus the volume of the atheroma plaque can be estimated as:

$$\nabla \cdot v = \frac{\partial C_{F,w}}{\partial t} Vol_{foam\ cell} \tag{6.50}$$

where v is the velocity of the material points and $Vol_{foam\ cell}$ is the volume of one foam cells, which can be estimated knowing the radius of a foam cell. The diameter of a macrophage is 21 μm (Krombach *et al.*, 1997), and Cannon and Swanson (1992) calculated the phagocytic capacity of the macrophages, concluding that these cells are capable of ingesting particles until 3 times their volume or 1.44 times their diameter. Thus, a diameter of 30.24 μm has been considered for the foam cells, and considering this cell as spherical:

$$Vol_{foam\ cell} = \frac{4}{3} \pi {R_F}^3 C_{F,w}, \tag{6.51}$$

where R_F is the radius of a foam cell.

6.3.4 Parameter values

The values and physiological meaning of the parameters in this and the subsequent equations are given in Table 6.1.

Parameter	Description	Value	Reference
ρ_b	Blood density	1050 $\frac{kg}{m^3}$	(Milnor, 1989)
μ_b	Viscosity density	0.0035 Pa $\cdot$ s	(Milnor, 1989)
ρ_b	Plasma density	1000 $\frac{kg}{m^3}$	(Milnor, 1989)
μ_b	Plasma density	0.001 Pa $\cdot$ s	(Milnor, 1989)
κ_w	Flow conductivity	$1.2 \cdot 10^{-18}$ m^2	(Vargas *et al.*, 1979)
$D_{LDL,l}$	LDL diffusion coefficient in the blood	$5 \cdot 10^{-12}$ $\frac{m^2}{s}$	(Curry, 1984)
$D_{m,l}$	Monocytes diffusion coefficient in the blood	$1 \cdot 10^{-10}$ $\frac{m^2}{s}$	(Petty *et al.*, 1980)
$D_{LDL,w}$	LDL diffusive coefficient in the plasma	$8 \cdot 10^{-11}$ $\frac{m^2}{s}$	(Prosi *et al.*, 2005; Dabagh *et al.*, 2009)
d_{LDL}	Degradation rate of LDL	$3.0 \cdot 10^{-4}$ s^{-1}	(Esterbauer *et al.*, 1989)
$D_{m,w}$	Monocytes diffusion coefficient in the plasma	$8 \cdot 10^{-13}$ $\frac{m^2}{s}$	(Budu-Grajdeanu *et al.*, 2008)
d_m	Rate of monocytes differentiated to macrophages.	$1.15 \cdot 10^{-6}$ s^{-1}	(Bulelzai and Dubbeldam, 2012)
m_d	Monocytes natural death	2.572 s^{-1}	(Krstic, 1997)
$D_{LDL_{ox},w}$	Oxidized LDL Diffusive coefficient in the plasma	$8 \cdot 10^{-11}$ $\frac{m^2}{s}$	(Prosi *et al.*, 2005; Dabagh *et al.*, 2009)
LDL_{oxr}	Rate of oxidized LDL uptaken by a macrophage	$0.0012 \cdot 10^{-15}$ $\frac{m^3}{cells\ s}$	Kruth *et al.* (2002)
$D_{M,w}$	Macrophages diffusive coefficient in the plasma	$1 \cdot 10^{-13}$	(Budu-Grajdeanu *et al.*, 2008)
M_{r1}	Oxidized LDL ingested to foam cell formation	$2.0375 \cdot 10^{-6}$ $\frac{m^3}{mol\ s}$	(Zhao *et al.*, 2006)
M_{r2}	Rate of foam cell formation	$9.25 \cdot 10^{-22}$ $\frac{m^3}{cells\ s}$	(Zhao *et al.*, 2006)
R_F	Radius of a foam cell	30.24 μm	(Krombach *et al.*, 1997)

Table 6.1: List of parameters related to the biochemical model.

6.4 Numerical example

In order to demonstrate the performance of the presented scheme equations, a computational model of an coronary artery is presented. A commercial finite element code, Comsol Multiphysics, Version 5.2 (COMSOL), was used to implement the model.

6.4.1 Geometrical model and mesh

The computational geometry corresponds to an idealized axisymmetric representation of a coronary artery as shown in Figure 6.5.a. The general dimensions of the model are 1.85 mm and 0.1702 mm of inner radius and arterial wall thickness, respectively, in accordance with the dimensions of a standard coronary artery (Dodge *et al.*, 1992; Gradus-Pizlo *et al.*, 2003). The length of the model is determined for the distance needed to obtain completely developed flow, and it has been assesses as 40 mm. Furthermore, a stenosis rate of 55% is included in the geometry in order to reproduce a recirculation zone comparable to those that develop at arterial bifurcations. The artery wall is composed by one layer which corresponds to the intima and media layer together.

Moreover, a fine mesh was created in the lumen and artery wall as Figure 6.5.b shown. The lumen was meshed with 22848 triangular elements and the arterial wall was meshed with 38610 triangular elements. Furthermore, grid independence tests were performed successfully for both fluid flow and LDL transport calculations.

6.4.2 Results

The equations were computed on the presented geometrical model simulating the plaque growth during ten years. The obtained results are presented below.

6.4.2.1 STEP 1 - Steady-state diffusion and convection along the lumen

The velocity along the artery lumen is presented in Figure 6.6.a. It can be observed that the flow is full development. The maximum velocity reached is 1.59 $\frac{m}{s}$ and it occurs in central part of the blood vessel after the stenosis area. Furthermore, the streamlines of the velocity are shown in order to identify the recirculation zones upstream of the stenosis. This zones of reverse flow indicate the place where the initiation of the atheroma plaque will be places. In addition, Figure 6.6.b. shows the pressure along the coronary artery where a drop pressure is observed due to the stenosis and the boundary conditions.

However, the most important part of the step 1 simulation is the computation of the WSS distribution along the coronary artery model since this distribution triggers the initiation of the atherosclerosis lesion. Therefore, Figure 6.7.a shows the contour map of this variable, showing a detail of the area where the WSS is lower. The WSS along the lumen wall varies from 1 to 2 Pa. For the sake of clarity, the WSS along the

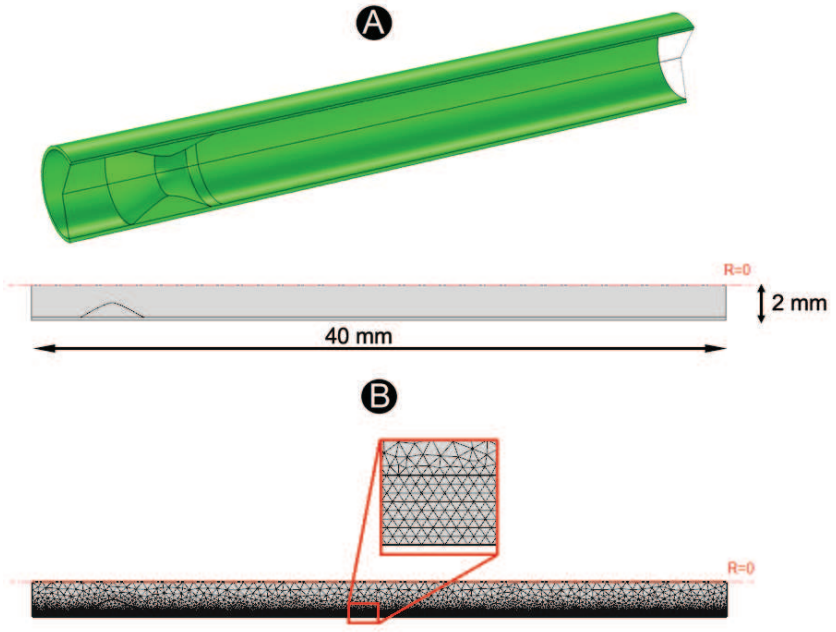

Figure 6.5: A - 3D Idealized geometry of an atherosclerotic coronary artery stenosed 40% of its area in order to obtain turbulent flow downstream and longitudinal section of this artery where the dashed center line represents the axis of symmetry. B - Longitudinal section of the used mesh, showing a detail of the artery wall mesh.

z coordinate has been plotted in Figure 6.7.b, showing that the minimum WSS occurs at z value of 0.022 mm.

6.4.2.2 STEP 2 - Time dependent diffusion and convection along the artery wall

Figure 6.8 shows the concentration evolution of each specie as the time increases. The curves are depicted for two points placed at the z coordinate where the WSS is minimum as it is shown in the legend of the Figure. Viewing the results, the LDL concentration reaches $68 \cdot 10^{-6}$ $\frac{mol}{m^3}$ at the beggaring and after that it remains constant at $68 \cdot 10^{-6}$ $\frac{mol}{m^3}$ as the time increases since the LDL solute flux is independent on the time, varying just with the WSS fluctuations. However, the oxidized LDL is accumulated as the time increases, reaching an equilibrium state of approximately 0.95 $\frac{mol}{m^3}$ at nine years. This equilibrium is produced due to the fact that there is not oxidized WSS at the beginning, then the LDL becomes oxidized and therefore the DL oxidized concentration increases. However, at the same time, the macrophages are ingested oxidized LDL. Thus, after 9 years the incoming and removal oxidized LDL concentration are compensated, producing a stable concentration of oxidized LDL. Furthermore, the concentration remains constant along the section of the artery wall since the oxidized LDL concentration is similar for both depicted points. The monocytes flux depends on the oxidized LDL con-

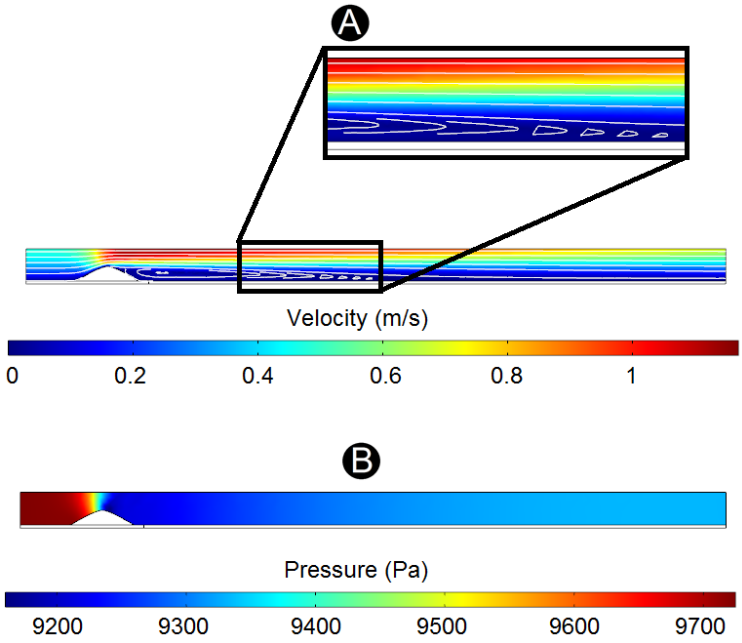

Figure 6.6: A - Velocity and streamlines of the lumen flow. B - Pressure distribution along the coronary artery model.

centration, since the monocytes flux is regulated by the concentration of this substance. Thus, the tendency of the monocytes concentration as the time increases is similar to that obtained for the oxidized LDL, reaching an equilibrium of $2 \cdot 10^{13}$ at nine years of atheroma plaque growth. Furthermore, the monocytes flux and removal, either due to natural death or the macrophage differentiation, modulates the obtained concentration. The macrophages evolution experiments a rapidly increase at the first days, after that it slightly decreases due to the initiation of foam cell formation. Finally, for the foam cell concentration, it is observed that it increases eternally. Since the oxidized LDL concentration has been reached an equilibrium, there is still oxidized LDL and therefore a monocytes flux. The foam cell increases will grow until the completely removal of the oxidized LDL.

Moreover, the contour maps of each biological specie considered at 10 years are shown in Figure 6.9, which a zoom in the zone of interest. This contour maps show how each specie is distributed along the artery wall. For all studied species, higher concentrations are observed in the zone where the WSS is lowest. It is observed that the LDL concentration is higher near to the lumen due to there is a constant flux of LDL at this boundary. Nevertheless, the oxidized LDL contour map shows higher concentration of this specie far away of the lumen surface due to the convention effects. Finally, the monocytes, macrophages and foam cell concentrations are approximately constant along the section of the artery.

Finally, Figure 6.10 shows the volumetric growth due to the foam cell formation.

The color legend indicates the displacements of each point in m. The stenosis after 10 years is approximately of 40% of the coronary artery section.

6.5 Discussion

A mathematical and computational model of atheromatous plaque emergence which allows the lesion to grow in particular area in relation with hemodynamics of the blood flow has been built. The atheroma plaque growth is a complex process, involving a number of biological processes and species. However, despite that the developed model is relatively simple, it captures some of the main features of atherosclerosis lesion formation. Consequently, the presented model is in good agreement with the clinical hypothesis that correlates atherosclerosis occurrence with low wall shear stress. Moreover, the obtained results are reasonable within the biological process of atheroma plaque growth. In particular, it realistically predicts the stenosis evolution due to the appearance of low WSS since a stenosis of approximately 40% of the lumen area has been obtained after 10 years, which is clinically viable. However, the results can not be validated since the appropriate experiments which directly measured the concentration of each specie at the human artery wall along the time are not available currently.

This model can be considered as a forward step to understand the atheroma plaque development. However, it should be further improved and several limitations of it should be mentioned. Concerning the mathematical model, firstly several important biological species such as cytokines, smooth muscle cells or collagen have been missed. However, the presented equations models the initiation of atherosclerosis lesions and the mentioned species play an important role in the latter stages of the atheroma plaque formation. Furthermore, other substances such as free radicals which oxidize the LDL and the processes in which they are involved, are also neglected. Secondly, the model parameters were obtained from a wide variety of experiments on many different human or animal models. However, a few parameters have been estimated attending the order of magnitude of these parameters and making choices that gave biologically reasonable results. Relating to the presented computational example, the model should be proved at geometries with bifurcations and even in 3D real geometries.

Despite these limitations, and according to the results obtained,it can be concluded that the functional regulation of the endothelium by local hemodynamic shear stress provides a model for understanding the focal propensity of atherosclerosis in the setting of systemic factors and may help guide future therapeutic strategies.

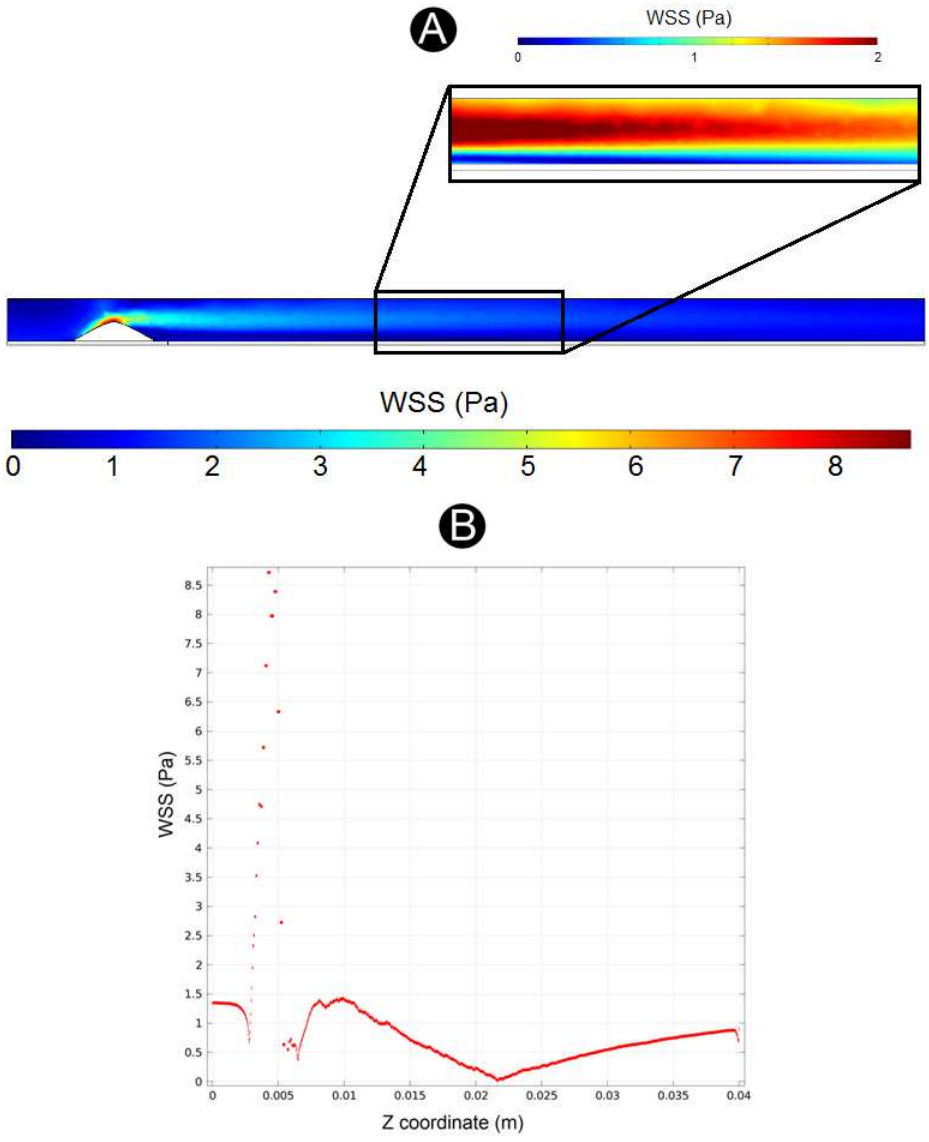

Figure 6.7: A - WSS contour map along the model. B - WSS versus z coordinate (m).

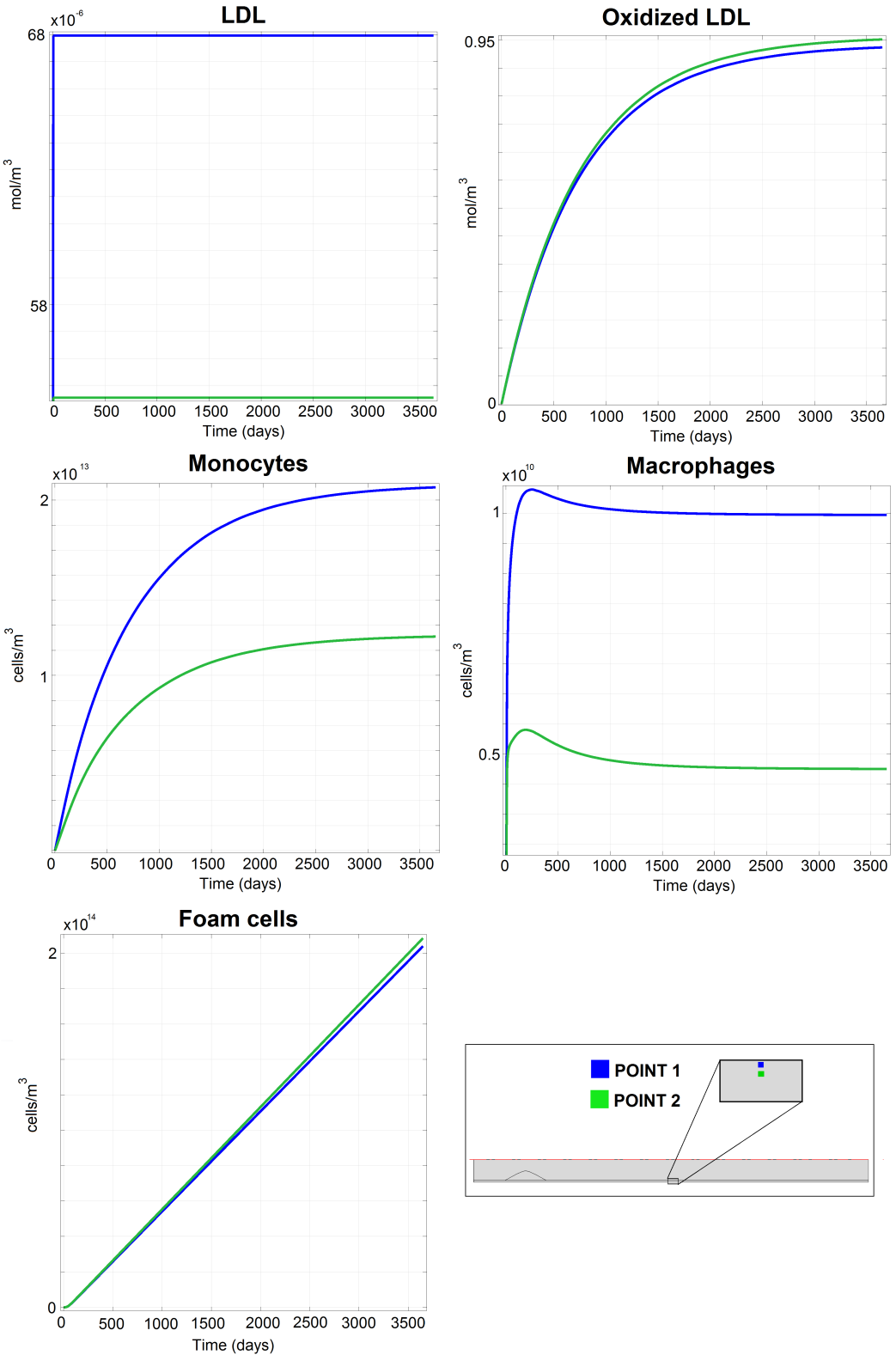

Figure 6.8: Concentration evolution for each considered species as the time increases.

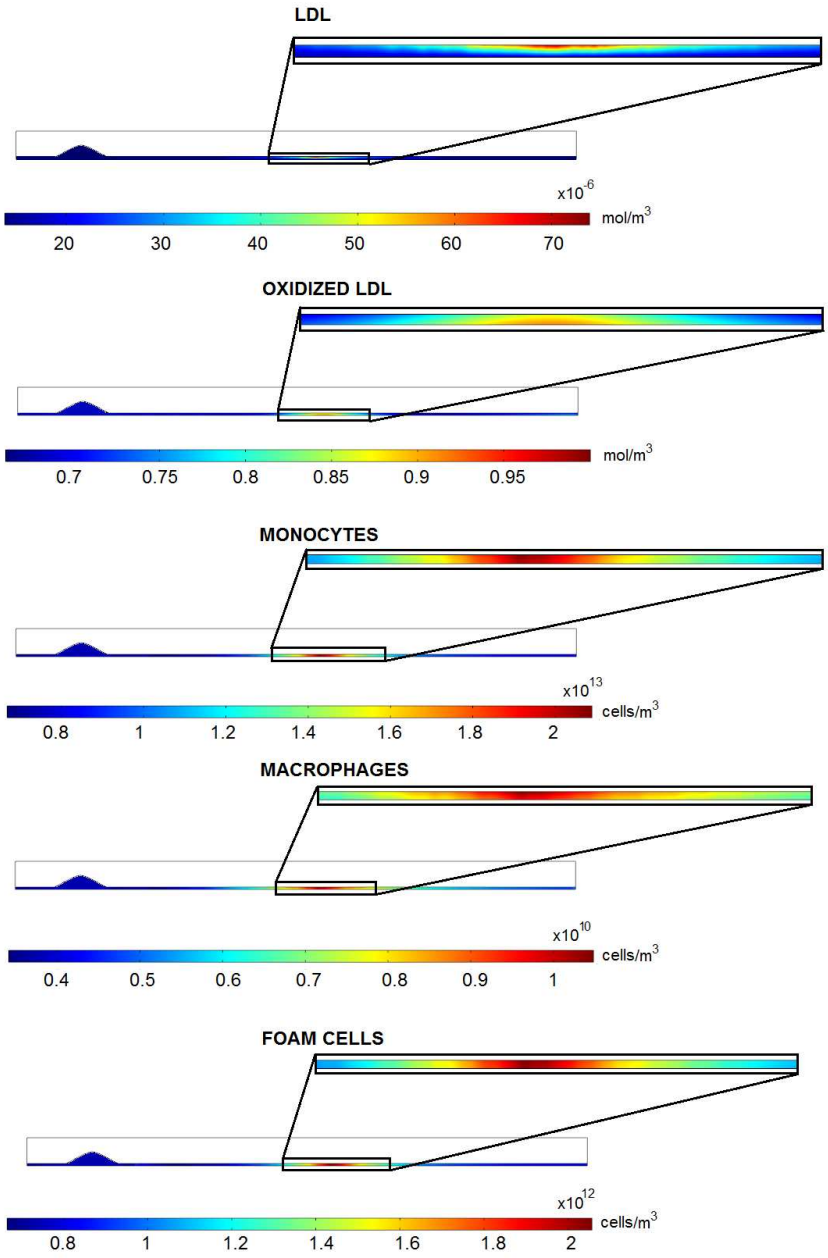

Figure 6.9: Contour maps of the concentration of each considered specie at 10 years.

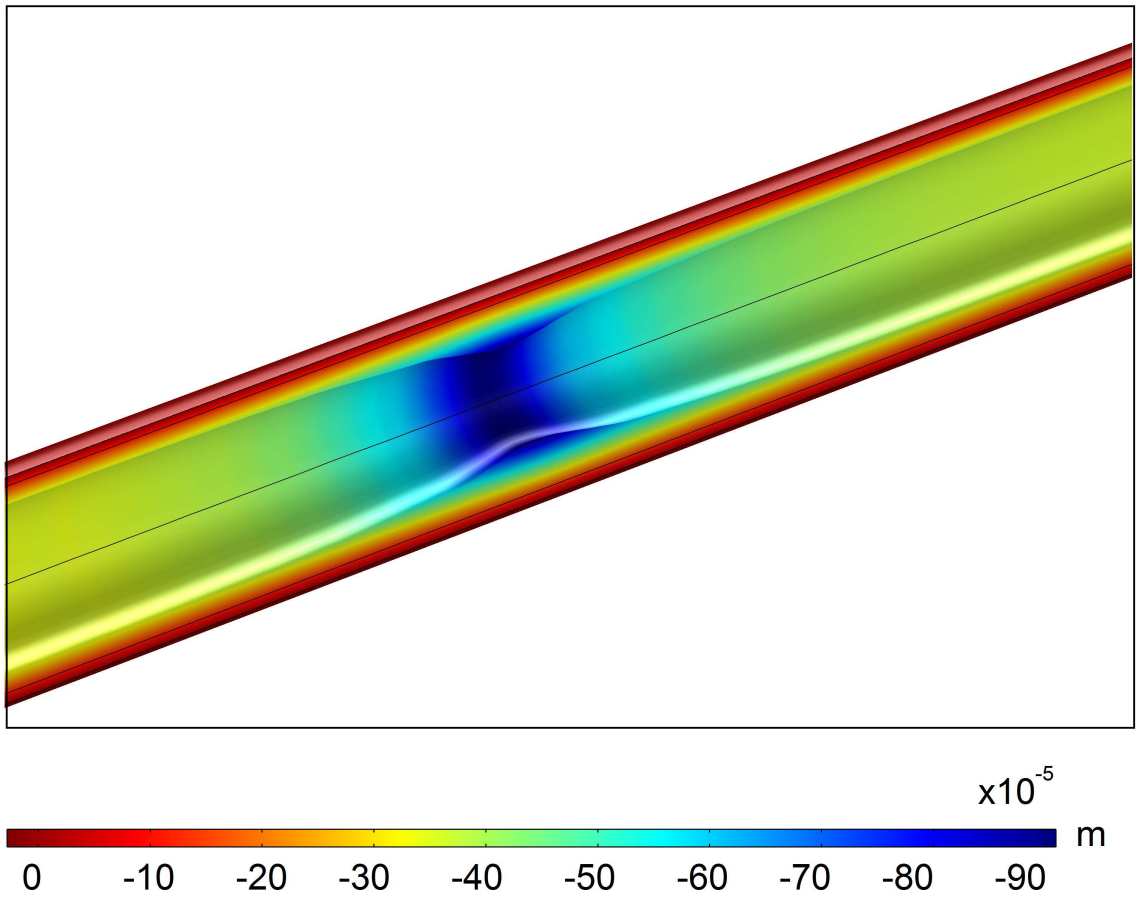

Figure 6.10: Total volumetric growth after 10 years.

Chapter 7

Conclusions and original contributions

A brief summary of the work developed in this Thesis together with the main conclusions, the original contributions, and future open lines are presented in this Chapter.

Contents

7.1 Conclusions

The most important conclusions of this Thesis can be grouped in three broad categories. The first one comprises the experimental aspects. The second group is related to the mechanical, mathematical and numerical aspects of the developments presented above, including their implementation. Finally, the third one groups the clinical and biomechanical conclusions of this work.

7.1.1 Experimental aspects

- A special own designed inflation experimental system was setup to perform *in situ* inflation tests on blood vessels of small animals. Moreover, a methodology and

protocol, which allow to characterize the mechanical behaviour of mice aorta by means of *in situ* inflation tests, has been developed.

- Regarding the mechanical behaviour of the ApoE$^{-/-}$ and control mice aorta, significant differences were not found in the aortic wall stiffness of the control mice for different ages. But on the contrary, statistical correlations were found in the stiffness of the ApoE$^{-/-}$ mice with the age and the time on a diet. Furthermore, comparing between both strains, the behaviour of the aortic tissue obtaining by inflation tests is statistically different since the beginning of the lesions in ApoE$^{-/-}$ mice.

- Any important evidence of atheroma plaque is observed for ApoE$^{-/-}$ mice during the first weeks of diet neither visually nor histological. However, atherosclerotic lesions are widespread throughout the whole aortic tree in advanced stages of the disease. For control mice, atheroma plaque were not found neither in the morphological lesion evaluation nor in the histological analyses performed. Thus, both the histological analyses and the quantification of atheroma plaque are correlated to the pressure-stretch behaviour obtained by means of *in situ* inflation tests.

- A significant correlation between the gain in body weight and cholesterol and triglycerides levels for each studied animal with the diet is highlighted.

- Significant differences were found on elastic and secant modules along the whole aortic tree when ApoE$^{-/-}$ and control mice are compared. Moreover, an almost linear relation has been observed between these modules and the age for ApoE$^{-/-}$ mice, and a constant behaviour for the control mice case. However, analogous behaviour of both strains studied at high pressures (from 200 mmHg to 250 mmHg) was observed, showing similar tangent modules for both ApoE$^{-/-}$ and control mice for all weeks studied. And the t-test for paired samples performed on the tangent modulus results was not statistically significant. This fact could be related to the breakdown of the elastin in the aortic wall of old ApoE$^{-/-}$. The integrity of the medial elastin in the conduit vessels is a major determinant of the arterial elasticity and the capacitive function of these arteries. However, this is just an hypothesis and further analyses should be carried out in order to prove it.

- Also, a linear relationship was found between the longitudinal residual stress of ApoE$^{-/-}$ mice and the age. However, they remain practically constant for control mice. Comparing the results obtained for both strains, significant differences were observed between control and ApoE$^{-/-}$ mice at 30 and 40 weeks on a diet, and between those ApoE$^{-/-}$ mice with initial atherosclerotic lesions and those with severe atherosclerosis developed.

7.1.2 Mechanical, mathematical and numerical aspects

- The physiological and morphological behaviour of the atheroma plaque have been characterized by means of the 3D parametric computational simulations of an idealized coronary artery. The results of this parametric study show the importance of using 3D geometries to obtain accurate MPS contour maps on atherosclerotic blood vessels, and therefore, to predict the atheroma plaque vulnerability risk. It has been shown that 2D plane strain models tend to overestimate the MPS contour maps, providing an unrealistic information about atheroma plaque vulnerability. Furthermore, 3D models allow the inclusion of some essential 3D features such as the anisotropy of the wall vessel or the longitudinal residual stress. Residual stress should be included in the 3D models to asses atheroma plaque rupture since the crucial influence of the residual stresses in the stress distribution was clearly exposed. Longitudinal residual stress tends to increase the MPS, however, the inclusion of circumferential residual stress produces the opposite effect, decreasing the MPS.

- The hypothesis of using an idealized geometry to perform the 3D parametric study has been validated thanks to a patient-specific coronary vessel reconstruction obtained by IVUS. The MPS contour maps as well as the maximum MPS obtained for the real geometry are similar to those found for an idealized geometry with the same geometrical dimensions.

- A FSI parametric study of an idealized coronary artery model has been developed. The results of this parametric study have been compared with those obtained in other 3D parametric study where only static blood pressure was considered. The results related to the MPS distribution on the atherosclerotic vessel of both parametric studies were similar, showing that the fluid shear stress is insignificant when compared to the effect of tensile wall stresses as a direct component in plaque fracture dynamics. Furthermore, the FSI models allow to calculate the WSS distribution, which is considered essential in plaque formation and growth.

- MLT such as ANN and SVM techniques are able to complement FEM simulations to predict the maximum MPS on an idealized coronary model with a good error tolerance and avoiding the high time consuming 3D FE analysis. Furthermore, the presence of high nonlinearities in the problem, as reflected by the results of classical linear regression model, reinforces the use of such alternative techniques to solve the regression problem.

- Microcalcification influence study on the atheroma plaque vulnerability suggests that the use of inappropriate material properties for the microcalcification tissue could produce conflicting results. The role of microcalcifications in the vulnerable plaque rupture mechanics is still debated; some studies suggest the microcalcifications increase the plaque vulnerability, while other studies indicate beneficial

effects in stabilizing the plaque. It has been shown that the controversy of the results found in the literature could be related to the use of microcalcification material properties too stiff in some studies.

- The atheroma plaque growth model based on differential equations of reaction-diffusion-convection was able to simulate the development of the atherosclerosis disease. Although merely qualitative, simulations predicted how the different substances, which play a role in the atheroma plaque formation, interact. It can be considered as a first step to the understanding of this pathology.

7.1.3 Clinical aspects

- The influence of five geometrical factors in the atheroma plaque vulnerability has been studied; the fibrous cap thickness, the stenosis ratio and the lipid core length, width and angle. The most influential parameter on the atheroma plaque rupture is the fibrous cap thickness, producing an increase of the risk rupture when this parameter decreases. Traditionally, coronary atheroma plaques with a thin fibrous cap thickness have been considered as prone to rupture, measuring just this parameters by the clinicians to asses atheroma plaque vulnerability. However, the obtained results indicate that the lipid core length and width are also important factors in the risk of plaque rupture.

- A parametric tool, using machine learning techniques (ANN and SVM) to assist the clinicians on decisions of the vulnerability of the atheroma plaque has been developed. Identifying vulnerable patients before plaque rupture occurs would help clinicians to provide early treatment as well as to take preventive measures.

- The microcalcification location is more influential (microcalcification angle and eccentricity) than the microcalcification size on the atheroma plaque vulnerability. However, the influence of the microcalcifications has no been really significative.

- Concerning the performed parametric study which compares the negative and positive atheroma plaque remodeling, it can be concluded that plaques with positive remodeling are always more vulnerable than those with negative remodeling.

- The sensitive analyses performed reveal that the hypertension and the stiffness of the blood vessel wall adversely affect to the plaque vulnerability risk.

- The FSI models are not relevant to predict atheroma plaque rupture, however, the hemodynamic forces play an essential role on the initiation, formation and growth of atherosclerotic lesions.

7.2 Original contributions

Next, the original contributions carried out during the period of this thesis are exposed below.

- The first 3D FE parametric study incorporating longitudinal and circumferential residual stress to asses plaque vulnerability has been carried out. The most influential parameter on the arterial wall MPS distribution as well as the limits of each parameter which define atheroma plaque vulnerability have been identified. Furthermore, the first study which assesses the influence of the residual stress on the atheroma plaque vulnerability risk has been developed. Furthermore, a specific-patient coronary geometry has been segmented in order to validate the assumption of idealized 3D geometry.

- The first parametric study to asses the role of the microcalcification in plaque stability which incorporates the size, position and material properties of a microcalcification has been developed.

- The vulnerability risk of an atheroma plaque with positive and negative remodeling has been compared through a parametric study, showing that plaques with positive remodeling are more prone to rupture than those with negative.

- A new parametric tool based on MLT such as ANN or SVM has been developed. This tool uses the MLT algorithms to predict the atheroma plaque rupture in terms of four of the most influential geometrical factors in the plaque rupture which are the input of the MLT: fibrous cap thickness, stenosis ratio and lipid core width and length. The output predicted by the MLT is the maximum MPS occurred in an atherosclerotic coronary vessel with the input dimensions.

- An inflation *in situ* system for very small diameters vessels as well as a protocol to perform *in situ* inflation test has been designed.

- The mechanical properties of the ApoE$^{-/-}$ and C57BL/6J mice aorta were studied first by *in situ* inflation tests to asses the influence of the age and diet on the plaque development. Furthermore, the aortic longitudinal residual stretch was also measured, an histological study and morphological observations of the lesions of each specimen have been carried out.

- The first simple model of the atheroma plaque growth based on differential reaction-diffusion-convection equations has been developed. This model is able to illustrate the biological process occurring during the atheroma plaque development.

7.2.1 Publications directly related to the thesis

1. Cilla, M., Peña, E., and Martínez M.A. 3D computational parametric analysis of eccentric atheroma plaque influence of axial and circumferential residual

stresses. *Biomechanical and Modeling Mechanobiology*, 11(7):1001-13 (2012).

2. Cilla, M., Martínez, J., Peña, E., and Martínez M.A. Machine Learning Techniques as a Helpful Tool Toward Determination of Plaque Vulnerability. *IEEE Transactions on Biomedical Enginering*, 9(4):1155-61 (2012).

3. Cilla, M., Monterde, D., Peña, E., and Martínez M.A. Does microcalcification increase the risk of rupture? *Proceedings of the Institution of Mechanical Engineers, Part H, Journal of Engineering in Medicine*, Submitted for publication.

4. Cilla, M., Peña, E., Martínez M.A. and D.J., Kelly Comparison of the vulnerability risk for positive versus negative atheroma plaque growth. *Journal of Biomechanics*, Under review.

5. Cilla, M., Pérez, M.M, Peña, E., and Martínez M.A. Arterial Stiffening due to Atherosclerosis in Apolipoprotein E-Deficient Mice. Effect of diet and age. *Atherosclerosis*, Submitted for publication.

6. Cilla, M., Borrás I., Peña, E., Martínez M.A. and Malvè M. Parametric analysis of atherosclerotic plaques by fluid structure interaction. Influence on the mechanics of the vulnerability. *Annals of Biomedical Engineering.*, In preparation.

7. Cilla, M., Peña, E., and Martínez M.A. On the time dependent mathematical model of atherome plaque formation. *Journal of Theoretical Biology.*, In preparation.

7.2.2 Publications within the biomechanical scope not included in this thesis

1. Araña, M., Peña, E., Abizanda, G., Cilla, M., Ochoa, I., Gavira, J.J., Doblaré, M., Pelacho, B., and Prósper F. Preparation and characterization of ADSC-cellularized patches for cardiovascular application. *Acta Biomaterialia*, Submitted for publication.

2. Araña, M., Peña, E., Abizanda, G., Cilla, M., Pérez, M.M., Gavira, J.J., Pelacho, B., and Prósper F. Cardiac remodeling after implantation of a collagen scaffolds with adipose derived stem cells. *Biomaterials*, In preparation.

7.2.3 Congress contributions

The following communications have been presented during the development of this thesis:

1. Cilla, M., Peña, E., Martínez M.A., and Doblaré, M., Estudio paramétrico tridimensional de factores geométricos en la vulnerabilidad de la placa de atheroma.

XXVII Congreso Anual de la Sociedad Española de Ingeniería Biomédica (CASEIB), Cádiz (Spain), 2009.

2. Cilla, M., Peña, E., Martínez M.A., and Doblaré, M., Computational modelling of atherome plaque: biomechanical factors in the risk of plaque rupture. *IV European Congress on Computational Mechanics (ECCM IV): Solids, Structures and Coupled Problems in Engineering*, Paris (France), 2010.

3. Cilla, M., Peña, E., Martínez M.A., and Doblaré, M., 3D parametric study of the biomechanical factors in evaluating the risk of plaque rupture. *17th Congress of the European Society of Biomechanics (ESB)*, Edinburgh, Scotland (United Kingdom), 2010.

4. Cilla, M., Peña, E., and Martínez M.A., Red Neuronal Artificial para la toma de decisiones en la vulnerabilidad de laca de ateroma. *Congress on Numerical Methods in Engineering (CNME)*, Coimbra, (Portugal), 2011.

5. Cilla, M., Martínez, J., Peña, E., and Martínez M.A., Red Neuronal Artificial para la toma de decisiones en la vulnerabilidad de laca de ateroma. *I Reunión del Capítulo Nacional de la Sociedad Europea de Biomecánica (ESB)*, Zaragoza, (Spain), 2011.

6. Cilla, M., Monterde, D., Peña, E., and Martínez M.A., The microcalcification influence on the ateroma plaque vulnerability. *I Jornada de Jóvenes Investigadores I3A*, Zaragoza, (Spain), 2012.

7. Cilla, M., Pérez, M.M., Peña, E., and Martínez M.A., Mechanical properties of atheroma plaque along the length of the aorta in ApoE$^{-/-}$ mice model. *18th Congress of the European Society of Biomechanics (ESB)*, Lisbon (Portugal), 2012.

8. Cilla, M., Peña, E., and Martínez M.A., A 3D parametric study of eccentric atheroma plaque: influence of Geometrical factors and residual stress. *18th Congress of the European Society of Biomechanics (ESB)*, Lisbon (Portugal), 2012.

9. Cilla, M., Martínez, J., Peña, E., and Martínez M.A., Atheroma plaque vulnerability prediction using Machine Learning Techniques. *XXIII International Congress of Theoretical and Applied Mechanics (ICTAM)*, Pekin, (China), 2012.

10. Cilla, M., Pérez M.M, J., Peña, E., and Martínez M.A., Propiedades mecánicas de la aorta durante el proceso de formación de placa aterosclerótica en ratones ApoE$^{-/-}$. *II Reunión del Capítulo Nacional de la Sociedad Europea de Biomecánica (ESB)*, Sevilla, (Spain), 2012.

7.3 Future work

The research presented in this Thesis is a small contribution to the understanding of the atheroma plaque process. Next, several work lines to continue the research here presented are:

- Analysis of other important data such as the circumferential residual stress by measuring the aperture angle or the cholesterol and triglycerides levels or other markers directly related to the atherosclerotic lesions. Furthermore, histological and immunohistochemistry studies should be carried out in order to quantify the microstructure and the main components of the atheroma plaque in order to correlate the results of these studies with the atheroma plaque growth model.

- To develop an study similar to the performed in ApoE$^{-/-}$ and control mice, but with rabbits. It has been proved that rabbits develop lesions more similar to those found in humans. Moreover, the size of the rabbit samples allow to perform the inflation test measuring the longitudinal stiffness or uniaxial and biaxial tests, that it was not possible for the mice experimental tests carried out.

- The study and constitutive modelling of the viscoelastic properties and plastic phenomena occurring in atherosclerotic tissues.

- Development of a hyperelastic constitutive law to model the mechanical properties of aortic tissue belonging to ApoE$^{-/-}$ and C57BL/6J mice. This model would be able to reproduce the pressure-stretch behaviour obtained by the *in situ* inflation tests.

- Acquisition of a great number of real patient-specific geometries. Reconstruction and simulation of these geometries by means of the finite element method in order to validate the results obtained in the 3D parametric study. Additionally, re-training the tool based on Machine Learning Techniques with the data obtained in the reconstructed geometries is proposed in order to develop a parametric tool for the clinical practice based on real data.

- Inclusion of new parameters which define positive and negative remodeling to the 3D idealized parametric study in order to detect which parameters are more influential on the atheroma plaque vulnerability and the limits of each parameter that define the vulnerable area. No idealized and parametric 3D studies have attempted to analyze the influence of residual stresses on the biomechanical stability of vulnerable coronary plaques with positive remodeling.

- Extension of the FSI study in order to simulate the 625 cases which result from combining all the parameter between them. Moreover, the inclusion of longitudinal and circumferential residual stresses to the FSI model is proposed. Furthermore, the obtaining of other important influential variables on the atheroma

plaque appearance such as the oscillatory shear index (OSI) or the WSS spatial gradient or the WSS angle gradient would be interesting.

- Development of more complex an atheroma plaque growing model. Inclusion of more biological agents and process related to the atheroma plaque formation such as enzymes and free radicals in the endothelium which regulate the oxidation of LDL. The increasing of the complexity of the model growth allow to provide more precise information about the atherosclerotic disease process. Furthermore, the model should be implemented in real patient-specific geometries.

- Execution of a sensitive study of the parameters used in the growth model in order to asses the influence on the obtained results. Furthermore, it should be taken account the difficulty of founding experimental parameter and constant values for this kind of models. Therefore, the development of own experimental test in order to obtain these parameters and constants is also proposed as future work.

- Implementation of the growth model to more complex geometries such as coronary or carotid arteries with bifurcations.

Appendices

Appendix A

Continuum mechanics

A brief review of the most important continuum mechanics concepts used through this Thesis are presented in this Appendix, where a basic continuum mechanics knowledge is assumed. Main mathematical concepts are presented from an engineering perspective, in the fashion of texts like Holzapfel *et al.* (2000). Accordingly, the results are restricted to the three dimensional cartesian space so that some relevant mathematical concepts such as co- and contra-variance are not introduced. For more rigorous derivations, the interested reader is referred to, e.g., Ciarlet (1988) and Marsden and Hughes (1994).

Essential finite strains kinematics are introduced emphasizing concepts like the multiplicative split of the deformation gradient tensor, which is of paramount importance in the computational modelling of soft biological tissues, like blood vessels. Different measures of stress are introduced, and their particular expressions for incompressible and compressible hyperelastic materials are presented. The use of structural tensors to model anisotropy is briefly reported, and expressions for the calculation of the tangent operator are given.

Standard notation is used, where scalars are denoted by plain letters, vectors and second-order tensors are named with bold symbols ($\boldsymbol{A}$), and fourth-order tensors are represented $\mathbf{A}$. In addition, the usual convention to use upper-case letters to denote variables in the material configuration, and lower-case to write spatial quantities is also followed, as well as the Einstein summation rule for repeated index summation.

This summary of basic continuum mechanics, which has been adapted from Alastrué (2008) and Holzapfel (2000), has been included for completeness.

Contents

A.1 Essential kinematics

Let $\mathcal{B}_0 \subset \mathbb{E}^3$ be a reference or rather material configuration of a body B of interest. The notation $\boldsymbol{\varphi} : \mathcal{B}_0 \times \mathcal{T} \to \mathcal{B}_t$ represents the mapping which transforms the referential position of a material point $\boldsymbol{X} \in \mathcal{B}_0$ to its spatial position $\boldsymbol{x} = \boldsymbol{\varphi}(\boldsymbol{X}, t) \in \mathcal{B}_t \subset \mathbb{E}^3$, where $\mathcal{B}_t$ represents the deformed configuration at time $t \in \mathcal{T} \subset \mathbb{R}$ (see Figure A.1). The mapping $\boldsymbol{\varphi}$ represents a motion of the body B that establishes the trajectory of a given point when moving from its reference position $\boldsymbol{X}$ to $\boldsymbol{x}$. It will be assumed that motion to has continuous derivatives with respect to space and time, and to be uniquely invertible so that $\boldsymbol{\varphi}^{-1}(\boldsymbol{x}, t)$ takes the points of the configuration $\mathcal{B}_t$ to the reference one $\mathcal{B}_0$.

Assuming $\boldsymbol{X}$, $\boldsymbol{Y} \in \mathcal{B}_0$ being neighbouring points, that is, very "close" points, we denote the (material) length of the material length element

$$\mathrm{d}\boldsymbol{X} \,=\, \boldsymbol{Y} - \boldsymbol{X} \,=\, \mathrm{d}\epsilon\, \boldsymbol{a}_0. \tag{A.1}$$

where $\mathrm{d}\epsilon = \|\boldsymbol{Y} - \boldsymbol{X}\|$, and the $\boldsymbol{a}_0$ vector, which is naturally associated to the material configuration $\mathcal{B}_0$, is defined as

$$\boldsymbol{a}_0 \,=\, \frac{\boldsymbol{Y} - \boldsymbol{X}}{\|\boldsymbol{Y} - \boldsymbol{X}\|}, \qquad \text{with} \qquad \|\boldsymbol{a}_0\| \,=\, 1, \tag{A.2}$$

describing the direction of a material line element at the point $\boldsymbol{X}$, that can be imagined as a fibre.

Next, the two-point deformation gradient tensor is defined as

$$\boldsymbol{F}(\boldsymbol{X},\, t) \,:=\, \frac{\partial \boldsymbol{\varphi}(\boldsymbol{X},\, t)}{\partial \boldsymbol{X}} \,=\, \frac{\partial \boldsymbol{x}}{\partial \boldsymbol{X}} \qquad \text{or} \qquad F_{aA} \,:=\, \frac{\partial \varphi_a}{\partial X_A} \,=\, \frac{\partial x_a}{\partial X_A}, \tag{A.3}$$

which linearly approximates the relative motion $\mathrm{d}\boldsymbol{x} = (\boldsymbol{y} - \boldsymbol{x})$ as

$$\mathrm{d}\boldsymbol{x} \,=\, \boldsymbol{F} \cdot \mathrm{d}\boldsymbol{X} \,=\, \boldsymbol{F} \cdot [\boldsymbol{Y} - \boldsymbol{X}]\,. \tag{A.4}$$

Note, that the closer $\boldsymbol{Y}$ and $\boldsymbol{X}$ are, the smaller is $\mathrm{d}\epsilon = \|\boldsymbol{Y} - \boldsymbol{X}\|$ and the better is the approximation (see, e.g., Holzapfel *et al.*, 2000, for a detailed derivation).

Then, the stretch vector $\boldsymbol{a}$ in the direction of the unit vector $\boldsymbol{a}_0$ at $\boldsymbol{X} \in \mathcal{B}_0$ is defined as

$$\boldsymbol{a}(\boldsymbol{X},\, t) \,:=\, \boldsymbol{F}(\boldsymbol{X},\, t) \cdot \boldsymbol{a}_0, \tag{A.5}$$

with length $\lambda := \|\boldsymbol{a}\|$, representing the stretch in the direction of $\boldsymbol{a}$, Figure A.1. Note that this operation, that provides the spatial orientation of a material vector, will be referred as the push-forward of a vector quantity.

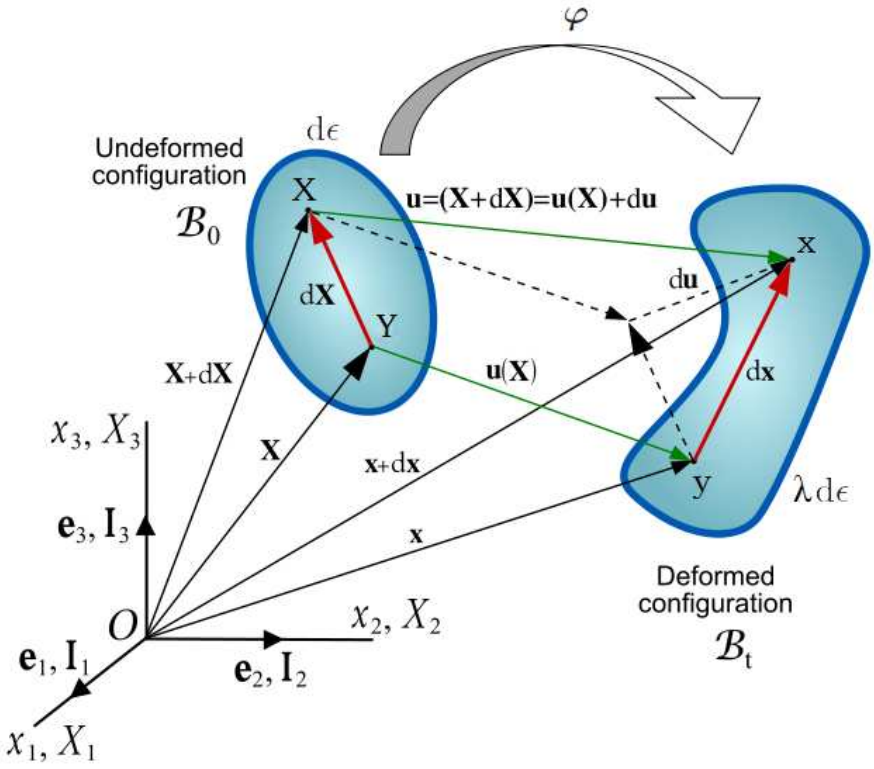

Figure A.1: Sketch of the deformation of a solid including the representation of a length element from the material to the spatial configurations $\mathcal{B}_0$ and $\mathcal{B}_t$, respectively.

Thus, the square of stretch can be expressed as

$$\lambda^2 = \boldsymbol{F}\cdot\boldsymbol{a}_0\cdot\boldsymbol{F}\cdot\boldsymbol{a}_0 = \boldsymbol{a}_0\cdot\boldsymbol{F}^{\mathrm{t}}\cdot\boldsymbol{F}\cdot\boldsymbol{a}_0. \tag{A.6}$$

With these quantities at hand, we respectively introduce the right and left Cauchy-Green tensors

$$\begin{aligned} \boldsymbol{C} &:= \boldsymbol{F}^{\mathrm{t}}\cdot\boldsymbol{F} \quad \text{or} \quad C_{AB} := F_{aA}F_{aB}, \\ \boldsymbol{b} &:= \boldsymbol{F}\cdot\boldsymbol{F}^{\mathrm{t}} \quad \text{or} \quad b_{ab} := F_{aA}F_{bA}, \end{aligned} \tag{A.7}$$

which are symmetric and positive-definite.

The polar decomposition of the deformation gradient tensor, which is a fundamental theorem of mechanics, allows to express it as

$$\boldsymbol{F} = \boldsymbol{R}\cdot\boldsymbol{U} = \boldsymbol{v}\cdot\boldsymbol{R} \quad \text{or} \quad F_{aA} = R_{aB}U_{BA} = v_{ab}R_{bA}, \tag{A.8}$$

where the rotation tensor $\boldsymbol{R}$ satisfies the relation $\boldsymbol{R}^{\mathrm{t}} = \boldsymbol{R}^{-1}$, and the stretch tensors $\boldsymbol{U}$ and $\boldsymbol{v}$ are unique positive definite symmetric tensors defined in the material and spatial frameworks, respectively (see, e.g., Marsden and Hughes, 1994). Hence, the application of (A.8) on the right and left Cauchy-Green strain tensors in (A.7) gives

$$\boldsymbol{C} = \boldsymbol{U}^2 \quad \text{or} \quad \boldsymbol{b} = \boldsymbol{v}^2. \tag{A.9}$$

Next, the Jacobian determinant, characterising the local volume ratio, is introduced

$$J := \det(\boldsymbol{F}) = [\det(\boldsymbol{C})]^{1/2} > 0. \tag{A.10}$$

In order to model the mechanical response under deformations causing volume variations, and those purely shear deformations, the deformation gradient tensor is multiplicative decomposed as

$$\boldsymbol{F} := J^{1/3}\boldsymbol{I} \cdot \bar{\boldsymbol{F}}. \tag{A.11}$$

Thereby, deformation is split into the volumetric part, $J^{1/3}\boldsymbol{I}$, where $\boldsymbol{I}$ represents the second-order identity tensor, and an isochoric contribution, $\bar{\boldsymbol{F}}$, so that $\det(\bar{\boldsymbol{F}}) = 1$. With these quantities at hand, the isochoric counterparts of the right and left Cauchy-Green deformation tensors in Equation (A.7) associated with $\bar{\boldsymbol{F}}$ are defined as

$$\bar{\boldsymbol{C}} := \bar{\boldsymbol{F}}^{\mathrm{t}} \cdot \bar{\boldsymbol{F}} := J^{-2/3}\boldsymbol{C}, \qquad \bar{\boldsymbol{b}} := \bar{\boldsymbol{F}} \cdot \bar{\boldsymbol{F}}^{\mathrm{t}} := J^{-2/3}\boldsymbol{b}. \tag{A.12}$$

Furthermore, by analogy with Equation (A.12), we introduce the vector

$$\bar{\boldsymbol{a}} := \bar{\boldsymbol{F}} \cdot \boldsymbol{a}_0 = J^{-1/3}\boldsymbol{a}, \tag{A.13}$$

which corresponds to the isochoric push-forward of the material orientation $\boldsymbol{a}_0$. Accordingly, the isochoric stretch is computed as

$$\bar{\lambda} := \|\bar{\boldsymbol{a}}\| = J^{-1/3}\|\boldsymbol{a}\|. \tag{A.14}$$

A.2 Stress

Consider a configuration $\mathcal{B}_t \subset \mathbb{E}^3$ of a continuum deformable body B of interest with boundary surface $\partial\mathcal{B}_t$ at time t as represented in Figure A.2.

The existence of forces acting both on the surface of the body, the so-called external forces and on the inner points of the body, namely the internal forces, is postulated. It will be assumed that this body is cut by a plane passing though a spatial point $\boldsymbol{x} \in \mathcal{B}_t$. A differential surface element $\mathrm{d}s$ in the cutting plane around $\boldsymbol{x}$, characterized by its outward oriented normal $\boldsymbol{n}$, is considered (see Figure A.2). Then, the resultant of the internal forces are $\mathrm{d}\boldsymbol{f} = \boldsymbol{t}\,\mathrm{d}s$, where $\boldsymbol{t}$ represents the Cauchy traction vector exerted on $\mathrm{d}s$ with outward normal $\boldsymbol{n}$. Accordingly, $\mathrm{d}\boldsymbol{f}$ can be expressed as a function of the counterpart surface element $\mathrm{d}S$ (associated to the $\boldsymbol{X} \in \mathcal{B}_0$ point), and first Piola-Kirchhoff traction vector $\boldsymbol{T}$, defined in the reference configuration as

$$\mathrm{d}\boldsymbol{f} = \boldsymbol{f}\,\mathrm{d}s = \boldsymbol{T}\mathrm{d}S \tag{A.15}$$

$$\boldsymbol{t} = \boldsymbol{t}(\boldsymbol{x}, t, \boldsymbol{n}), \qquad \boldsymbol{T} = \boldsymbol{T}(\boldsymbol{X}, t, \boldsymbol{N}), \tag{A.16}$$

where $\boldsymbol{t}$ and $\boldsymbol{T}$ are usually defined as surface traction, stress vectors, of just loads.

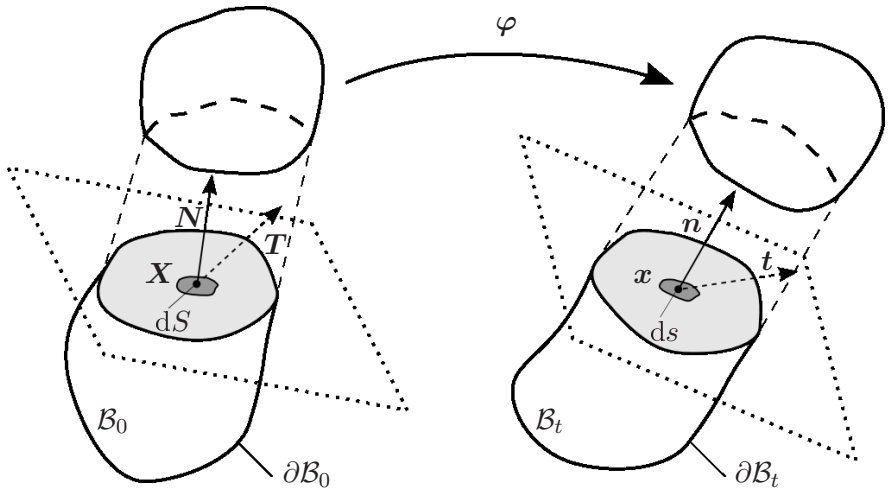

Figure A.2: Infinitesimal surface elements with outward normal and their associated traction vectors.

Cauchy's theorem is now introduced, so it is assumed the existence of unique second-order tensor fields satisfying

$$\left.\begin{array}{lll} \boldsymbol{t}(\boldsymbol{x},\, t,\, \boldsymbol{n}) \,=\, \boldsymbol{\sigma}(\boldsymbol{x},\, t)\cdot\boldsymbol{n} & \text{or} & t_a \,=\, \sigma_{ab}n_b \\ \boldsymbol{T}(\boldsymbol{X},\, t,\, \boldsymbol{N}) \,=\, \boldsymbol{P}(\boldsymbol{X},\, t)\cdot\boldsymbol{N} & \text{or} & T_A \,=\, P_{aA}n_A \end{array}\right\} \tag{A.17}$$

where $\boldsymbol{\sigma}$ denotes the symmetric spatial Cauchy stress tensor, while $\boldsymbol{P}$ characterizes the two-point first Piola-Kirchhoff stress tensor that, similarly to $\boldsymbol{F}$, relates spatial quantities to the material frame.

Since force does not depend on the body geometry, it is possible to find a relation between the Cauchy stress and the first Piola-Kirchhoff stress tensor. By combining Equation (A.15) with (A.16), and (A.17) the important transformations

$$\boldsymbol{t}(\boldsymbol{x},\, t,\, \boldsymbol{n})\,\mathrm{d}s \,=\, \boldsymbol{T}(\boldsymbol{X},\, t,\, \boldsymbol{N})\,\mathrm{d}S, \tag{A.18}$$

$$\boldsymbol{\sigma}(\boldsymbol{x},\, t)\cdot\boldsymbol{n}\,\mathrm{d}s \,=\, \boldsymbol{P}(\boldsymbol{X},\, t)\cdot\boldsymbol{N}\,\mathrm{d}S, \tag{A.19}$$

are obtained.

With these quantities at hand, and making use of Nanson's formula $\mathrm{d}s = J\boldsymbol{F}^{-\mathrm{t}}\mathrm{d}V$, which relates elements in the reference and deformed configurations by making use of the volume ratio (Equation (A.10)), $\boldsymbol{P}$ may be written as a function of $\boldsymbol{\sigma}$, i.e.

$$\boldsymbol{P} \,=\, J\boldsymbol{\sigma}\cdot\boldsymbol{F}^{-\mathrm{t}} \qquad \text{or} \qquad P_{aA} \,=\, J\sigma_{ab}F^{-1}_{Ab} \tag{A.20}$$

Then, the explicit expression of the Cauchy stress tensor is obtained as the inverse of the relation (A.20) as

$$\boldsymbol{\sigma} \,=\, J^{-1}\boldsymbol{P}\cdot\boldsymbol{F}^{\mathrm{t}} \,=\, \boldsymbol{\sigma}^{\mathrm{t}} \qquad \text{or} \qquad \sigma_{ab} \,=\, JP_{aA}F_{bA} \,=\, \sigma_{ba}, \tag{A.21}$$

which necessarily implies

$$\boldsymbol{P}\cdot\boldsymbol{F}^{\mathrm{t}} \;=\; \boldsymbol{F}\cdot\boldsymbol{P}^{\mathrm{t}}, \tag{A.22}$$

revealing that $\boldsymbol{P}$ is a, in general, non-symmetric tensor with nine independent components.

In addition to these two measures of stress, numerous additional definitions of stress tensors have been proposed. Among them, the spatial Kirchhoff stress tensor, which differs from the Cauchy stress tensor by the local volume ratio J, is used, i.e.

$$\boldsymbol{\tau} \;=\; J\boldsymbol{\sigma} \qquad \text{or} \qquad \tau_{ab} \;=\; J\sigma_{ab}. \tag{A.23}$$

In addition, the second Piola-Kirchhoff stress tensor which, although lacking of any physical interpretation, is very useful for the formulation of constitutive equations and is a frequently used stress measure in computational mechanics may be expressed as the pull-back operation on the contravariant spatial tensor field $\boldsymbol{\tau}^{\sharp}$

$$\boldsymbol{S} \;=\; \boldsymbol{F}^{-1}\cdot\boldsymbol{\tau}\cdot\boldsymbol{F}^{-\mathrm{t}} \qquad \text{or} \qquad S_{AB} \;=\; F^{-1}_{Aa}F^{-1}_{Bb}\tau_{ab}. \tag{A.24}$$

Thus, the Kirchhoff stress tensor can be expressed as the push-forward of $\boldsymbol{S}$ as

$$\boldsymbol{\tau} \;=\; \boldsymbol{F}\cdot\boldsymbol{S}\cdot\boldsymbol{F}^{\mathrm{t}} \qquad \text{or} \qquad \tau_{ab} \;=\; F_{aA}F_{bB}S_{AB}. \tag{A.25}$$

By combining Equation (A.24) and (A.23), it is possible to relate $\boldsymbol{S}$ with $\boldsymbol{\sigma}$ through the transformation

$$\begin{aligned} &\boldsymbol{S} \;=\; J\boldsymbol{F}^{-1}\cdot\boldsymbol{\sigma}\cdot\boldsymbol{F}^{-\mathrm{t}} \;=\; \boldsymbol{F}^{-1}\cdot\boldsymbol{P} \;=\; \boldsymbol{S}^{\mathrm{t}} \qquad \text{or} \\ &S_{AB} \;=\; JF^{-1}_{Aa}F^{-1}_{Bb}\sigma_{ab} \;=\; F^{-1}_{Aa}P_{aB} \;=\; S_{BA}, \end{aligned} \tag{A.26}$$

and inversely

$$\boldsymbol{\sigma} \;=\; J^{-1}\boldsymbol{F}\cdot\boldsymbol{S}\cdot\boldsymbol{F}^{\mathrm{t}} \qquad \text{or} \qquad \sigma_{ab} \;=\; J^{-1}F_{aA}F_{bB}S_{AB}. \tag{A.27}$$

Hence, from (A.26), the fundamental relation

$$\boldsymbol{P} \;=\; \boldsymbol{F}\cdot\boldsymbol{S} \qquad \text{or} \qquad P_{aA} \;=\; F_{aB}S_{BA}, \tag{A.28}$$

between the first Piola-Kirchhoff stress tensor $\boldsymbol{P}$ and the symmetric second Piola-Kirchhoff stress tensor $\boldsymbol{S}$, is found.

A.3 Hyperelastic constitutive laws

A constitutive law is said to be hyperelastic if its strain energy density function per reference volume unit, is a solely function of the deformation, that is, $\Psi(\boldsymbol{F})$. Since neither thermal effects nor entropy variations are considered, the strain energy function must coincide with the free energy variation in these conditions, namely $\mathrm{d}W \equiv \mathrm{d}\Psi$.

For a hyperelastic strain energy function, it is fulfilled that

$$\boldsymbol{P} = \frac{\partial \Psi(\boldsymbol{F})}{\partial \boldsymbol{F}} \qquad \text{or} \qquad P_{aA} = \frac{\partial \Psi}{\partial F_{aA}}. \tag{A.29}$$

Considering the strain energy function to be a function of right Cauchy-Green tensor, Equation (A.7), alternative expressions for the Piola-Kirchhoff stress tensors $\boldsymbol{P}$ and $\boldsymbol{S}$ may be obtained

$$\begin{aligned} \boldsymbol{P} &= 2\,\boldsymbol{F} \cdot \frac{\partial \Psi(\boldsymbol{C})}{\partial \boldsymbol{C}} \qquad && \text{or} \qquad P_{aA} = 2\,F_{aB}\frac{\partial \Psi}{\partial C_{BA}}, \\ \boldsymbol{S} &= 2\,\frac{\partial \Psi(\boldsymbol{C})}{\partial \boldsymbol{C}} \qquad && \text{or} \qquad S_{AB} = 2\,F_{aB}\frac{\partial \Psi}{\partial C_{AB}}, \end{aligned} \tag{A.30}$$

whereas the Cauchy stress can be obtained by applying the transformations in (A.21) and (A.27) to $\boldsymbol{P}$ and $\boldsymbol{S}$, respectively.

For convenience, it is commonly required that the strain energy function vanishes in the reference configuration, i.e. where $\boldsymbol{F} = \boldsymbol{I}$. This normalization condition implies that no energy is stored in the body in the undeformed state, and therefore

$$\Psi = \Psi(\boldsymbol{I}) = 0. \tag{A.31}$$

Since, from physical observations, it has been observed that the strain energy increases with deformation it will be required, in addition to (A.31), that

$$\Psi = \Psi(\boldsymbol{F}) > 0. \tag{A.32}$$

Moreover, it will be assumed that the strain energy density function has no other stationary point in the strain space. Note that relations (A.31) and (A.32) ensure that the residual stress in the reference configuration, namely the residual stress, is zero and, therefore, the reference configuration is stress-free.

Another requirement, for behaviour at finite deformations, is related to the changes of local volume, whose ratio is represented by the Jacobian determinant J, Equation (A.10). This implies that $\Psi \mapsto +\infty$ if $J = \det(\boldsymbol{F})$ approximates to $+\infty$ or $+0$, which is physically means that an infinite amount of energy is required to expand a material volume to the infinite range or to compress until vanishing it.

The strain energy function be invariant under rigid solid motions or changes of the observer. In other words, the strain energy function must be objective, which means that translations or rotations of the deformed configuration in the space do not change the amount of stored energy. Therefore, Ψ cannot be an arbitrary function of $\boldsymbol{F}$, but must rather satisfy the constraint

$$\Psi(\boldsymbol{F}) = \Psi(\boldsymbol{Q} \cdot \boldsymbol{F}), \tag{A.33}$$

with $\boldsymbol{Q} \in \mathbb{Q}^3_+$.

A feasible way to obtain equivalent formulations of (A.33) is obtained by choosing $\boldsymbol{Q} \equiv \boldsymbol{R}^{\mathrm{t}}$. Then, the right part of (A.33) reads $\Psi(\boldsymbol{R}^{\mathrm{t}} \cdot \boldsymbol{R} \cdot \boldsymbol{U}) = \Psi(\boldsymbol{U})$, which means that

the strain energy is independent of the rotational part of $\boldsymbol{F}$. Consequently, objectivity can be reached by expressing the strain energy function in terms of the six independent components of $\boldsymbol{C} = \boldsymbol{U}^2$,

$$\Psi(\boldsymbol{F}) \;=\; \Psi(\boldsymbol{C}). \tag{A.34}$$

Accordingly, the strain energy density function can be expressed as a function of the principal invariants of its argument (see Truesdell and Noll, 2004, for a detailed proof) which, for second order tensor, are obtained from the solution of its characteristic equation

$$\det(\boldsymbol{A} \,-\, \lambda_i \boldsymbol{I}) \;=\; -\lambda_i^3 + I_1\lambda_i^2 - I_2\lambda_i - I_3 \;=\; 0, \tag{A.35}$$

where λ_i, $i = 1,\, 2,\, 3$ represent the eigenvalues of $\boldsymbol{A}$, and $I_i(\boldsymbol{A})$, $i = 1,\, 2,\, 3$ are the so-called principal scalar invariants of $\boldsymbol{A}$ given by

$$\left.\begin{aligned} I_1(\boldsymbol{A}) \;&=\; \mathrm{tr}(\boldsymbol{A}) \;=\; \lambda_1 + \lambda_2 + \lambda_3, \\ I_2(\boldsymbol{A}) \;&=\; \frac{1}{2}\left[[\mathrm{tr}(\boldsymbol{A})]^2 - \mathrm{tr}(\boldsymbol{A}^2)\right] \;=\; \lambda_1\lambda_2 + \lambda_1\lambda_3 + \lambda_2\lambda_3, \\ I_3(\boldsymbol{A}) \;&=\; \det(\boldsymbol{A}) \;=\; \lambda_1\lambda_2\lambda_3. \end{aligned}\right\} \tag{A.36}$$

With these quantities at hand, it is possible to represent a symmetric tensor by means of its eigenvalues, λ_i, $i = 1,\, 2,\, 3$, and the eigenvectors associated to $\boldsymbol{A}$, which form the orthonormal basis $\{\hat{\boldsymbol{n}}_{1,\,2,\,3}\}$. Using the unit tensor, $\boldsymbol{I} = \hat{\boldsymbol{n}}_i \otimes \hat{\boldsymbol{n}}_i$, the spectral decomposition of $\boldsymbol{A}$ is expressed as

$$\boldsymbol{A} \;=\; \sum_{i=1}^{3} \lambda_i\, \hat{\boldsymbol{n}}_i \otimes \hat{\boldsymbol{n}}_i. \tag{A.37}$$

Taking advantage of the spectral representation, it is possible to express the second Piola-Kirchhoff stress, Equation (A.30), in terms of its eigenvalues S_a, $a = 1,\, 2,\, 3$, and the orthonormal basis $\hat{\boldsymbol{N}}_a$, $a = 1, 2, 3$, formed by the eigenvectors of $\boldsymbol{C}$, i.e.

$$\boldsymbol{S} \;=\; \sum_{a=1}^{3} \frac{1}{\lambda_a}\frac{\partial \Psi}{\partial \lambda_a} \hat{\boldsymbol{N}}_a \otimes \hat{\boldsymbol{N}}_a, \tag{A.38}$$

where the eigenvalues of $\boldsymbol{S}$ are

$$S_a \;=\; 2\,\frac{\partial \Psi}{\partial \lambda_a^2} \;=\; \frac{1}{\lambda_a}\frac{\partial \Psi}{\partial \lambda_a}. \tag{A.39}$$

A.3.1 Isotropic constitutive laws

Since the strain energy function is invariant under rotations, it may be expressed in terms of the principal invariants of its argument, which is a fundamental result for isotropic scalar functions. Having this in mind, (A.34) can be expressed as a function of the invariants of the right Cauchy-Green tensor $\boldsymbol{C}$ as

$$\Psi(\boldsymbol{C}) \;=\; \Psi(I_1(\boldsymbol{C}),\, I_2(\boldsymbol{C}),\, I_3(\boldsymbol{C})), \tag{A.40}$$

where the invariants are computed following (A.36).

In order to determine the stress response, the chain rule is applied on Equation (A.30), i.e.

$$\boldsymbol{S} = 2\sum_{a=1}^{3}\frac{\partial\Psi}{\partial I_a}\frac{\partial I_a}{\partial\boldsymbol{C}}, \tag{A.41}$$

in which the derivatives of the invariants with respect to $\boldsymbol{C}$ are

$$\frac{\partial I_1}{\partial\boldsymbol{C}} = \boldsymbol{I}, \qquad \frac{\partial I_2}{\partial\boldsymbol{C}} = I_1\boldsymbol{I} - \boldsymbol{C}, \qquad \frac{\partial I_3}{\partial\boldsymbol{C}} = I_3\boldsymbol{C}^{-1}. \tag{A.42}$$

Therefore, by replacing these quantities in (A.41) it is obtained

$$\boldsymbol{S} = 2\left[\left[\frac{\partial\Psi}{\partial I_1} + I_1\frac{\partial\Psi}{\partial I_2}\right]\boldsymbol{I} - \frac{\partial\Psi}{\partial I_2}\boldsymbol{C} + I_3\frac{\partial\Psi}{\partial I_3}\boldsymbol{C}^{-1}\right], \tag{A.43}$$

that is a general representation of the stresses for an isotropic material, in which Ψ can adopt any scalar-valued form of the right Cauchy-Green tensor.

Next, the application of Equation (A.27) allows obtaining the expression of the Cauchy-stress tensor, which after some straightforward algebraic manipulations, reads

$$\boldsymbol{\sigma} = 2J^{-1}\left[\left[I_2\frac{\partial\Psi}{\partial I_2} + I_3\frac{\partial\Psi}{\partial I_3}\right]\boldsymbol{I} + \frac{\partial\Psi}{\partial I_1}\boldsymbol{b} - I_3\frac{\partial\Psi}{\partial I_2}\boldsymbol{b}^{-1}\right]. \tag{A.44}$$

A.3.1.1 Stress tensors for incompressible materials

For the particular case of an incompressible hyperelastic material, the strain energy function

$$\Psi = \Psi(\boldsymbol{C}) + \mathrm{p}\,[J-1] \tag{A.45}$$

is postulated, where the strain energy Ψ is defined for $J := \det(\boldsymbol{F}) = 1$. There, compressibility is kinematically constrained by means of the scalar p, which serves as a Lagrange multiplier, usually identified with the hydrostatic pressure. Note that this scalar can be only determined from the equilibrium equation and the boundary conditions, and represents a workless reaction to the kinematic constraint in the deformation field.

Then, the stress expressions in the material configuration is obtained from (A.30) as

$$\boldsymbol{S} = -\mathrm{p}\boldsymbol{C}^{-1} + 2\,\frac{\partial\Psi(\boldsymbol{C})}{\partial\boldsymbol{C}}, \tag{A.46}$$

whereas the application of the push-forward (A.27) on this result renders the Cauchy stress expression

$$\boldsymbol{\sigma} = -\mathrm{p}\boldsymbol{I} + 2J^{-1}\,\boldsymbol{F}\cdot\frac{\partial\Psi(\boldsymbol{C})}{\partial\boldsymbol{C}}\cdot\boldsymbol{F}^{\mathrm{t}}. \tag{A.47}$$

These are general expressions for incompressible hyperelastic materials.

Regarding the representation of Ψ as a function of the invariants of $\boldsymbol{C}$, and considering that $\det\boldsymbol{C} = J^2 = I_3$, which is kinematically constrained to $I_3 = 1$, it turns out that

I_1 and I_2 are the only independent deformation variables. A suitable representation of the strain-energy function for incompressible hyperelastic materials, in view of (A.40), is

$$\Psi = \Psi(I_1(\boldsymbol{C}), I_2(\boldsymbol{C})) + \frac{1}{2}\mathrm{p}\,[I_3 - 1]\,, \tag{A.48}$$

where p/2 is an indeterminate Lagrange multiplier. Then, by analogy with the procedure applied in (A.43), the application of the chain rule together with the constraint $I_3 = 1$ turns into

$$\Psi = -p\boldsymbol{C}^{-1} + 2\left[\frac{\partial\Psi}{\partial I_1} + I_1\frac{\partial\Psi}{\partial I_2}\right]\boldsymbol{I} - 2\frac{\partial\Psi}{\partial I_2}\boldsymbol{C}, \tag{A.49}$$

and the Cauchy stress expression reads

$$\boldsymbol{\sigma} = -\mathrm{p}\boldsymbol{I} + 2\frac{\partial\Psi}{\partial I_1}\boldsymbol{b} - 2\frac{\partial\Psi}{\partial I_2}\boldsymbol{b}^{-1}. \tag{A.50}$$

Note that this expression is only valid for incompressible materials.

A.3.1.2 Stress tensors for compressible materials

The multiplicative split of the deformation gradient tensor into isochoric and bulk contributions in Equation (A.11), can be applied to model compressible materials which exhibit different behaviours under bulk ans shear deformations. This approach was firstly introduced by Flory (1961), and has been widely used to model a variety of phenomena in finite strains mechanics. Among them, it is possible to apply it to model materials for which local volume changing deformations need of much higher exterior work than the volume preserving ones, known as quasi-incompressible.

This concept has also important advantages in computational mechanics, where the separate treatment of isochoric and deviatoric parts presents noticeable numerical advantages.

In order to calculate the stress response for compressible hyperelastic materials, it is necessary to introduce the derivative of isochoric Cauchy-Green tensor $\bar{\boldsymbol{C}}$, Equation (A.12), relative to $\boldsymbol{C}$. For this purpose, the constitutive relations

$$\frac{\partial J}{\partial \boldsymbol{C}} = \frac{J}{2}\boldsymbol{C}^{-1} \qquad \text{and} \qquad \frac{\partial J^{-2/3}}{\partial \boldsymbol{C}} = -\frac{J^{-2/3}}{3}\boldsymbol{C}^{-1} \tag{A.51}$$

are needed.

With these relations at hand, the desired derivative is obtained as

$$\frac{\partial\bar{\boldsymbol{C}}}{\partial\boldsymbol{C}} = J^{-2/3}\left[\mathbf{I} - \frac{1}{3}\boldsymbol{C}\otimes\boldsymbol{C}^{-1}\right], \tag{A.52}$$

where $\mathbf{I}$ denotes de fourth-order unit tensor.

Next, following the assumptions represented in Equation (A.45), and based on the kinematical conditions in (A.12), the strain energy function is expressed

$$\Psi(\boldsymbol{C}) = \Psi_{\mathrm{vol}}(J) + \Psi_{\mathrm{ich}}(\bar{\boldsymbol{C}}), \tag{A.53}$$

where Ψ_{vol} accounts for the strain energy due to volume changes and Ψ_{ich} represents the strain energy corresponding to purely isochoric deformations.

Following the procedure previously presented, the second Piola-Kirchhoff stress tensor is obtained by derivation of (A.53) with respect to the right Cauchy-Green tensor, Equation (A.30). Thus, the stress tensor consists of a purely volumetric and a purely isochoric contributions, i.e. $\boldsymbol{S}_{\text{vol}}$ and $\boldsymbol{S}_{\text{ich}}$, so the total stress is

$$\boldsymbol{S} = \boldsymbol{S}_{\text{vol}} + \boldsymbol{S}_{\text{ich}}, \tag{A.54}$$

based on the definitions

$$\boldsymbol{S}_{\text{vol}} = J\, p\, \boldsymbol{C}^{-1} \tag{A.55}$$

$$\boldsymbol{S}_{\text{ich}} = J^{-2/3}\left[\mathbf{I} - \frac{1}{3}\boldsymbol{C}^{-1}\otimes\boldsymbol{C}\right] : \bar{\boldsymbol{S}} = \mathbf{P} : \bar{\boldsymbol{S}}, \tag{A.56}$$

where $\mathbf{P} = J^{-2/3}\left[\mathbf{I} - \frac{1}{3}\boldsymbol{C}^{-1}\otimes\boldsymbol{C}\right]$ is the fourth-order projection tensor, and the constitutive relations for the hydrostatic pressure p and fictitious second Piola-Kirchhoff stress $\bar{\boldsymbol{S}}$ defined by

$$p = \frac{\partial \Psi_{\text{vol}}(J)}{\partial J} \tag{A.57}$$

$$\bar{\boldsymbol{S}} = 2\,\frac{\partial \Psi_{\text{ich}}(\bar{\boldsymbol{S}})}{\partial \bar{\boldsymbol{C}}} = 2\left[\left[\frac{\partial \Psi}{\partial \bar{I}_1} + \bar{I}_1\frac{\partial \Psi}{\partial \bar{I}_2}\right]\boldsymbol{I} + \frac{\partial \Psi}{\partial \bar{I}_2}\boldsymbol{C}\right], \tag{A.58}$$

where $\bar{I}_1$ and $\bar{I}_2$ are the first and second invariants of $\bar{\boldsymbol{C}}$, Equation (A.36). Note that it is possible to obtain the Cauchy stress tensor by applying the push-forward, defined in Equation (A.27), on (A.54).

A.3.1.3 Tangent operator

Since most problems involving hyperelastic materials undergoing finite strains are non-linear, the computation of the tangent operator is frequently required in computational mechanics methods in order to linearise the problem. This linearised version can be solved by means of the intensive application of iterative schemes, which provide an approximate solution of the original problem. The tangent operator, which is basically the derivative of the stress with respect to the strain, is of crucial importance in order to optimize the convergence of those numerical procedures.

The tangent operator, also known as elasticity tensor when dealing with elastic constitutive laws, is defined in the reference configuration as

$$\mathbf{C} = 2\,\frac{\partial \boldsymbol{S}(\boldsymbol{C})}{\partial \boldsymbol{C}} \qquad \text{or} \qquad C_{ABCD} = 2\,\frac{\partial S_{AB}}{\partial C_{CD}}, \tag{A.59}$$

which corresponds to a fourth-order tensor with 81 components. Nevertheless, the number of independent components is reduced to 36 due to the symmetries of $\boldsymbol{S}$ and $\boldsymbol{C}$,

see (A.26), so it is satisfied that $\mathbf{C}$ is symmetric in its first and second subscripts, AB, and in its third and fourth subscripts, CD. Thus, it is said that the elasticity tensor has minor symmetries, i.e.

$$C_{ABCD} = C_{BACD} = C_{ABDC} \tag{A.60}$$

If the existence of a scalar-valued strain energy Ψ function is assumed, $\boldsymbol{S}$ can be derived from Ψ according to (A.30), so the elasticity tensor can be expressed

$$\mathbf{C} = 4\,\frac{\partial^2 \Psi(\boldsymbol{C})}{\partial \boldsymbol{C} \partial \boldsymbol{C}} \qquad \text{or} \qquad C_{ABCD} = 4\,\frac{\partial \Psi}{\partial C_{AB} \partial C_{CD}}, \tag{A.61}$$

which implies that $\mathbf{C}$ posses major symmetries, i.e.

$$\mathbf{C} = \mathbf{C}^{\mathrm{t}} \qquad \text{or} \qquad C_{ABCD} = C_{CDAB} \tag{A.62}$$

so that there are only 21 independent components at each strain rate.

The elasticity tensor in the spatial description $\mathbf{c}$ is defined as the push-forward of $\mathbf{C}$ times a factor J^{-1} (Marsden and Hughes, 1994)

$$\mathsf{c}_{abcd} = J^{-1}\, F_{aA}\, F_{bB}\, F_{cC}\, F_{dD}\, C_{ABCD}, \tag{A.63}$$

which has the same symmetries of $\mathbf{C}$.

Based on the kinematic decomposition of the deformation gradient tensor presented in (A.11), and according to the additive split of the strain energy density function into volumetric and isochoric contributions in (A.53), it is possible to write the elasticity tensor in the decoupled form

$$\mathbf{C} = 2\,\frac{\partial \boldsymbol{S}(\boldsymbol{C})}{\partial \boldsymbol{C}} = \mathbf{C}_{\mathrm{vol}} + \mathbf{C}_{\mathrm{ich}}, \tag{A.64}$$

which represents the completion of the additive split of the stress response, Equation (A.54).

In order to calculate the volumetric component of the elasticity tensor, the fourth-order tensor $\partial \boldsymbol{C}/\partial \boldsymbol{C}^{-1}$ is required. For convenience, the notation

$$\frac{\partial \boldsymbol{C}^{-1}}{\partial \boldsymbol{C}} = -\boldsymbol{C}^{-1} \odot \boldsymbol{C}^{-1} \tag{A.65}$$

is introduced, were the symbol $\odot$ denotes the tensor product rule

$$-\left[\boldsymbol{C}^{-1} \odot \boldsymbol{C}^{-1}\right] = -\frac{1}{2}\left[C^{-1}_{AC}\, C^{-1}_{BD} + C^{-1}_{AD}\, C^{-1}_{BC}\right] = \frac{\partial C^{-1}_{AB}}{\partial C_{CD}}. \tag{A.66}$$

Then, the chain rule is applied to Equation (A.55) so the volumetric part of the elasticity tensor in the material configuration is

$$\mathbf{C}_{\mathrm{vol}} = 2\,\frac{\partial \boldsymbol{S}_{\mathrm{vol}}}{\partial \boldsymbol{C}} = J\,\tilde{p}\,\boldsymbol{C}^{-1} \otimes \boldsymbol{C}^{-1} + 2\,J\,p\,\boldsymbol{C}^{-1} \odot \boldsymbol{C}^{-1}, \tag{A.67}$$

where p is defined in (A.57), and the scalar function $\tilde{p} = p + J\,\partial p/\partial J$ has been introduced for the sake of clarity.

The same procedure followed in the obtaining of $\mathbf{C}_{\text{vol}}$ can be applied in order to obtain the material description of the isochoric elasticity tensor for a compressible material $\mathbf{C}_{\text{ich}}$, which can be obtained from (A.30) and (A.56) as

$$\begin{aligned}\mathbf{C}_{\text{ich}} &= 2\,\frac{\partial \boldsymbol{S}_{\text{ich}}}{\partial \boldsymbol{C}} = 2\,\frac{\partial\left[J^{-2/3}\mathbf{P} : \bar{\boldsymbol{S}}\right]}{\partial \boldsymbol{C}} \\ &= \mathbf{P} : \bar{\mathbf{C}} : \mathbf{P}^{\text{t}} + \frac{2}{3}\Bigg[\left[J^{-2/3}\bar{\boldsymbol{S}} : \boldsymbol{C}\right]\tilde{\mathbf{P}} - \left[\boldsymbol{C}^{-1}\otimes \boldsymbol{S}_{\text{ich}} + \boldsymbol{S}_{\text{ich}}\otimes \boldsymbol{C}^{-1}\right]\Bigg],\end{aligned} \tag{A.68}$$

where

$$\bar{\mathbf{C}} = 2\,J^{-4/3}\frac{\partial \bar{\boldsymbol{S}}}{\partial \bar{\boldsymbol{C}}} \tag{A.69}$$

$$\tilde{\mathbf{P}} = \boldsymbol{C}^{-1}\odot \boldsymbol{C}^{-1} - \frac{1}{3}\boldsymbol{C}^{-1}\otimes \boldsymbol{C}^{-1} \tag{A.70}$$

Starting from (A.56), the application of the chain leads to

$$\begin{aligned}\mathbf{C}_{\text{ich}} &= 4\,J^{-4/3}\Bigg[\left[\bar{\Psi}_{11} + 2\bar{\Psi}_{21}\bar{I}_1 + \bar{\Psi}_2\bar{I}_1 + \bar{\Psi}_{22}\bar{I}_1^2\right]\boldsymbol{I}\otimes\boldsymbol{I} \\ &+ \bar{\Psi}_{22}\,\bar{\boldsymbol{C}}\otimes\bar{\boldsymbol{C}} - \bar{\Psi}_2\,\mathbf{I} \\ &+ \frac{1}{9}\left[\bar{\Psi}_{11}\bar{I}_1^2 + 4\bar{\Psi}_1\bar{I}_1 + 3\bar{\Psi}_{21}\bar{I}_1\bar{I}_2 + 2\bar{\Psi}_{22}\bar{I}_{22}^2 + 8\bar{\Psi}_2\bar{I}_2\right]\bar{\boldsymbol{C}}^{-1}\otimes\bar{\boldsymbol{C}}^{-1} \\ &- \left[\bar{\Psi}_{21} + \bar{\Psi}_{22}\bar{I}_1\right]\left[\bar{\boldsymbol{C}}\otimes\boldsymbol{I} + \boldsymbol{I}\otimes\bar{\boldsymbol{C}}\right] \\ &- \frac{1}{3}\left[\bar{\Psi}_1 - 2\bar{\Psi}_2\bar{I}_1 + \bar{\Psi}_{11}\bar{I}_1 + \bar{\Psi}_{21}\bar{I}_1^2\right]\left[\bar{\boldsymbol{C}}^{-1}\otimes\boldsymbol{I} + \boldsymbol{I}\otimes\bar{\boldsymbol{C}}^{-1}\right] \\ &+ \frac{1}{3}\left[\bar{\Psi}_2 - \bar{\Psi}_{21}\bar{I}_1 + 2\bar{\Psi}_{22}\bar{I}_2\right]\left[\bar{\boldsymbol{C}}\otimes\boldsymbol{C}^{-1} + \boldsymbol{C}^{-1}\otimes\bar{\boldsymbol{C}}\right]\Bigg],\end{aligned} \tag{A.71}$$

where the notation $\bar{\Psi}_i,\ i = 1, 2$ represents the derivative of $\bar{\Psi}$ with respect to the ith invariant, and $\bar{\Psi}_{ij},\ i = 1, 2,\ j = 1, 2$ means the second derivative with respect to the i and j invariants.

By analogy with the spectral decomposition of the stress in (A.37), it is possible to express the elasticity tensor as a function of the principal stretches. Considering the strain energy density function $\Psi = \Psi(\lambda_1, \lambda_2, \lambda_3)$, the spectral form of the elasticity tensor in the material description reads

$$\begin{aligned}\mathbf{C} &= \sum_{a,b=1}^{3}\frac{1}{\lambda_b}\frac{\partial S_a}{\partial \lambda_b}\,\hat{\boldsymbol{N}}_a\otimes\hat{\boldsymbol{N}}_a\otimes\hat{\boldsymbol{N}}_b\otimes\hat{\boldsymbol{N}}_b \\ &+ \sum_{\substack{a,b=1\\ a\neq b}}^{3}\frac{S_b - S_a}{\lambda_b^2 - \lambda_a^2}\left[\hat{\boldsymbol{N}}_a\otimes\hat{\boldsymbol{N}}_b\otimes\hat{\boldsymbol{N}}_a\otimes\hat{\boldsymbol{N}}_b + \hat{\boldsymbol{N}}_a\otimes\hat{\boldsymbol{N}}_b\otimes\hat{\boldsymbol{N}}_b\otimes\hat{\boldsymbol{N}}_a\right],\end{aligned} \tag{A.72}$$

where the second Piola-Kirchhoff stress eigenvalues $S_i,\ i = 1, 2, 3$ are defined in (A.39).

A.3.2 Anisotropic constitutive laws

The inclusion of structural tensors into constitutive laws (Spencer, 1971) is nowadays the most widely used technique to introduce anisotropy in material models (see, e.g., Weiss *et al.*, 1996). By means of this approach, the effect of anisotropy is represented by unit vectors in the reference configuration. Thus, the strain energy density function of material with n directions of anisotropy reads

$$\Psi = \Psi(\boldsymbol{C}, \boldsymbol{a}_1, \cdots, \boldsymbol{a}_n). \tag{A.73}$$

Since the sense of the vectors $\boldsymbol{a}_i$, $i \in [1, n]$ is immaterial, the strain energy function Ψ is frequently taken as an even function of $\boldsymbol{a}_i$, so (A.73) can be expressed

$$\Psi = \Psi(\boldsymbol{C}, \boldsymbol{A}_1, \cdots, \boldsymbol{A}_n), \tag{A.74}$$

where $\boldsymbol{A}_i$, are structural tensor characterizing the anisotropic response of the material associated to the referential unit vector $\boldsymbol{a}_i$ as

$$\boldsymbol{A}_i = \boldsymbol{a}_i \otimes \boldsymbol{a}_i. \tag{A.75}$$

As well as for the isotropic case, the modelling of incompressible and compressible materials render different expression for the stress and elastic tensor quantities. Based on the kinematic assumption (A.11), together with the additive split of the strain energy density function in (A.53), it is possible to express the strain energy function for anisotropic materials as

$$\Psi = \Psi_{\text{vol}}(J) + \Psi_{\text{ich}}(\bar{\boldsymbol{C}}, \boldsymbol{A}_1, \cdots, \boldsymbol{A}_n). \tag{A.76}$$

A.3.2.1 Fundamental quantities for compressible hyperelastic materials with two directions of anisotropy

Although Equation (A.76) is defined for n directions of anisotropy, soft biological tissues are frequently assumed to posses one direction of anisotropy, which provides a transversely isotropic behaviour (Humphrey and Yin, 1987), or two directions, as widely assumed in blood vessels modelling (Holzapfel *et al.*, 2000).

Accounting for these assumptions, the isochoric pseudo-invariants

$$\bar{I}_4(\bar{\boldsymbol{C}}, \boldsymbol{a}_1) = \boldsymbol{a}_1 \cdot \bar{\boldsymbol{C}} \cdot \boldsymbol{a}_1 \tag{A.77}$$

$$\bar{I}_5(\bar{\boldsymbol{C}}, \boldsymbol{a}_1) = \boldsymbol{a}_1 \cdot \bar{\boldsymbol{C}}^2 \cdot \boldsymbol{a}_1 \tag{A.78}$$

$$\bar{I}_6(\bar{\boldsymbol{C}}, \boldsymbol{a}_2) = \boldsymbol{a}_2 \cdot \bar{\boldsymbol{C}} \cdot \boldsymbol{a}_2 \tag{A.79}$$

$$\bar{I}_7(\bar{\boldsymbol{C}}, \boldsymbol{a}_2) = \boldsymbol{a}_2 \cdot \bar{\boldsymbol{C}}^2 \cdot \boldsymbol{a}_2 \tag{A.80}$$

$$\bar{I}_8(\bar{\boldsymbol{C}}, \boldsymbol{a}_1, \boldsymbol{a}_2) = [\boldsymbol{a}_1 \cdot \boldsymbol{a}_2]\, \boldsymbol{a}_1 \cdot \bar{\boldsymbol{C}} \cdot \boldsymbol{a}_2 \tag{A.81}$$

$$\bar{I}_9(\boldsymbol{a}_1, \boldsymbol{a}_2) = [\boldsymbol{a}_1 \cdot \boldsymbol{a}_2]^2 \tag{A.82}$$

associated to the anisotropic behaviour are introduced. Then, (A.76) can be expressed as a function of invariants as

$$\Psi \,=\, \Psi_{\text{vol}}(J) \,+\, \Psi_{\text{ich}}(\bar{I}_1,\, \bar{I}_2,\, \bar{I}_4,\, \bar{I}_5,\, \bar{I}_6,\, \bar{I}_7,\, \bar{I}_8). \tag{A.83}$$

Note that, since $\bar{I}_9$ is a constant, it has been removed from the strain energy function.

In order to obtain the constitutive equation for the isochoric part of (A.83), Equation (A.30) is applied. Then, the second Piola-Kirchhoff stress tensor reads

$$\boldsymbol{S}_{\text{ich}} \,=\, 2\,\frac{\partial \Psi_{\text{ich}}}{\partial \boldsymbol{C}} \,=\, 2\sum_{\substack{j=1\\ j\neq 3}}^{8} \frac{\partial \Psi_{\text{ich}}}{\partial \bar{I}_j}\frac{\partial \bar{I}_j}{\partial \bar{\boldsymbol{C}}} : \frac{\partial \bar{\boldsymbol{C}}}{\partial \boldsymbol{C}}, \tag{A.84}$$

where the derivatives of the pseudo-invariants are

$$\frac{\partial \bar{I}_4}{\partial \bar{\boldsymbol{C}}} \,=\, \boldsymbol{a}_1 \otimes \boldsymbol{a}_1, \tag{A.85}$$

$$\frac{\partial \bar{I}_5}{\partial \bar{\boldsymbol{C}}} \,=\, \boldsymbol{a}_1 \otimes \left[\bar{\boldsymbol{C}} \cdot \boldsymbol{a}_1\right] \,+\, \left[\bar{\boldsymbol{C}} \cdot \boldsymbol{a}_1\right] \otimes \boldsymbol{a}_1, \tag{A.86}$$

$$\frac{\partial \bar{I}_6}{\partial \bar{\boldsymbol{C}}} \,=\, \boldsymbol{a}_2 \otimes \boldsymbol{a}_2, \tag{A.87}$$

$$\frac{\partial \bar{I}_7}{\partial \bar{\boldsymbol{C}}} \,=\, \boldsymbol{a}_2 \otimes \left[\bar{\boldsymbol{C}} \cdot \boldsymbol{a}_1\right] \,+\, \left[\bar{\boldsymbol{C}} \cdot \boldsymbol{a}_2\right] \otimes \boldsymbol{a}_2, \tag{A.88}$$

$$\frac{\partial \bar{I}_8}{\partial \bar{\boldsymbol{C}}} \,=\, \frac{1}{2}\left[\boldsymbol{a}_1 \cdot \boldsymbol{a}_2\right]\left[\boldsymbol{a}_1 \otimes \boldsymbol{a}_2 + \boldsymbol{a}_2 \otimes \boldsymbol{a}_1\right]. \tag{A.89}$$

Having in mind these quantities, and considering the expression for the isochoric contribution to the second Piola-Kirchhoff stress tensor in Equation (A.56), the anisotropic isochoric stress in the material frame can be expressed, after some straightforward algebraic computations, as a function of the fictitious second Piola-Kirchhoff stress tensor, as defined in (A.58). For case under analysis, $\bar{\boldsymbol{S}}$ reads

$$\begin{aligned}
\bar{\boldsymbol{S}} \,&=\, 2\,\frac{\partial \Psi_{\text{ich}}}{\partial \bar{\boldsymbol{C}}} \,=\, 2\sum_{\substack{j=1\\ j\neq 3}}^{8} \frac{\partial \Psi_{\text{ich}}}{\partial \bar{I}_j}\frac{\partial \bar{I}_j}{\partial \bar{\boldsymbol{C}}} \\
&=\, 2\Big[\bar{\Psi}_1\,\boldsymbol{I} \,+\, \bar{\Psi}_2\,\bar{\boldsymbol{C}} \\
&+\, \bar{\Psi}_4\,\boldsymbol{a}_1 \otimes \boldsymbol{a}_1 \,+\, \bar{\Psi}_5\Big[\boldsymbol{a}_1 \otimes \left[\boldsymbol{a}_1 \cdot \bar{\boldsymbol{C}}\right] + \left[\boldsymbol{a}_1 \cdot \bar{\boldsymbol{C}}\right] \otimes \boldsymbol{a}_1\Big] \\
&+\, \bar{\Psi}_6\,\boldsymbol{a}_2 \otimes \boldsymbol{a}_2 \,+\, \bar{\Psi}_7\Big[\boldsymbol{a}_2 \otimes \left[\boldsymbol{a}_2 \cdot \bar{\boldsymbol{C}}\right] + \left[\boldsymbol{a}_2 \cdot \bar{\boldsymbol{C}}\right] \otimes \boldsymbol{a}_2\Big] \\
&+\, \frac{\bar{\Psi}_8}{2}\left[\boldsymbol{a}_1 \cdot \boldsymbol{a}_2\right]\left[\boldsymbol{a}_1 \otimes \boldsymbol{a}_2 + \boldsymbol{a}_2 \otimes \boldsymbol{a}_1\right]\Big],
\end{aligned} \tag{A.90}$$

Note that the spatial counterpart of (A.90) is obtained from the application of the push-forward operation in (A.27).

According to the decoupled representation of stress, the split representation of the elasticity tensor presented in (A.64) separates between volumetric and isochoric contributions. Thereby, the isochoric contribution to the elasticity tensor is computed following Equation (A.68), where the fictitious elasticity tensor reads

$$
\begin{aligned}
\bar{\mathsf{C}} &= 2\,\frac{\partial \bar{\boldsymbol{S}}}{\partial \bar{\boldsymbol{C}}} = 4\,\frac{\partial \Psi_{\text{ich}}(\bar{I}_1,\,\bar{I}_2,\,\bar{I}_4,\cdots,\,\bar{I}_8)}{\partial \bar{\boldsymbol{C}}} \\
&= 4\,J^{-4/3}\Bigg\{ \left[\bar{\Psi}_{11} + 2\bar{I}_1\bar{\Psi}_{12} + \bar{\Psi}_2 + \bar{I}_1^2\bar{\Psi}_{22}\right]\boldsymbol{I}\otimes\boldsymbol{I} \\
&- \left[\bar{\Psi}_{12} + \bar{I}_1\bar{\Psi}_{22}\right]\left[\boldsymbol{I}\otimes\bar{\boldsymbol{C}} + \bar{\boldsymbol{C}}\otimes\boldsymbol{I}\right] - \bar{\Psi}_{22}\,\bar{\boldsymbol{C}}\otimes\bar{\boldsymbol{C}} - \bar{\Psi}_2\,\mathbf{I} \\
&+ \left[\bar{\Psi}_{14} + \bar{I}_1\bar{\Psi}_{24}\right]\left[\boldsymbol{I}\otimes\boldsymbol{a}_1\otimes\boldsymbol{a}_1 + \boldsymbol{a}_1\otimes\boldsymbol{a}_1\otimes\boldsymbol{I}\right] \\
&- \bar{\Psi}_{24}\left[\bar{\boldsymbol{C}}\otimes\boldsymbol{a}_1\otimes\boldsymbol{a}_1 + \boldsymbol{a}_1\otimes\boldsymbol{a}_1\otimes\bar{\boldsymbol{C}}\right] \\
&+ \bar{\Psi}_{44}\,\boldsymbol{a}_1\otimes\boldsymbol{a}_1\otimes\boldsymbol{a}_1\otimes\boldsymbol{a}_1 + \left[\bar{\Psi}_{15} + \bar{I}_1\bar{\Psi}_{25}\right]\left[\boldsymbol{I}\otimes\frac{\partial\bar{I}_5}{\partial\bar{\boldsymbol{C}}} + \frac{\partial\bar{I}_5}{\partial\bar{\boldsymbol{C}}}\otimes\boldsymbol{I}\right] \\
&- \bar{\Psi}_{25}\left[\bar{\boldsymbol{C}}\otimes\frac{\partial\bar{I}_5}{\partial\bar{\boldsymbol{C}}} + \frac{\partial\bar{I}_5}{\partial\bar{\boldsymbol{C}}}\otimes\bar{\boldsymbol{C}}\right] + \bar{\Psi}_{55}\left[\frac{\partial\bar{I}_5}{\partial\bar{\boldsymbol{C}}}\otimes\frac{\partial\bar{I}_5}{\partial\bar{\boldsymbol{C}}}\right] \\
&+ \bar{\Psi}_{45}\left[\boldsymbol{a}_1\otimes\boldsymbol{a}_1\otimes\frac{\partial\bar{I}_5}{\partial\bar{\boldsymbol{C}}} + \frac{\partial\bar{I}_5}{\partial\bar{\boldsymbol{C}}}\otimes\boldsymbol{a}_1\otimes\boldsymbol{a}_1\right] + \bar{\Psi}_5\,\frac{\partial^2\bar{I}_5}{\partial\bar{\boldsymbol{C}}\partial\bar{\boldsymbol{C}}} \\
&+ \left[\bar{\Psi}_{16} + \bar{I}_1\bar{\Psi}_{26}\right]\left[\boldsymbol{I}\otimes\boldsymbol{a}_2\otimes\boldsymbol{a}_2 + \boldsymbol{a}_2\otimes\boldsymbol{a}_2\otimes\boldsymbol{I}\right] \\
&- \bar{\Psi}_{26}\left[\bar{\boldsymbol{C}}\otimes\boldsymbol{a}_2\otimes\boldsymbol{a}_2 + \boldsymbol{a}_2\otimes\boldsymbol{a}_2\otimes\bar{\boldsymbol{C}}\right] \\
&+ \bar{\Psi}_{66}\,\boldsymbol{a}_2\otimes\boldsymbol{a}_2\otimes\boldsymbol{a}_2\otimes\boldsymbol{a}_2 + \left[\bar{\Psi}_{17} + \bar{I}_1\bar{\Psi}_{27}\right]\left[\boldsymbol{I}\otimes\frac{\partial\bar{I}_7}{\partial\bar{\boldsymbol{C}}} + \frac{\partial\bar{I}_7}{\partial\bar{\boldsymbol{C}}}\otimes\boldsymbol{I}\right] \\
&- \bar{\Psi}_{27}\left[\bar{\boldsymbol{C}}\otimes\frac{\partial\bar{I}_7}{\partial\bar{\boldsymbol{C}}} + \frac{\partial\bar{I}_7}{\partial\bar{\boldsymbol{C}}}\otimes\bar{\boldsymbol{C}}\right] + \bar{\Psi}_{77}\left[\frac{\partial\bar{I}_7}{\partial\bar{\boldsymbol{C}}}\otimes\frac{\partial\bar{I}_7}{\partial\bar{\boldsymbol{C}}}\right] \\
&+ \bar{\Psi}_{67}\left[\boldsymbol{a}_2\otimes\boldsymbol{a}_2\otimes\frac{\partial\bar{I}_7}{\partial\bar{\boldsymbol{C}}} + \frac{\partial\bar{I}_7}{\partial\bar{\boldsymbol{C}}}\otimes\boldsymbol{a}_2\otimes\boldsymbol{a}_2\right] + \bar{\Psi}_7\,\frac{\partial^2\bar{I}_7}{\partial\bar{\boldsymbol{C}}\partial\bar{\boldsymbol{C}}} \\
&+ \frac{1}{2}\Bigg[\bar{\Psi}_{81}\,\boldsymbol{I} + \bar{\Psi}_{82}\left[\bar{I}_1 - \bar{\boldsymbol{C}}\right] + \bar{\Psi}_{84}\,\boldsymbol{a}_1\otimes\boldsymbol{a}_1 + \bar{\Psi}_{85}\,\frac{\partial\bar{I}_5}{\partial\bar{\boldsymbol{C}}} \\
&+ \bar{\Psi}_{86}\,\boldsymbol{a}_2\otimes\boldsymbol{a}_2 + \bar{\Psi}_{87}\,\frac{\partial\bar{I}_7}{\partial\bar{\boldsymbol{C}}} + \frac{\bar{\Psi}_{88}}{2}\,\frac{\partial\bar{I}_8}{\partial\bar{\boldsymbol{C}}}\Bigg]\otimes\frac{\partial\bar{I}_8}{\partial\bar{\boldsymbol{C}}}\Bigg\},
\end{aligned}
\tag{A.91}
$$

for the present case. In order to calculate this tensor, the second derivative of $\bar{I}_5$ and $\bar{I}_7$ with respect to $\bar{\boldsymbol{C}}$, read

$$
\frac{\partial\bar{I}_5}{\partial\bar{C}_{AB}\bar{C}_{CD}} = \frac{1}{2}\big[a_{1A}\left[a_{1D}\delta_{CD} + a_{1C}\delta_{BD}\right] + a_{1B}\left[a_{1D}\delta_{AC} + a_{1C}\delta_{AD}\right]\big], \tag{A.92}
$$

$$
\frac{\partial\bar{I}_7}{\partial\bar{C}_{AB}\bar{C}_{CD}} = \frac{1}{2}\big[a_{2A}\left[a_{2D}\delta_{CD} + a_{2C}\delta_{BD}\right] + a_{2B}\left[a_{2D}\delta_{AC} + a_{2C}\delta_{AD}\right]\big], \tag{A.93}
$$

where δ_{IJ} is the Dirac delta function.

The spatial fictitious elasticity tensor is obtained from the application of (A.63) on (A.91).

Appendix B

Customize the commercial software ABAQUS by means of Python scripts

The ABAQUS scripting interface allows to customize ABAQUS to suit specific requirements by means of a Python script. A brief summary of Python programming language and the main advantages of using this object-oriented programming language combining with ABAQUS software are presented in this Appendix. Furthermore, the Phyton scripts developed to several specific task along this Thesis such as the creation of all the model geometries described in Chapters 2, 3 and 4 or the post-processing of the obtained results of the models simulated in Chapters 2, 3 and 4, are included.

Contents

B.1 Python programming language

Python is a general purpose high level programming language that combines an imperative object-oriented core with features from functional and scripting languages. It is intended to be expressive, easy to learn and to support writing clean and readable code. Since its creation in 1989, it has become widely used for web development and scripting as well as other tasks such as scientific computing and development of GUI (Graphical User Interface) applications. It is maintained as an open source community project guided by its creator Guido van Rossum (Van Rossum, 2011, see for more details).

The version of Python used in this thesis is Python 3.1.3, which was released on November 2010. It should also work for Python 3.0 and 3.1, since there have been no changes to the language that would break compatibility.

B.2 Customize ABAQUS software

ABAQUS software counts on tools that allow to modify and extend their capabilities to enable a wide range of users to generate more efficient ABAQUS solutions. There are many ways to customize ABAQUS products:

- User subroutines: Allow to change the way ABAQUS Standard and ABAQUS Explicit compute analysis results.
- Environment files: Allow to change various default settings.
- Kernel scripts: Allow to create new functions to perform modeling or postprocessing tasks.
- GUI scripts: Allow to create new graphical user interfaces.

The kernel scripts and the graphical user interface scripts can be created by using the open source language Python for scripting and customization. Python scripts allows to accomplish tasks in ABAQUS that would be time consuming or practically impossible in the GUI ABAQUS CAE (Complete Abaqus Environment). Using a script, several requirements such as repetitive tasks, vary parameters of a simulation as part of an optimization, parametric study or extract information from large output databases can be automated. Furthermore, user interfaces that customize the look and feel of ABAQUS can even be created.

The behavior of ABAQUS pre and post processing to suit the specific requirements can be customized. Thus, Python can be used for accessing ABAQUS results on the output database (.odb) file, for scripting with ABAQUS CAE and ABAQUS Viewer, and general, for accomplishing varied programming tasks. On this Thesis, scripts to modify the ABAQUS environment (.cae) and to access to the output database (.odb) files have been programmed.

B.3 Programmed Python code

In this Thesis, several scripts have been implemented in order to accomplish two kind of tasks. The tasks that the Python code performed are:

- Script Python to build the models: Each model described in Chapters 2, 3 and 4 have been created from an ABAQUS CAE file. This .cae file contained the geometry of a 3D coronary artery model with the boundary conditions defined,

the different materials and sections created and assigned. Thus, the script modifies the dimensions of each model in order to obtain the possible relevant anatomical diversity. To accomplish this goal, the geometrical parameter studied in each parametric study have been continuously varied. After that, the models are seeded and meshed by means of this script and, finally, the job is created in order to simulate it.

- Script Python to extract results: In total, counting all the models simulated in Chapters 2, 3 and 4, a considerable number of models have been computed, thereby it is impossible to carry out the post processing tasks manually. A script which extracts specific results from the output database file has been developed. Specifically, the script collects the maximum MPS from the .odb files.

B.3.1 Script Python to build the models

Below, the script code to build the geometry of the models is presented. The code corresponds to the 3D parametric study described in Chapter 2 and 4. For the rest of the parametric studies presented in Chapter 3 the same Python code but with small modifications has been used. These modifications are due to the different parameters considered in each parametric studies. However, the code structure, the commands and the tasks performed are similar.

Specifically, when this script code is running on the ABAQUS CAE interface, 625 models in 3D are built and the corresponding .inp files (input files) are created. The .inp file is named according the values of the geometrical parameters of the created geometry. Notice that depending of the boundary conditions included in the .cae file, the 625 models will correspond to the cases without residual stress included or with just axial residual stress considered or with circumferential and longitudinal residual stress included.

Additionally, others scripts based on C programming language were created to run each created model (.inp) by the Python script in our computer cluster, and after that, to rank the results in different folders to handle them. Each folder created is named equals to the .inp file and contains the corresponding files to this simulation.

```
# Header
  from abaqus import *
  from abaqusConstants import *
  import _main_
  def Parameter_variation():
    import section
    import regionToolset
    import displayGroupMdbToolset as dgm
    import part
    import material
```

```
import assembly
import step
import interaction
import load
import mesh
import job
import sketch
import visualization
import xyPlot
import displayGroupOdbToolset as dgo
import connectorBehavior
```

Variation of parameters: Lipid core length (l), lumen radius (r) and fibrous cap thickness (fc). The lipid core width range is presented below due to the value of this parameter depends to the lumen radius and the fibrous cap thickness values

```
lenght=[1,2,4,6,8]
radius=[0.7,0.8,0.85,0.9,1]
thickness=[0.025,0.05,0.1,0.15,0.25]
```

Beginning of "for" loops

```
for l in length:
 j=0
 for r in radius:
 j=j+1
 i=0
  for fc in thickness:
  i=i+1
  k=0
  b=2.15-r-fc
  w=[b*0.3,b*0.45,b*0.6,b*0.75,b*0.9]
   for w in width:
    k=k+1
```

Modification of the parameters value in the models, parts and sketches

```
modelname='Model'+'_'+str(l)
p = mdb.models[modelname].parts['Coronary']
s = p.features['Partition face-2'].sketch
mdb.models[modelname].ConstrainedSketch(name='_edit_', objectToCopy=s)
s2 = mdb.models[modelname].sketches['_edit_']
g, v, d, c = s2.geometry, s2.vertices, s2.dimensions, s2.constraints
s2.setPrimaryObject(option=SUPERIMPOSE)
```

```
p.projectReferencesOntoSketch(sketch=s2,
 upToFeature=p.features['Partition face-2'], filter=COPLANAR_EDGES)]
d[2].setValues(value=r, )
p = mdb.models[modelname].parts['Coronary']
p.features['Partition face-2'].setValues(sketch=s2)
del mdb.models[modelname].sketches['_edit_']
p = mdb.models[modelname].parts['Coronary']
p = mdb.models[modelname].parts['Coronary']
p.regenerate()
p = mdb.models[modelname].parts['Coronary']
s = p.features['Partition face-4'].sketch
mdb.models[modelname].ConstrainedSketch(name='_edit_', objectToCopy=s)
s1 = mdb.models[modelname].sketches['_edit_']
g, v, d, c = s1.geometry, s1.vertices, s1.dimensions, s1.constraints
s1.setPrimaryObject(option=SUPERIMPOSE)
p.projectReferencesOntoSketch(sketch=s1,
 upToFeature=p.features['Partition face-4'], filter=COPLANAR_EDGES)
d[2].setValues(value=fc, )
d[2].setValues(value=w, )
s1.unsetPrimaryObject()
p = mdb.models[modelname].parts['Coronary']
p.features['Partition face-4'].setValues(sketch=s1)
del mdb.models[modelname].sketches['_edit_']
p = mdb.models[modelname].parts['Coronary']
p.regenerate()
```

Mesh the model

```
session.viewports['Viewport: 1'].partDisplay.setValues(mesh=ON)
session.viewports['Viewport: 1'].partDisplay.meshOptions.setValues(
 meshTechnique=ON)
a = mdb.models[modelname].rootAssembly
session.viewports['Viewport: 1'].setValues(displayedObject=a)
a.regenerate()
a = mdb.models[modelname].rootAssembly
session.viewports['Viewport: 1'].assemblyDisplay.setValues(mesh=ON, loads=OFF,
 bcs=OFF, predefinedFields=OFF, connectors=OFF)
session.viewports['Viewport: 1'].assemblyDisplay.meshOptions.setValues(
 meshTechnique=ON)
a = mdb.models[modelname].rootAssembly
c1 = a.instances['Coronary-1'].cells
pickedRegions = c1.getSequenceFromMask(mask=('[#1ff ]', ), )
```

```
a.setMeshControls(regions=pickedRegions, elemShape=TET, technique=FREE)
elemType1 = mesh.ElemType(elemCode=C3D8R, elemLibrary=STANDARD)
elemType2 = mesh.ElemType(elemCode=C3D6, elemLibrary=STANDARD)
elemType3 = mesh.ElemType(elemCode=C3D4H, elemLibrary=STANDARD)
a = mdb.models[modelname].rootAssembly
c1 = a.instances['Coronary-1'].cells
cells1 = c1.getSequenceFromMask(mask=('[#1ff ]', ), )
pickedRegions =(cells1, )
a.setElementType(regions=pickedRegions, elemTypes=(elemType1, elemType2,
  elemType3))
a = mdb.models[modelname].rootAssembly
partInstances =(a.instances['Coronary-1'], )
a.generateMesh(regions=partInstances)
session.viewports['Viewport: 1'].assemblyDisplay.setValues(mesh=OFF)
session.viewports['Viewport: 1'].assemblyDisplay.meshOptions.setValues(
  meshTechnique=OFF)

# Create the job
        jobname='Case'+'_l_'+str(l)+'_r_'+str(j)+'_fc_'+str(i)+'_w_'+str(k)
        mdb.Job(contactPrint=OFF, description='', echoPrint=OFF,
          explicitPrecision=SINGLE, historyPrint=OFF,
          memory=50, memoryUnits=PERCENTAGE,
          model=modelname, modelPrint=OFF, multiprocessingMode=DEFAULT,
          name=jobname, nodalOutputPrecision=SINGLE, numCpus=4,
          numDomains=4,parallelizationMethodExplicit=DOMAIN, type=ANALYSIS)
        mdb.jobs[modelname].writeInput(consistencyChecking=OFF)

# End of "for" loops
```

B.3.2 Script Python to obtain results

Once, the result files of each model are ranked in different folders, the post processing process occurs by means of the following Python script. This script creates an ABAQUS report (.rpt) from the .odb file with the MPS field for each node sorted. After that, a code written in MATLAB is used to find the maximum MPS at the critical zones (fibrous cap and plaque shoulders) of each .rpt file.

```
# Header
  from abaqus import *
  from abaqusConstants import *
  import _main_
  def Obtain_MPS():
```

```
import section
import regionToolset
import displayGroupMdbToolset as dgm
import part
import material
import assembly
import step
import interaction
import load
import mesh
import job
import sketch
import visualization
import xyPlot
import displayGroupOdbToolset as dgo
import connectorBehavior

# Beginning of "for" loops. Necessary to open the different files
for l in length:
 j=0
 for r in radius:
 j=j+1
 i=0
  for fc in thickness:
  i=i+1
  k=0
  b=2.15-r-fc
  w=[b*0.3,b*0.45,b*0.6,b*0.75,b*0.9]
   for w in width:
    k=k+1

# Open each .odb file and extract the Maximal Principal Stress field
        jobname='Case'+'_l_'+str(l)+'_r_'+str(j)+'_fc_'+str(i)+'_w_'+str(k)
        root='/home/gemm/mcilla/'+jobname+'/'+jobname+'.odb'
        o1 = session.openOdb(name=root)
        session.viewports['Viewport: 1'].setValues(displayedObject=o1)
        odb = session.odbs[root]
        session.fieldReportOptions.setValues(printMinMax=OFF)
        session.writeFieldReport(fileName=jobname+'.rpt', append=ON,
         sortItem='Node Label', odb=odb, step=0, frame=1, outputPosition=NODAL,
         variable=(('S', INTEGRATION_POINT,
```

((INVARIANT, 'Max. Principal'),)),))

Bibliography

Abè, H., Hayashi, K., Sato, M., 1996. Data Book on Mechanical Properties of Living Cells, Tissues, and Organs. Springer-Verlag.

Agianniotis, A., Rachev, A., Stergiopulos, N., 2012a. Active axial stress in mouse aorta. Journal of Biomechanics 45 (11), 1924–1927.

Agianniotis, A., Stergiopulos, N., 2012b. Wall properties of the apolipoprotein E-deficient mouse aorta. Atherosclerosis 223 (2), 314–320.

Ai, L., Vafai, K., 2006. A coupling model for macromolecule transport in a stenosed arterial wall. International Journal of Heat and Mass Transfer 49, 1568–1591.

Alastrué, V., 2008. Some inelastic problems in the modelling of blood vessels. Applications to non-physiological states and vascular surgery. PhD thesis, University of Zaragoza.

Alastrué, V., Martínez, M. A., Doblaré, M., Menzel, A., 2009a. Anisotropic microsphere-based finite elasticity applied to blood vessel modelling. Journal of the Mechanics and Physics of Solids 57, 178–203.

Alastrué, V., Martínez, M. A., Menzel, A., Doblaré, M., 2009b. On the use of non-linear transformations for the evaluation of anisotropic rotationally symmetric directional integrals. Application to the stress analysis in fibred soft tissues. International Journal for Numerical Methods in Engineering 79 (4), 474–504.

Alastrué, V., Peña, E., Martínez, M. A., Doblaré, M., 2007b. Assessing the use of the "opening angle method" to enforce residual stresses in patient-specific arteries. Annals of Biomedical Engineering 35, 1821–1837.

Alastrué, V., Rodríguez, J. F., Calvo, B., Doblaré, M., 2007a. Structural damage models for fibrous biological soft tissues. International Journal of Solids and Structures 44, 5894–5911.

Allender, S., Scarborough, P., Peto, V., Rayner, M., 2008. European cardiovascular disease statistics 2008 edition. Health Economics.

Alpaydin, E., 2001. Introduction to Machine Learning. MIT Press.

Altman, R., 2003. Risk factors in coronary atherosclerosis athero-inflammation: The meeting point. Thrombosis Journal 1, 4.

Anderson, T. W., 1958. An introduction to multivariate statistical. New York. John Wiley.

Anthony, M., Barlett, P., 1999. Neural network learning: Theoretical foundations. Cambridge University Press.

Antkowiak, M., 2006. Artificial neural networks vs. support vector machines for skin diseases recognition. Master's Thesis in Computing Science, Umea University, Sweden.

Aoki, T., Ku, D. N., 1993. Collapse of diseased arteries with eccentric cross section. Journal of Biomechanics 26, 133–142.

Armentano, R., Megnien, J. L., Simon, A., Bellenfant, F., Barra, J., Levenson, J., 1995. Effects of hypertension on viscoelasticity of carotid and femoral arteries in humans. Hypertension 26, 48–54.

Armentano, R., Santana, D., Cabrera, E., Graf, S., Perez, H., German, Y. Z., Saldias, M. D. C., Alvarez, I., 2006. An *in vitro* study of cryopreserved and fresh human arteries: A comparison with ePTFE prostheses and human arteries studied non-invasively *in vivo*. Cryobiology 52, 17–26.

Arroyo, L. H., Lee, R. T., 1999. Mechanisms of plaque rupture: Mechanical and biologic interactions. Cardiovascular Research 41, 369–375.

Arruda, E. M., Boyce, M. C., 1993. A three-dimensional constitutive model for the large stretch behavior of rubber elastic materials. Journal of the Mechanics and Physics of Solids 41(2), 389–412.

Asakura, T., Karino, T., 1990. Flow patterns and spatial distribution of atherosclerotic lesions in human coronary arteries. Circulation Research 66 (4), 1045–1066.

Ashwini, S., Soundararajan, D. K., Hunter, W. J., Agrawal, D. K., 2003. Comparison of vascular smooth muscle cell apoptosis and fibrous cap morphology in symptomatic and asymptomatic carotid artery disease. Annals of Vascular surgery 17, 1–8.

Auer, M., Stollberger, R., Regitnig, P., Ebner, F., Holzapfel, G. A., 2006. 3-D reconstruction of tissue components for atherosclerotic human arteries using *ex vivo* high-resolution MRI. Medical Imaging 25, 345–357.

Balcells, M., Suarez, M. F., Vazquez, M., Edelman, E. R., 2005. Cells in fluidic environments are sensitive to flow frequency. Journal of Cellular Physiology 204, 329–335.

Baldewsing, R. A., de Korte, C. L., Schaar, J. A., Mastik, F., Van der Steen, A. F., 2004. Finite element modeling and intravascular ultrasound elastography of vulnerable plaques: Parameter variation. Ultrasonics 42, 723–729.

Ballyk, P. D., Walsh, C., Butany, J., Ojha, M., 1997. Compliance mismatch may promote graft-artery intimal hyperplasia by altering suture-line stresses. Journal of Biomechanics 31 (3), 229–237.

Balossino, R., Gervaso, F., Migliavacca, F., Dubini, G., 2008. Effects of different stent designs on local hemodynamics in stented arteries. Journal of Biomechanics 41, 1053–1061.

Bank, A. J., Versluis, A., Dodge, S. M., Douglas, W. H., 2000. Ahterosclerotic plaque rupture: A fatigue process? Medical Hypotheses 55, 480–484.

Barger, A. C., Beeuwkee, R., Lainey, L. L., Silverman, K. J., 1984. Hypothesis: Vasa vasorum and neovascularization of coronary arteries. A possible role in the pathophyiology of atherosclerosis. The New England Journal of Medicine 310, 175–177.

Batista, G., Monard, M. C., 2003. An analysis of four missing data treatment methods for supervised learning. Applied Artificial Intelligence 17, 519–533.

Bažant, P., Oh, B. H., 1986. Efficient numerical integration on the surface of a sphere. ZAMM - Journal of Applied Mathematics and Mechanics / Zeitschrift für Angewandte Mathematik und Mechanik 66, 37–49.

Beattie, D., Xu, C., Vito, R., Glagov, S., Whang, M. C., 1998. Mechanical analysis of heterogeneous, atherosclerotic human aorta. ASME Journal of Biomechanical Engineering 120, 602–607.

Berger, J. O., 1985. Statistical decision theory and bayesian analysis. Springer.

Berger, S. A., Jou, L. D., 2000. Flow in stenotic vessels. Annual Reviews of Fluid Mechanics 32, 347–382.

Bertolotti, C., Deplano, V., 2000. Three-dimensional numerical simulations of flow through a stenosed coronary bypass. Journal of Biomechanics 33, 1011–1022.

Bhatt, D. L., Topol, E. J., 2002. Need to test the arterial inflammation hypothesis. Circulation 106, 136–140.

Billiar, K. L., Sacks, M. S., 2000. Biaxial mechanical properties of the native and glutaraldehyde-treated aortic valve cusp: Part II - A structural constitutive model. ASME Journal of Biomechanical Engineering 122, 327–335.

Bishop, C. M., 1994. Neural networks and their applications. Review. Scientific Instruments 65, 1803–1832.

Bishop, C. M., 1995. Neural networks and pattern recognition. Oxford University Press.

Bluestein, D., Alemu, Y., Avrahami, I., Gharib, M., Dumont, K., Ricotta, J. J., Einav, S., 2008. Influence of microcalcifications on vulnerable plaque mechanics using FSI modelling. Journal of Biomechanics 41, 1111–1118.

Bobryshev, Y. V., 2006. Monocyte recruitment and foam cell formation in atherosclerosis. Micron 37, 208–222.

Bonetti, P. O., Lerman, L. O., Lerman, A., 2003. Endothelial dysfunction. A marker of atherosclerotic risk. Arteriosclerosis, Thrombosis, and Vascular Biology 23, 168–175.

Boser, B. E., Guyon, I. M., Vapnik, V. N., 1992. A training algorithm for optimal margin classifier. Proceedings of the fifth annual workshop on Computational learning theory 1, 144–152.

Bourdarias, C., Gerbi, S., Oddou, C., Ohayon, J., 2003. A three dimensional finite element method for a biological active soft tissue. ESAIM: Proceedings 12, 8–11.

Bousquet, G., Elissee, A., 2002. Stability and generalization. Journal of machine learning research 2, 499–526.

Bousquet, O., Elissee, A., 2001. Algorithmic stability and generalization performance. Advances in neural information processing systems. Editors: Leen T. K., Dietterich T. G. and Tresp V. MIT Press.

Bovendeerd, P., Borsje, P., Arts, T., Van de Vosse, F., 2006. Dependence of intramyocardial pressure and coronary flow on ventricular loading and contractility: A model study. Annals of Biomedical Engineering 34 (12), 1833–1845.

Breslow, J. L., 1993. Transgenic mouse models of lipoprotein metabolism and atherosclerosis. Proceedings of the National Academy of Sciences 90 (18), 8314–8318.

Briley-Saebo, K. C., Mulder, W. J. M., Mani, V., Hyafil, F., Amirbekian, V., Aguinaldo, J. G. S., Fisher, E. A., Fayad, Z. A., 2007. Magnetic resonance imaging of vulnerable atherosclerotic plaques: Current imaging strategies and molecular imaging probes. Journal of Magnetic Resonance Imaging 26, 460–479.

Broisat, A., Toczek, J., Mesnier, N., Tracqui, P., Ghezzi, C., Ohayon, J., Riou, L. M., 2011. Assessing low levels of mechanical stress in aortic atherosclerotic lesions from apolipoprotein E -/- mice - Brief report. Arteriosclerosis, Thrombosis, and Vascular Biology 31, 1007–1010.

Brown, M. P., Grundy, W. N., Lin, D., Cristianini, N., Sugnet, C. W., Furey, T. S., Ares, M., Haussler, D., 2000. Knowledge-based analysis of microarray gene expression data by using Support Vector Machines. Proceedings of the National Academy of Sciences 97 (1), 262–267.

Budu-Grajdeanu, P., Schugart, R. C., Friedman, A., Valentine, C., Agarwal, A. K., Rovin, B. H., 2008. A mathematical model of venous neointimal hyperplasia formation. Theoretical Biology and Medical Modelling 1, 5–2.

Buja, L. M., Kita, T., Goldstein, J. L., Watanabe, Y., Brown, M. S., 1983. Cellular pathology of progressive atherosclerosis in the WHHL rabbit. An animal model of familial hypercholesterolemia. Arteriosclerosis, Thrombosis, and Vascular Biology 3 (1), 87–101.

Bulelzai, M. A. K., Dubbeldam, J. L. A., 2012. Long time evolution of atherosclerotic plaques. Journal of Theoretical Biology 297, 1–10.

Bulter, S. L., Kohles, S. S., Thielke, R. J., Chen, C., Vanderby, R., 1997. Interstitial fluid flow in tendons or ligaments: A porous medium finite element simulation. Medical & Biological Engineering & Computing 35, 742–746.

Burges, C. J. C., 1998. A tutorial on Support Vector Machines for pattern recognition. Data Mining and Knowledge Discovery 2 (2), 121–167.

Burke, A. P., Farb, A., Malcom, G. T., Liang, Y.-h., Smialek, J., Virmani, R., 1997. Coronary risk factors and plaque morphology in men with coronary disease who died suddenly. New England Journal of Medicine 336 (18), 1276–1282.

Cabrera Fischer, E. I., Bia, D., Camus, J. M., Zacalo, Y., De Forteza, E., Armentano, R. L., 2006. Adventitia-dependent mechanical properties of brachiocephalic ovine arteries in *in vivo* and *in vitro* studies. Acta Physiologica 188 (2), 103–111.

Calvez, V., Ebde, A., Meunier, N., Raoult, A., 2009. Mathematical modelling of the atherosclerotic plaque formation. ESAIM: Proceedings 28, 1–12.

Calvez, V., Houot, J. G., Meunier, N., Raoult, A., Rusnakova, G., 2010. Mathematical and numerical modeling of early atherosclerotic lesions. ESAIM: Proceedings 30, 1–14.

Cancel, L., Fitting, A., Tarbell, J. M., 2007. *In vitro* study of LDL transport under pressurized (convective) conditions. American Journal of Physiology - Heart and Circulatory Physiology 293, 126–132.

Caner, F. C., Carol, I., 2006. Microplane constitutive model and computational framework for blood vessel tissue. ASME Journal of Biomechanical Engineering 128 (3), 419–427.

Cannon, G. J., Swanson, J. A., 1992. The macrophage capacity for phagocytosis. Journal of Cell Science 101, 907–913.

Carbonell, J., 1983. Learning by analogy in machine learning: An artificial intelligence approach. Michalski, R. and Carbonell, J. (editors). San Francisco: Morgan Kaufmann.

Carboni, M., Desch, G. W., Weizsacker, H. W., 2007. Passive mechanical properties of porcine left circumflex artery and its mathematical description. Medical Engineering & Physics 29 (1), 8–16.

Cardamone, L., Valentín, A., Eberth, J. F., Humphrey, J. D., 2009. Origin of axial prestretch and residual stress in arteries. Biomechanics and Modeling in Mechanobiology 8 (6), 431–446.

Carew, T. E., Vaishnav, R. N., Patel, D. J., 1968. Compressibility of the arterial wall. Circulation Research 23, 61–86.

Carmeliet, P., Moons, L., Lijnen, R., Baes, M., Lemaitre, V., Tipping, P., Drew, A., Eeckhout, Y., Shapiro, S., Lupu, F., Collen, D., Dec. 1997. Urokinase-generated plasmin activates matrix metalloproteinases during aneurysm formation. Nature Genetics 17 (4), 439–444.

Carmines, D. V., McElhaney, J. H., Stack, R., 1991. A piece-wise nonlinear elastic stress expression of human and pig coronary-arteries tested *in vitro*. Journal of Biomechanics 24(10), 899–906.

Caro, C. G., Fitz-Gerald, J. M., Schroter, R. C., 1971. Atheroma and arterial wall shear. Observation and proposal of a shear dependent mass transfer mechanism for atherogenesis. Proceedings of the Royal Society B: Biological Sciences 177 (1046), 109–159.

Caro, C. G., Pedley, T. J., Schroter, R. C., Seed, W. A., 1978. The mechanics of the circulation. Oxford University Press, Oxford.

Carol, I., Jirásek, M., Bažant, Z. P., 2004. A framework for microplane models at large strain, with application to hyperelasticity. International Journal of Solids And Structures 41 (2), 511–557.

Chatzizisis, Y. S., Coskun, A. U., Jonas, M., Edelman, E. R., Feldman, C. L., Stone, P. H., 2007. Role of endothelial shear stress in the natural history of coronary atherosclerosis and vascular remodeling. Journal of the American College of Cardiology 49 (25), 2379–2393.

Chau, A. H., Chan, R. C., Shishkov, M., MacNeill, B., Iftimia, N., Tearney, G. J., Kamm, R. D., Bouma, B. E., Kaazempur-Mofrad, M. R., 2004. Mechanical analysis of

atherosclerotic plaques based on optical coherence tomography. Annals of Biomedical Engineering 32, 1494–1503.

Cheng, G. C., Loree, H. M., Kamm, R. D., Fishbein, M. C., Lee, R. T., 1993. Distribution of circumferential stress in ruptured and stable atherosclerotic lesions. A structural analysis with histopathological correlation. Circulation 87, 1179–1187.

Cheung, N., 2001. Machine Learning Techniques for medical analysis. School of Information Technology and Electrical Engineering. University of Queensland.

Chiastra, C., Morlacchi, S., Pereira, S., Dubini, G., Migliavacca, F., 2012. Computational fluid dynamics of stented coronary bifurcations studied with a hybrid discretization method. European Journal of Mechanics B/Fluids (2012) 35, 76–84.

Chien, S., 2003. Molecular and mechanical bases of focal lipid accumulation in arterial wall. Progress in Biophysics and Molecular Biology 83, 131–151.

Chien, S., 2008. Effects of disturbed flow on endothelial cells. Annals of Biomedical Engineering 36 (4), 554–562.

Chiu, J.-J., Chien, S., 2011. Effects of disturbed flow on vascular endothelium: Pathophysiological basis and clinical perspectives. Physiological Reviews 91, 327–387.

Chiu, J. J., Wang, D. L., Chien, S., Skalak, R., Usami, S., 1998. Effects of disturbed flow on endothelial cells. ASME Journal of Biomechanical Engineering 120, 2–8.

Chun, Y., Dalin, T., Satya, A., 2010. Three-dimensional carotid plaque progression simulation using meshless generalized finite difference method based on multi-year MRI patient-tracking data. Computer Modeling in Engineering & Sciences 57, 51–76.

Chung, S., Vafai, K., 2012. Low-density lipoprotein transport within a multi-layered arterial wall-effect of the atherosclerotic plaque/stenosis. Journal of Biomechanics doi:10.1016/j.jbiomech.2012.09.022.

Chuong, C. J., Fung, Y. C., 1984. Compressibility and constitutive equation of arterial wall in radial compression experiments. Journal of Biomechanics 17 (1), 35–40.

Chuong, C. J., Fung, Y. C., 1986. On residual stress in arteries. ASME Journal of Biomechanical Engineering 108, 189–192.

Ciarlet, P. G., 1988. Mathematical elasticity. Volume I: Three-dimensional elasticity. Vol. 6. North-Hollad.

Cilla, M., Peña, E., Martínez, M. A., 2012a. 3D computational parametric analysis of eccentric atheroma plaque. Influence of axial residual stresses. Biomechanics and Modeling in Mechanobiology 11 (7), 1001–1013.

Ciofalo, M., Collins, M. W., Hennessy, T. R., 1998. Nanoscale fluid dynamics in physiological processes: A review study. Boston: WIT Press.

Clark, J. M., Glagov, S., 1985. Transmural organization of the arterial media. The lamellar unit revisited. Artheriosclerosis 5 (1), 19–34.

Cobbold, C. A., Sherratt, J. A., Maxwell, S. J. R., 2002. Lipoprotein oxidation and its significance for atherosclerosis: A mathematical approach. Bulletin of Mathematical Biology 64, 65–95.

Coleman, R., Hayek, T., Keidar, S., Aviram, M., 2006. A mouse model for human atherosclerosis: Long-term histopathological study of lesion development in the aortic arch of apolipoprotein E-deficient (E0) mice. Acta Histochemica 108 (6), 415–424.

Collins, M. J., Bersi, M., Wilson, E., Humphrey, J. D., 2011. Mechanical properties of suprarenal and infrarenal abdominal aorta: Implications for mouse models of aneurysms. Medical Engineering & Physics 33 (10), 1262–1269.

Cook, M. J., 1965. The anatomy of the mouse. Academic Press, New York.

Cortes, C., Vapnik, V. N., 1995. Support vector networks. Machine Learning 20 (3), 273–297.

Corti, R., Farkouh, M. E., Badimon, J. J., 2002. The vulnerable plaque and acute coronary syndromes. American Journal of Medicine 113, 668–680.

Cosman, P. C., Oehler, K. L., Riskin, E. A., Gray, R. M., 1993. Using vector quantization for image processing. Proceedings of the IEEE 81, 1326–1341.

Cox, M. A. J., Driessen, N. J. B., Boerboom, R. A., Bouten, C. V. C., Baaijens, F. P. T., 2008. Mechanical characterization of anisotropic planar biological soft tissues using finite indentation: Experimental feasibility. Journal of Biomechanics 41 (2), 422–429.

Cox, M. A. J., Driessen, N. J. B., Bouten, C. V. C., Baaijens, F. P. T., 2006. Mechanical characterization of anisotropic planar biological soft tissues using large indentation: A computational feasibility study. ASME Journal of Biomechanical Engineering 128 (3), 428–436.

Cox, R. H., 1978. Passive mechanics and connective tissue composition of canine arteries. American Journal of Physiology - Heart and Circulatory Physiology 234 (5), 533–541.

Creane, A., Maher, E., Sultan, S., Hynes, N., Kelly, D. J., Lally, C., 2010. Finite element modelling of diseased carotid bifurcations generated from *in vivo* computerised tomographic angiography. Computers in Biology and Medicine 40, 419–429.

Curry, F. E., 1974. Hydrodynamic description of osmotic reflection coefficient with application to pore theory of transcapillary exchange. Microvascular Research 8, 236–252.

Curry, F. E., 1984. Mechanics and thermodynamics of transcapillary exchange. Handbook of physiology. The Cardiovascular System. Microcirculation. American Physiological Society, Bethesda, MD.

Dabagh, M., Jalali, P., Tarbell, J. M., 2009. The transport of LDL across the deformable arterial wall: The effect of endothelial cell turnover and intimal deformation under hypertension. American Journal of Physiology - Heart and Circulatory Physiology 297 (3), 983–996.

Daugherty, A., 2002. Mouse models of atherosclerosis. American Journal of the Medical Sciences 323 (1), 3–10.

Daughtery, A., Cassis, L. A., 2004. Mouse models of abdominal aortic aneurysms. Arteriosclerosis, Thrombosis, and Vascular Biology 24, 429–434.

Davies, J. E., Whinnett, Z. I., Francis, D. P., Manisty, C. H., Aguado-Sierra, J., Willson, K., Foale, R. A., Malik, I. S., Hughes, A. D., Parker, K. H., Mayet, J., 2006. Evidence of a dominant backward-propagating suction wave responsible for diastolic coronary filling in humans, attenuated in left ventricular hypertrophy. Circulation 113 (14), 1768–1778.

Davies, M. J., 1996. Stability and instability: Two faces of coronary atherosclerosis: The Paul Dudley White lecture 1995. Circulation 94, 2013–2020.

Davies, M. J., 2000. The pathophysiology of acute coronary syndromes. Heart 83, 361–366.

Davies, M. J., Richardson, P. D., Woolf, N., Katz, D. R., Mann, J., 1993. Risk of thrombosis in human atherosclerotic plaques: Role of extracellular lipid, macrophage, and smooth muscle cell content. British Heart Journal 69, 377–381.

Davies, M. J., Woolf, N., Rowles, P. M., Pepper, J., 1988. Morphology of the endothelium over atherosclerotic plaques in human coronary arteries. British Heart Journal 60 (6), 459–464.

Davignon, J., Ganz, P., 2004. Role of endothelial dysfunction in atherosclerosis. Circulation 109 (23), 27–32.

Davis, E. C., 1995. Elastic lamina growth in the developing mouse aorta. Journal of Histochemistry & Cytochemistry 43 (11), 1115–1123.

Delfino, A., Moore, J. E., Jr. Meister, J., 1994. Lateral deformation and movement effects on flow through distensible tube models of blood vessels. Biorheology 31, 533–547.

Demiray, H., 1972. A note on the elasticity of soft biological tissues. Journal of Biomechanics 5, 309–311.

Demiray, H., Vito, R. P., 1991. A layered cylindrical shell model for an aorta. International Journal of Engineering Science 29 (1), 47–54.

Demiray, H., Weizsacker, H. W., Pascale, K., Erbay, H., 1988. A stress-strain relation for a rat abdominal aorta. Journal of Biomechanics 21, 369–374.

Di Lullo, G. A., Sweeney, S. M., Körkkö, J., Ala-Kokko, L., San Antonio, J. D., 2002. Mapping the ligand-binding sites and disease-associated mutations on the most abundant protein in the human. Type I Collagen. The Journal of Biological Chemistry 277 (6), 4223–4231.

Di Tomaso, G., Diaz-Zuccarini, V., Pichardo-Almarza, C., 2011. A multiscale model of atherosclerotic plaque formation at its early stage. IEEE Transactions on Biomedical Engineering 58, 3460–3463.

Dimmeler, S., Hermann, C., Galle, J., Zeiher, A. M., 1999. Upregulation of superoxide dismutase and nitric oxide synthase mediates the apoptosis-suppressive effects of shear stress on endothelial cells. Arteriosclerosis, Thrombosis, and Vascular Biology 19 (3), 656–664.

Dobrin, P. B., Rovick, A. A., 1969. Influence of vascular smooth muscle on contractile mechanics and elasticity of arteries. American Journal of Physiology – Legacy Content 217 (6), 1644–1651.

Dodge, J. T., Brown, B. G., Bolson, E. L., Dodge, H. T., 1992. Lumen diameter of normal human coronary arteries influence of age, sex, anatomic variation, and left ventricular hypertrophy or dilation. Circulation 86, 232–246.

Doetschman, T., Gregg, R. G., Maeda, N., Hooper, M. L., Melton, D. W., Thompson, S., Smithies, O., 1987. Targetted correction of a mutant HPRT gene in mouse embryonic stem cells. Nature 330, 576–578.

Douglas, A. F., Christopher, S., Amankulor, N., Din, R., Poullis, M., Amin-Hanjani, S., Ghogawala, Z., 2011. Extracranial carotid plaque length and parent vessel diameter significantly affect baseline ipsilateral intracranial blood flow. Neurosurgery 69, 114–121.

Driessen, N. J., Bouten, C. V., Baaijens, F. P., 2005. Improved prediction of the collagen fiber architecture in the aortic heart valve. ASME Journal of Biomechanical Engineering 127 (2), 329–336.

Drobnik, J., Dabrowski, R., Szczepanowska, A., Giernat, L., Lorenc, J., 2000. Response of aorta connective tissue matrix to injury caused by vasopressin-induced hypertension or hypercholesterolemia. Journal of Physiology and Pharmacology 51, 521–533.

Drucker, H., Burges, C., Kaufman, L., Smola, A., Vapnik, V., 1997. Support Vector regression Machines. MIT Press.

Dunmore, B. J., McCarthy, M. J., 2007. Ischemic symptoms are linked to immaturity of microvessels within plaques. Journal of Vascular surgery 45 (1), 115–159.

Dye, W. W., Gleason, R. L., Wilson, E., Humphrey, J. D., 2007. Altered biomechanical properties of carotid arteries in two mouse models of muscular dystrophy. Journal of Applied Physiology 103, 664–672.

Eberth, J. F., Cardamone, L., Humphrey, J. D., 2011. Evolving biaxial mechanical properties of mouse carotid arteries in hypertension. Journal of Biomechanics 44 (14), 2532–2537.

Efron, B., Tibshirani, R., 1997. Improvements on cross-validation: The 632+ bootstrap method. Journal of the American Statistical Association 92, 548–560.

El Khatib, N., Genieys, S., Kazmierczak, B., Volpert, V., 2009. Mathematical modelling of atherosclerosis as an inflammatory disease. Philosophical Transactions of the Royal Society A: Mathematical, Physical and Engineering Sciences 367 (1908), 4877–4886.

El Khatib, N., Genieys, S., Volpert, V., 2007. Atherosclerosis initiation modeled as an inflammatory process. Mathematical Modelling of Natural Phenomena 2, 126–141.

Eriksson, E. E., Xie, X., Werr, J., Thoren, P., Lindbom, L., 2001. Importance of primary capture and l-selectin-dependent secondary capture in leukocyte accumulation in inflammation and atherosclerosis *in vivo*. The Journal of Experimental Medicine 194 (2), 205–218.

Eriksson, J., Gulliksson, M., Lindström, P., Wedin, P. A., 1998. Regularization tools for training large feed-forward neural networks using automatic differentation. Optimization Methods and Software 10, 49–69.

Esterbauer, H., Striegl, G., Puhl, H., Rotheneder, M., 1989. Continuous monitoring of *in vitro* oxidation of human low density lipoprotein. Free radical research communications 6 (1), 67–75.

Ethier, C. R., 2002. Computational modeling of mass transfer and links to atherosclerosis. Annals of Biomedical Engineering 30, 461–471.

Evans, B., Fisher, D., 1992. Process delay analyses using decision-tree induction. Technical report CS92-06, Department of Computer Science, Vanderbilt University, Nashville, Tennessee.

Faggiotto, A., Ross, R., Harker, L., 1984. Studies of hypercholesterolemia in the nonhuman primate. I - Changes that lead to fatty streak formation. Arteriosclerosis, Thrombosis, and Vascular Biology 4 (4), 323–340.

Falk, E., 1989. Morphologic features of unstable atherothrombotic plaques underlying acute coronary syndromes. The American Journal of Cardiology 63 (10), E114–E120.

Falk, E., 1992. Why do plaques rupture? Circulation 86, 30–42.

Falk, E., Shah, P. K., Fuster, V., 1995. Coronary plaque disruption. Circulation 92 (3), 657–671.

Fayad, Z. A., Fuster, V., 2001. Clinical imaging of the high-risk or vulnerable atherosclerotic plaque. Circulation Research 89, 305–316.

Fayyad, U. M., Weir, N., Djorgovski, S., 1993. A machine learning system for automated cataloging of large scale sky surveys. Proceedings of the Tenth International Conference on Machine Learning and Applications. 1, 112–119.

Fei, D. Y., Thomas, J. D., Rittgers, S. E., 1994. The effect of angle and flow rate upon hemodynamics in distal graft anastomoses: A numerical model study. ASME Journal of Biomechanical Engineering 116, 331–336.

Figueroa, A., Vignon-Clementel, I., Jansen, K., Hughes, T., Taylor, C., 2006. A coupled momentum method for modeling blood flow in three-dimensional deformable arteries. Computer Methods in Applied Mechanics and Engineering 195, 5685–5706.

Finet, G., Ohayon, J., Rioufol, G., 2004. Biomechanical interaction between cap thickness, lipid core composition and blood pressure in vulnerable coronary plaque: Impact on stability or instability. Coronary Artery Disease 15, 13–20.

Finlay, H. M., Whittaker, P., Canham, P. B., 1998. Collagen organization in the branching region of human brain arteries. Stroke 29 (8), 1595–1601.

Finn, A. V., Nakano, M., Narula, J., Kolodgie, F. D., Virmani, R., 2010. Concept of vulnerable/unstable plaque. Arteriosclerosis, Thrombosis, and Vascular Biology 30 (7), 1282–1292.

Fisher, R. A., 1925. Statistical methods for research worker. Macmillan Pub Co.

Flory, P. J., 1961. Thermodynamic relations for high elastic materials. Transactions of the Faraday Society 57, 829–838.

Fok, P. W., 2012. Mathematical model of intimal thickening in atherosclerosis: Vessel stenosis as a free boundary problem. Journal of Theoretical Biology 314, 23–33.

Franklin, K. J., 1928. The physiology and pharmacology of veins. Physiological Reviews 8, 346–364.

Fridez, P., Zulliger, M., Bobard, F., Montorzi, G., Miyazaki, H., Hayashi, K., Stergiopulos, N., 2003. Geometrical, functional, and histomorphometric adaptation of rat carotid artery in induced hypertension. Journal of Biomechanics 36 (5), 671–680.

Friedrich, G. J., Moes, N. Y., Mühlberger, V. A., Gabl, C., Mikuz, G.and Hausmann, D., Fitzgerald, P. J., Yock, P. G., 1994. Detection of intralesional calcium by intracoronary ultrasound depends on the histologic pattern. American Journal of Physiology - Heart 128, 435–441.

Frigui, H., Krishnapuram, R., 1998. A robust competitive clustering algorithm with applications in computer vision. IEEE Transactions on Pattern Analysis and Machine Intelligence 21, 450–465.

Fruchart, J. C., Nierman, M. C., Stroes, E. S. G., Kastelein, J. J. P., Duriez, P., 2004. New risk factors for atherosclerosis and patient risk assessment. Circulation 109 (23), supplement 1, 15–19.

Fry, D. L., 1985. Mathematical models of arterial transmural transport. American Journal of Physiology 248, 240–263.

Fry, D. L., 1987. Mass transport, atherogenesis and risk. Arteriosclerosis 7, 88–100.

Fujii, K., Carlier, S. G., Mintz, G. S., Wijns, W., Colombo, A., Böse, D., Erbel, R., de Ribamar Costa, J., Jr, Kimura, M., Sano, K., Costa, R. A., Lui, J., Stone, G. W., Moses, J. W., Leon, M. B., 2005. Association of plaque characterization by intravascular ultrasound virtual histology and arterial remodeling. The American Journal of Cardiology 96, 1476–1483.

Fung, Y. C., 1990. Biomechanics. Mechanical properties of living tissues. Springer-Verlag.

Fung, Y. C., Fronek, K., Patitucci, P., 1979. Pseudoelasticity of arteries and the choice of its mathematical expression. American Journal of Physiology 237, 620–631.

Fung, Y. C., Liu, S. Q., 1991. Changes of zero-stress state of rat pulmonary arteries in hypoxic hypertension. Journal of Applied Physiology 70, 2455–2470.

Fung, Y. C., Liu, S. Q., 1992. Strain distribution in small blood vessels with zero-stress state taken into consideration. American Journal of Physiology - Heart and Circulatory Physiology 262 (2), 544–552.

Fuster, V., 2002. Assessing and modifying the vulnerable atherosclerotic plaque. John Wiley & Sons.

Fuster, V., Fayad, Z. A., Moreno, P. R., Poon, M., Corti, R., Badimon, J. J., 2005. Atherothrombosis and high-risk plaque. Part II: Approaches by noninvasive computed tomographic/magnetic resonance imaging. Journal of the American College of Cardiology 46, 1209–1218.

Fuster, V., Kelly, B. B., 2010. Promoting cardiovascular health in the developing world: A critical challenge to achieve global health. Committee on preventing the global

epidemic of cardiovascular disease: Meeting the challenges in developing countries; Institute of medicine. Washington, D.C: National Academies Press.

Gao, H., Long, Q., 2008. Effects of varied lipid core volume and fibrous cap thickness on stress distribution in carotid arterial plaques. Journal of Biomechanics 41, 3053–3059.

García, A., Peña, E., Laborda, A., Lostalé, F., De Gregorio, M. A., Doblaré, M., Martínez, M. A., 2011. Experimental study and constitutive modelling of the passive mechanical properties of the porcine carotid artery and its relation to histological analysis. Implications in animal cardiovascular device trials. Medical Engineering & Physics 33, 665–676.

Gasser, T. C., 2001. Physical an numerical modelling of balloon angioplasty. PhD thesis, Graz University of Technology.

Gasser, T. C., Holzapfel, G. A., 2002. A rate-independent elastoplastic constitutive model for (biological) fiber-reinforced composites at finite strains: Continuum basis, algorithmic and finite element implementation. Computational Mechanics 29, 340–360.

Gasser, T. C., Ogden, R. W., Holzapfel, G. A., 2006. Hyperelastic modelling of arterial layers with distributed collagen fibre orientations. Journal of The Royal Society of Interface 3, 15–35.

Gaziano, T., Gaziano, J. M., 2009. Global burden of cardiovascular disease, in heart disease: A textbook of cardiovascular medicine. 9th edition, E Braunwald (editors). Philadelphia, Elsevier Saunders.

Gefen, A., 2012. Patient-specific modeling in tomorrow's medicine. Series: Studies in mechanobiology, tissue engineering and biomaterials, Volume 9. Springer.

Gerrity, R. G., 1981. The role of the monocyte in atherogenesis. I- Transition of blood-borne monocytes into foam cells in fatty lesions. American Journal of Pathology 103, 181–190.

Gertz, S. D., Roberts, W. C., 1990. Hemodynamic shear force in rupture of coronary arterial atherosclerotic plaques. The American Journal of Cardiology 66, 1368–1372.

Gessaghi, V. C., Raschi, M. A., Tanoni, D. Y., Perazzo, C. A., Larreteguy, A. E., 2011. Growth model for cholesterol accumulation in the wall of a simplified 3D geometry of the carotid bifurcation. Computer Methods in Applied Mechanics and Engineering 200, 2117–2125.

Getz, S. D., Roberts, W. C., 1990. Hemodynamic shear force in rupture of coronary arterial atherosclerotic plaques. American Journal of Cardiology 66, 1368–1372.

Giannoglou, G., Soulis, J., Fermakis, T., Zioupos, G., Giannakoulas, G., Louridas, G., 2002. Wall shear stress differences between proximal and distal left coronary artery bifurcations. Abstract of European Heart Journal 1, 686.

Giannoglou, G., Soulis, J., Fermakis, T. M., Fermakis, D., Louridas, G., 1986. Haemodynamic factors and the important role of local low static pressure in coronary wall thickening. International Journal of Cardiology 2002 (1), 27–40.

Gijsen, F., Wentzel, J., Thury, A., Lamers, B., Schuurbiers, J., Serruys, P., der Steen, A. V., 2006. A new imaging technique to study 3-D plaque and shear stress distribution in human coronary artery bifurcations *in vivo*. Journal of Biomechanics 40, 2349–2357.

Gijsen, F. J. H., Wentzel, J. J., Thury, A., Mastik, F., Schaar, J. A., Schuurbiers, J. C. H., Slager, C. J., Van der Giessen, W. J., de Feyter, P. J., Van der Steen, A. F. W., Serruys, P. W., 2008. Strain distribution over plaques in human coronary arteries relates to shear stress. American Journal of Physiology - Heart and Circulatory Physiology 295 (4), 1608–1614.

Gill, P., Murray, W., Wright, M., 1981. Practical Optimization. London, Academic Press.

Glagov, S., Weisenberg, E., Zarins, C. K., Stankunavicius, R., Kolettis, G. J., 1987. Compensatory enlargement of human atherosclerotic coronary arteries. New England Journal of Medicine 316, 1371–1375.

Gleason, R. L., Wilson, E., Humphrey, J. D., 2007. Biaxial biomechanical adaptations of mouse carotid arteries cultured at altered axial extension. Journal of Biomechanics 40 (4), 766–776.

Glowinska, B., Urban, M., Koput, A., Galar, M., 2003. New atherosclerosis risk factors in obese, hypertensive and diabetic children and adolescents. Atherosclerosis 167 (2), 275–286.

Gluck, M., Rumelhart, D., 1989. Neuroscience and connectionist theory. The developments in connectionist theory. Hillsdale, N. J.: Erlbaum Associates.

Gniadecka, M., Alshede, P. P., Sigurdsson, S., Wessel, S., 2004. Melanoma diagnosis by Raman spectroscopy and neural networks: Structure alterations in proteins and lipids in intact cancer tissue. Journal of Investigative Dermatology 122, 443–449.

Goergen, C. J., Azuma, J., Barr, K. N., Magdefessel, L., Kallop, D. Y., Gogineni, A., 2011. Influences of aortic motion and curvature on vessel expansion in murine experimental aneurysms. Arteriosclerosis, Thrombosis, and Vascular Biology 31, 270–279.

Goldstein, J. L., Brown, M. S., 1977. The low-density lipoprotein pathway and its relation to atherosclerosis. Annual Review of Biochemistry 46, 897–930.

Gori, F., Boghi, A., 2011. Three-dimensional numerical simulation of blood flow in two coronary stents. Numerical Heat Transfer, Part A: Applications: An International Journal of Computation and Methodology 59 (4), 231–246.

Goubergrits, L., Wellnhofer, E., Kertzscher, U., Affeld, K., Petz, C., Hege, C., 2007. Coronary artery wss profiling using a geometry reconstruction based on biplane angiography. Annals of Biomedical Engineering 37 (4), 682–691.

Gow, B., Hadfield, C., 1979. The elasticity of canine and human coronary arteries with reference to postmortem changes. Circulation Research 45 (5), 588–594.

Gradus-Pizlo, I., Bigelow, B., Mahomed, Y., Sawada, S. G., Rieger, K., Feigenbaum, H., 2003. Left anterior descending coronary artery wall thickness measured by high-frequency transthoracic and epicardial echocardiography includes adventitia. American Journal of Cardiology 91, 27–32.

Green, J. F., 1982. Fundamental cardiovascular and pulmonary physiology. An integrated approach for medicine. Philadelphia: LEA and FEBIGER.

Greenwald, S. E., Moore, J. E. J., Rachev, A., Kane, T., Meister, J. J., 1997. Experimental investigation of the distribution of residual strains in the artery wall. ASME Journal of Biomechanical Engineering 119 (4), 438–444.

Grieder, E. B., Strandberg, J. D., 2003. The contribution of laboratory animals to medical progress-past, present, and future. In Handbook of laboratory animal science, 2nd edition. CRC Press, Boca Raton, FL.

Groen, H. C., Gijsen, F. J., Van Der Lugt, A., Ferguson, M. S., hatsukami, T. S., Van Der Steen, A. F., Yuan, C., Wentzel, J. J., 2007. Plaque rupture in the carotid artery is localized at the high shear stress region: A case report. Stroke 38 (8), 2379–2381.

Groen, H. C., Gijsen, F. J., Van Der Lugt, A., Ferguson, M. S., hatsukami, T. S., Van Der Steen, A. F., Yuan, C., Wentzel, J. J., 2008. High shear stress influences plaque vulnerability. Netherlands heart journal 16 (7), 280–283.

Grundy, S. M., 2002. Obesity, metabolic syndrome, and coronary atherosclerosis. Circulation 105, 2696–2698.

Guarino, A. J., Tulenko, T. N., Wrenn, S. P., 2006. Sphingomyelinase-to-LDL molar ratio determines low density lipoprotein aggregation size: Biological significance. Chemistry and Physics of Lipids 142, 33 – 42.

Guo, X., Kassab, G. S., 2003. Variation of mechanical properties along the length of the aorta in C57BL/6 mice. American Journal of Physiology - Heart and Circulatory Physiology 285 (6), 2614–2622.

Guo, X., Kassab, G. S., 2004. Distribution of stress and strain along the porcine aorta and coronary arterial tree. American Journal of Physiology - Heart and Circulatory Physiology 286 (6), 2361–2368.

Gurney, K., 1997. An introduction to neural networks. London: Routledge.

Hallow, K. M., Taylor, W. R., Rachev, A., Vito, R. P., 2009. Markers of inflammation collocate with increased wall stress in human coronary arterial plaque. Biomechanics and modeling in mechanobiology 1, 1–14.

Hamlin, R. L., Altschuld, R. A., 2001. Extrapolation from mouse to man. Circulation: Cardiovascular Imaging. 4, 2–4.

Han, H. C., Fung, Y. C., 1991. Species dependence of the zero-stress state of aorta-pig versus rat. ASME Journal of Biomechanical Engineering 113 (4), 446–451.

Handels, H., Rob, T., Kreusch, J., Wolff, H. H., Poopl, S. J., 1999. A feature selection for optimized skin tumor recognition using genetic algorithms. Artificial Intelligence in Medicine 16, 283–297.

Hanke, H., Lenz, C., Finking, G., 2001. The discovery of the pathophysiological aspects of atherosclerosis - A review. Acta Chirurgica Belgica 101, 162–169.

Haussler, D., 1992. Decision theoretic generalizations of the PAC model for neural net and other learning applications. Information and computation 100 (1), 78–150.

Hayashi, K., Handa, H., Nagasawa, S., Okumura, A., Moritake, K., 1980. Stiffness and elastic behavior of human intracranial and extracranial arteries. Journal of Biomechanics 13 (2), 175–179.

Hayashi, K., Imai, Y., 1997. Tensile property of atheromatous plaque and an analysis of stress in atherosclerotic wall. Journal of Biomechanics 30, 573–579.

Hayashi, K., Mori, K., Miyazaki, H., 2003. Biomechanical response of femoral vein to chronic elevation of blood pressure in rabbits. American Journal of Physiology - Heart and Circulatory Physiology 284 (2), 511–518.

Hayashi, K., Washizu, T., Tsushima, N., Kiraly, R. J., Nose, Y., 1981. Mechanical properties of aortas and pulmonary arteries of calves implanted with cardiac prostheses. Journal of Biomechanics 14(3), 173–182.

Hayenga, H. N., Trache, A., Trzeciakowski, J., Humphrey, J. D., 2011. Regional atherosclerotic plaque properties in ApoE-/- mice quantified by atomic force, immunofluorescence, and light microscopy. Journal of Vascular Research 48 (6), 495–504.

Hebb, D. O., 1949. The organization of behaviour. New York. John Wiley & Sons.

Himburg, H. A., Friedman, M. H., 2006. Correspondence of low mean shear and high harmonic content in the porcine iliac arteries. ASME Journal of Biomechanical Engineering 128 (6), 852–856.

Himburg, H. A., Grzybowski, D. M., Hazel, A. L., LaMack, J. A., Li, X. M., Friedman, M. H., 2004. Spatial comparison between wall shear stress measures and porcine arterial endothelial permeability. American Journal of Physiology - Heart and Circulatory Physiology 286, 1916–1922.

Hirano, T., Takahashi, T., Saito, S., Tajima, H., Ebara, T., Adachi, M., 2001. Apoprotein C-III deficiency markedly stimulates triglyceride secretion *in vivo*: Comparison with apoprotein E. American Journal of Physiology - Endocrinology and Metabolism 281 (4), E665–E669.

Hodge, V., Austin, J., 2004. A survey of outlier detection methodologies. Artificial Intelligence Review 22 (2), 85–126.

Hofker, M. H., Van Vlijmen, B. J. M., Havekes, L. M., 1998. Transgenic mouse models to study the role of apoe in hyperlipidemia and atherosclerosis. Atherosclerosis 137, 1–11.

Holzapfel, G., Sommer, G., Auer, M., Regitnig, P., Ogden, R., 2007. Layer-specific 3D residual deformations of human aortas with non-atherosclerotic intimal thickening. Annals of Biomedical Engineering 35, 530–545.

Holzapfel, G. A., 2000. Nonlinear Solid Mechanics: A Continuum Approach for Engineering. John Wiley & Sons.

Holzapfel, G. A., 2006. Determination of material models for arterial walls from uniaxial extension tests and histological structure. Journal of Theoretical Biology 238 (2), 290–302.

Holzapfel, G. A., Gasser, C. T., Sommer, G., Regitnig, P., 2005b. Determination of the layer-specific mechanical properties of human coronary arteries with non-atherosclerotic intimal thickening, and related constitutive modelling. American Journal of Physiology - Heart and Circulatory Physiology 289, 2048–2058.

Holzapfel, G. A., Gasser, T. C., 2001. A viscoelastic model for fiber-reinforced composites at finite strains: Continuum basis, computational aspects and applications. Computer Methods in Applied Mechanics and Engineering 190 (34), 4379–4403.

Holzapfel, G. A., Gasser, T. C., Ogden, R. W., 2000. A new constitutive framework for arterial wall mechanics and a comparative study of material models. Journal of Elasticity 61, 1–48.

Holzapfel, G. A., Ogden, R. W., 2003. Biomechanics of soft tissue in cardiovascular systems. Springer Wien New York.

Holzapfel, G. A., Ogden, R. W., 2010. Modelling the layer-specific 3D residual stresses in arteries, with an application to the human aorta. Journal of the Royal society of Interface 7, 787–799.

Holzapfel, G. A., Sommer, G., Regitnig, P., 2004. Anisotropic mechanical properties of tissue components in human atherosclerotic plaques. ASME Journal of Biomechanical Engineering 126, 657–665.

Holzapfel, G. A., Stadler, M., Gasser, C. T., 2005a. Changes in the mechanical environment of stenotic arteries during interaction with stents: Computational assessment of parametric stent designs. ASME Journal of Biomechanical Engineering 127, 166–180.

Holzapfel, G. A., Stadler, M., Schulze-Bauer, C. A. J., 2002. A layer specific three-dimensional model for the simulation of balloon angioplasty using magnetic resonance imaging and mechanical testing. Annals of Biomedical Engineering 30, 753–767.

Holzapfel, G. A., Weizsäcker, H. W., 1998. Biomechanical behavior of the arterial wall and its numerical characterization. Computers in Biology and Medicine 28, 377–392.

Hong, J., Wei, L., Fu, C., Tan, W., 2008. Blood flow and macromolecular transport in complex blood vessels. Clinical Biomechanics 23, Supplement 1, 125–129.

Howarth, S., Li, Z. Y., Trivedi, R. A., U-King-Im, J. M., Graves, M. J., Kirkpatrick, P. J., Gillard, J. H., 2007. Correlation of macrophage location and plaque stress distribution using USPIO-enhanced MRI in a patient with symptomatic severe carotid stenosis: A new insight into risk stratification. British journal of Neurosurgery 21 (4), 396–398.

Howley, T., Madden, M. G., 2005. The genetic kernel support vector machine: Description and evaluation. Kluwer Academic Publishers. Printed in the Netherlands.

Hoyt Jr., R. E., Hawkins, J. V., St Clair, M. B., Kennett, M. J., 2007. The mouse in biomedical research (2nd Edition). Academic Press.

Hrapko, M., Van Dommelen, J. A., Peters, G. W., Wismans, J. S., 2008. The influence of test conditions on characterization of the mechanical properties of brain tissue. ASME Journal of Biomechanical Engineering 130 (3), 031003.

Huang, H., Virmani, R., Younis, H., Burke, A. P., Kamm, R. D., Lee, R. T., 2001. The impact of calcification on the biomechanical stability of atherosclerotic plaques. Circulation 103, 1051–1056.

Huang, M., Kecman, V., 2005. Gene extraction for cancer diagnosis by support vector machines. Artificial Intelligence in Medicine 35, 185–194.

Huang, Y., Guo, X., Kassab, G. S., 2006. Axial nonuniformity of geometric and mechanical properties of mouse aorta is increased during postnatal growth. American Journal of Physiology - Heart and Circulatory Physiology 290 (2), 657–664.

Huang, Y., Rumschitzki, D., Chien, S., Weinbaum, S., 1994. A fiber-matrix model for the growth of macromolecular leakage spots in the arterial intima. ASME Journal of Biomechanical Engineering 116, 430–445.

Huang, Z. J., Tarbell, J. M., 1997. Numerical simulation of mass transfer in porous media of blood vessel walls. American Journal of Physiology 273, 464–477.

Hume, D., 1748. An enquiry concerning human understanding. Oxford University Press, USA, New Edition edition (1999).

Humphrey, J. D., 2001. Stress, strain, and mechanotransduction in cells. ASME Journal of Biomechanical Engineering 123 (6), 638–641.

Humphrey, J. D., 2002b. Cardiovascular solid mechanics: Cells, tissues, and organs. Springer-Verlag.

Humphrey, J. D., Eberth, J. F., Dye, W. W., Gleason, R. L., 2009. Fundamental role of axial stress in compensatory adaptations by arteries. Journal of Biomechanics 42 (1), 1–8.

Humphrey, J. D., Na, S., 2002a. Elastodynamics and arterial wall stress. Annals of Biomedical Engineering 30 (4), 509–523.

Humphrey, J. D., Yin, F. C., 1987. A new constitutive formulation for characterizing the mechanical behavior of soft tissues. Biophysical Journal 53 (4), 564–570.

Huo, Y., Choy, J. S., Svendsen, M., Sinha, A. K., Kassab, G. S., 2009a. Effects of vessel compliance on flow pattern in porcine epicardial right coronary arterial tree. Journal of Biomechanics 42 (5), 594–602.

Huo, Y., Kassab, G., 2009b. Effects of vessel compliance and hematocrit on wall shear stress in a model of the entire coronary arterial tree. Journal of Applied Physiology 107, 500–505.

Huyghe, J. M., Arts, T., Campen, D. H. V., Reneman, R. S., 1992. Porous medium finite element model of the beating left ventricle. American Journal of Physiology 262, 1256–1267.

Huyghe, J. M., Schroder, Y., Baaijens, F. P. T., 2004. Bioengineering: The future of poromechanics. 17th ASCE Engineering Mechanics Conference, University of Delaware, Newark, DE.

Hyun, S., Kleinstreuer, C., Archie, J. P., 2000. Hemodynamics analyses of arterial expansions with implications to thrombosis and restenosis. Medical Engineering & Physics 22 (1), 13–27.

Ibragimov, A. I., McNeal, C. J., Ritter, L. R., Walton, J. R., 2006. A mathematical model of atherogenesis as an inflammatory response. Mathematical Medicine and Biology 22 (4), 305–333.

Ignatowski, A. C., 1908. Influence of animal food on the organism of rabbits. St. Petersburg Izvest Imp Voyenno-Med 16, 154–173.

Iliceto, S., Marangelli, V., Memmola, C., Rizzon, P., 1991. Transesophageal Doppler echocardiography evaluation of coronary blood flow velocity in baseline conditions and during dipyridamole-dipyridamole-induced coronary vasodilation. Circulation 83, 61–69.

Imoto, K., Hiro, T., Fujii, T., Murashige, A., Fukumoto, Y., Hashimoto, G., Okamura, T., Yamada, J., Mori, K., Matsuzaki, M., 2005. Longitudinal structural determinants of atherosclerotic plaque vulnerability: A computational analysis of stress distribution using vessel models and three-dimensional intravascular ultrasound imaging. Journal of the American College of Cardiology 46, 1507–1515.

Itchhaporia, D., Almassy, R., Kaufman, L., Snow, P., Oetgen, W., 1995. Artificial neural networks can predict significant coronary disease. Journal of the American College of Cardiology 25, 328.

Itchhaporia, D., Snow, P. B., Almassy, R. J., Oetgen, W. J., 1996. Artificial neural networks: Current status in cardiovascular medicine. Journal of the American College of Cardiology 28 (2), 515–521.

Iwaki, T., Yamashita, H., Hayakawa, T., 2001. A color atlas of sectional anatomy of the mouse. Adthree, Tokyo.

Jabbour, K., 1987. Automated load forecasting assistant. Proccedings of the IEEE Power Engineering Society Summer Meeting.

Jaroslav, V., Jiri, S., Dita, V., Karel, V., 1999. Residual strain in human atherosclerotic coronary arteries and age related geometrical changes. Bio-Medical Materials and Engineering 9, 311–317.

Jaroslav, V., Karel, V., Radomir, C., Svatava, K., Miroslav, S., Lukas, H., 2002. Age related constitutive laws and stress distribution in human main coronary arteries with reference to residual strain. Bio- Medical Materials and Engineering 12, 121–134.

Jawien, J., Nastalek, P., Korbut., R., 2004. Mouse models of experimental atherosclerosis. Journal of Physiology and Pharmacology 55 (3), 503–517.

Johnston, B. M., Johnston, P. R., Corney, S., Kilpatrick, D., 2004. Non-newtonian blood flow in human right coronary arteries: Steady state simulations. Journal of Biomechanics 37, 709–720.

Johnston, B. M., Johnston, P. R., Corney, S., Kilpatrick, D., 2006. Non-newtonian blood flow in human right coronary arteries: Transient simulations. Journal of Biomechanics 39 (6), 1116–1128.

Kaazempur-Mofrad, M. R., Isasi, A. G., Younis, H. F., Chan, R. C., Hinton, D. P., Sukhova, G., LaMuraglia, G. M., Lee, R. T., Kamm, R. D., 2004. Characterization of the atherosclerotic carotid bifurcation using MRI, finite element modeling, and histology. Annals of Biomedical Engineering 32 (7), 932–946.

Kalita, P., Schaefer, R., 2008. Mechanical models of artery walls. Archives of Computational Methods in Engineering 15 (1), 1–36.

Karner, G., Perktold, K., 2000. Effect of endothelial injury and increased blood pressure on albumin accumulation in the arterial wall: A numerical study. Journal of Biomechanics 33, 709–715.

Karner, G., Perktold, K., P., Z. H., 2001. Computational modeling of macromolecule transport in the arterial wall. Computer Methods in Biomechanics and Biomedical Engineering 4, 491–504.

Kasabov, N., Kozma, R., Kilgour, R., Laws, M., Taylor, J., Watts, M., Gray, A., 1999. A methodology for speech data analysis and a framework for adaptive speech recognition using fuzzy neural networks and self organising maps. Neuro-fuzzy Techniques for Intelligent Information Systems. Physica: Springer Verlag.

Katsuda, S., Waki, H., Yamasaki, M., Nagayama, T., O-Ishi, H., Katahira, K., Machida, N., Hasegawa, M., Shimizu, T., 2002. Postnatal changes in the rheological properties of the aorta in Sprague-Dawley rats. Experimental Animals 51 (1), 83–93.

Kedem, O., Katchalsky, A., 1958. Thermodynamic analysis of the permeability of biological membranes to non-electrolytes. Biochimica et Biophysica Acta 27, 229–246.

Khakpour, M., Vafai, K., 2008. Critical assessment of arterial transport models. International Journal of Heat and Mass Transfer 51, 807–822.

Khaled, A. R. A., Vafai, K., 2003. The role of porous media on modeling flow and heat transfer in biological tissues. International Journal of Heat and Mass Transfer 46, 4989–5003.

Khan, F. H., 2009. The elements of immunology. Pearson Education India.

King, V. L., Cassis, L. A., Daugherty, A., 2007. Interleukin-4 does not influence development of hypercholesterolemia or angiotensin. II-Induced atherosclerotic lesions in mice. American Journal of Pathology 171 (6), 2040–2047.

Kiousis, D. E., Gasser, T. C., Holzapfel, G. A., 2007. A numerical model to study the interaction of vascular stents with human atherosclerotic lesions. Annals of Biomedical Engineering 35 (11), 1857–1869.

Kiousis, D. E., Rubinigg, S. F., Auer, M., Holzapfel, G. A., 2009. A methodology to analyze changes in lipid core and calcification onto fibrous cap vulnerability: The human atherosclerotic carotid bifurcation as an illustratory example. ASME Journal of Biomechanical Engineering 131 (12), 121002.

Kips, J. G., Segers, P., Van Bortel, L. M., 2008. Identifying the vulnerable plaque: A review of invasive and non-invasive imaging modalities. Artery Research 2, 21–34.

Kock, S. A., Nygaard, J. V., Eldrup, N., Fründ, E.-T., Klaerke, A., Paaske, W. P., Falk, E., Kim, W. Y., 2008. Mechanical stresses in carotid plaques using MRI-based Fluid-Structure Interaction models. Journal of Biomechanics 41, 1651–1658.

Kohavi, R., 1995. A study of cross-validation and bootstrap for accuracy estimation and model selection. Proceedings of the Fourteenth International Joint Conference on Artificial Intelligence 1, 1137–1145.

Kolodner, J., 1993. Case-based reasoning. San Francisco. Morgan Kaufmann.

Kononenko, I., 2001. Machine learning for medical diagnosis: History, state of the art and perspective. Artificial Intelligence in Medicine 23 (1), 89–109.

Kotsiantis, S. B., 2007. Supervised machine learning: A review of classification techniques. IOS Press.

Koza, J., 1992. Genetic programming: On the programming of computers by means of natural selection. Cambridge, MA. MIT Press.

Krishna Kumar, R., Balakrishnan, K. R., 2005. Influence of lumen shape and vessel geometry on plaque stresses: Possible role in the increased vulnerability of a remodelled vessel and the shoulder of a plaque. Heart 91, 1459–1465.

Krishnamurthy, G., Ennis, D. B., Itoh, A., Bothe, W., Swanson-Birchill, J. C., Karlsson, M., Kuhl, E., Miller, D. C., Ingels, N. B., 2008. Material properties of the ovine mitral valve anterior leaflet *in vivo* from inverse finite element analysis. American Journal of Physiology - Heart and Circulatory Physiology 295, 1141–1149.

Krombach, F., Münzing, S., Allmeling, A. M., Gerlach, J. T., Behr, J., Dörger, M., 1997. Cell size of alveolar macrophages: An interspecies comparison. Environmental Health Perspectives 105, 1261–1263.

Krstic, R. V., 1997. Human microscopic anatomy: An atlas for students of medicine and biology. Springer-Verlag.

Kruth, H. S., Huang, W., Ishii, I., Zhang, W. Y., 2002. Macrophage foam cell formation with native low density lipoprotein. The Journal of Biological Chemistry 277 (37), 34573–34580.

Ku, D. N., 1997. Blood flow in arteries. Anna 29, 399–434.

Kumar, R. K., Balakrishnan, K. R., 2005. Influence of lumen shape and vessel geometry on plaque stresses: Possible role in the increased vulnerability to a remodeled vessel and the shoulder of a plaque. Heart 91 (11), 1459–1465.

Kyriacou, S. K., Schwab, C., Humphrey, J. D., 1996. Finite element analysis of nonlinear orthotropic hyperelastic membranes. Computational Mechanics 18, 269–278.

Landuyt, M., 2006. Structural quantification of collagen fibers in abdominal aortic aneurysms. Master's thesis. Royal Institute of Technology in Stockholm, Department of Solid Mechanics and Ghent University, Department of Civil Engineering.

Langley, P., Simon, H. A., 1995. Applications of machine learning and rule induction. Communications of the Association Computing Machinery 38 (11), 54–64.

Lanir, Y., 1979. A structural theory for the homogeneous biaxial stress-strain relationship in flat collageneous tissues. Journal of Biomechanics 12, 423–436.

Lanir, Y., Fung, Y. C., 1974a. Two-dimensional mechanical properties of rabbit skin-I. Experimental system. Journal of Biomechanics 7 (1), 29–34.

Lanir, Y., Fung, Y. C., 1974b. Two-dimensional mechanical properties of rabbit skin-II. Experimental results. Journal of Biomechanics 7 (2), 171–174.

Lantz, J., Karlsson, M., 2012. Large eddy simulation of LDL surface concentration in a subject specific human aorta. Journal of Biomechanics 45 (3), 537–542.

Lavrac, N., Keravnou, E., Zupan, B., 2000. Intelligent data analysis in medicine. Encyclopedia of Computer Science and Technology 9, 113–157.

Lawton, R. W., 1954. The thermoelastic behavior of isolated aortic strips of the dog. Circulation Research 2 (4), 344–353.

Le Cun, Y., Jackel, L. D., Boser, B., Denker, J. S., Graf, H. P., Guyon, I., Henderson, D., Howard, R. E., Hubbard, W., 1989. Handwritten digit recognition: Applications of neural network chips and automatic learning. Communications Magazine, IEEE 27, 41–46.

Lee, D., Chen, J. Y., 2000. Numerical simulation of flow fields in a tube with two branches. Journal of Biomechanics 33, 1305–1312.

Lee, R. T., 2000. Atherosclerotic lesion mechanisc versus biology. Zeitschrift fur Kardiologie 89, 80–84.

Lee, R. T., Grodzinsky, A. J., Frank, E. H., Kamm, R. D., Schoen, F. J., 1991. Structure-dependent dynamic mechanical behavior of fibrous caps from human atherosclerotic plaques. Circulation 83, 1764–1770.

Lee, R. T., Loree, H. M., Cheng, G. C., Lieberman, E. H., Jaramillo, N., Schoen, F. J., 1993. Computational structural analysis based on intravascular ultrasound imaging before *in vitro* angioplasty: Prediction of plaque fracture locations. Journal of the American College of Cardiology 21, 777–782.

Lee, R. T., Loree, H. M., Fishbein, M. C., 1994. High stress regions in saphenous vein bypass graft atherosclerotic lesions. Journal of the American College of Cardiology 24 (7), 1639–1644.

Lee, R. T., Schoen, F. J., Loree, H. M., Lark, M. W., Libby, P., 1996. Circumferential stress and matrix metalloproteinase 1 in human coronary atherosclerosis. Arteriosclerosis, Thrombosis, and Vascular Biology 16 (8), 1070–1073.

Lehoux, S., Tedgui, A., 2003. Cellular mechanics and gene expression in blood vessels. Journal of Biomechanics 36 (5), 631–643.

Lendon, C. L., Davies, M. J., Born, G. V. R., Richardson, P., 1991. Atherosclerotic plaque caps are locally weakened when macrophages density is increased. Atherosclerosis 87, 87–90.

Levesque, M. J., Liepsch, D., Moravec, S., Nerem, R. M., 1986. Correlation of endothelial-cell shape and wall shear-stress in a stenosed dog aorta. Arteriosclerosis 6, 220–229.

Li, M. X., Beech-Brandt, J. J., John, L. R., Hoskins, P. R., Easson, W. J., 2007a. Numerical analysis of pulsatile blood flow and vessel wall mechanics in different degrees of stenosis. Journal of Biomechanics 40 (16), 3715–3724.

Li, Z. Y., Howarth, S., Trivedi, R. A., U-King-Im, J. M., Graves, M. J., Brown, A., Wang, L., Gillard, J. H., 2006b. Stress analysis of carotid plaque rupture based on *in vivo* high resolution MRI. Journal of Biomechanics 39 (14), 2611–2622.

Li, Z. Y., Howarth, S. P. S., Tang, T., Gillard, J. H., 2006. How critical is fibrous cap thickness to carotid plaque stability? Stroke 37 (5), 1195–1199.

Li, Z. Y., Howarth, S. P. S., Tang, T., Graves, M. J., U-King-Im, J., Trivedi, R. A., Kirkpatrick, P. J., Gillard, J. H., 2007b. Structure analysis and magnetic resonance imaging predict plaque vulnerability: A study comparing symptomatic and asymptomatic individuals. Journal of vascular surgery 45 (4), 768–775.

Libby, P., Geng, Y. J., Aikawa, M., Schoenbeck, U., Mach, F., Cliton, S. K., Sukhova, G. K., Lee, R. T., 1996. Macrophages and atherosclerotic plaque stability, 7(5):330-335, 1996. Current opinion in Lipidology 7, 330–335.

Libby, P., Ridker, P. M., Hansson, G. K., 2011. Progress and challenges in translating the biology of atherosclerosis. Nature 473 (7347), 317–325.

Libby, P., Ridker, P. M., Maseri, A., 2002. Inflammation and atherosclerosis. Circulation 105, 1135–1143.

Liepsch, D., 2002. An introduction to biofluid mechanics-basic models and applications. Journal of Biomechanics 35, 415–435.

Lilliefors, H. W., 1967. On the kolmogorov-smirnov test for normality with mean and variance unknown. Journal of the American Statistical Association 62, 399–402.

Lin, D. H., Yin, F. C., 1998. A multiaxial constitutive law for mammalian left ventricular myocardium in steady-state barium contracture or tetanus. ASME Journal of Biomechanical Engineering 120, 504–517.

Lin, S. J., Jan, K. M., Chien, S., 1990. Role of dying endothelial cells in transendothelial macromolecular transport. Arteriosclerosis 10, 703–709.

Lin, S. J., Jan, K. M., Weinbaum, S., Chien, S., 1989. Transendothelial transport of low-density lipoprotein in association with cell mitosis in rat aorta. Arteriosclerosis 9, 230–236.

Lisboa, P. J., 2002. A review of evidence of health benefit from artificial neural networks in medical intervention. Neural Networks 15, 11–39.

Liu, H., Motoda, H., 2001. Instance selection and constructive data mining. Boston. Kluwer Academic Publishers.

Liu, Y. H., Chang, F., Lin, C. C., 2005. Language identification of character images using machine learning techniques. Document Analysis and Recognition, International Conference on 1, 630–634.

Lloyd-Jones, D., Adams, R., Carnethon, M., De Simone, G., Ferguson, T. B., Flegal, K., Ford, E., Furie, K., Go, A., Greenlund, K., Haase, N., Hailpern, S., Ho, M., Howard, V., Kissela, B., Kittner, S., Lackland, D., Lisabeth, L., Marelli, A., McDermott, M., Meigs, J., Mozaffarian, D., Nichol, G., O'Donnell, C., Roger, V., Rosamond, W., Sacco, R., Sorlie, P., Stafford, R., Steinberger, J., Thom, T., Wasserthiel-Smoller, S., Wong, N., Wylie-Rosett, J., Hong, Y., for the American Heart Association Statistics Committee, Subcommittee, S. S., 2009. Heart disease and stroke statistics–2009 update: A report from the american heart association statistics committee and stroke statistics subcommittee. Circulation 119, 21–181.

Long, Q., Xu, X. Y., Ariff, B., Thom, S. A., Hughes, A. D., Stanton, A. V., 2000. Reconstruction of blood flow patterns in a human carotid bifurcation: A combined CFD and MRI study. Journal of Magnetic Resonance Imaging 11, 299–311.

Long, Q., Xu, X. Y., Collins, M. W., Griffith, T. M., Bourne, M., 1997. Fluid dynamics of the aortic bifurcation using magnetic resonance imaging and computational fluid dynamics. Internal medicine (Clinical and Laboratory) 5, 35–42.

Long, Q., Xu, X. Y., Ramnarine, K. V., Hoskins, P., 2001. Numerical investigation of physiologically realistic pulsatile flow through arterial stenosis. Journal of Biomechanics 34, 1229–1242.

Loree, H. M., Grodzinsky, A. J., Park, S. Y., Gibson, L. J., Lee, R. T., 1994. Static circumferential tangential modulus of human atherosclerotic tissue. Journal of Biomechanics 27, 195–204.

Loree, H. M., Kamm, R. D., Atkinson, C. M., Lee, R. T., 1991. Turbulent pressure fluctuations on surface of model vascular stenosis. American Journal of Physiology - Heart and Circulatory Physiology 261, 644–650.

Loree, H. M., Kamm, R. D., Stringfellow, R. G., Lee, R. T., 1992. Effects of fibrous cap thickness on peak circumferential stress in model atherosclerotic vessels. Circulation Research 71, 850–858.

López, M., Martíinez, J., Matías, J. M., Taboada, J., Vilán, J. A., 2010a. Shape functional optimization with restrictions boosted with machine learning techniques. Journal of Computational and Applied Mathematics 234, 2609–2615.

López, M., Martínez, J., Matías, J. M., Taboada, J., Vilán, J. A., 2010b. Functional classification of ornamental stone using machine learning techniques. Journal of Computational and Applied Mathematics 234, 1338–1345.

Lusis, A. J., 2000. Atherosclerosis. Nature 407 (6801), 233–241.

Machii, M., Becker, A. E., 1997. Morphologic features of the normal aortic arch in neonates, infants, and children pertinent to growth. The Annals of Thoracic Surgery 64 (2), 511–515.

MacNeill, B. D., Lowe, H. C., Takano, M., Fuster, V., Jang, I. K., 2003. Intravascular modalities for detection of vulnerable plaque. Arteriosclerosis, Thrombosis, and Vascular Biology 23 (8), 1333–1342.

Maeda, N., Givens, R. C., Reddick, R. L., 2007a. The mouse in biomedical research (2nd Edition). Academic Press.

Maeda, N., Johnson, L., Kim, S., Hagaman, J., Friedman, M., Reddick, R., 2007b. Anatomical differences and atherosclerosis in apolipoprotein E-deficient mice with 129/SvEv and C57BL/6 genetic backgrounds. Atherosclerosis 195 (1), 75–82.

Maher, E., Creane, A., Sultan, S., Hynes, N., Lally, C., Kelly, D., 2009. Tensile and compressive properties of fresh human carotid atherosclerotic plaques. Journal of Biomechanics 42 (16), 2760–2767.

Maher, E., Creane, A., Sultan, S., Hynes, N., Lally, C., Kelly, D., 2011. Inelasticity of human carotid atherosclerotic plaque. Annals of Biomedical Engineering 39, 2445–2455.

Maldonado, N., Kelly-Arnold, A., Vengrenyuk, Y., Laudier, D., Fallon, J. T., Virmani, R., Cardoso, L., Weinbaum, S., 2012. A mechanistic analysis of the role of microcalcifications in atherosclerotic plaque stability: Potential implications for plaque rupture. American Journal of Physiology - Heart and Circulatory Physiology 303 (5), 619–628.

Malek, A. M., Alper, S. L., Izumo, S., 1999. Hemodynamic shear stress and its role in atherosclerosis. Journal of the American Medical Association 282 (1), 2035–2042.

Malvè, M., García, A., Ohayon, J., Martínez, M. A., 2012. Unsteady blood flow and mass transfer of a human left coronary artery bifurcation: FSI vs. CFD. International Communications in Heat and Mass Transfer 39 (6), 745–751.

Mandarino, W. A., Berceli, S. A., Sheppeck, R. A., Borovetz, H. S., 1992. Experimental determination of velocity profiles and wall shear rate along the rabbit aortoiliac bifurcation: Relationship to vessel wall low-density lipoprotein (LDL) metabolism. Journal of Biomechanics 25 (9), 985–993.

Marquardt, D. W., 1963. An algorithm for least-squares estimation of nonlinear parameters. SIAM Journal on Applied Mathematics 11, 431–441.

Marsden, J. E., Hughes, T. J. R., 1994. Mathematical Foundations of Elasticity. Dover, New York.

Martins, J. A. C., Pires, E. B., Salvado, R., Dinis, P. B., 1998. A numerical model of passive and active behavior of skeletal muscles. Computer Methods in Applied Mechanics and Engineering 151, 419–433.

Martínez, J., 2011. Clasificación Automática de Placas de Pizarra. Editorial Académica Española.

Mathers, C. D., Murray, C. J. L., 2006. Global burden of disease and risk factors, chapter the burden of disease and mortality by condition: Data, methods, and results for 2001. Oxford University Press , 45–240.

Matsumoto, T., Goto, T., Furukawa, T., Sato, M., 2004. Residual stress and strain in the lamellar unit of the porcine aorta: Experiment and analysis. Journal of Biomechanics 37 (6), 807–815.

Matsumoto, T., Hayashi, K., 1994. Mechanical and dimensional adaptation of rat aorta to hypertension. ASME Journal of Biomechanical Engineering 116, 279–283.

Matsumoto, T., Hayashi, K., 1996. Stress and strain distribution in hypertensive and normotensive rat aorta considering residual strain. ASME Journal of Biomechanical Engineering 118, 62–73.

Maurits, N. M., Loots, G. E., Veldman, A. E. P., 2007. The influence of vessel wall elasticity and peripheral resistance on the carotid artery flow waveform: a CFD model compared to *in vivo* ultrasound measurements. Journal of Biomechanics 40, 427–436.

McCord, B. N., Ku, D. N., 1993. Mechanical rupture of the atherosclerotic plaque fibrous cap. ASME 1993 Bioengineering Conference 24, 324–326.

McCulloch, W. S., Pitts, W. S., 1943. A logical calculus of the ideas inmanent in nervous activity. Bulletin of Mathematical Biophysics 5, 115–133.

Menzel, A., 2007. A fibre reorientation model for orthotropic multiplicative growth. Biomechanics And Modeling in Mechanobiology 6, 303–320.

Menzel, A., Steinmann, P., 2001. On the comparison of two strategies to formulate orthotropic hyperelasticity. Journal of Elasticity 62 (3), 171–201.

Menzel, A., Steinmann, P., 2003. A view on anisotropic finite hyper-elasticity. European Journal of Mechanics - A/Solids 22 (1), 71–87.

Mestas, J., Hughes, C. C., 2001. Of mice and not men: Differences between mouse and human immunology. The Journal of Immunology 172, 2731–2738.

Metha, J. L., Saldeen, T. G. P., Rand, K., 1998. Interactive role of infection, inflammation and traditional risk factors in atherosclerosis and coronary artery disease. The Journal of the American College of Cardiology 31, 1217–1225.

Meyer, D., Leisch, F., Hornik, K., 2003. The support vector machine under test. Neurocomputing 55 (1-2), 169–186.

Meyer, G., Merval, R., Tedgui, A., 1996. Effects of pressure-induced stretch and convection on low-density lipoprotein and albumin uptake in the rabbit aortic wall. Circulation Research 79, 532–540.

Michie, D., Spiegelhalter, D. J., Taylor, C. C., 1994. Machine learning, neural and statistical classification. Ellis Horwood.

Miller, K., 2001. How to test very soft biological tissues in extension? Journal of Biomechanics 34 (5), 651–657.

Milne-Thomson, L. M., 1958. Theoretical aerodynamics. London, Macmillan.

Milnor, W. R., 1989. Hemodynamics. 2nd Edition. Williams and Wilkins, Baltimore, MD.

Minsky, M., Papert, S., 1969. Perceptrons. Cambridge: MIT Press.

Mitchell, T., 1997. Machine learning. McGraw Hil.

Mizushige, K., Reisman, M., Buchbinder, M., Dittrich, H., DeMaria, A. N., 1993. Atheroma deformation during the cardiac cycle: Evaluation by intracoronary ultrasound. Circulation 88 - Supplement 1, 550.

Mooney, M., 1940. A theory of large elastic deformation. Journal of Applied Physics 11, 582–592.

Moore, J., Ethier, C., 1997. Oxygen mass transfer calculations in large arteries. ASME Journal of Biomechanical Engineering 119, 469–475.

Moreira, M., Fiesler., E., 1995. Neural networks with adaptive learning rate and momentum terms. Technical Report 95-04. Institut Dalle Morre D'Intelligence Artificielle Perceptive, Martigny, Valais, Switzerland.

Moreno, P. R., Flak, E., Palacios, I. F., Newell, J. B., Fuster, V., Fallon, J. T., 1994. Macrophage infiltration in acute coronary syndromes: Implication for plaque rupture. Circulation 90 (2), 775–778.

Moreno, P. R., Purushothaman, K. R., Fuster, V., O'Connor, W. N., 2002. Intimomedial interface damage and adventitial inflammation is increased beneath disrupted atherosclerosis in the aorta: Implications for plaque vulnerability. Circulation 105, 2504–2511.

Morlacchi, S., Chiastra, C., Gastaldi, D., Pennati, G., Dubini, G., Migliavacca, F., 2011. Sequential structural and fluid dynamic numerical simulations of a stented bifurcated coronary artery. ASME Journal of Biomechanical Engineering 133, 121010.

Mouse genome sequencing consortium, 2002. Initial sequencing and comparative analysis of the mouse genome. Nature 420, 520–562.

Naghavi, M., Falk, E., 2010. From vulnerable plaque to vulnerable patient. Contemporary Cardiology. Humana Press.

Naghavi, M., Libby, P., Falk, E., Casscells, S. W., Litovsky, S., Rumberger, J., Badimon, J. J., Stefanadis, C., Moreno, P., Pasterkamp, G., Fayad, Z., Stone, P. H., Waxman, S., Raggi, P., Madjid, M., Zarrabi, A., Burke, A., Yuan, C., Fitzgerald, P. J., Siscovick, D. S., de Korte, C. L., Aikawa, M., Juhani Airaksinen, K., Assmann, G., Becker, C. R., Chesebro, J. H., Farb, A., Galis, Z. S., Jackson, C., Jang, I.-K., Koenig, W., Lodder, R. A., March, K., Demirovic, J., Navab, M., Priori, S. G., Rekhter, M. D., Bahr, R., Grundy, S. M., Mehran, R., Colombo, A., Boerwinkle, E., Ballantyne, C., Insull, William, J., Schwartz, R. S., Vogel, R., Serruys, P. W., Hansson, G. K., Faxon, D. P., Kaul, S., Drexler, H., Greenland, P., Muller, J. E., Virmani, R., Ridker, P. M., Zipes, D. P., Shah, P. K., Willerson, J. T., 2003. From vulnerable plaque to vulnerable patient: A call for new definitions and risk assessment strategies: Part I. Circulation 108, 1664–1672.

Nakashima, Y., Plump, A. S., Raines, E. W., Breslow, J. L., Ross, R., 1994. ApoE-deficient mice develop lesions of all phases of atherosclerosis throughout the arterial tree. Arteriosclerosis, Thrombosis, and Vascular Biology 14 (1), 133–140.

National Institutes of Health, 2002. Detection, evaluation, and treatment of high blood cholesterol in adults. Third report of the National Cholesterol Education Program (NCEP). NIH Publication No. 02-5215 Expert Panel on.

Nemirovsky, D., 2003. Imaging of high-risk plaque. Cardiology 100 (4), 160–175.

Netter, F. H., 2010. Atlas of human anatomy. Elsevier Health Sciences.

Nguyen, T. D., Boyce, B. L., 2011. An inverse finite element method for determining the anisotropic properties of the cornea. Biomechanics and Modeling in Mechanobiology 10 (3), 323–337.

Nichols, W. W., O'Rourke., M. F., 1990. Mc donald's blood flow in arteries. 3rd edition., Philadelphia: Lea & Febiger.

Nilsson, J., 1986. Growth factors and the pathogenesis of atherosclerosis. Atherosclerosis 62 (3), 185–199.

Ogden, R. W., 1972. Large deformation isotropic elasticity I: On the correlation of theory and experiment for incompresible rubberlike solids. Proceedings of the Royal Society A: Mathematical, Physical and Engineering Sciences A326, 565–584.

Ogden, R. W., 2003. Nonlinear elasticity, anisotropy, material stability and residual stresses in soft tissues. Biomechanics of Soft Tissue in Cardiovascular Systems. CISM Courses and Lectures 441, 65–108.

Ogunrinade, O., Kameya, G. T., Truskey, G. A., 2002. Effect of fluid shear stress on the permeability of the arterial endothelium. Annals of Biomedical Engineering 30, 430–446.

Ohayon, J., Cai, H., Youk, P. S., Usson, Y., Azancot, A., 2002. A model of strutural and functional development of the normal human fetal left ventricle based on a global growth law. Computer Methods in Biomechanics and Biomedical Engineering 2, 113–126.

Ohayon, J., Dubreuil, O., Tracqui, P., Le Floc'h, S., Rioufol, G., Chalabreysse, L., Thivolet, F., Pettigrew, R. I., Finet, G., 2007. Influence of residual stress/strain on the biomechanical stability of vulnerable coronary plaques: Potential impact for evaluating the risk of plaque rupture. American Journal of Physiology - Heart and Circulatory Physiology 293, 1987–1996.

Ohayon, J., Finet, G., Gharib, A. M., Herzka, D. A., Tracqui, P., Heroux, J., Rioufol, G., Kotys, M. S., Elagha, A., Pettigrew, R. I., 2008. Necrotic core thickness and positive arterial remodeling index: Emergent biomechanical factors for evaluating the risk of plaque rupture. American Journal of Physiology - Heart and Circulatory Physiology 295, 717–727.

Ohayon, J., Finet, G., Treyve, F., Rioufol, G., Dubreuil., O., 2005. A three dimensional finite element analysis of stress distribution in a coronary atherosclerotic plaque: *In-vivo* prediction of plaque rupture location. Biomechanics Applied to Computer Assisted Surgery 17, 225–241.

Ohayon, J., Gharib, A. M., García, A., Heroux, J., Yazdani, S. K., Malvè, M., Tracqui, P., Martínez, M. A., Doblaré, M., Finet, G., Pettigrew, R. I., 2011. Is arterial wall-strain stiffening an additional process responsible for atherosclerosis in coronary bifurcations?: An *in vivo* study based on dynamic ct and mri. American Journal of Physiology - Heart and Circulatory Physiology 301, 1097–1106.

Ohayon, J., Mesnier, N., Broisat, A., Toczek, J., Riou, L., Tracqui, P., 2012. Elucidating atherosclerotic vulnerable plaque rupture by modeling cross substitution of ApoE-/- mouse and human plaque components stiffnesses. Biomechanics And Modeling in Mechanobiology 11, 801–813.

Ohayon, J., Teppaz, P., Finet, G., Rioufol, G., 2001. *In-vivo* prediction of human coronary plaque rupture location using intravascular and finite element method. Coronary Artery Disease 12, 655–663.

Olgac, U., Kurtcuoglu, V., Poulikakos, D., 2008. Computational modeling of coupled blood-wall mass transport of LDL: Effects of local wall shear stress. American Journal of Physiology - Heart and Circulatory Physiology 294 (2), 909–919.

Olgac, U., Poulikakos, D., Saur, S. C., Alkadhi, H., Kurtcuoglu, V., 2009. Patient-specific three-dimensional simulation of LDL accumulation in a human left coronary artery in its healthy and atherosclerotic states. American Journal of Physiology - Heart and Circulatory Physiology 296, 1969–1982.

Ougrinovskaia, A., Thompson, R., Myerscough, M., 2010. An ODE model of early stages of atherosclerosis: Mechanisms of the inflammatory response. Bulletin of Mathematical Biology 72, 1534–1561.

Oyen, M. L., 2011. Handbook of nanoindentation with biological applications. Pan Stanford Publishing Pte. Ltd. Singapore.

Ozolanta, I., Tetere, G., Purinya, B., Kasyanov, V., 1998. Changes in the mechanical properties, biochemical contents and wall structure of the human coronary arteries with age and sex. Medical Engineering & Physics 20 (7), 523–533.

Pandit, A., Lu, X., Wang, C., Kassab, G. S., 2005. Biaxial elastic material properties of porcine coronary media and adventitia. American Journal of Physiology - Heart 288, H2581–H2587.

Parker, D. B., 1985. Learning logic. Technical report TR-47. Center for computational research in economics and management science. MIT.

Pasterkamp, G., de Kleijn, D. P., Borst, C., 2000. Arterial remodeling in atherosclerosis, restenosis and after alteration of blood flow: Potential mechanisms and clinical implications. Cardiovascular Researcher 45, 843–852.

Patel, D. J., Janicki, J. S., Carew, T. E., 1969. Static anisotropic elastic properties of the aorta in living dogs. Circulation Research 25 (6), 765–779.

Peña, E.and Calvo, B., Martínez, M. A., Doblaré, M., 2007. An anisotropic visco-hyperelastic model for ligaments at finite strains: Formulation and computational aspects. International Journal of Solids and Structures 44, 760–778.

Peña, E., Alastrué, V., Laborda, A., Martínez, M. A., Doblare, M., 2010. A constitutive formulation of vascular tissue mechanics including viscoelasticity and softening behaviour. Journal of Biomechanics 43, 984–989.

Pedley, T. J., 1980. The fluid mechanics of large blood vessels. Cambridge University Press.

Perktold, K., Hofer, M., Rappitsch, G., Loew, M., Kuban, B. D., Friedman, M. H., 1997. Validated computation of physiologic flow in a realistic coronary artery branch. Journal of Biomechanics 31 (3), 217–228.

Perktold, K., Rappitsch, G., 1995. Mathematical modelling of local arterial flow and vessel mechanics. Computational methods for Fluid-Structure Interaction. Pitman Research Notes in Mathematics Series, Longman Science and Technology, Wiley, New York 1, 230–245.

Perktold, K., Resch, M., Florian, H., 1991. Pulsatile non-newtonian flow characteristics in a three-dimensional human carotid bifurcation model. ASME Journal of Biomechanical Engineering 113, 464–475.

Petersen, S., Peto, V., Rayner, M., Leal, J., Luengo-Fernandez, R., Gray, A., 2005. European cardiovascular disease statistics. Technical report. BHF: London.

Peterson, S. J., Okamoto, R. J., 2000. Effect of residual stress and heterogeneity on circumferential stress in the arterial wall. ASME Journal of Biomechanical Engineering 122, 454–456.

Petty, H. R., Smith, L. M., Fearont, D. T., McConnell, H. M., 1980. Lateral distribution and diffusion of the C3b receptor of complement, HLA antigens, and lipid probes in peripheral blood leukocytes. Proceedings of the National Academy of Sciences 77 (11), 6587–6591.

Platt, J. C., Christianini, N., Shave-Taylor, J., 2000. Large margin dags for multiclass classification. Advances in Neural Information Processing Systems 1, 547–443.

Plump, A. S., Smith, J. D., Hayek, T., Aalto-Setala, K., Walsh, A., Verstuyft, J. G., Rubin, E. M., Breslow, J. L., 1992. Severe hypercholesterolemia and atherosclerosis in apolipoprotein E-deficient mice created by homologous recombination in ES cells. Cell 71 (2), 343–353.

Poli, R., Cagnoni, S., Livi, R., Coppini, G., Valli, G., 1991. A neural network expert system for diagnosing and treating hypertension. Computer 3, 64–71.

Pollard, D., 1990. Empirical processes: Theory and applications. NSF-CBMS Regional conference series in probability and statitics. Institute of mathematical statistics - American statistical association.

Popper, K., 1934, 1959. The logic of scientific discovery. First English Ed., Hutchinson, First published as Logik Der Forschung in Vienna: Springer.

Preobrazhensky, S. N., Dolgov, V. V., Flegel, H. G., Repin, V. S., Smirnov, V. N., 1983. LDL uptake in rabbit arteries perfused in situ effect of HDL on intact and de-endothelialized vessels. Atherosclerosis 48 (2), 147–155.

Prosi, M., Zunino, P., Perktold, K., Quarteroni, A., 2005. Mathematical and numerical models for transfer of low-density lipoproteins through the arterial walls: A new methodology for the model set up with applications to the study of disturbed lumenal flow. Journal of Biomechanics 38, 903–917.

Puso, M. A., Weiss, J. A., 1998. Finite element implementation of anisotropic quasilinear viscoelasticity. ASME Journal of Biomechanical Engineering 120, 162–170.

Quarteroni, A., Tuveri, M., Veneziani, A., 2000. Computational vascular fluid dynamics: Problems, models, and methods. Computing and Visualization in Science 2, 163–197.

Quehenberger, O., 2005. Thematic review series: The immune system and atherogenesis. Molecular mechanisms regulating monocyte recruitment in atherosclerosis. The Journal of Lipid Research 46, 1582–1590.

Rabiner, L. R., 1989. A tutorial on hidden markov models and selected applications in speech recognition. Proceedings of the IEEE 77, 257–286.

Rachev, A., 1997. Theoretical study of the effect of stress-dependent remodeling on arterial geometry under hypertensive conditions. Journal of Biomechanics 30, 819–827.

Rachev, A., Greenwald, S. E., 2003. Residual strains in conduit arteries. Journal of Biomechanics 36 (5), 661–670.

Raggi, P., Callister, T. Q., Cooil, B., He, Z. X., Lippolis, N. J., Russo, D. J., Zelinger, A., Mahmarian, J. J., 2000. Identification of patients at increased risk of first unheralded acute myocardial infarction by electron-beam computed tomography. Circulation 101, 850–855.

Raghavan, M. L., Trivedi, S., Nagaraj, A., McPherson, D. D., Chandran, K. B., 2004. Three-dimensional finite element analysis of residual stress in arteries. Annals of Biomedical Engineering 32, 257–263.

Ramaswamy, S. D., Vigmostad, S. C., Wahle, A., Lai, Y. G., Olszewski, M. E., Braddy, K. C., Brennan, T. M. H., Rossen, J. D., Sonka, M., Chandran, K. B., 2004. Fluid dynamics analysis in a human anterior descending coronary artery with arterial motion. Annals of Biomedical Engineering 32, 1628–1641.

Rappitsch, G., Perktold, K., 1996. Pulsatile albumin transport in large arteries: A numerical simulation study. Journal of Biomechanics 118, 511–519.

Reddick, R. L., Zhang, S. H., Maeda, N., 1994. Atherosclerosis in mice lacking ApoE. Evaluation of lesional development and progression. Arteriosclerosis, Thrombosis, and Vascular Biology 14, 141–147.

Reinartz, T., 2002. A unifying view on instance selection. Data Mining and Knowledge Discovery 6, 191–210.

Reitman, J. S., Mahley, R. W., Fry, D. L., 1982. Yucatan miniature swine as a model for diet-induced atherosclerosis. Atherosclerosis 43 (1), 119–132.

Rhodin, J. A. G., 1980. Architecture of the vessel wall. Handbook of physiology. The cardiovascular system, volume 2. American Physiological Society, Bethesda, MD.

Rice, J. A., 2006. Mathematical statistics and data analysis. Duxbury Advanced.

Richardson, P. D., Davies, M. J., Born, G. V. R., 1989. Influence of plaque configuration and stress distribution on fissuring of coronary atherosclerotic plaques. The Lancet 334, 941–944.

Roach, M. R., Burton, A. C., 1957. The reason for the shape of the distensibility curves of arteries. Canadian Journal of Biochemistry and Physiology 35, 681–690.

Rodríguez, J., Goicolea, J. M., Gabaldón, F., 2007. A volumetric model for growth of arterial walls with arbitrary geometry and loads. Journal of Biomechanics 40 (5), 961–971.

Roger, V. L., Go, A. S., Lloyd-Jones, D. M., Adams, R. J., Berry, J. D., Brown, T. M., Carnethon, M. R., Dai, S., de Simone, G., Ford, E. S., Fox, C. S., Fullerton, H. J., Gillespie, C., Greenlund, K. J., Hailpern, S. M., Heit, J. A., Ho, P. M., Howard, V. J., Kissela, B. M., Kittner, S. J., Lackland, D. T., Lichtman, J. H., Lisabeth, L. D., Makuc, D. M., Marcus, G. M., Marelli, A., Matchar, D. B., McDermott, M. M., Meigs, J. B., Moy, C. S., Mozaffarian, D., Mussolino, M. E., Nichol, G., Paynter, N. P., Rosamond, W. D., Sorlie, P. D., Stafford, R. S., Turan, T. N., Turner, M. B., Wong, N. D., Wylie-Rosett, J., 2011. Heart disease and stroke statistics - 2011 Update. Circulation 123 (4), 18–209.

Roijers, R. B., Dutta, R. K., Cleutjens, J. P. M., Mutsaers, P. H. A., de Goeij, J. J. M., Van der Vusse, G. J., 2008. Early calcifications in human coronary arteries as determined with a proton microprobe. Analytical Chemistry 80, 55–61.

Rosenblatt, F., 1958. The perceptron: A probabilistic model for information storage and organization in the brain. Psychological Review 65, 386–408.

Rosenfeld, M. E., Tsukada, T., Chait, A., Bierman, E. L., Gown, A. M., Ross, R., 1987. Fatty streak expansion and maturation in watanabe heritable hyperlipemic and comparably hypercholesterolemic fat-fed rabbits. Arteriosclerosis, Thrombosis, and Vascular Biology 7 (1), 24–34.

Ross, M. H., Pawlina, W., 2010. Histology: A text and atlas. Churchill Livingstone.

Ross, R., 1986. The pathogenesis of atherosclerosis: An update. New England Journal of Medicine 314 (8), 488–500.

Ross, R., 1993. Atherosclerosis: a defense-mechanism gone. American Journal of Pathology 143, 987–1002.

Roy, C. S., 1881. The elastic properties of the arterial wall. The Journal of Physiology 3 (2), 125–159.

Roy, S., Silacci, P., Stergiopulos, N., 2005. Biomechanical proprieties of decellularized porcine common carotid arteries. American Journal of Physiology - Heart And Circulatory Physiology 289 (4), 1567–1576.

Rumelhart, D., Widrow, B., Lehr, M., 1994. The basic ideas in neural networks. Communications of the Association Computing Machinery 37, 87–92.

Rumelhart, D. E., Hinton, G. E., Williams, R. J., 1985. Learning internal representation by error propagation. ICS Report 8506. Institute for cognitive science. University of California at San Diego.

Sacks, M., 2000. Biaxial mechanical evaluation of planar biological materials. Journal of Elasticity 61, 199–246.

Saini, J., Berry, C., Greenwald, S., 1995. Effect of age and sex on residual stress in the aorta. Journal of Vascular Research 32, 398–405.

Salunke, N. V., Topoleski, L. D., Humphrey, J. D., Mergner, W. J., 2001. Compressive stress-relaxation of human atherosclerotic plaque. Journal of Biomedical Materials Research Part A 55, 236–241.

Santelices, L. C., Calano, S. J., Erhart, J. C., Prantil, R. L., Haney, J. L., Vorp, D. A., Ahearn, J. M., 2007. Experimental system for *ex vivo* measurement of murine aortic stiffness. Physiological Measurement 28 (8), 39–49.

Sastry, S., Bodson, M., 1989. Adaptive Control: Stability, convergence, and robustness. Prentice-Hall.

Scholkopf, B., Smola, A. J., Williamson, R. C., Bartlett, P. L., 2000. New support vector algorithms. Neural Computation 12, 1207–1245.

Scholkpof, B., Smola, A. J., 2002. Learning with kernels: Support vector machines, regularization, optimization, and beyond. MIT Press.

Schroeder, A. P., Falk, E., 1995. Vulnerable and dangerous coronary plaques. Atherosclerosis 118, Supplement, 141 – 149.

Schulze-Bauer, C. A. J., Mörth, C., Holzapfel, G. A., 2003. Passive biaxial mechanical response of agel human iliac arteries. ASME Journal of Biomechanical Engineering 125, 395–406.

Schulze-Bauer, C. A. J., Regitnig, P., Holzapfel, G. A., 2002. Mechanics of the human femoral adventitia including the high-pressure response. American Journal of Physiology - Heart and Circulatory Physiology 282 (6), 2427–2440.

Schwartz, C. J., Sprague, E. A., Kelley, J. L., Valente, A. J., Suenram, C. A., 1985. Aortic intimal monocyte recruitment in the normo and hypercholesterolemic baboon (*Papio Cynocephalus*). The European Journal of Pathology 405, 175–191.

Schwenke, D., Carew, T., 1989. Initiation of atherosclerotic lesions in cholesterol-fed rabbits, II: Selective retention of LDL vs. selective increases in LDL permeability in susceptible sites of arteries. Arteriosclerosis 9, 908–918.

Scotti, C. M., Finol, E. A., 2007. Compliant biomechanics of abdominal aortic aneurysms: A Fluid-Structure Interaction study. Computers and Structures 85, 1097–1113.

Sejnowski, T., Koch, C., Churchland, P., 1988. Computational neuroscience. Science 241, 1299–1306.

Seymour, G., 1993. Predictive Inference. New York, Chapman and Hall.

Sáez, P., Alastrué, V., Peña, E., M., D., Martínez, M. A., 2012. Anisotropic microsphere-based approach to damage in soft fibered tissue. Biomechanics and Modeling in Mechanobiology 11 (5), 595–608.

Shah, P., Falk, E., Badimon, J. J., Fernandez-Ortiz, A., Mailhac, A., Villareal-Levy, G., Fallon, J. T., Regnstrom, J., Fuster, V., 1995. Human monocyte-derived macrophages induce collagen breakdown in fibrous caps of atherosclerotic plaques: Potential role of matrix degrading metalloproteinases and implications for plaque rupture. Circulation 92 (6), 1565–1569.

Sheth, R. A., Maricevich, M., Mahmood, U., 2010. *In vivo* optical molecular imaging of matrix metalloproteinase activity in abdominal aortic aneurysms correlates with treatment effects on growth rate. Atherosclerosis 212, 181–187.

Silver, F. H., Snowhill, P. B., Foran, D. J., 2003. Mechanical behavior of vessel wall: A comparative study of aorta, vena cava, and carotid artery. Annals of Biomedical Engineering 31, 793–803.

Simon, B. R., Kaufmann, M. V., McAfee, M. A., Baldwin, A. L., 1998. Porohyperelastic finite element analysis of large arteries using Abaqus. ASME Journal of Biomechanical Engineering 120 (2), 296–298.

Singh, V., Tiwari, R. L., Dikshit, M., Barthwal, M. K., 2009. Models to study atherosclerosis: A mechanistic insight. Current Vascular Pharmacology 7 (1), 75–109.

Siogkas, P., Sakellarios, A., Exarchos, T. P., Athanasiou, L., Karvounis, E., Stefanou, K., Fotiou, E., Fotiadis, D. I., Naka, K. K., Michalis, L. K., Filipovic, N., Parodi, O., 2011. Multiscale-patient-specific artery and atherogenesis models. IEEE Transactions on Biomedical Engineering 58 (12), 3464–3468.

Sipahi, I., Tuzcu, E. M., Schoenhagen, P., Nicholls, S. J., Ozduran, V., Kapadia, S., Nissen, S. E., 2006. Compensatory enlargement of human coronary arteries during progression of atherosclerosis is unrelated to atheroma burden: Serial intravascular ultrasound observations from the reversal trial. European Heart Journal 27, 1664–1670.

Skalak, R., 1981. Growth as a finite displacement field. IUTAM Symposium on Finite Elasticity. Carlson, D. E., Shields, R. T.

Skalak, R., Dasgupta, G., Moss, M., Otten, E., Dullemeijer, P., Vilmann, H., 1982. Analytical description of growth. Journal of Theoretical Biology 94 (3), 555–577.

Slager, C. J., Wentzel, J. J., Gijsen, F. J., Schuurbiers, J. C., Van der Wal, A. C., Van der Steen, A. F., Serruys, P. W., 2005a. The role of shear stress in the generation of rupture-prone vulnerable plaques. Nature Clinical Practice Cardiovascular Medicine 2 (8), 401–407.

Slager, C. J., Wentzel, J. J., Gijsen, F. J., Thury, A., Van der Wal, A. C., Shaar, J. A., 2005b. The role of shear stress in the destabilization of vulnerable plaques and related therapeutic implications. Nature Clinical Practice Cardiovascular Medicine 9, 456–464.

Smedby, O., 1998. Geometrical risk factors for atherosclerosis in the femoral artery: A longitudinal angiographic study. Annals of Biomedical Engineering 26, 391–397.

Smith, D. D., Tan, X., Tawfik, O., Milne, G., Stechschulte, D. J., Dileepan, K. N., 2010. Increased aortic atherosclerotic plaque development in female apolipoprotein E-null mice is associated with elevated thromboxane A2 and decreased prostacyclin production. Journal of Physiology and Pharmacology 61 (3), 309–316.

Smith, J. D., Breslow, J. L., 1997. The emergence of mouse models of atherosclerosis and their relevance to clinical research. Journal of Internal Medicine 242 (2), 99–109.

Snelting-Havinga, I., Mommaas, M., Van Hinsbergh, V. W., Daha, M. R., Daems, W. T., Vermeer, B. J., 1989. Immunoelectron microscopic visualization of the transcytosis of low density lipoproteins in perfused rat arteries. European Journal of Cell Biology 48, 27–36.

Sobol, I. M., 2001. Global sensitivity indices for nonlinear mathematical models and their monte carlo estimates. Mathematics and Computers in Simulation 55, 271–280.

Sommer, G., Gasser, T. C., Regitnig, P., Auer, M., Holzapfel, G. A., 2008. Dissection properties of the human aortic media: An experimental study. ASME Journal of Biomechanical Engineering 130 (2), 021007.

Soulis, J., Fermakis, M., Giannoglou, G., Louridas, G., 2006. Wall shear stress in normal left coronary artery tree. Journal of Biomechanics 39, 742–749.

Spanish National Statistics Institute (INE), 2010. Report: Causes of death in Spain during 2009 and 2010.

Spencer, A. J. M., 1971. Theory of invariants. Continuum physics. Academic Press, New York , 239–253.

Stangeby, D., Ethier, C., 2002b. Computational analysis of coupled blood-wall arterial LDL transport. ASME Journal of Biomechanical Engineering 124, 1–8.

Stangeby, D. K., Ethier, C. R., 2002a. Coupled computational analysis of arterial ldl transport. Effects of hypertension. Computer Methods in Biomechanics and Biomedical Engineering 5, 233–241.

Stefano, D., Felice, R. F., Balbarini, A., 2009. Angiogenesis as risk factor for plaque vulnerability. Current Pharmaceutical Design 15 (10), 1095–1106.

Steinberg, D., Khoo, J. C., Glass, C. K., Palinski, W., Almazan, F., 1977. A new approach to determining the rates of recruitment of circulating leukocytes into tissues: Application to the measurement of leukocyte recruitment into atherosclerotic lesions. Proceedings of the National Academy of Sciences 94, 4040–4044.

Steinman, D. A., 2004. Image-based computational fluid dynamics: A new paradigm for monitoring hemodynamics and atherosclerosis. Current Drug Targets - Cardiovascular & Hematological Disorders 4 (2), 183–197.

Steinman, R., Cohn, Z. A., 1972. The interaction of soluble horseradish peroxidase with mouse peritoneal macrophages *in vitro*. The Journal of Cell Biology 55, 186–204.

Stergiopulos, N., Vulliémoz, S., Rachev, A., Meister, J. J., Greenwald, S. E., 2001. Assessing the homogeneity of the elastic properties and composition of the pig aortic media. Journal of Vascular Research 38 (3), 237–246.

Stone, M., 1974. Cross-validatory choice and assessment of statistical predictions. Journal of Royal Statistical Society Eries B 36, 111–147.

Stouffer, G., 2007. Cardiovascular hemodynamics for the clinician. Wiley-Blackwell.

Suciu, A., 1997. Effects of external forces on endothelial cells. PhD thesis. École Polytechnique Fédérale de Lausanne, Switzerland.

Sun, N., Wood, N. B., Hughes, A. D., Thom, S. A. M., Xu, X. Y., 2006. Fluid-wall modelling of mass transfer in an axisymmetric stenosis: Effects of sheardependent transport properties. Annals of Biomedical Engineering 34, 1119–1128.

Sun, W., Sacks, M. S., Scott, M. J., 2005. Effects of boundary conditions on the estimation of the planar biaxial mechanical properties of soft tissues. ASME Journal of Biomechanical Engineering 127 (4), 709–715.

Taber, L., Perucchio, R., 2000. Modeling heart development. Journal of Elasticity 61 (1), 165–197.

Taboada, J., Matías, J. M., Ordóñez, C., García, P. J., 2007. Creating a quality map of a slate deposit using support vector machines. Journal of Computational and Applied Mathematics 204, 84–94.

Tada, S., Tarbell, J. M., 2004. Internal elastic lamina affects the distribution of macromolecules in the arterial wall: A computational study. American Journal of Physiology 287, 905–913.

Takamizawa, K., Hayashi, K., 1987. Strain energy density function and uniform strain hypothesis for arterial mechanics. Journal of Biomechanics 20 (1), 7–17.

Takamizawa, K., Hayashi, K., 1988. Uniform strain hypothesis and thin-walled theory in arterial mechanics. Biorheology 25 (3), 555–565.

Tang, D., Teng, Z., Canton, G., Yang, C., Ferguson, M., Huang, X., Zheng, J., Woodard, P. K., Yuan, C., 2009. Sites of rupture in human atherosclerotic carotid plaques are associated with high structural stresses: An *in vivo* MRI-based 3D Fluid-Structure Interaction study. Stroke 40, 3258–3263.

Tang, D., Yang, C., Kobayashi, S., Ku, D. N., 2004. Effect of a lipid pool on stress/strain distributions in stenotic arteries: 3D Fluid-Structure Interactions (FSI) models. ASME Journal of Biomechanical Engineering 126, 363–370.

Tang, D., Yang, C., Kobayashi, S., Ku, N. D., 2002. Simulating cyclic artery compression using a 3D unsteady model with Fluid-Structure Interactions. Computers and Structures 80, 1651–1665.

Tang, D., Yang, C., Kobayashi, S., Zheng, J., P., V. R., 2003. Effect of stenosis asymmetry on blood flow and artery compression: A three dimensional Fluid- Structure Interaction model. Annals of Biomedical Engineering 31, 1182–1193.

Tang, D., Yang, C., Zheng, J., Woodard, P., Saffitz, J., Petruccelli, J., Sicard, G., Yuan, C., 2005a. Local maximal stress hypothesis and computational plaque vulnerability index for atherosclerotic plaque assessment. Annals of Biomedical Engineering 33, 1789–1801.

Tang, D., Yang, C., Zheng, J., Woodard, P. K., Saffitz, J. E., Sicard, G. A., Pilgram, T. K., Yuan, C., 2005b. Quantifying effects of plaque structure and material properties on stress distributions in human atherosclerotic plaques using 3D FSI models. ASME Journal of Biomechanical Engineering 127, 1185–1194.

Tang, T. Y., Howarth, S. P. S., Li, Z. Y., Miller, S. R., Graves, M. J., U-King-Im, J. M., Trivedi, R. A., Walsh, S. R., Brown, A. P., Kirkpatrick, P. J., Gaunt, M. E., Gillard, J. H., 2008. Correlation of carotid atheromatous plaque inflammation with biomechanical stress: Utility of USPIO enhanced MR imaging and finite element analysis. Atherosclerosis 196, 879–887.

Tarbell, J. M., 2003. Mass transport in arteries and the localization of atherosclerosis. Annual Review of Biomedical Engineering 5, 79–118.

Tarbell, J. M., Qiu, Y., 2000. The biomedical engineering handbook. CRC Press LLC. Editor: J.D. Bronzino.

Taylor, C., Humphrey, J., 2009. Open problems in computational vascular biomechanics: Hemodynamics and arterial wall mechanics. Computer Methods in Applied Mechanics and Engineering 198 (45), 3514–3523.

Tedgui, A., Lever, M. J., 1984. Filtration through damaged and undamaged rabbit thoracic aorta. American Journal of Physiology - Heart and Circulatory Physiology 247, 784–791.

Tezduyar, T., Sathe, S., Schwaab, M., Conklin, B., 2008. Arterial fluid mechanics modeling with the stabilized space-time Fluid-Structure Interaction technique. International Journal for Numerical Methods in Fluids 57, 601–629.

Thomas, K. R., Capecchi, M. R., 1987. Site-directed mutagenesis by gene targeting in mouse embryo-derived stem cells. Cell 51, 503–512.

Thubrikar, M. J., 2007. Vascular mechanics and pathology. Spinger Science.

Tompkins, R. G., Yarmush, M., J., S. J., K., C. C., A., S. K., B., S. M., 1989. Low-density lipoprotein transport in blood-vessel walls of squirrel-monkeys. American Journal of Physiology - Heart and Circulatory Physiology 257, 452–464.

Torii, R., Oshima, M., Kobayashi, T., Takagi, K., Tezduyar, T. E., 2006. Fluid-Structure Interaction modeling of aneurysmal conditions with high and normal blood pressures. Computational Mechanics 38, 482–490.

Torii, R., Oshima, M., Kobayashi, T., Takagi, K., Tezduyar, T. E., 2007. Influence of wall elasticity in patient-specific hemodynamic simulations. Computers and Fluids 36, 160–168.

Torii, R., Oshima, M., Kobayashi, T., Takagi, K., Tezduyar, T. E., 2010. Role of 0D peripheral vasculature model in Fluid-Structure Interaction modeling of aneurysms. Computational Mechanics 46, 43–52.

Torii, R., Wood, N., Hadjiloizou, N., Dowsey, A., Wright, A., Hughes, A., Davies, J., Francis, D., Mayet, J., Yang, G., McG, S., Thom, X. X., 2009. Fluid-Structure Interaction analysis of a patient-specific right coronary artery with physiological velocity and pressure waveforms. Communications in Numerical Methods in Engineering 55, 565–580.

Tracqui, P., Broisat, A., Toczek, J., Mesnier, N., Ohayon, J., Riou, L., 2011. Mapping elasticity moduli of atherosclerotic plaque *in situ* via atomic force microscopy. Journal of Structural Biology 174, 115–123.

Treloar, L. R. G., 1943a. The elasticity of a network of long-chain molecules - I. Transactions of the Faraday Society 39, 36–41.

Treloar, L. R. G., 1943b. The elasticity of a network of long-chain molecules - II. Transactions of the Faraday Society 39, 241–246.

Tricot, O., Mallat, Z., Heymes, C., Belmin, J., Lesèche, G., Tedgui, A., 2000. Relation between endothelial cell apoptosis and blood flow direction in human atherosclerotic plaques. Circulation 101 (21), 2450–2453.

Trivedi, R. A., U-king Im, J. M., Graves, M. J., Horsley, J., Goddard, M., Kirkpatrick, P. J., Gillard, J. H., 2004. MRI-derived measurements of fibrous-cap and lipid-core thickness: The potential for identifying vulnerable carotid plaques *in vivo*. Neuroradiology 46, 738–743.

Truesdell, C., Noll, W., 2004. The Non-Linear Field Theories of Mechanics. Springer-Verlag, 3rd edition.

Truskey, G. A., Roberts, W. L., Herrmann, R. A., A., M. R., 1992. Measurement of endothelial permeability to i-125 low-density lipoproteins in rabbit arteries by use of en face preparations. Circulation Research 71, 883–897.

Tu, J. V., 1996. Advantages and disadvantages of using artificial neural networks versus logistic regression for predicting medical outcomes. Journal of Clinical Epidemiology 49 (11), 1225–1231.

Vafai, K., Tien, C. L., 1981. Boundary and inertia effects on flow and heat transfer in porous media. International Journal of Heat and Mass Transfer 24, 195–203.

Vaishnav, R. N., Vossoughi, J., 1987. Residual-stress and strain in aortic segments. Journal of Biomechanics 20 (3), 235–239.

Vaishnav, R. N., Young, J. T., Patel, D. J., 1973. Distribution of stresses and of strain-energy density through the wall thickness in a canine aortic segment. Circulation Research 32 (5), 577–583.

Valanis, K. C., Landel, R. F., 1967. The strain-energy function of a hyperelastic material in terms of the extension ratios. Journal of Applied Physics 38, 2997–3002.

Valencia, A., Baeza, F., 2009. Numerical simulation of Fluid-Structure Interaction in stenotic arteries considering two layer nonlinear anisotropic structural model. International Communications in Heat and Mass Transfer 36, 137–142.

Valencia, A., Villanueva, M., 2006. Unsteady flow and mass transfer in models of stenotic arteries considering Fluid-Structure Interaction. International Communications in Heat and Mass Transfer 33, 966–975.

Valiant, L. G., 1984. A theory of the learn-able. Comunications of the ACM 27, 1134–1142.

Van Andel, C. J., Pistecky, P. V., Borst, C., 2003. Mechanical properties of porcine and human arteries: Implications for coronary anastomotic connectors. Annals of Thoracic Surgery 76 (1), 58–64.

Van der Giessen, A. G., Gijsen, F. J., Wentzel, J. J., Jairam, P. M., Van Walsum, T., Neefjes, L. A., Mollet, N. R., Niessen, W. J., Van de Vosse, F. N., de Feyter, P. J., Van der Steen, A. F., 2011. Small coronary calcifications are not detectable by 64-slice contrast enhanced computed tomography. International Journal of Cardiovascular Imaging 27 (1), 143–152.

Van der Wal, A. C., Becker, A. E., 1999. Atherosclerotic plaque rupture - Pathologic basis of plaque stability and instability. Cardiovascular Research 41, 334–344.

Van Ree, J. H., Van den Broek, W. J., Dahlmans, V. E. H., Groot, P. H. E., Vidgeon-Hart, M., Frants, R. R., Wieringa, B., Havekes, L. M., Hofker, M. H., 1994. Diet-induced hypercholesterolemia and atherosclerosis in heterozygous apolipoprotein E-deficient mice. Atherosclerosis 111 (1), 25–37.

Van Rossum, G., 2011. The Python language reference, release 3.2. Drake, Fred L. (editor).

Vande Geest, J. P., Sacks, M. S., Vorp, D. A., 2004. Age dependency of the biaxial biomechanical behavior of human abdominal aorta. ASME Journal of Biomechanical Engineering 126 (6), 815–822.

VanderLaan, P. A., Reardon, C. A., Getz, G. S., 2004. Site specificity of athero-sclerosis: site-selective responses to atherosclerotic modulators. Arteriosclerosis, Thrombosis, and Vascular Biology 24, 12–22.

VanEpps, J. S., Vorp, D. A., 2007. Mechanopathobiology of atherogenesis: A review. Journal of Surgical Research 142, 202–217.

Vanhecke, T. E., Miller, W. M., Franklin, B. A., Weber, J. E., McCullough, P. A., 2006. Awareness, knowledge, and perception of heart disease among adolescents. European Journal of Cardiovascular Prevention & Rehabilitation 13 (5), 718–723.

Vapnik, V., 1982. Estimation of dependences based on empirical data. Springer.

Vapnik, V., 1995. The Nature of Statistical Learning Theory. Springer-Verlag. New York.

Vapnik, V., 1998a. The support vector method of function estimation. Neural Networks and Machine Learning 1, 239–268.

Vapnik, V., Chervonenkis, A. Y., 1971. On the uniform convergence of relative frequencies of events to their probabilities. Theory of Probability and its Applications 16, 264–280.

Vapnik, V., Chervonenkis, A. Y., 1981. Necessary and sufficient conditions for the uniform convergence of means to their expectations. Theory of Probability and its Applications 26, 532–553.

Vapnik, V. N., 1998b. Statistical Learning Theory. John Wiley & Sons.

Vargas, C. B., Vargas, F. F., Pribyl, J. G., Blackshear, P. L., 1979. Hydraulic conductivity of the endothelial and outer layers of the rabbit aorta. American Journal of Physiology - Heart and Circulatory Physiology 236, 53–60.

Varnava, A. M., Davies, M. J., 2001. Relation between coronary artery remodelling (compensatory dilatation) and stenosis in human native coronary arteries. Heart 86, 207–211.

Varnava, A. M., Mills, P. G., Davies, M. J., 2002. Relationship between coronary artery remodeling and plaque vulnerability. Circulation 105, 939–943.

Vengrenyuk, Y., Carlier, S., Xanthos, S., Cardoso, L., Ganatos, P., Virmani, R., Einav, S., Gilchrist, L., Weinbaum, S., 2006. A hypothesis for vulnerable plaque rupture due to stress-induced debonding around cellular microcalcifications in thin fibrous caps. Proceedings of the National Academy of Sciences 103, 14678–14683.

Vengrenyuk, Y., Kaplan, T. J., Cardoso, L., Randolph, G. J., Weinbaum, S., 2010. Computational stress analysis of atherosclerotic plaques in ApoE knockout mice. Annals of Biomedical Engineering 38, 738–747.

Venter, J. C., Adams, M. D., Myers, E. W., Li, P. W., Mural, R. J., 2001. The sequence of the human genome. Science 291, 1304–1351.

Veress, A. I., Vince, D. G., Anderson, P. M., Cornhill, J. F., 2000. Vascular mechanics of the coronary artery. Zeitschrift Fur Kardiologie 89, Suplement 2, 92–100.

Versluis, A., Bank, A. J., Douglas, W. H., 2006. Fatigue and plaque rupture in myocardial infarction. Journal of Biomechanics 39, 339–347.

Vidyasagar, M., 1997. A theory of learning and generalization with applications to neural networks and control systems. Springer.

Virmani, R., Burke, A. P., Farb, A., Kolodgie, F. D., 2006. Pathology of the vulnerable plaque. Journal of the American College of Cardiology 47, 13–18.

Virmani, R., Burke, A. P., Kolodgie, F. D., Farb, A., 2003. Pathology of the thin-cap fibrouatheroma: A type of vulnerable plaque. Journal of Interventional Cardiology 16 (3), 267–272.

Virmani, R., Kolodgie, F. D., Burke, A. P., Farb, A., Schwartz, S. M., 2000. Lessons from sudden coronary death: A comprehensive morphological classification scheme for atherosclerotic lesions. Arteriosclerosis, Thrombosis, and Vascular Biology 20, 1262–1275.

Vito, R. P., Dixon, S. A., 2003. Blood vessel constitutive models: 1995-2002. Annual Review of Biomedical Engineering 5, 413–439.

Von Maltzahn, W. W., Besdo, D., Wiemer, W., 1981. Elastic properties of arteries: A nonlinear two-layer cylindrical model. Journal of Biomechanics 14 (6), 389–397.

Von Maltzahn, W. W., Warriyar, R. G., Keitzer, W. F., 1984. Experimental measurements of elastic properties of media and adventitia of bovine carotid arteries. Journal of Biomechanics 17 (11), 839–847.

Wada, S., Karino, T., 2000. Computational study on ldl transfer from flowing blood to arterial walls. Applications of Computational Mechanics to the Cardiovascular System 1, 157–173.

Wada, S., Koujiya, M., Karino, T., 2002. Theoretical study of the effect of local flow disturbances on the concentration of low-density lipoproteins at the luminal surface of end-to-end anastomosed vessels. Medical & Biological Engineering & Computing 40, 576–587.

Wagner, W. D., 1978. Risk factors in pigeons genetically selected for increased atherosclerosis susceptibility. Atherosclerosis 31 (4), 453–463.

Wang, C., García, M., Lu, X., Lanir, Y., Kassab, G. S., 2006. Three-dimensional mechanical properties of porcine coronary arteries: A validated two-layer model. American Journal of Physiology - Heart and Circulatory Physiology 291, 1200–1209.

Wang, H. H., 2001. Analytical models of atherosclerosis. Atherosclerosis 159, 1–7.

Wang, Y. X., Halks-Miller, M., Vergona, R., Sullivan, M. E., Fitch, R., Mallari, C., Martin-McNulty, B., da Cunha, V., Freay, A., Rubanyi, G. M., Kauser, K., 2000. Increased aortic stiffness assessed by pulse wave velocity in apolipoprotein E-deficient mice. American Journal of Physiology - Heart and Circulatory Physiology 278 (2), H428–H434.

Wasserman, L., 2005. All of nonparametric statistics. Springer.

Wehrens, R., Putter, H., Buydens, L., 2000. The bootstrap: A tutorial. Chemometrics and Intelligent Laboratory Systems 54, 35–52.

Weinbaum, S., Tzeghai, G., Ganatos, P., Pfeffer, R., S., C., 1985. Effect of cell turnover and leaky junctions on arterial macromolecular transport. American Journal of Physiology - Heart And Circulatory Physiology 248, 945–960.

Weiss, J. A., 1994. A constitutive model and finite element representation for transversely isotropic soft tissues. Ph.D. thesis, The University of Utah.

Weiss, J. A., Maker, B. N., Govindjee, S., 1996. Finite element implementation of incompressible, transversely isotropic hyperelasticity. Computer Methods in Applied Mechanics and Engineering 135, 107–128.

Weizsacker, H. W., Pinto, J. G., 1988. Isotropy and anisotropy of the arterial wall. Journal of Biomechanics 21 (6), 477–487.

Wells, S. M., Langille, B. L., Lee, J. M., Adamson, S. L., 1999. Determinants of mechanical properties in the developing ovine thoracic aorta. American Journal of Physiology - Heart and Circulatory Physiology 277 (4), H1385–H1391.

Wenk, J. F., 2011. Numerical modeling of stress in stenotic arteries with microcalcifications: A parameter sensitivity study. ASME Journal of Biomechanical Engineering 133, 014503.

Wenk, J. F., Papadopoulos, P., Zohdi, T. I., 2010. Numerical modeling of stress in stenotic arteries with microcalcifications: A micromechanical approximation. ASME Journal of Biomechanical Engineering 132 (9), 091011.

Werbos, P. J., 1974. Beyond regression: New tools for prediction and analysis in the behavioral sciences. PhD thesis, Harvard University.

Wessel, A., Sedmera, D., 2003. Developmental anatomy of the heart: A tale of mice and man. Physiological Genomics 15, 165–176.

Weydahl, E., Jr. Meister, J., 2001. Dynamic curvature strongly affects wall shear rates in a coronary artery bifurcation model. Journal of Biomechanics 34, 1189–1196.

Whitehall, B. L., Lu, S. C. Y., 1991. Machine learning in engineering automation: The present and the future. Computers in Industry 17, 91–100.

Widrow, B., Rumelhart, D. E., Lehr, M. A., 1994. Neural networks: Applications in industry, business, and science. Communications of the ACM. Communications of the Association Computing Machinery 37 (3), 93–105.

William Jr., I., 2009. The pathology of atherosclerosis: Plaque development and plaque responses to medical treatment. The American Journal of Medicine 122, Supplement 1, 3–14.

Williams, K., Tabas, I., 1995. The response-to-retention hypothesis of early atherogenesis. Arteriosclerosis, Thrombosis, and Vascular Biology 15, 551–561.

Williamson, S. D., Lam, Y., Younis, H. F., Huang, H., Patel, S., Kaazempur-Mofrad, M. R., Kamm, R. D., 2003. On the sensitivity of wall stresses in diseased arteries to variable material properties. ASME Journal of Biomechanical Engineering 125, 147–155.

Wolinsky, H., Glagov, S., 1964. Structural basis for the static mechanical properties of the aortic media. Circulation Research 14 (5), 400–413.

Wolinsky, H., Glagov, S., 1967. A lamellar unit of aortic medial structure and function in mammals. Circulation Research 20 (1), 99–111.

Wolpert, D. H., 1995. The relationship between PAC, the statistical physics framework, the Bayesian framework, and the VC framework. The Mathematics of Generalization. Addison-Wesley.

Wong, K., Thavornpattanapong, P., Cheung, S., Sun, Z., Tu, J., 2012. Effect of calcification on the mechanical stability of plaque based on a three-dimensional carotid bifurcation model. BMC Cardiovascular Disorders 12 (1), 7.

Wong, L. C. Y., Langille, B. L., 1996. Developmental remodeling of the internal elastic lamina of rabbit arteries: Effect of blood flow. Circulation Research 78 (5), 799–805.

World Health Organization. Regional Office for Europe, 2010. The european health report. Technical report. World Health Statistics (2008). World Health Organization.

World Health Organization. Regional Office for Europe, 2011. The european health report. Technical report. The 10 leading causes of death by broad income group (2008). World Health Organization.

Wu, H. C., Chen, S. Y. J., Shroff, S. G., Carroll, J. D., 2003. Stress analysis using anatomically realistic coronary tree. Medical Physics 30 (11), 2927–2936.

Yamagushi, T., Furuta, N., Nakayama, T., Kobayashi, T., 1996. Computations of the fluid and wall mechanical interactions in arterial diseases. ASME Journal of Biomechanical Engineering 31, 197–198.

Yamagushi, T., Kobayashi, T., Liu, H., 1998. Fluid-wall interactions in the collapse and ablation of an atheromatous plaque in coronary arteries. Procceding of the Third World Congress of Biomechanics, 1, 20.

Yang, N., Vafai, K., 2006. Modeling of low-density lipoprotein (LDL) transport in the artery. Effects of hypertension. International Journal of Heat and Mass Transfer 49, 850–867.

Yeoh, O. H., 1993. Some forms of the strain energy function for rubber. Rubber Chemistry and Technology 66, 754–771.

Younis, H. F., Kaazempur-Mofrad, M. R., Chan, R. C., Isasi, A. G., Hinton, D. P., Hinton, D. P., 2004. Hemodynamics and wall mechanics in human carotid bifurcation and its consequences for atherogenesis: Investigation of inter-individual variation. Biomechanics and Modeling in Mechanobiology 3 (1), 17–32.

Yu, L., Liu, H., 2004. Efficient feature selection via analysis of relevance and redundancy. Journal of Machine Learning Research 5, 1205–1224.

Yuan, F., Chien, S., Weinbaum, S., 1991. A new view of convective-diffusive transport processes in the arterial intima. ASME Journal of Biomechanical Engineering 113, 314–329.

Yuan, X. M., Brunk, U. T., Hazell, L., 2000. Atherosclerosis, gene expression, cell interactions and oxidation. Oxford University Press. Roger T. Dean, David T. Kell.

Zaragoza, C., Gómez-Guerrero, C., Martín-Ventura, J. L., Blanco-Colio, L., Lavin, B., Mallavia, B., Tarin, C., Mas, S., Ortíz, A., Egido, J., 2011. Animal models of cardiovascular diseases. Journal of Biomedicine and Biotechnology 3, 13–26.

Zarins, C. K., Giddens, D. P., Haradvaj, B. K. B., Sottiurai, V. S., Mabon, R. F., Glagov, S., 1983. Carotid bifurcation atherosclerosis. Quantitative correlation of plaque localization with flow velocity profiles and wall shear stress. Circulation Research 53, 502–514.

Zarins, C. K., Zatina, M. A., P., G. D., N., K. D., Glagov, S., 1987. Shear stress regulation of artery lumen diameter in experimental atherogenesis. Journal of Vascular Surgery 5, 413–420.

Zhang, S., Zhang, C., Yang, Q., 2002. Data preparation for data mining. Applied Artificial Intelligence 17, 375–381.

Zhang, S. H., Reddick, R. L., Piedrahita, J. A., Maeda, N., 1992. Spontaneous hypercholesterolemia and arterial lesions in mice lacking apolipoprotein E. Proceedings of the National Academy of Sciences 258 (5081), 468–471.

Zhao, B., Li, Y., Buono, C., Waldo, S. W., Jones, N. L., Mori, M., Kruth, H. S., 2006. Constitutive receptor-independent low density lipoprotein uptake and cholesterol accumulation by macrophages differentiated from human monocytes with macrophage-colony-stimulating factor (M-CSF). The Journal of Biological Chemistry 281 (23), 15757–15762.

Zhao, S. Z., Ariff, B., Long, Q., Hughes, A. D., Thom, S. A., Stanton, A. V., Xu, X. Y., 2002. Inter-individual variations in wall shear stress and mechanical stress distributions at the carotid artery bifurcation of healthy humans. Journal of Biomechanics 35 (10), 1367–1377.

Zheng, J., El Naqa, I., Rowold, F. E., Pilgram, T. K., Woodard, P. K., Saffitz, J. E., Tang, D., 2005. Quantitative assessment of coronary artery plaque vulnerability by high-resolution magnetic resonance imaging and computational biomechanics: A pilot study *ex vivo*. Magnetic Resonance in Medicine 54 (6), 1360–1368.

Zhou, J., Fung, Y. C., 1997. The degree of nonlinearity and anisotropy of blood vessel elasticity. Proceedings of the National Academy of Sciences 94, 14255–14260.

Zohdi, T. I., Holzapfel, G. A., Berger, S. A., 2004. A phenomenological model for atherosclerotic plaque growth and rupture. Journal of Theoretical Biology 227, 437 – 443.